Dissertation zur Erlangung des Doktorgrades

der Fakultät für Chemie und Pharmazie

der Ludwig-Maximilians-Universität München

Tethered Photopharmacology

Philipp Florian Willi Leippe

aus

Ulm, Deutschland

2018

Erklärung

Diese Dissertation wurde im Sinne von § 7 der Promotionsordnung vom 28. November 2011 von Herrn Prof. Dr. Dirk Trauner betreut.

Eidesstattliche Versicherung

Diese Dissertation wurde eigenständig und ohne unerlaubte Hilfe erarbeitet.

München, den 25. Mai 2018

Philipp Leippe

Dissertation eingereicht am:	29. Mai 2018
1. Gutachter:	Prof. Dr. Dirk Trauner
2. Gutachter:	Prof. Dr. Anja Hoffmann-Röder
Mündliche Prüfung am:	27. Juli 2018

Danksagung

Zunächst möchte ich meinem Doktorvater, Prof. Dr. Dirk Trauner, herzlich für die spannende Zeit in seinem Forschungslabor danken. Die *Trauner group* war und ist geprägt von wissenschaftlichem Können und Wissen auf höchstem Niveau, kombiniert mit unablässigem Forscherdrang und sucht ihresgleichen. Weiterhin möchte ich ihm für die Möglichkeit danken, für meine Forschungsarbeit auch andere Laboratorien in Lille und Heidelberg besuchen zu dürfen, als auch für die Möglichkeit, meine Forschung auf Konferenzen in Orten wie Harvard und Berlin präsentieren zu können.

Ein halbes Jahr meines Promotionsstudiums verbrachte ich in zwei Aufenthalten am Pasteur Institut in Lille, Frankreich. Dort arbeitete ich als Gast in den Laboratorien von Dr. Jérôme Vicogne und Dr. Colette Dissous. Ich möchte Jérôme und Colette für ihre sehr herzliche Aufnahme in Lille danken. Mein besonderer Dank gilt Jérôme, denn zu Beginn meiner Doktorarbeit war, als Absolvent eines Chemiestudiums mit Fokus auf organische Chemie, mein Wissen, was Biologie angeht, sehr limitiert. Jérôme hat mit viel Zeit und Geduld all meine ungeduldigen Fragen beantwortet und ich schätze mich glücklich, dass ich von seinem Wissen und seiner Kompetenz profitieren konnte.

Das letzte Jahr meines Promotionsstudiums verbrachte ich als Gast am Max-Planck-Institut für medizinische Forschung in Heidelberg. Ich möchte Prof. Dr. Kai Johnsson für seine großzügige Unterstützung danken, die es mir ermöglichte, in Heidelberg meine Doktorarbeit abzuschließen.

An dieser Stelle möchte ich Dr. Johannes Broichhagen für die Zusammenarbeit in München, Lausanne und Heidelberg als auch für seine Freundschaft herzlich danken. Des Weiteren möchte ich einige meiner längsten Labor-Freunde erwähnen; Mariia Palchyk, James Frank, Katharina Hüll und Tom Podewin, die das Labor zu einem Ort gemacht haben, an welchen man jeden Morgen gerne zurückkehrt. Vielen Dank auch für das Korrekturlesen an Helen Farrants und Johannes!

Zuallerletzt möchte ich meiner Familie für ihre immerwährende Unterstützung danken: Danke Mama Martina, Papa Matthias, Anna und Daria für eure liebevolle Art!

Corpora non agunt nisi fixata

PAUL EHRLICH, 1913

Publications

Sections of this work have been published in peer-reviewed journals:

(1) Broichhagen, J.; Damijonaitis, A.; Levitz, J.; Sokol, K. R.; **Leippe, P**.; Konrad, D.; Isacoff, E. Y.; Trauner, D. Orthogonal Optical Control of a G Protein-Coupled Receptor with a SNAP-Tethered Photochromic Ligand. *ACS Cent. Sci.* **2015**, *1* (7), 383–393.

(2) Levitz, J.; Broichhagen, J.; **Leippe, P**.; Konrad, D.; Trauner, D.; Isacoff, E. Y. Dual Optical Control and Mechanistic Insights into Photoswitchable Group II and III Metabotropic Glutamate Receptors. *Proc. Natl. Acad. Sci. U.S.A* **2017**, *114* (17), E3546-E3554.

(3) **Leippe, P.**; Koehler Leman, J.; Trauner, D. Specificity and Speed: Tethered Photopharmacology. *Biochemistry* **2017**, *56* (39), 5214–5220.

(4) Podewin, T.; Ast, J.; Broichhagen, J.; Fine, N.H.F., Nasteska, D.; **Leippe, P.;** Gailer, M., Buenaventura, T.; Kanda, N.; Jones, B.J., M'Kadmi, C.; Baneres, J.-L.; Marie, J.; Tomas, A., Trauner, D.; Hoffmann-Röder, A.; Hodson, D.J. Conditional and Reversible Activation of Class A and B G Protein-Coupled Receptors Using Tethered Pharmacology. *ACS Cent. Sci.* **2018**, *4* (2), 166–179.

Further publications in peer-reviewed journals include:

(5) Hartrampf, F. W. W.; Barber, D. M.; Gottschling, K.; **Leippe, P**.; Hollmann, M.; Trauner, D. Development of a Photoswitchable Antagonist of NMDA Receptors. *Tetrahedron* **2017**, *73* (33), 4905–4912.

(6) Westphal, M.; Schafroth, M. A.; Sarott, R.; Imhof, M.; Bold, C.; **Leippe, P.;** Dhopeshwarkar, A.; Grandner, J.; Katritch, V.; Mackie, K.; Trauner, D.; Carreira, E. M.; Frank, J. A. Synthesis of Photoswitchable Δ^9-Tetrahydrocannabinol Derivatives Enables Optical Control of Cannabinoid Receptor 1 Signaling. *J. Am. Chem. Soc.* **2017**.

Manuscripts in Preparation:

(7) **Leippe, P.**; Winter, N.; Sumser, M. P.; Trauner, D. Expanding the Toolbox of Photoswitchable Potassium Channel Blockers. *Submitted to ACS. Chem. Neurosci.*

(8) **Leippe, P.**; Broichhagen, J.; Maggio, K., Martoriati, A.; Morel, M.; Mougel, A.; Dissous, C.; Trauner, D.; Vicogne, J. Conversion of the Human Insulin Receptor into a Glutamate Receptor and a Photoreceptor

Project Affiliation Disclosure

In this statement, I proclaim that the findings in the following thesis are the results of an effort involving more individuals than myself. Not only have others significantly contributed to this work, but it was also influenced by many more people through discussions and an exchange of ideas. Alongside the supervision of Prof. Dr. Dirk Trauner, here I list, in no particular order, the individuals that significantly contributed to this work:

Chapter 1. Introduction to Tethered Photopharmacology

Dr. Julia Koehler Leman[1] (models of SNAP_mGluR2 and LihIR, as well as title art).

> [1]Center for Computational Biology, Flatiron Institute, Simons Foundation, 162 Fifth Avenue, New York, New York 10010, United States. Department of Biology and Center for Genomics and Systems Biology, New York University, New York, New York 10003, United States

Chapter 2. Optical Control of Receptor Tyrosine Kinases

Dr. Johannes Broichhagen[1], Dr. Katia Maggio[2], Dr. Alain Martoriati[2], Dr. Marion Morel[3], Alexandre Mougel[4], Dr. Colette Dissous[3], Dr. Jérôme Vicogne[4], Chiara Zambarda[1], Dr. Ada Cavalcanti-Adam[1].

> [1]Max Planck Institute for Medical Research, Jahnstr. 29, 69120 Heidelberg. [2]EA 4479, IFR 147, Université Lille 1 Sciences et Technologies, Villeneuve d'Ascq, France. [3]Center for Infection and Immunity of Lille, Inserm U1019, CNRS-UMR 8204, University Lille Nord de France, Institut Pasteur de Lille, Lille, France, 2EA. [4]UMR CNRS 8161 CNRS, Université de Lille, Institut Pasteur de Lille, 1 rue du Pr Calmette, 59021 Lille Cedex, France.

Chapter 3. Optical Control of Potassium Channels

Dr. Nils Winter[1] (synthesis), Dr. Cameron Lee[2] (antibody modifications).

> [1]Department of Chemistry and Center for Integrated Protein Science Munich, Ludwig-Maximilians-Universität München, Butenandtstrasse 5-13, 81377 Munich, Germany. [2]Novartis Institutes for BioMedical Research (NIBR), Boston, MA.

Chapter 4. Tethered Photopharmacology of the AMPA Receptor

Dr. Prashant Donthamsetti[1] (patch clamp), Dr. Ehud Isacoff[1,2,3].

> [1]Department of Molecular and Cell Biology, University of California,Berkeley, CA 94720. [2]Helen Wills Neuroscience Institute, University of California, Berkeley, CA 94720. [3]Bioscience Division, Lawrence Berkeley National Laboratory, Berkeley, CA 94720.

Chapter 5. Tethered Photopharmacology of the μ-Opioid Receptor

Nil Patel[1] and Seva Katrich[1] (molecular docking), Mariia Palchyk (technician), Niklas Bargenda (intern), Dr. Ahmed Ali[2] (AM-II), Manuel Gailer[2] (AzoDAMGO).

> [1]Department of Biological Sciences, Bridge Institute, University of Southern California, Los Angeles, CA 90089, USA. [2]Department of Chemistry and Center for Integrated Protein Science Munich, Ludwig-Maximilians-Universität München, Butenandtstrasse 5-13, 81377 Munich, Germany.

Chapter 6. Optical Control of the Smoothened Receptor

Alexander Gisnapp (intern), Johannes Morstein[1].

> [1]Department of Chemistry and Center for Integrated Protein Science Munich, Ludwig-Maximilians-Universität München, Butenandtstrasse 5-13, 81377 Munich, Germany.

Chapter 7. Photoswitchable Receptor Tyrosine Kinase Inhibitors

Simon Dresbach (intern).

Chapter 8. Further Synthesis and Biology

Lukas Brunner (intern).

Summary

Light as a trigger is ideal to perturb biological function due to its high spatial and temporal precision. This is evidenced by the ever-expanding arsenal of genetically-encoded optical tools available to scientists today. These tools are summarized by the umbrella term ‘optogenetics’ and have had an especially transformative impact on neuroscience, since light is able to match the high speed and precision of neuronal processes. Alternatively, ‘photopharmacology’ can be employed which describes the use of photoswitchable drugs acting on non-genetically modified targets to enable their optical control. As an extension of pharmacology, it offers the same advantages, such as acute onset and facile translatability from bench to bedside, but also suffers from some of pharmacology’s disadvantages, primarily from its lack of target selectivity. While this lack of selectivity is often regarded as an issue of ‘selectivity for one target over another’, side-effects also arise from a drugs’ action on the desired target but at the wrong site, *i.e.* the wrong cell or organ. While much effort in drug development is directed at identifying more and more selective drugs, many effective drugs that are widely prescribed have an extensive polypharmacology which we are only beginning to understand. This double-edged sword of polypharmacology may offer huge untapped potential, as long as its effects can be limited to a certain area. One possibility to spatially confine a drugs’ effect lies in the combination with genetic methods that allow for precise targeting to specific populations of cells. To this end, an anchoring-site can be genetically introduced into the cell of interest and subsequently be provided with function by labeling it with a drug, an approach that is described as ‘tethered pharmacology’. The photoswitchable variant thereof, ‘tethered photopharmacology’, provides reversibility as well as an additional layer of temporal control.

In this thesis, I will give a general introduction to the concept of tethered photopharmacology (chapter **1**). Then, I will describe an approach that employs tethered photoswitches to render chimeric receptor tyrosine kinases light-sensitive (chapter **2**). Next, I introduce an improved series of photoswitchable K$^+$ channel blockers and elaborate on antibody-photoswitch conjugates that target K$^+$ channels (chapter **3**). I will then describe the design of a tethered photoswitch for the wild-type AMPA receptor, and show its preliminary biological characterization (chapter **4**). Approaches towards expanding tethered photopharmacology to the μ-opioid receptor are described in chapter **5**. The synthesis of a freely-diffusible photoswitch for the smoothened receptor is presented in chapter **6**. In chapter **7**, the synthesis of photoswitchable kinase inhibitors is described. Lastly, chapter **8** summarizes miscellaneous work on various biological targets. In summary, I will demonstrate how the combination of synthetic chemistry with genetic engineering can afford new tools for elucidating biological questions, and outline future directions that tethered photopharmacology could take.

Chapters

Table of contents

1 Introduction to Tethered Photopharmacology

Pharmacology is concerned with the use, effects and mode of action of drugs. Traditionally, many drugs are small molecules (SM) that interact with a target protein and elicit a desired effect (Figure 1a). Such a drug can be chemically functionalized with a photoswitch (Figure 1b) to render it light-sensitive (Figure 1c). Upon illumination, these so-called photochromic ligands (PCLs) change their efficacy and/or affinity towards their biological target, which is a protein in most cases. Consequently, depending on the nature of the drug, the protein target can be activated, inhibited or modulated in a light-dependent fashion; or in other words, the target can be turned 'ON' or 'OFF'. Light is a powerful trigger since it offers unmatched spatiotemporal precision. This approach represents an extension of pharmacology and is appropriately termed *Photopharmacology*.[1] PCLs operate on wild-type proteins and have been created for a wide range of diverse targets, including ligand-gated ion channels (such as AMPA,[2,3] NMDA[4]), G protein-coupled receptors (GPCRs, such as μ-Opioid[5]), voltage-gated Na^+ and K^+ channels[6,7] and receptor-linked enzymes (such as the ANP receptor[8]).

Commonly used photoswitches are azobenzenes (Figure 1b), as they isomerize upon illumination with light (~320–350 nm) from their thermodynamically-favored, elongated *trans*-configuration to the bent *cis*-configuration. This isomerization is accompanied by a large change in geometry and in distance of the 4- and 4'-position (~13 Å to ~8 Å).[9] In addition, there is a large increase in polarity. The *cis*-isomer can isomerize back to the *trans*-isomer under thermal conditions with a half-life of milliseconds to days. This feature, as well as the switching wavelength, can be readily tuned by choosing the substitution pattern of the azobenzene.[10] For instance, azobenzene can also isomerize from *trans-* to *cis-* by illumination with light of longer wavelengths (~400–450 nm), when the electron density is increased by appropriate substitutions. Therefore, by using light of two different wavelengths, the switch can reversibly be toggled between its *trans*- and *cis*-configuration.

Another strategy to render proteins light-sensitive is by using a photoswitchable tethered ligand (PTL, Figure 1d and Figure 2a). Here, a cysteine-mutation is introduced to the target protein and covalently conjugated to a PTL molecule that incorporates a maleimide handle. In PTLs, the tether and photoswitch are not necessarily part of the pharmacophore, *i.e.* do not necessarily interact with the protein, and the *cis-trans* isomerization serves to position the ligand in or out of its binding pocket. Consequently, the cysteine mutation has to be carefully screened to identify a suitable mutation site and the position on the protein of interest (POI) has a large impact on the PTLs activity. Indeed, the site of mutation might even dictate whether the PTL acts as an agonist or as an antagonist.[11–13] The attachment site, along with length and geometry of the tether between maleimide and photoswitch, therefore determines the biological effect. The PTL approach is the first example of *Tethered Photopharmacology* and has successfully been applied to a variety of proteins such as K^+ channels (K_V,[14] TREK-1,[15] HyLighter[16]), ionotropic glutamate receptor (kainate[17] and NMDA[12]), metabotropic glutamate receptors,[11] pentameric ligand-gated ion channels (nAChR[18]) and trimeric ligand-gated ion channels (P2X[19]).

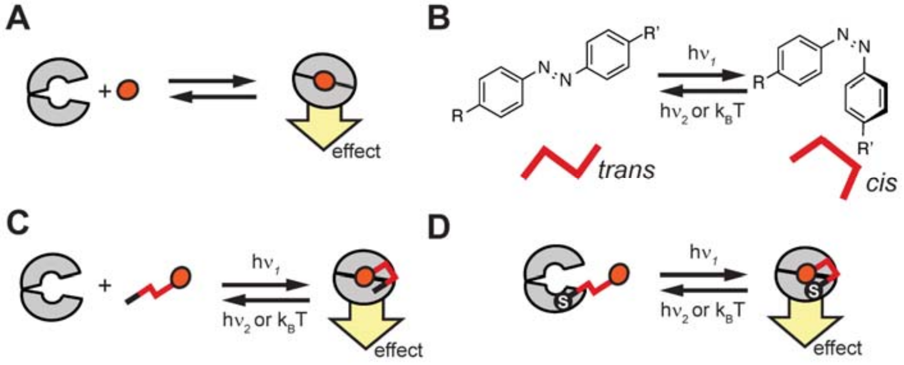

Figure 1. **Photopharmacology: controlling biological function with light. a)** A ligand (orange) interacts with a protein (grey), resulting in a biological effect. **b)** The photochromic ligand (PCL) concept. **c)** Photoisomerization of azobenzene upon illumination with different wavelengths of light ($h\nu_1$ and $h\nu_2$). **d)** The photoswitchable tethered ligand (PTL) concept.

Because of their genetically-encoded specificity and high spatiotemporal control, PTLs have found several applications for the optical control of biological systems, ranging from *in vitro* to *in vivo*.[20–22] In a notable example, PTLs could identify the role of Kolmer-Agduhr neurons in the spinal cord of freely moving zebrafish larvae.[22] To this end, the light-gated ionotropic ligand channel LiGluR was expressed in these neurons *via* transgenic zebrafish lines and then labelled with the PTL 'MAG1'. After stimulation by light, the larval fish showed 'spontaneous swim behavior', identifying a positive drive of Kolmer-Agduhr neurons to the underlying 'central pattern generator' neuronal network.

Despite many reported studies, a major drawback of these early examples of tethered photopharmacology lies in their reliance on cysteine-maleimide bioconjugation. *Prima facie*, the introduction of a unique cysteine is a relatively small change to the protein and is unlikely to affect its expression, trafficking and function. Nevertheless, cysteines introduce a considerable amount of free energy to the protein and the free thiol or thiolate can undergo redox reactions, especially when surface exposed, and may disrupt the pattern of disulfide bonds required for proper protein folding.[23] In addition, the requisite maleimide chemistry is less-than-ideal as maleimides undergo hydrolysis at physiological pH to form maleamic acid which in turn is unreactive towards sulfhydryls.[24] Lastly, the design of PTLs is complicated by the required mutational cysteine-screen to identify suitable conjugation sites.[25] As an alternative to cysteine-mutation, Chin and coworkers introduced unnatural amino acids to the MAPK Kinase MEK1 by Amber codon suppression (Figure 2d).[26] Here, the unnatural amino acid contains a strained alkene/alkyne in its side chain and is conjugated to a PTL termed photo-BOLT *via* bioorthogonal tetrazine click chemistry.[27] While this approach is attractive and allowed for the optical control over the MAPK signaling cascade, Amber codon suppression is technically challenging and photo-BOLT has not yet been applied to receptors or ion channels.

To overcome these limitations and to make tethered photopharmacology more applicable to *in vivo* experiments, we introduced photoswitchable orthogonal-remotely tethered ligands (PORTLs) for the metabotropic glutamate receptor 2 (mGluR2) in 2015.[28] The PORTL is composed of three parts: (i) photoswitchable ligand, (ii) a long and flexible linker and (iii) a bioconjugation motif. For bioconjugation, PORTLs rely on self-labeling protein tags, such as the SNAP-tag. The SNAP-tag is a ~20 kDa mutant of the DNA-repair protein *O*^{6}-alkylguanine-DNA alkyltransferase that reacts specifically and rapidly (rate constant ~10^5 - 10^6 M^{-1} s^{-1})[29] with *O*^{6}-alkylated benzyl guanine (BG) derivatives in a single turn-over reaction (Figure 2b).[30] The SNAP-tag is cloned to the POI, usually as an *N*- or *C*-terminal fusion protein; but, if required, a circularly permutated SNAP-tag can also be introduced into flexible loops. SNAP-fusions are well tolerated by many transmembrane proteins, are usually used for fluorophore labelling, and a wealth of SNAP-tagged receptors are commercially available, which can be readily repurposed for PORTLs.[31] Benzyl guanines are essentially inert in aqueous buffers to regular cysteines or other nucleophiles that are present under physiological conditions. The SNAP-receptor gains light-sensitivity only after covalent attachment of the PORTL (Figure 2c). Since the PORTL attachment site is remote, the self-labeling protein tag can also be attached to a protein in vicinity of the protein target. In the case of a transmembrane protein, the tag can be localized to the cell membrane by fusion with a membrane anchor and laterally act on the endogenously expressed target receptor. This was described very recently for the AMPA and muscarinic acetylcholine (mACh) receptors by Tadross and coworkers (Figure 2e) in an approach termed ‘drugs acutely-restricted by tethering’ (DART).[32] The anchored self-labeling protein tag was labelled with a non-photoswitchable, tethered antagonist, which then acted remotely on wild-type AMPA receptors. Clearly, the same strategy readily applies to PORTLs. We term these molecules acting from a separate, close-by protein on an endogenous receptor ‘*para*-PORTL’ (*para* from the Greek word for beside, next to, near; Figure 2f).

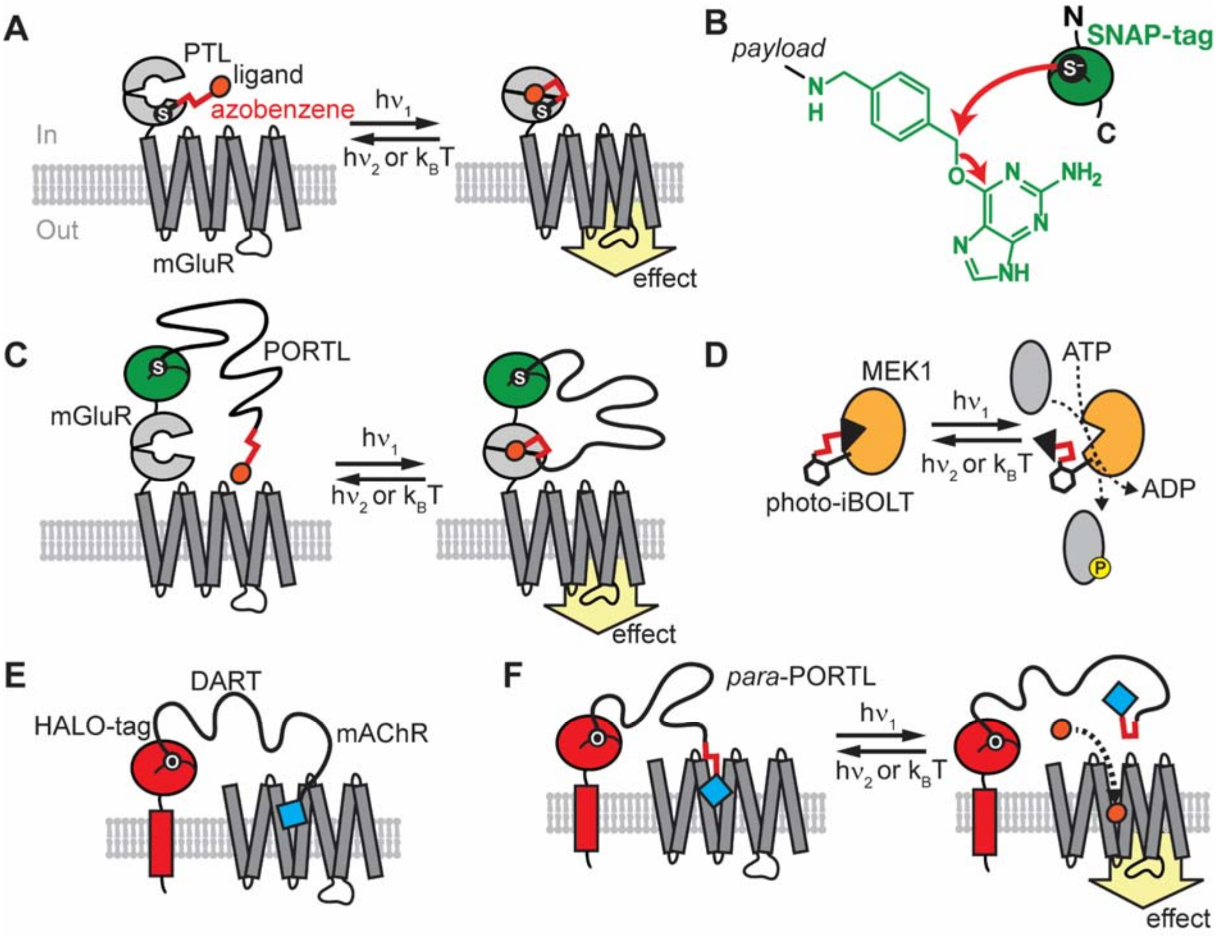

Figure 2. **Tethered Photopharmacology: from photoswitchable tethered ligands to photoswitchable orthogonal remotely-tethered ligands. a)** The photoswitchable tethered ligand (PTL) approach relies on a cysteine mutation which is conjugated to a photoswitch *via* cysteine-maleimide chemistry. **b)** In the photoswitchable orthogonal remotely-tethered ligand (PORTL) approach, a self-labeling protein tag (*e.g.* SNAP-tag) is employed as bioconjugation method. The SNAP-tag reacts specifically with benzyl guanine-functionalized payloads. Guanine is released in this reaction and the payload is covalently and permanently attached to the SNAP-tag. **c)** In the PORTL strategy, the SNAP-tag is genetically introduced as a fusion to the metabotropic glutamate receptor. The light-sensitivity is only gained after labelling with the PORTL and upon illumination with light of different wavelengths the receptor can be turned ON and OFF in a reversible fashion. **d)** The photo-BOLT system by Chin and coworkers.[26] Photo-BOLT relies on a photoswitchable inhibitor which is bolted the MAPK Kinase to MEK1 *via* a bioorthogonal 'Click' reaction with an unnatural amino acid. **e)** The approach by Tadross and coworkers where a self-labeling Halo-tag fused to a membrane anchor was expressed and labelled it with a 'drug-acutely restricted by tethering' (DART).[32] The DART then acts inhibitory and remotely on endogenous receptors present on the cell membrane. This approach was demonstrated for the ligand-ion channel AMPA and extended to the muscarinic acetylcholine receptor (mAChR). **f)** A combination of DART and PORTL gives rise to the *para*-PORTL, allowing the PORTL approach to be extended to endogenous receptors.

PORTL was pioneered on the mGlu receptors. These belong to the Class C subgroup of the GPCR superfamily and are widely, but not exclusively, expressed in neurons. mGluRs feature a large extracellular ligand binding domain (LBD) that binds the excitatory neurotransmitter glutamate.[33] Glutamate is sandwiched between two large lobes connected by a flexible hinge region. The binding event results in a large conformational change which resembles the movement of the venus flytrap plant *Dionaea muscipula* upon catching its prey. Consequently, the LBD is commonly referred to as a 'Venus flytrap domain'. The conformational change is transmitted through a rigid, cysteine-rich domain (CRD) to the helical seven transmembrane-domain (7 TMD), which in turn couples to a G-protein. There are eight subtypes of mGluR with distinct biological functions that are hard to discriminate by traditional pharmacology. Tethered (photo)pharmacology can provide a solution, by encoding the SNAP-tag on mGluR subtypes, subtype-specific activation by light can be achieved after labeling with a PORTL molecule (BGAG$_{12}$). Figure 3 serves as a model to visualize size and dimensions of the dimeric SNAP_mGluR2 fusion after labelling with BGAG$_{12}$, for calibration a sphere with 5 nm diameter is shown (grey sphere).

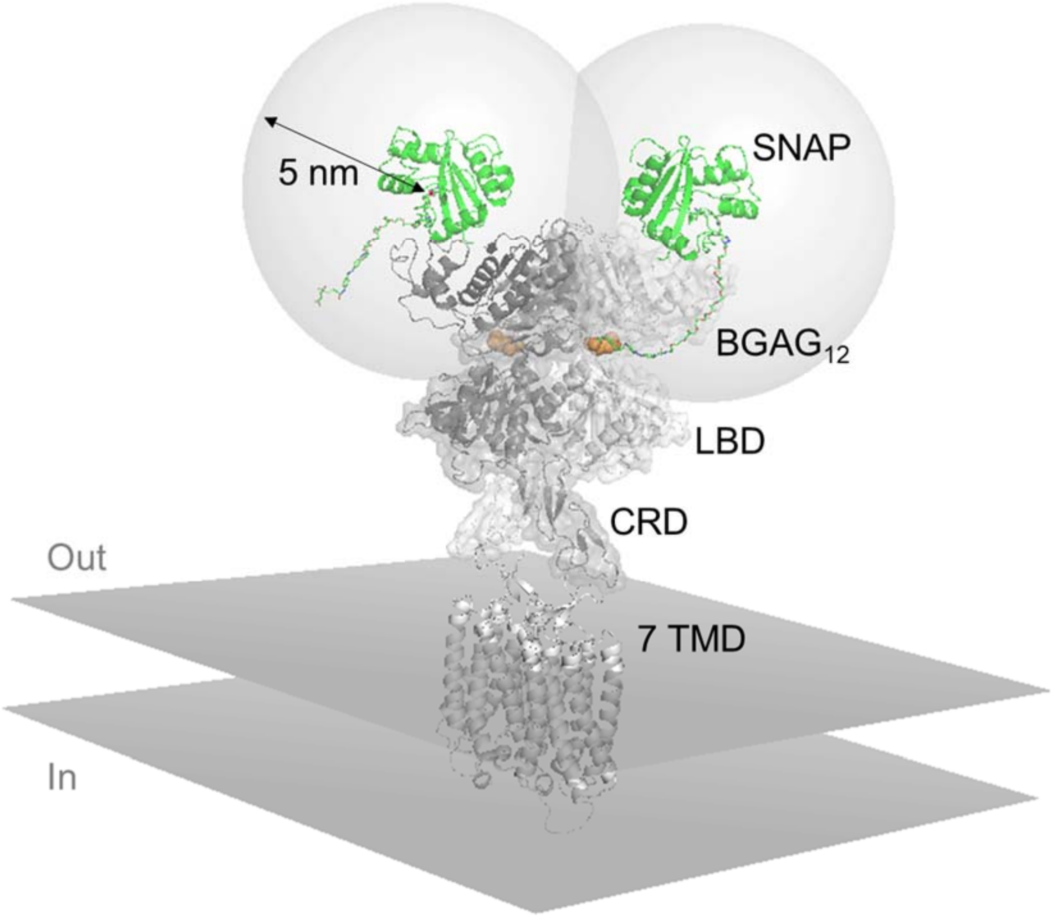

Figure 3. **Model of a dimeric SNAP-mGluR2 labelled with the PORTL (BGAG$_{12}$).** Grey: mGluR2, green: SNAP-tag, orange: glutamate, multicolored: BGAG$_{12}$. Abbreviations: LBD ligand binding domain, CRD cysteine-rich domain, 7 TMD seven-helix transmembrane domain. Please note that this model is modeled after the glutamate-unbound LBD crystal structure and

only serves to illustrate concept, relative size and dimensions of the labelled construct. (pdb: 5kzq, 4or2, 5cni, 3kzy)

The remoteness of the bioconjugation site has several consequences for the design of PORTL molecules:

(i) A long, flexible, soluble and inert linker is required to span the distance between ligand binding site and bioconjugation handle. Polyethylene glycol (PEG) linkers fulfill these criteria; they are harmless, water soluble and do not adhere to protein surfaces. In addition, they are commercially available as monodisperse polymers of distinct lengths, facilitating syntheses of small libraries of PORTLs with increasing linker lengths.

(ii) In contrast to the PTL approach, it is unlikely that photoswitching results in a significant change of length or pointing angle of the ligand headgroup due to the long overall length and flexibility of the linker.

(iii) Similar to a PCL, the biological activity is caused by a change in efficacy or affinity upon photoswitching, and the photoswitch is necessarily a part of the pharmacophore. Therefore, photoswitching results in a change of affinity or efficacy of the PORTL. PORTLs can therefore be conceptualized as ‘PCLs on a leash’.

(iv) The tethering ensures high local concentrations, since the tether is rarely in its fully extended conformation due to statistical sampling of the space. Even by low estimates, the effective molarity (M_{eff}) of the headgroup is in the millimolar range.[32,34]

(v) The high EM allows photoswitchable ligands to be employed with low or modest target affinities. It is important that the inactive form of the photoswitch has negligible affinity, otherwise the high M_{eff} might result in background activity.

(vi) The high EM can be advantageous in more complex experiments, *e.g.* application of PORTLs by intracranial injections, since it allows wash-free application at low-doses that produce no effect in free solution.

(vii) This is important since the PORTL molecule inherits its parent-drugs’ selectivity profile and gains its target specificity only after bioconjugation. The PORTL only produces an effect after capture by the self-labeling protein tag and the resulting increase in local concentration.

(viii) Most bioconjugation reactions follow second-order rate constants and low doses of PORTL molecules require reactions with high rates. Only a handful of methods like self-labeling proteins and strain-promoted inverse electron-demand Diels-Alder cycloaddition fulfil this requirement.

A PORTL can be thought of as a molecule with two or more separate functional parts connected by a linker (Figure 4). In the case of mGluR PORTLs, the molecules are made up of a photoswitchable pharmacophore that consists of an azobenzene (violet/blue) and a glutamate headgroup (orange) on one side and is fused *via* the long PEG linker (black) to a benzylguanine (BG, green) on the other side. The different parts can be interchanged and synthetically tailored to the specific need or application. The bioconjugation motif can be chosen as BG (for SNAP), benzylcytosine (BC, bright green, for CLIP) or chloroalkane (for Halo). The tether can be shortened or extended to adjust the EM or the tether can be branched to bear additional functionality, *e.g.* a second photoswitchable headgroup or a fluorophore. The substitution pattern of the azobenzene can be changed to tune the activation/deactivation wavelength, *e.g.* activation by violet (380 nm) or blue light (460 nm). mGluR PORTLs are denoted as follows: B**X**AG$_{\mathbf{n,y}}$ B = benzyl; X = G (guanine) or C (cytosine); A = azobenzene; G = glutamate, n = number of PEG repeats; y = activation wavelength (no number equals 380 nm). In addition, ClAG $_{\mathbf{n,y}}$ describes the Halo-tag reactive variant (Cl = Chloro). The combination of PORTLs with orthogonal reactivity (BG/BC) and activation wavelengths (380/460 nm) offers the opportunity to simultaneously control more than one receptor subtype in the same cell. We recently demonstrated this by expressing CLIP_mGluR2 and SNAP_mGluR7 in the same cell, labelling with B**C**AG$_{12}$/B**G**AG$_{12,460}$ and activating/deactivating both subtypes independently from each other.[35]

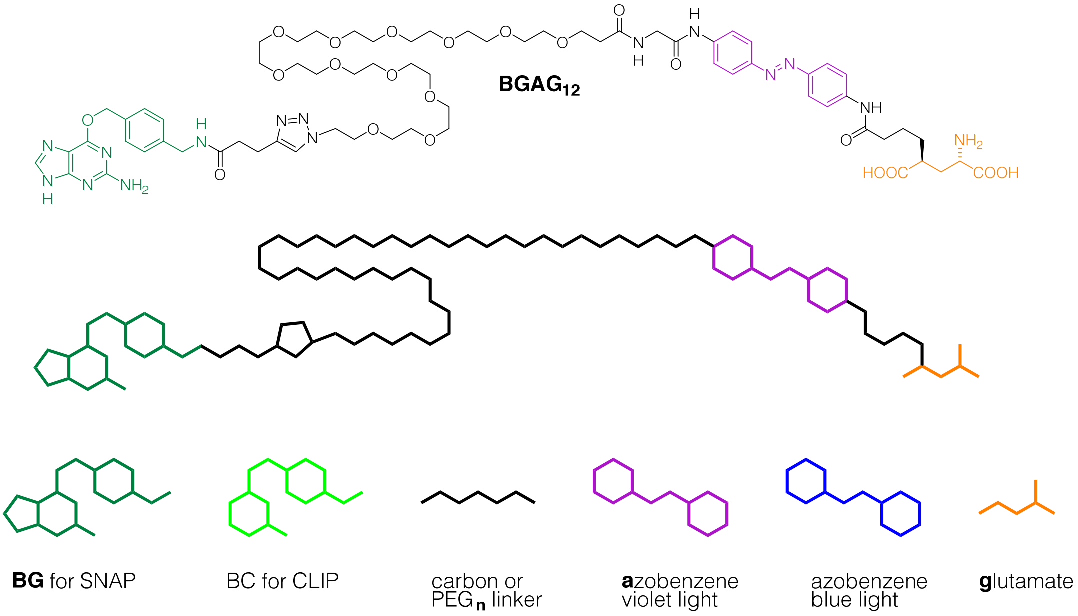

Figure 4. **Chemistry LEGO:** PORTLs for the metabotropic glutamate receptors (mGluRs). The different functional parts are highlighted to show the high modularity and interchangeability of these multivalent molecules.[36]

Very recently, Berry *et al.* virally expressed SNAP_mGluR2 in retinal ganglion cells (RGCs) of blind *rd1* mice and labelled it with $BGAG_{12,460}$.[37] One intravitreal injection at a concentration of 500 nM was enough to produce a uniform OFF light response upon exposure of these *rd1* retinae to light that is similar to the OFF light response of wild-type mice retinae. Then, LiGluR (*vide supra*, PTL-conjugated light-gated ion channel) was additionally targeted to RGCs to restore ON light responses as previously described.[21,38] Together, SNAP_mGluR2 and LiGluR could restore ON and OFF light responses. This restored visual acuity (*i.e.* clarity of vision) in living, blind *rd1* mice. The mice could differentiate between parallel and perpendicular bars of light in behavioral light-avoidance experiments. When $BGAG_{12,460}$ was employed together with the FDA-approved excipient additive β-cyclodextrine, compound release was slowed and light-guided behavior of mice persisted for a remarkable duration of 6 weeks after one single intravitreal injection. This impressive and elegant work highlights the robustness and practicability of PORTL molecules and their potential for *in vivo* applications. The eye is an attractive organ for gene therapy due to its immune privilege which circumvents immunogenicity of the viral vector. In addition, viral particles can be delivered directly by subretinal injection. Due to these advantages, Luxturna®, a treatment to restore vision in patients with RPE65 mutation-associated retinal dystrophy, was the first gene therapy approved for human patients by the FDA in late 2017.[39] Today, it seems plausible that the PORTL technology may find applications in human medicine, wherever gene therapy can deliver or alter the target protein. However, gene therapy is still in its infancy and immunogenicity of the exogenous gene and its mode of delivery is hard to predict.

In principle, PORTL molecules don't necessitate tethering to the receptor itself or even a protein in its vicinity but could also be linked *via* strong binders that furnish target specificity (Figure 5a). Such strong binders can be full-size antibodies, which can be synthetically modified with PORTLs (Figure 5b). Due to the advances with antibody-drug conjugates (ADCs), the chemistry of antibody-modification has been refined to a high level of sophistication[40] and could be exploited for the synthesis of antibody-photoswitch conjugates (APCs). Nevertheless, smaller biologics that are more easily produced and modified might be more amenable to this approach. Recombinant single chain immunoglobulin (Ig) derivatives like nanobodies (Nb) as well as non-Ig antibody-mimetics such as monobodies, anticalins or affibodies[41] can be expressed with high yields from bacteria and can straightforwardly be modified to carry a SNAP-tag or an unnatural amino acid for subsequent PORTL labelling.[42] Very recently, Farrants *et al.* capitalized on this idea by cloning the SNAP-tag on a Nb.[43] In this case, the Nb recognizes GFP,[44] which is fused *N*-terminally with mGluR2. After conjugation of SNAP-Nb with $BGAG_{12}$, robust photoactivation of GFP_mGluR2 was achieved. Up to now, this represents the most remote attachment site of PORTL molecules. Genetic modification is still required to make the GFP-fusion but the outlined principles should apply to nanobodies that target the receptor itself. Allosteric nanobodies for the extracellular domain of mGluR2 have been developed as of now[45] and they could be modified and loaded with BGAGs to ultimately photocontrol endogenous receptors without any genetic modification.

Even more ambitiously, the biological binder could be replaced by a small molecule that binds allosterically in a subtype-selective manner. Subtype-selective agonists or antagonists for mGluRs have been challenging to develop due to the high similarity of the orthosteric glutamate binding pocket,[33] but a variety of positive and negative allosteric modulators (PAMs and NAMs) exist.[46] A bivalent molecule of an allosteric modulator tethered to a photoswitch could be synthesized; for mGluR2, the high-affinity PAM 'BINA' could be employed (Figure 5b). Exploiting the high-affinity of BINA for mGluR2, the low-affinity glutamate-photoswitch could be targeted to the allosteric site. This leads to an increase in M_{eff} around the receptor and the photoswitch then acts on the orthosteric site through its long tether. These high-affinity PCLs would be fully synthetic and significantly smaller, which could aid their biodistribution and bioavailability. In addition, the high-affinity PCLs forego the need for biological binders, which could be hampered by immunogenicity.

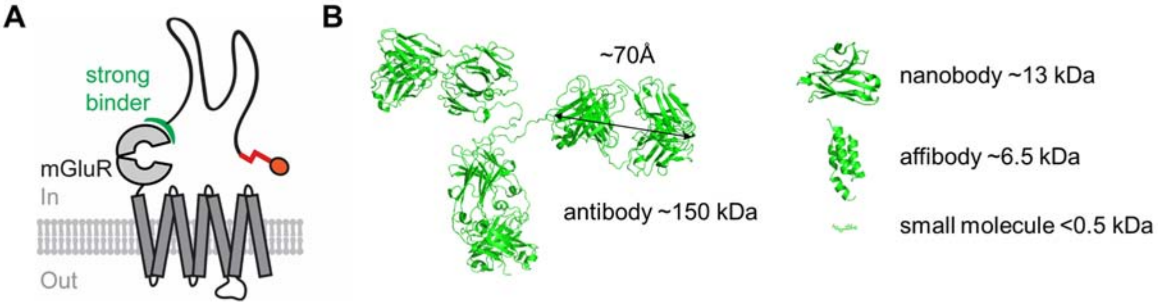

Figure 5. **Strategies without genetic modification of the target receptor. a)** PORTLs can be endowed with target specificity by fusion to a strong allosteric binder. **b)** This binder can be a full-size antibody, or smaller protein binders like nanobodies or affibodies. Even more, the binding can be assumed by allosteric modulators (BINA), to obtain fully-synthetic, high-affinity PORTLs (pdb: 1igt, 3g9a, 2kzi). The structures in b) are true to scale.

In this thesis, I seize the opportunities outlined in this introduction. However, its main focus lies on an approach that employs PORTL molecules to render chimeric receptor tyrosine kinases light-sensitive (chapter **2**). Next, I introduce an improved series of photoswitchable K^+ channel blockers and elaborate on antibody-photoswitch conjugates that target K^+ channels in chapter **3**. I will then describe the design of a *para*-PORTL for the AMPA receptor, and show its preliminary biological characterization in chapter **4**. Approaches towards expanding the PORTL concept to the *μ*-opioid receptor are described in chapter **5**. The synthesis of a PCL for the smoothened receptor is presented in chapter **6**. In chapter **7**, the synthesis of photoswitchable kinase inhibitors is described. Lastly, chapter **8** summarizes miscellaneous work on various biological targets.

2 Optical Control of Receptor Tyrosine Kinases

2.1 Abstract

Understanding the complex orchestra between a signaling ligand, its target receptor and the signaling events followed by receptor activation is crucial to deciphering cell and animal behavior. Many ligands, their receptors and effector proteins are today understood to the molecular detail. However, the spatial and temporal precision of receptor activation and the dynamics of their interactions with intracellular signaling and effector proteins remain poorly understood. To date, central questions in cell signaling remain enigmatic: How are signals integrated along the signaling cascades? How are signaling patterns like oscillation or waves created, sensed and processed? What are the dynamics of signaling complexes that assemble upon receptor activation? What role does receptor internalization play? To elucidate these questions, a tool that allows for repeated, reversible, and adjustable activation of a cell signaling pathway is required. Here, I present the engineering and characterization of light-activatable receptor tyrosine kinases by a fusion of synthetic chemistry with molecular biology.

2.2 Introduction

In mammals, three major classes of transmembrane receptors are involved in the transmission of extracellular input signals to the cytosol. (i) Ligand-gated ion channels transmit fast and short-lasting signals by changing the cell's electrical potential. For instance, these receptors are involved in synaptic transmission in the brain. (ii) G protein-coupled receptors (GPCRs) are responsible for a myriad of functions ranging from sensing light over olfactory stimuli to regulating metabolism. (iii) Receptor linked enzymes (RLEs), of which the major class are receptor tyrosine kinases (RTKs), sense growth factors and hormones. RTKs are involved in the control of critical cellular processes like metabolism and cell cycle control, and constitute an important target for diabetes and cancer therapy.[47]

58 RTKs have been described in humans. They consist of a large extracellular domain (ECD) connected to an intracellular kinase (TK) domain by a single-pass transmembrane (TM) α-helix (Figure 6a). According to the canonical picture of RTK activation, they mostly exist as monomers at the cell membrane and dimerize or oligomerize upon ligand binding, triggering activation of their intracellular TK domains. The insulin receptor (IR) is an exception, as it exists as preformed dimers in its inactive form (Figure 6b). Furthermore, in the inactive receptor, the TK domains are auto-inhibited and only have residual kinase activity. Upon ligand binding, the receptors undergo a conformational change, which results in juxtaposition and *trans*-autophosphorylation of the inhibitory loop of the TK domains. In other words, the TK domains cross-phosphorylate each other triggering a large increase in kinase activity. Subsequently,

many of the receptor's intracellular tyrosine residues are phosphorylated, which produces binding sites for adapter proteins. A host of receptor-specific and common adaptors assemble around the phosphorylated TK domain and various signaling pathways are activated. Among these are the AKT/PKB (protein kinase B) and the canonical Ras/MAP (mitogen-activated protein) kinase pathways, whose activations can be followed by the increase in phosphorylation of AKT and Erk1/2 (MAP Kinase), respectively.

An unusual kind of an RTK was cloned in 2003 from the parasitic worm *Schistosoma mansoni* (SmVKR*).*[48] As expected for an RTK, phylogenetic and structural analysis of *SmVKR* indicated a high similarity of the intracellular domain to that of the IR. Surprisingly, and in stark contrast to typical RTKs, the ligand binding domain showed a high sequence homology with the venus flytrap domains (VFT) from Class C GPCRs, such as the $GABA_B$ or the mGlu receptors. Accordingly, this novel class of RTKs was named *Venus Kinase Receptors* (VKRs).

Later, the amino acid L-arginine (L-arg) was identified as the ligand for SmVKR and it was shown that L-arg binding to the VFT functionally results in phosphorylation of its TKD.[49] In the parasitic worm, SmVKR is involved in oogenesis (*i.e.* sexual reproduction), which occurs in the mammalian host. Therefore, inhibition of SmVKR is an attractive target in the hunt for new drugs for this hard-to-treat parasitic disease. Moreover, VKRs recently gained increased attention due to their discovery in other pathogen vectors such as the malaria-spreading mosquito *Aedes aegypti*.[50] In later studies, genes encoding VKRs have been identified in in a large variety of invertebrates (and particularly in insects) and it is now evident that they form a special and distinct class of RTKs, which is absent in vertebrates.[51]

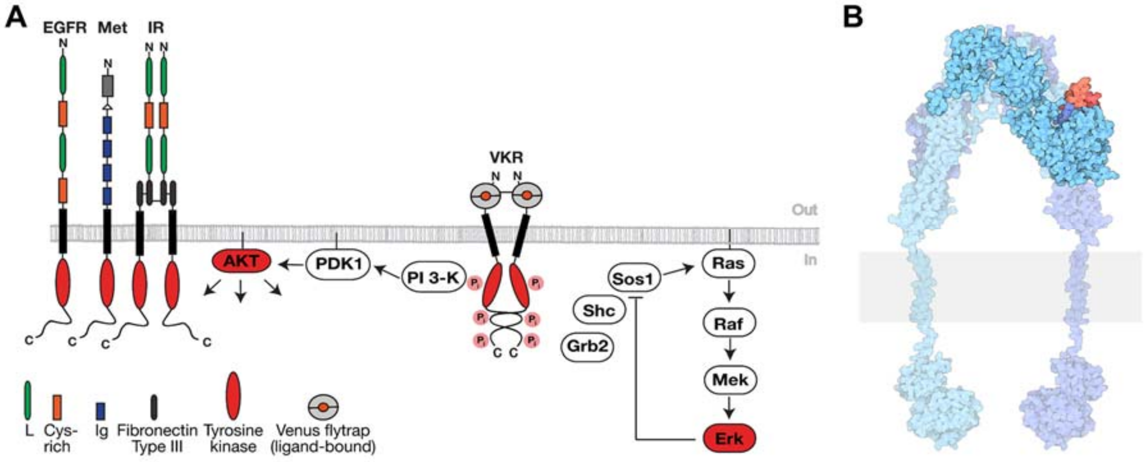

Figure 6. **Structure of receptor tyrosine kinases and Venus Kinase Receptors. a)** RTKs are made up by a large extracellular domain connected to a tyrosine kinase domain *via* a single-pass α-helix. In VKRs, the large extracellular domain is replaced by a venus flytrap domain. Upon stimulation of RTKs or VKRs by their ligands, networks of signaling proteins are activated, among them are the AKT and the MAPK pathways. **b)** The insulin receptor dimer,

adapted from Goodsell.[52] Its ECD adopts an inverted V-shape and binds insulin (red) on its outer edge.

Early investigations of the biology of VKRs were carried out in oocytes from the frog *Xenopus laevis* (Figure 7). The immature, fully-grown oocyte (Dumont Stage 6) is in a G2-arrested state, in which it can remain for a long time. Only induction by external stimuli abolishes this arrest state, and the oocyte then maturates and is primed for fertilization. This maturation is accompanied by germinal vesicle breakdown (GVBD), which can be easily observed by the appearance of a white spot on the pigmented, brown animal pole of the oocyte. In the female frog, this maturation is triggered by the steroid hormone progesterone, which acts through an unknown receptor to activate intracellular kinase-dependent signaling pathways. These are amplified by positive feedback loops so that the stimulation is irreversible, *i.e.* the oocyte switches binary from an 'OFF' (immature) to an 'ON' (mature) state.[53] GVBD can also be triggered by other molecules that induce downstream kinase activity, *e.g.* insulin, which likely binds to endogenously expressed insulin receptor-like growth factor (IGF) 1 receptor.[54] Oocytes are large in diameter (~1 mm) and are a robust assay for kinase activity. After injection of exogenous RNA encoding for VKRs, they can be used for highly-sensitive and qualitative tests for kinase-activity by simple observation of GVBD in response to potential ligands. In addition, the molecular components of the RTK-downstream signaling cascade are present in the oocyte, enabling the identification of VKR effectors and interaction partners. Taken together, these features make *Xenopus* oocytes an ideal model system to study RTKs.

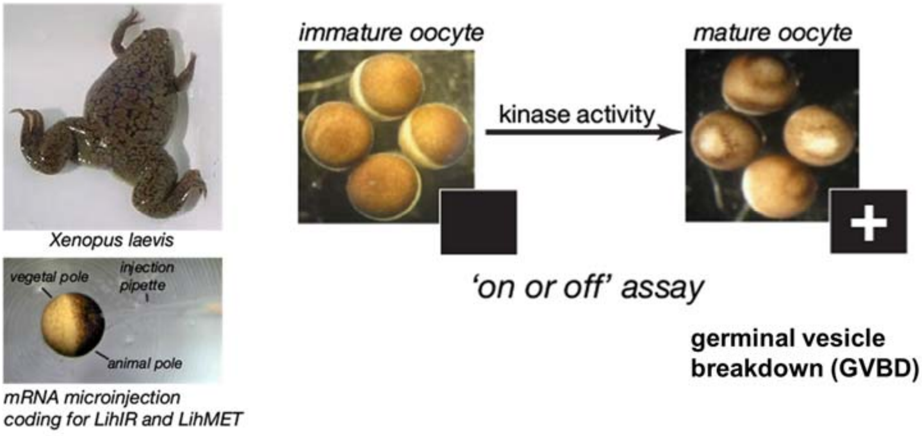

Figure 7. ***Xenopus laevis* oocytes as assay system for kinase activity.** The oocytes of female *Xenopus laevis* frogs (upper left) are large in diameter (~1 mm) and can be microinjected with mRNA (bottom left) for expression of proteins. Oocytes undergo germinal vesicle breakdown (GVBD) in response to outside stimuli that result in an increase of kinase activity. GVBD can be observed by the formation of a white spot on the brown animal pole of the oocyte (right).

Due to the successes of photopharmacology on receptors that contain a LBD with a venus flytrap motif, such as the glutamate-gated ion channels AMPA and NMDA, the ANP or mGlu and $GABA_b$ receptors, we became interested in the presence of these VFD in other membrane proteins. Indeed, it seems that this widespread motif originates from ancient periplasmic binding proteins (PBPs) found in prokaryotes and that their evolutionary fusion with transmembrane proteins gave rise to small-molecule binding receptors.[55] Photopharmacology relies on small-molecule photoswitches. RTKs are not amenable to photopharmacology at first sight, since they sense large peptide molecules such as insulin (MW = 5.8 kDa), and it is unlikely that incorporation and photoswitching of a small-molecule changes the shape or geometry of such a large molecule enough to have a large impact on ligand binding.

In this context, we came across the VKRs in 2008. Due to their late cloning and notable absence from classical animal models such as *Drosophila melanogaster* and *C. elegans,* the biological role of VKRs, their downstream signaling pathways, and their ligands were still largely unclear. Nevertheless, we envisioned that these VKRs could be repurposed and made light-sensitive by utilizing a photoswitch based on their small-molecule ligand. To this end, the VKR from the honeybee *Apis mellifera* (AmVKR) was chosen.[56] Work on the AmVKR was initiated by Dr. Harald Janovjak and conducted together with Dr. Johannes Broichhagen during their time in the Trauner laboratory. This work was started in close collaboration with Dr. Colette Dissous and Dr. Jerome Vicogne, who discovered the VKRs in 2003. From the start, the work on AmVKR was hampered by three main issues in mammalian cells:

(i) bad (surface-) expression,
(ii) unclear downstream signaling and
(iii) an incomplete picture of its ligands (supposedly including L-arginine).

Despite extensive work on AmVKR, these hurdles could not be overcome (see PhD thesis Dr. Johannes Broichhagen). Consequently, it was decided to discontinue work on invertebrate VKRs but instead engineer chimeric receptors guided by the VKR structure but based on mammalian protein domains.

2.3 Results and Discussion

2.3.1 Design

Chimeric receptors were constructed based on three RTKs, the (i) human insulin receptor (hIR), (ii) the epidermal growth factor receptor (EGFR) and (iii) the hepatocyte growth factor receptor (HGFR or Met). The extracellular domain (ECD) was completely removed after the transmembrane (TM) α-helix and fused to the rat mGluR2 domain, including its rigid cysteine-rich domain (CRD). The mGluR2 domain additionally carries a SNAP-tag for bioconjugation on its *N*-terminus and originates from the SNAP_mGluR2 construct which was already validated for photoswitching with PORTL molecules (BGAGs, see chapter 1).[28] Between mGluR2-CRD and TM, an additional 2-3 amino acids were introduced to allow for some flexibility. In addition, the construct carries the non-cleavable signal peptide from mGluR5 on its *N*-terminus, to ensure trafficking to the cell-membrane, and an HA epitope for immunoprecipitation or immunodetection. These constructs were termed LihIR, LiEGFR and LiMet and are supposedly a) activated by glutamate and b) activatable by light after labelling with the photoswitch (BGAG). See Figure 8 for visualization of the molecular components and their approximate sizes.

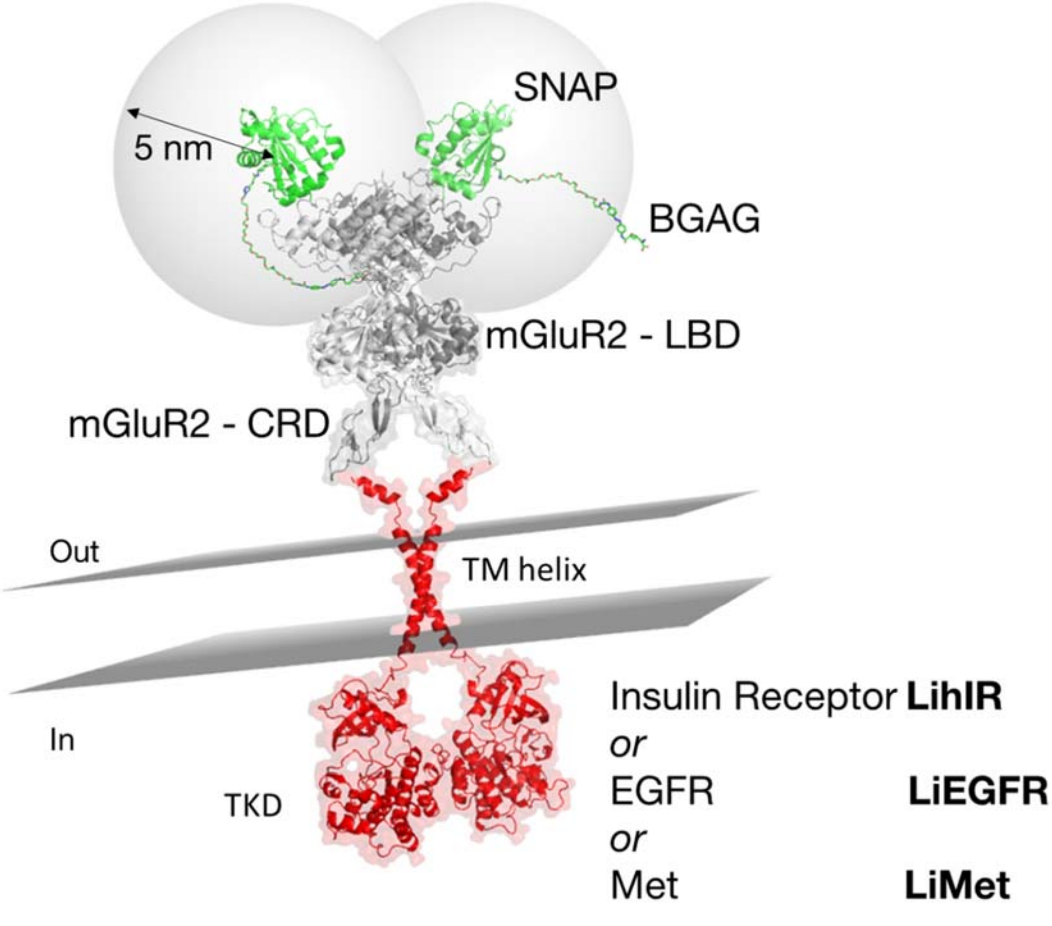

Figure 8. **LiRTK model.** Red: RTK domains, grey: mGluR2 domains, green: SNAP-tag, multicolor: BGAG PORTL; abbreviations: TKD tyrosine kinase domain, TM (transmembrane), LBD ligand binding domain. (pdb: 3kzy, 5kzq, 2mfr, 1irk)

2.3.2 Activation of LiRTKs by L-Glutamate in *Xenopus Oocytes*

Since the LiRTKs are engineered receptors, several questions have to be carefully investigated:

(i) Are LiRTKs expressed?

(ii) Are they inactive in absence of L-glutamate or are they constitutively active?

(iii) Do LiRTKs show an increase in kinase activity in response to addition of L-glutamate?

(iv) Does the glutamate-based photoswitch BGAG$_8$ activate the receptor upon illumination with light of the appropriate wavelength?

We produced mRNA coding for LihIR, LiMet and LiEGFR and expressed them in defollucillated *Xenopus laevis* oocytes by microinjection. It should to be noted that LiEGFR could not be expressed in oocytes, probably due to an intrinsic incompatibility of the EGFR TKD with the oocyte expression system.

Then, L-glutamate (L-glu) was added (~4 h after microinjection) and stimulation of kinase-activity was qualitatively assayed on the next day (after ~18 h) by observing and counting the appearance of the white spot on the brown animal pole of the oocyte (more than 14 out of 20 = GVBD; less than 6 = no GVBD; indicated by + or – on the bottom of Figure 9).

Experiments where protein is detected, by Western Blotting (WB), had to be completed within 5 h after microinjection, because cleavage and degradation of receptor proteins was observed at later time points. Accordingly, all treatments, *e.g.* addition of L-glu, were conducted ~4 h post-microinjection. After 5 h post-microinjection, the oocytes (n = 2 x 20 per condition/column on WB) were lysed and the lysate was divided into two equal parts. One part was used to directly detect cytosolic, high-abundance signaling proteins by WB, such as Akt and Erk. The other part was subjected to immunoprecipitation (IP) and then WB. Progesterone (PG) was included as a positive control, to confirm the health and correct development stage of the oocytes and rule out variances due the oocyte-donating animal.

Several conclusions can be drawn from GVBD and immunoblotting assays with L-glu stimulated oocytes (Figure 9):

(i) Expression of LihIR and LiMet was confirmed by detection of their HA epitope (top lane ‘HA’).

(ii) LihIR and LiMET have no effect on GVBD or phosphorylation of Akt and Erk in absence of stimulation by L-glu.

(iii) Oocytes expressing LihIR and LiMet undergo GVBD in response to L-glu.

(iv) Oocytes expressing LihIR and LiMet are phosphorylated/activated on RTKs upon stimulation by L-glu (PY100 lane)

(v) This results in phosphorylation of the two major signaling proteins Akt and Erk (pAkt and pErk lanes).

(vi) As negative control oocytes were injected with mRNA for dead kinase mutants of the LiRTKs (a single point mutation in the TKD which completely abolishes kinases activity). These do not show GVBD or phosphorylation under the stimulating condition, showing that L-glu acts through the LiRTK and that the effect is due to kinase activity.

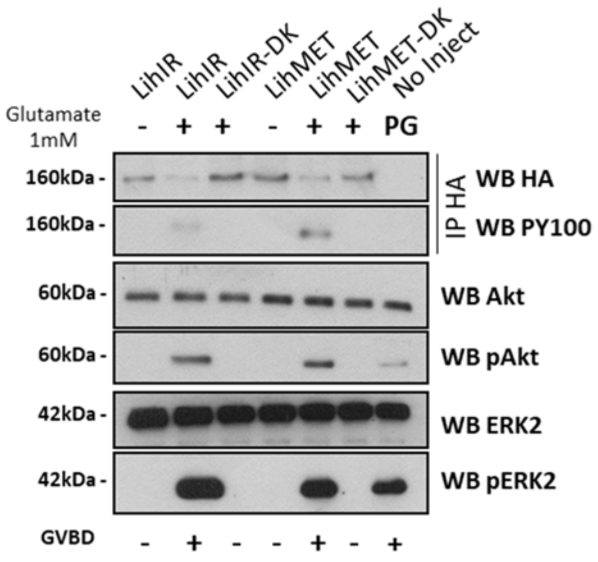

Figure 9. **LihIR and LiMet are sensitive to L-glutamate.** 20 oocytes each were used for each IP, WB and GVBD (in total 60 oocytes per vertical lane). DK= dead kinase, neg. ctrl.; PG = progesterone, pos. ctr.

These experiments were performed at least in three separate, independent experiments using oocytes from different animals (see supporting information for additional and uncropped original blots) and indicates that we are able to convert the human receptors for insulin and for the hepatocyte growth factor into glutamate receptors by replacing their extracellular domain with the ligand binding domain from the metabotropic glutamate receptor.

2.3.3 Activation of LiRTKs by Light

Encouraged by these results, we next assayed if the photoswitch together with light stimulation can elicit the same effects as L-glu alone. Again, LihIR, LiMet and their dead kinase mutants were expressed in oocytes by microinjection of RNA. 3 h post-injection, the oocytes were placed into a labelling solution containing 100 μM $BGAG_8$ (the PORTL molecule) in buffer. After 1 h incubation at r.t., the oocytes were removed from the labelling solution and placed into fresh buffer. Then, light stimulation was performed from the top using a UV handheld lamp (power 12 W, excitation ~350 nm) as follows: 1 min illumination, 5 min dark, 5 cycles. As before, one set of oocytes (n = 20 eggs) was observed and counted for GVDB after ~18 h. The second set (n = 20 eggs) was subjected to IP and WP for protein detection of chimeras. The third set (n = 20 eggs) was used for detection of cytosolic signaling proteins.

Several observations and conclusions can be drawn from GVBD and immunoblotting assays with light-stimulated oocytes (Figure 10):

(i) Oocytes expressing chimeras and labelled with $BGAG_8$ are inactive in the dark.
(ii) When illuminated with UV light, the oocytes undergo GVBD, and are phosphorylated both on receptor level and on downstream signaling level.
(iii) AG_8 is a negative labeling control and lacks the BG for bioconjugation. Oocytes treated with AG_8 are not affected by illumination.
(iv) No effect is observed with the dead kinase mutants.
(v) Non-injected oocytes serve as another control to show that neither $BGAG_8$ or AG_8 have an effect in absence of chimera.

Taken together, this is conclusive evidence that we are able to convert the insulin and the hepatocyte growth factor receptor into light-activatable receptors.

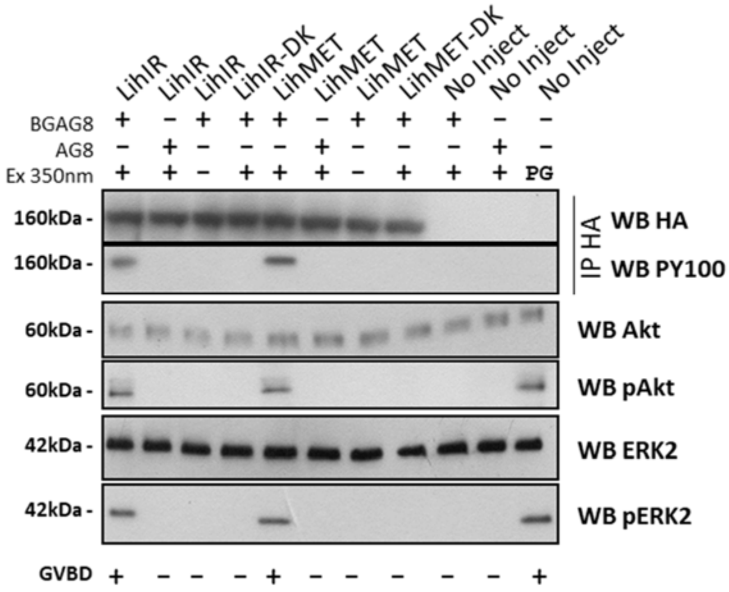

Figure 10. **LihIR and LiMet labelled with $BGAG_8$ can be activated by light.** 20 oocytes each were used for each IP, WB and GVBD (in total 60 oocytes per vertical lane). DK = dead kinase, neg. ctrl.; PG = progesterone, pos. ctr.; $BGAG_8$ = PORTL molecule; AG_8 = PORTL without the bioconjugation motif, negative labeling control.

2.3.4 Influence of the TMD of LihIR on Chimera Activation

Due to their relevance to human medicine, RTKs have been the focus of extensive research efforts. Nevertheless, it still remains unclear how the information from ligand-binding to the ECD is relayed to the TKD, partly due to the challenges of expressing full-length RTKs for biophysical and structural characterization by X-Ray crystallography or Cryo-EM.[57,58] It is an astonishing feat that in receptors of over 1300 amino acids in size (only one monomer) this critical part of signal transduction is accomplished by a single transmembrane *α*-helix of only around 20-25 amino acids. The hIR TM helix has a repeat of three isoleucines at its *N*-terminal, membrane embedded part, and we reasoned that by adding or removing one isoleucine we could reposition the helix inside of the membrane (*i.e.* ‘push’ our ‘pull’ it out of the membrane) which should have a large impact on receptor activation. Accordingly, we cloned a ‘extended’ and a ‘truncated’ version of LihIR and investigated them in oocytes (Figure 11). Strikingly, the truncation by only one amino acid completely abolished kinase activity. On the other hand, the extension was not entirely deleterious but lowered LihIRs apparent affinity for glutamate. 1 mM L-glu is sufficient to induce full GVBD in oocytes for the ‘normal’ LihIR, while the extended variant only underwent full GVBD at 5 mM. In addition, the extended variant did activate the Erk and JNK pathways but not the AKT pathway. This confirms the crucial role of the TM helix in the LihIR construct and could be an interesting entry point for the generation of variants with reduced affinities or altered downstream signaling.

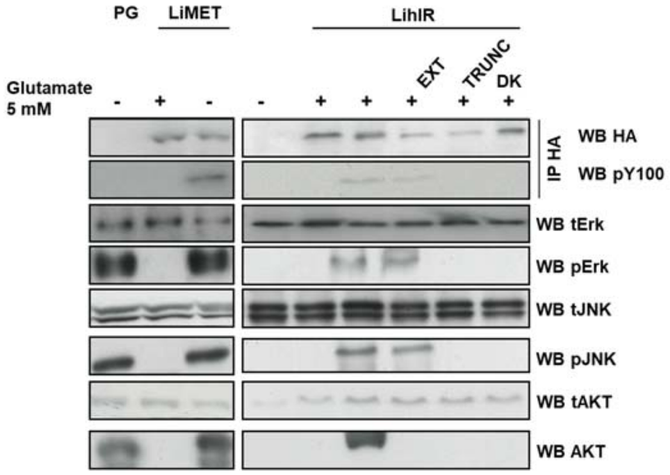

Figure 11. **Influence of a single amino acid insertion or deletion in the fusion region**. 20 oocytes each were used for each IP, WB and GVBD (in total 60 oocytes per vertical lane). DK = dead kinase, neg. ctrl.; PG = progesterone, pos. ctr

2.3.5 Activation of LiRTKs by Light in Mammalian Cells

LiRTKs would be an even more useful tool if they could be expressed in mammalian cells. To this end, LiRTKs were subcloned on a bicistronic vector (pIRES2-AcGFP1). By bicistronic expression, the expression levels of LiRTKs and GFP are linked, and it was anticipated that this would allow for selection of populations of cells with different expression levels by fluorescence-activated cell sorting (FACS). Cell lines were chosen with no or little expression of the parent wild-type RTK to avoid issues due to hetero-dimerization of wild-type RTKs with LiRTKs. Several cell lines were investigated for expression of the LiRTKs, including Hela, HEK293T, MCF7, MDCK-II and PC12. Many experimental and technical issues were encountered. For instance, Hela and HEK293T cells had high background phosphorylation levels of AKT and Erk, making any further increases due to LiRTK activity difficult to observe. On the other hand, MCF7 did not respond well to transfection by electroporation and in general were extremely tedious to culture due to their tendency to form piles when growing on culture dishes. Lastly, PC12 partially underwent differentiation into neuronal precursor cells when expressing LiRTKs, which made the further culturing impossible. Due to these issues, it was later decided to focus on MDCK-II cells expressing LihIR and LiEGFR.

MDCK-II cells were transfected with LihIR and LiEGFR (on pIRES2_AcGFP1) (and their dead kinase mutants) by electroporation. Then cells were selected by antibiotic resistance to Geneticin® and FACS-sorted for GFP expression. These cells were then employed for the subsequent experiments.

Expression of LiRTKs in mammalian cells was technically challenging. In contrast to the experiments in *Xenopus* oocytes, a high level of background phosphorylation was observed, which could be due to several reasons:

(i) L-glu is present in the growth medium used for mammalian cells, fetal calf serum (FCS) contains ~1 mM L-glu.[59] Therefore, normal growth medium (10% FCS) contains ~100 μM L-glu stemming from serum alone. This is likely enough to fully activate the chimera, since the EC_{50} of L-glu for mGluR2 is in the two-digit micromolar range.[60]

(ii) RTKs are never fully *cis*-autoinhibited since this would preclude the initial *trans*-phosphorylation that is required for receptor activation. The TKD is therefore thought to 'breathe' between states of high or low kinase activity.[47] In addition, overexpression of RTKs leads to constitutive activation in absence of ligand.[61] Therefore, the expression levels of the chimeras are very likely to have a crucial influence on their background activity and stimuli-responsiveness.

(iii) The activated chimera activates downstream signaling pathways that promote cell survival and proliferation. Therefore, cells are selected during culturing that express activated chimera in absence of stimulation, *i.e.* highly expressing cells where an increase in activation can be hard to observe.

These issues are also amplified by the biochemical assays used to detect RTK activation. Most commonly, RTK activation is observed by an increase in phosphorylation, detected by immunoblotting with phospho-specific anti-RTK antibodies. These antibodies usually detect low amounts of phospho-protein, and are in are visualized and amplified by a HRP-conjugated secondary antibody. Therefore, a low percentage of phospho-protein of an overexpressed RTK is enough to saturate the signal on the only semi-quantitative method of WB. In contrast, the detection of phosphorylated downstream proteins might be easier since these pathways can compensate for the high level of continuous activation during the cell culturing by downregulation, making them more responsive to an additional stimulation.

First experiments were performed by L-glu addition to cells expressing LiRTKs, and in many cases, an increase in downstream Erk phosphorylation was observed. Nevertheless, reproducibility of these experiments was an issue, possibly due to unidentified interactions of L-glu with endogenous proteins, obscuring the results. Consequently, chimera activation was probed by light after labeling with the PORTL molecule $BGAG_8$. This is the ‘cleaner’ experimental approach, limiting off-target effects, since $BGAG_8$ is bioorthogonal and excess molecule is washed out after the labeling reaction. Light was applied using LED arrays as previously described and should not cause any phototoxic effects at the employed intensities and durations.[62]

Accordingly, MDCK-II cells stably expressing LihIR were labelled with 10 μM $BGAG_8$ in the dark and at 37°C for 45-60 min in reduced medium (0.5% FCS/OptiMEM/0.1% DMSO), which in addition serves to starve the cells and lower the background phosphorylation of Erk/Akt. Then, the labeling medium was removed, replaced with HBSS/HEPES and cells were constantly illuminated with an LED array equipped with 24 LEDs (380 nm or 505 nm) for the indicated time at 37°C. Two controls were included, one where cells were not starved, and the other to exclude unspecific effects of DMSO vehicle or light application. Directly after the indicated illumination time, cells were washed with ice-cold PBS, placed on ice, lysed and subjected to WB (Figure 12). While no increase in phosphorylation of LihIR was be observed, likely due to the reasons outlined above, a transient increase in phosphorylation of Erk was observed that peaked around 2 minutes and decreased to basal levels at 10 min. Longer illumination of 15 or 20 min did not lead to increased or sustained receptor activation. Control cells that were only treated with the vehicle (0.1% DMSO) did not show any effects upon illumination (‘neg’). Non-transfected (‘mock’) cells were treated exactly like the 20 min time point LihIR cells and did not show any increase on Erk level, ruling out non-specific effects by the illumination.

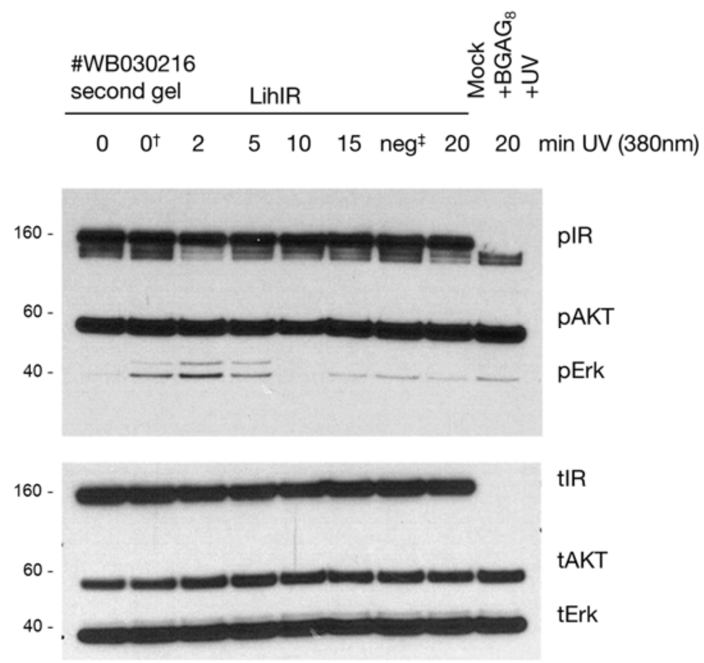

Figure 12. **Activation of LihIR by light in MDCK-II cells.** †Non-starved cells. ‡Negative control, cells treated exactly like 15 min time point, but only incubated with 0.1% DMSO (instead BGAG$_8$). Mock control is non-transfected MDCK-II cells treated like the 20 min time point cell.

Following the same protocol, MDCK-II cells expressing LiEGFR were assayed, but this time different light protocols were followed (Figure 13). It should to be noted, that after an initial bout of violet light (380 nm), which isomerizes the photoswitch to its *cis*-isomer, the LiRTK should, on these timescales, stay 'ON' due to its bistability. Only after illumination with green light (here: 505 nm), the photoswitch isomerizes back to *trans-,* turning the LiRTK 'OFF'. The experiment was conducted in a duplicate in presence of the EGFR-inhibitor Gefitinib (1 μM), as negative control.

By comparison of the pErk level of illuminated conditions B-F to the dark pErk level in A, several conclusions can be made:

(i) **A:** dark panel.

(ii) **B:** Illumination with green light for 20 min leads to a small increase on pErk level, which is consistent with the fact that the PSS under green light contains a higher percentage of *cis*-isomer than the PSS in the dark.

(iii) **C:** Illumination with violet light for 20 min leads to activation of the chimera with a ~3-fold increase in Erk phosphorylation that is sustained over 20 min in the dark.

(iv) **D:** Similar to C, Illumination with violet light for 30 min leads to activation of the chimera followed by 10 min in the dark leads to a ~3-fold increase in Erk phosphorylation. This indicates that thermal relaxation in the dark from *cis*- to *trans*- is likely not occurring to a significant at these timescales.

(v) **E:** The largest increase in Erk phosphorylation was observed in cells illuminated with green light for 20 min followed by activating violet light for 20 min. The increase in pErk is ~5-fold.

(vi) **F:** Reversing the wavelengths of E, *i.e.* first violet and then green light, ceases the activation of the receptor, observed by the decrease in pErk to 'green' levels (compare to B). This decrease is unlikely due to downregulation of Erk itself (compare to C and D). Therefore, F serves as an indication that the photoswitching of the receptor is reversible, *i.e.* that the LiRTK can not only be switched 'ON' but also 'OFF'.

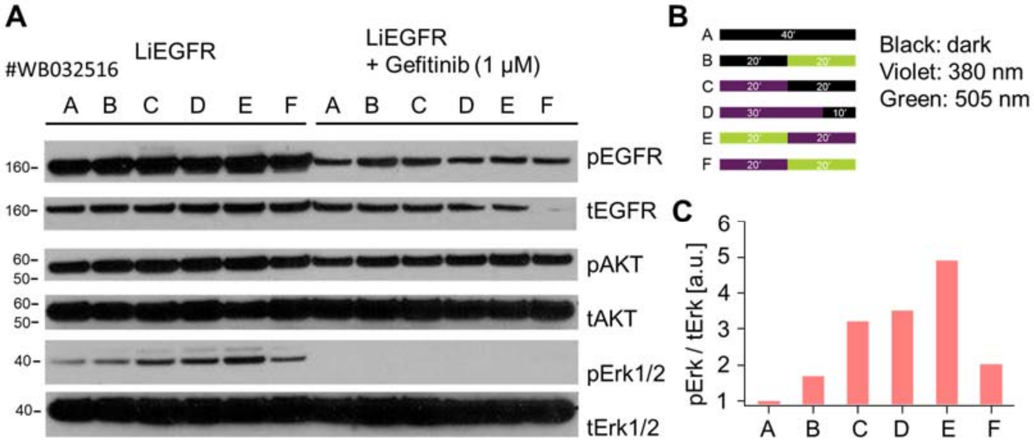

Figure 13. **Activation of LiEGFR by light in MDCK-II cells. a)** WB, **b)** Light-stimulation protocol (time in minutes). **c)** Bands were integrated with ImageJ and pErk divided by tErk, then normalized to pErk/tErk of condition A (=1). The absence of the tEGFR in the rightmost lane is an experimental artifact.

In summary, both LihIR and LiEGFR could be activated by light after labelling with the photoswitch BGAG$_8$. The downstream Erk activation *via* LihIR was only transient, while LiEGFR light-stimulation led to sustained Erk phosphorylation. This indicates that the LiRTK inherits their parent RTKs signaling features. Therefore, LiRTK can potentially be used for time- and spatially-resolved studies of the events following RTK activation. The reversibility of ON and OFF photoswitching could be illustrated by following different light protocols for LiEGFR stimulation. It should be noted that western blotting is not an appropriate method for observing signaling events in a time-resolved manner. Great care was taken not to introduce outside variances, cells were treated exactly in the same manner except the different light protocols. Nevertheless, WB is only a semi-quantitative method and integrates the signal over a population of a few hundred thousand cells. However, signaling pathways should be studied on a single cell level since every cell is different and integrates outside stimulation. The bulk observation can be misleading and misrepresent the single-cell events. One textbook example of this is the maturation (GVBD) of *Xenopus* oocytes (vide supra).[53,63] Despite these limitations, the experiments shown above are a strong indication that LiRTKs are indeed activated by light.

Lastly, the astonishing events are highlighted here that have to happen on a molecular level to cause a light-induced effect on Erk phosphorylation: (i) a photoswitch is covalently attached to a protein, (ii) absorbs a photon of the appropriate energy and isomerizes to *cis*-, (iii) this induces ‘closure’ of the venus-flytrap, ligand-binding domain, (iv) which in turn is transmitted through the cell membrane to the intracellular tyrosine kinase domain, (v) ultimately resulting in kinase activation and initiation of downstream signaling events.

2.3.6 Control of Cell Adhesion in MDCK-II Cells Expressing LiEGFR

A431 cells overexpressing EGFR loose cell-to-cell adhesion upon addition of EGF (unpublished observations by Chiara Zambarda, Growth Factor Mechanobiology Group, MPI for Medical Research Heidelberg). To observe and analyze this, cells were seeded on micropatterned dishes, where cells can only attach and grow on circular islands. These dishes are produced by adapting published protocols,[64,65] where a glass coverslip was PEGylated and this layer was removed by UV irradiation through a mask, *i.e.* photomasking. The A431 cells were seeded on these dishes to form round, confluent islets of cells and upon EGF addition, the cells seemed to ‘contract’, forming a pile in the islet’s middle. This can then be quantified by comparing the areas that are covered by cells before and after EGF addition.

We asked if cells expressing LiEGFR upon L-glu addition exhibit the same behavior as the A431 upon EGF addition. To this end, MDCK-II cells expressing LiEGFR were seeded on the micropatterned dishes and a timelapse video with a 30 sec frame rate was recorded (Figure 14). Before stimulation, the cells move around and completely fill out the round islets. Upon addition of L-glu (to a final conc. of 1 mM, 1/100 dilution from 100 mM stock) at t = 10 min, the cells lose cell-to-cell adhesion (see t = 11, 13, 18 min). In overall, the cell islets ‘contract’, a process that is immediate and rapid and can be followed on a minute timescale. The response is reversible, and the cells relax and re-expand to the previous state (t = 40 min).

Importantly, the negative controls (MDCK-II ‘mock’, non-transfected) and MDCK-II/LiEGFR_dK (dead kinase mutant) do not contract after L-glu addition (see chapter 2.5.4). MDCK/LiEGFR_LBD cells that express a mutant with lower affinity for L-glu (R57A)[66], exhibit the contraction but to a smaller extent, *i.e.* less cells contract and less pronounced.

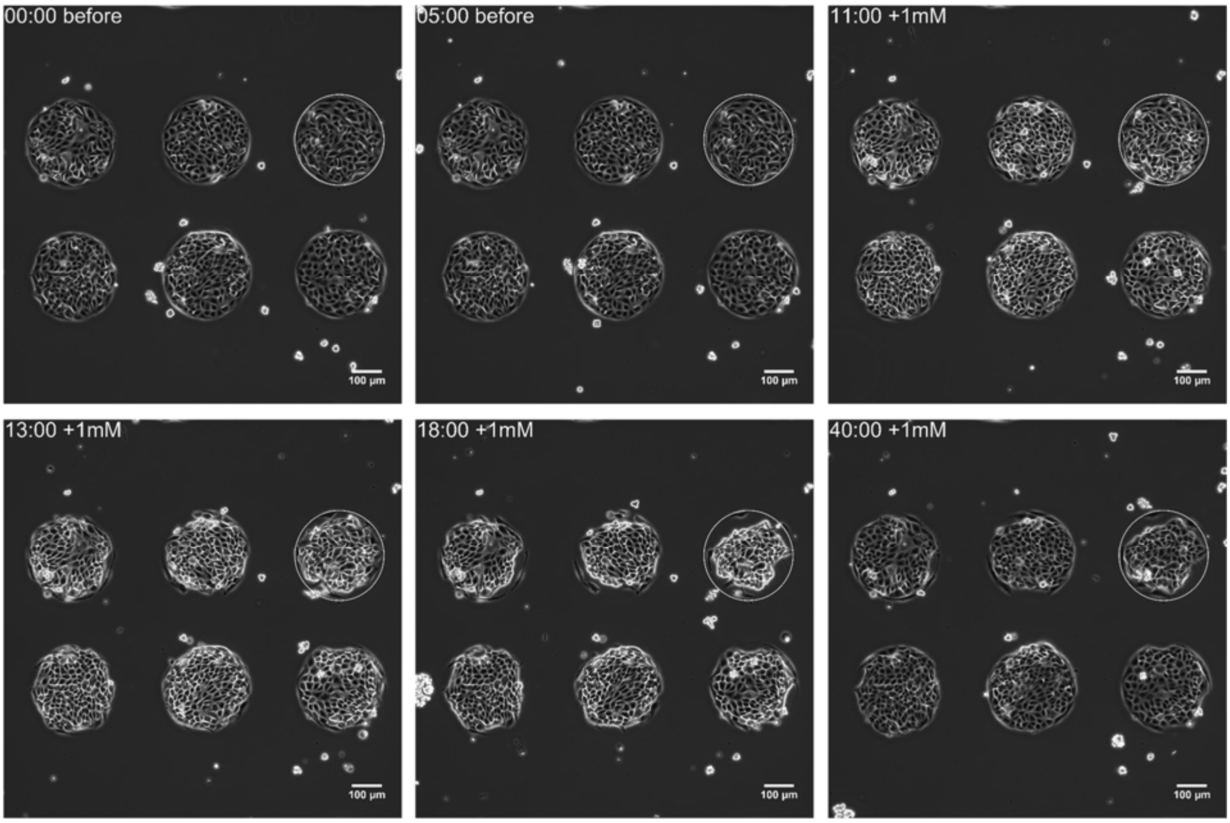

Figure 14. **Time-lapse of MDCK-II cells stably expressing LiEGFR.** L-glu (1 mM) was added after t = 10 min. For clarity, the upper right islet is marked with a white circle, representing the area covered by cells at t = 0 min.

The contraction of MDCK-II/LiEGFR is similar to the response of A431-EGFR upon EGF addition (unpublished results from Chiara Zambarda) but more heterogeneous. On a single cell level, it is obvious that some MDCK-II/LiEGFR cells show a strong response, but that other cells do not contract at all. This is most likely due to highly variable levels of receptor expression, which is a common issue of traditional stable expression from cDNA.[67] Experiments are underway to directly detect the LiEGFR receptor on cell-to-cell level by immunofluorescence.

That RTKs such as EGFR can influence the mechanobiology of cells is an active and new field of research and the knowledge of the mechanisms underlying these observations and their significance is incomplete. In collaboration with the 'Growth Factor Mechanobiology' group we are actively working on identifying the molecular components underlying the signal transduction that must lie between binding of EGF/L-glu and the phenotypic response ('contraction'). In addition, we are planning to adapt these experiments for labelling with the photoswitch 'BGAG$_8$' and producing the same contraction with light.

2.4 Summary and Outlook

Here, several Receptor Tyrosine Kinases (RTKs) were converted into glutamate receptors and then into photoreceptors. This was accomplished by engineering chimeric receptors in analogy to Venus Kinase Receptors (VKRs), a special class of RTKs only found in invertebrates. We cloned chimeras featuring the venus-flytrap, ligand-binding domain of the metabotropic glutamate receptor 2 and the intracellular domains from a selection of human RTKs. In addition, these chimeras carry a self-labeling protein tag (*i.e.* SNAP-tag) on its extracellular *N*-terminus. Experiments in a *Xenopus laevis* assay indicate that LiRTKs can be activated by the amino acid L-glutamate (L-glu). Moreover, after reaction of the SNAP-tag with a photoswitchable orthogonal remotely-tethered ligand (PORTL), the LiRTK gains light sensitivity. The labeled LiRTK can be activated by light in both the *Xenopus laevis* assay and in mammalian MDCK-II cells. We demonstrated that this approach is not only applicable to the insulin receptor but also to other RTKs, such as EGFR and Met.

These LiRTKs can be expressed in mammalian cells, and enable optical control over the downstream MAPK signaling pathway. Moreover, they can control the mechanobiology of epithelial cells; in MDCK-II/LiEGFR cells stimulation by L-glu leads to a loss of cell-to-cell adhesion.

While we could clearly demonstrate the LiRTK concept, all conclusions in mammalian cells are based on downstream observations, such as Erk activation or cell contraction. We are still in the process of observing the activation of the receptor by light or L-glu on the receptor level itself, *i.e.* the increase in RTK kinase activity. Investigations are ongoing to produce mammalian cells lines expressing LiRTKs on a more physiological level. In combination with microscopy-based readouts, these cell lines will allow perturbation of LiRTKs by light in a spatiotemporally defined manner, while observing the readout in real-time.

2.5 Supporting Information

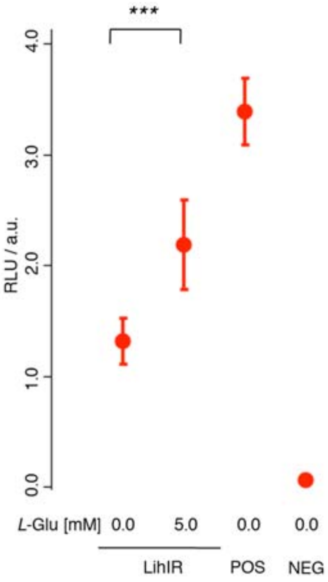

Supporting Figure 1. Elk1/SRF (from Qiagen) transcriptional dual luciferase readout of Erk activity in Hela cells transfected with LihIR and stimulated with L-glu.

2.5.1 Xenopus Laevis Oocytes

RNA was produced by mMESSAGE mMACHINE™ T7 Transcription Kit (Invitrogen #AM1344) according to the manufacturer's instructions.

mRNA preparation:

DNA was linearized by digesting 5 μg of DNA (on pcDNA3.1 vector) by the FastDigest (ThermoScientific, #00151181) protocol with PmeI (MssI) (Thermo Scientific, #FD1344) for 1.5 h at 37 °C. Afterwards, subsequent addition of 250 μL absolute EtOH, followed by 10 μL of 3 M NaOAc was carried out before storing the solution at -20 °C overnight for precipitation of the linearized plasmid, which was then isolated by centrifugation for 20 minutes at 12,000 rpm at 4 °C. After removal of the supernatant, DNA was dissolved in 15 μL dH_2O and 1 μg was reverse-transcribed by using the mMessage mMachine T7 transcription kit (life technologies, #AM1344) according to the manufacturer's instructions. Pure mRNA was taken up in nuclease-free water, aliquoted and stored at -20 °C.

Injection and treatment:

Female frogs were anesthetized, oocytes were surgically harvested, washed and stored in ND96 buffer. Oocytes were defolliculated manually with forceps before injection with cRNA (60 ng) coding for the construct. L-Glutamate was added to reach the appropriate final concentration for stimulation (1 mM or 5 mM) 3 h after cRNA Injection. GVBD was observed after 15 h.

For immunoprecipitation and western blotting, the oocytes were lysed 5 h after cRNA injection (*i.e.* before GVBD).

For the light-stimulation experiments, oocytes were incubated at 19°C for 1 h with BGAG$_8$ (1% DMSO in ND96 buffer), 3 h after cRNA injection was performed. The oocytes were transferred back to ND96 buffer and illuminated at 365 nm in cycles (12 W, 1 min UV, 5 min dark, 5 repetitions). GVBD was observed after approximately after 15 h.

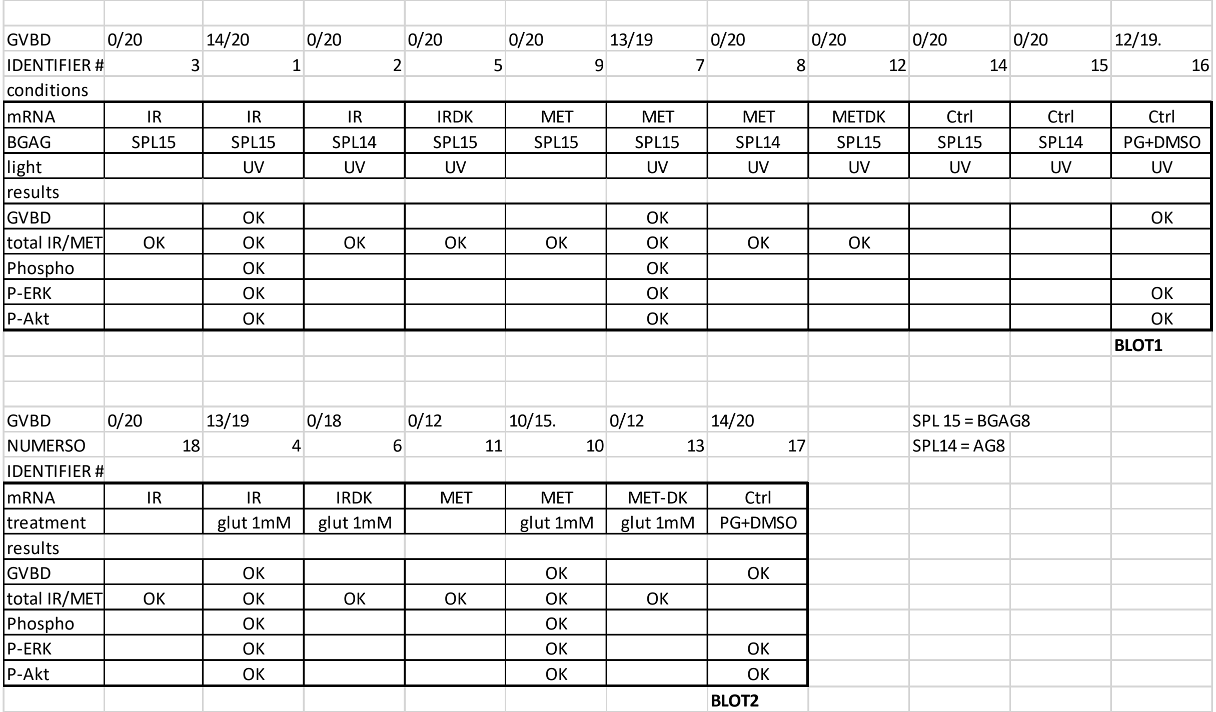

GVBD	0/20	14/20	0/20	0/20	0/20	13/19	0/20	0/20	0/20	0/20	12/19.
IDENTIFIER #	3	1	2	5	9	7	8	12	14	15	16
conditions											
mRNA	IR	IR	IR	IRDK	MET	MET	MET	METDK	Ctrl	Ctrl	Ctrl
BGAG	SPL15	SPL15	SPL14	SPL15	SPL15	SPL15	SPL14	SPL15	SPL15	SPL14	PG+DMSO
light		UV	UV	UV		UV	UV	UV	UV	UV	UV
results											
GVBD		OK				OK					OK
total IR/MET	OK	OK	OK	OK	OK	OK	OK	OK			
Phospho		OK				OK					
P-ERK		OK				OK					OK
P-Akt		OK				OK					OK
											BLOT1
GVBD	0/20	13/19	0/18	0/12	10/15.	0/12	14/20		SPL 15 = BGAG8		
NUMERSO	18	4	6	11	10	13	17		SPL14 = AG8		
IDENTIFIER #											
mRNA	IR	IR	IRDK	MET	MET	MET-DK	Ctrl				
treatment		glut 1mM	glut 1mM		glut 1mM	glut 1mM	PG+DMSO				
results											
GVBD		OK			OK		OK				
total IR/MET	OK	OK	OK	OK	OK	OK					
Phospho		OK			OK						
P-ERK		OK			OK		OK				
P-Akt		OK			OK		OK				
							BLOT2				

Supporting Figure 2: **GVBD scores and WB identifiers/layout. July 2017**

Original Blots (July 2017):


6 juillet 2017
Mb
même protocole
charge contrôle de la manip ②
③ IR
④ IR stim.
③ ④ 1 2 3 5 7 8 9 12 14 15 16
200
150
100
75
anti HA
③ ④ 1 2 3 5 7 8 9 12 14 15 16
200
150
100
75
anti PY

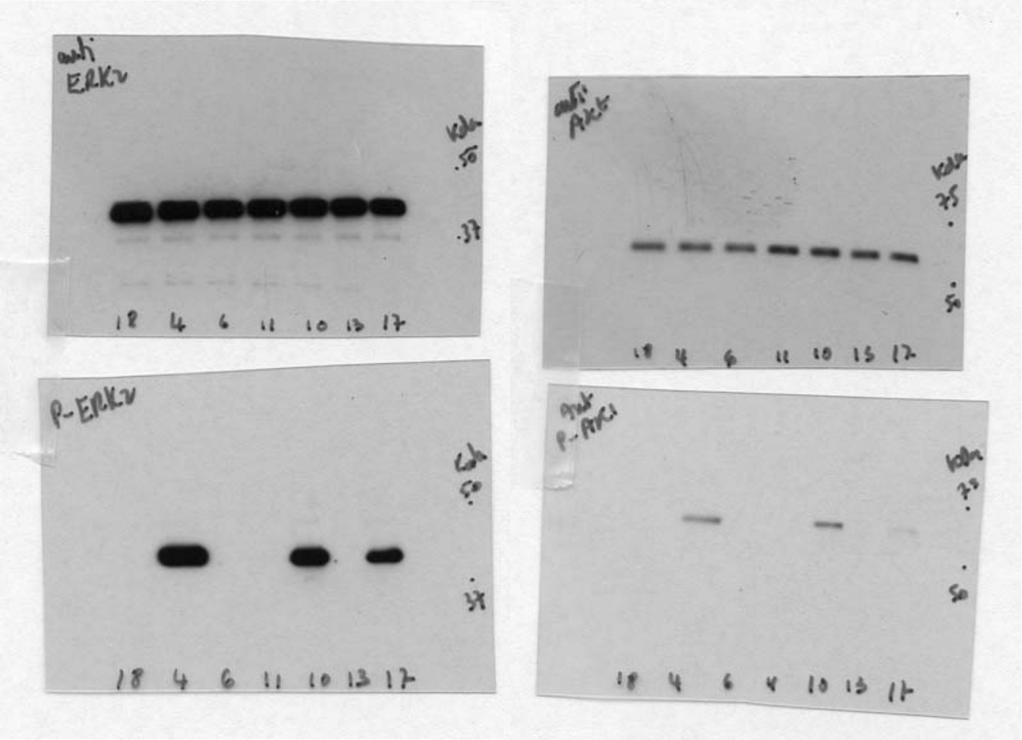
anti ERK2
kDa
50
37
18 4 6 11 10 13 17
anti AKT
kDa
75
50
18 4 6 11 10 13 17
P-ERK2
kDa
50
37
18 4 6 11 10 13 17
anti P-AKT
kDa
75
50
18 4 6 4 10 13 17

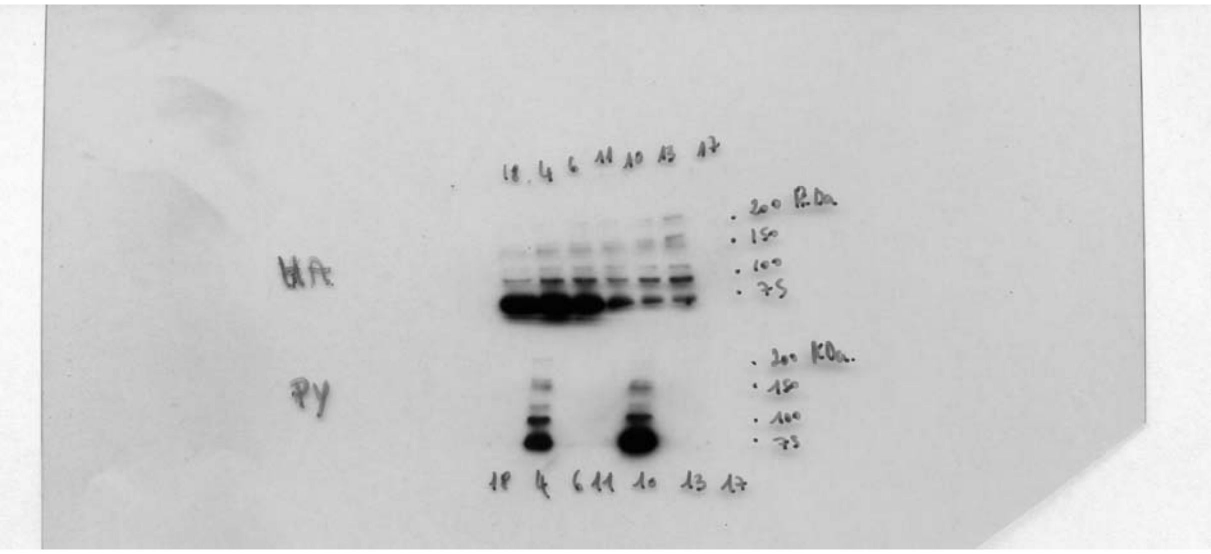
18 4 6 11 10 13 17
200 kDa
150
100
75
HA
200 kDa
150
100
75
PY
18 4 6 11 10 13 17

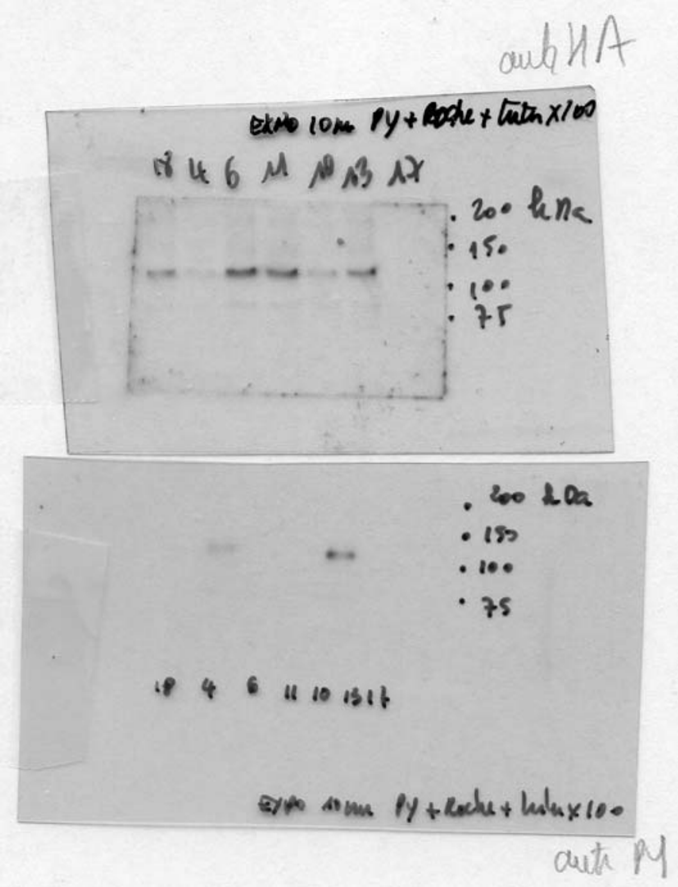
anti HA
Expo 10 min PY + Roche + Triton X100
18 4 6 11 10 13 17
200 kDa
150
100
75
200 kDa
150
100
75
18 4 6 11 10 13 17
Expo 10 min PY + Roche + Triton X100
anti PY

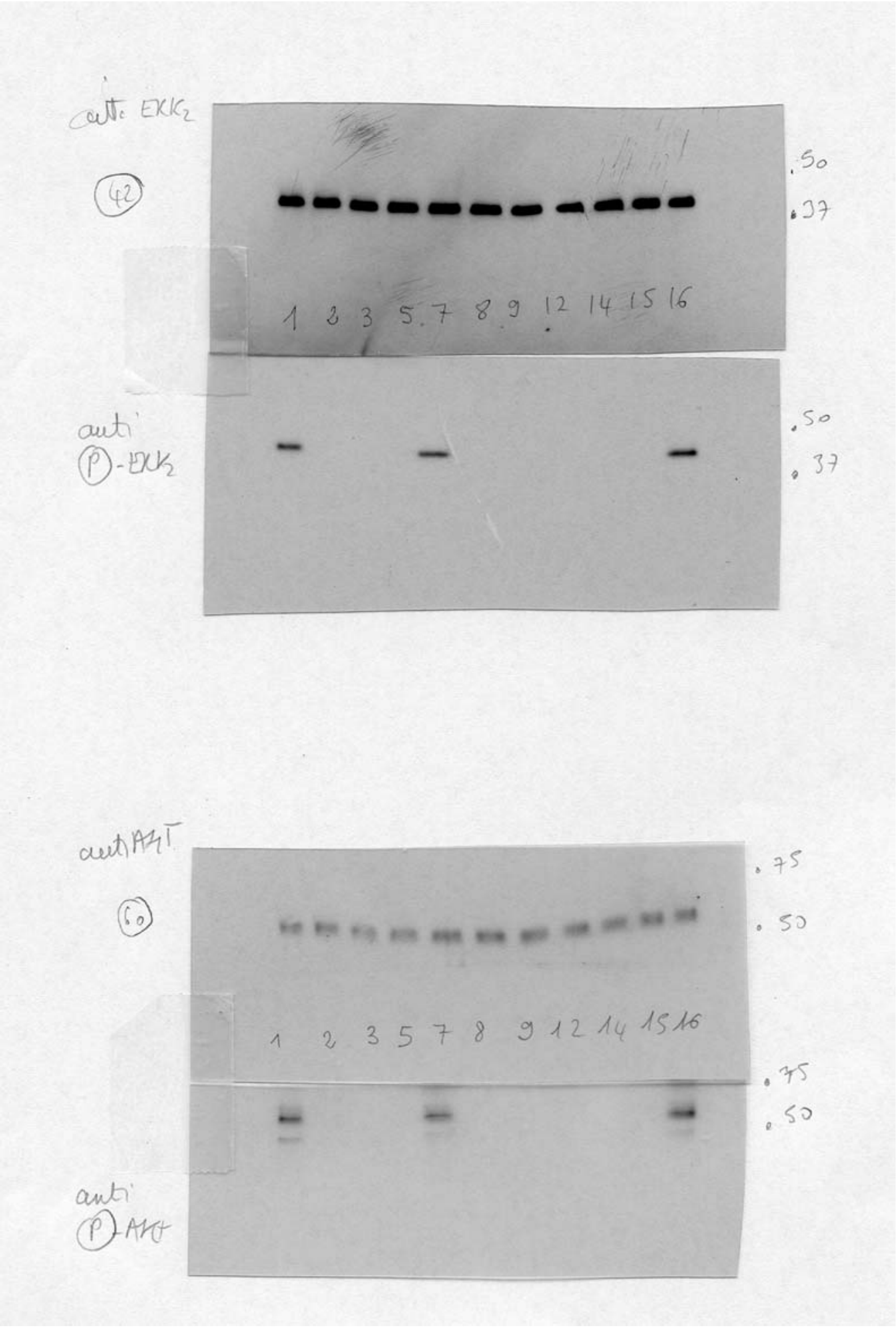
anti ERK2
42
.50
.37
1 2 3 5 7 8 9 12 14 15 16
anti
(P)-ERK2
.50
.37
anti AKT
60
.75
.50
1 2 3 5 7 8 9 12 14 15 16
.75
.50
anti
(P)-AKT

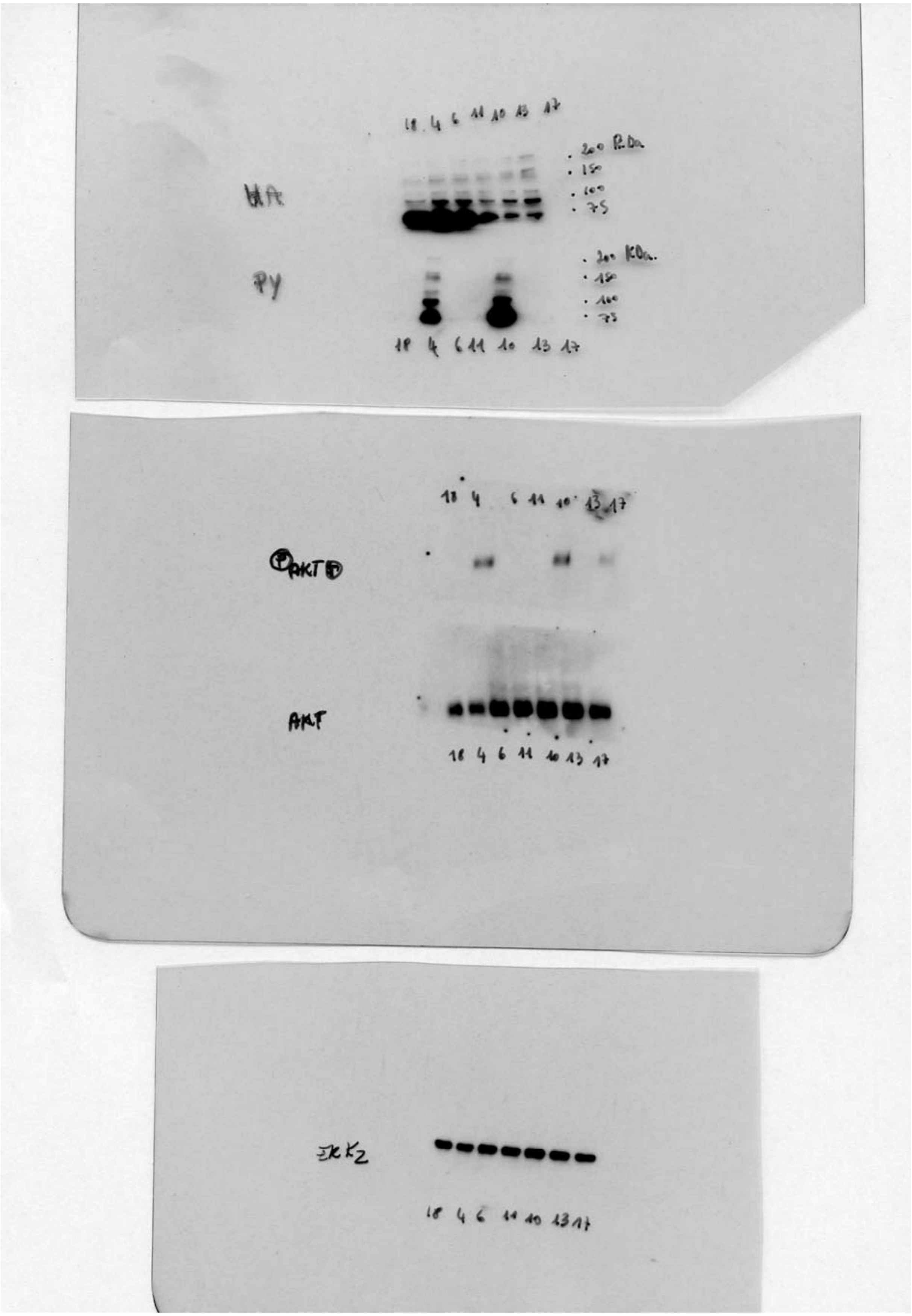
18 4 6 11 10 13 17
HA
200 kDa
150
100
75
Py
200 kDa
150
100
75
18 4 6 11 10 13 17
18 4 6 11 10 13 17
ⓅAKTⓅ
AKT
18 4 6 11 10 13 17
ERK2
18 4 6 11 10 13 17

Original Blots (November 2014):

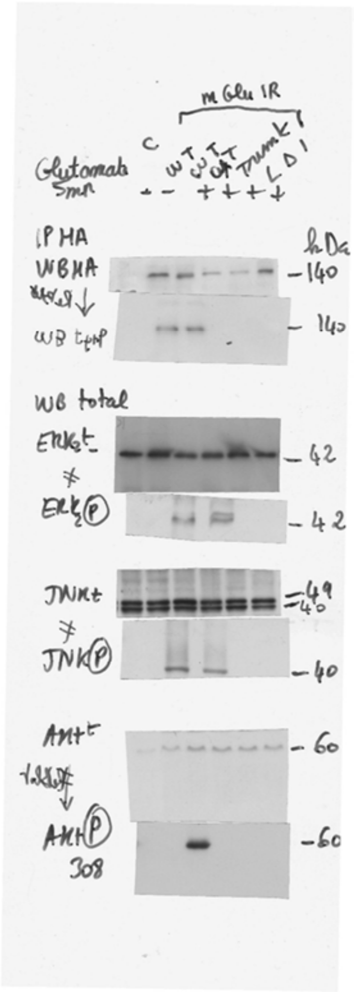

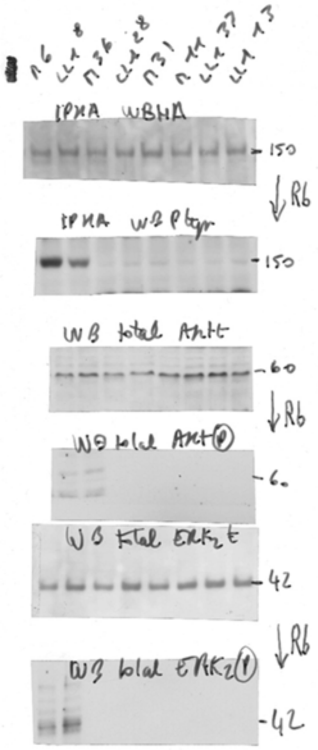

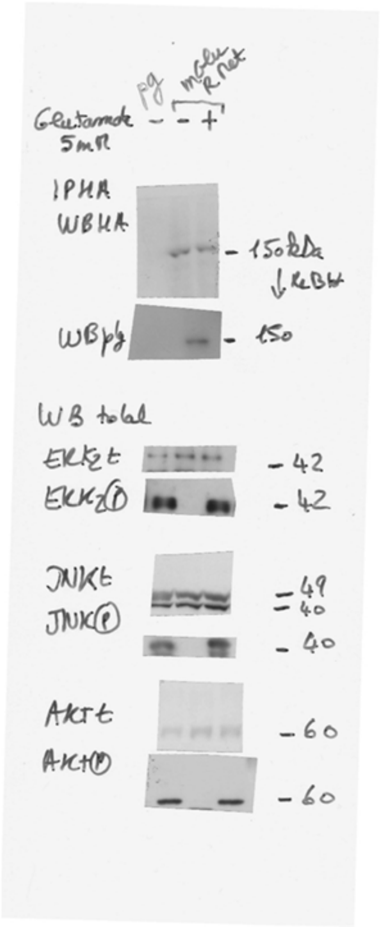

Original Blots (November 2016):

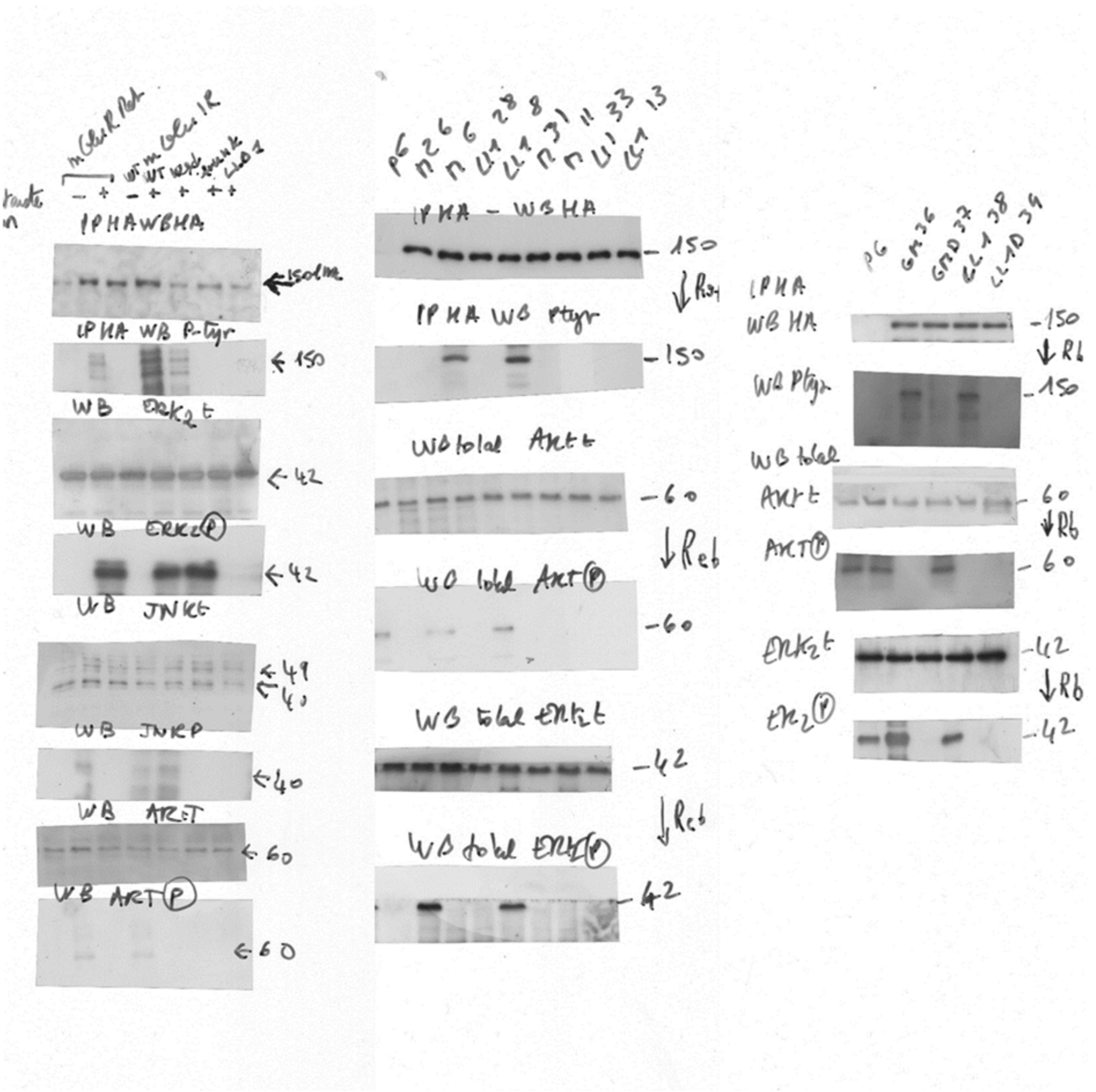

Cropped bots (spring 2016):

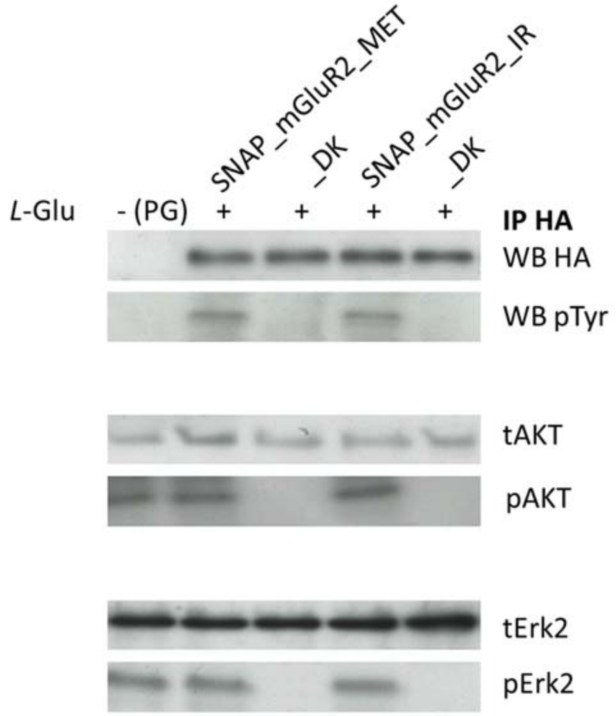

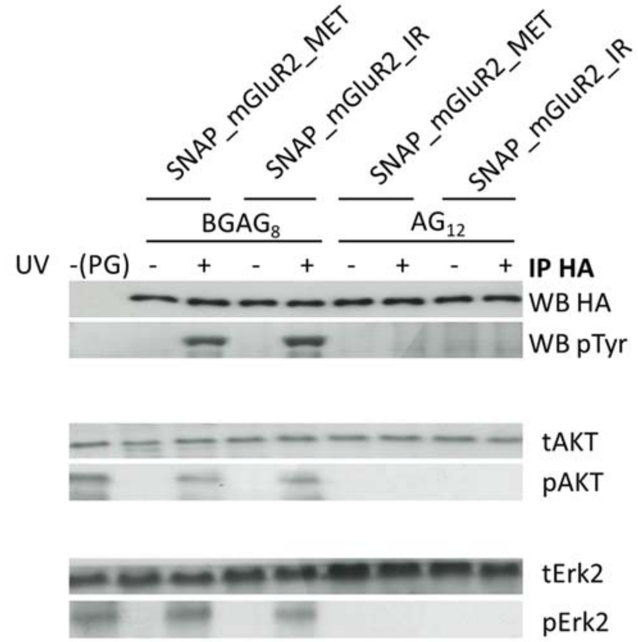

2.5.2 Western Blotting

Western blotting protocol:

• Cells were placed on ice, medium was removed and washed with cold PBS (2mL).

• Cell lysis buffer was prepared: 0.5 vol% phosphatase inhibitor (Sigma, #P5726-5ML) and 0.25 vol% protease (Sigma, #P8340) inhibitor were added to 100 μL cold RIPA-SDS buffer.

• Cell lysis buffer was added to the wells and the cells were scrubbed off and transferred to a 1.5 mL Eppendorf tube. The cell suspension was centrifuged (14000 rpm, 4 °C). The supernatant was transferred carefully to a new tube without disturbing the DNA pellet.

• For determination of protein concentrations, a BCA assay was performed using a BCA kit (ThermoScientific, #23225) on a colorimetric platereader (Thermo Scientific, MultiscanEX) according to the the manufacturer's instructions.

• For each sample 20-30 μg of protein was added to 7.5 μL of NuPAGE blue LDS sample buffer (4X, life technologies, #NP0007) and 3 μL Redox buffer (10X) and filled up to a total volume of 30 μL with ddH_2O. Samples were heated to 70 °C for 10 min prior to loading on a SDS-PAGE gel (4-12% NuPAGE Bis-Tris Plus Gel, life technologies, #BG04120BOX or #WG1401BOX). Electrophoresis was carried out at 80-180 V.

• Protein was transferred on a PVDF membrane (1.5-2 h, 55-65 V) before blocking the membrane with caseine blocking buffer for 30 min at r.t., then the primary antibody (usual dilution 1/1000 in recommended primary antibody buffer) was added and incubated at 4 °C overnight under agitation. The membrane was washed 5 times 5-10 min each with PBS (0.05% Tween-20) before the secondary antibody was added (1/30000 dilution in blocking buffer) and incubated at r.t. for 30-45 min under agitation. The membrane was washed 2 times, 5-10 min each, with PBS (0.05% Tween-20) and one time with cold PBS.

• After removal of washing buffer, the membrane was treated with chemiluminiscent substrate (Pico, Thermo Scientific, #34080 or Dura, Thermo Scientific, #34076F) according to the manufacturer's instructions. CL-XPosure X-ray film (Thermo Scientific, #OK196129) was exposed to luminiscence signal for a duration of 30 seconds to 20 minutes prior to development. Blots were scanned and processed with ImageJ for integration of signals.

• For incubation with a different primary antibody, the membrane was stripped with stripping

buffer (Gene Bio Application, #CST0100) and washed with 2 times with PBS (0.05% Tween-20) before repeating the above steps.

2.5.3 Supplementary Western Blots (cropped)

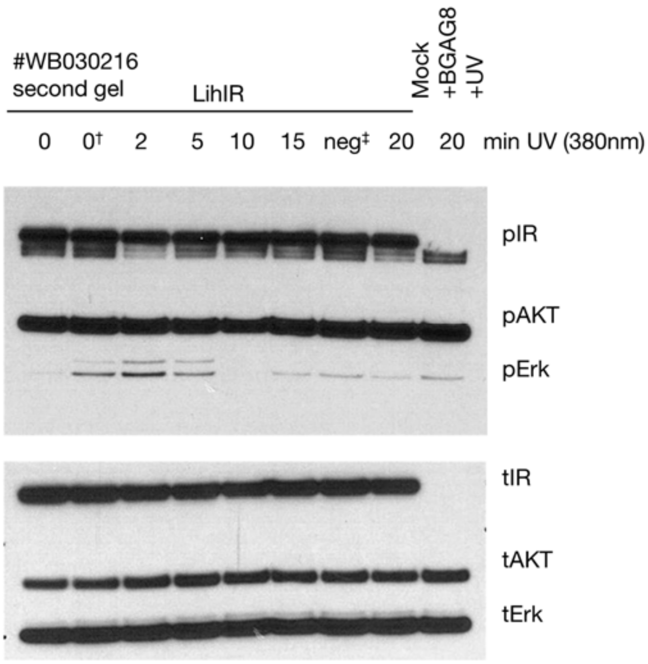

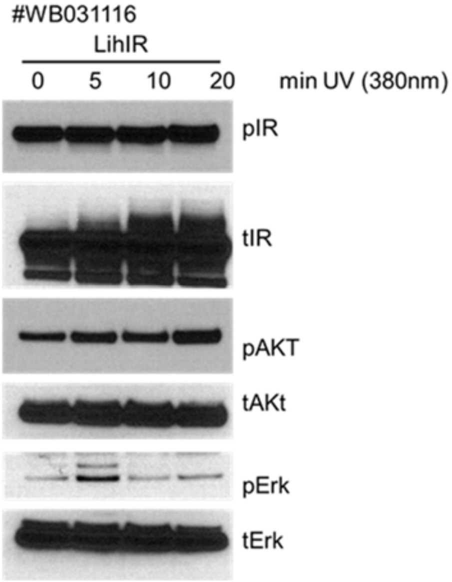

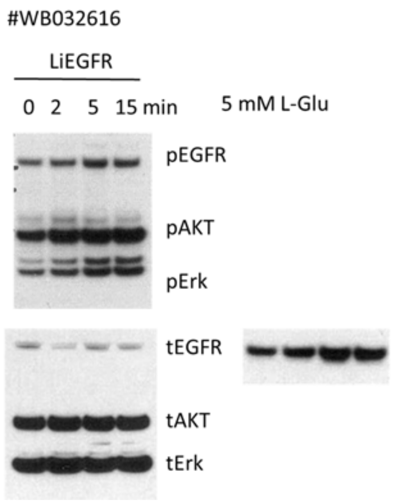
#WB032616
LiEGFR
0 2 5 15 min
5 mM L-Glu
pEGFR
pAKT
pErk
tEGFR
tAKT
tErk

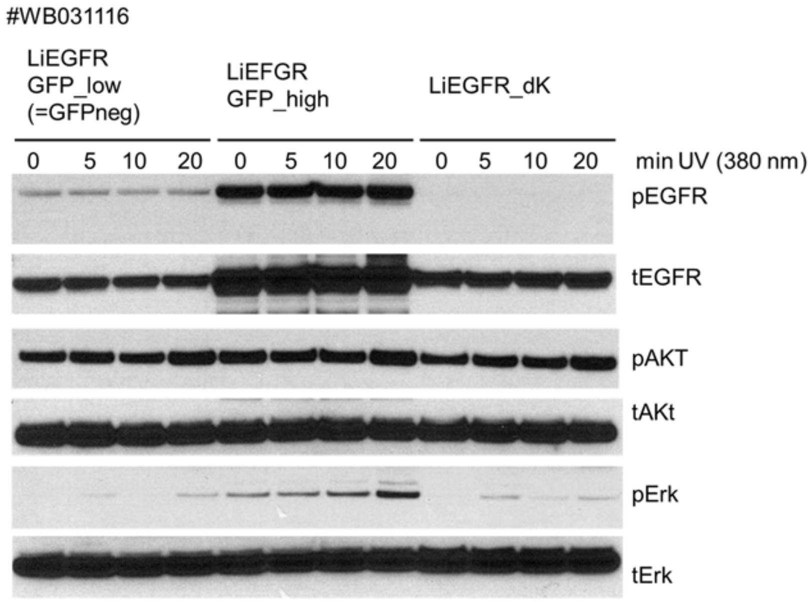
#WB031116
LiEGFR GFP_low (=GFPneg)
LiEFGR GFP_high
LiEGFR_dK
0 5 10 20 0 5 10 20 0 5 10 20
min UV (380 nm)
pEGFR
tEGFR
pAKT
tAKt
pErk
tErk

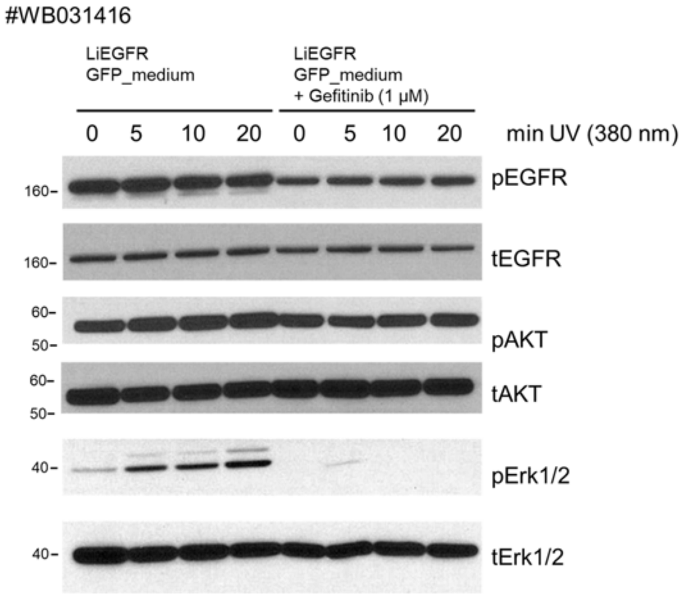

2.5.4 Supporting Contraction Timelapse Videos

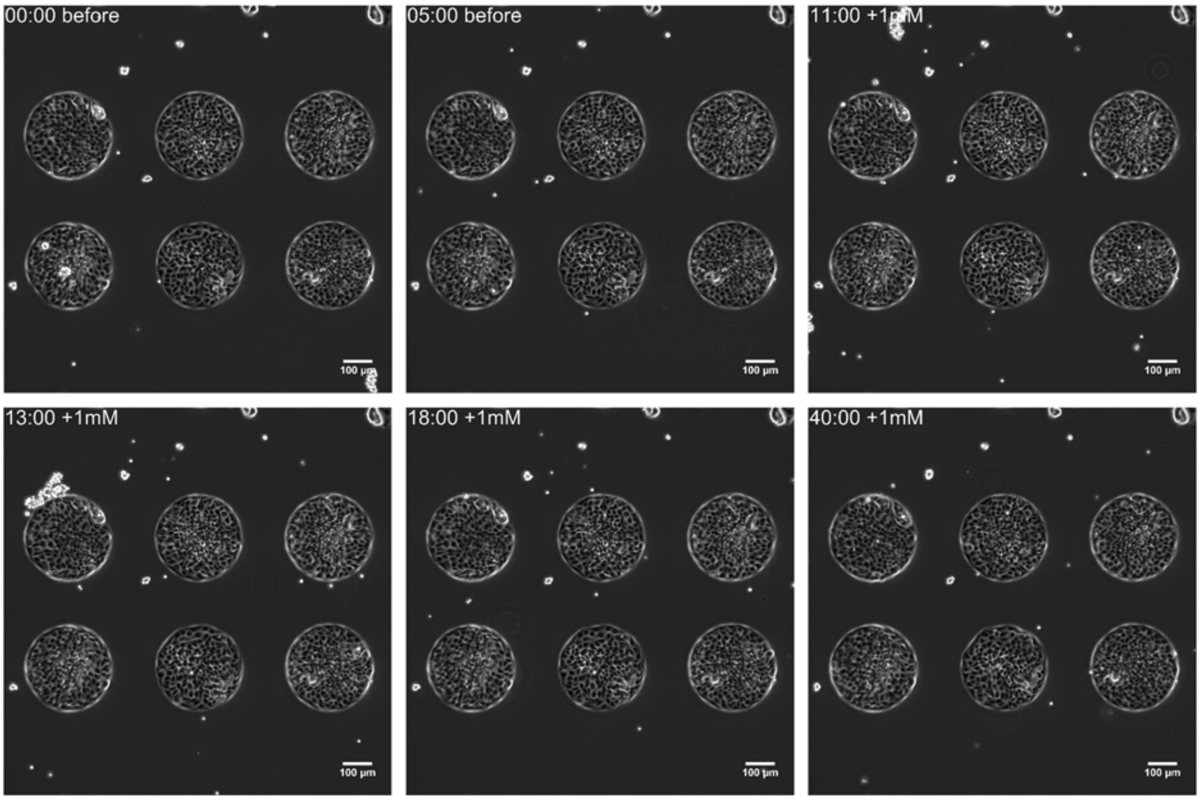

Supporting figure: MDCK-II mock cells (non-transfected). L-Glu (1 mM) was added at t = 10 min.

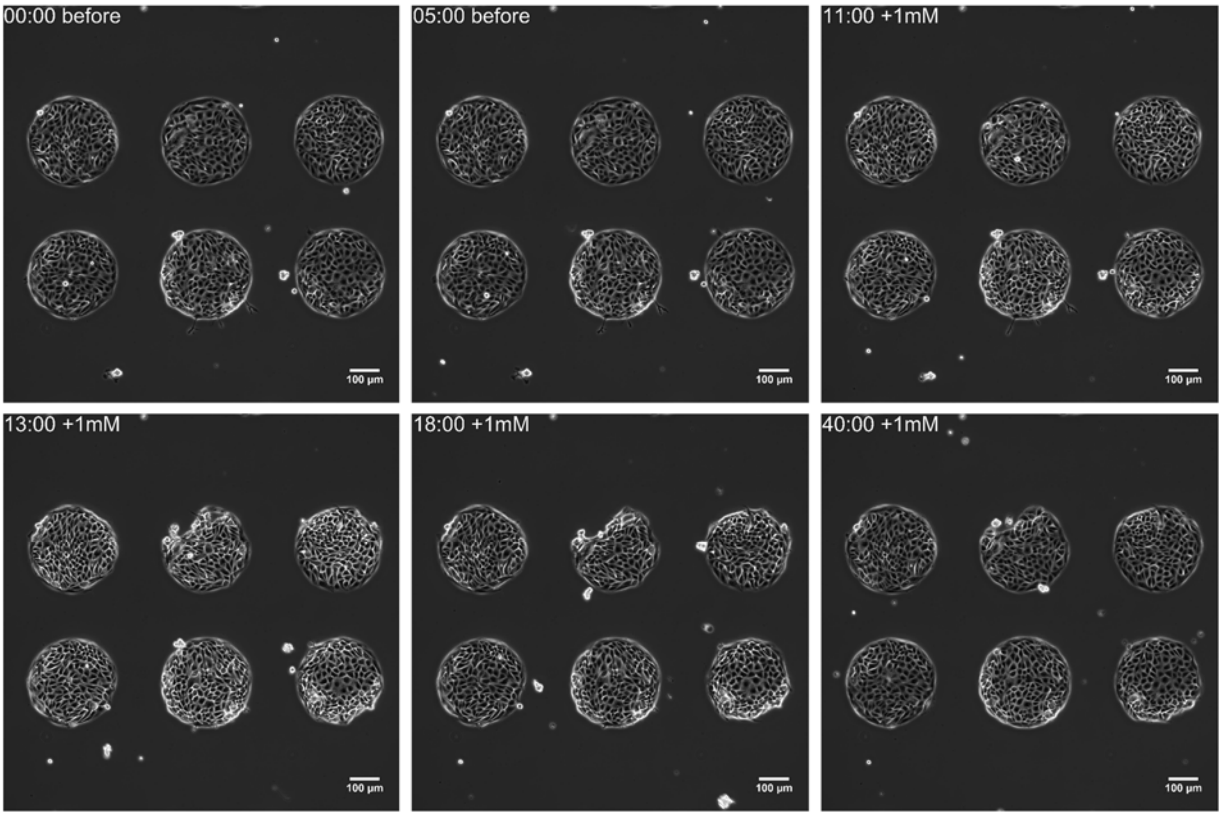

Supporting figure: MDCK-II/LiEGFR_LBD (low-affinity mutant). L-Glu (1 mM) was added at t = 10 min.

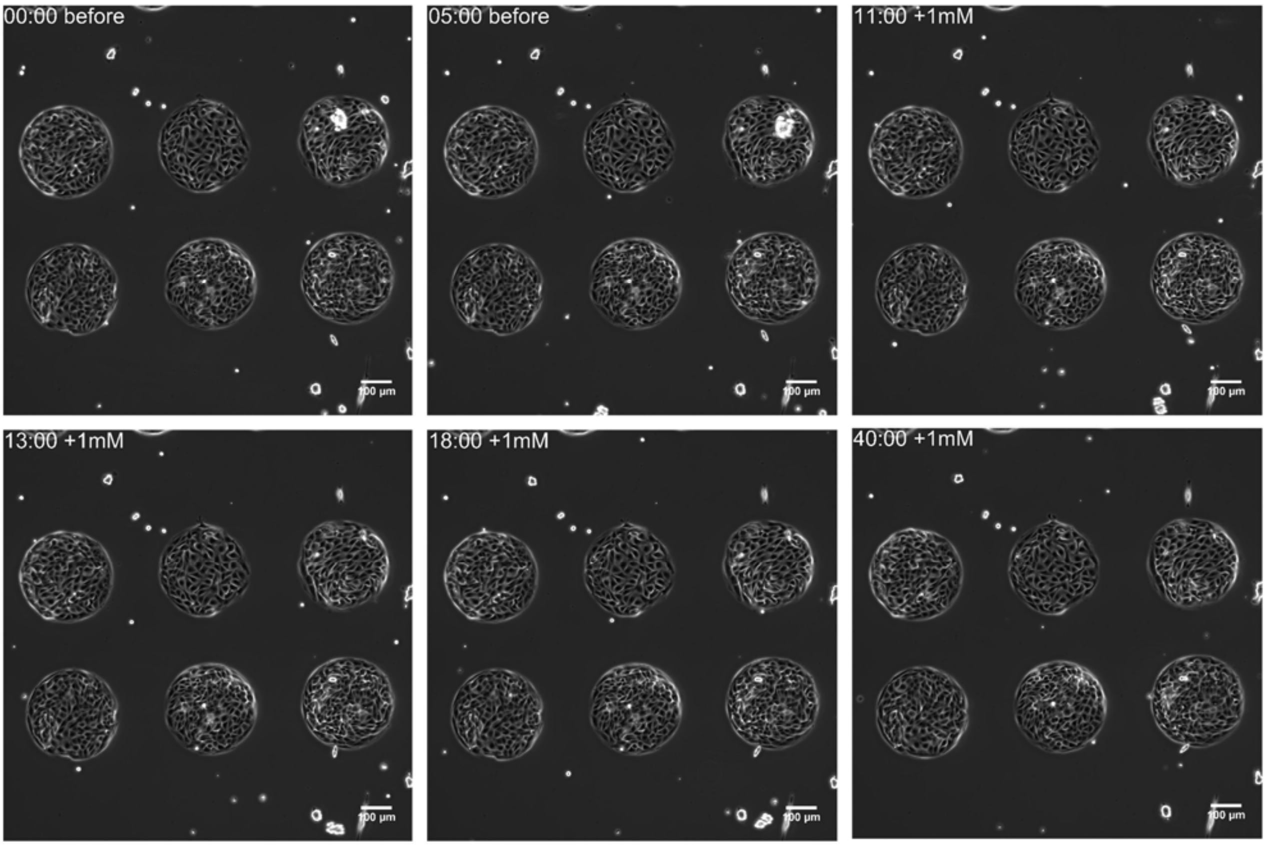

Supporting figure: MDCK-II/LiEGFR_dk (dead-kinase mutant). L-Glu (1 mM) was added at t = 10 min.

2.5.5 Plasmid Maps and DNA Sequences

2.5.5.1 LihIR

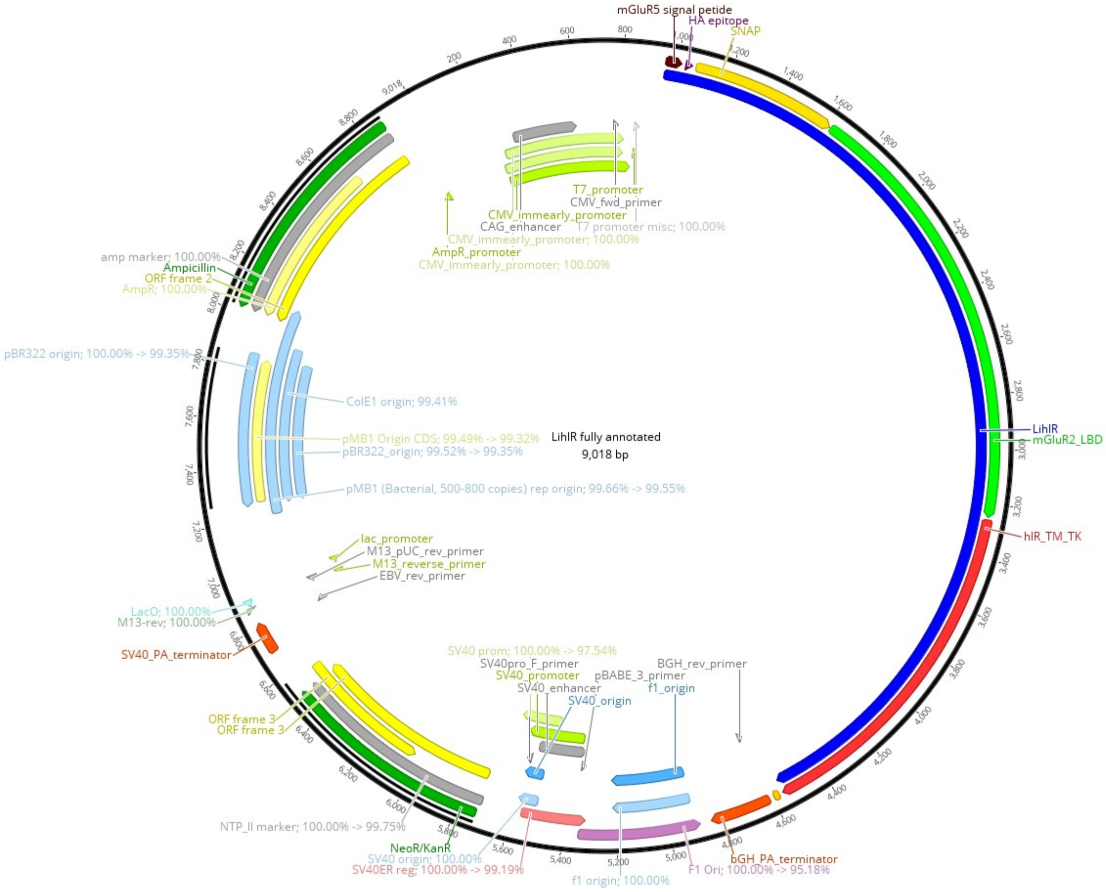

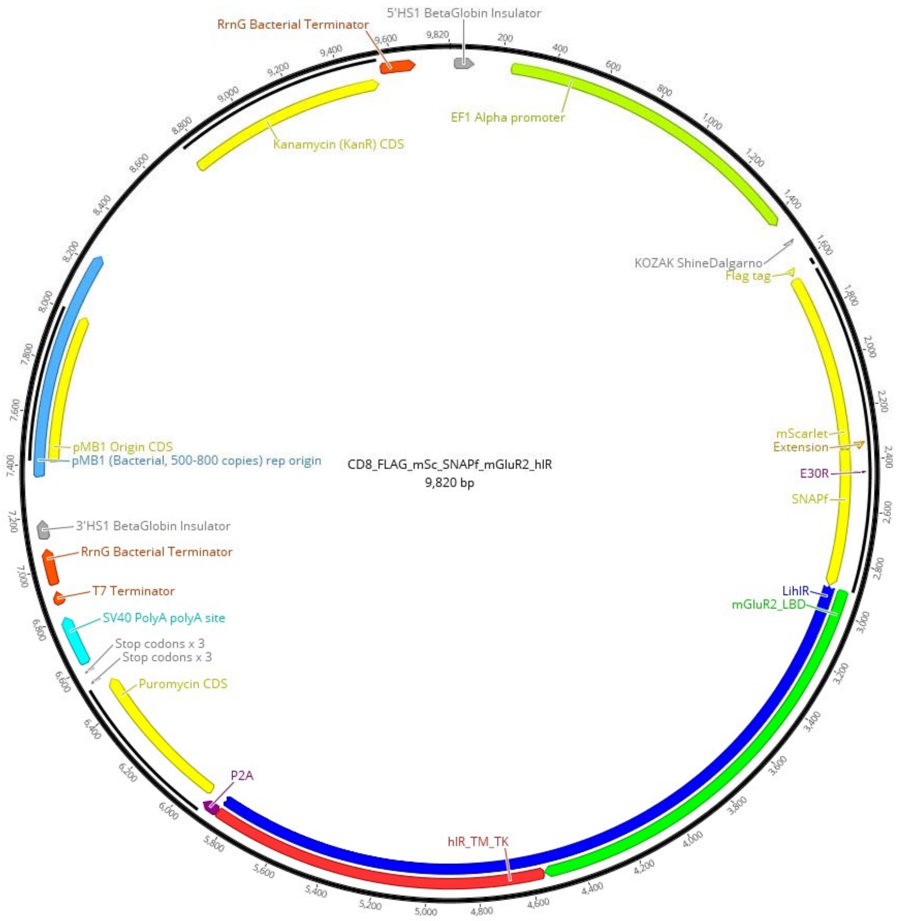
5'HS1 BetaGlobin Insulator
RrnG Bacterial Terminator
EF1 Alpha promoter
Kanamycin (KanR) CDS
KOZAK ShineDalgarno
Flag tag
mScarlet
Extension
E30R
SNAPf
LihIR
mGluR2_LBD
hIR_TM_TK
P2A
Puromycin CDS
Stop codons x 3
Stop codons x 3
SV40 PolyA polyA site
T7 Terminator
RrnG Bacterial Terminator
3'HS1 BetaGlobin Insulator
pMB1 Origin CDS
pMB1 (Bacterial, 500-800 copies) rep origin
CD8_FLAG_mSc_SNAPf_mGluR2_hIR
9,820 bp
9,820
200
400
600
800
1,000
1,200
1,400
1,600
1,800
2,000
2,200
2,400
2,600
2,800
3,000
3,200
3,400
3,600
3,800
4,000
4,200
4,400
4,600
4,800
5,000
5,200
5,400
5,600
5,800
6,000
6,200
6,400
6,600
6,800
7,000
7,200
7,400
7,600
7,800
8,000
8,200
8,400
8,600
8,800
9,000
9,200
9,400
9,600

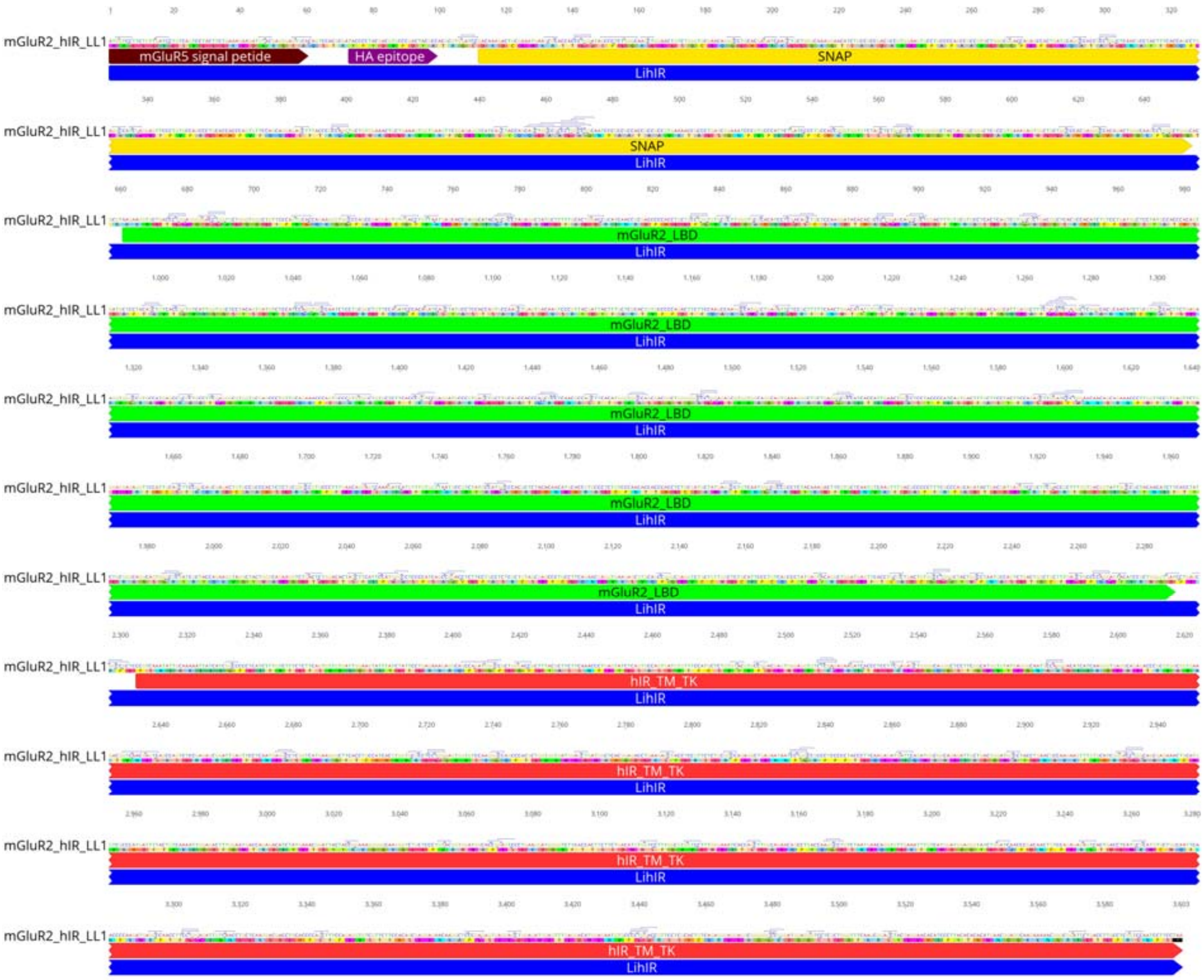
mGluR2_hIR_LL1
mGluR5 signal petide
HA epitope
SNAP
LihIR
mGluR2_LBD
hIR_TM_TK

2.5.5.2 LiMet


mGluR2-MET.xdna
mGluR5 signal petide; 100.00%
HA epitope; 100.00%
SNAP; 100.00%
mGluR2_LBD; 100.00%
MET_TK_TM; 100.00%

2.5.5.3 LiEGFR

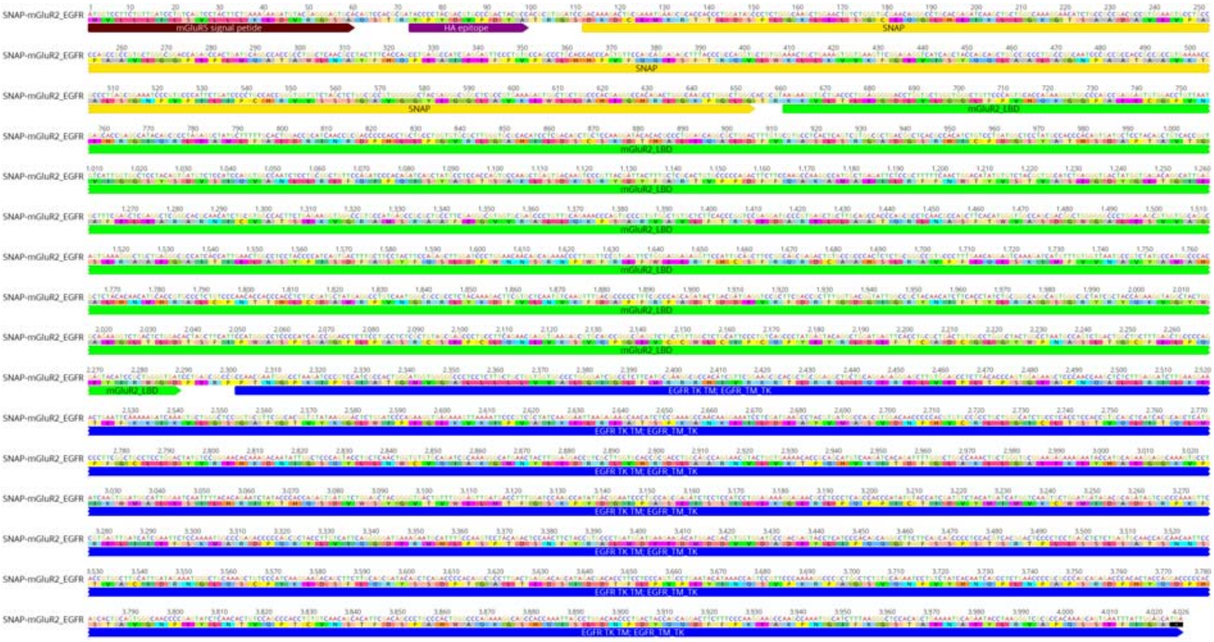
SNAP-mGluR2_EGFR
mGluR5 signal petide
HA epitope
SNAP
mGluR2_LBD
EGFR TK TM; EGFR_TM_TK

2.5.5.4 KTR-Erk_mScarlet

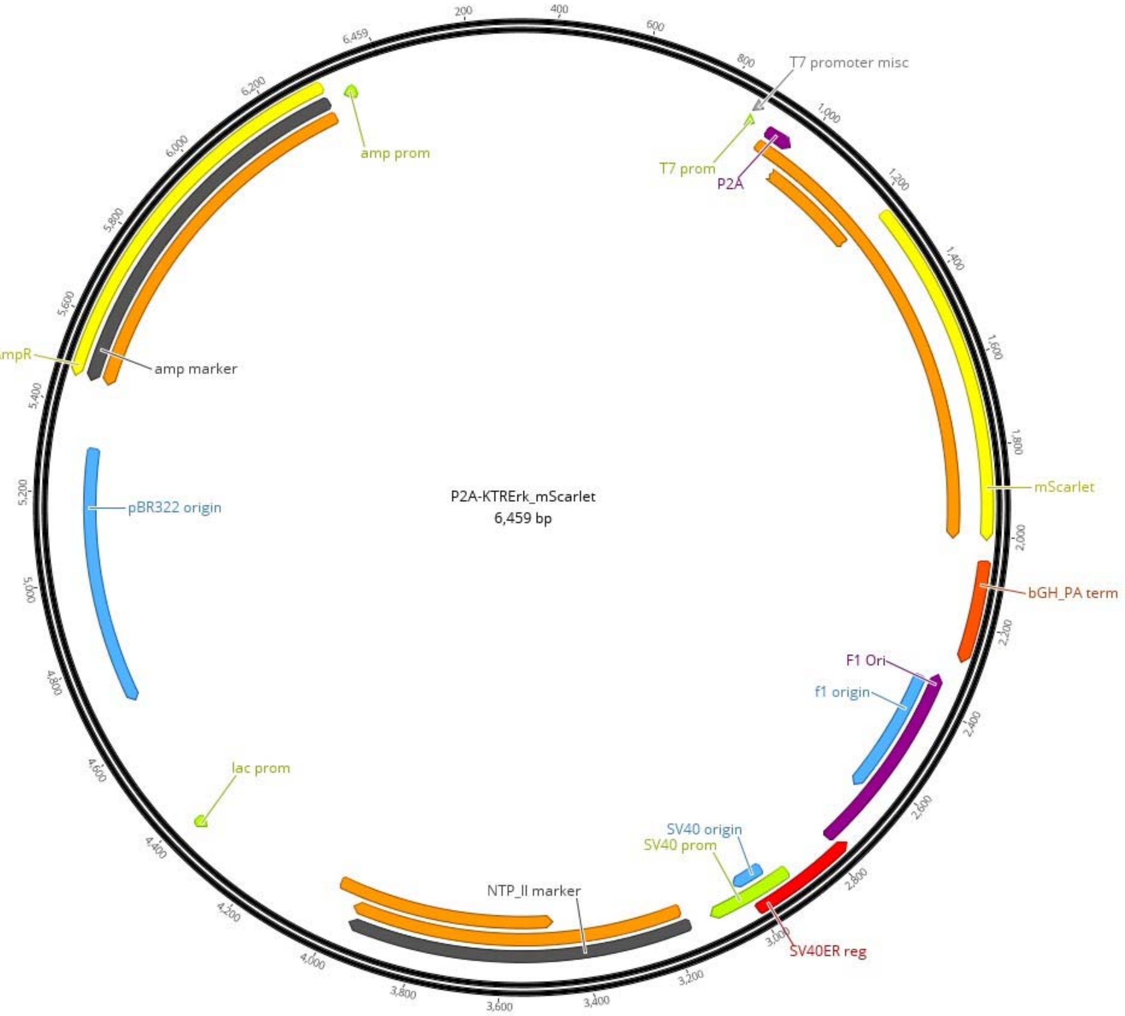

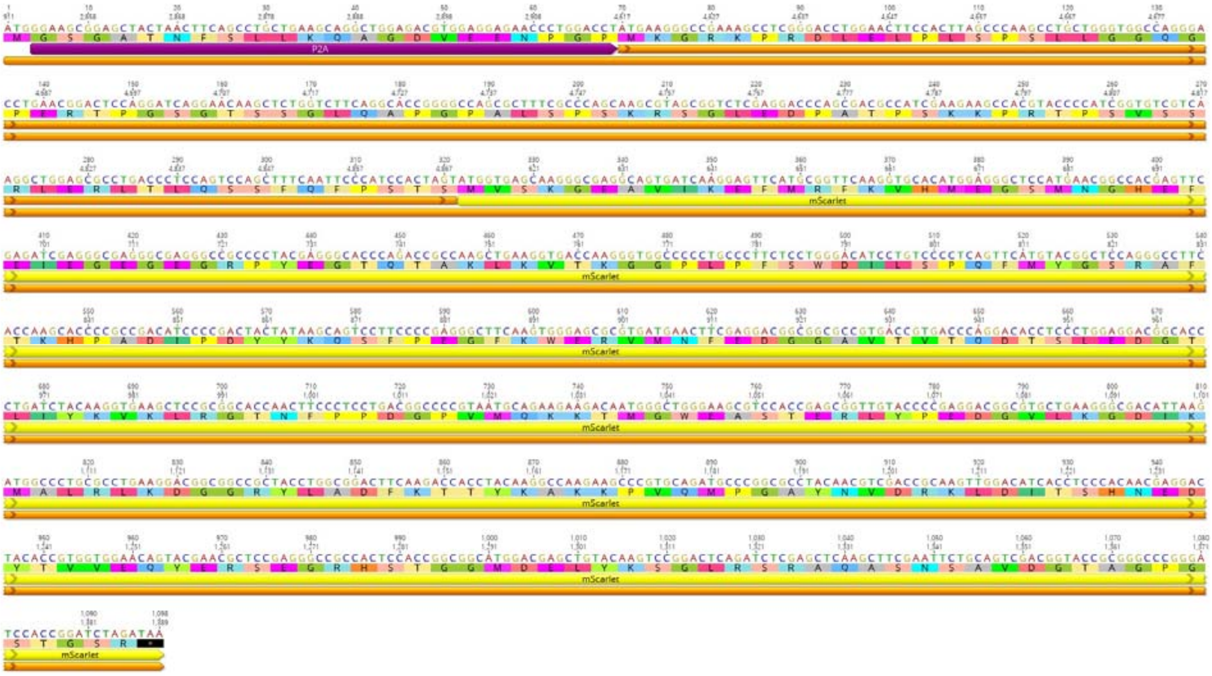

```
ATGGGAAGCGGAGCTACTAACTTCAGCCTGCTGAAGCAGGCTGGAGACGTGGAGGAGAACCCTGGACCTATGAAGGGCCGAAAGCCTCGGGACCTGGAACTTCCACTTAGCCCAAGCCTGCTGGGTGGCCAGGGA
CCTGAACGGACTCCAGGATCAGGAACAAGCTCTGGTCTTCAGGCACCGGGGCCAGCGCTTTCGCCCAGCAAGCGTAGCGGTCTCGAGGACCCAGCGACGCCATCGAAGAAGCCACGTACCCCATCGGTGTCGTCA
AGGCTGGAGCGCCTGACCCTCCAGTCCAGCTTTCAATTCCCATCCACTAGTATGGTGAGCAAGGGCGAGGCAGTGATCAAGGAGTTCATGCGGTTCAAGGTGCACATGGAGGGCTCCATGAACGGCCACGAGTTC
GAGATCGAGGGCGAGGGCGAGGGCCGCCCCTACGAGGGCACCCAGACCGCCAAGCTGAAGGTGACCAAGGGTGGCCCCCTGCCCTTCTCCTGGGACATCCTGTCCCCTCAGTTCATGTACGGCTCCAGGGCCTTC
ACCAAGCACCCCGCCGACATCCCCGACTACTATAAGCAGTCCTTCCCCGAGGGCTTCAAGTGGGAGCGCGTGATGAACTTCGAGGACGGCGGCGCCGTGACCGTGACCCAGGACACCTCCCTGGAGGACGGCACC
CTGATCTACAAGGTGAAGCTCCGCGGCACCAACTTCCCTCCTGACGGCCCCGTAATGCAGAAGAAGACAATGGGCTGGGAAGCGTCCACCGAGCGGTTGTACCCCGAGGACGGCGTGCTGAAGGGCGACATTAAG
ATGGCCCTGCGCCTGAAGGACGGCGGCCGCTACCTGGCGGACTTCAAGACCACCTACAAGGCCAAGAAGCCCGTGCAGATGCCCGGCGCCTACAACGTCGACCGCAAGTTGGACATCACCTCCCACAACGAGGAC
TACACCGTGGTGGAACAGTACGAACGCTCCGAGGGCCGCCACTCCACCGGCGGCATGGACGAGCTGTACAAGTCCGGACTCAGATCTCGAGCTCAAGCTTCGAATTCTGCAGTCGACGGTACCGCGGGCCCGGGA
TCCACCGGATCTAGATAA
```

2.5.6 Fluorescent Erk reporters

To take full advantage of the spatiotemporal precision that a light-activatable LiRTKs offer, the experimental setup has to be performed so that both light-stimulation as well as the downstream readout can be performed with a resolution of milliseconds to minutes. To this end, a downstream Erk readout could be employed, more specifically 'kinase translocation reporters' (KTRs).[68,69] These consist of a fluorescent protein (FP) fused to a combined nuclear localization and nuclear export sequence (NLS and NES). The NLS/NES sequence is engineered to be a substrate for the Erk kinase, and is phosphorylated upon Erk activation in such a way that the KTR construct is exported from the nucleus into the cytosol. This enables real-time measurement of Erk activity by following the ratio of FP between the nucleus and the cytosol. The available, published KTR-Erk reporters are not compatible with the LiRTKs because they are fluorescent at wavelengths that are required for the activation/deactivation of the LiRTKs. Therefore, a KTR-Erk sensor was cloned utilizing the monomeric, bright FP 'mScarlet' with maximum absorbance at 569 nm, which is red-shifted enough to allow for orthogonal ON/OFF photoswitching of the LiRTKs.[70]

The advanced, fully-motorized DMi8 inverted wide field microscope (Leica) is an attractive platform for these experiments. It allows automatization of the protocols for light stimulation and readout, and at the same time allows the light to be applied only to a part of the dish, to demonstrated the spatial features of light activation. Complex, customized protocols can be easily programmed, *e.g.* light stimulation for N seconds on position XYZ is followed by a fluorescent readout at time M.

To validate the KTR-Erk Sensor, it was transiently transfected in Hela cells and saturating insulin was added. Indeed, the translocation of KTR-Erk_mScarlet out of the nucleus could be followed in real-time peaking at 16 min, which normalized to baseline levels 30 minutes post-stimulation (Figure 15).

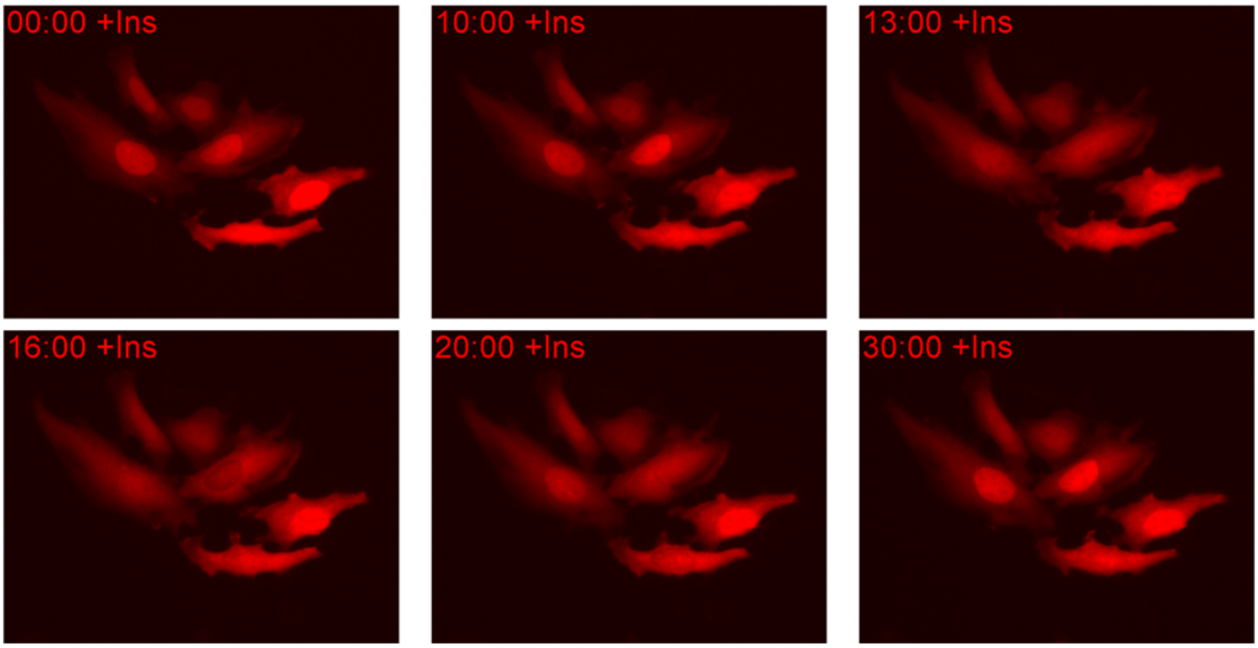

Figure 15. **Hela cells transfected with KTR-Erk_mScarlet and stimulated with insulin.** Several time points are depicted (minutes).

2.5.7 Compounds

Detailed experimental procedures for the synthesis of all employed photoswitches are described in:

Broichhagen, J., Damijonaitis, A., Levitz, J., Sokol, K.R., Leippe, P., Konrad, D., Isacoff, E.Y., Trauner, D., 2015. Orthogonal Optical Control of a G Protein-Coupled Receptor with a SNAP-Tethered Photochromic Ligand. ACS Cent. Sci. 1, 383–393.

3 Optical Control of Potassium Channels

3.1 Introduction

Neurons are excitable cells that generate electrical signals, called action potentials. Upon receiving information, they propagate these signals along their cell body and transmit them to other neurons by synaptic transmission.

Action potentials are primarily shaped by two components: a transient inward current of Na$^+$ ions and a delayed outward current of K$^+$ ions. When a neuron is depolarized from its resting potential (around -70 mV) to threshold potentials (around -50 mV) by a cationic neurotransmitter-gated channel (*e.g.* AMPA), voltage-gated Na$^+$ (Na$_v$) channels open (Figure 16). This causes a rapid and transient inward flow of Na$^+$ ions along their concentration gradient, resulting in a sudden further depolarization of the membrane. The depolarization induces a delayed opening of voltage-gated K$^+$ (K$_v$) channels. K$^+$ ions then flow outwards, since K$^+$ ion concentration is higher inside than outside of the cell. The efflux of K$^+$ repolarizes and resets the membrane potential to its resting value and primes the neuron for a new action potential.

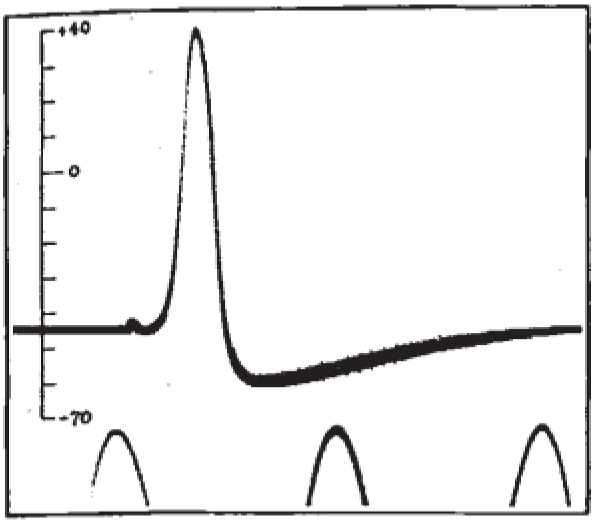

Figure 16. **The first recorded action potential from Hodgkin and Huxley in 1939.**[71] The action potential was recorded between the in- and outside of a giant axon from squids.

Action potentials are at the heart of neuronal signal transduction and the interplay between many neurons connected to networks and circuits in the brain is the foundation of animal behavior. To sculpt the circuitries' responses to input signals, action potentials come in many shapes and frequencies. Contributing to that diversity in excitability, K$^+$ channels exhibit a broad variety of gating properties. This is manifested in the large number of different K$^+$ channel subtypes expressed in neurons. In total, four families encode a total of 78 K$^+$ channel subtypes:

voltage-gated (K_V), two-pore domain (K_{2P}), Ca^{2+}-activated (K_{Ca}) and inwardly-rectifying (K_{ir}). The largest family, K_v channels, counting 40 different genes in the human genome.[72] K^+ channels constitute important drug targets for a variety of diseases, not only in the CNS but also for metabolic or autoimmune disorders. Unfortunately, it has been difficult to target K^+ channels in a subtype-selective manner with traditional pharmacology, since most K^+ channel modulators interact with the pore region, a region with high sequence homology among subtypes. Due to this absence of selective openers or blockers, the target identification of K^+ channels has largely been limited to information obtained from genetic diseases or rodent knockout models, greatly slowing down ion channel drug discovery.[73]

The physiological action of K^+ channels takes place on a millisecond timescale. Therefore, tools that allow perturbation of K^+ channels on this timescale are highly useful, such as photoswitchable channel blockers. In 2004, Trauner, Kramer and Isacoff described such a photoswitchable blocker for the Shaker K^+ channel.[14] These blockers are based on tetraethylammonium (TEA), a quaternary ammonium (QA) and an unselective blocker of K^+ channels. TEA was modified with a photoswitchable azobenzene and this enabled optical control over Shaker channel gating and allowed for remote control of neuronal firing by light in neurons. These compounds based on QAs, such as MAQ,[14] AAQ[74] and DENAQ[75] have shown great promise in the field of vision restoration (Figure 18a). In particular, DENAQ confers light-sensitivity to degenerated retinae from blind mice and is a potential treatment for eye diseases, *e.g.* retinitis pigmentosa and age-related macular degeneration.[75] These compounds primarily act through intracellular block of the TEA binding site of K^+ channels and are use-dependent, open-state blockers.[6] Despite their potential, one drawback has been their low target affinity with effective concentrations in the high micromolar to single-digit millimolar range.[6] This is presumably due to their permanent charge, which prevents these molecules from efficiently crossing the cell membrane to reach their site of action. While this issue is partly compensated for by uptake through pore channels such as P2X7, the comparatively low potency remains a challenging issue.[76] In the first part of the chapter, this matter is overcome with the design, synthesis and electrophysiological characterization of an improved series of photoswitchable channel blockers based on the non-charged local anesthetic bupivacaine (Chapter 3.2.1).

One way to furnish photoswitchable blockers with target specificity for a K^+ channel subtype could lie in the fusion of small-molecule drugs with antibodies. The field of antibody-drug conjugates (ADCs) was mostly pioneered in cancer therapy. There, conjugation of cytotoxic drugs to antibodies that recognize specific markers on cancer cells allow drugs to be targeted to specific populations, without harming the healthy surrounding tissue. These advances culminated in FDA approvals for drugs like trastuzumab emtansine (Kadcycla®), which has shown efficacy in HER2 positive breast cancer. Fueled by these successes, the requisite chemistry of antibody-drug conjugates (ADCs) has been refined to a satisfying degree of sophistication over the last decade.[40] We envisioned that by attaching a photoswitchable K^+ channel blocker to an antibody, we could photoswitch endogenous K^+ channels with subtype specificity. K_v channels are mostly buried in the membrane with only the loop between transmembrane helices S1 and S2 accessible from the extracellular side (Figure 17a). In the second chapter, we describe the synthesis of antibody-photoswitch conjugates (APCs) targeting the S1-S2 loop of $K_v1.1$ and $K_v2.1$ and their electrophysiological characterization (Chapter 3.2.2).

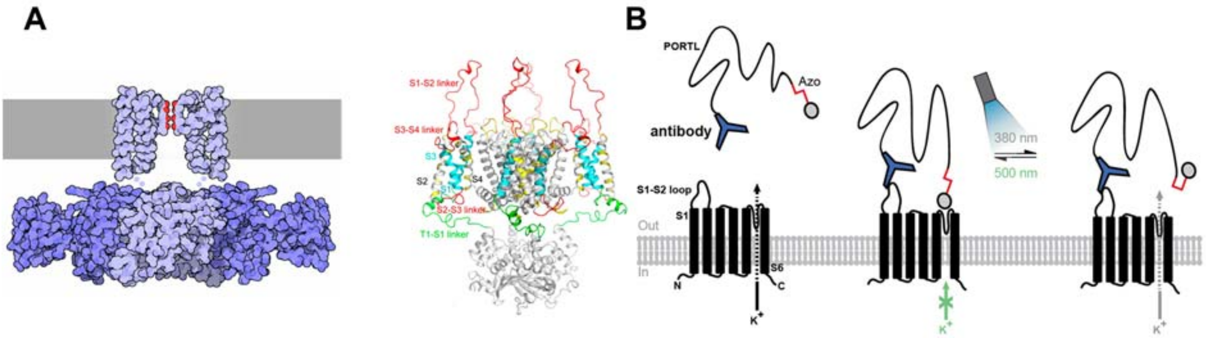

Figure 17. **Concept of antibody-photoswitch conjugates a)** left: Scheme based on the bacterial MthK, adapted from David Goodsell[77] right: Shaker K^+ structure **b)** A photochromic blocker is tethered to an antibody. The antibody binds to the exposed S1-S2-loop allowing the remotely attached photochromic blocker to light-gate the channel.

3.2 Results and Discussion

3.2.1 Photochromic Blockers Based on Bupivacaine

One strategy to equip drugs with light-sensitivity is termed 'azo-extension'.[78] In this approach, furnishing drugs with a photoswitch is achieved by identifying positions in their chemical structure where modification changes the biological activity but where the modification is not completely deleterious. After functionalizing that position with a photoswitch, it is likely that photoisomerization leads to light-dependent change in biological activity. Accordingly, we envisioned to install an azobenzene in the *para*-position of the pipecolic amide of bupivacaine (Figure 18b). Isomerization of the azobenzene from its *cis*- to its *trans*-configuration by light should then change the PCLs efficacy and/or affinity to the K^+ channel, enabling optical control over K^+ currents (Figure 18c). It should be noted that bupivacaine contains an asymmetric carbon but is sold and used as a racemic mixture. Therefore, the synthesis was planned without stereoselectivity and in a modular fashion to yield a short series of three azobupivacaines **AB1-3** bearing different substituents on the azobenzene to finetune switching wavelengths and photswitching kinetics.

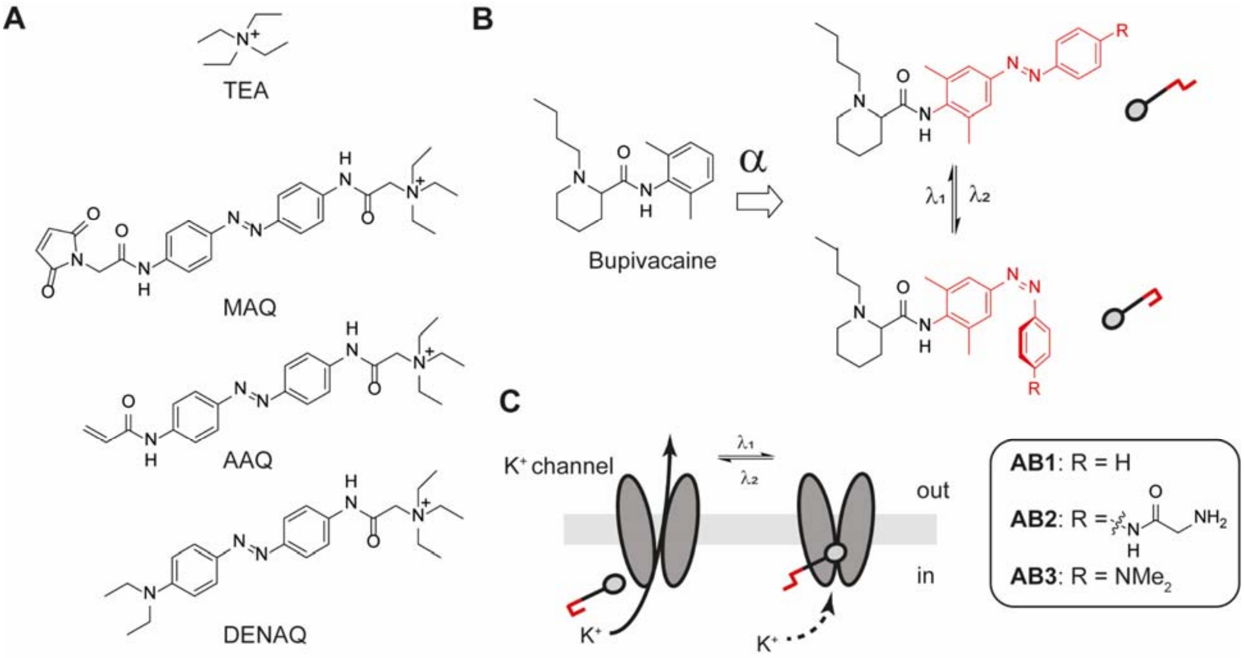

Figure 18. **Logic and design of photoswitchable azobupivacaines AB1-3**. **a)** Photoswitchable blockers based on TEA. **b)** 'Azo-extension' strategy of azobupivacaines. **c)** Azobupivacaines **AB1-3** block channels in one configuration while allow ion flow in the other.

The synthesis of **AB1-3** commenced with acyl chloride formation of pipecolic acid (**1**) followed by amide bond formation with 4-bromo-2,6-dimethylaniline to give pipecholyl xylidine **2**. Direct treatment of **2** with *n*-butylbromide furnished tertiary amine **3** in fair overall yields (Scheme 1). Pd-catalyzed amination of **3** using LiHMDS as the nitrogen source, followed by direct deprotection of the silyl groups furnished aniline **4** as the common precursor for further derivatization. **AB1** was then accessed by a Baeyer-Mills reaction of **4** with nitrosobenzene. Treatment of **4** with *t*-BuONO followed by trapping of the resultant diazonium ion with *N,N*-dimethylaniline furnished **AB3** in moderate yields. Aniline **6** was obtained from **4** after Baeyer-Mills reaction with 4-nitronitrosobenzene followed by reduction of the nitro group using sodium sulfite. Amide bond formation of **6** with chloroacetyl chloride, followed by a Finkelstein reaction and careful substitution with ammonia furnished **AB2** in good overall yields.

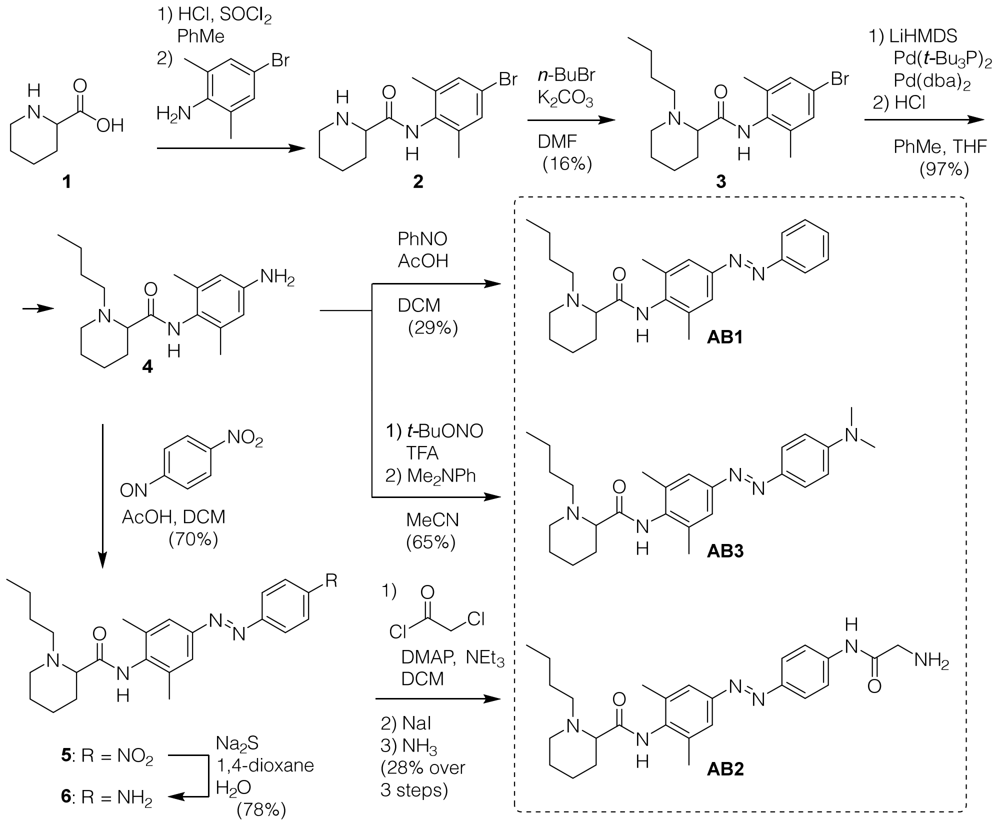

Scheme 1: **Synthesis of AB1-3.**

Next, the photoswitching properties of **AB1-3** were evaluated by means of UV/Vis spectroscopy. The optimal wavelengths for *cis*-to-*trans* isomerization were determined in a wavelength-screen by changing the illumination wavelength while looking at minimal/maximal extinction at the absorbance maximum near the π-π^* transition, as described previously.[79] UV/Vis spectra of **AB1-3** were then recorded under illumination of these optimal switching wavelengths (Figure 19, upper panels; **AB1**: λ_{cis} = 360 nm (light gray), λ_{trans} = 420 nm (violet); **AB2**: λ_{cis} = 380 nm (dark gray), λ_{trans} = 500 nm (green); **AB3**: λ_{cis} = 460 nm (blue); no illumination is black in all cases. Both **AB1** and **AB2** exhibit bistable behavior, *e.g.* slow thermal relaxation back to the *trans*-isomer in the dark (Figure 19, lower panel). This is an advantageous property in photoswitches since it allows to switch using a short bout of light as opposed to constant illumination. **AB3** is red-shifted and exhibits fast thermal relaxation in the dark. Red-shifting can be beneficial in applications such as vision restoration, where a quick turn-off in the dark is required. In addition, longer-wavelength light allows deeper tissue penetration.

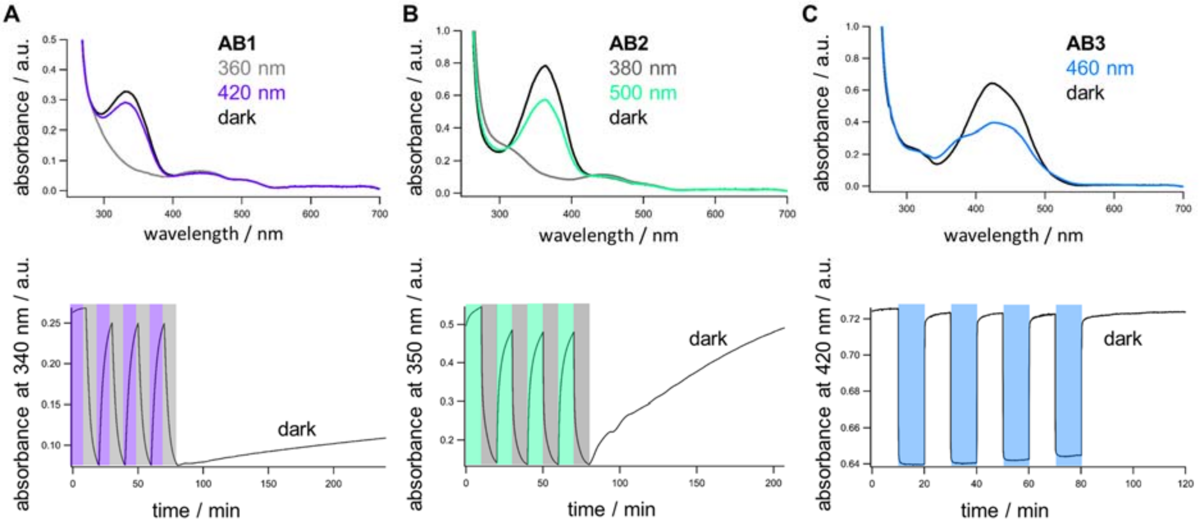

Figure 19. Top: UV/Vis spectra of **AB1-3** (15 μM in DMSO) in the dark (black) and illuminated at the indicated wavelengths. Bottom: Photoswitching is stable over many cycles. **a)** Black: dark-adapted, violet: 420 nm, light gray: 360 nm; **b)** Black: dark-adapted, green: 500 nm, dark gray: 380 nm and **c)** Black: dark-adapted, blue: 460 nm.

To evaluate the effect of **AB**s on K_v channels, HEK293T cells were transiently transfected with the slowly-desensitizing, delayed-rectifier K_v2.1 channel. Prior to compound wash-in, a current-voltage(IV) -curve was recorded for normalization to account for cell-to-cell variances like size, conductance or expression. In particular, K^+ currents were evoked by depolarization from -80 to +40 mV in whole-cell voltage-clamp mode. Then, **AB**s were washed in and illuminated with the appropriate wavelength to isomerize to the *trans*-configuration (*i.e.* violet/green or dark) while recording two IV-curves (Figure 20a). Maximum block was only achieved after the second IV (*trans*-) which is consistent with the mechanism of a use-dependent open channel blocker.[80] Next, two IV-curves were recorded under the appropriate switching wavelengths to the *cis*-configuration (grey) to unblock the channel. The block was more pronounced at high voltages which indicates a channel block from the intracellular side (Figure 20b).[80] We tested **AB1-3** at different concentrations and determined **AB2** as the most potent compound, showing the maximum photodependent block at 5 μM (Figure 20c and Supporting Figure 3). As such, **AB2** blocks 70.1 ± 1.5% of K^+ current under green light, of which 58.8 ± 4.7% can be relieved under UV-illumination (Figure 20b,c). Interestingly, the substitution at the *para*-position of the azobenzene impacts potency greatly since both **AB1** and **AB3** showed a decreased block (Figure 20c). At a high concentration of 100 μM **AB1** blocked under violet light with $I_{max} = 0.22 \pm 0.03$ and unblocked under UV-light with $I_{max} = 0.64 \pm 0.03$ (n = 4 cells). **AB3** was only soluble up to 50 μM in extracellular buffer and at this concentration blocked currents in the dark with $I_{max} = 0.25 \pm 0.06$ while unblocking under blue illumination with $I_{max} = 0.67 \pm 0.07$ (n = 4 cells).

To ultimately highlight the reversibility and rapid speed of block and unblock with **AB2**, we switched between UV/green illumination while holding the cell at +20 mV (Figure 20d).

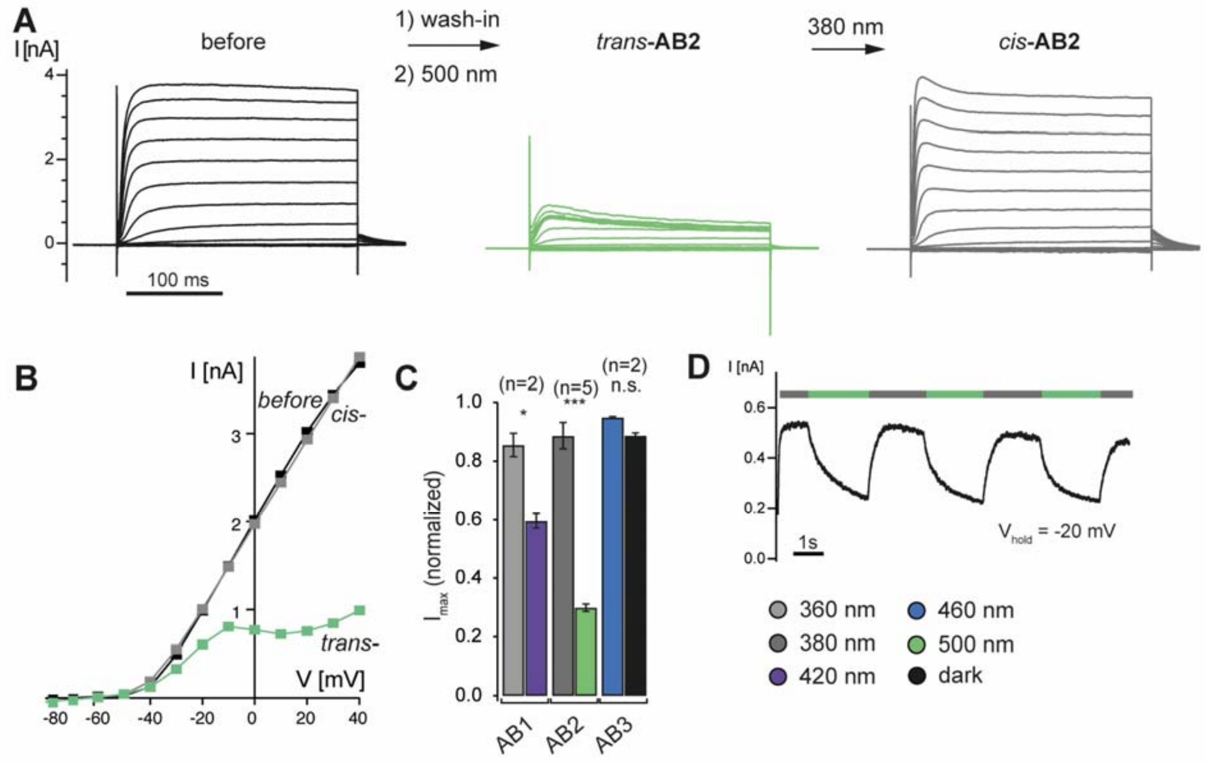

Figure 20. **Light-gated K_v2.1 currents by AB1-3 in HEK293T cells transiently transfected with K_v2.1**. **a)** After recording an initial IV-curve in 10 mV steps from -80 to +40 mV, **AB2** (5 μM) was washed in, followed by illumination with green light (500 nm) to isomerize **AB2** to its *trans*-configuration, leading to a block of K^+ current. After isomerization to its *cis*-configuration by UV-light (380 nm), the blocking could be reversed. **b)** Representative single-cell IV-curve before wash-in, and in presence of **AB2** under illumination with 380 or 500 nm. **c)** Maximum light-gated currents were normalized to the maximum current before wash-in in the dark. **AB1** (5 μM) opened the channel under UV-light (360 nm) with $I_{max.}$ = 0.86 ± 0.04, while blocking under violet light (420 nm) (I_{max} =0.60 ± 0.03). **AB2** (5 μM) showed currents of I_{max} = 0.89 ± 0.05 under UV-light (380 nm) and $I_{max.}$ = 0.30 ± 0.01 under green light (500 nm). **AB3** showed no significant block at 5 μM with $I_{max.}$ (460 nm) = 0.95 ± 0.01 and $I_{max.}$ (dark) = 0.89 ± 0.01. **d)** To demonstrate the reversibility and fast kinetics of block and unblock, the cell was held at -20 mV while switching with UV/green light (380/500 nm) in presence of **AB2** (5 μM).

TREK-1 is a two-pore domain K^+ (K_{2p}) channel which is widely expressed in the central nervous system (CNS) and exhibits unique physiological and pharmacological properties.[81] Initially described as ‘background’ or ‘leak’ channel, this channel was cloned in 1996.[82] It is described as an outward rectifier but has a comparatively high probability of opening at negatively membrane potentials. Therefore, TREK-1 opening sets the membrane potential closer to the potassium equilibrium potential. TREK-1 is activated by a variety of molecules, such as lipids and general anesthetics, but is also responsive to nociceptive stimuli like membrane stretch.[83]

TREK-1 is implicated in processes ranging from neuroprotection, anesthesia and pain, to mood disorders such as depression. It also constitutes a fairly novel drug target.[84,85] TREK-1 is only weakly sensitive to quaternary ammoniums like TEA.[86] Therefore, optical control of TREK-1 blockade using the photoswitch MAQ could only be enabled at very high local concentrations by tethering MAQ to a genetically introduced cysteine at its pore region.[15] While this elegant approach could unravel TREK-1 contributions to hippocampal $GABA_b$ signaling, it is limited by the requirement of genetic modification, and by the inherent drawbacks of cysteine-maleimide chemistry, such as reactivity towards glutathione or hydrolysis. We were intrigued by the first description of 'leak' channels in myelinated nerves in 1992, which identified bupivacaine as a leak channel blocker,[87] and accordingly hypothesized that azobupivacaines could photoswitch this channel. First, the inability of permanently charged PCLs to block TREK-1 was reassessed. Indeed, after transfection of HEK293T cells with TREK-1, no block by AAQ in neither the *cis*- nor its *trans*- configuration was observed, even at 100 μM (Supporting Figure 4). Then, **AB1-3** (Figure 21a) were tested by looking at the IV-relationship from -80 to +40 mV. Again, one IV-curve for normalization was recorded before wash-in of compounds **AB1-3.** The cell was then illuminated with light of the appropriate wavelength for the *trans*-isomerization. (*i.e.* violet/green nm or dark). The channel was then unblocked by illumination with UV or blue light. Interestingly, and in contrast to the experiments with $K_v2.1$, **AB1** emerged as the most efficacious compound for potentiating TREK-1 currents (Figure 18b and Supporting Figure 5). *cis*-**AB1** potentiates TREK-1 at 100 µM with a maximum normalized current of $I_{max,\ norm.} = 1.20 \pm 0.06$ while *trans*-**AB1** blocks the channel efficiently with $I_{max,\ norm.} = 0.39 \pm 0.07$ (Figure 21c). Two aspects of TREK-1 blockade by **AB1-3** were different in comparison to $K_v2.1$. First, TREK-1 blocking and unblocking was fully apparent at the first recorded IV-step. Secondly, the percentage of block did not increase at positive potentials. Together, this points to a different mechanism of channel blockade on TREK-1 compared to $K_v2.1$.

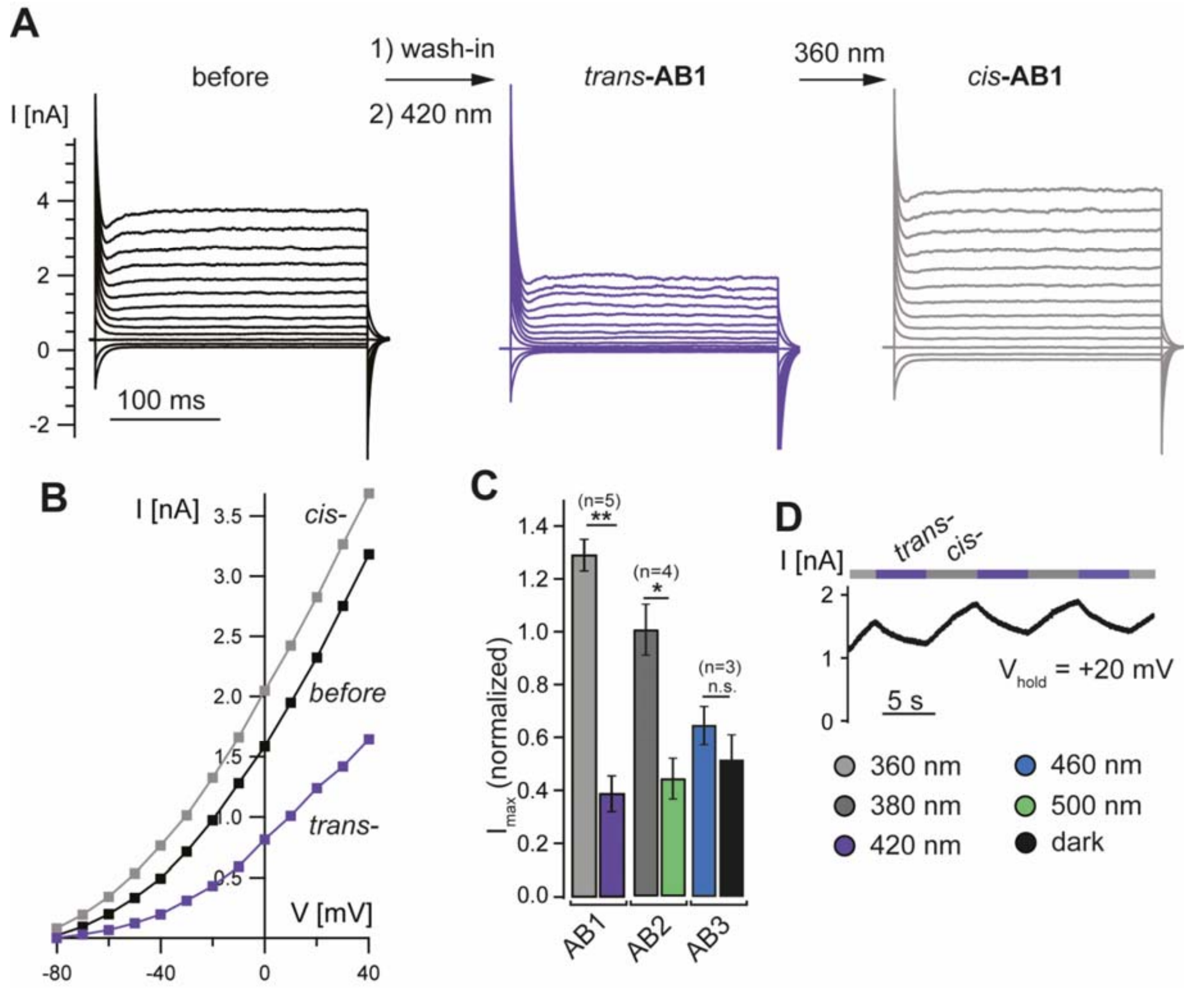

Figure 21. **Light-gated TREK-1 currents by AB1-3 in HEK293T cells transiently transfected with TREK-1. a)** After recording an initial IV-curve in 10 mV steps from -80 to +40 mV, **AB1** (100 μM) was washed in, followed by illumination with violet light (420 nm) to isomerize to *trans*-**AB1***,* leading to a block of K$^+$ current. After isomerization to *cis*-**AB1** by UV-light (360 nm), the block was not only reversed but the channel was potentiated to larger currents than before wash-in. **b)** Representative single-cell IV-curve before wash-in, and in presence **AB1** under illumination with UV-light (360 nm) and violet light (420 nm). **c)** Over multiple cells, maximum light-gated currents were normalized to the maximum current before wash-in in the dark. **AB1** (100 μM) opened the channel under UV light (360 nm) with $I_{max.} = 1.29 \pm 0.06$, while blocking under violet light (420 nm, $I_{max} = 0.39 \pm 0.07$). **AB2** (100 μM) showed currents of $I_{max} = 1.01 \pm 0.10$ under UV light (380 nm) and $I_{max.} = 0.44 \pm 0.08$ under green light (500 nm). **AB3** (50 μM) blocked the current in in *trans*-configuration ($I_{max.} = 0.50 \pm 0.10$) but could not be unblocked significantly under illumination with blue light (460 nm, $I_{max.} = 0.63 \pm 0.07$). **d)** To demonstrate the reversibility and fast kinetics of block and unblock, the cell was held at +20 mV while switching with UV/violet light (360/420 nm) in presence of **AB1** (100 μM).

Having set the stage in transfected cells, we tested **AB2** for effects in coronal brain slices of the mouse hippocampus CA2 region, where $K_V2.1$ is highly expressed.[88] Action potentials (APs) were evoked in whole-cell current-clamp mode by injection of an above-threshold current. In the dark, *trans*-**AB2** allowed for AP firing by inhibiting potassium channels. Due to the bistable behavior of **AB2**, a short flash of UV-light (380 nm) was sufficient to silence AP firing (Figure 22a). Silencing and unsilencing could be performed on a millisecond timescale (Figure 22b). Similar to HEK293T cells, transiently transfected with TREK-1, K$^+$ currents were blocked rapidly by switching between UV/green light (380/500 nm) in brain slices (Figure 22c).

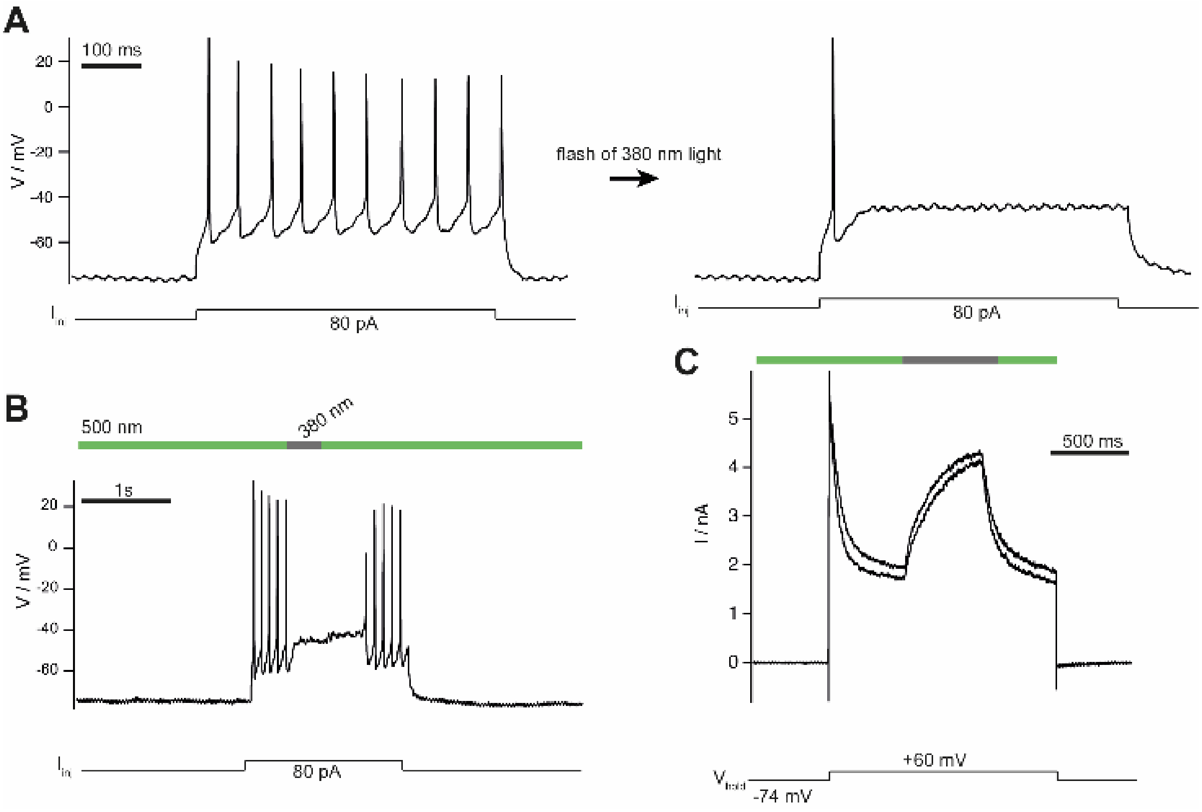

Figure 22. **Optical control of AP firing of hippocampal neurons in acute brain slices**. **a)** A short flash of UV light (380 nm) was sufficient to silence AP firing. **b)** Switching between silenced and unsilenced mode proceeds in milliseconds **c)** K$^+$ current was evoked by depolarization to +60 mV and potentiated by switching UV/green light (380/500 nm).

In conclusion, we report three novel photoswitchable channel blockers which operate on K_V2.1 at low concentrations. In addition, these compounds act as photochromic blockers on the K_{2P} channel TREK-1. An opposing trend in efficacy in dependence on the azobenzene could be observed between the two channels. TREK-1 could not accommodate large substitutions on the azobenzene with the smallest photoswitch **AB1** exhibiting the largest potentiation of K$^+$ current. Furthermore, the *cis*-configuration could not only relieve the block, but showed an agonistic effect, potentiating the K$^+$ currents towards larger values. On K_V2.1, the glycine-substituted **AB2** proved to be the most potent photoswitch.

Potassium channels are implicated in processes ranging from cancer and metabolism to neurological and cardiovascular diseases. However, this huge therapeutic potential has remained largely untapped due to the lack of selective pharmacology, which additionally limited target validation to genetic knockout models.[72] While photoswitchable blockers like azobupivacaine inherit their parent drugs' unselectivity, the additional layer of control by confining its activity in area and in time using light makes them a useful tool. The beauty of photopharmacology lies in its simplicity: it requires no genetic manipulation and can be applied as normal drugs while only requiring additional delivery of light, which is often already developed due to the abundance of fluorescence and microscopy techniques in life science research. Currently, we are actively working on equipping azobupivacaines and other photoswitchable blockers with additional functionality. By tethering these photoswitches to nanobodies, monobodies, toxins or other easily-modifiable, small protein-based strong binders that can take over the function of a full-sized antibody, we hope to combine the advantages of small-molecule photoswitches with the specificity of antibody binding (chapter 3.2.2).

3.2.2 Antibody-Photoswitch Conjugates (APCs)

The potential for using antibodies that target extracellular epitopes to deliver payloads subtype-specifically to K_v channels was exemplified and highlighted by Sack *et al.* in 2013. There, the use of a singlet-oxygen generating, porphyrin-labelled anti-K_v4.2-IgG was describe to selectively photoablate K_v4.2 channels.[89] The photosensitizer porphyrin was attached by lysine labelling with activated NHS-esters. A photosensitizer has multiple turnovers and singlet-oxygen has a long half-maximal reactive distance of approximately 40 Å.[90] Therefore, the stoichiometry of porphyrin:antibody, as well as the exact location of conjugation, is unlikely to have a large influence on photoablation. Our approach of antibody-photoswitch conjugates (APCs) was aimed at linking photoswitchable blockers to antibodies and in this fashion equip them with subtype specificity. Since these blockers have to physically reach the external TEA blocking site rather than acting from a remote distance, a more controllable method than lysine labelling was necessary for antibody modification. More specifically, a method was required that labels residues at a defined stoichiometry and at a defined location on wild-type, commercially-available antibodies. The selected conjugation strategy is inspired by patent procedures from Novartis.[91,92] These describe how the four interchain disulfides are mildly reduced by TCEP in presence of the doubly-alkylating agent 1,3-dichloroacetone. The 1,3-dichloroacetone immediately and *in situ* rebridges the heavy and light chains of the antibody and inserts a ketone. The ketone is subsequently reacted with the aminooxy bioconjugation handle to irreversibly form an oxime and yield the APCs (Figure 23).

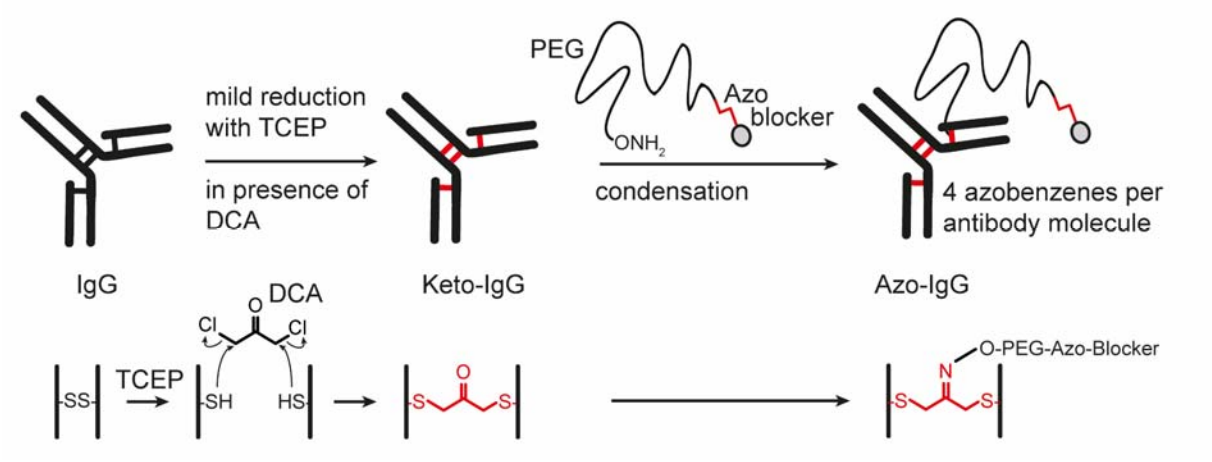

Figure 23. **Strategy for antibody-photoswitch conjugation.** Mild reduction by TCEP only occurs on the four interchain disulfide (black), which is not disrupting the IgG structure and is directly trapped by the double-alkylating agent 1,3-dichloroacetone. The rebridged keto-IgG is not susceptible to further reduction anymore and the inserted ketone serves as a bioconjugation handle. The photoswitchable blocker is attached to an aminooxy group *via* a long PEG-tether. The aminooxy group reacts in an irreversible, bioorthogonal reaction with the ketone to form an oxime, linking the antibody-photoswitch conjugate (APC).

To span the distance between the antibody and the TEA binding site on the K^+ channel, a long, flexible linker is required. As an estimation, a 'molecular tape' measure of maleimide-QA compounds with increasing linker lengths was described by Miller *et al.* in 2000. They concluded that the transmembrane-extracellular ends of the most distant S1 and S3 helices of the Shaker channel are only at a distance of around 30 Å away from the pore mouth. Therefore, we hoped that the monodisperse PEG_{12} linker, which has an approximate end-to-end distance of 46 Å according to the manufacturer (see SI for details), would be sufficient to span the gap of the antibody binding site on the closer S1-S2 loop to the external TEA blocking site, even when considering the additional bulk of the antibody. Even though most channel blockers (except MAQ) work from the intracellular side, we hoped to block the external TEA site by ensuring very high local concentrations around the channel by the antibody-binding. A careful survey of commercially available antibodies for K_V's was conducted. The antibody had to fulfil several important criteria: (i) binding to extracellular epitopes, (ii) it must be monoclonal and (ii) it must have been validated in a few applications, such as immunohistology. In addition, the antibody had to target channels with an external TEA binding site. We found two antibodies from the UC Davis Neuromab facility targeting $K_V1.1$ (clone K36/15) and $K_V2.1$ (clone K39/25) that fulfilled these criteria and selected them for our APCs.

Next, we moved to the synthesis of the photoswitch **3.5**. It was accessed through a 4 step reaction sequence. **3.8** was prepared in a 4 step sequence from the commercial dye disperse red and then reacted with PhthNO-PEG12-NHS-ester. This was followed by amide coupling with the betaine **3.3** and deprotection of the phthalimide using hydrazine hydrate to afford the final bioconjugation-ready aminooxy photoswitch **3.5.**

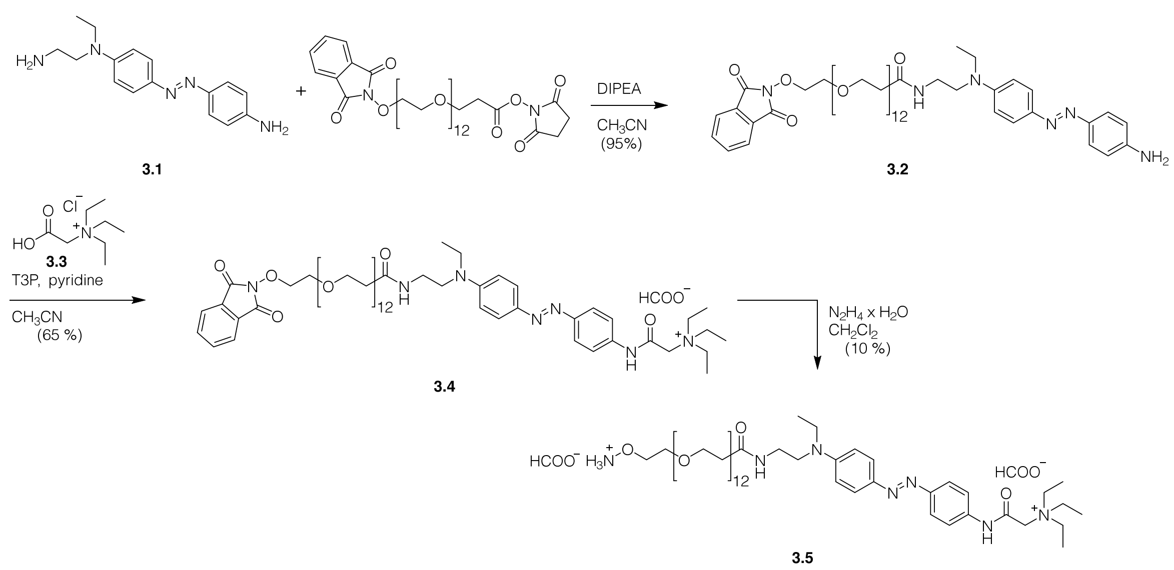

Scheme 2. **Synthesis of the red-shifted 3.5.**

Next, the conditions of the aforementioned patent procedures were optimized to the microgram scale using a cheap, control-antibody MOPC-21 (mouse IgG1, kappa monoclonal isotype control, see chapters 3.4.2.1, 3.4.2.2 and 3.4.2.3). Then, K_v1.1- and K_v2.1-IgGs were conjugated with **3.5** and checked for intactness on SDS-PAGE (Figure 24a). The shift to higher molecular weight for the **3.5** (MW = 1042) conjugated Azo-K_v1.1- and Azo-K_v2.1-IgGs was easily observable. The antibody/azobenzene ratio was estimated from absorbance spectroscopy by nanodrop. Due to the high extinction coefficients of azobenzenes, the absorption of the photoswitch moiety can easily be observed at low concentrations (typical APC concentration 1-10 μM). The absorption at 280 nm was taken for estimation of antibody concentration and the absorption at 460 nm for determining the azobenzene concentration. Using the appropriate extinction coefficients for antibody and azobenzene, the approximate conjugation ratio was determined to be very close to the theoretical value of 4 azobenzenes per antibody (see chapter 3.4.2.5 for an example calculation). Next, to check for specific antibody-antigen binding, HEK293T cells were transfected with plasmids for K_v1.1 (rat) and K_v2.1 (rat), lysed, and analyzed by western blot. Both modified antibodies bound to K_v1.1 (expected MW 57 kDa) and K_v2.1 (expected MW 105-125 kDa, Figure 24b) as expected.

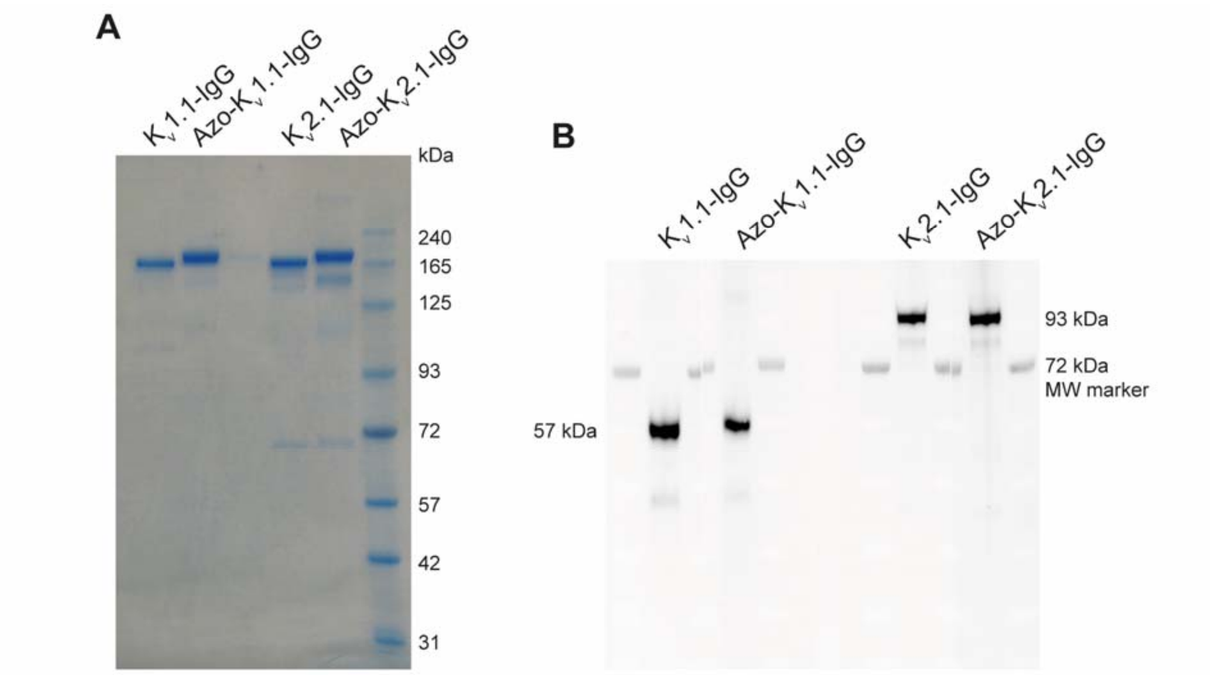

Figure 24. **K_v1.1-IgGs and K_v2.1-IgGs conjugated to 3.5. a)** SDS-PAGE of the IgGs under non-reducing conditions. The rightmost lane is the molecular weight maker. **b)** HEK293T cells were transiently transfected either with K_v1.1 (rat) or K_v2.1 (rat) and YFP as transfection control. The lysate was immunoblotted and probed with the indicated wild-type, or conjugated IgG (1 *μ*g/mL). Detection was performed using a PE conjugated fluorescent anti-mouse secondary AB (Biolegend #406708 or #407108). In between the sample lanes, lanes were charged with molecular weight marker, which fluoresces at 72 kDa.

After having the modified antibodies in hand, functional characterization at the electrophysiology setup was performed. HEK293T cells were transfected with K_v1.1 or K_v2.1 and multiple conditions were explored for the incubation with the Azo-K_v-IgGs:

- Incubation at 2 *μ*g/mL or 10 *μ*g/mL Azo-K_v-IgG directly added to the extracellular bath solution, at r.t. for a duration of 15-60 min.
- Application through a second “puffing” pipette (pressurized ejection of compound). The pipette was positioned in the near vicinity of the patched cell, ejection of up to 1 mg/mL of Azo-K_v-IgG.
- Incubation at higher concentrations in the incubator, at 37 °C for 30 min (up to 20 *μ*g/mL) in reduced serum medium (OptiMEM).

K^+ currents were then evoked by ramps or IV-steps from -80 to +40 mV under illumination of either blue light (460 nm, *cis*-isomer) or in the dark (*trans*-isomer), while looking for light-dependent blockade of the ion channel. Unfortunately, under none of the tested labelling conditions any effects of illumination could be observed and the data is therefore not shown here.

At this stage, we hypothesized that the lack of observed photoswitching could be due to the red-shifted nature of the photoswitch. In our hands, red-shifted azobenzenes require higher light intensities for the *cis*-isomerization with the photostationary state (PSS) showing a larger percentage of *trans*-isomer due to the fast thermal relaxation in aqueous environments. The block of the red-shifted **3.5** APCs is expected to occur by the *trans*-isomer, *i.e.* in the dark. Therefore, incubation with the APC in the absence of illumination should lead to a decrease in K^+ current. Indeed, this could be observed in a few isolated cells but in the absence of clear photoswitching effects, *i.e.* unblock/opening of the channel by illumination to the *cis*-isomer, the effects of the APC on K_v channel gating were hard to decipher and inconclusive.

In pursuit of a functional photoswitch, we opted to use an amide-substituted azobenzene which should exhibit bistable photoswitching behavior, *i.e.* slow thermal back-relaxation in the dark, allowing for a PSS with a higher percentage of *cis*-isomer. In addition, we simplified the synthesis, since the purification after final phthalimide deprotection of **3.5** was problematic due to the high reactivity of the aminooxy moiety, even with trace amounts of ketones. Therefore, the synthesis was redesigned such as to bear a Boc-group instead of the phthalimide to enable clean deprotection with neat TFA without a final chromatographical purification step. The synthesis yielded the bistable, aminooxy-photoswitch **3.8** (Scheme 3) in 4 steps starting from **3.6.** To streamline our efforts, it was decided to focus on the $K_v2.1$ channel from this point on.

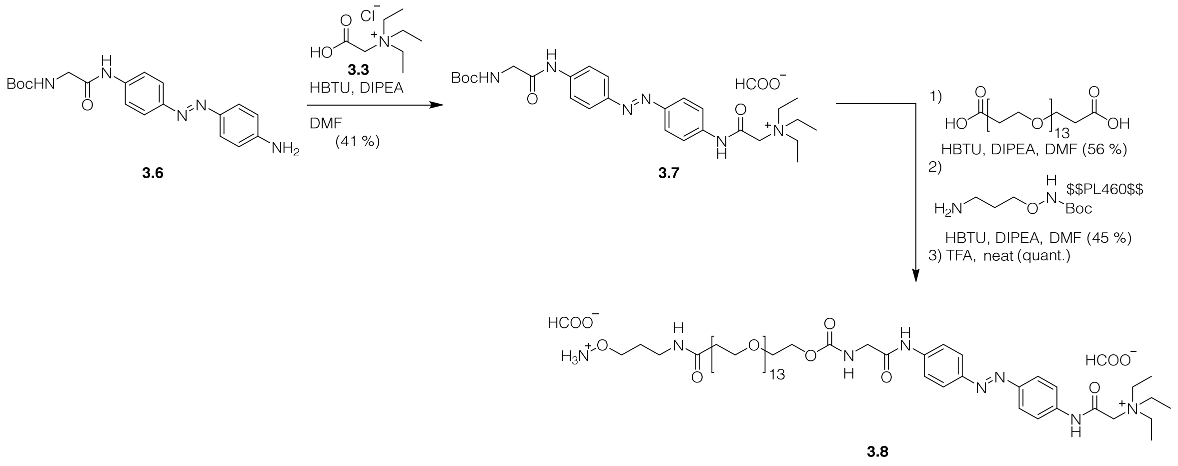

Scheme 3. **Synthesis of bistable 3.8.**

The **3.8**-conjugated Kv2.1-IgG antibody was again evaluated for quality by SDS-PAGE and western blot. We performed the SDS-PAGE under non-reducing as well as reducing conditions (by DTT+β-ME heated to 70°C for 10 min, Figure 25a). While wild-type, unmodified, IgGs are reduced to heavy and light chains, the ketone- or azo-inserted IgGs are not susceptible to further reduction. There is a distinct shift in mobility after attachment of the azobenzene.

UV/Vis-spectroscopy confirmed a conjugation ratio close to 4. Specificity of the modified antibodies was confirmed by immunblot (Figure 25b).

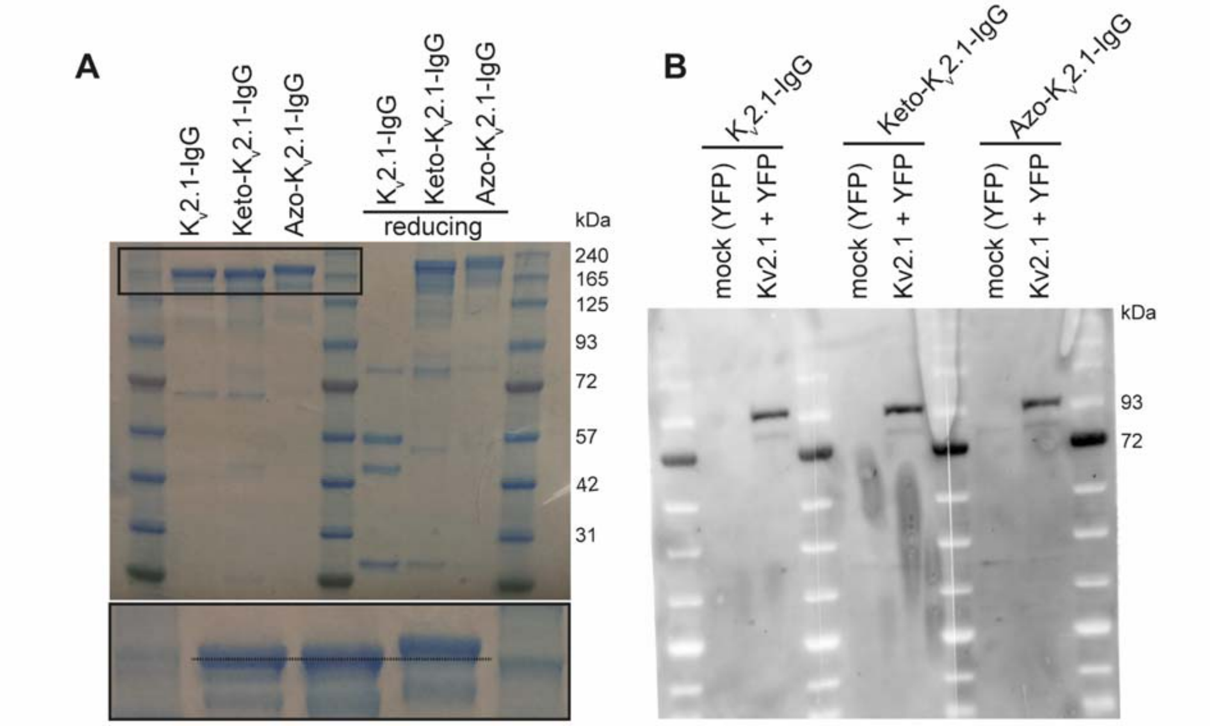

Figure 25. **K_v2.1-IgGs conjugated to 3.8. a)** SDS-PAGE of the IgGs under non-reducing (left) or reducing conditions (right). **b)** HEK293T cells were transfected with K_v2.1 and YFP, mock transfection with YFP alone served as negative control. The lysate was immunoblotted and probed with the indicated conjugated IgG (1 *µ*g/mL). was performed using a PE conjugated anti-mouse secondary AB (Biolegend #407108).

In addition, the **3.8**-K_v2.1-IgG conjugate was evaluated in fixed cells by confocal imaging with the hope of observing antibody-antigen binding in a setting more transferable to the electrophysiological patch-clamp setup (in contrast to western blots). Therefore, HEK293T cells transiently transfected with GFP_K_v2.1 (*C*-terminal fusion protein) were incubated for 6 h at 37°C degrees with **3.8-**K_v2.1-IgG (10 *µ*g/mL) and secondary Alexa-647 conjugated antibody (10 *µ*g/mL). Confocal images confirmed colocalization of the green GFP_K_v2.1 and the Alexa 647 signal, although some unspecific binding of the secondary antibody was observed in the Alexa 647 channel (Figure 26).

The patch-clamp experiments were repeated using the same aforementioned antibody incubation methods **3.8**-K_v2.1-IgG. IV-steps and ramps were recorded under either UV-light (380 nm, *cis*-isomer) or green light (500 nm, *trans*-isomer). After an exhaustive set of experiments, mostly varying antibody incubation conditions (*i.e.* concentrations, additives, buffers, incubation time and temperature; data not shown), no light-dependent effects on K_v2.1 gating could be observed.

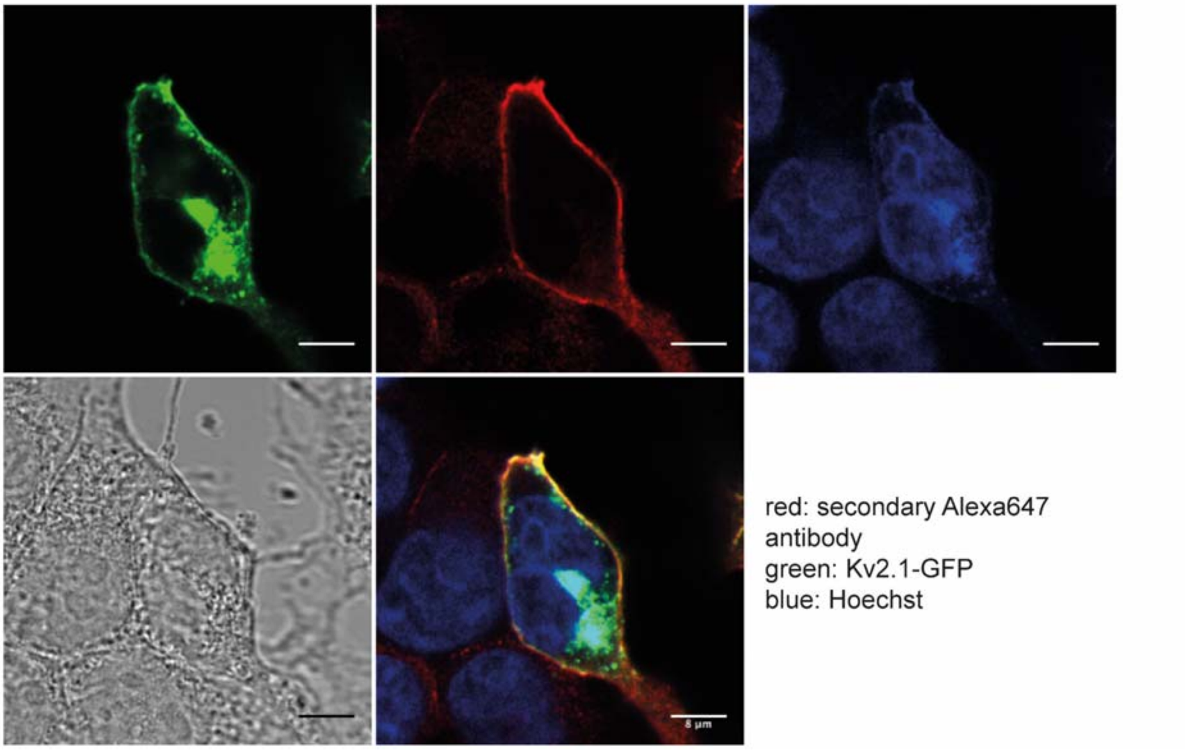

Figure 26. HEK293T cells were transfected with K$_v$2.1_GFP, fixed and incubated with Azo-K$_v$2.1-IgG (**3.8** conjugate). Secondary antibody conjugation was performed using an Alexa Fluor 647 goat anti-mouse antibody (ThermoFisher Scientific #A-21241).

Altogether, we successfully synthesized and characterized a set of APCs for K$_v$1.1 and K$_v$2.1. The binding of APCs to the K$_v$1.1 and K$_v$2.1 channel was confirmed both by western blot and live-cell imaging. Discouragingly, none of the APCs showed any light-dependent effects in patch-clamp experiments. Taken together, we hypothesized that the linker between the photoswitch and the bioconjugation handle (aminooxy group) must be the issue. The linker could be preventing the photoswitch from reaching its site of action, either by its nature (hydrophilic *vs* hydrophobic), length (too short), or by its placement on the photoswitch. To investigate this, we returned to K$_v$2.1 experiments with freely diffusible photoswitche-linker comibnations. The PEGylated compounds **3.9** and bupivacaine-based **3.10** were tested. In addition, we prepared two compounds with a hydrophobic chain fused to the azobenzene, **3.11** and **3.12** (Scheme 4). The compounds were tested at either 50 μM or 100 μM, depending on solubility (n = 3 cells each). In short, none of the compounds showed any light-dependent block of K$_v$2.1.

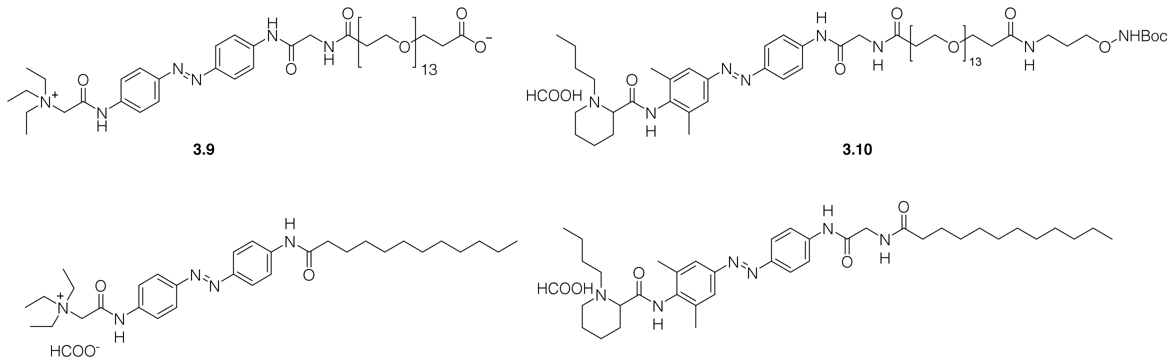

3.9 **3.10** **3.11** **3.12**

Scheme 4. **Further compounds tested in patch clamp experiments on K_V2.1.**

In conclusion, basic parameters of the structure-activity relationship of photoswitchable blockers are still unclear. Since the basic structure of these blocker allow a wide variety of substitutions in *para*-position to the azobenzene,[6] our intuition initially guided us to attach the long chain necessary for this APC approach on this position. It now seems clear that attachment of a linker on this position is deleterious to channel block and that further work must be directed at identifying novel linker-photoswitch combinations.

3.3 Summary and Outlook

A short series of novel photoswitches based on the general anesthetic bupivacaine, termed azobupicacaines **AB1-3**, was presented. **AB1-3** are non-permanently charged and enable optical control over the voltage-gated K^+ channel $K_v2.1$ at one to two orders of magnitude lower concentrations than the previously described, quaternary-ammonium (QA) ion based photoswitches. In addition, **AB1-3** light-gate the two-pore domain K^+ channel TREK-1 by exploiting a mode of action different from QA block and without use-dependence. An opposing trend in efficacy was observed for the effects on $K_v2.1$ and TREK-1 varying with the azobenzenes substituents, which could serve as the entry point for an improved, more-selective generation of azobupivacaines. **AB1-3** efficiently control the hyperpolarization of hippocampal neurons in acute mouse brain slices and using light as the trigger, **AB1-3** could efficiently silence and unsilence action potential firing in a reversible manner.

In addition, the synthesis and characterization of antibody-photoswitch conjugates (APCs) based on the combination of small-molecule photochromic blockers with subtype-specific K^+ channel antibodies is described. While the preparation of APCs in a very defined manner without interfering with the antibody-antigen binding could be exemplified, APCs targeting extracellular epitopes of $K_v1.1$ and $K_v2.1$ did not exhibit any functional effects. More specifically, the APCs did not show opening or blockage of $K_v1.1$ or $K_v2.1$ channels after incubation and upon illumination. Therefore, the influence of the tether between the antibody and photoswitchable head group was reevaluated. It now seems clear that the placement of the tether is a crucial determinant of the K_v channel blockade. Future work should be directed at deciphering the structure-activity relationship of the small-molecule photochromic blockers. In addition, future APCs should be based on bivalent photoswitch-fluorophore combinations to confirm the antibody binding during the electrophysiological experiments *in situ*.

3.4 Supporting Information

3.4.1 Synthesis

Synthesis of AzoBupivacaines (ABs) 1-3 was performed by Dr. Nils Winter and are described in his thesis.

3.4.1.1 (*E*)-*N*-(4-((4-Aminophenyl)diazenyl)phenyl)-*N*-ethylethane-1,2-diamine (**3.1**)

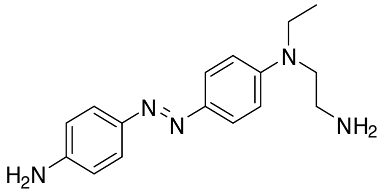

3.1 was synthesized as previously described in 4 steps from the commercially available dye Disperse Red 1.[93]

TLC ($NEt_3/MeOH/CH_2Cl_2 = 0.1/1/9$) = 0.30.

^{1}H NMR (400 MHz, $CDCl_3$) δ 7.86 – 7.70 (m, 4H), 6.86 – 6.71 (m, 4H), 4.08 – 3.92 (m, 2H), 3.49 (dq, J = 11.4, 6.9 Hz, 3H), 2.99 (t, J = 6.8 Hz, 2H), 1.68 (s, 3H), 1.24 (q, J = 7.1 Hz, 2H).

^{13}C NMR (101 MHz, $CDCl_3$) δ 149.6, 148.1, 146.1, 143.6, 124.4, 124.1, 114.84, 111.4, 53.4, 45.6, 39.9, 12.2.

HRMS (ESI): *m/z* calc. $C_{16}H_{22}N_5^+$ $(M+H)^+$: 284.1870, found: 284.1871.

***t*$_R$** (LCMS; MeCN/H_2O/formic acid = 10/90/0.1 → 100/0/0.1 over 10 min) = 4.04 (*cis*), 4.13 min (*trans*).

UV/Vis (LCMS): λ_{max1} = 420 nm, λ_{max2} = 446 nm.

3.4.1.2 *N*-(Carboxymethyl)-*N,N,N*-triethylethanammonium chloride (**3.3**)

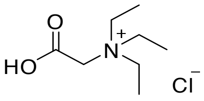

In a round-bottomed flask, triethylamine (2.00 g, 19.8 mmol) and methyl bromoacetate (3.02 g, 19.7 mmol) were combined. A magnetic stirring bar was added and the reaction mixture was stirred at room temperature. Within 1 h, the reaction mixture had solidified. After 4 h, 37% HCl (10 mL) was added and the reaction mixture was heated at 100 °C with stirring for 4 h. The reaction mixture was concentrated under reduced pressure, providing a white solid that was washed with diethyl ether. The crude product was dissolved in a minimal amount of water and then precipitated with acetone. The white solid was collected by filtration and dried under vacuum to yield the desired product (1.54 g, 39%).

^{1}H NMR (400 MHz, D_2O) δ 3.97 (s, 2H), 3.52 (q, J = 7.3 Hz, 6H), 1.26 (t, J = 7.3 Hz, 9H).

3.4.1.3 (*E*)-*N*-(2-((4-((4-Aminophenyl)diazenyl)phenyl)(ethyl)amino)ethyl)-1-((1,3-dioxoisoindolin-2-yl)oxy)-3,6,9,12,15,18,21,24,27,30,33,36-dodecaoxanonatriacontan-39-amide (**3.2**)

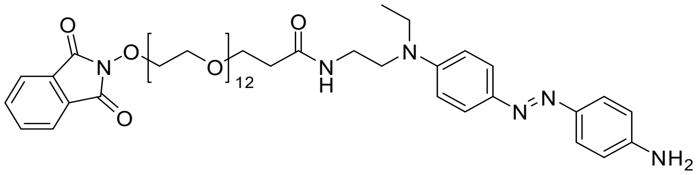

In a small vial with a magnetic stirring bar, Phth-NO-dPEG(12)-NHS (Iris Biotech #PEG4630, 20.0 mg, 23.2 µmol, 1.0 equiv.) was dissolved in 1mL of anhydrous CH_3CN, and to this solution were added **3.1** (13.2 mg, 46.6 µmol, 2.0 equiv.) and DIPEA (6 µL, 46.5 µmol, 2.0 equiv.). The orange reaction mixture was stirred at r.t. overnight. The reaction mixture was concentrated under reduced pressure and the crude product was dissolved in 0.1% aq. formic acid. The crude material was purified by reverse-phase chromatography on a 5 g SepPak C8 SPE cartridge (0%-30% CH_3CN/H_2O + 0.1% FA). The product containing fractions were lyophilized to provide **3.2** as a glassy orange solid (22.8 mg, 95%).

TLC ($NEt_3/MeOH/CH_2Cl_2 = 0.1/1/9$) = 0.67.

^{1}H NMR (400 MHz, CD_3CN) δ 7.81 (s, 4H), 7.69 (d, *J* = 8.9 Hz, 2H), 7.61 (d, *J* = 8.6 Hz, 2H), 6.85 (d, *J* = 8.9 Hz, 2H), 6.80 – 6.66 (m, 3H), 4.60 (s, 2H), 4.31 – 4.24 (m, 2H), 3.79 – 3.72 (m, 2H), 3.63 (t, *J* = 6.1 Hz, 2H), 3.59 – 3.41 (m, 48H), 3.36 (q, *J* = 6.4 Hz, 2H), 2.33 (t, *J* = 6.0 Hz, 2H), 1.16 (t, *J* = 7.0 Hz, 3H).

HRMS (ESI): *m/z* calc. for $C_{51}H_{76}N_6O_{16}^+$ $(M+H)^+$: 1029.5391, found 1029.5424; *m/z* calc. for $C_{51}H_{77}N_6O_{16}$ $(M+2H)^+$: 515.2732, found: 515.2739.

***t*$_R$** (LCMS; MeCN/H_2O/formic acid = 10/90/0.1 → 100/0/0.1 over 10 min) = 6.44 min.

UV/Vis (LCMS): λ_{max1} = 452 nm.

3.4.1.4 (*E*)-2-((4-((4-((1-((1,3-Dioxoisoindolin-2-yl)oxy)-39-oxo-3,6,9,12,15,18,21,24,27,30,33,36-dodecaoxa-40-azadotetracontan-42-yl)(ethyl)amino)phenyl)diazenyl)phenyl)amino)-*N,N,N*-triethyl-2-oxoethan-1-ammonium formate (**3.4**)

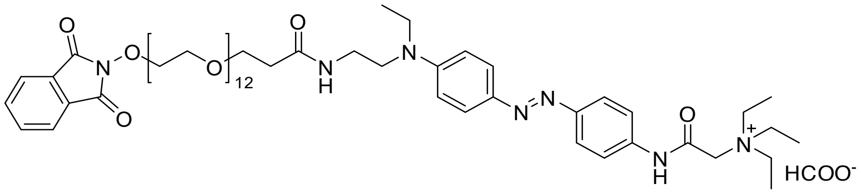

In a small vial with a magnetic stirring bar, **3.3** (22.8 mg, 22.2 μmol, 1.0 equiv) was dissolved in 2 mL of dry CH_3CN, and to this solution were added **3.2** (21.7 mg, 110.9 μmol, 5.0 equiv.) and pyridine (88 μL, 1.11 mmol, 50 equiv.). T3P (50% wt in EtOAc, 706 μL, 1.11 mmol, 50 equiv.) was added to the reaction mixture, which was stirred r.t. overnight. The next day, the reaction mixture was concentrated under reduced pressure and the crude product was dissolved in 0.1% aqueous formic acid. The crude was purified by reverse phase chromatography on a 5g SepPak C8 SPE cartridge (0%-20% CH_3CN/H_2O + 0.1% FA). The product-containing fractions were lyophilized to provide **3.4** as an orange solid (17.4 mg, 65%).

^{1}H NMR (400 MHz, CD_3CN) δ 12.79 (br s, 1H), 8.60 (s, 1H), 7.79 (d, *J* = 9.7 Hz, 10H), 6.85 (dd, *J* = 20.3, 7.4 Hz, 3H), 4.54 (br s, 2H), 4.31 – 4.23 (m, 2H), 3.75 (t, *J* = 4.2 Hz, 2H), 3.63 (t, *J* = 6.1 Hz, 2H), 3.56 – 3.46 (m, 48H), 3.37 (q, *J* = 6.4 Hz, 3H), 2.65 (br s, 6H), 2.34 (t, *J* = 6.1 Hz, 2H), 1.32 (br s, 9H), 1.17 (t, *J* = 7.0 Hz, 3H).

HRMS (ESI): *m/z* calc. for $C_{59}H_{93}N_7O_{17}^+$ (M^+): 1170.6544, found 1170.6599; *m/z* calc. for $C_{59}H_{93}N_7O_{17}$ ($M^+ + H^+$): 585.8309, found 585.8320.

$\boldsymbol{t_R}$ (LCMS; MeCN/H_2O/formic acid = 10/90/0.1 → 100/0/0.1 over 10 min) = 6.20 min.

UV/Vis (LCMS): λ_{max1} = 451 nm.

3.4.1.5 (*E*)-2-((4-((4-((1-(Amoxy)-39-oxo-3,6,9,12,15,18,21,24,27,30,33,36-dodecaoxa-40-azadotetracontan-42-yl)(ethyl)amino)phenyl)diazenyl)phenyl)amino)-*N,N,N*-triethyl-2-oxoethan-1-amine diformate **(3.5)**

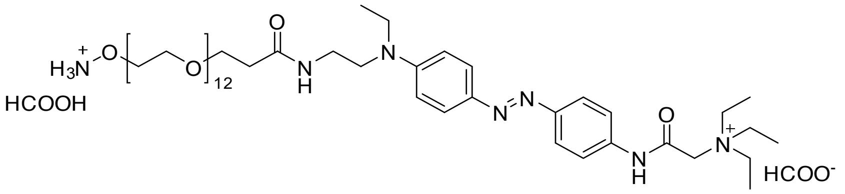

In a small vial with a magnetic stirring bar, **3.4** (10.8 mg, 8.9 μmol) was dissolved in 2 mL of anhydrous CH_2Cl_2, and to this solution was added hydrazine hydrate (89 μL, 1.8 mmol). A white precipitate formed almost immediately and the reaction mixture was stirred at r.t. overnight. After 0.5 h, an aliquot of the reaction mixture was diluted in acetonitrile (1 mL) containing a few drops of methyl ethyl ketone (MEK) for LCMS analysis— the major peak observed has *m/z* values consistent with the expected oxime condensation product (*m/z* = +365.5 and +547,8 for M+2H and M+H, respectively). The solvent was evaporated under a stream of nitrogen and the crude product was dissolved in 0.1% aq. formic acid. The crude material was purified by reverse phase chromatography on a 5g SepPak C8 SPE cartridge (0%-20% CH_3CN/H_2O + 0.1% FA). Two major orange-colored bands were collected and aliquots were analyzed by LCMS after diluting in acetonitrile containing MEK. The earlier eluting orange band has *m/z* values consistent with the expected MEK oxime condensation product. The later eluting orange band has *m/z* values consistent with the formaldehyde oxime condensation product (+351,5, +526,7 for M+2H and M+H, respectively). The desired product-containing fractions were lyophilized to provide **3.5** as an orange solid (1.2 mg 10%). The formaldehyde oxime condensation product was discarded. The aminoxy compound was dissolved in water to provide a 5 mM stock solution and stored at –20°C when not being used.

tt_R (LCMS; MeCN/H_2O/formic acid = 10/90/0.1 → 100/0/0.1 over 10 min) = 6.20 min.

LRMS (ESI): *m/z* calc. for $C_{55}H_{97}N_7O_{15}^{2+}$ (M^++MEK+H^+) 547.7.

UV/Vis (LCMS): λ_{max1} = 454 nm.

HRMS (ESI): *m/z* calc. for $C_{51}H_{91}N_7O_{15}^{2+}$ (M^++CH_2O+ H^+): 520.8281, found 520.8291.

Note: The aminooxy compound was highly reactive and requires careful handling to avoid any sources of ketones or aldehydes. In fact, it was observed that extra-pure formic acid which is routinely used in LCMS and HRMS systems has sufficient amounts of formaldehyde contamination to react aminoxy compounds fully to the condensed product. Due to the low isolated amounts and high reactivity, no NMR spectra were recorded.

3.4.1.6 *tert*-Butyl (3-(1,3-dioxoisoindolin-2-yl)propoxy)carbamate **(3.13)**

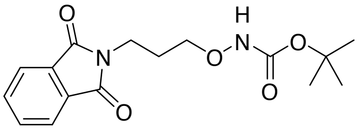

N-(3-Bromopropyl)phthalimide (2.45 mg, 9.10 mmol, 1.0 equiv.), *N*-hydroxycarbamate (1.33 g, 10.00 mmol, 1.1 equiv.) were mixed in dry toluene (20 mL) under a nitrogen atmosphere before addition of DBU (1.50 mL, 10.00 mmol, 1.1 equiv.). The reaction mixture was heated to 110 °C for several hours while stirring vigorously. An orange-brow oil separated from the solution. The reaction mixture was extracted with DCM (200 mL) against citrate solution (10% wt to pH = 5.5 with HCl, 200 mL). The organic layer was washed with citrate solution (10% wt to pH = 5.5 with HCl, 3x200 mL) and then dried over $MgSO_4$ before concentration *in vacuo*. The crude material was purified by flash column chromatography (DCM/EtOAc = 9/1) to yield 1.85 g of the desired product as a white solid (0.42 mmol, 63%).

TLC (DCM/EtOAc= 9/1) = 0.67, stain: ninhydrin.

^{1}H NMR (400 MHz, Methanol-d_4) δ 7.89 – 7.83 (m, 2H), 7.83 – 7.76 (m, 2H), 3.84 (t, *J* = 6.3 Hz, 2H), 3.78 (t, *J* = 7.1 Hz, 2H), 1.97 (p, *J* = 6.6 Hz, 2H), 1.46 (s, 9H).

3.4.1.7 *tert*-Butyl (3-aminopropoxy)carbamate **(3.14)**

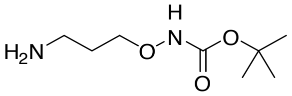

3.13 was dissolved in MeOH (9.3 mL) and hydrazine hydrate (5.8 mL) was added. The reaction mixture was stirred at r.t. overnight before concentration to dryness *in vacuo.* The residue was triturated, suspended in $CHCl_3$ and filtered. The solid was washed with a copious of $CHCl_3$ before the filtrate was concentrated to yield a yellowish oil. After purification by flash column chromatography (MeOH/DCM/aq. NH_3 = 20/80/1), **3.14** was obtained as colorless solid (606 mg, 3.18 mmol, 55%)

^{1}H NMR (400 MHz, $CDCl_3$) δ 3.93 (t, *J* = 6.0 Hz, 2H), 2.84 (t, *J* = 6.6 Hz, 2H), 1.76 (p, *J* = 6.3 Hz, 2H), 1.46 (s, 9H).

^{13}C NMR (101 MHz, $CDCl_3$) δ 157.0, 81.6, 74.9, 39.2, 31.5, 28.2.

HRMS (ESI): *m/z* calc. for $C_8H_{19}O_3N_2^+$ (M+H$^+$): 191.1390, found 191.1390.

3.4.1.8 (*E*)-2-((4-((4-(2-((*tert*-Butoxycarbonyl)amino)acetamido)phenyl)diazenyl)phenyl)amino)-*N,N,N*-triethyl-2-oxoethan-1-ammonium formate **(3.7)**

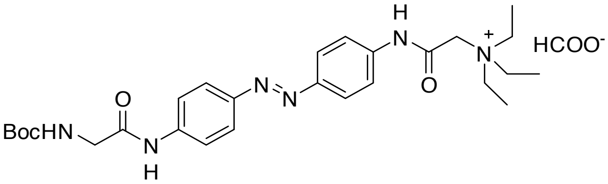

tert-Butyl (*E*)-(2-((4-((4-aminophenyl)diazenyl)phenyl)amino)-2-oxoethyl)carbamate **3.6** (55 mg, 0.15 mmol, 1.0 equiv.), **3.3** (45 mg, 0.23 mmol, 1.5 equiv.), HBTU (68 mg, 0.18 mmol, 1.2 equiv.) were combined in DMF (1 mL) and DIPEA (52 μL, 0.30 mmol, 2.0 equiv.) was added. Reaction progress was monitored by LCMS and judged to be complete after ca. 30 min. The reaction mixture was acidified using a few drops of formic acid and purified on a 2 g SepPak C18 SPE cartridge (0%-30% CH_3CN/H_2O + 0.1% FA). Product containing fractions were identified by LCMS, combined and concentrated *in vacuo* to dryness to yield the desired product as a yellow-orange glaze (34 mg, 61 μmol, 41%).

^{1}H NMR (400 MHz, Methanol-*d*$_4$) δ 7.89 (t, *J* = 8.4 Hz, 4H), 7.78 (t, *J* = 8.5 Hz, 4H), 4.19 (d, *J* = 4.7 Hz, 2H), 3.90 (s, 2H), 3.67 (q, *J* = 7.2 Hz, 6H), 1.48 (s, 9H), 1.39 (t, *J* = 7.2 Hz, 9H).

^{13}C NMR (400 MHz, Methanol-*d*$_4$) δ 169.4, 161.8, 157.2, 149.4, 148.7, 141.1, 139.8, 126.5, 123.3, 123.2, 120.1, 119.7, 79.4, 56.2, 54.4, 43.7, 27.3, 6.6.

HRMS (ESI): *m/z* calc. for $C_{27}H_{39}O_4N_6^+$ (M+H$^+$):511.3027, found 511.3024.

3.4.1.9 (*E*)-1,4-Dioxo-1-((4-((4-(2-triethylammonio)acetamido)phenyl)diazenyl)phenyl)amino)-7,10,13,16,19,22,25,28,31,34,37,40,43-tridecaoxa-3-azahexatetracontan-46-oate **(3.9)**

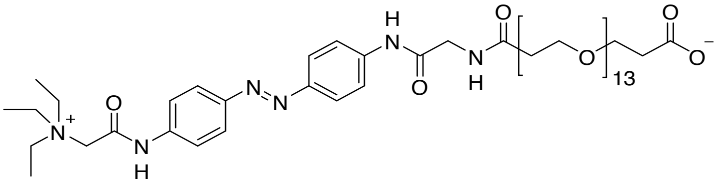

3.7 (34 mg, 62 μmol, 1.0 equiv.) was deprotected at r.t. for 10 min using 1 mL neat TFA. TFA was removed in a gentle stream of nitrogen before the residue was dried under HV. The residue was dissolved in DMF, before sequential addition of PEG13-diacid (polypure #37137-1295, 51 mg, 74 μmol, 1.2 equiv.), HBTU (25 mg, 66 μmol, 1.05 equiv.) and DIPEA (53 μL, 0.30 mmol, 5.0 equiv.). The reaction mixture was stirred for 1 h at r.t. when LCMS analysis indicated full conversion. The reaction mixture was acidified using a few drops of FA and purified on a 5 g SepPak C18 SPE cartridge (0%-25% CH_3CN/H_2O + 0.1% FA). Product containing fractions were identified by LCMS, combined and dried *in vacuo* to yield the desired product as an orange glaze (38 mg, 35 μmol, 56%).

HRMS (ESI): *m/z* calc. for $C_{52}H_{85}O_{18}N_6^-$ (M-H)$^-$: 1081.5926, found:1081.5922.

3.4.1.10 (*E*)-2-((4-((4-(50-(Ammoniooxy)-4,46-dioxo-7,10,13,16,19,22,25,28,31,34,37,40,43-tridecaoxa-3,47-diazapentacontanamido)phenyl)diazenyl)phenyl)amino)-*N,N,N*-triethyl-2-oxoethan-1-ammonium bis-(trifluroacetate) (**3.8**)

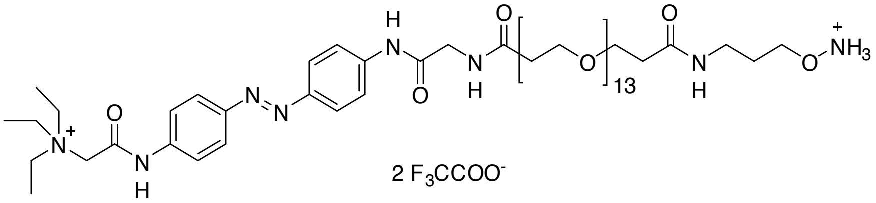

3.9 (100 μL of 0.1M in DMF, 10 μmol, 1.0 equiv.) and **3.14** (24 μL of 0.5M in DMF, 12 μmol, 1.2 equiv.) were combined and HBTU (5.0 mg, 12 μmol, 1.2 equiv.) and DIPEA (4.2 μL, 24 μmol, 2.0 equiv.) were added. The reaction was stirred at r.t. overnight before LCMS analysis indicated incomplete conversion. Therefore, the same amounts of all reagents except **3.9** were added to the reaction mixture again. After an additional hour of stirring, the reaction mixture was acidified using a few drops of FA and purified on a 5 g SepPak C18 SPE cartridge (0%-

30% CH_3CN/H_2O + 0.1% FA). Product containing fractions were identified by LCMS and dried *in vacuo* to yield the desired product as an orange glaze (5.8 mg, 4.5 μmol, 45%).

HRMS (ESI): *m/z* calc. for $C_{60}H_{102}O_{20}N_8^-$ (M-H)$^-$: 1254.7210, found: 1254.7197

For deprotection, neat TFA (0.2 mL) was added and allowed to stand at r.t. for 10 min before removal of all volatiles in a gentle stream of nitrogen. The residue was dried under HV. Quantitative yield was assumed. A small quantity of the product was tested for reactivity and purity by addition of a drop of acetone. LCMS analysis showed one clean peak with an *m/z* (+) of 1195, consistent with the expected *m/z* of the acetone condensation product.

^{1}H NMR (400 MHz, DMSO-*d*$_6$) δ 11.05 (s, 1H), 10.65 (s, 4H), 10.36 (s, 1H), 8.30 (t, *J* = 5.6 Hz, 1H), 7.91 (td, *J* = 12.0, 7.2 Hz, 5H), 7.81 (dd, *J* = 9.1, 2.8 Hz, 4H), 4.24 (d, *J* = 4.3 Hz, 2H), 4.03 – 3.90 (m, 5H), 3.51 (s, 65H), 3.11 (q, *J* = 6.6 Hz, 2H), 2.44 (t, *J* = 6.5 Hz, 2H), 2.31 (t, *J* = 6.4 Hz, 3H), 1.71 (t, *J* = 6.7 Hz, 2H), 1.28 (q, *J* = 7.2 Hz, 10H).

^{13}C NMR (101 MHz, DMSO) δ 171.1, 170.6, 168.8, 162.8, 158.8, 158.5, 158.1, 148.9, 148.0, 142.3, 140.6, 124.1, 123.9, 120.6, 119.8, 72.6, 70.2, 70.1, 70.0, 70.0, 67.2, 67.2, 56.8, 55.4, 54.5, 43.3, 36.6, 36.3, 35.5, 28.0, 7.9.

HRMS (ESI): *m/z* calc. for $C_{58}H_{97}N_8O_{18}^-$ (M+acetone-2H)$^-$: 1193.6926, found: 1193.6928; *m/z* calc. for $C_{58}H_{99}N_8O_{18}^+$ (M+acetone)$^+$: 1195.7077, found:1195.7086.

3.4.1.11 (*E*)-1-Butyl-2-((4-((4-(2,2-dimethyl-4,11,53-trioxo-3,6,14,17,20,23,26,29,32,35,38,41,44,47,50-pentadecaoxa-5,10,54-triazahexapentacontan-56-amido)-3,5-dimethylphenyl)diazenyl)phenyl)carbamoyl)piperidin-1-ium formate (**3.10**)

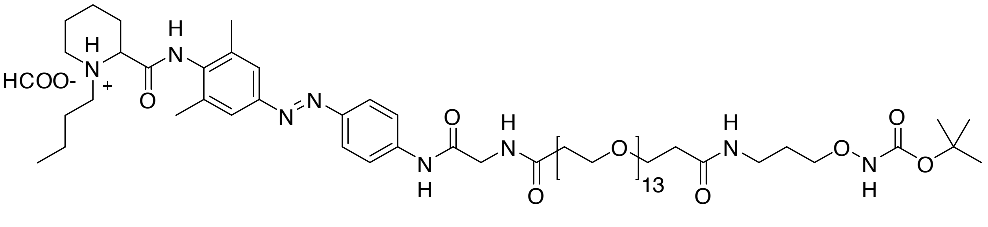

(*E*)-*N*-(4-((4-(2-aminoacetamido)phenyl)diazenyl)-2,6-dimethylphenyl)-1-butylpiperidine-2-carboxamide (27 mg, 59 μmol, 1.0 equiv.), PEG13-diacid (polypure #37137-1295, 49 mg, 71 μmol, 1.2 equiv.), DIPEA (51 μL, 0.30 mmol, 5 equiv.) and HBTU (24 mg, 62 μmol, 1.05 equiv.) were added to DMF (0.5 Ml). The reaction mixture was stirred for 1 h at r.t., when LCMS analysis indicated full conversion of the starting azobenzene. The reaction mixture was acidified with a few drops of FA and purified on a 5 g SepPak C18 SPE cartridge (0%-40% CH_3CN/H_2O + 0.1% FA). Product containing fractions were identified by LCMS, combined and dried *in vacuo* to obtain the desired product as a yellow solid (32 mg, 28 μmol, 48%).

HRMS (ESI): *m/z* calc. for $C_{56}H_{91}N_6O_{18}^-$ (M-H)$^-$: 1135.6395, found:1135.6394.

The entire product of the previous step was dissolved in DMF (0.7 mL) and **3.14** (6.5 mg, 34 μmol, 1.2 equiv.), HBTU (13 mg, 34 μmol, 1.2 equiv.) and DIPEA (10 μL, 56 μmol, 2.0 equiv.) were added. The reaction mixture was stirred overnight at r.t., when LCMS analysis indicated full conversion of the starting azobenzene. The reaction mixture was acidified with a few drops of FA and purified on a 5g SepPak C18 SPE cartridge (0%-40% CH_3CN/H_2O + 0.1% FA). Product containing fractions were identified by LCMS, combined and dried *in vacuo* to obtain the desired product as a yellow solid (18 mg, 13 μmol, 22% over 2 steps).

HRMS (ESI): *m/z* calc. for $C_{64}H_{107}N_8O_{20}^-$ $(M-H)^-$: 1307.7607, found: 1307.7606.

3.4.1.12 (*E*)-N-(4-((4-aminophenyl)diazenyl)phenyl)dodecanamide (**3.15**)

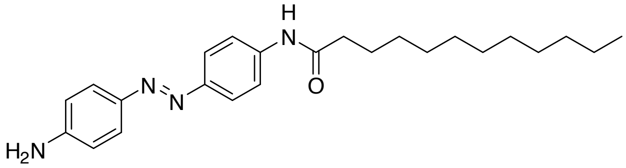

4,4‘-diazoniline (212 mg, 1 mmol, 2.0 equiv.), dodecanoic acid (100 mg, 0.5 mmol, 1.0 equiv.), HBTU (209 mg, 0.55 mmol, 1.1 equiv.) and DIPEA (0.17 mL, 1 mmol, 2.0 equiv.) were combined in DMF (2 mL). The reaction was stirred at r.t. overnight. The product was extracted against aq. 10% LiCl, water (2x) and brine. The organic layer was dried over $MgSO_4$ and concentrated *in vacuo* to yield the desired product as a yellow solid (134 mg, 0.34 mmol, 68%).

^{1}H NMR (400 MHz, $CDCl_3$) δ 7.74 (dd, *J* = 21.7, 8.6 Hz, 4H), 7.58 (d, *J* = 8.5 Hz, 2H), 7.22 (s, 1H), 6.67 (d, *J* = 8.5 Hz, 2H), 3.96 (s, 2H), 2.31 (t, *J* = 7.6 Hz, 2H), 1.67 (p, *J* = 7.5 Hz, 2H), 1.37 – 1.10 (m, 16H), 0.81 (t, *J* = 6.7 Hz, 3H).

^{13}C NMR (101 MHz, $CDCl_3$) δ 171.4, 149.4, 149.3, 145.6, 139.4, 124.9, 123.4, 119.7, 114.7, 38.0, 31.9, 29.6, 29.6, 29.5, 29.4, 29.4, 29.3, 25.6, 22.7, 14.2.

HRMS (ESI): *m/z* calc. for $C_{24}H_{35}N_4O^+$ $(M+H)^+$: 395.2805, found: 395.2808.

***t*$_R$** (LCMS; MeCN/H_2O/formic acid = 10/90/0.1 → 100/0/0.1 over 10 min) = 7.16 min.

UV/Vis (LCMS): λ_{max} = 394 nm.

3.4.1.13 (*E*)-2-((4-((4-dodecanamidophenyl)diazenyl)phenyl)amino)-*N,N,N*-triethyl-2-oxoethan-1-ammonium formate (**3.11**)

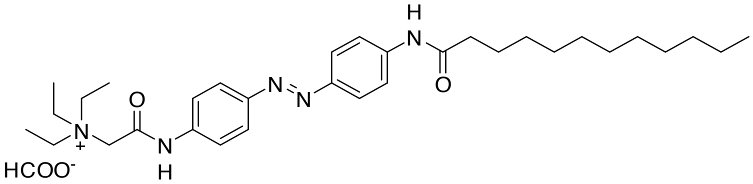

3.15 (40 mg, 0.10 mmol, 1.0 equiv), **3.3** (22 mg, 0.11 mmol, 1.1 equiv.), HBTU (42 mg, 0.11 mmol, 1.1 equiv) and DIPEA (35 *µ*L, 0.20 mmol, 2.0 equiv.) were combined in DMF (1 Ml). After 3.5 h, the reaction mixture was acidified with a few drops of FA and purified on a 5g SepPak C8 SPE cartridge (0%-45% CH_3CN/H_2O + 0.1% FA). Product containing fractions were identified by LCMS, combined and dried *in vacuo* to obtain the desired product as a yellow foam (15 mg, 28 *µ*mol, 28%).

^{1}H NMR (400 MHz, DMSO-d_6) δ 12.20 (br s, 1H), 10.31 (s, 1H), 8.50 (s, 1H), 7.93 – 7.74 (m, 8H), 4.45 (s, 2H), 3.55 (q, *J* = 8.4, 7.5 Hz, 6H), 2.35 (t, *J* = 7.4 Hz, 2H), 1.27 (dd, *J* = 16.1, 8.6 Hz, 26H), 1.64 – 1.55 (m, 2H), 0.84 (t, *J* = 6.5 Hz, 3H).

^{13}C NMR (101 MHz, DMSO) δ 172.3, 163.2, 148.7, 147.8, 142.7, 141.2, 123.9, 123.8, 120.6, 119.6, 56.9, 54.5, 37.0, 31.8, 29.5, 29.5, 29.4, 29.3, 29.2, 29.1, 25.5, 22.6, 14.4, 7.9.

HRMS (ESI): *m/z* calc. for $C_{32}H_{50}N_5O_2^+$ $(M)^+$: 536.3959, found: 536.3965.

***t*$_R$** (LCMS; MeCN/H_2O/formic acid = 10/90/0.1 → 100/0/0.1 over 10 min) = 5.18 min.

UV/Vis (LCMS): λ_{max} = 368 nm.

3.4.1.14 (*E*)-1-Butyl-2-((4-((4-(2-dodecanamidoacetamido)phenyl)diazenyl)phenyl)carbamoyl)piperidin-1-ium formate (**3.12**)

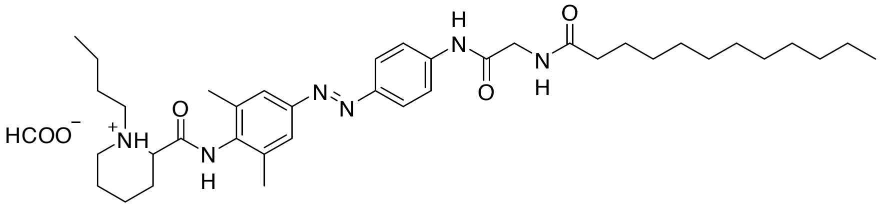

(*E*)-*N*-(4-((4-(2-Amminoacetamido)phenyl)diazenyl)-2,6-dimethylphenyl)-1-butylpiperidine-2-carboxamide (23 mg, 43 *µ*mol, 1.0 equiv.), dodecanoic acid (8.6 mg, 43 *µ*mol, 1.0 equiv.), HBTU (18 mg, 47 *µ*moL, 1.1 equiv.) and DIPEA (38 *µ*L, 0.22 mmol, 5.0 equiv.) were combined in DMF (1 mL) and stirred for 45 min at r.t. when LCMS analysis indicated full conversion. The reaction mixture was acidified with a few drops of FA and purified on a 5 g SepPak C18 SPE cartridge (0%-50% CH_3CN/H_2O + 0.1% FA). Product containing fractions were identified by LCMS, combined and dried *in vacuo* to obtain the desired product as a yellow foam (25 mg, 39 *µ*mol, 91%).

^{1}H NMR (400 MHz, DMSO-d_6) δ 10.35 (s, 1H), 9.44 (s, 1H), 8.20 (t, *J* = 5.9 Hz, 1H), 8.15 (s, 1H), 7.87 (d, *J* = 8.8 Hz, 2H), 7.81 (d, *J* = 8.8 Hz, 2H), 7.59 (s, 2H), 3.91 (d, *J* = 5.8 Hz, 2H), 3.22 – 3.12 (m, 1H), 3.10 – 2.98 (m, 1H), 2.78 – 2.64 (m, 1H), 2.35 (s, 1H), 2.24 (s, 6H), 2.16

(t, *J* = 7.4 Hz, 2H), 1.92 (d, *J* = 11.6 Hz, 1H), 1.73 (d, *J* = 10.1 Hz, 2H), 1.53 (dt, *J* = 14.8, 6.5 Hz, 5H), 1.25 (d, *J* = 6.8 Hz, 17H), 0.87 (dt, *J* = 17.7, 7.1 Hz, 6H).

^{13}C NMR (101 MHz, DMSO-d_6) δ 173.3, 168.9, 163.6, 150.6, 148.0, 142.4, 138.0, 137.0, 124.1, 122.1, 119.7, 67.4, 56.2, 51.5, 43.3, 35.6, 31.8, 30.3, 29.5, 29.4, 29.3, 29.2, 29.1, 28.1, 25.7, 24.8, 23.2, 22.6, 20.6, 19.3, 18.8, 14.4, 14.4.

HRMS (ESI): *m/z* calc. for $C_{38}H_{59}N_6O_3^+$ (M)$^+$: 647.4643, found: 647.4652.

***t*$_R$** (LCMS; MeCN/H_2O/formic acid = 10/90/0.1 → 100/0/0.1 over 10 min) 4.70 min.

UV/Vis (LCMS): λ_{max} = 356 nm.

3.4.2 Antibody Modifications

3.4.2.1 Determining the detection limit of Antibody-detection by SDS-PAGE

To determine the limit of detection for full size IgGs as well as well as evaluate reduction conditions of IgGs to heavy and light chains on SDS-PAGE gels (NuPAGE 4-12% Bis-Tris, 12 well) in combination with InstantBlue Coomassie (Expedeon) protein stain, a dilution series was performed.

Lanes were loaded with MOPC-21-IgG as follows:

Per lane: total volume 30 *μ*L, TCEP 0 (non-reducing) or 0.017 M (reducing)

Lanes: 1: 0.025 *μ*g, 2: 0.025 +TCEP, 3: 0.375 *μ*g, 4: 0.375 *μ*g + TCEP, 5: 0.75 *μ*g, 6: 0.75 *μ*g + TCEP, 7: 1.5 *μ*g, 8: 1.5 *μ*g + TCEP

Gel was run for 75 min at 200 V in the ThermoScientific Mini Gel Tank. Gel was removed from its casing and stained overnight with InstantBlue Coomassie (Expedeon).

As little as 0.325 *μ*g of MOPC-21-IgG could be detected using these conditions. Reducing conditions showed no full-size antibody but two bands migrating further on the gel, indicative of quantitative reduction of IgG to heavy and light chains.

3.4.2.2 Optimization of antibody modification procedure to the microgram scale

The ketone insertion reaction procedure was adapted for microgram scale reactions from procedures described in US patents #US2015032126 and #US20150150998.

Optimization of IgG reduction by TCEP:

20 pmol of MOPC-21 IgG (3 *μ*g) were reduced using increasing amounts of TCEP (0 nmol, 0.8 nmol, 1.2 nmol, 1.6 nmol, 2.0 nmol, 2.4 nmol, 2.8 nmol, 3.2 nmol, 3.6 nmol, 500 nmol) were

incubated at 4 °C for 30 min. Then, the samples were analyzed per SDS-PAGE and with InstantBlue Coomassie (Expedeon) staining.

Observations:

An increasing trend with higher TCEP equivalents towards reduction was observed. Only with 500 nmol TCEP, full reduction was observed. Possibly, in absence of the alkylating agent DCA the antibody is reoxidized to the full-size IgG when using only a small amount of TCEP.

Optimization of Ketone insertion:

IgG reacted with DCA and TCEP under different stochiometries. The reaction was allowed to proceed in 0.25 M TRIS Ph 7.3 (total volume 30 μL) at 4 °C overnight followed SDS-PAGE and InstantBlue Coomassie (Expedeon) staining. If antibody is reduced by TCEP and DCA is inserted, it is expected that only one clean band at the full-size IgG is present. The modified antibody with the inserted ketone can't be reduced by the reducing gel conditions.

Lanes were loaded as followed:

Tube /lane	1	2	3	4	5	6	7
IgG (μg)	1.5	1.5	1.5	1.5	1.5	1.5	1.5
pmol IgG	20	20	20	20	20	20	20
TCEP (equiv.)	120	120	180	180	240	240	300
DCA (equiv.)	4000	4000	4000	4000	4000	4000	4000
Reducing gel?	N	Y	N	Y	N	Y	N

Observations:

Cleanest bands were for lane 6 and 7. Therefore, it was concluded that 240-300 equiv TCEP in presence of 4000 equiv. is the optimal stoichiometry for ketone insertion.

3.4.2.3 Final conditions for all antibody modifications

General procedure for the synthesis of keto-IgGs (procedure is shown with keto-MOPC-21 IgG)

Stock solutions:

A 0.1 mg/mL stock solution of MOPC-21 (BioXCell, catalog # BE0083) was prepared by diluting 7.4 μL of 6.75 mg/mL stock with 493 μL of 0.25 M pH 7.3 TRIS buffer. A 20 mg/mL stock solution of 1,3-dichloroacetone (DCA) was prepared by dissolving 26.2 mg of DCA in 1.31 mL DMSO. A 4 mM stock solution of TCEP x HCl was prepared by diluting 10 μL of 0.5 M TCEP x HCl with 1.25 mL milliQ water. The 0.5 M stock solution of TCEP x HCl was prepared by dissolving 69.7 mg of TCEP x HCl in 0.486 mL milliQ water.

Reaction:

In a microcentrifuge tube at room temperature, 6.8 μL of 20 mg/mL DCA was combined with 400 μL of 0.1 mg/mL MOPC-21 (4000:1 DCA:IgG). The tube was vortexed and cooled to 4 °C. In a separate microcentrifuge tube, 20 μL of 4 mM freshly prepared TCEP x HCl was added and cooled to 4 °C. Using a pipette, the entire volume of the MOPC-21/DCA solution was added to the TCEP x HCl solution and the resulting solution was mixed thoroughly by repeated pipetting (300:1 TCEP:IgG). The reaction mixture allowed to stand at 4 °C overnight. The antibody was purified the next morning by membrane filtration using an Amicon centrifugal filter with 10 kDa MWCO (10 min, 14000 rcf). After concentration, the retentate was diluted to ~500 μL with PBS pH 7.4 and concentration was repeated. In total, seven concentration steps were performed, using PBS pH 7.4 as diluent each time. The final retentate was collected via centrifugation according to the manufacturer's instructions into a tared tube and then weighed to determine the retentate volume (60.5 mg = 60.5 μL, assuming d = 1 mg/μL). The concentration of keto-MOPC-21 was determined by absorbance spectroscopy: A_{280} = 0.628, corresponding to 0.46 mg/mL using ε_{280} of 1.36 $\text{mL}\cdot\text{mg}^{-1}\cdot\text{cm}^{-1}$. Recovery of keto-MOPC-21 was 70% (28 μg).

The following samples were analyzed by SDS-PAGE on a NuPage 4-12% Bis-Tris gel with MES running buffer at 200V for 25 min:

- Keto-MOPC-21 (0.69 μg) diluted with PBS and NuPage LDS sample buffer
- Keto-MOPC-21 (0.69 μg) diluted with PBS and reduced with 1 μL 1M TCEP x HCl for 15 min at 37 °C, then diluted with NuPage LDS sample buffer
- MOPC-21 (1 μg) diluted with 0.25 M pH 7.3 Tris and NuPage LDS sample buffer
- MOPC-21 (1 μg) diluted with 0.25 M pH 7.3 Tris and reduced with 1 μL 1 M TCEP x HCl for 15 min at 37°C, then diluted with NuPage LDS sample buffer
- Blue-Elf Protein MW Markers (Jena Bioscience)

The gel was removed from its plastic casing and stained using InstantBlue Coomassie (Expedeon). Keto-MOPC-21 and MOPC-21 were observed to migrate near the 165 kDa MW marker, consistent with an intact IgG (~150 kDa). The reduced MOPC-21 migrated as two bands near the 24 kDa and 57 kDa MW markers, consistent with complete reduction of the interchain disulfide bonds yielding separate HC (~50 kDa) and LC (~25 kDa). The reduced keto-MOPC-21 migrated near the 165 kDa MW marker, consistent with successful crosslinking with DCA, where reduction-insensitive thioether bonds have replaced disulfides.

General procedure for the synthesis of oxime-IgGs (procedure is shown for CF488DI-anti-K_v2.1-IgG)

Stock solutions:

A 1 M stock solution of 3,5-diaminobenzoic acid (DABA) was freshly prepared by dissolving 49.6 mg DABA in 326 μL DMSO.

A 5 mg/mL stock solution of CF488DI aminooxy (Biotium, catalog #92177) was prepared by dissolving 1 mg CF488DI aminooxy in 200 μL DMSO.

Reaction:

Keto-Kv2.1-IgG was prepared from 10 μg anti-Kv2.1 IgG (Antibodies Incorporated, catalog #75-159) following the general procedure for keto-IgG synthesis. To purified keto-Kv2.1-IgG in PBS pH 7.4 at room temperature in a microcentrifuge tube was added PBS pH 7.4 (26.3 μL), DMSO (17.4 μL), 1M DABA (10 μL), and 5mg/mL CF488DI aminooxy (2.6 μL, 300 eq). The keto-Kv2.1-IgG target concentration was 0.1mg/mL, the DMSO target concentration was 30% vol/vol, and the DABA target concentration was 0.1 M. The reaction mixture was stored at r.t., protected from light, overnight. The next morning the reaction was diluted to ~500 μL by addition of PBS pH 7.4 and the antibody was purified by membrane filtration using an Amicon centrifugal filter with 10 kDa MWCO (10 min, 14000 rcf) using the same procedure as described for keto-IgG purification. The final retentate was collected *via* centrifugation according to the manufacturer's instructions into a tared tube and then weighed to determine the retentate volume (41.8 mg = 41.8 μL, assuming d = 1 mg/μL). The concentration of CF488DI-oxime-Kv2.1-IgG was determined by absorbance spectroscopy: A_{280} = 0.12, corresponding to 88 μg/mL using ε_{280} of $1.36 mL\cdot mg^{-1}\cdot cm^{-1}$. An absorbance peak at 466 nm was observed, indicative of successful conjugation: A_{466} = 0.16. Recovery of CF488DI-oxime-Kv2.1-IgG was 37% (3.7 μg) over two steps.

The following samples were analyzed by SDS-PAGE on a NuPage 4-12% Bis-Tris gel with MES running buffer at 200V for 25min:

- Keto-Kv2.1-IgG (0.31 μg) diluted with PBS and NuPage LDS sample buffer
- CF488DI-oxime-Kv2.1-IgG (0.18 μg) diluted with PBS and NuPage LDS sample buffer
- MOPC-21 (0.25, 0.5, 1, and 2 μg) diluted with PBS and NuPage LDS sample buffer

- Blue-Elf Protein MW Markers (Jena Bioscience)

The gel was removed from its plastic casing and imaged with a Bio-Rad fluorescent imager using settings for Alexa Fluor 488. After fluorescent imaging, the gel was stained using InstantBlue Coomassie (Expedeon). In the Coomassie-stained gel, CF488DI-oxime-Kv2.1-IgG migrated at a position very similar to keto-Kv2.1-IgG, MOPC-21, and the 165 kDa MW marker. The band intensity was slightly less than the 0.25 μg MOPC-21 band, consistent with the CF488DI-oxime-Kv2.1-IgG stock concentration being ~100 μg/mL. The band migrating near the 165kDa MW marker for CF488DI-oxime-Kv2.1-IgG fluoresced intensely, indicating successful conjugation. The presence of multiple weakly-fluorescing, faster-migrating bands was also noted for this sample (these bands were not apparent in the Coomassie-stained gel).

Notes: DMSO was added to improve solubility of CF488DI aminooxy in the reaction mixture.

3.4.2.4 Synthesis of keto-anti-K_v2.1-IgG

Procedure as described for MOPC-21 IgG.

Amounts:

- 100 μL anti-K_v2.1-IgG (1.07 mg/mL, 107 ng), 900 μL 0.25 M TRIS pH 7.3
- 17 μL DCA (20 mg/mL)
- 50 μL freshly prepared 4 mM TCEP x HCl

Weight of retentate after Amicon filtration: 51.8 mg = 51.8 μL, assuming d = 1 mg/μL. The concentration of keto-anti-K_v2.1-IgG was determined by absorbance spectroscopy: A_{280} = 2.162, corresponding to 1.59 mg/mL using ε_{280} of 1.36 mL·mg^{-1}·cm^{-1}. Recovery of keto-anti-K_v2.1-IgG was 77% (82.4 ng).

3.4.2.5 Synthesis of **3.8**-anti-K_v2.1-IgG conjugates

Procedure as described for CF488DI-anti-K_v2.1-IgG.

Amounts:

- 31.4 μL keto-anti-K_v2.1-IgG (1.59 mg/mL, 50 μg)
- 6 μL DABA (1 M in DMSO)
- 96 nmol **3.8** (9.6 μL of 10 mM stock)
- PBS pH 7.4 (13 μL)

Weight of retentate after Amicon filtration: 44.6 μg = 44.6 μL, assuming d = 1 mg/μL.

The concentration of keto-anti-K_v2.1-IgG was determined by absorbance spectroscopy: A_{280} = 1.468, corresponding to 1.08 mg/mL using ε_{280} of 1.36 mL·mg^{-1}·cm^{-1}. Recovery of keto-anti-

K_v2.1-IgG was 96% (1.08 mg/mL * 44.6 μL = 48.2 μg). Using m_a (IgG) = 156 kDa, this amounts to 309 pmol (48.2 μg / (156,000 g/mol)). A second absorption peak at 367 nm was indicative of successful conjugation with azobenzene: A_{367} = 0.638. This corresponds to a concentration of 26.4 μM of azobenzene **3.8** using ε_{280} of 20000 $mL \cdot mol^{-1} \cdot cm^{-1}$ (which is an averaged absorption of a bis-amide sustituted azobenzene) which amounts to 1.18 nmol (26.4 μM * 44.6 μL). This accounts to a conjugation ratio of 3.82 molecules of **3.8** per anti-Kv2.1-IgG antibody (1.18 nmol / 309 pmol).

3.4.3 Cell Culture and Electrophysiology

Plasmids

K_v1.1, K_v2.1 and GFP_ K_v2.1 on pcDNA3.1 were a kind gift from James Trimmer (UC Davis).

TREK-1 and TREK-2 on pcDNA3.1 were a kind gift from Joshua Levitz (Cornell).

Cell Culture and whole-cell electrophysiology. HEK293T (obtained from Leibniz-Institute DSMZ: #305) cells were maintained in Dulbecco's modified Eagle's medium (DMEM) supplemented with 10% fetal calf serum (Biochrom, Merk Millipore, Germany) in a 10% CO_2 atmosphere at 37 °C and were split at 80-90% confluency. Medium was removed and the cells were washed with PBS before cell detachment with trypsin. Cells were taken up in fresh medium and counted. 40-60,000 cells were plated on acid-etched glass coverslips in 500 μL full medium. DNA (per coverslip: TREK1 (50 ng) and YFP (50 ng) or GFP_ K_v2.1 (50 ng)) was diluted in jetPRIME® buffer (per coverslip: 50 μL) and jetPRIME® transfection reagent (per coverslip: 0.5 μL) was added. After mixing and 10 min incubation, the DNA-jetPRIME® mixture was added to the cells. Medium was exchanged after 4-5 hours. Electrophysiology was performed 16-36 h post-transfection. Electrophysiology was performed using a standard electrophysiology setup equipped with a HEKA Patch Clamp EPC10 USB amplifier and PatchMaster software (HEKA Electronic). Micropipettes were generated from "Science Products GB200-F-8P with filament" pipettes using a Narishige PC-10 or PC-100 vertical puller. The patch pipette resistance varied between 5-9 MΩ. The bath solution contained (in mM): NaCl (137), KCl (4), $MgCl_2$ (1), $CaCl_2$ (1.8), HEPES (10), D-glucose (10), pH to 7.4 with NaOH. The pipette solution contained (in mM): KCl (12), K-gluconate (140), HEPES (10), MgATP (4), Na_2GTP (0.4), NaCl (4), pH to 7.4 with KOH. All analyzed cells were first visualized to contain YFP or GFP_K_v2.1 by irradiation at 480 nm using a Polychrome V (Till Photonics) monochromator. All patch clamp experiments were performed at room temperature. For photoswitching, light was applied using the epifluorescence coupling equipped with a Polychrome V (Till Photonics) monochromator.

3.4.4 Brain Slice Preparation

Hippocampal brain slices were prepared from mice strain C57Bl6JRj (postnatal day 10-14) as described previously.[2] Briefly, mice were euthanized, the skull was quickly removed and the brain placed in ice cold saline solution saturated with carbogen (95/5 = O_2/CO_2). The saline solution contained (in mM): 87 NaCl, 2.5 KCl, 1.25 NaH_2PO_4, 25 $NaHCO_3$, 0.5 $CaCl_2$, 7 $MgCl_2$, 25 D-glucose, 75 sucrose. Coronal brain slices of 250 mM thickness were prepared using Campden vibrating microtome 7000smz-2. Prior to recording, the brain slice was placed in artificial cerebrospinal fluid and saturated carbogen (95/5 = O_2/CO_2). The artificial cerebrospinal fluid contained (in mM): 125 NaCl, 2.5 KCl, 1.25 NaH_2PO_4, 1 $MgCl_2$, 2 $CaCl_2$, 26 $NaHCO_3$, and 20 D-glucose. Experiments were performed in continuous flow of aCSF in presence of **AB2** (50 μM).

3.4.5 Supporting Figures

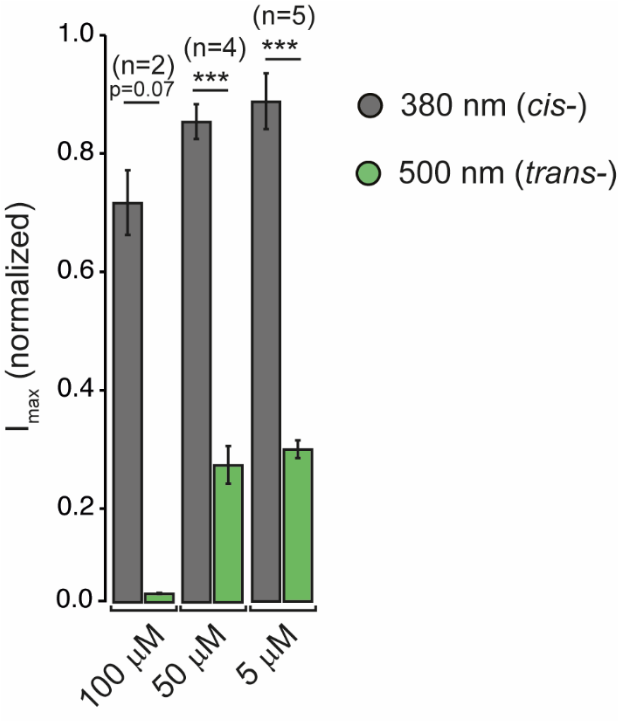

Supporting Figure 3. **Light-dependent dose response of AB2 block of K_v2.1.**

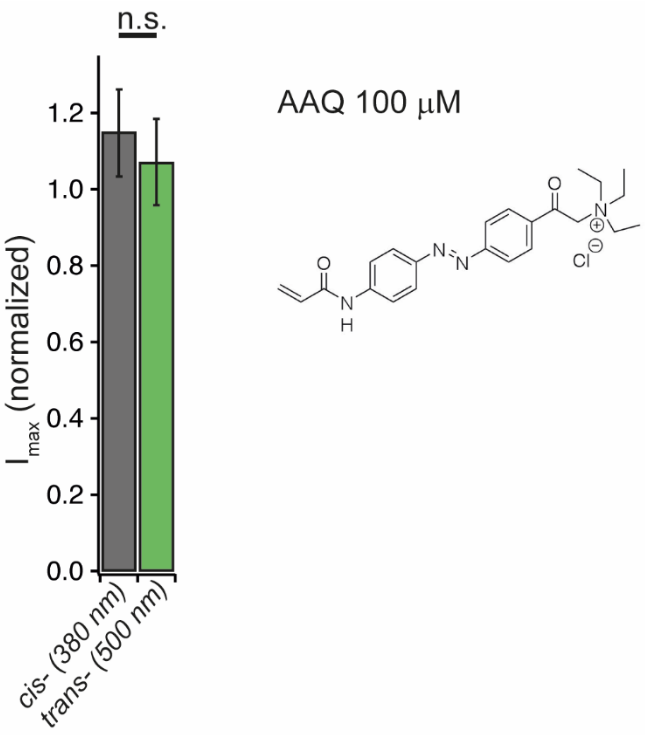

Supporting Figure 4. **The permanently-charged photoswitchable blocker AAQ has no effect on TREK-1 upon isomerization.**

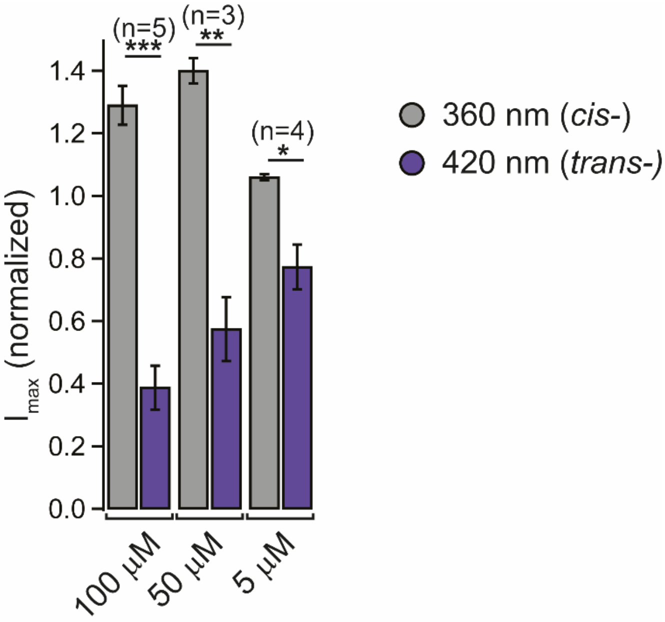

Supporting Figure 5. **Light-dependent dose response of AB1 block of TREK-1.**

3.4.6 Immunohistochemsitry

Expression of $K_v1.1$ and $K_v2.1$ in HEK293T cells with transient transfection:

Day 1

seed HEK293T cells on a LabTek (coated with Fibronectin) or on an ibidi slide.

• Prepare Fibronectin-solution (50 µL Fibronectin stock solution (1 mg/mL) + 4.95 mL 1x PBS + Mg, Ca). Transfer 400 µL of Fibronectin solution into LabTek wells (LabTeks II #1.5). Incubate LabTek at 37°C, 10% CO2 for 45 min. Then, remove Fibronectine solution.

• Plate HEK293T cells (1.4 104 cells / 400 µL cell culture medium (DMEM/10% FCS) per well) into LabTek chambers. Incubate HEK293T cells at 37°C, 10% CO2 for approximately 24 h.

Day 2

Transfection of the HEK293T cells.
• On the next day, inspect HEK293T cells whether they grew sufficiently.
• Prepare transfection mix in the following order (Transfection mix per well of LabTek II #1.5)
- Add Opti-MEM (40 µL Opti-MEM - x µL (DNA) into a new reaction tube.
- Add appropriate volume of DNA (usually x µL of a 100 ng/µL dilution).
- Add 0.6 µL TurboFect to each reaction mix, mix thoroughly, incubate transfection mixtures for 20 min at room temperature.
- Meanwhile remove half of the cell culture medium (200 µL) from LabTeks harbouring cells.
• After incubation of transfection mixtures, add transfection mixtures to cells drop by drop. After adding the transfection mixtures, rock LabTeks gently back and forth to dispense transfection mixture. Incubate cells at 37 °C, 10 % CO2 for 4 h - 6 h.
• After incubation, remove the transfection mixture from plated cells and add 400 µL of DMEM/10 % FCS in each well. Incubate cells at 37°C, 10 % CO2 overnight.

Day 3

On the next day, inspect HEK293T cells and check for florescence using the UV lamp and appropriate filters on the microscope (cell culture).
Labelling with one Antibody in HEK293T cells (with fixation but not with permeabilisation).
• wash with 2 x 200 µL DPBS
• fix the cells with 1 x 200 µL PFA (4%) in PEM, 20 min 21 °C, fixation
• wash with 2 x 200 µL DPBS
• block with 1 x 200 µL DPBS + 1% BSA, 45 min 21 °C, blocking
• stain with 1 x 200 µL antibody (1 µg/mL) in DPBS + 1 % BSA, 18 h 4 °C
• wash with 3 x 200 µL DPBS

At this point cells can be imaged by fluorescence microscopy.

Labelling with **two** Antibodies in HEK293T cells (with fixation but not with permeabilisation).

- wash with 2 x 200 μL DPBS
- fix the cells with 1 x 200 μL PFA (4%) in PEM, 20 min 21 °C, fixation
- wash with 2 x 200 μL DPBS
- block with 1 x 200 μL DPBS + 1% BSA, 45 min 21 °C, blocking
- stain with 1 x 200 μL antibody 1 (2, 4 or 8 μg/mL) in DPBS + 1 % BSA, 18 h 4 °C

Day 4

- wash with 2 x 200 μL DPBS
- stain with 1 x 200 μL antibody 2 (1 μg/mL) in DPBS + 1% BSA, 10 h 4 or 21 °C
- wash with 3 x 200 μL DPBS

At this point cells can be imaged by fluorescence microscopy

3.4.7 Spectral Data

3.4.7.1 (*E*)-*N*-(4-((4-Aminophenyl)diazenyl)phenyl)-*N*-ethylethane-1,2-diamine (**3.1**)

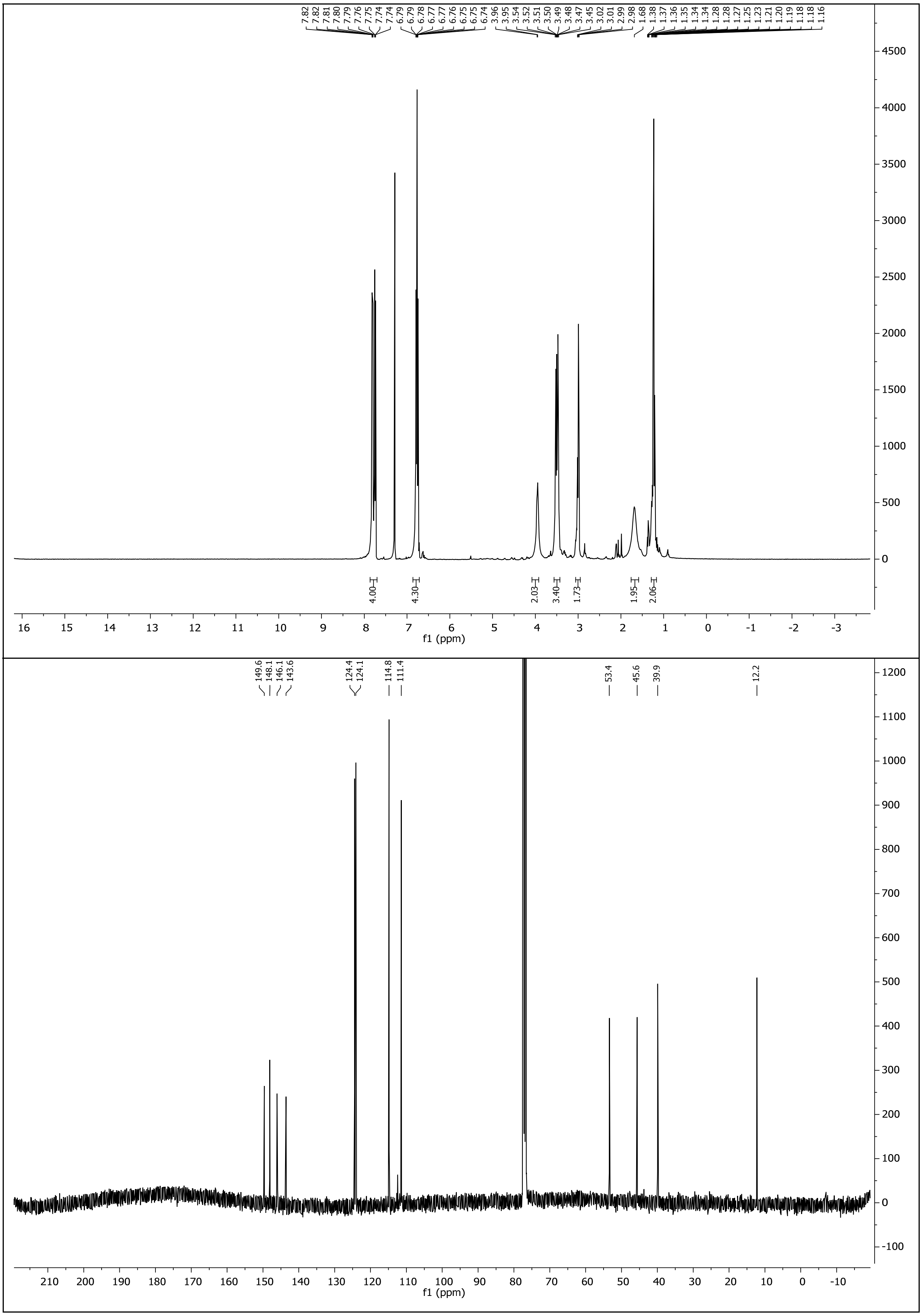

3.4.7.2 *N*-(Carboxymethyl)-*N,N,N*-triethylethanammonium chloride (**3.3**)

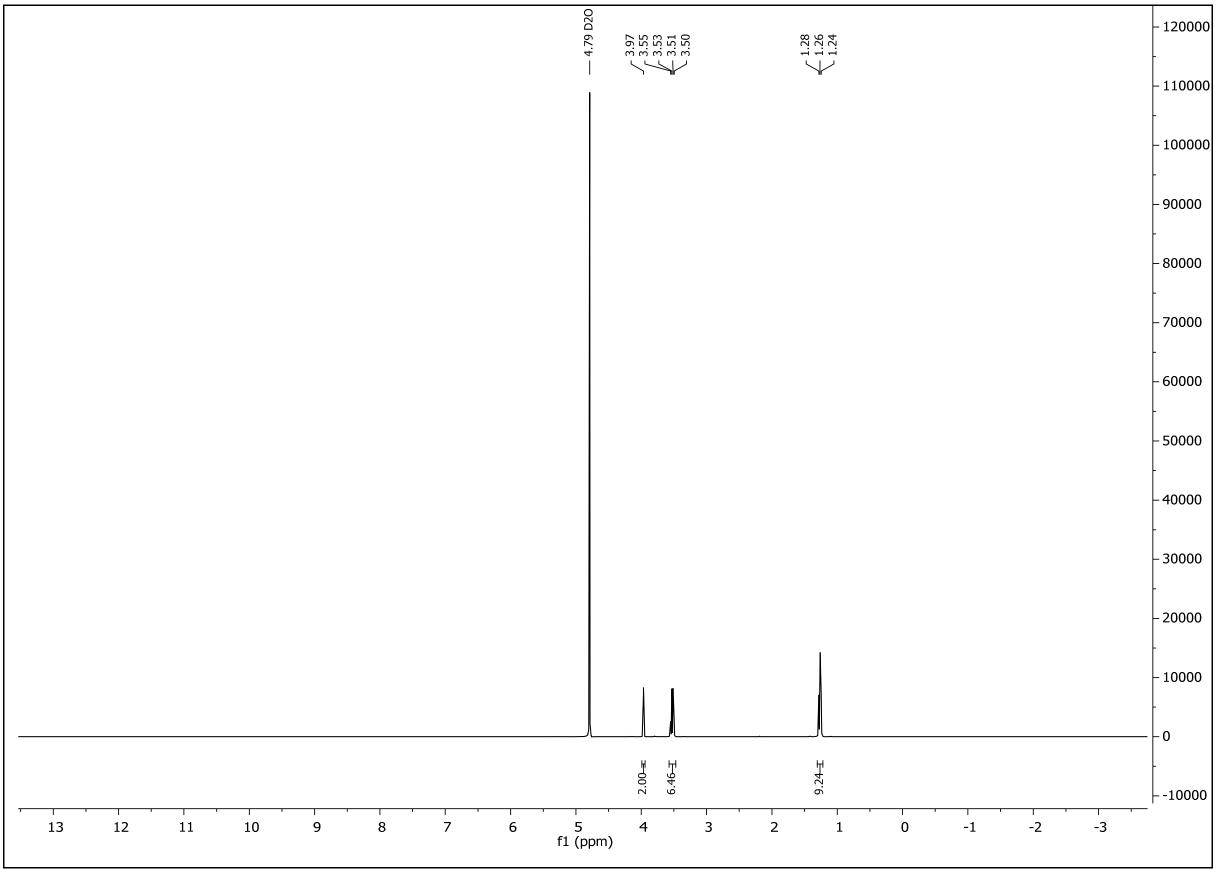

3.4.7.3 (*E*)-*N*-(2-((4-((4-Aminophenyl)diazenyl)phenyl)(ethyl)amino)ethyl)-1-((1,3-dioxoisoindolin-2-yl)oxy)-3,6,9,12,15,18,21,24,27,30,33,36-dodecaoxanonatriacontan-39-amide (**3.2**)

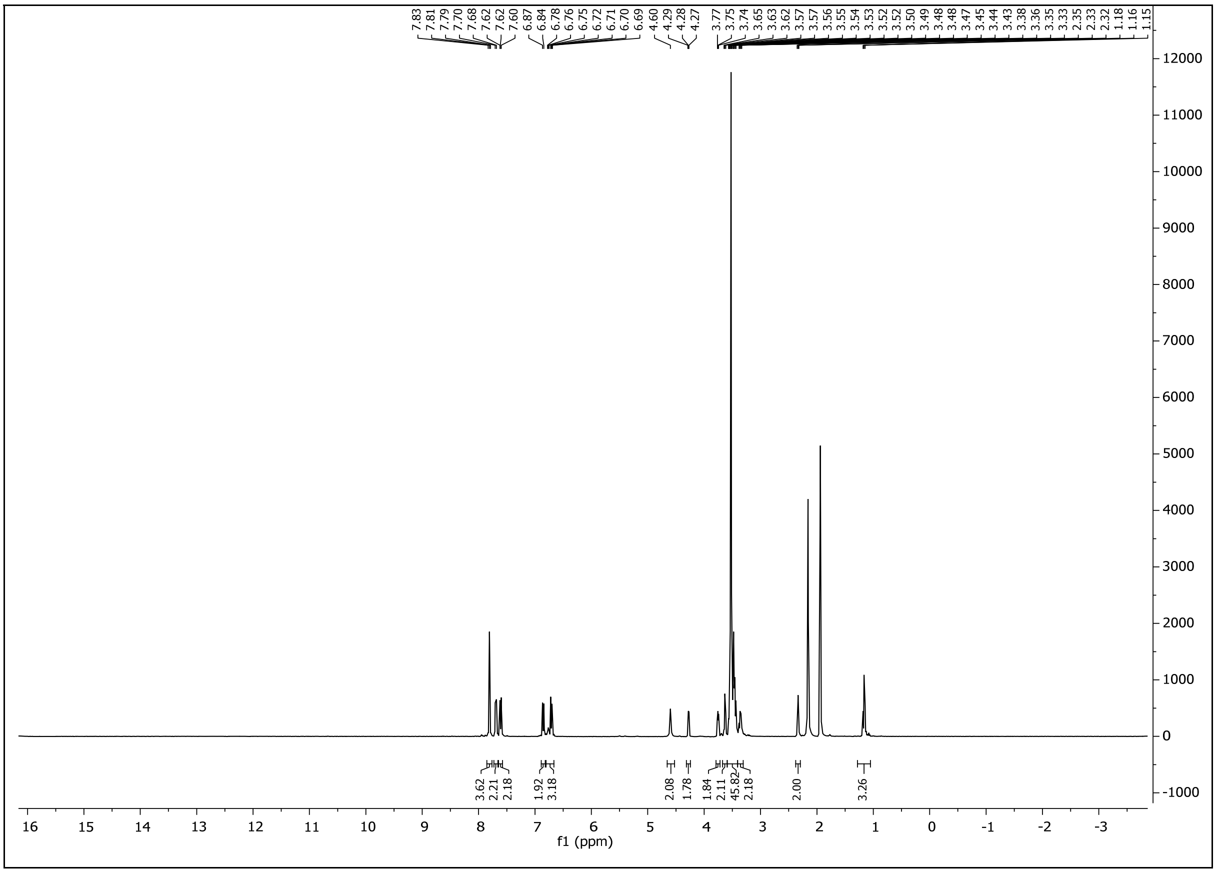

3.4.7.4 (*E*)-2-((4-((4-((1-((1,3-Dioxoisoindolin-2-yl)oxy)-39-oxo-3,6,9,12,15,18,21,24,27,30,33,36-dodecaoxa-40-azadotetracontan-42-yl)(ethyl)amino)phenyl)diazenyl)phenyl)amino)-*N,N,N*-triethyl-2-oxoethan-1-ammonium formate (**3.4**)

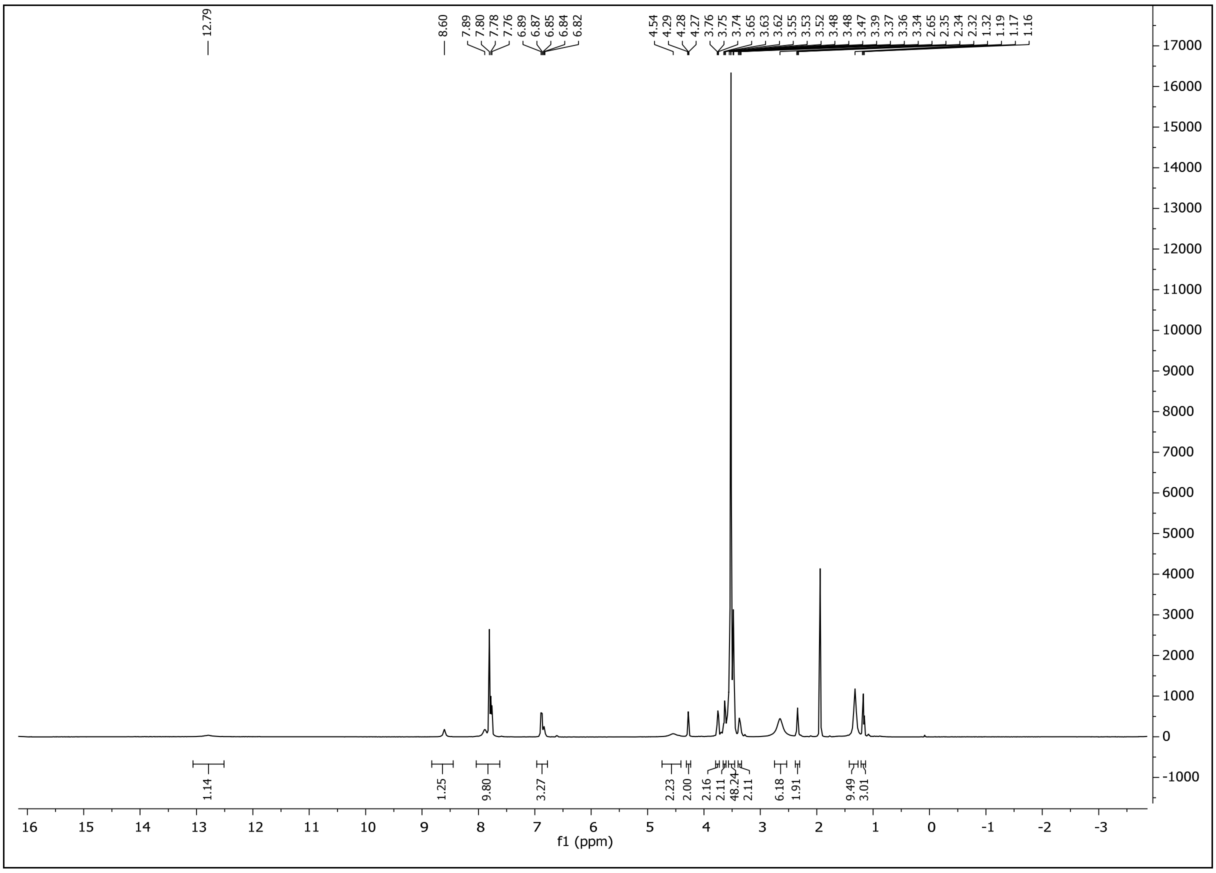

3.4.7.5 *tert*-Butyl (3-(1,3-dioxoisoindolin-2-yl)propoxy)carbamate (**3.13**)

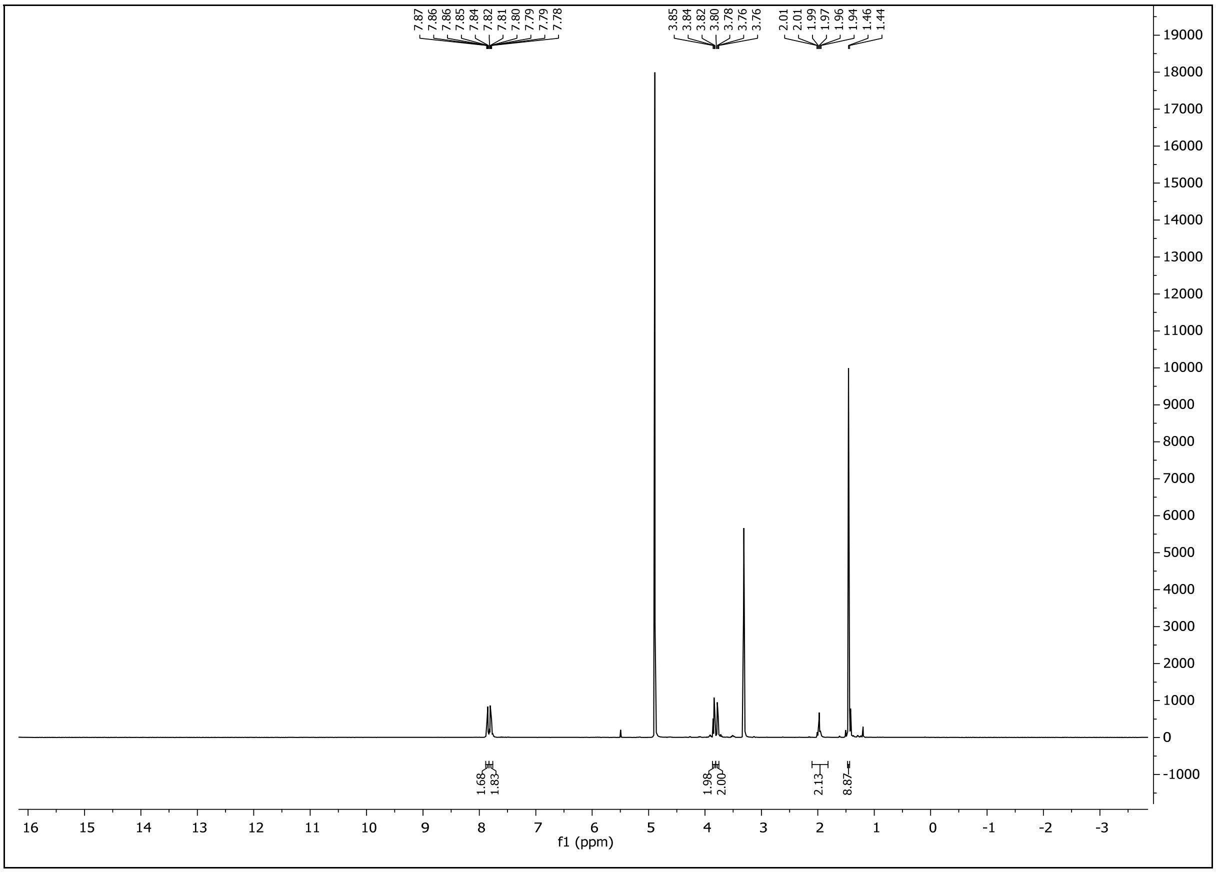

3.4.7.6 *tert*-Butyl (3-aminopropoxy)carbamate (**3.14**)

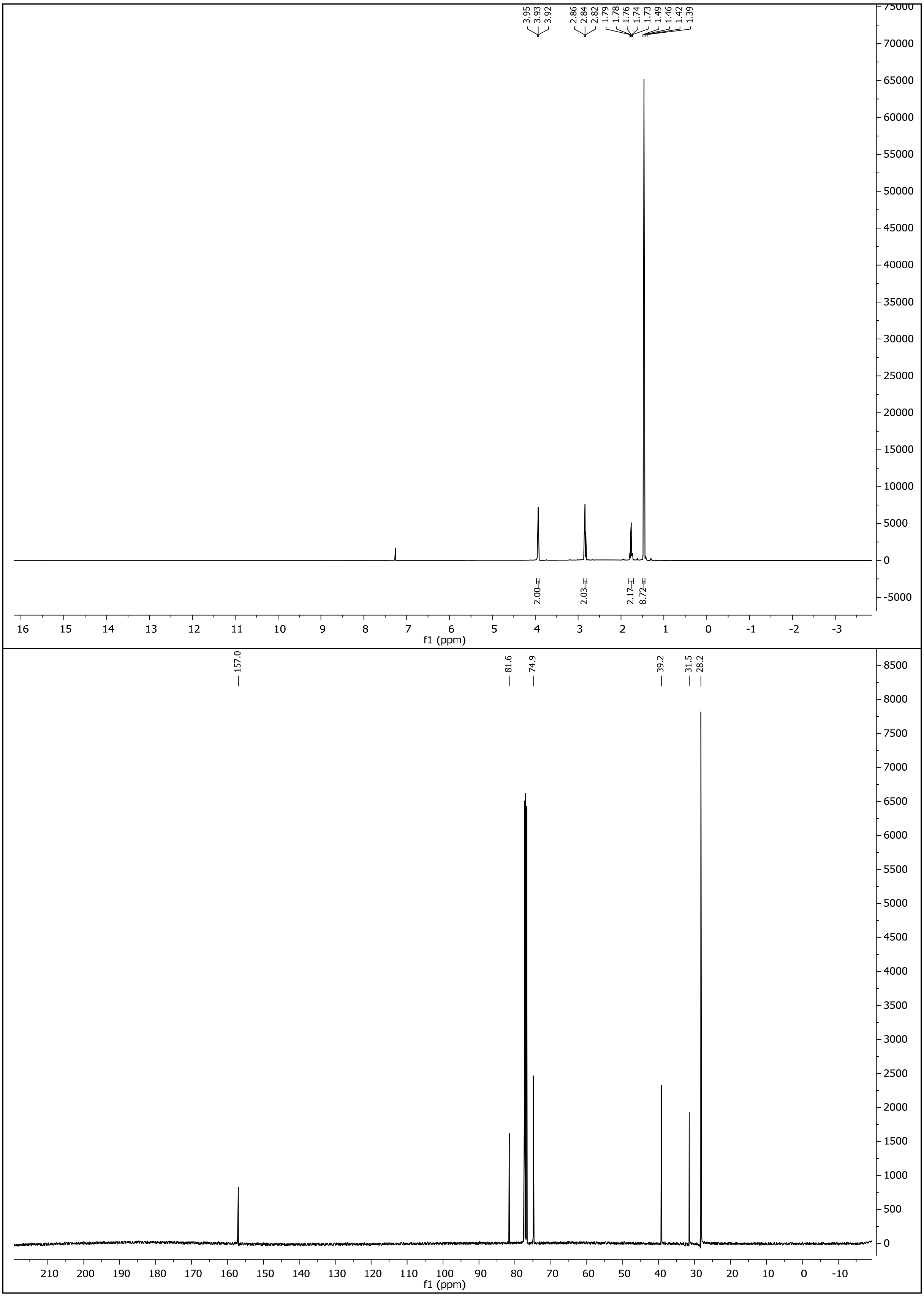

3.4.7.7 (*E*)-2-((4-((4-(2-((*tert*-Butoxycarbonyl)amino)acetamido)phenyl)diazenyl)phenyl) amino)-*N,N,N*-triethyl-2-oxoethan-1-ammonium formate (**3.7**)

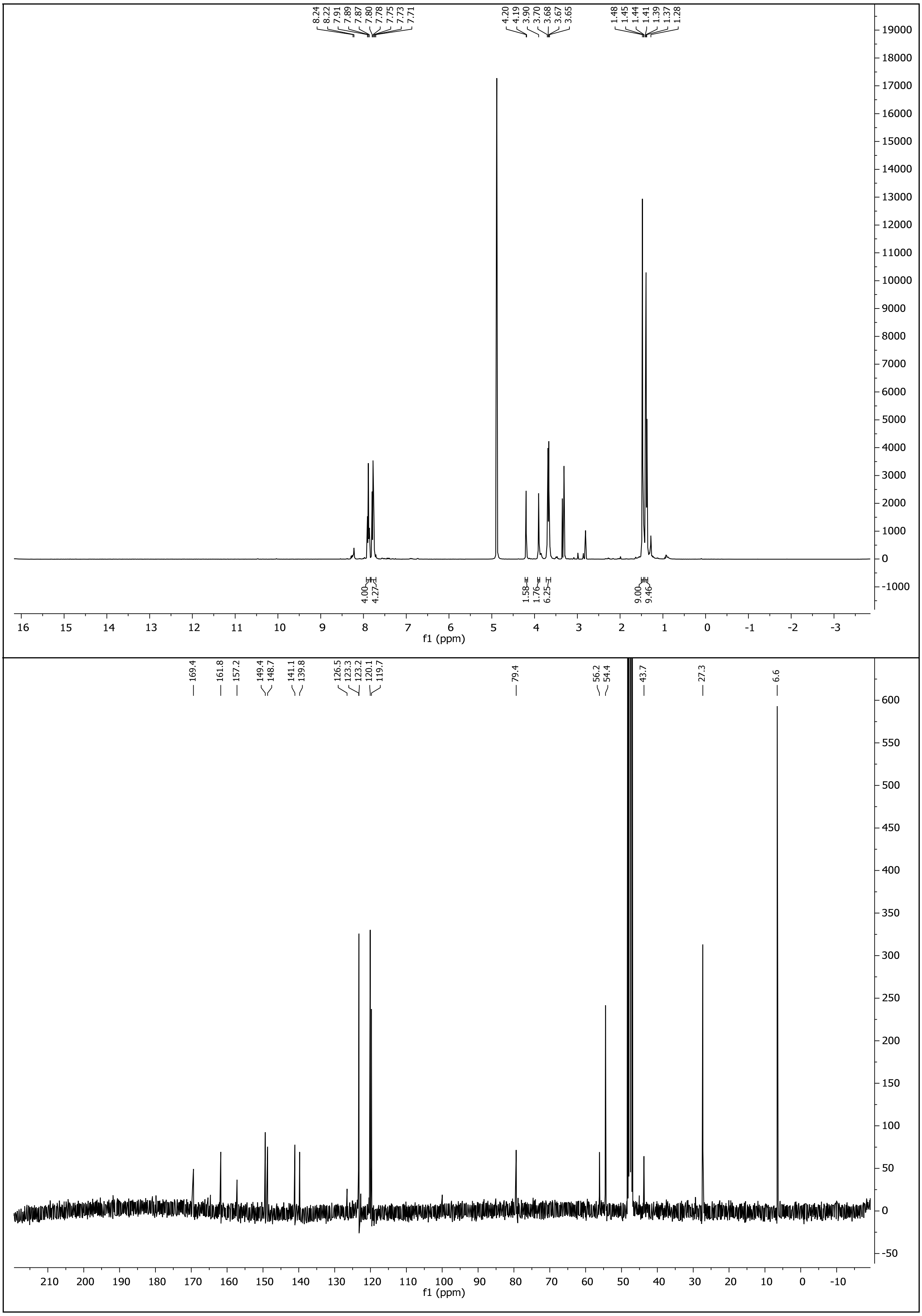

3.4.7.8 (*E*)-2-((4-((4-(50-(Ammoniooxy)-4,46-dioxo-7,10,13,16,19,22,25,28,31,34,37,40,43-tridecaoxa-3,47-diazapentacontanamido)phenyl)diazenyl)phenyl)amino)-*N,N,N*-triethyl-2-oxoethan-1-ammonium bis-(trifluroacetate) (**3.8**)

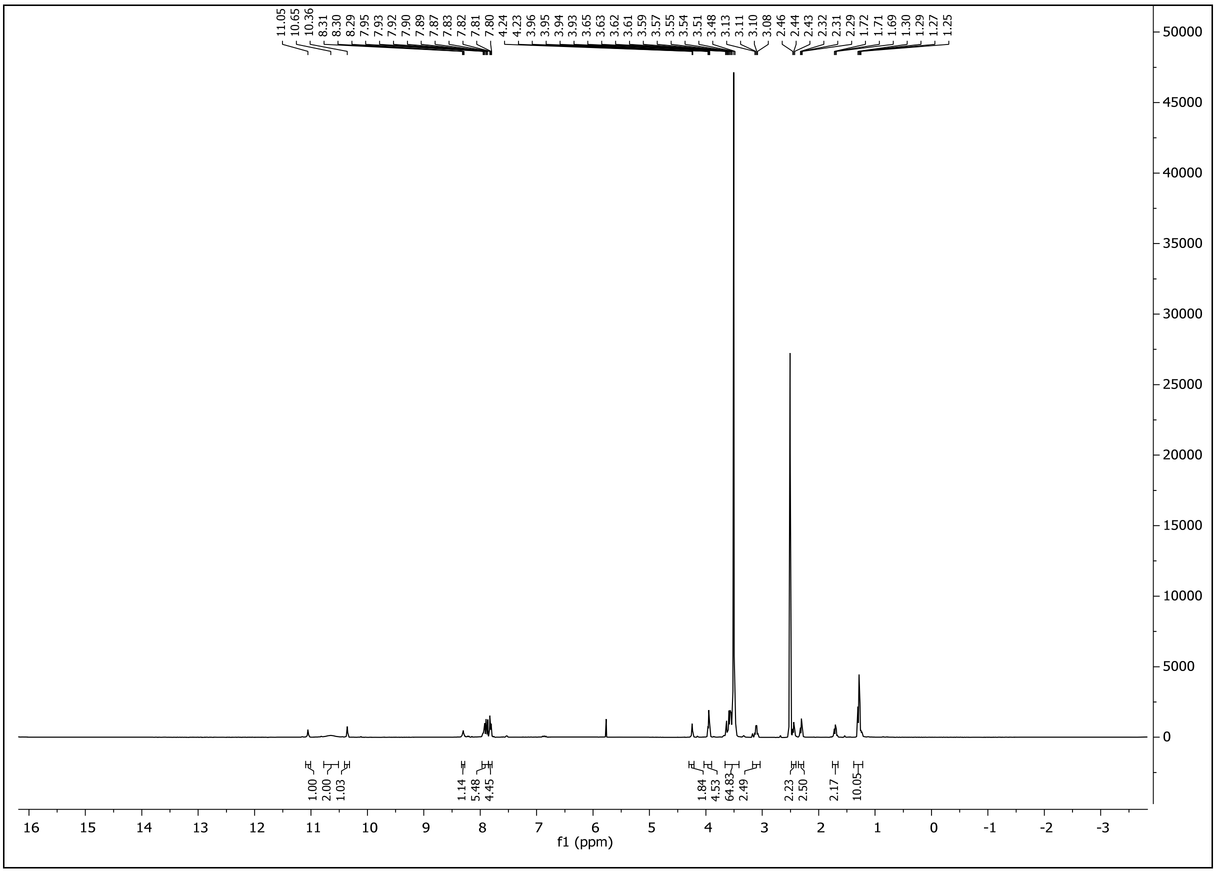

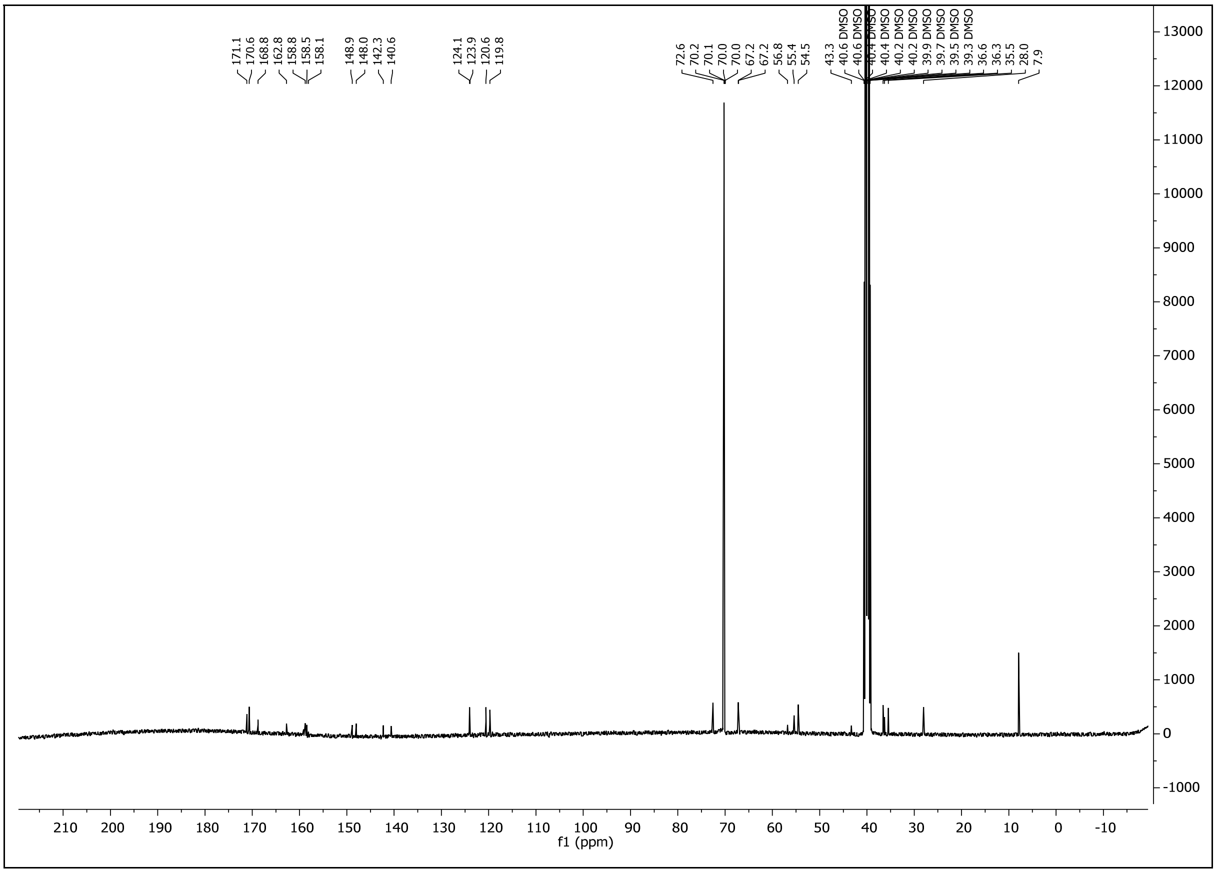

3.4.7.9 (*E*)-N-(4-((4-aminophenyl)diazenyl)phenyl)dodecanamide (**3.15**)

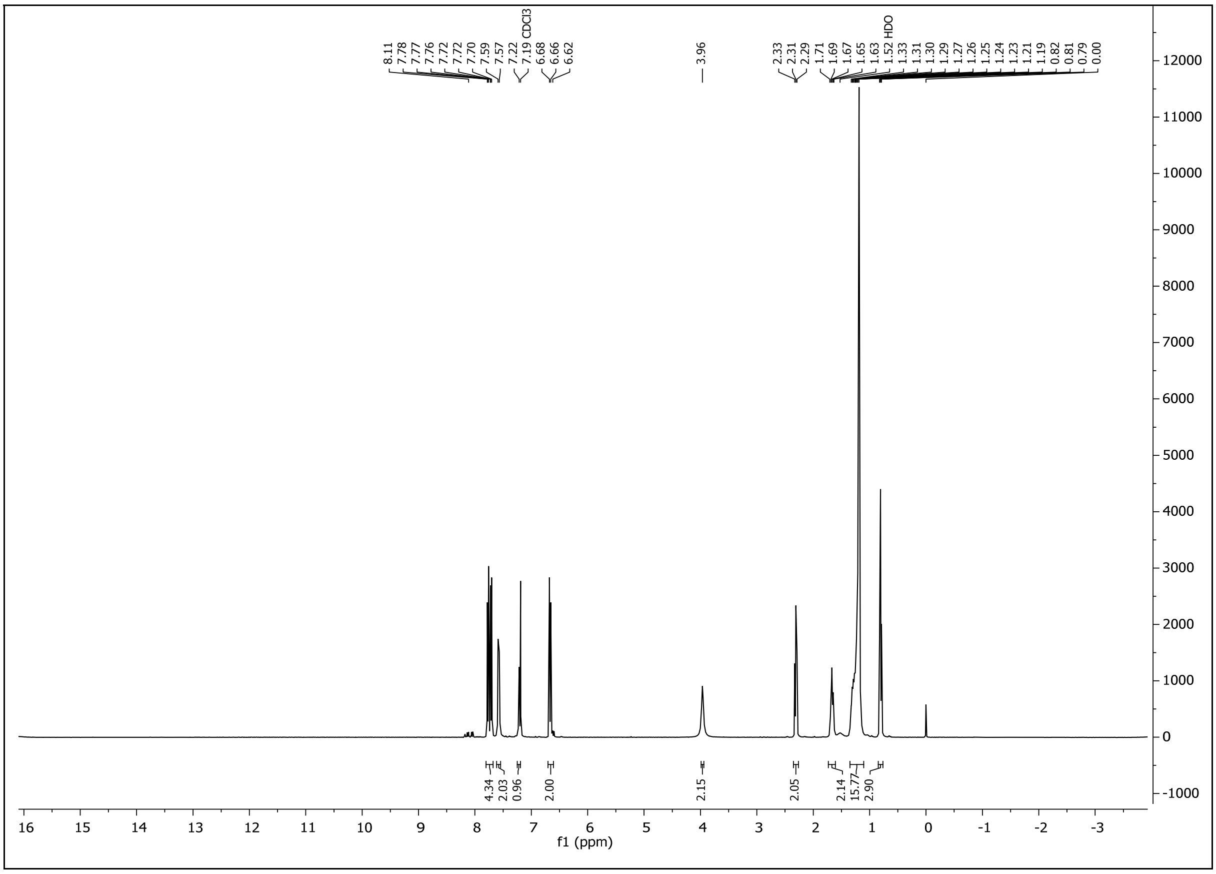

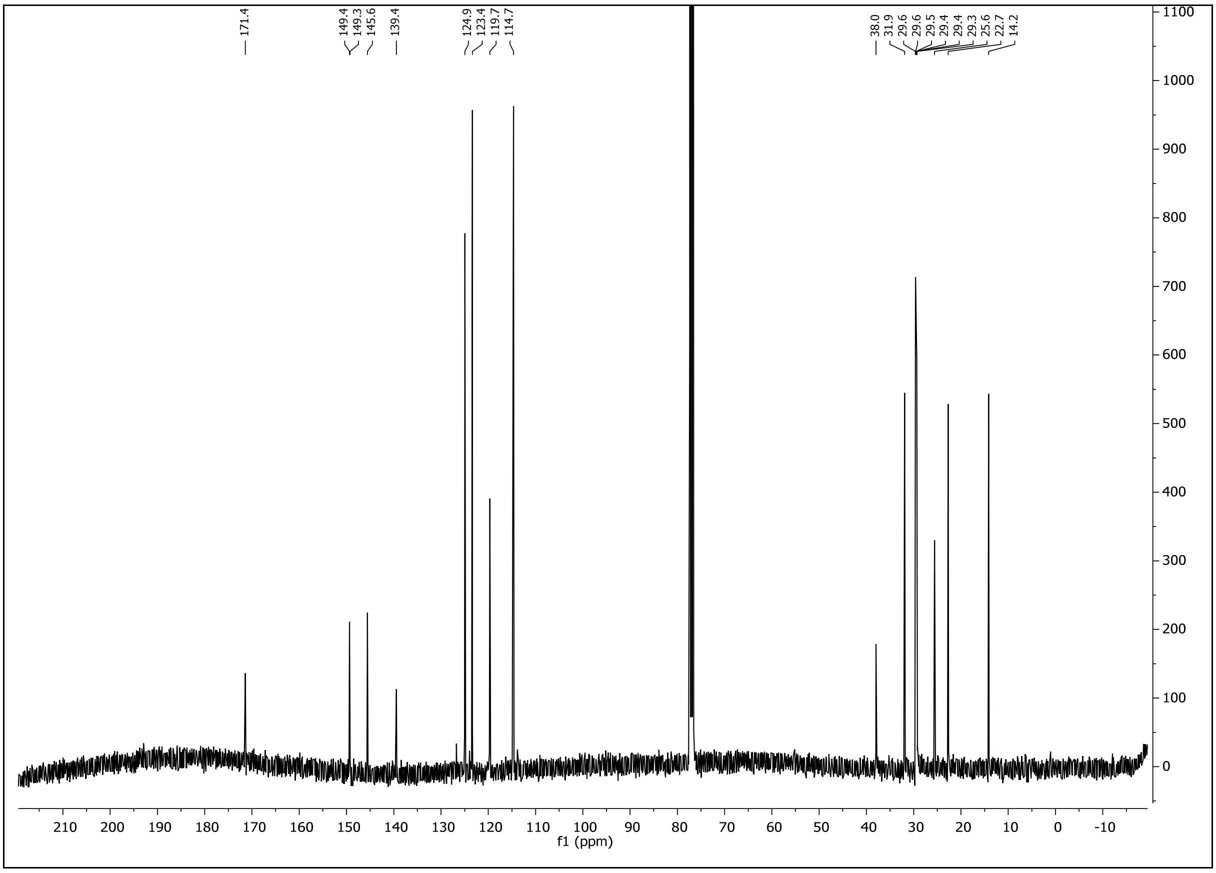
171.4
149.4
149.3
145.6
139.4
124.9
123.4
119.7
114.7
38.0
31.9
29.6
29.6
29.5
29.4
29.4
29.3
25.6
22.7
14.2
1100
1000
900
800
700
600
500
400
300
200
100
0
210
200
190
180
170
160
150
140
130
120
110
100
90
80
70
60
50
40
30
20
10
0
-10
f1 (ppm)

3.4.7.10 (*E*)-2-((4-((4-dodecanamidophenyl)diazenyl)phenyl)amino)-*N,N,N*-triethyl-2-oxoethan-1-ammonium formate (**3.11**)

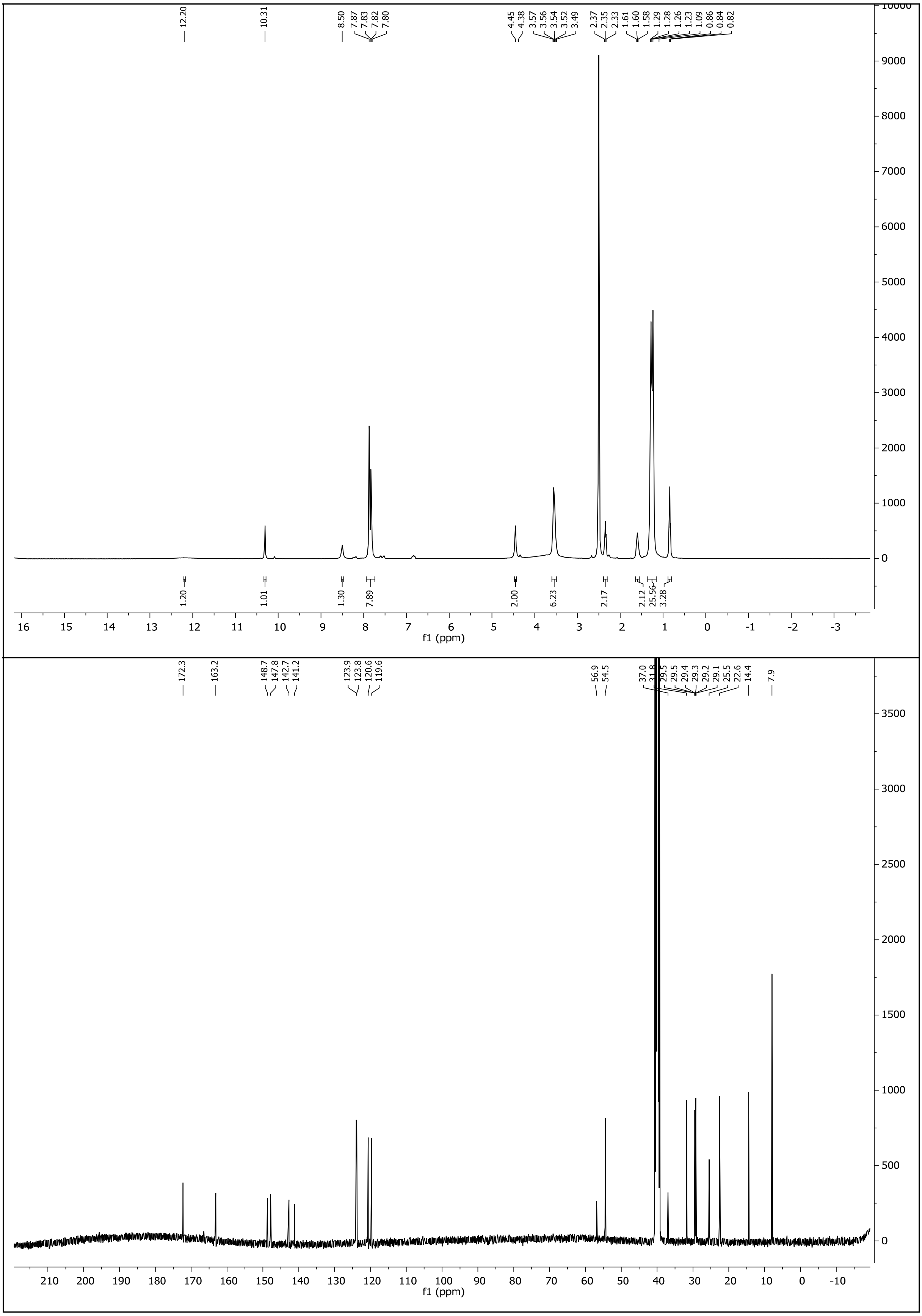

3.4.7.11 (*E*)-1-Butyl-2-((4-((4-(2-dodecanamidoacetamido)phenyl)diazenyl)phenyl)carbamoyl)piperidin-1-ium formate (**3.12**)

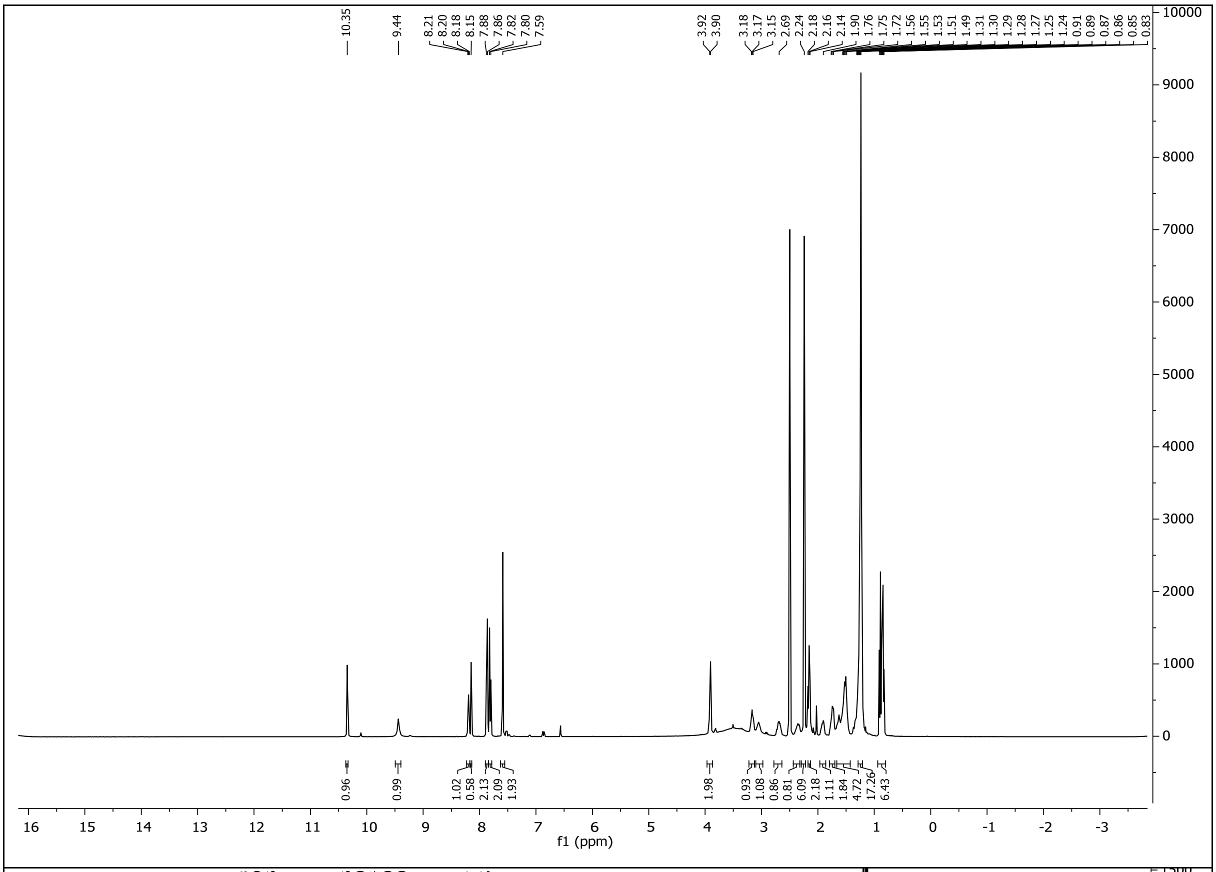

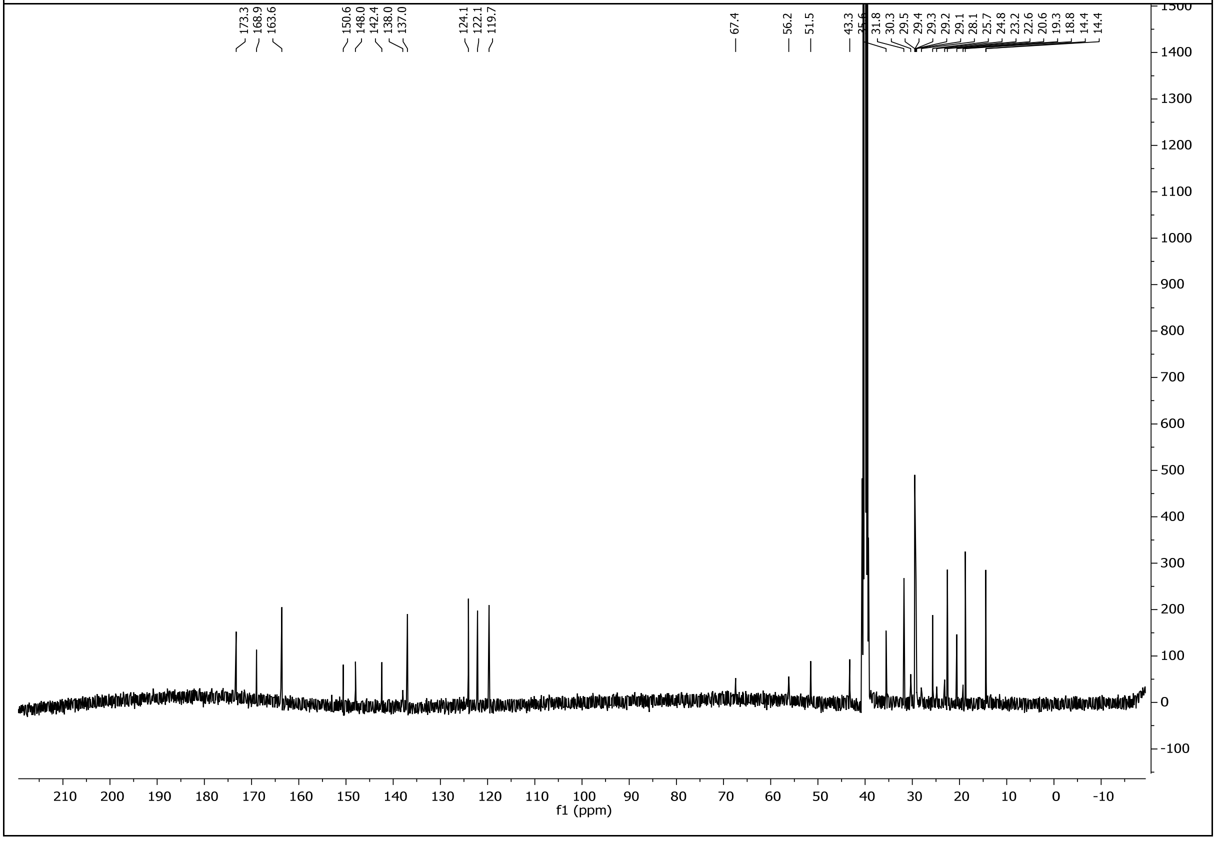

4 Tethered Photopharmacology of the AMPA Receptor

4.1 Introduction

Ionotropic glutamate receptors (iGluRs) are the major mediators of excitatory synaptic transmission. Upon arrival of an action potential in the axon-terminal of the presynaptic neuron, glutamate is released into the synaptic cleft. This spike in glutamate concentration opens postsynaptically expressed iGluRs, triggering an efflux of K^+ and an influx of Na^+ and/or Ca^{2+} ions, resulting in a depolarization of the cell membrane and an excitatory postsynaptic potential (EPSP). Above-threshold EPSPs can in turn trigger voltage-gated Na^+ channels and hence generate an action potential. To date, 18 iGluR subunits have been identified which are classified according to their sensitivity to agonists (AMPA, kainate, and NMDA). Among these, AMPA receptors carry the bulk of the fast excitatory current, producing fast-rising, quickly-desensitizing and high-amplitude EPSPs with a time to peak of around 1 ms.[94] AMPA receptors are tetramers composed of four closely relates subtypes (GluA1-4) which predominantly form a symmetric 'dimer of dimers' of GluA2 with either GluA1, GluA3 or GluA4.[95] While traditional pharmacology has been crucial to identify the different iGluR classes and untangle their contributions to synaptic transmission, its utility is limited not only by their imperfect selectivity profile but also by the ubiquity and abundance of iGluR expression, which at the same time is highly regulated and varied. For instance, AMPA receptors are not only defined by their subunit composition but are also subject to alternative splicing or editing, giving rise to a huge number of possible subunit combinations.[95] Adding another layer of complexity, their precise function is influenced by expression level, location or trafficking and is modulated by auxiliary and regulatory proteins.[95–97] Even more so, when moving from this molecular level to a circuitry of neurons it is easy to see how a systemic application of drugs with limited subtype-selectivity is a tool far too crude to study events of glutamergic synaptic transmission in detail.

One possibility of studying proteins in one population of cells over another is by genetic targeting. For instance, membrane-tethered toxins can be expressed in specific cell populations and block endogenous ion channels.[98] One drawback of this method compared to pharmacology is the lack of acute onset which could cause complications such as compensatory gene expression. Shields *et al.* described an alternative strategy termed 'drugs acutely restricted by tethering' (DART) to combine the cell-type specificity and endogenous-protein specificity of genetic methods with the acute onset of pharmacology (Figure 27a).[32] Therein, the AMPAR antagonist YM90K is synthetically modified with bioconjugation motif (Halo-tag ligand), separated by a long PEG_{36} chain as tether. The Halo-tag is a self-labelling protein tag (size: ~34 kDa) derived from the a bacterial haloalkane dehalogenase.[99] It reacts with chloroalkanes (Halo-tag ligand) with high speed and specificity. The Halo-tag is fused to a membrane anchor, and by expressing it in AMPAR-positive cells and subsequent labelling with the tethered antagonist, endogenous AMPARs can be antagonized. The large advantages of this approach over other genetically encoded approaches lie in the inactivity of the Halo-tag prior to application of the tethered antagonist and that it does not require modification of the receptor itself. We envisioned that we could equip this tethered DART antagonist with another layer of control by incorporation of the photoswitch ShuBQX-3 (Figure 27b). ShuBQX-3 is a photoswitchable antagonist of the AMPAR and was introduced by the Trauner group in 2017.[79] It is derived from quinoxaline-2,3-dione antagonists such as DNQX or zonampanel/YM90K which allow for a variety of substitutions in the 6-position of their core structure. Applied as a freely diffusible photoswitch, it is an antagonist in its *trans*-form, blocking glutamate-induced AMPAR currents entirely. Upon illumination and isomerization to the *cis*-configuration, about 50% of the block is relieved (in presence of 300 μM L-glu). The envisioned hybrid molecule of ShuBXQ-3 and YM90K-DART that is termed '*para*-PORTL' (Figure 27c). It represents a refinement of the photoswitchable orthogonal remotely-tethered ligands (PORTL) demonstrated in 2015 for the SNAP-tagged metabotropic glutamate receptors (mGluRs; see chapter 1 for more details on PORTL).[28] While the SNAP-tag in the PORTL concept resides on the receptor of interest, the tag in *para*-PORTL is even further removed to a protein its near vicinity, *e.g.* a membrane anchor or a membrane-bound auxiliary or regulatory protein (*para from the Greek word for beside, next to, near*).

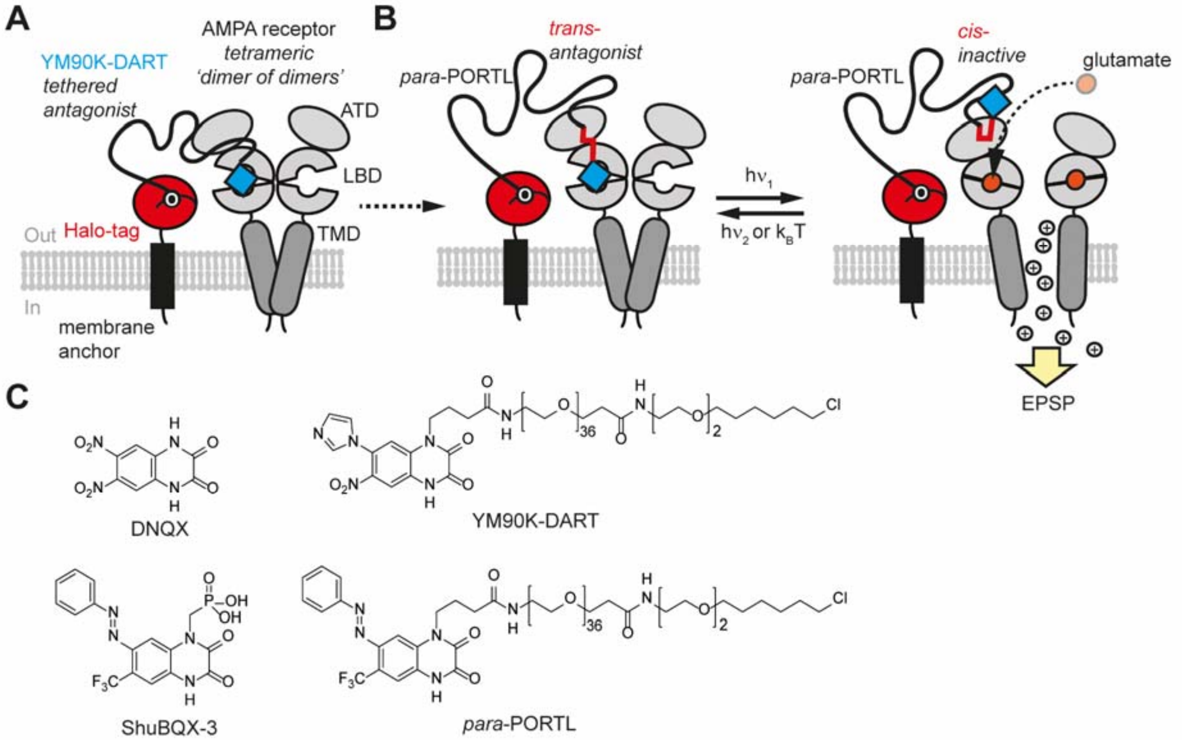

Figure 27. ***para*-PORTL concept and design. a)** Drugs acutely restricted by tethering (DART) by Shields *et al.*[32] **b)** By incorporating a photoswitch in the DART molecule, optical control can

be achieved by the obtained *para*-PORTL. (ATD: amino terminal domain, LBD: ligand binding domain, TMD: transmembrane domain, EPSP: excitatory postsynaptic potential).

4.2 Results and Discussion

The synthesis of *para*-PORTL **4.10** was started by a nucleophilic aromatic substitution of electron-poor, commercially available starting material **4.1** with the ethyl ester of 4-aminobutanoic acid (Scheme 5). The reaction was carried out with a limiting two equivalents of cesium carbonate in DMSO to avoid ester hydrolysis. **4.2** was then coupled to 1-Boc-1-phenylhydrazine **4.3** in a Buchwald-Hartwig cross-coupling reaction employing palladium diacetate as catalyst and *t*-Bu_3P as ligand. **4.4** was subsequently reduced by palladium on carbon and hydrogen gas to afford aniline **4.5.** A condensation reaction with oxalyl chloride furnished quinoxaline-2,3-dione **4.6.** The ester was saponified by sodium hydroxide in a mixture of MeOH and THF, providing the free acid **4.7.** A PEG_{36} tether was then installed by amide coupling to H_2N-PEG_{36}-COO*t*Bu. By addition of neat TFA, the molecule was deprotected globally to obtain the azobenzene moiety and the free acid handle. Finally, amide coupling to Halo-Tag ligand afforded the *para*-PORTL **4.10** over a total of 8 linear synthetic steps.

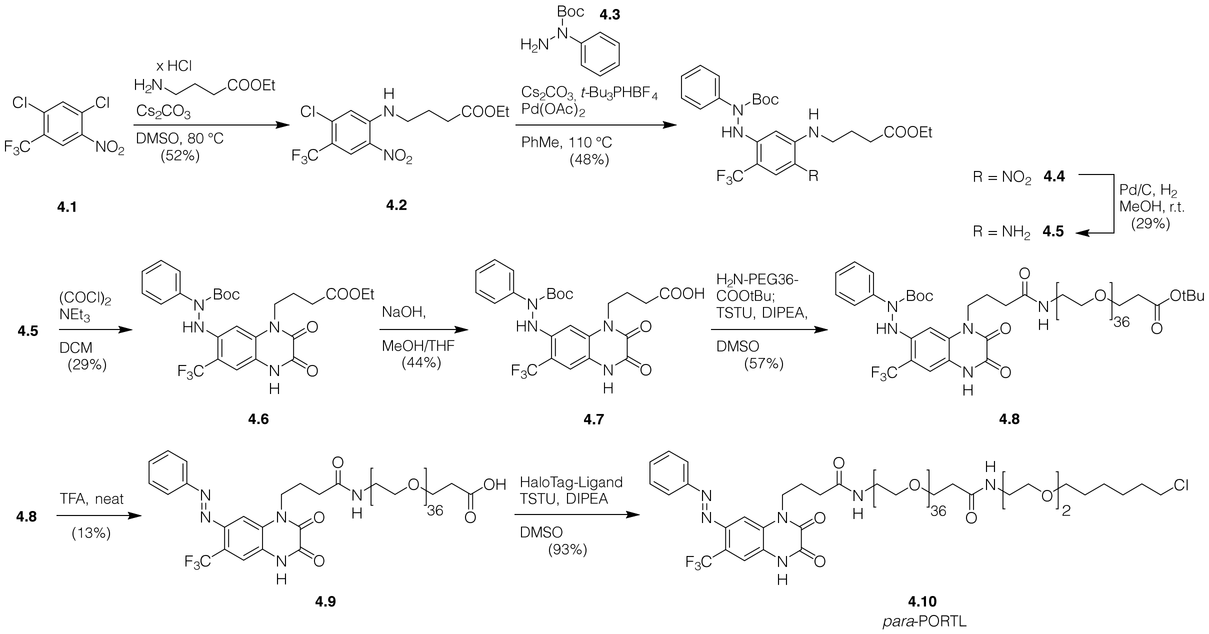

Scheme 5. **Synthesis of *para*-PORTL 4.10.**

The *para*-PORTL **4.10** was then evaluated in an *in vitro* labelling experiment. To this end, purified Halo-tag protein (MW ~34 kDa) was incubated with a fourfold excess of **4.10** and then directly loaded on a SDS-PAGE precast gel (Figure 28). The clean shift to higher molecular weight is indicative of successful labeling with **4.10.** As positive control, Halo-tag protein was labelled with the fluorescent Halo-TMR, which is 6-carboxytetramethylrhodamine amide coupled to Halo-tag ligand (Lane 3 in a) and b). To determine if **4.10** labels the Halo-tag protein to completion, it was labelled in a first reaction with **4.10** and afterwards in a second reaction with Halo-TMR. The absence of TMR fluorescence is indicative of full labelling in the first reaction with **4.10** (lane 4 in b)**.**

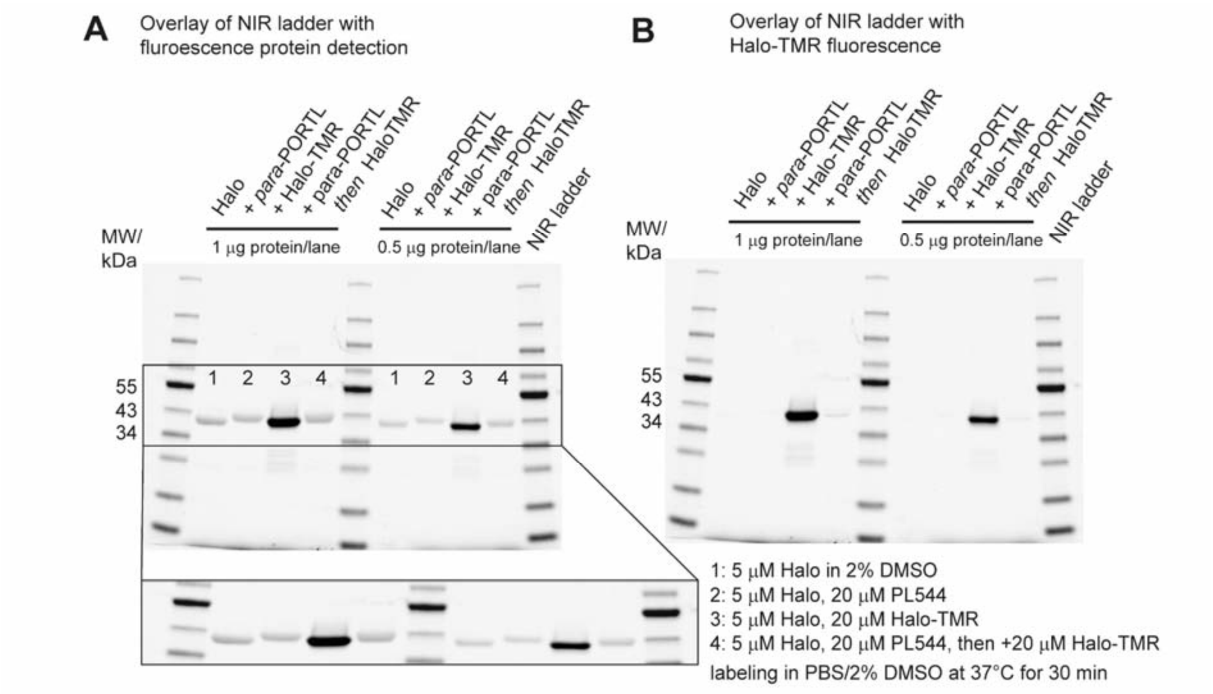

Figure 28. **In vitro labelling of purified Halo-tag protein with para-PORTL 4.10. a)** Protein was labelled as indicated and total protein amount was detected by UV-induced fluorescence (Bio-Rad Mini-Protean stain-free™ precast gels). Overlay with near-infrared fluorescent ladder. The Halo-tag protein shows a clear shift in molecular weight upon reaction with the ca. 2.3 kDa *para*-PORTL (lane 1 and 2). TMR-labelled Halo-tag shows bleed-through into the protein detection channel (lane 3). The Halo-tag is labelled to completion by the para-PORTL, a later incubation with Halo-TMR leads to no TMR-labelling (lane 4). **b)** Same as a) but TMR-fluorescence channel.

As of now, the electrophysiological evaluation of **4.10** is only in its very early stages. In preliminary experiments, **4.10** was tested by Dr. Prashant Donthamsetti (Isacoff lab, UC Berkeley) in patch-clamp recordings (Figure 37). The AMPAR (GluA1, non-desensitizing mutant) was opened by application of L-glu (1 mM). **4.10** was then able to photoblock 11.9 ± 2.3% of the inward current (n = 9 cells) after photoisomerization to *cis* (380 nm, grey). Under blue light (460 nm), no effect was observed. The small block observed with orange light (600 nm) is likely an effect of the light's first harmonic oscillation (300 nm), which is isomerizing a fraction of **4.10** to *cis*. Therefore, **4.10** is inactive in its *trans*-configuration while the *cis*-isomer acts as a competitive antagonist.

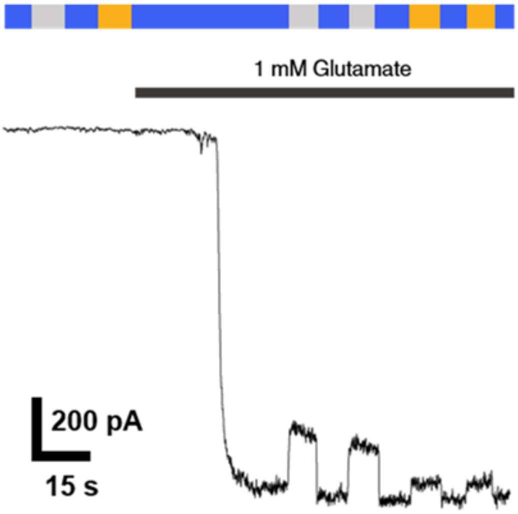

Figure 29. **Photoblock of AMPAR by *para*-PORTL 4.10.** Blue: 460 nm, grey: 360 nm, orange: 600 nm.

That the *cis*-isomer of **4.10** is the active configuration is unexpected and in stark contrast to the initial expectations (compare to Figure 27). The freely diffusible photoswitch ShuBQX-3 was active in its *trans*-isomer.[3] In addition to being *trans*-active, ShuBQX-3 exhibited a strong bathochromic shift in switching wavelengths. More specifically, in DMSO or in aqueous Ringer-Buffer, ShuBQX-3 behaved like a normal azobenzene in UV/Vis experiments, with optimal switching wavelengths of 380 nm (*trans* to *cis*) and 460 nm (*cis* to *trans*). However, when ShuBQX-3 was applied to HEK293T cells expressing AMPAR, the optimal wavelength for *trans*- to *cis*-isomerization in patch-clamp experiments was 460 nm. In an attempt to explain this bathochromic shift, the authors consulted the X-ray structure of MPXQ bound to the AMPAR.[100] In this structure, the guanidinium moiety of an arginine (R-485) is positioned near the quinoxaline-2,3,-dione core of the antagonist MPQX. Consequently, the authors ascribed the observed bathochromic shift to similar interactions of this arginine with the quinoxaline-2,3-dione core of ShuBQX-3. This was corroborated by UV/Vis-experiments in which a DMSO solution of ShuBQX-3 was spiked with L-arginine or guanidine (20 equiv.). In both cases, a bathochromic shift was observed that was comparable to the one observed in the patch-clamp experiments. In conclusion, *trans*-ShuBQX-3 binds competitively (with L-glu) to AMPAR, the interaction with arginine results in the bathochromic shift, and the receptor-bound *trans*-ShuBQX-3 is isomerized to *cis* by illumination with blue light (460 nm). This triggers the release of ShuBQX-3 from the binding pocket.

In **4.10**, the installation of the PEG chain likely restrains the positioning of the quinoxaline-2,3-dione core in the AMPAR binding pocket. Therefore, *trans*-**4.10** cannot be accommodated anymore while the ‘smaller’ *cis*-isomer still fits into the binding pocket, antagonizing the receptor. Unfortunately, the amplitude of photoblock under physiological concentrations of L-glu (1 mM) is likely too low to efficiently block AMPAR-mediated synaptic transmission in neurons, which is the primary goal.

In the PORTL concept, the use of low-affinity ligands can be advantageous (see chapter 1). Improvements of photoblock will therefore not be aimed at improving the affinity but rather at increasing the effective concentration of tethered **4.10** around the AMPAR. This will be tackled by two strategies, i) cloning of Halo-membrane anchors that position **4.10** more efficaciously and ii) by introducing multivalent, dendritic ligands that have multiple photoswitches attached to one bioconjugation motif.

4.3 Conclusion and Outlook

A novel approach, termed *para*-PORTL, is illustrated on the AMPA receptor which represents an improvement and a refinement of the PORTL concept. In *para*-PORTL, the bioconjugation tag is removed from the receptor itself to a protein in its near vicinity, *e.g.* an auxiliary or a scaffold protein. Since no modification of the receptor is required, the *para*-PORTL concept better reflects the underlying receptor biology. The biological investigation is currently underway in collaboration with the Isacoff laboratory and first experiments were promising, showing a light-dependent block of AMPAR (GluA1-L497Y, non-desensitizing point mutant).

Due to their central role in synaptic transmission, dysregulation or dysfunction of AMPA receptors often result in neurological diseases with massive human cost such as epilepsy or Alzheimer's.[101,102] *para*-PORTLs permit perturbation of endogenous AMPA receptors with light and could be an useful tool to study physiological and pathophysiological processes with AMPAR contribution. For instance, the subunit composition governs the ratio of Ca^{2+} impermeable (CI) and permeable (CP) AMPA receptors, which is a major determinant of excitotoxicity and is linked to diseases like amyotrophic lateral sclerosis.[103] The ratio of CP/CI-AMPARs is also influenced by their association with auxiliary subunits of which a large variety has been identified, such as transmembrane AMPA receptor regulatory proteins (γ2-8 TARPs), cornichons, Shisas and GSG1L.[104] By fusing a Halo-tag to the different auxiliary subunits and labelling with a *para*-PORTL molecule, associated populations of AMPARs may be blocked and unblocked using light. This could help to break down contributions of subunit-AMPAR complexes to disease states.

4.4 Supporting Information

4.4.1 Synthesis

LCMS was performed on a Shimadzu MS2020 connected to a Nexerra UHPLC system equipped with a Waters ACQUITY UPLC BEH C18 1.7 µm 2.1x50 mm column. Buffer A: 0.05% HCOOH in H_2O Buffer B: 0.05% HCOOH in acetonitrile. Analytical gradient was from 10% to 90% B within 4.0 min with 1 mL/min flow.

4.4.1.1 Ethyl 4-((5-chloro-2-nitro-4-(trifluoromethyl)phenyl)amino)butanoate (**4.2**)

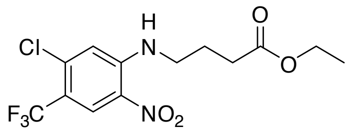

1,5-Dichloro-2-nitro-4-(trifluoromethyl)benzene (2.01 g, 7.73 mmol, 1.04 equiv.) and ethyl 4-aminobutanoate (1.25 g, 7.46 mmol, 1.0 equiv.), cesium carbonate (6.00 g, 15.35 mmol, 2.96 equiv.) and DMSO (30 mL) were heated to 80 °C overnight. The reaction mixture was diluted with water (600 mL) and extracted with EtOAc (4 x 400 mL). The combined organic layers were washed against water (400 mL), 10% aq. LiCl solution (400 mL) and brine (400 mL), and dried over $MgSO_4$ before concentration *in vacuo*. The residue was purified by flash column chromatography (EtOAc/hexanes = 1/5) to yield the desired product as a citron-yellow, waxy solid (1.37 g,3.86 mmol, 52%).

TLC (EtOAc/hexanes = 1/5): 0.30 (UV + yellow color).

^{1}H NMR (400 MHz, $CDCl_3$) δ 8.52 (d, J = 0.7 Hz, 1H), 8.40 – 8.18 (m, 1H), 7.04 (s, 1H), 4.18 (q, J = 7.1 Hz, 2H), 3.42 (td, J = 7.2, 5.5 Hz, 2H), 2.47 (t, J = 6.9 Hz, 2H), 2.19 – 1.99 (m, 2H), 1.28 (t, J = 7.2 Hz, 3H).

^{13}C NMR (101 MHz, $CDCl_3$): δ 172.53, 146.68, 139.76, 129.38, 127.24 (q, J = 5.7 Hz), 122.34 (q, J = 271.6 Hz), 116.04, 115.42 (q, J = 33.4 Hz), 60.88, 42.58, 31.20, 23.79, 14.21.

Note: Purity ca. 95%. Ca. 5% contamination with the free acid. The impurity had no impact on subsequent reactions.

HRMS (ESI): *m/z* calc. for $C_{13}H_{15}ClF_3N_2O_4^+$ $(M+H)^+$: 355.0667, found: 355.0667.

t

4.4.1.2 *tert*-Butyl 1-phenylhydrazine-1-carboxylate (**4.3**)

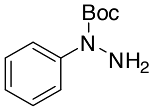

4.3 was prepared according to a published procedure.[105] Analytical data matched those reported.

^{1}H NMR (400 MHz, $CDCl_3$) δ 7.52 – 7.41 (m, 2H), 7.42 – 7.27 (m, 2H), 7.13 (ddt, *J* = 8.6, 7.0, 1.2 Hz, 1H), 4.23 (s, 3H), 1.52 (s, 9H).

4.4.1.3 *tert*-Butyl 2-(5-((4-ethoxy-4-oxobutyl)amino)-4-nitro-2-(trifluoromethyl)phenyl)-1-phenylhydrazine-1-carboxylate (**4.4**)

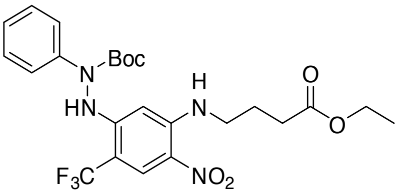

4.2 (1.06 g, 3.00 mmol, 1.0 equiv.), *tert*-butyl 1-phenylhydrazine-1-carboxylate (750 mg, 3.60 mmol, 1.2 equiv.), cesium carbonate (1.37 g, 4.20 mmol, 1.4 equiv.), tBu_3PHBF_4 (174 mg, 0.60 mmol, 0.2 equiv.), $Pd(OAc)_2$ (67.4 mg, 0.30 mmol, 0.1 equiv.) and toluene (50 mL) were combined in a pressure flask, purged with Argon, sealed and heated to 110 °C for 24 h. The reaction mixture was allowed to cool to r.t., filtered over celite, washing with a copious of EtOAc. The filtrate was concentrated *in vacuo* and purified by flash column chromatography 100% DCM) to yield the product as a yellow gum (754 mg, 1.43 mmol, 48%).

TLC (100% DCM): 0.27 (UV+yellow color); SM: 0.49 (UV+yellow color).

^{1}H NMR (400 MHz, $CDCl_3$) *δ* 8.40 (d, *J* = 0.9 Hz, 1H), 8.35 – 8.27 (m, 1H), 7.51 – 7.45 (m, 2H), 7.32 – 7.26 (m, 2H), 7.14 – 7.08 (m, 2H), 6.07 (s, 1H), 4.05 (q, *J* = 7.1 Hz, 2H), 3.13 (td, *J* = 7.0, 5.5 Hz, 2H), 2.27 (t, *J* = 7.2 Hz, 2H), 1.83 (p, *J* = 7.1 Hz, 2H), 1.38 (s, 9H), 1.18 (t, *J* = 7.1 Hz, 3H).

^{13}C NMR (101 MHz, $CDCl_3$): δ 172.5, 152.9, 150.4, 148.6, 141.2, 129.1, 128.2 (q, J = 5.5 Hz), 125.6, 125.3, 121.5, 103.6 (d, J = 33.0 Hz), 93.6, 83.6, 60.8, 42.4, 31.5, 28.2, 23.8, 14.4.

Note: CF_3 carbon not observed.

HRMS (ESI): *m/z* calc. for $C_{24}H_{30}F_3N_4O_6^+$ $(M+H)^+$: 527.2112, found: 527.2117.

t_R (LCMS) = 3.96 min.

UV/Vis (LCMS): λ_{max1} = 239 nm, λ_{max2} = 351 nm (broad).

4.4.1.4 *tert*-Butyl 2-(4-amino-5-((4-ethoxy-4-oxobutyl)amino)-2-(trifluoromethyl)phenyl)-1-phenylhydrazine-1-carboxylate (**4.5**)

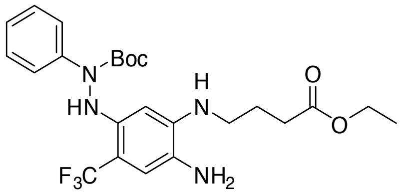

4.4 (486 mg, 0.92 mmol, 1.0 equiv.) was dissolved in MeOH (10 mL) and Pd/C (10 wt % Pd, 195 mg, 0.18 mmol, 0.2 equiv.) was added. The reaction flask was flushed with hydrogen (3x). The resulting mixture was stirred at r.t. overnight. The reaction mixture was filtered over celite, washing with EtOAc. The filtrate was concentrated and purified by flash column chromatography (2% MeOH/DCM) to give the product as a brownish, viscous oil (133 mg, 0.27 mmol, 29%)

TLC (5% MeOH/DCM): 0.38 (UV+ninhydrin).

^{1}H NMR (400 MHz, $CDCl_3$) δ = 7.54 (dt, *J* = 8.1, 1.1 Hz, 2H), 7.30 – 7.20 (m, 2H), 7.08 – 6.99 (m, 1H), 6.93 – 6.66 (m, 2H), 6.04 (s, 1H), 4.05 (q, *J* = 7.2 Hz, 2H), 2.96 (s, 3H), 2.32 (t, *J* = 7.3 Hz, 2H), 1.83 (p, *J* = 7.0 Hz, 2H), 1.33 (s, 9H), 1.17 (t, *J* = 7.1 Hz, 3H).

^{13}C NMR (101 MHz, $CDCl_3$): δ = 173.8, 153.7, 143.8, 142.5, 128.6, 128.6, 124.9, 124.5, 121.4, 116.9, 95.1, 82.4, 60.7, 42.9, 32.1, 28.0, 24.2, 14.2.

Note: CF_3 carbon not observed, C-F couplings not observed.

HRMS (ESI): *m/z* calc. for $C_{24}H_{32}F_3N_4O_4^+$ $(M+H)^+$: 497.2370, found: 497.2371.

t_R (LCMS) = 2.85 min.

UV/Vis (LCMS): λ_{max1} = 198 nm, λ_{max2} = 233 nm, λ_{max3} = 269 nm.

4.4.1.5 *tert*-Butyl 2-(4-(4-ethoxy-4-oxobutyl)-2,3-dioxo-7-(trifluoromethyl)-1,2,3,4-tetrahydroquinoxalin-6-yl)-1-phenylhydrazine-1-carboxylate (**4.6**)

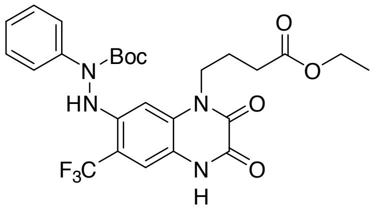

4.5 (133 mg, 0.27 mmol, 1.0 equiv.) was dissolved in DCM (2.7 mL). Triethylamine (82 µL, 0.59 mmol, 2.2 equiv.) and oxalyl chloride (2 M in DCM, 160 µL, 0.32 mmol, 1.2 equiv.) were sequentially added. The reaction mixture was stirred at r.t. for 30 min, quenched by addition of a drop of MeOH and directly purified by flash column chromatography (5% MeOH/DCM). The product was obtained as a brown oil (43.5 mg, 79 µmol, 29%).

TLC (5% MeOH/DCM): 0.19 (UV).

^{1}H NMR (400 MHz, $CDCl_3$) δ = 7.69 – 7.61 (m, 2H), 7.51 (d, *J* = 5.7 Hz, 1H), 7.39 – 7.28 (m, 2H), 7.19 – 7.10 (m, 1H), 7.05 (d, *J* = 1.8 Hz, 1H), 6.92 (s, 1H), 4.19 – 4.05 (m, 4H), 2.34 (t, *J* = 7.0 Hz, 2H), 1.85 (p, *J* = 7.1 Hz, 2H), 1.44 (s, 9H), 1.24 (t, *J* = 7.1 Hz, 3H).

Note: NH proton of the quinoxaline-2,3-dione is not observed.

^{13}C NMR (101 MHz, $CDCl_3$): δ = 172.2, 155.3, 154.3, 153.3, 143.0, 141.6, 130.4, 128.8, 125.2, 121.6, 123.7 (d, *J* = 272.2 Hz), 117.4, 115.6 (d, *J* = 5.8 Hz), 110.7 (d, *J* = 32.5 Hz), 99.4, 83.3, 60.7, 42.8, 31.1, 28.0, 21.8, 14.2.

HRMS (ESI): *m/z* calc. for $C_{26}H_{30}F_3N_4O_6^+$ $(M+H)^+$: 551.2112, found: 551.2115.

***t*$_R$** (LCMS) = 3.23 min.

UV/Vis (LCMS): λ_{max1} = 224 nm, λ_{max2} = 337 nm.

4.4.1.6 4-(7-(2-(*tert*-Butoxycarbonyl)-2-phenylhydrazineyl)-2,3-dioxo-6-(trifluoromethyl)-3,4-dihydroquinoxalin-1(2H)-yl)butanoic acid (**4.7**)

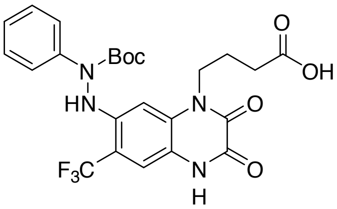

4.6 (43.5 mg, 79 µmol, 1.0 equiv.) was dissolved in THF/MeOH (1 mL/0.5 mL) and aq. NaOH (1 M, 0.16 mL, 0.16 mmol, 2.0 equiv.) was added. The reaction was stirred at r.t. for 1 h, then acidified by addition of 50 µL AcOH. The reaction mixture was concentrated *in vacuo* to dryness. The residue was taken up in 900 µL DMSO and 100 µL water and centrifuged (14,000 rcf, 2 min). The supernatant was purified by HPLC. Product containing fractions were combined and freeze-dried. The desired product was obtained in 44% yield (18.1 mg, 35 µmol).

^{1}H NMR (400 MHz, DMSO-*d*$_6$) δ = 11.85 (s, 1H), 8.64 (s, 1H), 7.73 – 7.46 (m, 2H), 7.46 – 7.25 (m, 3H), 7.23 – 7.04 (m, 1H), 6.64 (s, 1H), 3.95 (t, *J* = 7.3 Hz, 2H), 2.29 (t, *J* = 7.3 Hz, 2H), 1.72 (t, *J* = 7.3 Hz, 2H), 1.38 (s, 9H).

Note: NH proton of the quinoxaline-2,3-dione is not observed.

^{13}C NMR (101 MHz, $CDCl_3$): δ = 174.0, 156.1, 153.6, 153.1, 142.7, 141.7, 131.1, 128.8, 124.5 (d, J = 272.5 Hz), 125.5, 123.5, 118.5, 114.2 (q, J = 5.2 Hz), 107.2 (q, J = 31.7 Hz), 98.3, 81.8, 42.3, 31.4, 28.2, 22.1.

HRMS (ESI): *m/z* calc. for $C_{24}H_{26}F_3N_4O_6^+$ $(M+H)^+$: 523.1799, found: 523.1801.

***t*$_R$** (LCMS) = 2.78 min.

UV/Vis (LCMS): λ_{max1} = 198 nm, λ_{max2} = 224 nm, λ_{max3} = 337 nm..

4.4.1.7 *tert*-Butyl 116-(7-(2-(tert-butoxycarbonyl)-2-phenylhydrazineyl)-2,3-dioxo-6-(trifluoromethyl)-3,4-dihydroquinoxalin-1(2H)-yl)-113-oxo-4,7,10,13,19,22,25,28,31,34,37,40,43,46,49,52,55,58,61,64,67,70,73,76,79,82,85,88,91,94,97,100,103,106,109-pentatriacontaoxa-112-azahexadecahectanoate (**4.8**)

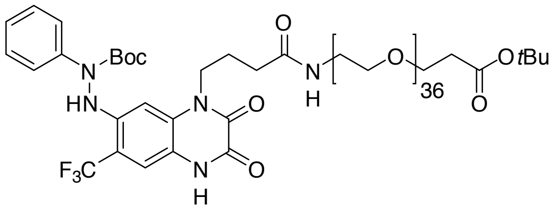

4.7 (13.1 mg, 25 µmol, 1.0 equiv.) was dissolved in DMSO (0.8 mL) and DIPEA (9.2 µL, 53 µmol, 2.1 equiv.) and TSTU (9.0 mg, 30 µmol, 1.2 equiv.) were added. The reaction mixture was stirred at r.t. for 30 min, before additional DIPEA (18.5 µL, 106 µmol, 4.2 equiv.) and NH_2-PEG36-COO*t*Bu (Iris Biotech #PEG3710, 52.0 mg, 30 µmol 1.2 equiv.) were added. The reaction mixture was stirred at r.t. overnight before it was acidified by addition of 40 µL of AcOH. The reaction mixture was centrifuged (14,000 rcf, 2 min) and the supernatant was subjected to HPLC purification. The product was obtained after freeze-drying of product containing fractions in 57% yield (32.0 mg, 14 µmol).

HRMS (ESI): *m/z* calc. for $C_{103}H_{184}F_3N_5O_{43}^{2+}$ $(M+2H)^{2+}$: 1118.6170, found: 1118.6170.

***t*$_R$** (LCMS) = 3.29 min.

UV/Vis (LCMS): λ_{max1} = 198 nm, λ_{max2} = 225 nm, λ_{max3} = 337 nm.

4.4.1.8 (*E*)-116-(2,3-Dioxo-7-(phenyldiazenyl)-6-(trifluoromethyl)-3,4-dihydroquinoxalin-1(2H)-yl)-113-oxo-4,7,10,13,19,22,25,28,31,34,37,40,43,46,49,52,55,58,61,64,67,70,73,76,79,82,85,88,91,94,97,100,103,106,109-pentatriacontaoxa-112-azahexadecahectanoic acid (**4.9**)

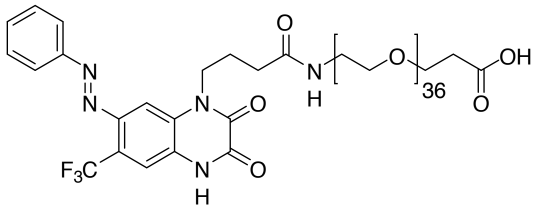

Precooled TFA (0.5 mL) was added to **4.7** (32.0 mg, 14 *µ*mol, 1.0 equiv.) on ice. The reaction mixture quickly turned to an orange color and as allowed to stand on ice for 10 min and analyzed by LCMS. Then, the reaction mixture was allowed to warm to r.t. and allowed to stand for an additional 30 min and again analyzed by LCMS. TFA was removed by a gentle stream of nitrogen. The residue was taken up in 900 *µ*L DMSO and 100 *µ*L water, centrifuged (14,000 rcf, 2 min) and the supernatant was subjected to HPLC purification. The product was obtained as an orange, viscous oil (3.9 mg, 1.9 *µ*mol, 13%)

Note: Due to wrong mass assignments in the LCMS analysis, the reaction progress was incorrectly judged to be incomplete after 10 min on ice. Degradation of the product was observed upon warming to r.t.. If this reaction was repeated, longer reaction times on ice and addition of a cation scavenger (e.g. a drop of water or anisole) are recommended.

LRMS (ESI): *m/z* calc. $C_{94}H_{167}F_3N_5O_{41}^{3+}$for (M+3H)$^{3+}$: 692.4, found: 693.4

HRMS (ESI): *m/z* calc. $C_{94}H_{166}F_3N_5O_{41}^{3+}$for (M+2H)$^{2+}$: 1039.5516 found: 1039.5524.

t_R (LCMS) = 2.94 min.

UV/Vis (LCMS): λ_{max1} = 220 nm, λ_{max2} = 263 nm, λ_{max3} = 291, λ_{max4} = 360 nm.

4.4.1.9 (*E*)-N-(2-(2-((6-Chlorohexyl)oxy)ethoxy)ethyl)-1-(4-(2,3-dioxo-7-(phenyldiazenyl)-6-(trifluoromethyl)-3,4-dihydroquinoxalin-1(2H)-yl)butanamido)-3,6,9,12,15,18,21,24,27,30,33,36,39,42,45,48,51,54,57,60,63,66,69,72,75,78,81,84,87,90,93,99,102,105,108-pentatriacontaoxaundecahectan-111-amide (**4.10**)

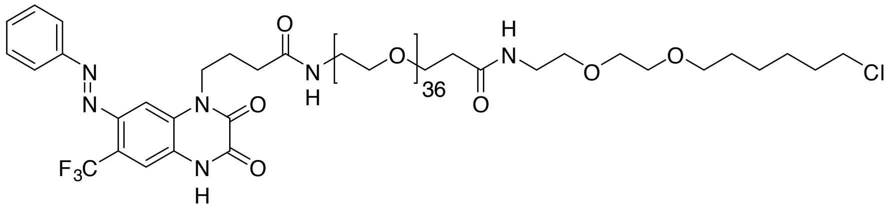

4.9 (3.9 mg, 1.9 *μ*mol, 1.0 equiv.), DIPEA (2 *μ*L, 11.5 *μ*mol, 6.0 equiv.) and TSTU (0.7 mg, 2.4 *μ*mol, 1.3 equiv.) were combined in DMSO (200 *μ*L) and stirred at r.t. for 30 min. 2-(2-((6-Chlorohexyl)oxy)ethoxy)ethan-1-amine (HaloTag-ligand, 1.2 mg, 3.8 *μ*mol, 2.0 equiv.) was prepared in a 4 mL dram vial and the solution of the activated acid was added in one portion. The reaction mixture was stirred at r.t. overnight. The reaction mixture was acidified by a drop of AcOH, centrifuged (14,000 rcf, 2 min) and the supernatant was subjected to HPLC purification. The product was obtained as an orange, viscous oil (1.8 *μ*mol, 95%)

^{1}H NMR (400 MHz, $CDCl_3$) δ 8.08 – 8.01 (m, 2H, *trans*), 8.00 (s, 1H, *trans*), 7.70 (s, 1H, *trans*), 7.65 – 7.56 (m, 3H, *trans*), 7.34 (t, *J* = 7.8 Hz, 1H, *cis*), 7.24 – 7.16 (m, 0H, *cis*), 7.00 – 6.92 (m, 1H, *cis*), 6.48 (s, 0H, *cis*), 4.39 – 4.29 (m, 2H), 3.92 – 3.85 (m, 1H), 3.84 – 3.77 (m, 1H), 3.73 (t, *J* = 6.2 Hz, 3H), 3.66 – 3.56 (m, 191H), 2.46 (t, *J* = 6.2 Hz, 3H), 2.40 (t, *J* = 7.0 Hz, 2H), 2.11 (q, *J* = 7.1 Hz, 3H), 1.83 – 1.71 (m, 3H), 1.60 (p, *J* = 6.8 Hz, 3H), 1.52 – 1.31 (m, 5H).

Note: Mixture of cis- and trans-isomers. To assign cis- and trans- peaks, the NMR tube was illuminated by a UV-handheld lamp for a few minutes and directly measured by NMR (see chapter 4.4.2.7).

HRMS (ESI): *m/z* calc. for $C_{104}H_{187}ClF_3N_6O_{42}^{3+}$ $(M+3H)^{3+}$: 761.7446, found: 761.7451.

t_R (LCMS) = 3.30 min.

UV/Vis (LCMS): λ_{max1} = 219 nm, λ_{max2} = 263 nm, λ_{max3} = 291, λ_{max4} = 360 nm.

4.4.2 Spectral Data

4.4.2.1 Ethyl 4-((5-chloro-2-nitro-4-(trifluoromethyl)phenyl)amino)butanoate (**4.2**)

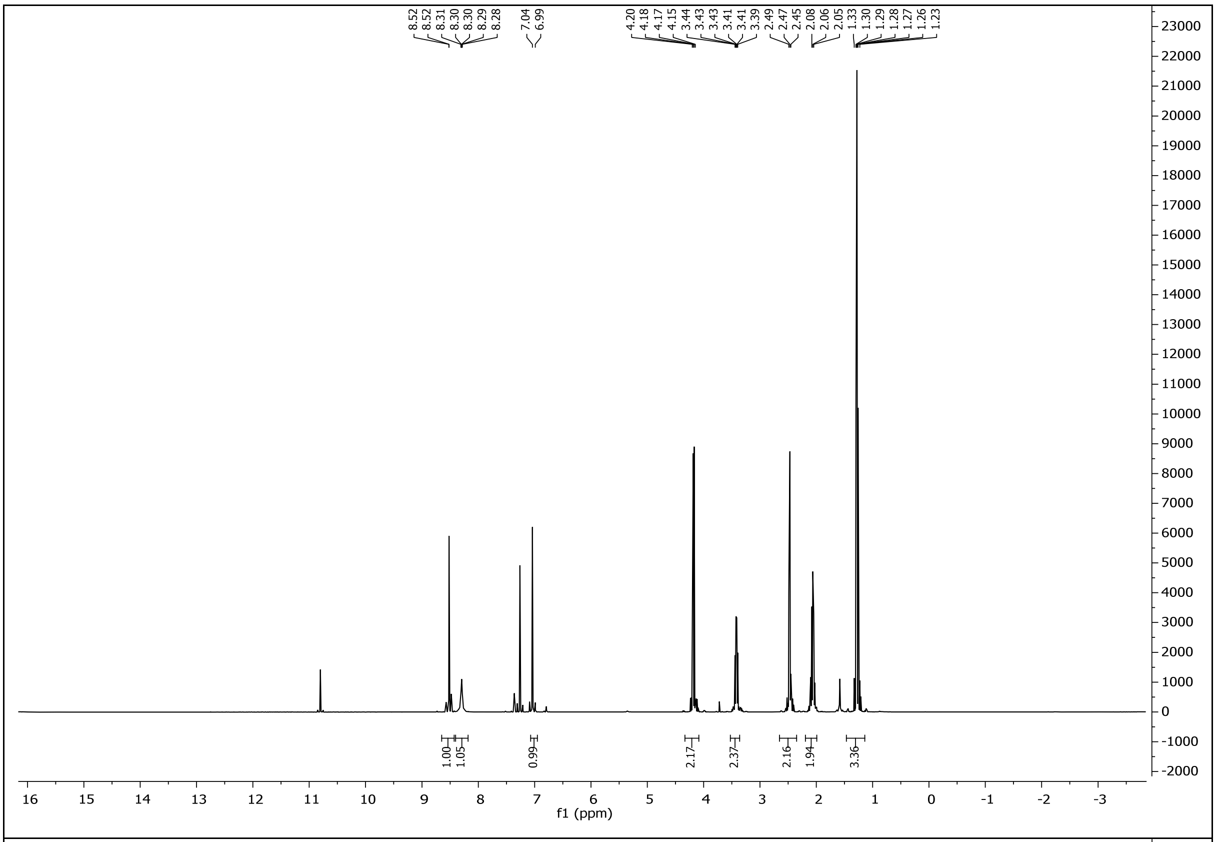

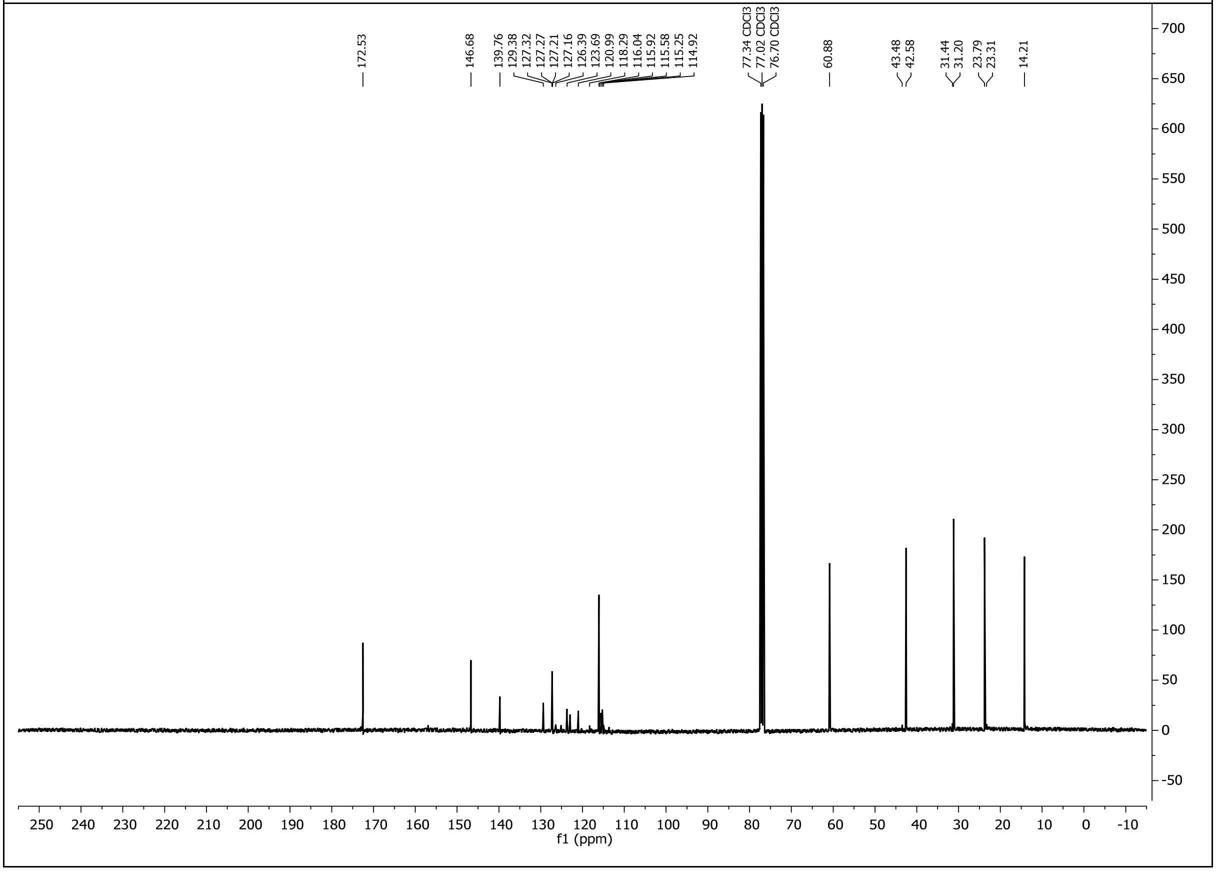

4.4.2.2 *tert*-Butyl 1-phenylhydrazine-1-carboxylate (**4.3**)

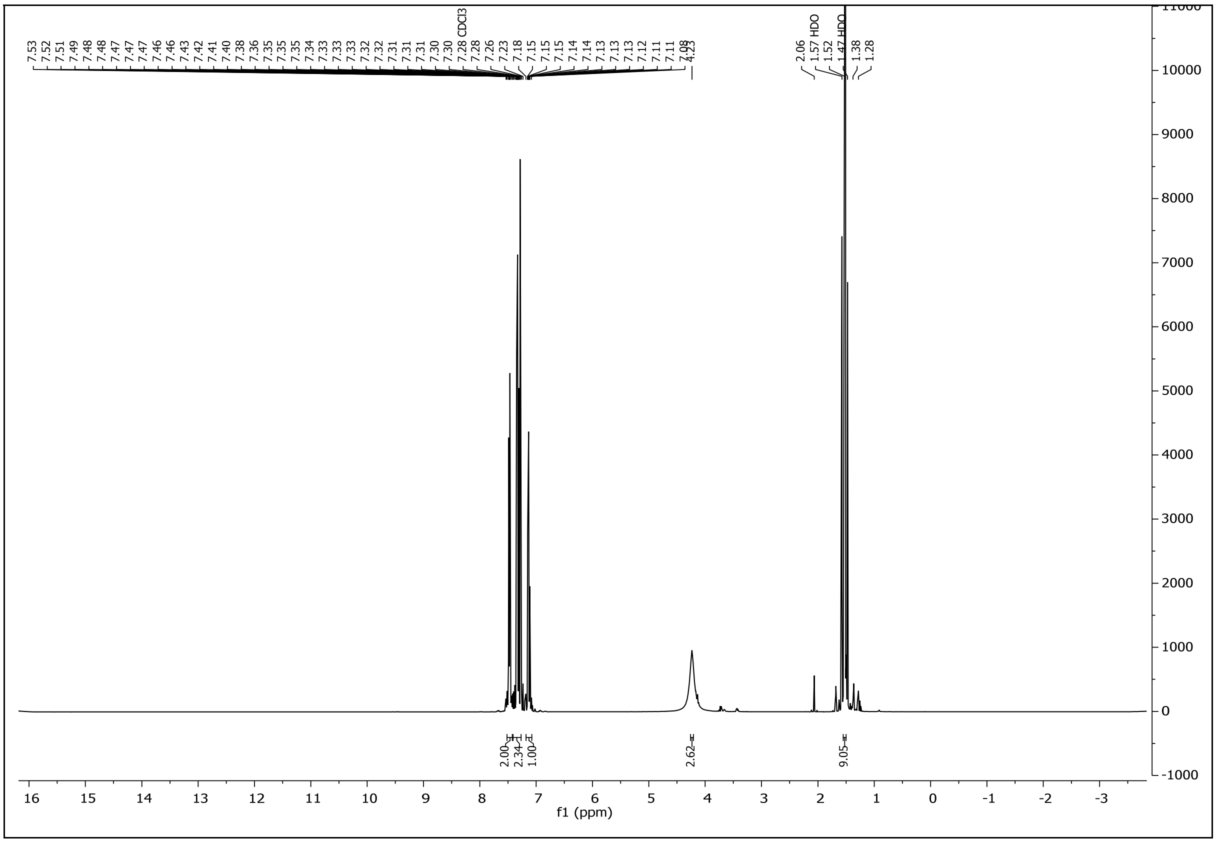

4.4.2.3 *tert*-Butyl 2-(5-((4-ethoxy-4-oxobutyl)amino)-4-nitro-2-(trifluoromethyl)phenyl)-1-phenylhydrazine-1-carboxylate (**4.4**)

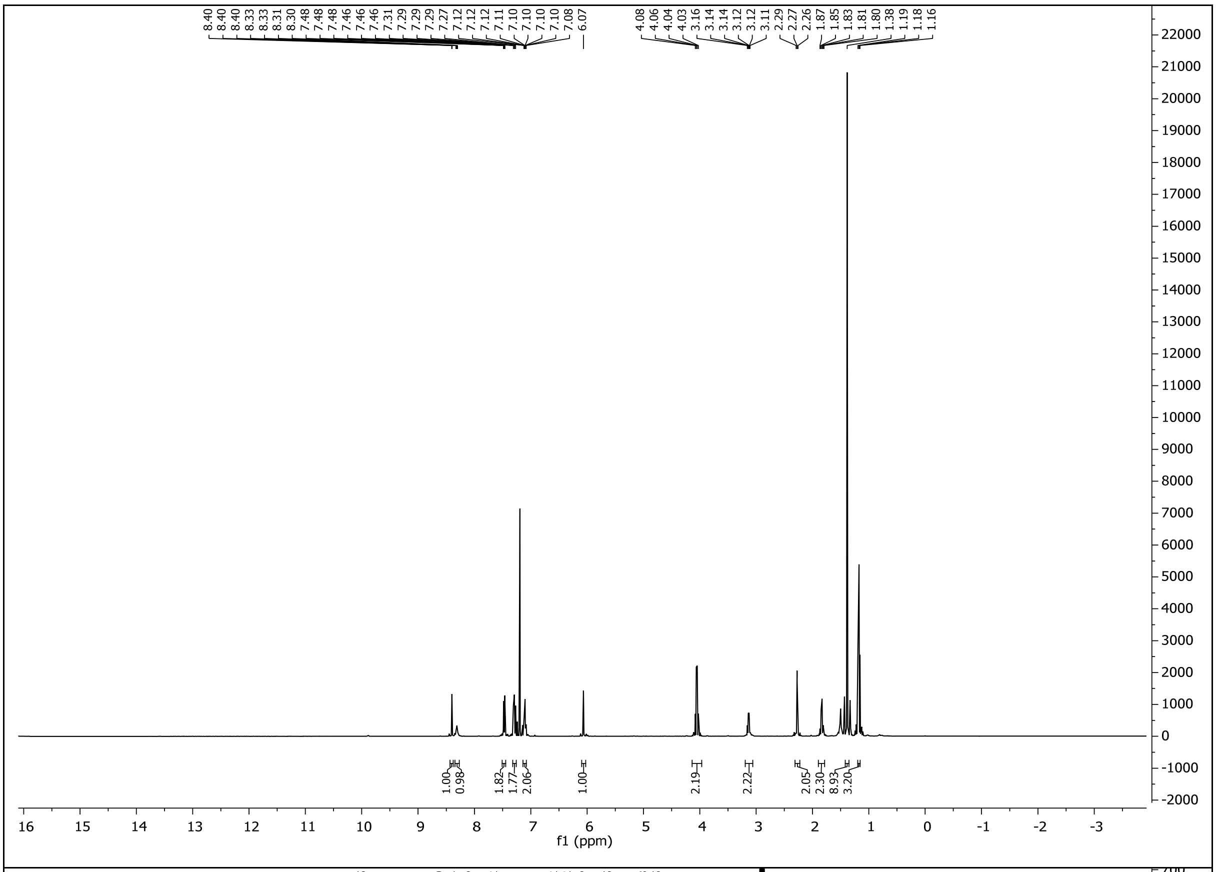

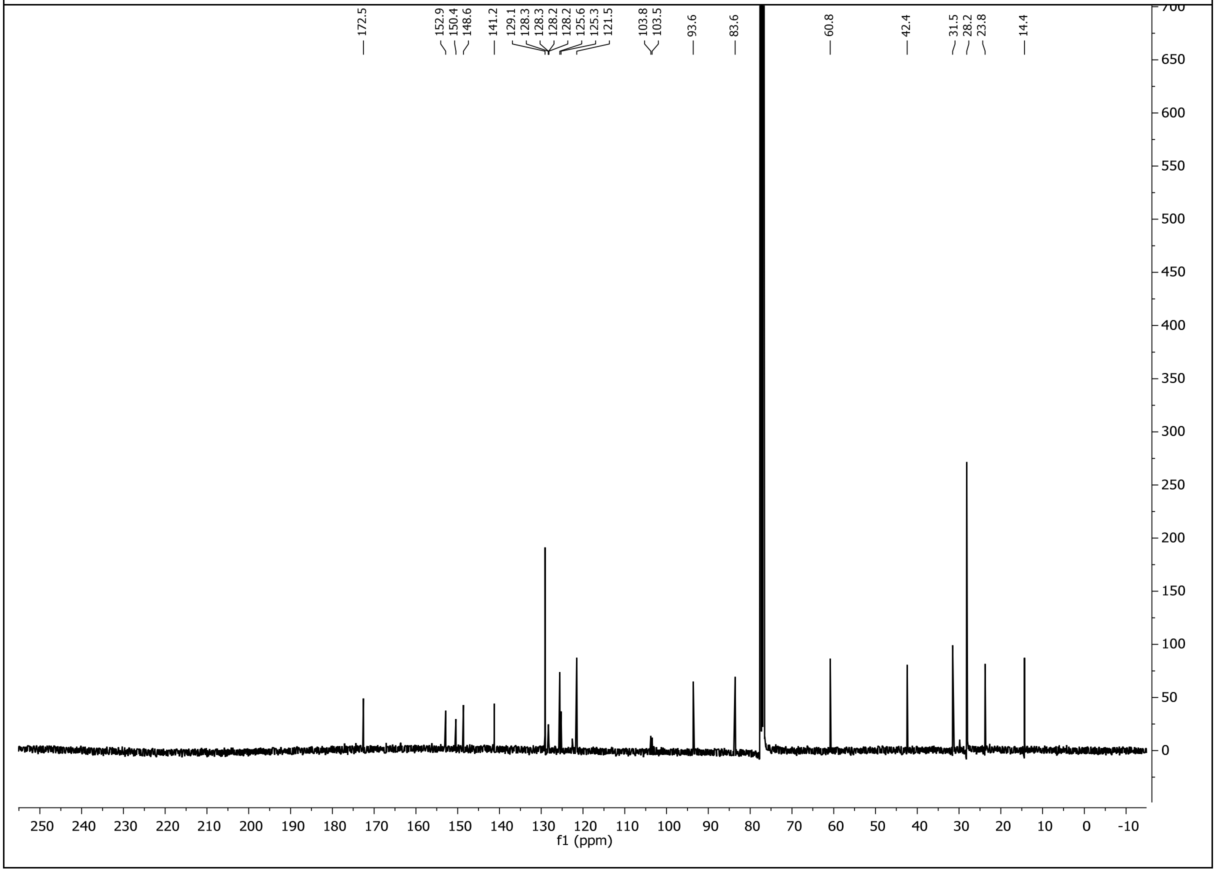

4.4.2.4 *tert*-Butyl 2-(4-amino-5-((4-ethoxy-4-oxobutyl)amino)-2-(trifluoromethyl)phenyl)-1-phenylhydrazine-1-carboxylate (**4.5**)

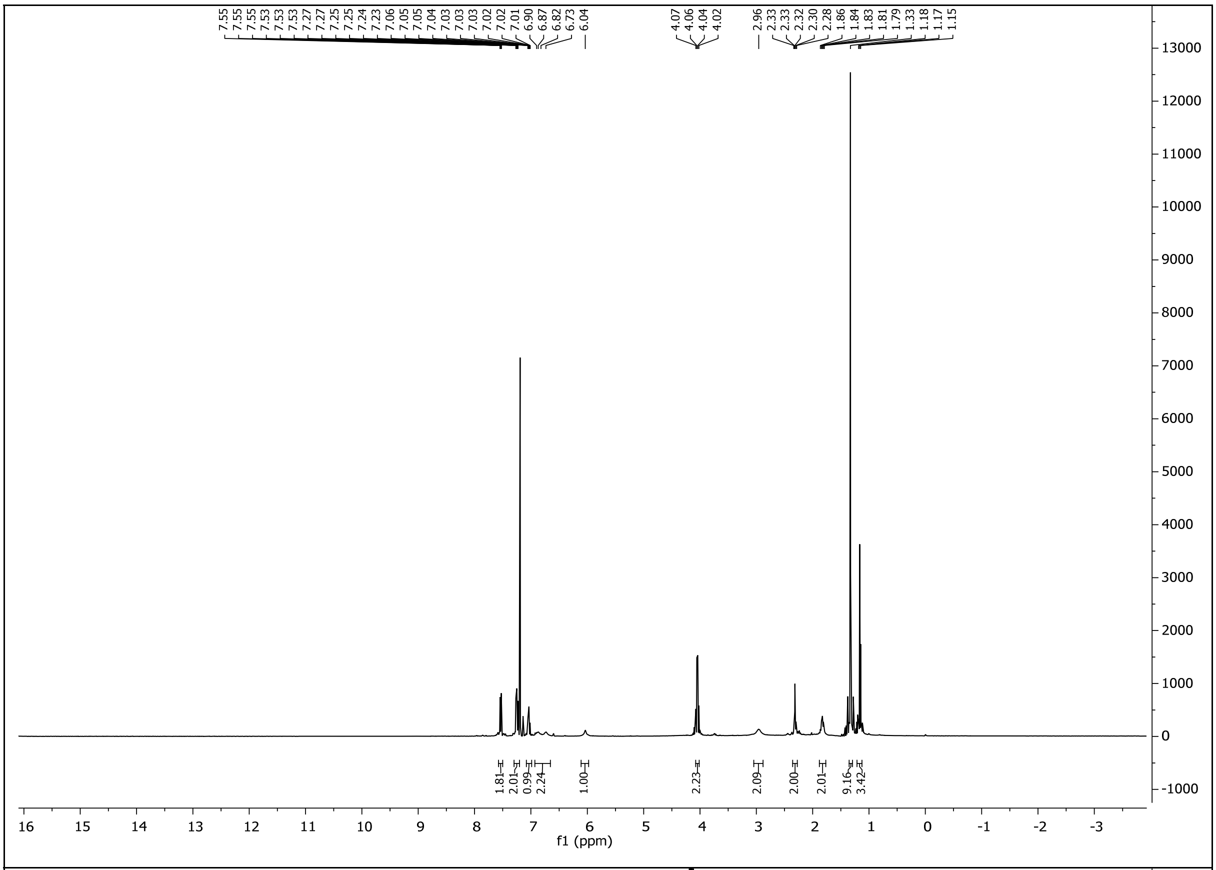

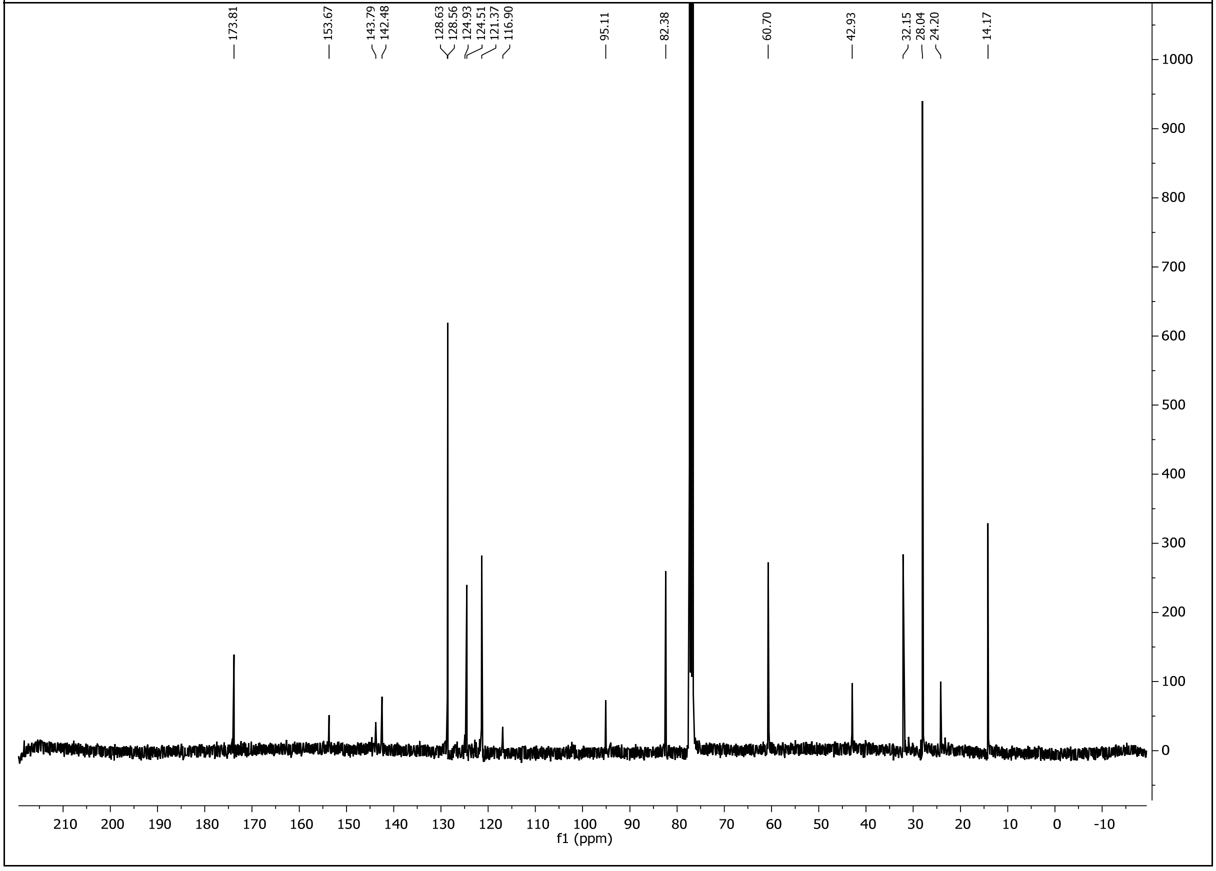

4.4.2.5 tert-butyl 2-(4-(4-ethoxy-4-oxobutyl)-2,3-dioxo-7-(trifluoromethyl)-1,2,3,4-tetrahydroquinoxalin-6-yl)-1-phenylhydrazine-1-carboxylate (**4.6**)

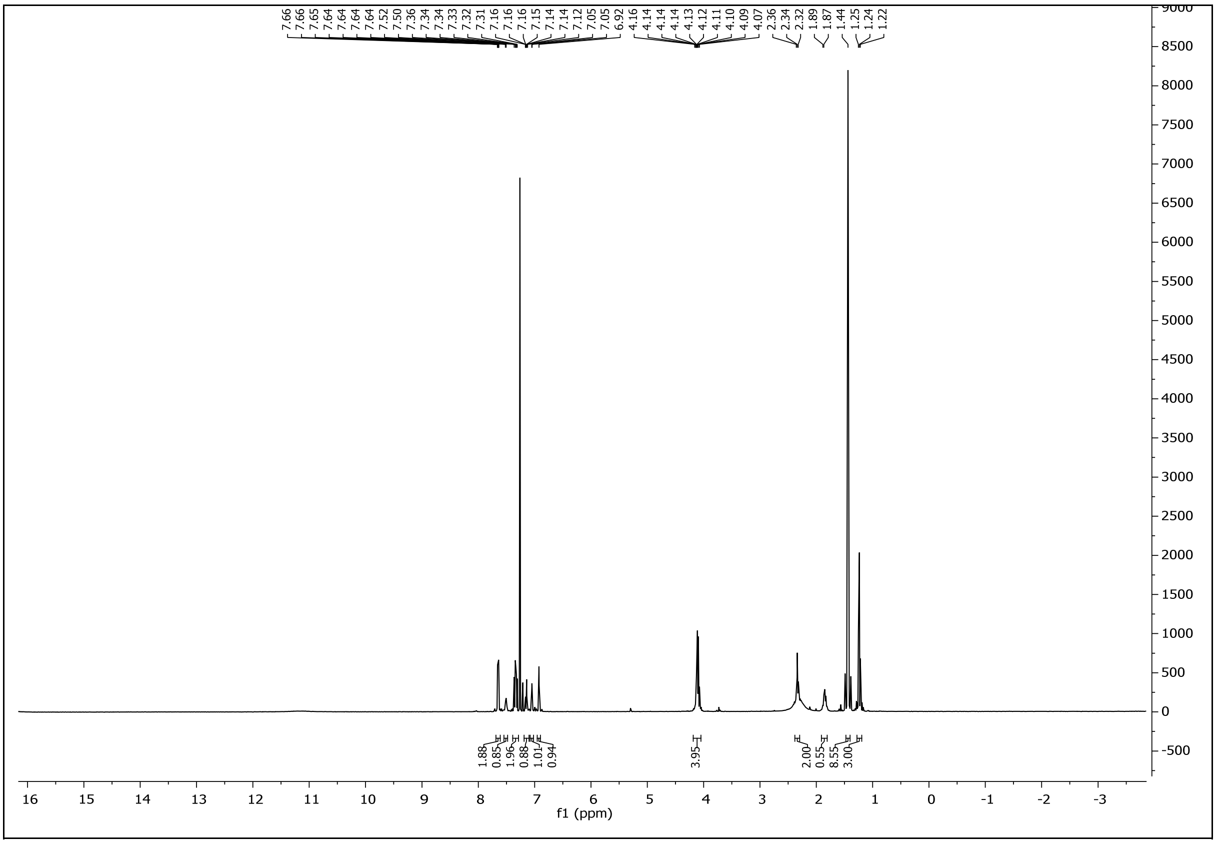

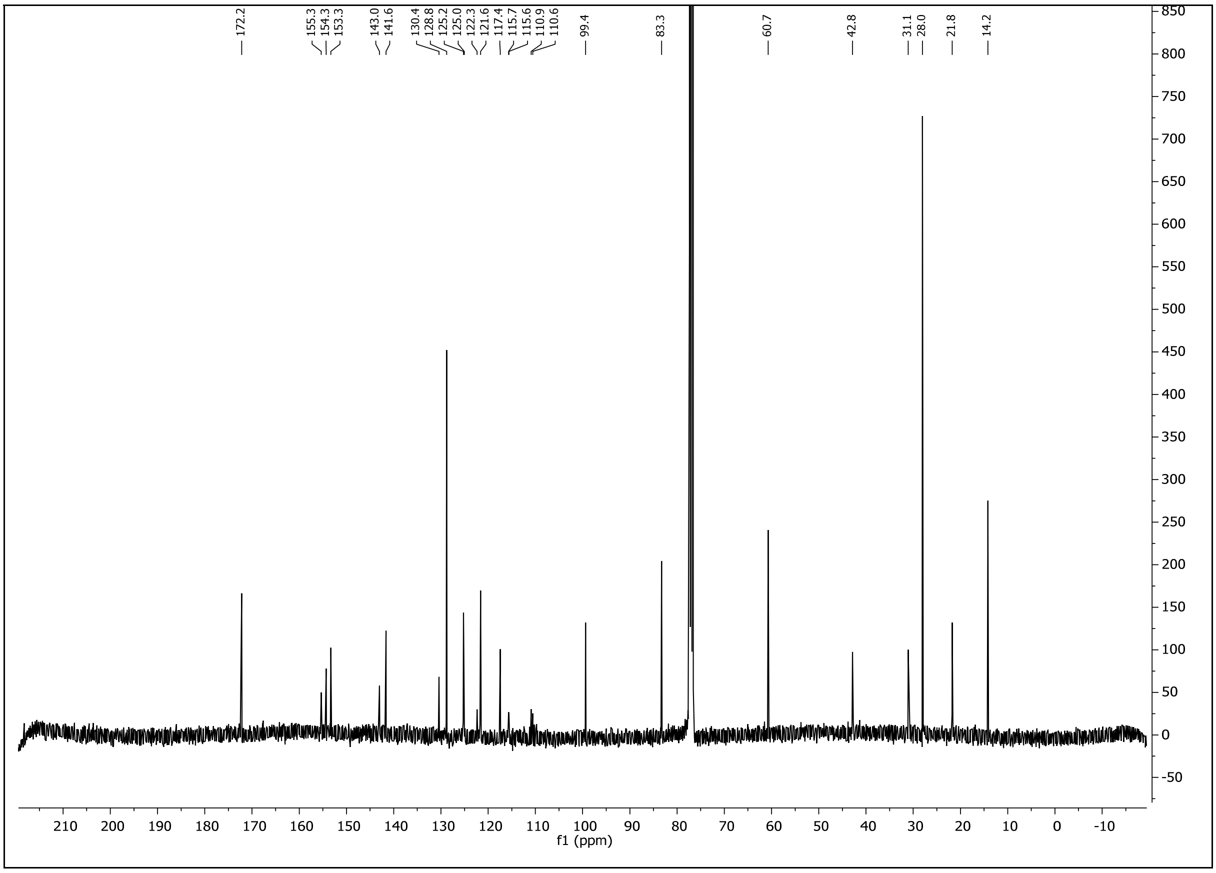
172.2
155.3
154.3
153.3
143.0
141.6
130.4
128.8
125.2
125.0
122.3
121.6
117.4
115.7
115.6
110.9
110.6
99.4
83.3
60.7
42.8
31.1
28.0
21.8
14.2
850
800
750
700
650
600
550
500
450
400
350
300
250
200
150
100
50
0
-50
210
200
190
180
170
160
150
140
130
120
110
100
90
80
70
60
50
40
30
20
10
0
-10
f1 (ppm)

4.4.2.6 4-(7-(2-(tert-butoxycarbonyl)-2-phenylhydrazineyl)-2,3-dioxo-6-(trifluoromethyl)-3,4-dihydroquinoxalin-1(2H)-yl)butanoic acid (**4.7**)

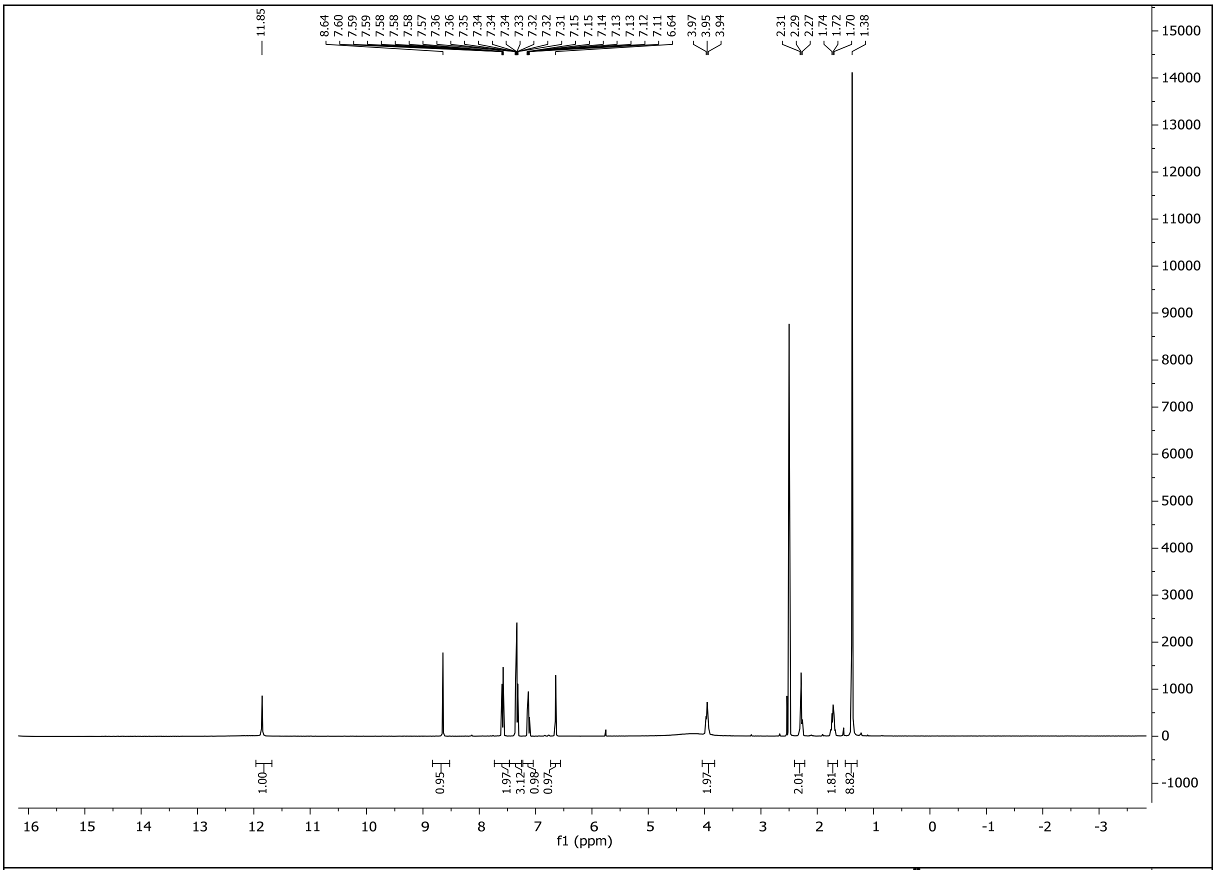

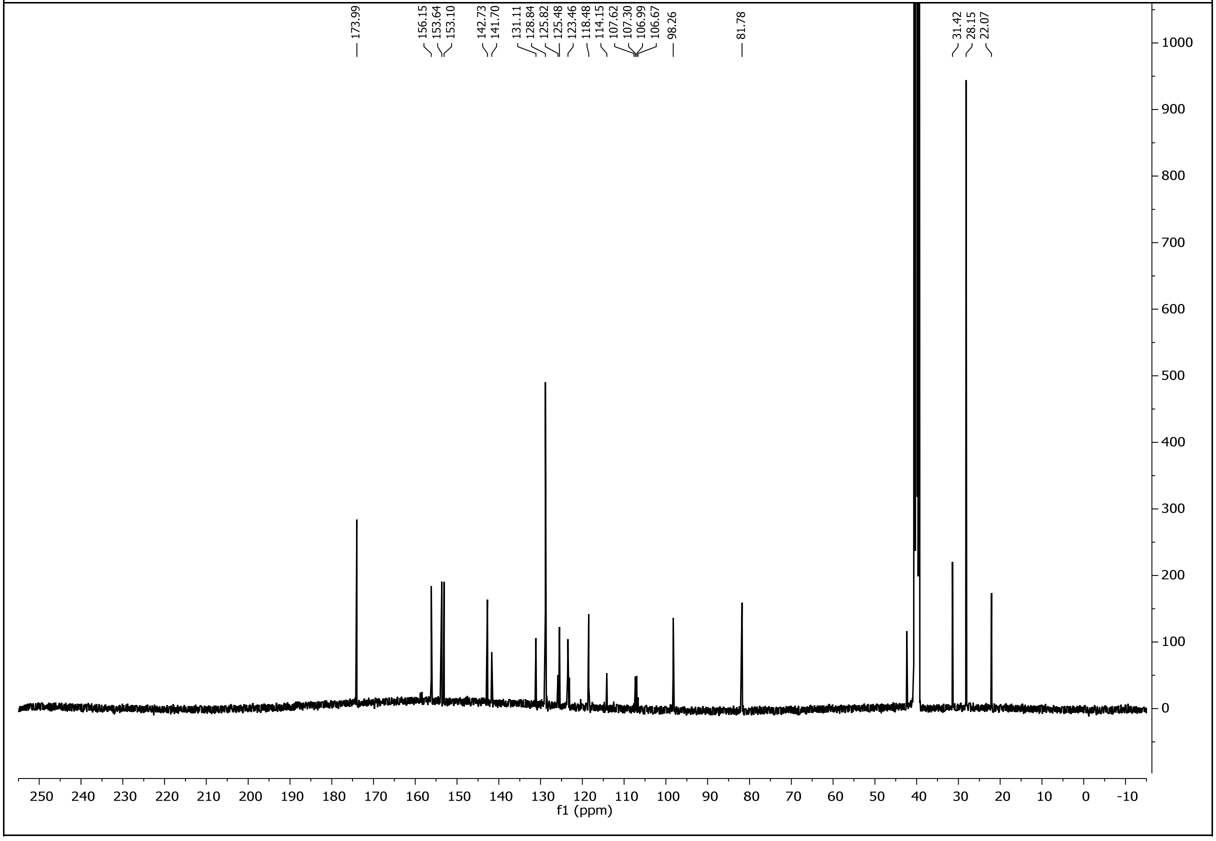

4.4.2.7 (*E*)-*N*-(2-(2-((6-chlorohexyl)oxy)ethoxy)ethyl)-1-(4-(2,3-dioxo-7-(phenyldiazenyl)-6-(trifluoromethyl)-3,4-dihydroquinoxalin-1(2*H*)-yl)butanamido)-3,6,9,12,15,18,21,24,27,30,33,36,39,42,45,48,51,54,57,60,63,66,69,72,75,78,81,84,87,90,93,99,102,105,108-pentatriacontaoxaundecahectan-111-amide (**4.10**)

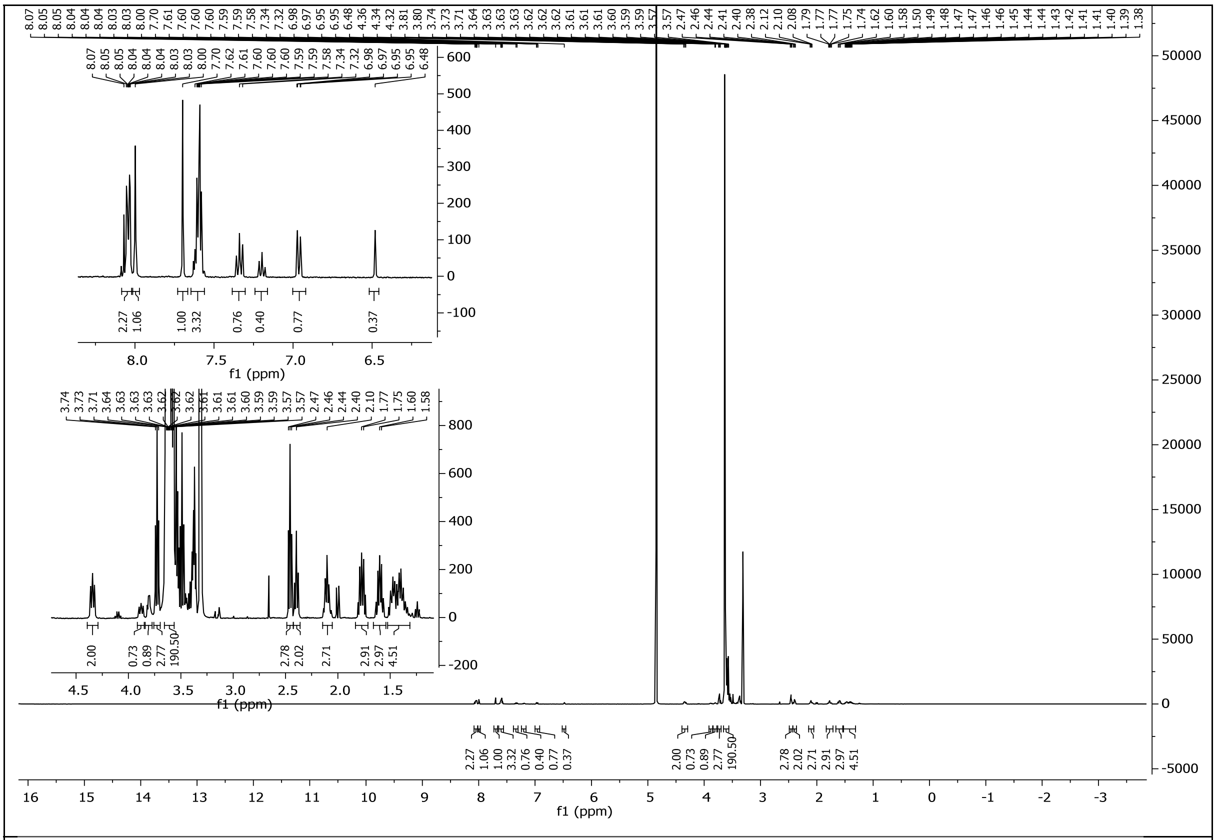

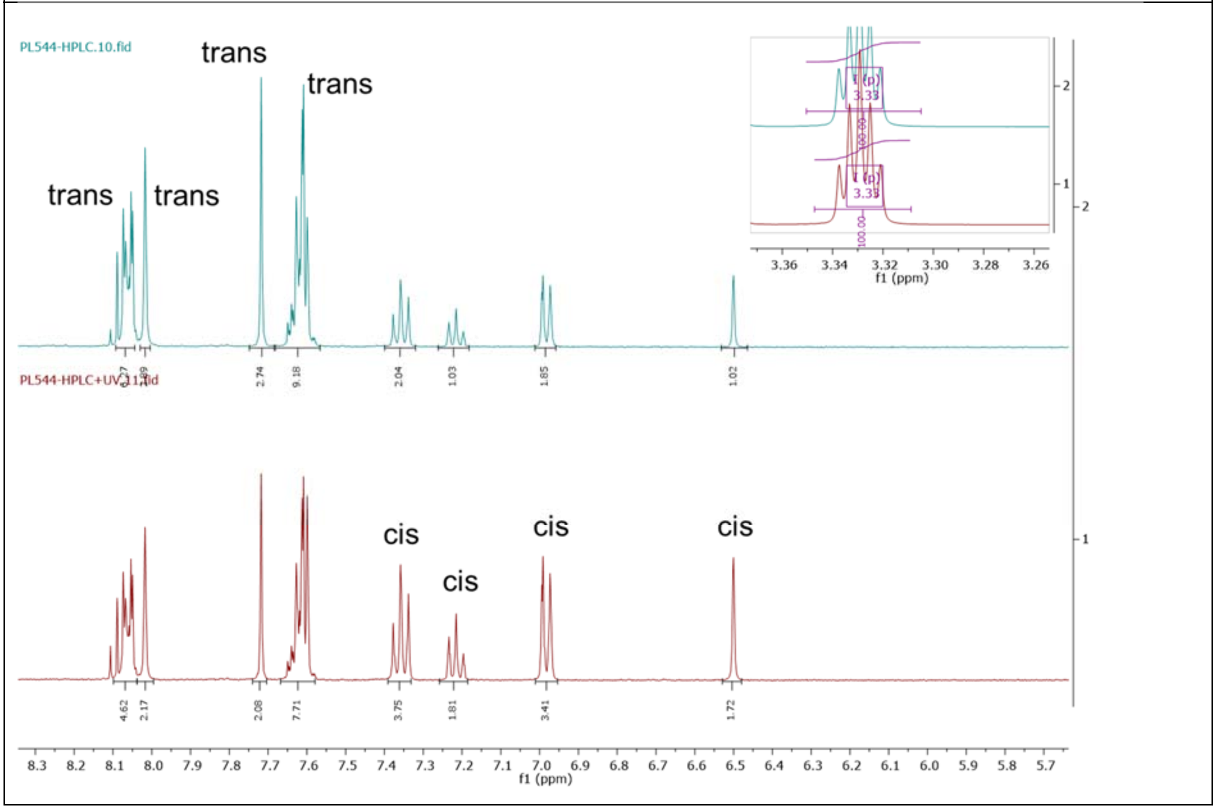

5 Tethered Photopharmacology of the *μ*-Opioid Receptor

5.1 Introduction

Since antiquity, morphine and related opiates have widely been used for pain relief. As opiates also induce euphoria, they also have been abused recreationally for hundreds of years. The mechanistic target of opiates is the *μ*-opioid receptor (MOR), which is a class A GPCR. In contrast to Class B or C GPCRs, it features no large extracellular domain and consists of 7 transmembrane helices (Figure 30a). Its third intracellular loop is coupled to an inhibitory $G_{i/o}$ protein (colored red in Figure 30a). Upon receptor stimulation, the trimeric $G_{i/o}$ protein binds GTP and dissociates into α- and βγ-subunits. The α-subunit inhibits adenylyl cyclase, resulting in decreased cAMP levels, while the βγ-subunit opens G protein-coupled inwardly-rectifying potassium (GIRK) channels. In addition, MOR, like other GPCRs, can signal in G protein-independent fashion, *e.g.* through β-arrestin or activation of downstream kinases.

The MOR is also the target of non-opiate opioids such as fentanyl and tramadol (Figure 30b). Fentanyl is a highly-addictive and extremely potent agonist with an EC_{50} around 1 nM[106] and is used as analgesic in the clinic, together with many structural analogs. In recent years, fentanyl abuse has increased dramatically, especially in the US. It now is the major cause for lethal opioid overdoses with deaths peaking at roughly 64,000 in 2017, and still rising. At these numbers, opioid overdoses cause more deaths in the US than gun violence or car accidents.[107] Especially fentanyl is dangerous because it produces respiratory depression to a larger extent than other opioids.[108]

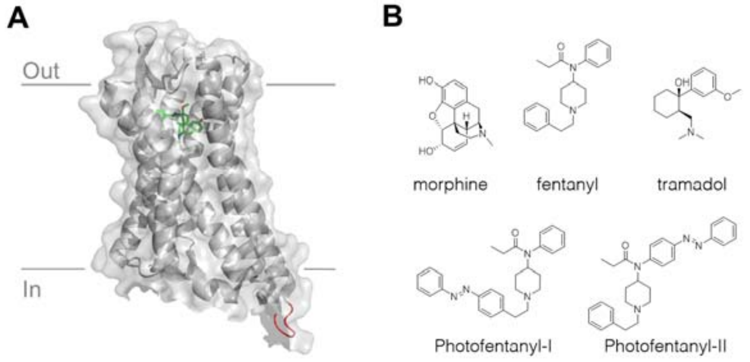

Figure 30. **Structure and Pharmacology of the *μ*-opioid receptor. a)** Structure of the active-state MOR bound to the synthetic agonist BU72. The intracellular loop that binds to the G protein is highlighted in red. (pdp 5C1M) **b)** The MOR has an extensive pharmacology and a few examples of MOR agonists are shown (top). Photofentanyl-I (PF-I) and Photofentanyl-II (PF-II) according to Schönberger *et al.*[5] PF-II exhibited light-dependent agonism on MOR, while PF-I was inactive.

To develop novel therapies and fight drug addiction it is important to understand the molecular processes underlying tolerance and addiction. In the last decades, considerable effort has been directed into the mechanisms of acute MOR signaling, receptor regulation and tolerance and their implications on drug tolerance and addiction.[109] Novel tools that permit the perturbation of MOR with the high spatiotemporal precision that light offers could be highly useful to decipher the relationship of receptor activation and regulation to drug tolerance.

In line with this, we wanted to extend the PORTL concept (see chapter 1) to the MOR. Our group published a freely-diffusible photochromic agonist (PCL) for the MOR in 2014.[5] There, fentanyl was furnished with an azobenzene in two different positions to give access to Photofentanyl-I (PF-I) and Photofentanyl-II (PF-II, Figure 30b). While PF-I was inactive, PF-II was an agonist in its *trans*-isomer, *i.e.* in the dark, activating MOR while its *cis*-isomer was inactive. This was observed by reading out the opening of GIRK channels by voltage-clamp electrophysiology.

A suitable point of attachment of the flexible PEG-linker needed to be identified. The PEG-chain is required as a tether between the photoswitchable agonist and the bioconjugation motif. To this end, we turned to Nil Patel and Seva Katrich (USC) for molecular docking studies. Based on the active-state MOR structure (pdb 5C1M), PF-II with PEG chains in different positions was docked computationally. Initially, intuition guided us to propose a structure with the PEG chain attached to the *para*-position of the azobenzene. Our reasoning was such that this position already tolerated the introduction of the azobenzene, making it likely that increasing the bulk there by attaching the PEG chain could be accommodated by the receptor. PF-II adopts a similar binding mode as fentanyl itself (Figure 31a) with the azobenzene sticking out in direction of the extracellular space. The PEGylated PF-II binds comparably, albeit with reduced scores due to steric constraints around the linker. It should be noted that the *N*-terminus of MOR in the crystal structure is modified and that its correct conformation is hard to predict precisely.

We also considered to attach the PEG linker on the propionic amide residue (Figure 31b) but the linker clearly clashes with the protein, with no exit tunnel remaining.

In a last design, we proposed to attach an acrylic acid moiety on the phenethyl residue. This was inspired by a recent report that described synthetic modification of fentanyl in that fashion.[106] Subsequently, the acrylic acid was used to attach a PEG chain *via* amide coupling and this did not disrupt the fentanyl's analgesic properties. Accordingly, we hypothesized that the acrylic acid and the PEG chain might be tolerated at the same position on PF-II. The docking study revealed that the PEGylated fentanyl can flip in the binding pocket, and therefore allow exit of the PEG chain. Unfortunately, this flip was not possible in the PF-II derivative due to the presence of the azobenzene.

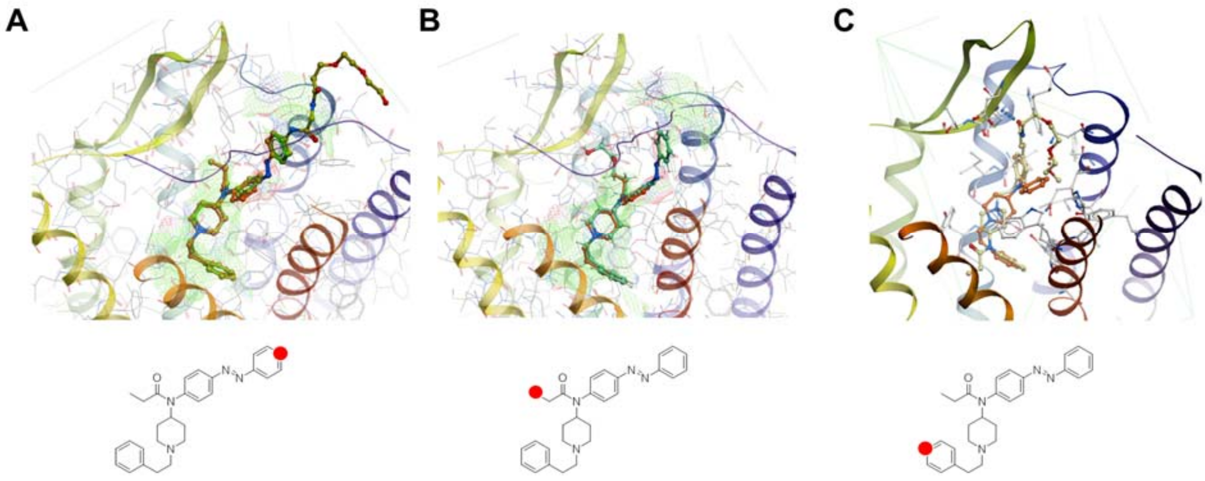

Figure 31. **Docking studies with various linker attachment points on PF-II. a)** Overlay of docked structures for fentanyl (orange sticks), PF-II (green sticks) and tethered PF-II (yellow sticks). **b)** Overlay of docked structures for fentanyl (orange) and tethered PF-II (turquoise). **c)** Overlay of fentanyl orange sticks) and a PEGylated acrylic acid derivative of fentanyl from Averick and coworkers[106] (beige sticks). The PEGylated acrylic acid derivative of PF-II could not be accommodated by the MOR receptor. Computational models are based on active-state MOR structure (pdb 5C1M) and were performed by Nil Patel and Seva Katritch (USC).

According to the docking studies, we proposed the design of fentanyl-based PORTLs according to design A. PF-II was to be modified in *para*-position on the azobenzene, including a long PEG chain as tether, linking the photoswitch to a benzylguanine (BG) for SNAP-tag labelling (Figure 32).

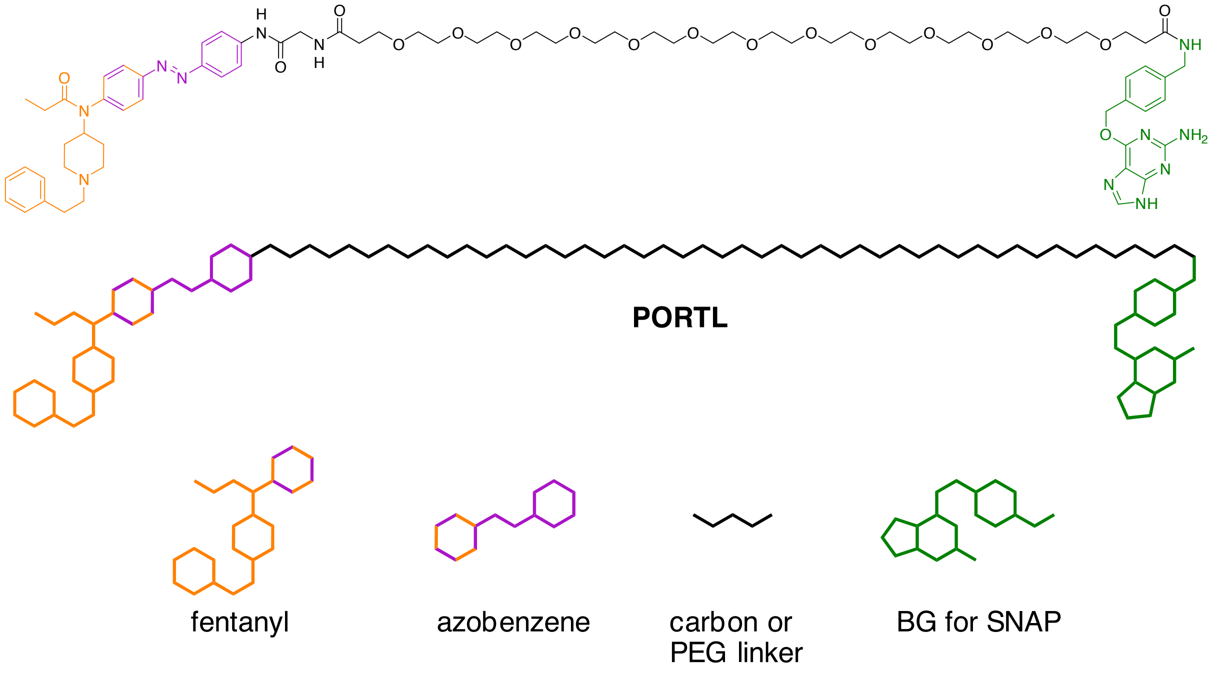

Figure 32. **Design of fentanyl-based PORTL molecules.**

5.2 Results and Discussion

5.2.1 Synthesis of the PCL Core

Early syntheses aimed at installing a protected amine in *para*-position to the azobenzene for further derivatization. It quickly became apparent that the acylation with propionyl chloride was problematic. With electron-withdrawing substituents on the azobenzene, the acylation reaction with propionyl chloride only gave very low conversions and upon heating gave the doubly reacted Michael-addition product. Therefore, it was attempted to use the *N,N*-diallyl-derivative as electron-rich protecting group for in a *para*-position of the azobenzene. While the acylation proceeded with high yield, deprotection of the *N,N*-diallyl amine failed under all conditions tested, *i.e.* basic (KO*t*Bu) or catalytic (Ruthenium catalysts). To circumvent this issue, the electron-rich, red-shifted fentanyl PORTL was synthesized first. The synthesis was commenced by reductive amination of *N*-methylaniline with *N*-Boc-3-aminopropanal to give **5.3** (Scheme 6)**.** Azobenzene **5.4** was obtained by Azo-coupling with the tetrafluoroborate salt of the 4-nitrobenzenediazonium electrophile. The aniline **5.5** was obtained after reduction by sodium sulfide in a THF/water mixture and reductively aminated with *N*-phenethylpiperidin-4-one to afford **5.6.** The final red-shifted photoswitch **5.8** was then obtained after acylation with propionyl chloride and Boc-deprotection by EtOAc saturated with gaseous HCl.

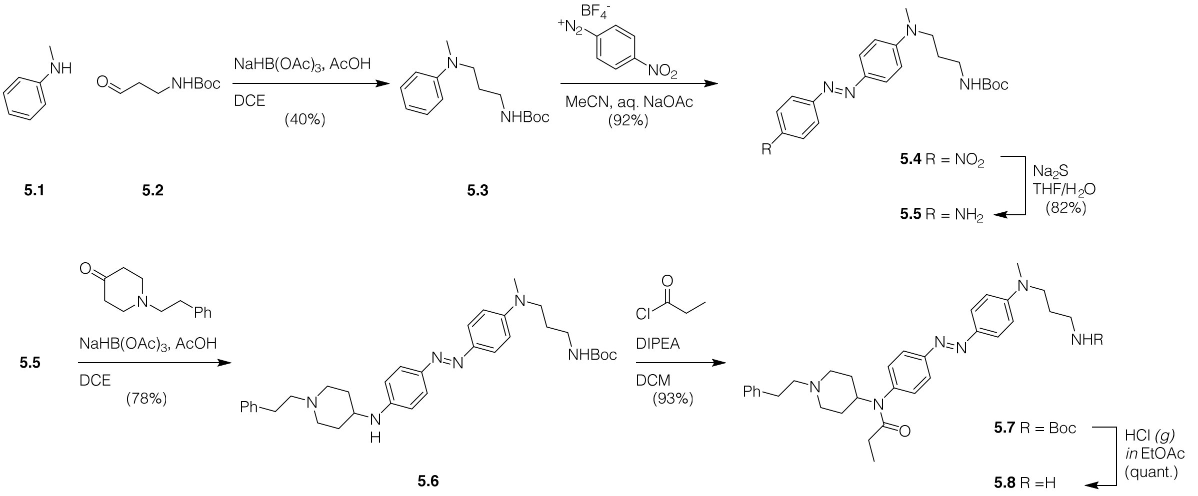

Scheme 6. **Synthesis of red-shifted photopharmacophore 5.8:**

Since Photofentanyl-II is a *cis*-active photoswitch, it was anticipated that a *bis*-amide substituted photoswitch might prove more suitable since it can be isomerized to *cis* more efficiently than red-shifted azobenzenes. Therefore, the synthesis of the photoswitch with bistable photostationary states was started by amide coupling of Boc-glycine with an excess of 4,4'-azodianiline to yield **5.10** (Scheme 7). The final photoswitch **5.13** was then obtained in the same manner as for the red-shifted photoswitch by the sequence of reductive amination, acylation and deprotection.

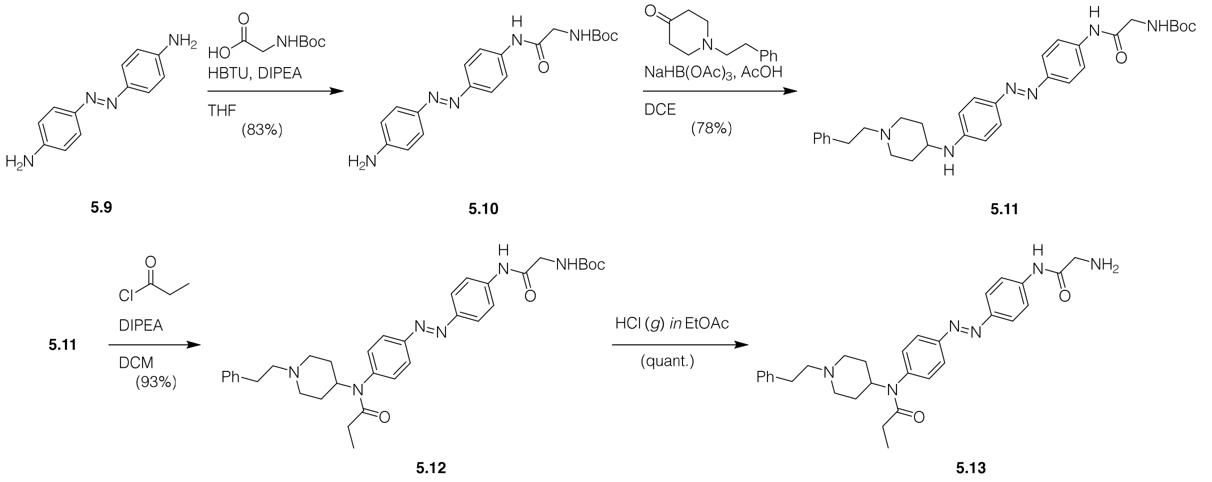

Scheme 7 **Synthesis of photopharmacophore 5.13.**

To investigate if the substitutions on the azobenzene are tolerated by the *μ*-Opioid receptor (MOR), **5.8** and **5.13** were tested by electrophysiology. The *μ*-Opioid receptor is coupled to a $G_{i/o}$ protein, of which the activated βγ subunit couples to inwardly-rectifying K^+ channels (GIRKs). Therefore, activation of MOR can be read-out indirectly by measuring the K^+ flux over the cell membrane *via* patch-clamp at appropriate K^+ concentrations/holding potentials. The GIRK read-out very closely reflects both the conformational changes underlying receptor activation as well as the downstream activation of effectors. Therefore, HEK293 cells stably expressing GIRK1/2 were transiently transfected with *N*-terminally SNAP-tagged MOR. Two variants of SNAP-MOR were used that differed in species (rat or mouse), in signal peptide and in linker sequences between the domain. One construct was cloned by Helen Farrants (Johnsson group, MPIMF Heidelberg) and the other was a kind gift of J. T. Williams (OHSU). Both were validated for expression and surface fluorophore labelling by the respective research groups, for details maps see supporting information.

HEK293 cells stably expressing GIRK1/2 (HEK-GIRK, kind gift from Sonja Kleinlogel)[110] were transfected with the SNAP_MOR constructs and tested for functional activation by wash-in of peptide agonist Leu-Enkephalin (LE) at a saturating concentration. In later experiments, DAMGO was used as positive control instead, since it is more stable towards hydrolysis (Supporting Figure 6). Both constructs were functional as confirmed by wash-in currents of LE or DAMGO.

Then, the photoswitches **5.8** and **5.13** were tested. After establishing a patch in whole-cell mode, the compound was washed in and photoswitching was attempted (Figure 33). Both compounds were active in their *trans*-configuration and could be switched ON and OFF with illumination at the respective wavelength.

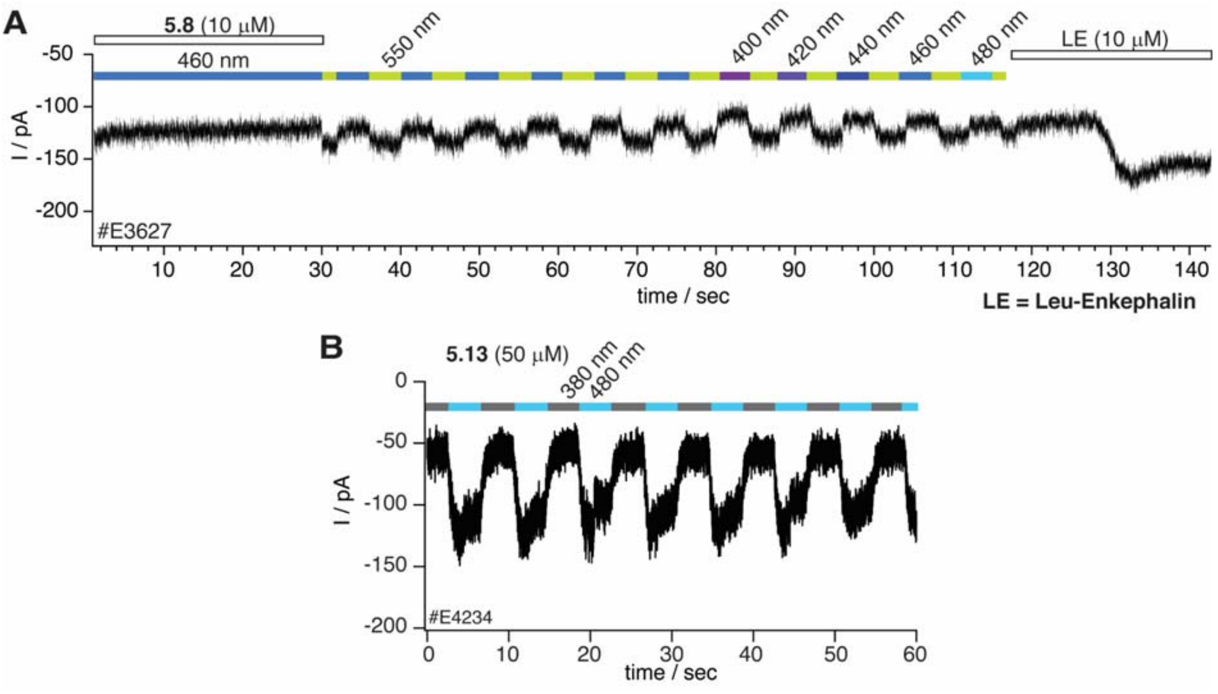

Figure 33. **Patch-clamp data of the freely diffusible photoswitches.** HEK-GIRK cells were transiently transfected with SNAP_MOR. Then, photoswitch was washed in and photoswitching was performed at the indicated wavelengths.

5.2.2 Synthesis of PORTLs

After establishing that the feely-diffusible, photoswitchable cores enable optical control over the SNAP_MOR constructs, the final PORTL molecules **5.14** and **5.15** were accessed by a sequence of amide couplings, deprotection and/or 'click' azide-alkyne cycloadditions (Scheme 8). Issues with copper-catalyzed azide-alkyne cycloadditions (CuAAC) were encountered on a related project, the benzylguanine-azo-glutamate (BGAGs) PORTL molecules.[28] The BGAGs with amides in 4,4'-position of the azobenzene required unusually high catalytic loadings of Cu(I) and high temperatures to drive the CuAAC to completion. Even more surprising, the red-shifted BGAG_{460}, where one amide is changed to a dialkylamine, was entirely unreactive in CuAAC under all conditions tested. In the end, BGAG_{460} was synthesized using strain-promoted azide-alkyne cycloaddition (SpAAC) with a strained dibenzocyclooctyne. We hypothesized that the PEG chains are coordinating to the copper-ions, rendering them unavailable for catalysis. To avoid this issues, the synthesis of MOR PORTLs was directly planned *via* SpAAC. Next, the MOR PORTLs **5.14** and **5.15** were tested by electrophysiology. HEK293 cells expressing SNAP_MOR and GIRK1/2 were labelled with MOR PORTLs at micromolar concentrations (1 - 10 μM) at 37 °C for 30-90 min. The labelling solution was then replaced with extracellular buffer, cells were patched and illuminated at the appropriate wavelengths to isomerize to *cis.* If no effect was observed upon illumination, the agonists Leu-Enkephalin (LE) or DAMGO were washed in as positive control to confirm expression of

SNAP_MOR and GIRK1/2. Negative experiments were at least repeated twice and are not shown here. Unfortunately, neither **5.14** nor **5.15** showed any light-dependent currents. Both compounds feature dibenzocyclooctyne which represents a large hydrophobic moiety. Even at low concentrations of 1 μM, precipitation of the compounds in labelling solution was observed. Accordingly, we hypothesized that the lack of light-dependent currents could be explained by failure to label due to low aqueous solubility of the PORTLs. First, the SpAAC was replaced by CuAAC (**5.19**), but led to incomplete conversion and was replaced by amide couplings (**5.16** and **5.17**). **5.16** and **5.17** were both assayed for photoswitching in patch-clamp experiments, but again no light-dependent effects were observed. In a last attempt, the PEG tether was replaced by a simple C10 carbon chain, and this compound was directly washed in at 50 μM, but again, no photoswitching could be observed.

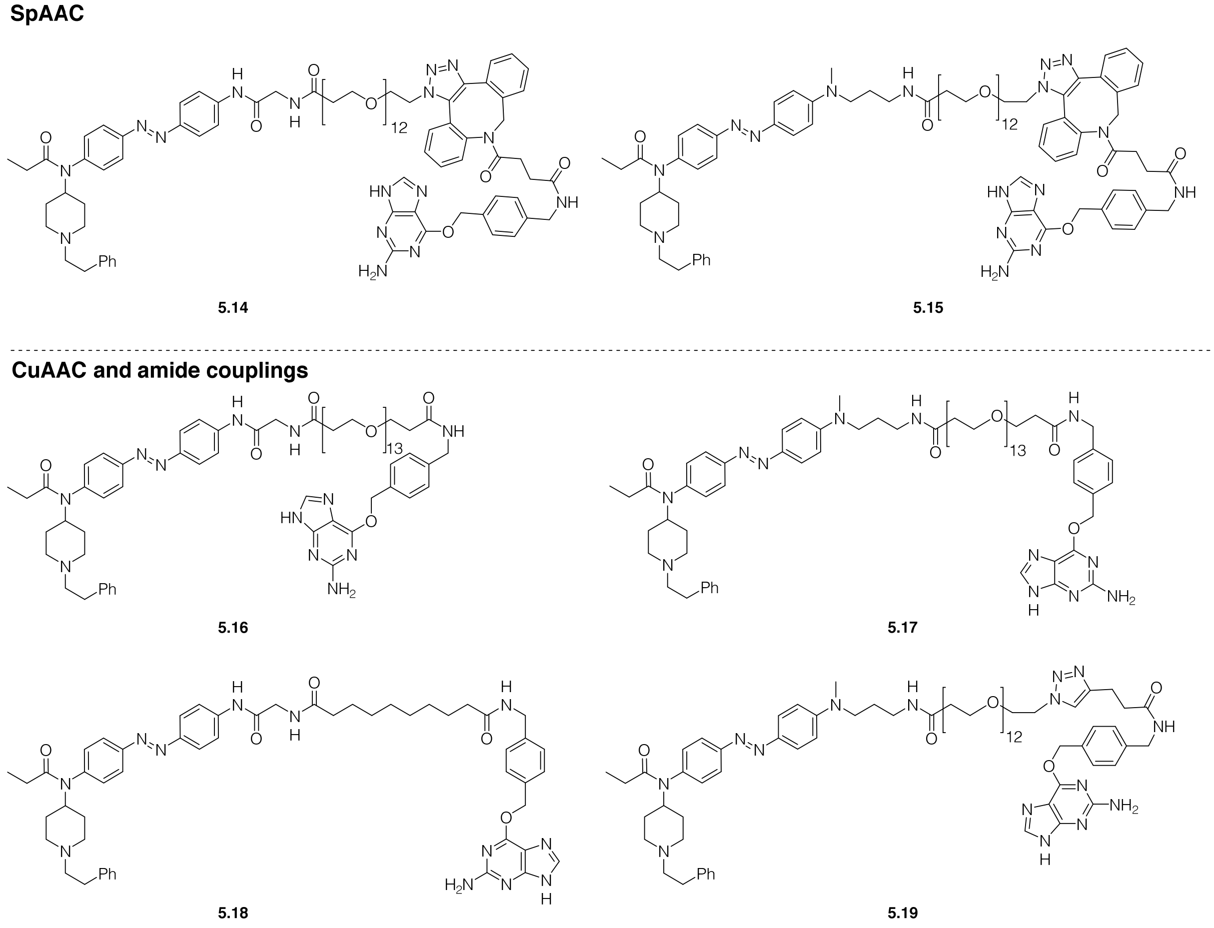

Scheme 8. **Final MOR PORTLs.**

5.2.3 Cis-stable Photoswitches

Ideally, PCLs are inactive in the dark and only elicit a biological effect upon illumination. Since PF-II and the related photoswitches **5.8** and **5.13** are trans-active, *i.e.* dark active, we sought to reverse the azobenzene logic. Siewertsen *et al.* reported a bridged 5,6-dihydrodibenzo[c,g][1,2]diazocine in 2009.[111] In these 'bridged' azobenzenes, the *cis*-isomer is the thermodynamically stable configuration and can be photoisomerized to the *trans*-configuration by violet/blue light with wavelengths around 370-400 nm. The thermal back-isomerization is usually slow for this type of a photoswitch. Green light around 480-550 nm triggers the photoisomerization back from the *trans*- to the *cis*-isomer.[111,112]

While the *cis*-stable, bridged azobenzenes have been employed for optical control of biological systems before,[113] it has not yet been shown that a *trans*-active PCL can be converted into a *cis*-active switch by replacing its azobenzene with the bridged variant. One synthesis by Woolley et al.[113] exists for the diamino-substituted, *cis*-stable photoswitch core **5.24**. In this synthesis, the diazene is formed by intramolecular reductive coupling of the nitro groups. This is reported with a mixture of Zn dust and $Ba(OH)_2$ in ethanol followed by treatment with HgO. This procedure was attempted multiple times in the Trauner laboratory but was not reproducible in our hands. Therefore, we revisited an alternative route towards the *cis*-stable photoswitch that was developed by Dr. David Woodmansee and remains unpublished to date. With minor modifications to these procedures, the *cis*-stable photoswitch **5.24** could be accessed through a 4-step reaction sequence with satisfying and reproducible yields.

The synthesis commenced with a radical bromination of 2,2'-ethylene dianiline. The aniline groups were then oxidatively coupled by treatment with *m*CPBA in DCM. The reaction yielded a mixture of the desired azobenzene2 and the further oxidized azoxy byproducts. Theoretically, two equivalents of *m*CPBA are required to oxidize the aniline to the nitroso, which subsequently reacts with the other aniline to the azobenzene in an intramolecular Baeyer-Mills-reaction. By portion wise addition of 2.0 equivalents of *m*CPBA to **5.21** in DCM, the amount of azoxy byproducuts could be minimized and the desired bridged azobenzene **5.22** could be isolated in 30% yield. Finally, by Buchwald-Hartwig coupling of **5.22** with *tert*-butyl carbamate and Boc-deprotection in neat TFA, the *cis*-stable azobenzene **5.24** was accessed.

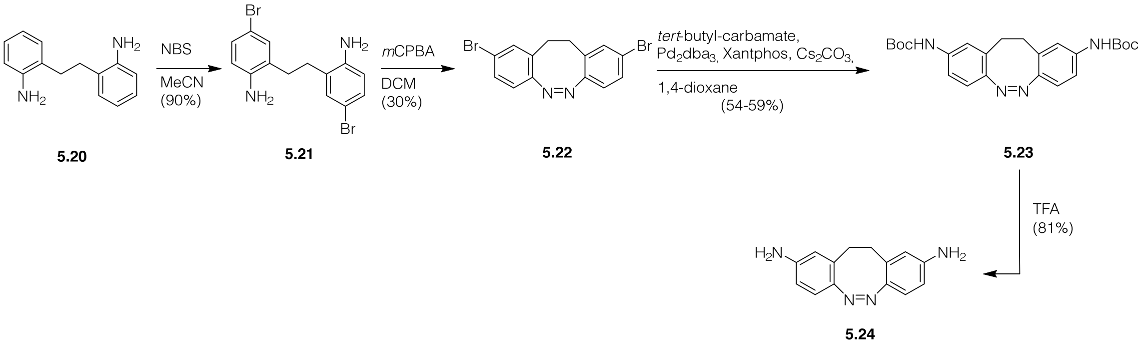

Scheme 9. **Synthesis of cis-stable azobenzene 5.24.**

Single crystals of **5.22** suitable for X-ray crystallography could be obtained (Figure 34). The 4- and 4'-positions are 6.1 Å apart, very similar in comparison with normal *cis*-azobenzene[114] (6.2

Å). The dihedral angle is 7.9°, very similar to the value of 7.7° for *cis*-azobenzene. The phenyl rings in cis-azobenzene are not arranged planar but are rotated by 57° around the C-N bond, an angle of 90° would represent the planar arrangement. In *cis*-**5.22** this angle is 71°. Therefore, the phenyl rings in the *cis*-**5.22** are more planar to each other than in cis-azobenzene, which is the major difference in their geometry.

Next, the optimal wavelengths for the photoisomerization was determined by changing the illumination wavelength while recording the absorbance at the *trans*-**5.22** absorbance maximum at 492 nm (Figure 34d). The optimal switching wavelengths for *cis*-to-*trans* are 400 nm and >490 nm for *trans*-to-*cis* photoisomerization.

The photoisomerization leads to a change in absorption (Figure 34e), which can easily observed by the color change of the **5.22**-solution (Figure 34b). The photoisomerization can be performed over multiple cycles with no observable decay or degradation (Figure 34f). In the dark, thermal relaxation of **5.22** is slow and it can therefore be considered as bistable photoswitch on the timescales that are relevant for MOR-targeting photoswitches (Figure 34g).

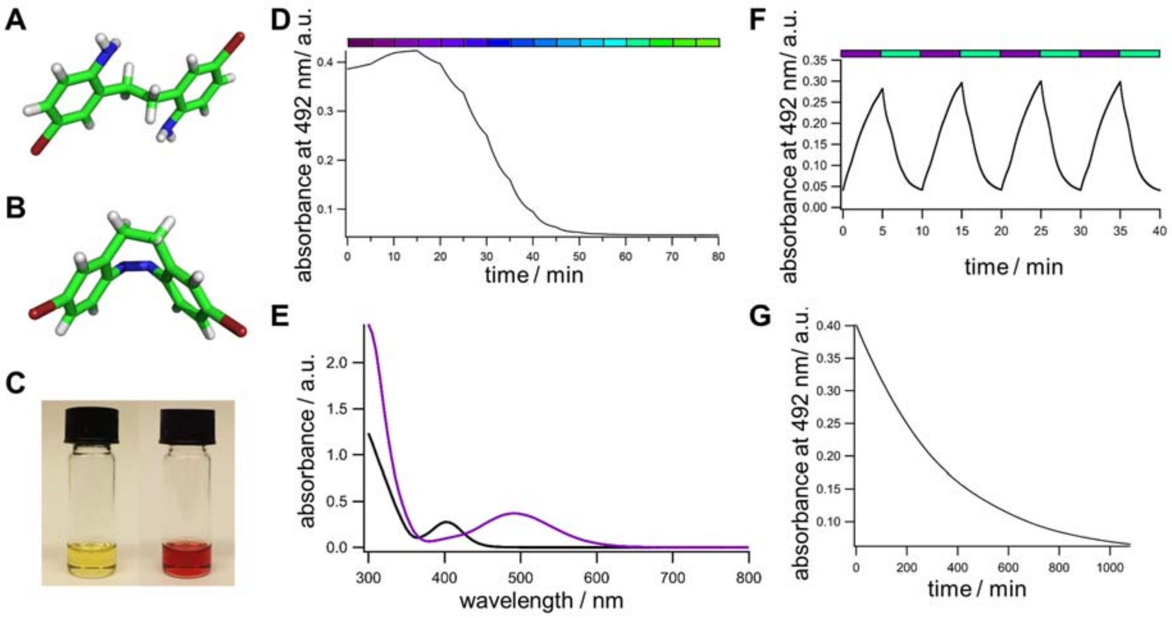

Figure 34. **Photophysical properites of 5.22. a)** X-Ray crystal structure of precursor **5.21. b)** X-Ray crystal structure of the **cis**-isomer of **5.22. c)** A solution of **5.22** in DMSO. Left: dark-adapted, *cis*-configuration; right: after illumination with violet light (λ = 400 nm) in the *trans*-configuration. **d)** Wavelength screen in 10 nm steps from 380 nm to 530 nm. **e)** UV/Vis spectrum in the dark-adapted state of **5.22** (black) and after illumination with violet light (λ = 400 nm). **f)** Switching was performed by illumination with violet (λ = 400 nm) and green light (λ = 500 nm). **g)** Dark relaxation proceeds with a time constant of τ = 349 min. All spectrums were recorded at a concentration of 0.5 mM **5.22** in DMSO.

After establishing the synthesis of the *cis*-stable azobenzene, the final steps towards a *cis*-stable PCL were performed. **5.24** was amide coupled with Boc-protected glycine. Then, the phenethylpiperidine moiety was attached *via* reductive amination to yield **5.26**. The final *cis*-stable photoswitch **5.27** was obtained after acylation using propionylchloride and deprotection by HCl gas in EtOAc.

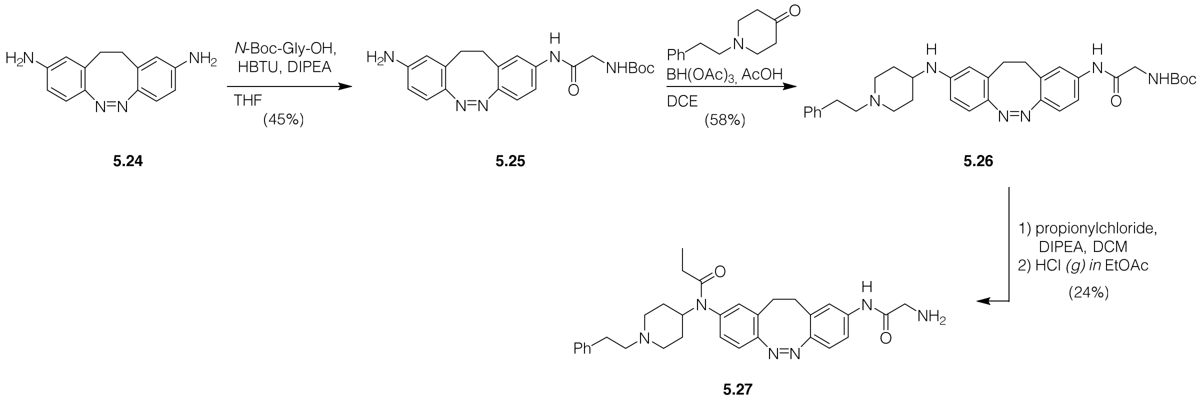

Scheme 10. **Synthesis of the cis-stable photofentanyl 5.27.**

The photoswitch **5.27** was tested at a (high) concentration of 50 *μ*M by patch-clamp electrophysiology in HEK-GIRK cells transfected with SNAP_MOR. Unfortunately, no light-dependent effects could be observed (Supporting Figure 7).

5.2.4 Further synthesis

The following compound was synthesized according to the design in Figure 31c by Dr. Ahmed Ali.

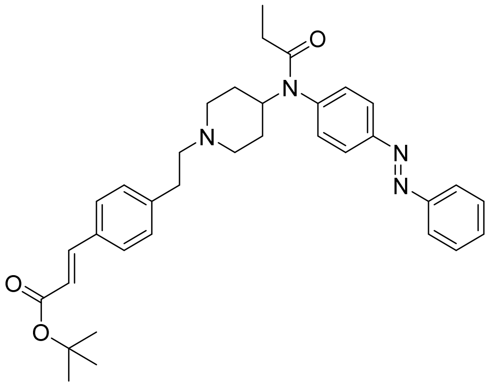

Scheme 11. **Structure of AM-II.**

AM-II was tested for effects in SNAP_MOR expressing HEK-GIRK cells. Unfortunately, no wash-in currents and no photoswitching could be observed (n = 5). For electrophysiological characterization see Supporting Figure 8.

In collaboration with Manuel Gailer (Hoffmann-Röder group, LMU Munich), a photoswitchable version (AzoDAMGO) of the synthetic enkephalin DAMGO was synthesized. To this end, an azobenzene was installed on the phenylalanine of DAMGO (Scheme 12). AzoDAMGO was tested for effects in MOR-transfected HEK-GIRK assays, but no effects were observed (n = 8). For electrophysiological characterization see Supporting Figure 9.

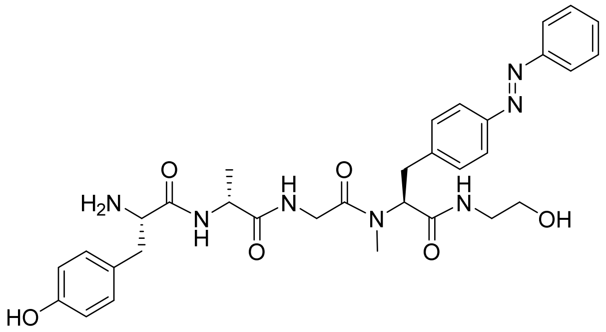

AzoDAMGO

Scheme 12. **Structure of AzoDAMGO.**

5.3 Summary and Outlook

A variety of photoswitchable derivatives of fentanyl was synthesized. Some of the freely-diffusible photoswitches enabled photoswitching of the *μ*-opioid receptor (MOR). Unfortunately, attachment of the PEG chain, that is required to span the distance between bioconjugation site and ligand binding site, was deleterious to photoswitching. None of the PEGylated photoswitches activated the MOR, neither in their *trans*- nor in their *cis*-configuration.

In an attempt to reverse the logic of photofentanyl-II, its azobenzene was replaced with a cis-stable, ethylene-bridged variant to yield **5.27**. **5.27** was not active on the MOR receptor in both its *cis*- and *trans*-configuration.

In conclusion, future PORTL molecules for the MOR should not be designed based on fentanyl. Molecular docking studies were performed with photoswitchable variants of carfentanyl (not shown). These molecules adapt a different position in the MOR binding site and molecular docking suggests that carfentanyl-based photoswitches might be more amenable to the PORTL approach.

5.4 Supporting Information

5.4.1 Synthesis

5.4.1.1 *tert*-Butyl (*E*)-(2-((4-((4-aminophenyl)diazenyl)phenyl)amino)-2-oxoethyl)carbamate (**3.6, 5.10**)

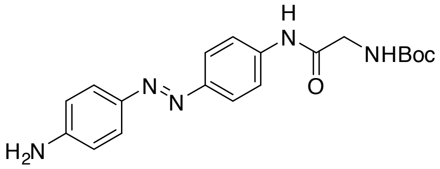

4,4'-Diazoaniline (1.00 g, 4.71 mmol, 2.0 equiv.), *N*-Boc-Gly-OH (413 mg, 2.36 mmol, 1.0 equiv.), HBTU (1.79 g, 4.72 mmol, 2.0 equiv.) and DIPEA (1.64 mL, 9.40 mmol, 4.0 equiv.) were added successively to a round bottom flask filled with dry THF (20 mL) at 0 °C. The reaction mixture was stirred at 0 °C for 45 min before it was allowed to warm to r.t. After 3 h the solvent was removed *in vacuo* and the residue was partitioned between EtOAc and 1 mM HCl. The organic layer was washed with water (1x) and brine (1x) before drying over $MgSO_4$. After purification by flash column chromatography (1/2 = EtOAc/DCM) 725 mg (1.96 mmol) of the product were obtained as an orange solid in in 83% yield.

TLC (2/1 = EtOAc/DCM) = 0.61.

^{1}H NMR (400 MHz, MeOH-*d*$_4$) δ = 7.67 (d, *J* = 8.9 Hz, 2H), 7.63 – 7.54 (m, 4H), 6.67 – 6.57 (m, 2H), 3.79 (s, 2H), 1.38 (s, 9H).

^{13}C NMR (101 MHz, MeOH-*d*$_4$): δ = 169.2, 157.2, 151.9, 149.2, 144.3, 139.6, 124.6, 122.4, 119.8, 113.8, 79.3, 48.2, 48.0, 47.8, 47.6, 47.4, 47.2, 46.9, 43.7, 27.3.

HRMS (ESI): *m/z* calc. for $C_{19}H_{24}N_5O_3^+$ $(M+H)^+$: 370.1874, found: 370.1873.

***t*$_R$** (LCMS; MeCN/H_2O/formic acid = 10/90/0.1 → 100/0/0.1 over 10 min) = 6.52 (*cis*), 6.67 min (*trans*).

UV/Vis (LCMS): λ_{max} = 389 nm.

5.4.1.2 *tert*-Butyl (*E*)-(2-oxo-2-((4-((4-((1-phenethylpiperidin-4-yl)amino)phenyl)diazenyl) phenyl)amino)ethyl)carbamate (5.11)

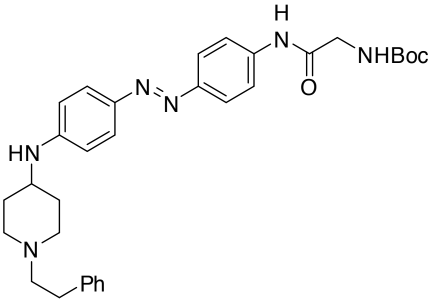

3.6 (200 mg, 0.54 mmol, 1.0 equiv.), *N*-phenethylpiperidin-4-one1 (110 mg, 0.54 mmol, 1.0 equiv.), sodium triacetoxyborohydride (160 mg, 0.76 mmol, 1.4 equiv.), AcOH (30 *μ*L, 0.54 mmol, 1.0 equiv.) were added successively to dry DCE (5 mL). The reaction mixture was was stirred for 18 h at r.t. before the solvent was removed *in vacuo*. The residue was extracted with EtOAc against $NaHCO_3$, water and brine. The organic layer was dried over $MgSO_4$. After purification by flash column chromatography (3/2 = DCM/EtOAc -> EtOAc) the product was obtained as an orange solid (68 mg, 0.12 mmol) in 23% yield.

TLC (2/3 = EtOAc/DCM) = 0.20 (PAA stain, SM: orange-yellow, product: violet).

^{1}H NMR (400 MHz, MeOH-*d*$_4$) δ = 77.70 – 7.54 (m, 6H), 7.22 – 7.03 (m, 5H), 6.65 – 6.52 (m, 2H), 3.78 (s, 2H), 3.33 (tt, *J* = 10.1, 4.1 Hz, 1H), 2.94 (d, *J* = 11.6 Hz, 2H), 2.77 – 2.68 (m, 2H), 2.57 – 2.48 (m, 2H), 2.25 – 2.14 (m, 2H), 2.03 – 1.93 (m, 2H), 1.55 – 1.41 (m, 2H), 1.38 (s, 9H).

^{13}C NMR (101 MHz, MeOH-*d*$_4$): δ = 175.48, 163.51, 157.28, 155.63, 149.98, 146.13, 145.72, 134.68, 134.48, 132.11, 131.11, 128.64, 126.13, 118.21, 85.65, 66.57, 58.27, 55.29, 49.98, 39.12, 37.50, 33.61.

HRMS (ESI): *m/z* calc. for $C_{32}H_{41}N_6O_3^+$ $(M+H)^+$: 557.3235, found: 557.3236.

***t*$_R$** (LCMS; MeCN/H_2O/formic acid = 10/90/0.1 → 100/0/0.1 over 10 min) = 5.99 min.

UV/Vis (LCMS): λ_{max} = 420 nm.

5.4.1.3 *tert*-Butyl (*E*)-(2-oxo-2-((4-((4-(*N*-(1-phenethylpiperidin-4-yl)propionamido)phenyl)diazenyl)phenyl)amino)ethyl)carbamate (5.12)

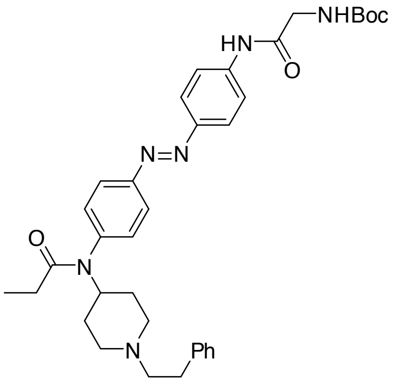

5.11 (58 mg, 0.104 mmol, 1.0 equiv.) was dissolved in dry DCM (5 mL) under a nitrogen atmosphere before addition of dry DIPEA (45 μL, 0.260 mmol, 2.5 equiv.) and propionyl chloride (11 μL, 0.125 mmol, 1.2 equiv.). After stirring at r.t. for 36 h, reaction progress was checked by LCMS, judged to be incomplete and more propionyl chloride was added (11 μL, 0.125 mmol, 1.2 equiv.). After stirring for further 4.5 h at r.t., the reaction was quenched by addition of a few drops of MeOH before it was loaded directly on a silica column for purification (96/4 → 95/5 = MeOH/DCM). The product was obtained as an orange solid (50 mg, 81.6 μmol) in 79% yield.

TLC (MeOH/DCM = 95/5) = 0.30. (*Product and starting material run co-polar on TLC; PAA stain: SM violet, product yellow.).*

^{1}H NMR (400 MHz, $CDCl_3$) δ = 8.86 (s, 1H), 7.90 – 7.80 (m, 4H), 7.70 – 7.60 (m, 2H), 7.21 – 7.05 (m, 7H), 5.49 (t, *J* = 5.9 Hz, 1H), 4.63 (tt, *J* = 11.4, 3.4 Hz, 1H), 3.93 (d, *J* = 5.8 Hz, 2H), 2.96 (d, *J* = 11.2 Hz, 2H), 2.71 – 2.62 (m, 2H), 2.53 – 2.44 (m, 2H), 2.12 (t, *J* = 11.6 Hz, 2H), 1.92 (q, *J* = 7.4 Hz, 2H), 1.78 (d, *J* = 11.3 Hz, 2H), 1.51 – 1.36 (m, 11H), 0.97 (t, *J* = 7.4 Hz, 3H).

^{13}C NMR (101 MHz, $CDCl_3$): δ = 173.5, 168.2, 156.7, 152.2, 148.9, 140.8, 140.0, 131.1, 128.6, 128.4, 126.1, 124.2, 123.5, 119.9, 80.8, 60.3, 53.0, 52.5, 45.6, 33.7, 30.5, 28.7, 28.3, 9.7.

HRMS (ESI): *m/z* calc. for $C_{35}H_{45}N_6O_4^+$ $(M+H)^+$: 613.3497, found: 613.3498.

t_R (LCMS; MeCN/H_2O/formic acid = 10/90/0.1 → 100/0/0.1 over 10 min) = 5.57 (*cis*), 5.89 (*trans*).

UV/Vis (LCMS): λ_{max} = 365 nm.

5.4.1.4 (*E*)-*N*-(4-((4-(2-Aminoacetamido)phenyl)diazenyl)phenyl)-*N*-(1-phenethylpiperidin-4-yl)propionamide (**5.13**)

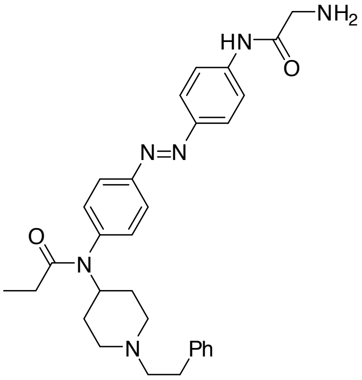

5.12 (18 mg, 29 μmol) was dissolved in dry EtOAc (1 mL) and sat. HCl in EtOAc (3 mL) was added. After stirring for 1 h at r.t., the precipitate was filtered off and dried under HV to yield the product as an orange HCl salt in quantitative yield (19 mg).

^{1}H NMR (400 MHz, D_2O) δ = 7.82 (dd, *J* = 8.6, 5.0 Hz, 4H), 7.70 – 7.60 (m, 2H), 7.33 (ddd, *J* = 7.8, 5.6, 1.9 Hz, 4H), 7.29 – 7.20 (m, 3H), 4.68 (tt, *J* = 8.6, 3.3 Hz, 1H), 3.99 (s, 2H), 3.60 – 3.53 (m, 2H), 3.31 – 3.23 (m, 2H), 3.16 – 3.04 (m, 2H), 2.95 (dd, *J* = 9.8, 6.4 Hz, 2H), 2.11 – 1.99 (m, 2H), 1.94 (q, *J* = 7.6 Hz, 2H), 1.61 (qd, *J* = 12.9, 3.8 Hz, 2H), 0.90 (t, *J* = 7.4 Hz, 3H).

^{13}C NMR (101 MHz, D_2O): δ = 176.7, 165.4, 151.9, 148.6, 140.1, 139.5, 136.1, 130.8, 129.0, 128.6, 127.3, 123.9, 123.5, 121.0, 57.4, 51.9, 50.2, 41.1, 29.8, 28.3, 27.3, 8.9.

HRMS (ESI): *m/z* calc. for $C_{30}H_{37}N_6O_2^+$ $(M+H)^+$: 513.2973, found:513.2970.

***t*$_R$** (LCMS; MeCN/H_2O/formic acid = 10/90/0.1 → 100/0/0.1 over 10 min) = 5.13 min.

UV/Vis (LCMS): λ_{max} = 365 nm.

5.4.1.5 (*E*)-1-Azido-*N*-(2-oxo-2-((4-((4-(*N*-(1-phenethylpiperidin-4-yl)propionamido)phenyl)diazenyl)phenyl)amino)ethyl)-3,6,9,12,15,18,21,24,27,30,33,36-dodecaoxanonatriacontan-39-amide (**5.28**)

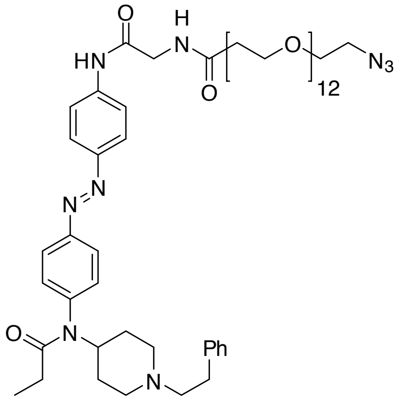

5.13 (19 mg, 32.4 μmol, 1.0 equiv.) and N_3-PEG12-NHS-ester (baseclick #BCL-033, 72 mg, 97.2 μmol, 3.0 equiv.) were dissolved in dry DMF (1 ml), dry DIPEA (56 μL, 320 μmol, 10 equiv.) was added and the reaction mixture was stirred at r.t. Reaction progress was monitored by LCMS and judged to be complete after 1 h. The reaction mixture was loaded directly on a C18 column (Waters Sep-Pak C18 5g) using a gradient of 1 mM HCl and MeCN (100/0 → 60/40 = 1 mM HCl/MeCN). Product containing fractions were identified by LCMS, combined and freeze-dried to obtain the product as a yellow solid in 66% yield (24.3 mg, 21.3 μmol).

HRMS (ESI): *m/z* calc. for $C_{57}H_{86}O_{15}N_9^-$ (M-H)$^-$: 1136.6249, found: 1136.6252.

t_R (LCMS; MeCN/H_2O/formic acid = 10/90/0.1 → 100/0/0.1 over 10 min) = 5.29 min (*cis*), 5.44 (*trans*).

UV/Vis (LCMS): λ_{max1} = 362 nm.

5.4.1.6 BG-DBCO

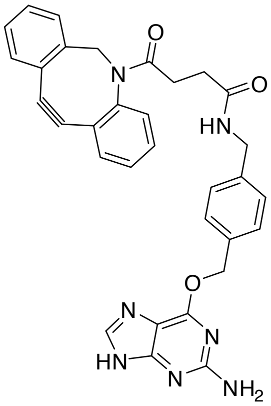

6-((4-(Aminomethyl)benzyl)oxy)-9*H*-purin-2-amine, BG-NH_2, (14.9 mg, 55 μmol, 1.1 equiv.) and DBCO-NHS-ester (Jena Bioscience #CLK-A133-100, 20.1 mg, 5´0 μmol, 1.0 equiv.) were combined in dry DMF (500 μL) and dry DIPEA (16.7 μL, 100 μmol, 2.0 equiv.) was added. Reaction progress was monitored by LCMS and judged to be complete after 5.5 h. The reaction mixture was directly loaded on a C8 column (Waters Sep-Pak C8 2g) and eluted with a gradient of 1 mM HCl and MeCN (100/0 → 60/40 = 1 mM HCl/MeCN). Product containing fractions were identified by LCMS, conbined and freeze-dried to obtain the product as a colorless solid (8.0 mg 14.3 μmol, 29%).

^{1}H NMR (400 MHz, DMSO-*d_6*) δ = 8.53 (s, 1H), 8.29 (t, J = 5.9 Hz, 1H), 7.74 – 7.60 (m, 2H), 7.55 – 7.26 (m, 8H), 7.21 (d, J = 7.9 Hz, 2H), 5.53 (s, 2H), 5.04 (d, J = 14.0 jkHz, 1H), 4.18 (d, J = 5.9 Hz, 2H), 3.63 (d, J = 14.0 Hz, 1H), 2.61 (t, J = 8.0 Hz, 1H), 2.29 (t, J = 7.6 Hz, 1H), 2.09 (ddd, J = 15.4, 7.7, 5.7 Hz, 1H), 1.80 (ddd, J = 16.4, 7.6, 5.7 Hz, 1H).

^{13}C NMR (101 MHz, DMSO-d_6) δ = 171.6, 171.5, 152.0, 148.9, 140.4, 134.4, 132.9, 130.1, 129.4, 129.3, 128.6, 128.5, 128.2, 127.8, 127.7, 127.3, 125.6, 123.0, 121.9, 114.7, 108.6, 68.5, 55.4, 42.2, 30.8, 30.1.

HRMS (ESI): *m/z* calc. for $C_{32}H_{26}O_3N_7^-$ $(M-H)^-$: 556.2103, found: 556.2109.

t_R (LCMS; MeCN/H_2O/formic acid = 10/90/0.1 → 100/0/0.1 over 10 min) = 5.75 min.

UV/Vis (LCMS): λ_{max} = 290 nm.

5.4.1.7 (*E*)-1-(8-(4-((4-(((2-Amino-9*H*-purin-6-yl)oxy)methyl)benzyl)amino)-4-oxobutanoyl)-8,9-dihydro-1*H*-dibenzo[b,f][1,2,3]triazolo[4,5-d]azocin-1-yl)-*N*-(2-oxo-2-((4-((4-(*N*-(1-phenethylpiperidin-4-yl)propionamido)phenyl)diazenyl)phenyl)amino)ethyl)-3,6,9,12,15,18,21,24,27,30,33,36-dodecaoxanonatriacontan-39-amide (**5.14**)

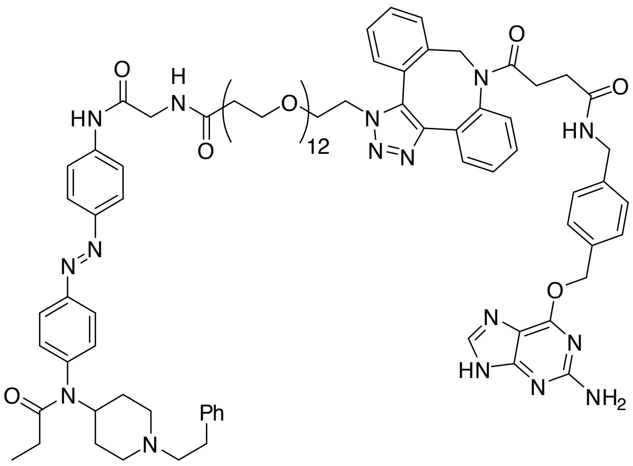

5.28 (4.1 mg, 3.9 µmol, 1.0 equiv.) and BG-DBCO (2.2 mg, 3.9 µmol, 1.0 equiv.) were combined in dry DMSO (300 µL) and stirred o.n. at r.t. The product was directly loaded on a C8 column (Waters Sep-Pak C8 2g) and eluted with a gradient of 1 mM HCl and MeCN (100/0 → 60/40 = 1 mM HCl/MeCN). Product containing fractions were identified by LCMS, combined and freeze dried to obtain the desired product as an orange solid (3.2 mg, 1.9 µmol, 49%).

5.4.1.8 *tert*-Butyl (3-(methyl(phenyl)amino)propyl)carbamate (**5.3**)

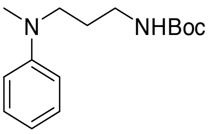

N-Methylaniline (338 µL, 3.13 mmol, 1.1 equiv.), *N*-Boc-3-aminopropanal (400 mg, 2.85 mmol, 1.0 equiv.), AcOH (171 µL, 3 mmol, 1.1 equiv.) and sodium triacetoxyborohydride (1.02 g, 4.8 mmol, 1.7 equiv.) were added successively to dry DCE (15 mL). The reaction mixture was stirred for 4.5 h at r.t., before it was extracted with DCM against $NaHCO_3$ (aq. sat.). The organic layer was washed against $NaHCO_3$ (aq. sat.), brine and dried over $MgSO_4$ before purification by flash column chromatography (98/2 = DCM/MeOH), the product was obtained as colorless and viscous oil (298 mg, 1.13mmol) in 40% yield.

TLC (DCM/MeOH = 98/2) = 0.40. (stain: ninhydrin)

^{1}H NMR (400 MHz, $CDCl_3$) δ = 7.20 – 7.11 (m, 2H), 6.64 (d, J = 7.7 Hz, 3H), 4.51 (s, 1H), 3.33 – 3.24 (m, 2H), 3.10 (q, J = 6.7 Hz, 2H), 2.85 (s, 3H), 1.70 (p, J = 7.1 Hz, 2H), 1.37 (s, 9H).

^{13}C NMR (101 MHz, $CDCl_3$) δ = 156.0, 149.2, 129.2, 116.4, 112.4, 79.3, 50.3, 38.6, 38.5, 28.4, 27.3.

HRMS (ESI): *m/z* calc. for $C_{15}H_{25}N_2O_2^+$ $(M+H)^+$: 265.1911, found: 265.1916.

5.4.1.9 *tert*-Butyl (*E*)-(3-(methyl(4-((4-nitrophenyl)diazenyl)phenyl)amino)propyl)carbamate (**5.4**)

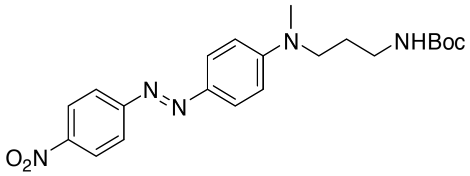

5.3 (250 mg, 0.95 mmol, 1.0 equiv.) was dissolved in a mixture of MeCN (10 mL) and 1 M aq. NaOAc (10 mL) and cooled to 0 °C. 4-Nitrobenzenediazonium tetrafluoroborate was dissolved in MeCN (10 mL), cooled to 0 °C and added dropwise to the solution containing **5.3.** After complete addition, the reaction mixture was allowed to warm to r.t. and stirred for 20 min. The reaction mixture was portioned between DCM (100 mL) and water (30 mL). The organic layer was washed with water (2 x 50 mL), brine (50 mL) and dried over $MgSO_4$. After purification by flash column chromatography (DCM -> 98/2 = DCM/MeOH), the product was obtained as a red solid (358 mg, 0.87 mmol) in 92% yield.

TLC (DCM/MeOH = 98/2) = 0.33.

^{1}H NMR (400 MHz, $CDCl_3$) δ = 8.36 – 8.28 (m, 2H), 7.97 – 7.86 (m, 4H), 6.79 – 6.70 (m, 2H), 4.59 (s, 1H), 3.56 – 3.47 (m, 2H), 3.21 (q, J = 6.8 Hz, 2H), 3.10 (s, 3H), 1.86 (p, J = 7.0 Hz, 2H), 1.46 (s, 9H).

^{13}C NMR (101 MHz, $CDCl_3$) δ = 156.8, 156.0, 152.3, 147.4, 143.7, 126.2, 124.7, 122.6, 111.4, 77.2, 50.1, 38.8, 38.3, 28.4, 27.8.

HRMS (ESI): *m/z* calc. for $C_{21}H_{26}N_5O_4^-$ $(M-H)^-$: 412.1990, found: 412.1990.

***t*$_R$** (LCMS; MeCN/H_2O/formic acid = 10/90/0.1 → 100/0/0.1 over 10 min) = 9.19 min.

UV/Vis (LCMS): λ_{max} = 550 nm (broad).

5.4.1.10 *tert*-Butyl (*E*)-(3-((4-((4-aminophenyl)diazenyl)phenyl)(methyl)amino)propyl) carbamate (**5.5**)

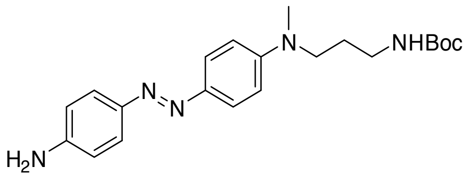

5.4 (350 mg, 0.85 mmol) was dissolved in a mixture of THF (20 mL) and water (20 mL). Sodium sulfide (65%, monohydrate, 407 mg, 3.39 mmol, 4.0 equiv.) was added and the reaction mixture heated to 80 °C for 1 h before it was allowed to cool to r.t. addition of water (75 mL) and $NaHCO_3$ (aq. sat., 75 mL). The aqueous phase was extracted with DCM (3x 75 mL). The combined organic layers were washed with $NaHCO_3$ (aq. sat., 100 mL), water (100 mL), brine (100 mL) and dried over $MgSO_4$. Purification by flash column chromatography (97.5/2.5 = DCM/MeOH) gave the product as an orange solid (280 mg, 0.73 mmol) in 86% yield.

^{1}H NMR (400 MHz, $CDCl_3$) δ = 7.78 – 7.63 (m, 4H), 6.67 (dd, J = 8.8, 2.1 Hz, 4H), 4.52 (s, 1H), 3.92 (s, 2H), 3.39 (t, J = 7.3 Hz, 2H), 3.12 (q, J = 6.7 Hz, 2H), 2.96 (s, 3H), 1.75 (p, J = 7.1 Hz, 2H), 1.39 (d, J = 3.3 Hz, 9H).

^{13}C NMR (101 MHz, $CDCl_3$) δ = 156.0, 150.5, 150.4, 148.2, 124.4, 124.2, 114.8, 111.6, 79.4, 50.1, 38.7, 38.4, 28.4, 27.6.

HRMS (ESI): *m/z* calc. for $C_{21}H_{28}O_2N_5^-$ $(M-H)^-$: 382.2248 found: 382.2251.

t_R (LCMS; MeCN/H_2O/formic acid = 10/90/0.1 → 100/0/0.1 over 10 min) = 7.73 min.

UV/Vis (LCMS): λ_{max1} = 442 nm.

5.4.1.11 *tert*-Butyl (*E*)-(3-(methyl(4-((4-((1-phenethylpiperidin-4-yl)amino)phenyl)diazenyl)phenyl)amino)propyl)carbamate (**5.6**)

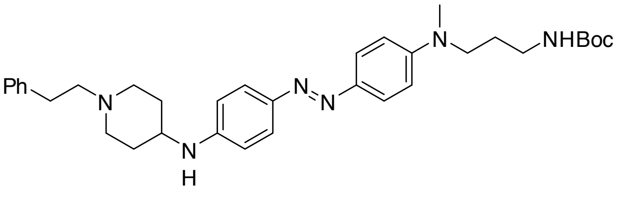

5.5 (96 mg, 0.25 mmol, 1.0 equiv.), *N*-phenethylpiperidin-4-one (51 mg, 0.25 mmol, 1.0 equiv.), sodium triacetoxyborohydride (85 mg, 0.40 mmol, 1.6 equiv.) and AcOH (14 µL, 0.25 mmol, 1.0 equiv.) were combined in dry DCE (5 mL). The reaction mixture was stirred at r.t. for 17 h before it was directly purified by flash column chromatography (DCM/MeOH = 98/2 -> 96/4 -> 94/6). The product was obtained as a red solid (111 mg, 0.19 mmol) in 78% yield.

^{1}H NMR (400 MHz, $CDCl_3$) *δ* = 7.77 (ddd, *J* = 14.5, 9.2, 2.3 Hz, 4H), 7.35 – 7.26 (m, 2H), 7.22 (dt, *J* = 6.7, 2.5 Hz, 4H), 6.77 – 6.69 (m, 2H), 6.68 – 6.60 (m, 2H), 4.58 (s, 1H), 4.06 – 3.53 (m, 1H), 3.54 – 3.39 (m, 4H), 3.24 – 3.10 (m, 4H), 3.03 (s, 3H), 2.97 – 2.88 (m, 2H), 2.79 (t, *J* = 8.2 Hz, 2H), 2.51 – 2.33 (m, 6H), 2.26 – 2.12 (m, 4H), 1.86 – 1.65 (m, 2H), 1.46 (s, 9H).

^{13}C NMR (101 MHz, $CDCl_3$) δ = 156.1, 150.5, 148.4, 145.3, 144.0, 128.9, 128.7, 126.6, 124.5, 124.4, 112.9, 111.7, 77.4, 59.9, 52.0, 50.2, 38.8, 38.6, 32.8, 31.4, 28.6, 27.7.

HRMS (ESI): *m/z* calc. for $C_{34}H_{47}O_2N_6^+$ $(M+H)^+$: 571.3755 found: 571.3767.

t_R (LCMS; MeCN/H_2O/formic acid = 10/90/0.1 → 100/0/0.1 over 10 min) = 6.70 min.

UV/Vis (LCMS): λ_{max} = 458 nm.

Note: Acetic acid impurity.

5.4.1.12 *tert*-Butyl (*E*)-(3-(methyl(4-((4-(*N*-(1-phenethylpiperidin-4-yl)propionamido)phenyl)diazenyl)phenyl)amino)propyl)carbamate (**5.7**)

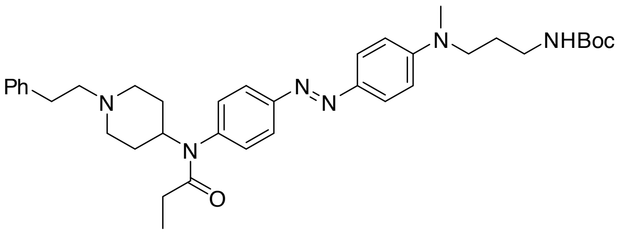

5.6 (55 mg, 96 μmol, 1.0 equiv.) was dissolved in dry DCM (1.8 mL) before addition of dry DIPEA (42 μL, 240 μmol, 2.5 equiv.) and propionyl chloride (10 μL, 115 μmol, 1.2 equiv.). The reaction mixture was stirred overnight at r.t. before it was directly purified by flash column chromatography (DCM/MeOH = 96/4) to yield the product as a red solid (56 mg, 89 μmol) in 93% yield.

TLC (DCM/MeOH = 96/4) = 0.16. (*Product and starting material run copular on TLC, PAA stain: SM yellow, product pink.)*

^{1}H NMR (400 MHz, $CDCl_3$) *δ* = 7.85 – 7.64 (m, 4H), 7.17 (dd, *J* = 8.9, 2.7 Hz, 2H), 7.14 – 7.05 (m, 5H), 6.72 – 6.61 (m, 2H), 4.69 – 4.58 (m, 1H), 4.56 (s, 1H), 3.42 (t, *J* = 7.3 Hz, 2H), 3.13 (q, *J* = 6.7 Hz, 2H), 3.00 (s, 3H), 2.94 (dd, *J* = 8.7, 3.6 Hz, 2H), 2.71 – 2.53 (m, 2H), 2.52 – 2.42 (m, 2H), 2.16 – 2.02 (m, 2H), 1.92 (q, *J* = 7.4 Hz, 2H), 1.76 (q, *J* = 6.7 Hz, 4H), 1.50 – 1.41 (m, 2H), 1.39 (s, 9H), 0.96 (t, *J* = 7.4 Hz, 3H).

^{13}C NMR (101 MHz, $CDCl_3$) *δ* = 173.5, 156.0, 152.8, 151.5, 143.5, 140.2, 139.5, 131.0, 128.7, 128.4, 126.0, 125.4, 122.9, 111.4, 79.5, 60.5, 53.1, 52.4, 50.0, 38.7, 38.4, 33.8, 30.6, 28.7, 28.4, 27.7, 9.7.

HRMS (ESI): *m/z* calc. for $C_{37}H_{49}O_3N_6^-$ $(M-H)^-$: 625.3872, found: 625.3872

t$_R$ (LCMS; MeCN/H_2O/formic acid = 10/90/0.1 → 100/0/0.1 over 10 min) = 6.67 min.

UV/Vis (LCMS): λ_{max} = 455 nm.

5.4.1.13 (*E*)-*N*-(4-((4-((3-Aminopropyl)(methyl)amino)phenyl)diazenyl)phenyl)-*N*-(1-phenethylpiperidin-4-yl)propionamide dihydrochloride (**5.8**)

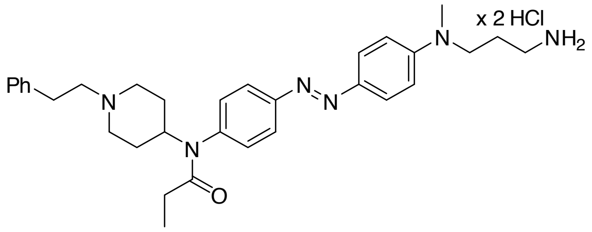

A saturated solution of HCl in dry EtOAc was freshly prepared by bubbling HCl through EtOAc for 1 h while stirring. **5.7** (56 mg, 89 μmol) was dissolved in dry EtOAc (2 mL) and HCl sat. in dry EtOAc (6 mL) was added. After stirring at r.t. for 3.5 h, the resulting precipitate was filtered off, washed with EtOAc and dissolved and transferred with dry MeOH. After solvent removal *in vacuo*, the product was dried under HV and obtained as a violet solid (54 mg, 90 μmol) in quantitative yield.

^{1}H NMR (400 MHz, D_2O) δ = 7.87 – 7.79 (m, 2H), 7.77 – 7.69 (m, 2H), 7.34 – 7.23 (m, 4H), 7.23 – 7.15 (m, 3H), 7.07 – 7.01 (m, 2H), 4.68 – 4.59 (m, 1H), 3.66 (t, *J* = 7.5 Hz, 2H), 3.54 (d, *J* = 12.6 Hz, 2H), 3.27 – 3.20 (m, 2H), 3.19 (s, 3H), 3.13 – 3.02 (m, 2H), 2.98 (t, *J* = 8.1 Hz, 2H), 2.91 (dd, *J* = 10.0, 6.5 Hz, 2H), 2.12 – 1.81 (m, 6H), 1.57 (tt, *J* = 14.0, 7.2 Hz, 2H), 0.85 (t, *J* = 7.5 Hz, 3H).

^{13}C NMR (101 MHz, D_2O) δ = 177.2, 154.5, 147.3, 140.9, 137.4, 136.1, 131.0, 129.0, 128.7, 128.7, 127.3, 121.0, 115.2, 57.5, 52.0, 50.5, 50.2, 39.6, 36.9, 29.8, 28.3, 27.4, 24.5, 8.9.

HRMS (ESI): *m/z* calc. for $C_{32}H_{43}ON_6^+$ $(M+H)^+$: 527.3493, found: 527.3498.

t_R (LCMS; MeCN/H_2O/formic acid = 10/90/0.1 → 100/0/0.1 over 10 min) = 5.65 min (broad peak).

UV/Vis (LCMS): λ_{max} = 430 nm.

5.4.1.14 (*E*)-1-Azido-*N*-(3-(methyl(4-((4-(*N*-(1-phenethylpiperidin-4-yl)propionamido)phenyl)diazenyl)phenyl)amino)propyl)-3,6,9,12,15,18,21,24,27,30,33,36-dodecaoxanonatriacontan-39-amide (**5.29**)

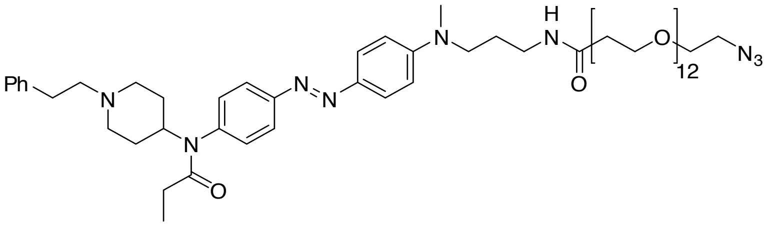

5.8 (8.1 mg, 14 μmol, 1.0 equiv.), N_3-PEG_{12}-NHS-ester (10 mg, 14 μmol, 1.0 equiv.) and dry DIPEA (14 μL, 81 μmol, 6.0 equiv.) were combined in dry DMF (1.25 mL). After stirring for 18 h at r.t. full conversion was confirmed by LCMS. The product was directly loaded on a C18 column (Waters Sep-Pak C18 2g) and eluted with a gradient of MeCN and 1 mM HCl (100/0 → 60/40 = 1 mM HCl/MeCN). Product containing fractions were identified by LCMS, combined and freeze-dried to obtain the product as a red solid (14.5 mg, 12.6 μmol) in 93% yield.

HRMS (ESI): *m/z* calc. for $C_{59}H_{94}O_{14}N_9^+$ $(M+H)^+$: 1152.6915, found: 1152.6924; *m/z* calc. for $C_{59}H_{92}O_{14}N_9^-$ $(M-H)^-$: 1150.6769, found: 1150.6766.

***t*R** (LCMS; MeCN/H_2O/formic acid = 10/90/0.1 → 100/0/0.1 over 10 min) = 5.86 min.

UV/Vis (LCMS): λ_{max} = 448 nm.

5.4.1.15 (*E*)-1-(8-(4-((4-(((2-Amino-9*H*-purin-6-yl)oxy)methyl)benzyl)amino)-4-oxobutanoyl)-8,9-dihydro-1*H*-dibenzo[b,f][1,2,3]triazolo[4,5-d]azocin-1-yl)-*N*-(3-((4-((4-(*N*-(1-phenethylpiperidin-4-yl)propionamido)phenyl)diazenyl)phenyl)-λ^2-azaneyl)propyl)-3,6,9,12,15,18,21,24,27,30,33,36-dodecaoxanonatriacontan-39-amide (**5.15**)

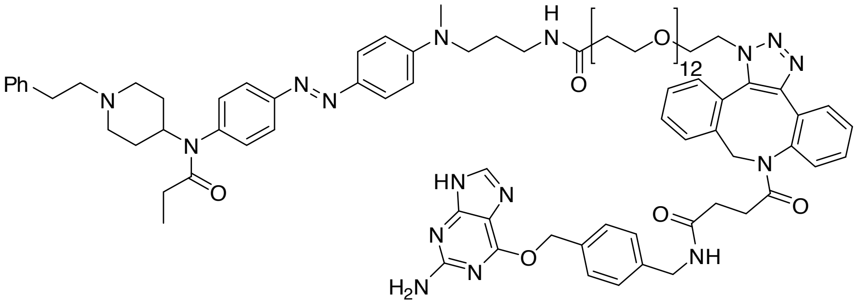

5.29 (5.8 mg, 5.0 μmol, 1.0 equiv.) and BG-DBCO (2.8 mg, 5.00 μmol, 1.0 equiv.) were combined in DMSO (400 μL) and stirred at r.t. for 3h before LCMS indicated near quantitative conversion. The reaction mixture was purified on a 2 g SepPak C18 SPE cartridge (gradient 0%-40% CH_3CN/H_2O + 0.1% FA). Product containing fractions were identified by LCMS, combined and freeze-dried to obtain the desired product as orange solid (6.2 mg, 3.6 μmol, 73%).

^{1}H NMR (400 MHz, DMSO-*d*$_6$) δ 7.89 – 7.76 (m, 5H), 7.60 – 7.46 (m, 2H), 7.41 – 7.30 (m, 5H), 7.33 – 7.14 (m, 7H), 6.88 – 6.79 (m, 2H), 5.84 (dd, *J* = 21.0, 16.8 Hz, 1H), 5.53 (s, 1H), 4.74 (d, *J* = 16.6 Hz, 2H), 4.53 – 4.42 (m, 2H), 4.32 (s, 1H), 4.18 (t, *J* = 4.9 Hz, 2H), 4.15 – 3.95 (m, 1H), 3.59 (dt, *J* = 17.0, 8.5 Hz, 5H), 3.50 – 3.33 (m, 47H), 3.20 (dd, *J* = 11.8, 5.3 Hz, 2H), 3.19 – 3.06 (m, 4H), 3.03 (s, 3H), 2.99 – 2.91 (m, 3H), 2.33 (s, 2H), 2.09 – 1.98 (m, 2H), 1.97 (s, 2H), 1.92 (d, *J* = 7.8 Hz, 2H), 1.66 (dp, *J* = 19.8, 7.2 Hz, 4H), 0.91 (t, *J* = 7.4 Hz, 3H).

HRMS (ESI): *m/z* calc. for $C_{91}H_{122}O_{17}N_{16}^{2+}$ $(M+2H)^{2+}$: 855.4581, found: 855.4594.

***t*$_R$** (LCMS; MeCN/H$_2$O/formic acid = 10/90/0.1 → 100/0/0.1 over 10 min) = 5.95 min.

UV/Vis (LCMS): λ_{max1} = 280 nm, λ_{max2} = 450 nm.

5.4.1.16 (*E*)-1-(4-(3-((4-(((2-Amino-9*H*-purin-6-yl)oxy)methyl)benzyl)amino)-3-oxopropyl)-1*H*-1,2,3-triazol-1-yl)-*N*-(3-((4-((4-(*N*-(1-phenethylpiperidin-4-yl)propionamido)phenyl)diazenyl)phenyl)-λ^2-azaneyl)propyl)-3,6,9,12,15,18,21,24,27,30,33,36-dodecaoxanonatriacontan-39-amide (**5.19**)

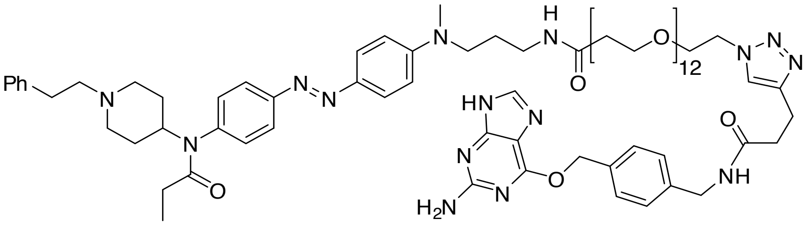

5.29 (8.7 mg, 7.6 μmol, 1.0 equiv.) and *N*-(4-(((2-amino-9H-purin-6-yl)oxy)methyl)benzyl)pent-4-ynamide (**BG-alkyne,** 2.7 mg, 7.6 μmol, 1.0 equiv.) were combined in DMSO (0.5 mL) and 100 μl of a 10 mM solution of each CuSO$_4$ and TBTA were added. Then sodium ascorbate was added in one portion (24 mg, 0.12 μmol, 16.0 equiv.). The reaction mixture was stirred at r.t. for several days before it was purified on a 2 g SepPak C18 SPE cartridge (gradient 0%-40% CH$_3$CN/H$_2$O + 0.1% FA). Product containing fractions were identified by LCMS, combined and freeze-dried to obtain the desired product as orange solid (3.5 mg, 2.3 μmol, 31%).

HRMS (ESI): *m/z* calc. for $C_{77}H_{113}O_{16}N_{15}^{2+}$ $(M+2H)^{2+}$: 751.9239 (100%), 752.4256 (83%); found: 751.9255, 752.4272.

***t*$_R$** (LCMS; MeCN/H$_2$O/formic acid = 10/90/0.1 → 100/0/0.1 over 10 min) = 6.30 min.

UV/Vis (LCMS): λ_{max1} = 224 nm, λ_{max2} = 450 nm.

5.4.1.17 (*E*)-N^1-(4-(((2-Amino-9*H*-purin-6-yl)oxy)methyl)benzyl)-N^{43}-(3-(methyl(4-((4-(*N*-(1-phenethylpiperidin-4-yl)propionamido)phenyl)diazenyl)phenyl)amino)propyl)-4,7,10,13,16,19,22,25,28,31,34,37,40-tridecaoxatritetracontanediamide (**5.17**)

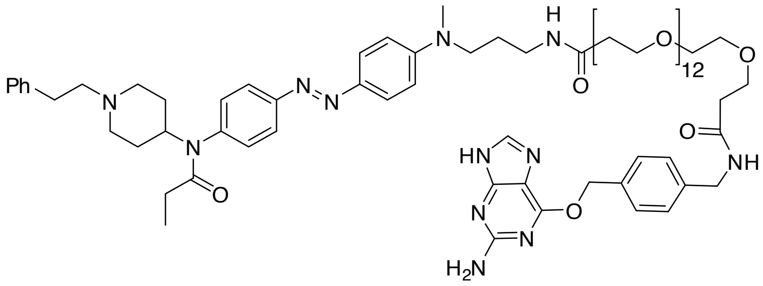

5.8 (41 mg, 68 μmol, 1.0 equiv.), PEG_{13}-diacid (polypure #37137-1295, 95 mg, 0.14 mmol, 2.0 equiv.), DIPEA (71 μL; 0.41 mmol, 6.0 equiv.) and HBTU (31 mg, 82 μmol, 1.2 equiv.) were combined in DMF (1 mL). The reaction mixture was stirred for 3.5 h before it was concentrated and purified by flash column chromatography (DCM/MeOH/AcOH/water = 90/10/1/1). The product was obtained as a dark red solid (75 mg, 63 μmol, 92%).

The product from the first amide coupling (22 mg, 18 μmol, 1.0 equiv.), 6-((4-(aminomethyl)benzyl)oxy)-9*H*-purin-2-amine (**BG-NH₂**, 6.0 mg, 22 μmol, 1.2 equiv.), DIPEA (13 μL, 74 μmol, 4 equiv.) and HBTU (8.4 mg, 22 μmol, 1.2 equiv.) were combined in DMF (0.7 mL) and stirred at r.t. for several hours. Then, the reaction mixture was concentrated and the residue purified by flash column chromatography (DCM/MeOH = 90/10 → 80/20). The product was obtained as a red solid (13 mg, 8.8 μmol, 48%).

HRMS (ESI): *m/z* calc. for $C_{75}H_{112}O_{17}N_{12}^{2+}$ $(M+2H)^{2+}$: 726.4129, found: 726.4147.

t_R (LCMS; MeCN/H_2O/formic acid = 40/60/0.1 → 100/0/0.1 over 10 min) = 2.1 min.

t_R (LCMS; MeCN/H_2O/formic acid = 10/90/0.1 → 100/0/0.1 over 10 min) = 9.8 min.

UV/Vis (LCMS): λ_{max} = 455 nm.

5.4.1.18 (*E*)-1,4-Dioxo-1-((4-((4-(*N*-(1-phenethylpiperidin-4-yl)propionamido)phenyl)diazenyl)phenyl)amino)-7,10,13,16,19,22,25,28,31,34,37,40,43-tridecaoxa-3-azahexatetracontan-46-oic acid (**5.30**)

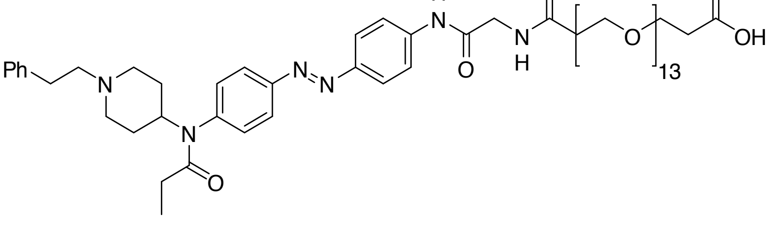

5.13 (17 mg, 30 *µ*mol, 1.0 equiv.), PEG$_{13}$-diacid (polypure #37137-1295, 20 mg, 30 *µ*mol, 1.0 equiv.), HBTU (12mg, 31 *µ*mol, 1.05 equiv.) and DIPEA (21 *µ*L, 0.12 mmol, 4.0 equiv.) were combined in DMF (0.3 mL) and stirred at r.t. overnight. The reaction mixture was directly purified by flash column chromatography (DCM/MeOH/AcOH = 90/10/1 → 70/30/1). The desired product was obtained as an orange solid (11 mg, 9 *µ*mol, 30%).

HRMS (ESI): *m/z* calc. for $C_{60}H_{91}O_{18}N_6^-$ $(M-H)^-$: 1183.6395, found: 1183.6361.

$\boldsymbol{t_R}$ (LCMS; MeCN/H_2O/formic acid = 10/90/0.1 → 100/0/0.1 over 10 min) = 3.20 min.

UV/Vis (LCMS): λ_{max} = 354 nm.

5.4.1.19 (*E*)-*N*^{1}-(4-(((2-amino-9*H*-purin-6-yl)oxy)methyl)benzyl)-*N*^{43}-(2-oxo-2-((4-((4-(*N*-(1-phenethylpiperidin-4-yl)propionamido)phenyl)diazenyl)phenyl)amino)ethyl)-4,7,10,13,16,19,22,25,28,31,34,37,40-tridecaoxatritetracontanediamide (**5.16**)

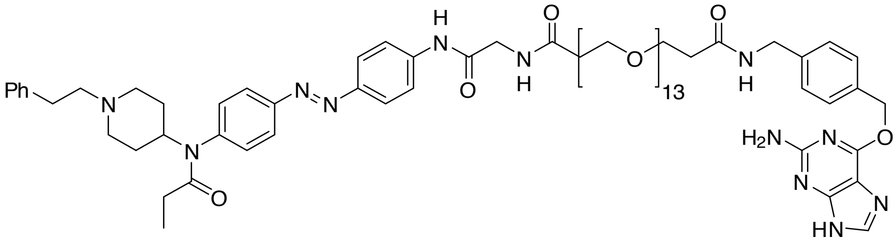

5.30 (11 mg, 9 *µ*mol, 1.0 equiv.), 6-((4-(aminomethyl)benzyl)oxy)-9*H*-purin-2-amine (**BG-NH2**, 3.2 mg, 12 *µ*mol, 1.3 equiv.), DIPEA (6.5 *µ*L, 38 *µ*mol, 4.0 equiv.) and HBTU (4.3 mg, 11 *µ*mol, 1.2 equiv.) were combined in DMF (0.5 mL) and stirred at r.t. overnight. The reaction mixture was purified on a 2 g SepPak C18 SPE cartridge (0%-30% = CH_3CN/H_2O + 0.1% FA). Product containing fractions were identified by LCMS, combined and freeze-dried to obtain the desired product as orange solid (2.0 mg, 1.4 *µ*mol, 16%).

HRMS (ESI): *m/z* calc. for $C_{73}H_{106}O_{18}N_{12}^{2+}$ $(M+2H)^+$: 719.3869, found: 719.3886.

$\boldsymbol{t_R}$ (LCMS; MeCN/H_2O/formic acid = 10/90/0.1 → 100/0/0.1 over 10 min) = 2.99 min.

UV/Vis (LCMS): λ_{max} = 355 nm.

5.4.1.20 (*E*)-*N*1-(4-(((2-Amino-9*H*-purin-6-yl)oxy)methyl)benzyl)-*N*10-(2-oxo-2-((4-((4-(*N*-(1-phenethylpiperidin-4-yl)propionamido)phenyl)diazenyl)phenyl) amino)ethyl)decanediamide (**5.18**)

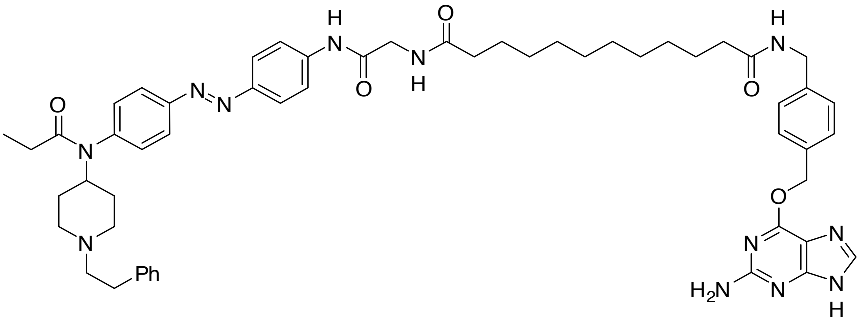

5.13 (13 mg, 25 μmol, 1.0 equiv.) was combined with dodecandioic acid (23 mg, 98 μmol, 4.0 equiv.), HBTU (10 mg, 27 μmol, 1.1 equiv.) and DIPEA (43 μL, 250 μmol, 10 equiv.) in DMF (0.5 mL). The reaction mixture was allowed to stir at r.t. for o.n., before it was acidified and purified on a 2 g SepPak C18 SPE cartridge (0%-40% CH_3CN in H_2O + 0.1% FA). Product containing fractions were identified by LCMS and combined. The product was obtained as an orange solid after removal of all volatiles (9.7 mg, 13 μmol, 55%)

The product from the previous step (9.7 mg, 13 μmol, 1.0 equiv.) was combined with **BG-NH$_2$** (4.0 mg, 15 μmol, 1.1 equiv.), HBTU (5.1 mg, 13 μmol, 1.0 equiv.) and DIPEA (4.7 μL, 27 μmol, 2.0 equiv.) in DMF (0.5 Ml): The reaction mixture was stirred at r.t. o.n., before it was acidified and purified on a 2 g SepPak C18 SPE cartridge (0%-35% CH_3CN in H_2O + 0.1% FA). Product containing fractions were identified by LCMS and combined. The product was obtained as an orange solid after removal of all volatiles (4.2 mg, 4.3 μmol, 32%)

HRMS (ESI): *m/z* calc. for $C_{55}H_{69}O_5N_{12}^+$ $(M+H)^+$: 977.5508, found: 977.5528; *m/z* calc. for $C_{55}H_{67}O_5N_{12}^-$ $(M-H)^-$: 975.5363, found: 975.5362.

5.4.1.21 2,2'-(Ethane-1,2-diyl)bis(4-bromoaniline) (**5.21**)

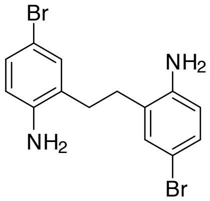

2,2'-(Ethane-1,2-diyl)dianiline (1.27 g, 6.0 mmol, 1.00 equiv.) was dissolved in 60 mL MeCN. The flask was wrapped in aluminum foil to keep the reaction in the dark and NBS (99%, 2.12 g, 11.8 mmol, 2.0 equiv.) was added in portions under vigorous stirring over a time of 6 h. After the addition was complete, the reaction mixture was stirred at r.t. overnight. Conversion was checked by LCMS and the reaction was judged to be complete. The solution was extracted with 50 mL EtOAc against 50 mL of 0.5 M aq. NaOH (4x). The combined aq. layers were back extracted with additional 4 x 50 mL EtOAc. All collected organic layers were combined, dried over $MgSO_4$ and concentrated *in vacuo*. The crude product was adsorbed on silica and loaded on a 4 x 20 cm column of silica. The product was eluted with 20-100% EtOAc/hexanes, yielding **5.21** as a yellow-brown solid (2.00 g, 5.4 mmol, 90%).

^{1}H NMR (400 MHz, DMSO-d$_6$) δ = 7.17 (d, *J* = 2.3 Hz, 2H), 7.03 (dd, *J* = 8.5, 2.3 Hz, 2H), 6.57 (d, *J* = 8.5 Hz, 2H), 5.12 (s, 4H), 2.61 (s, 4H).

^{13}C NMR (101 MHz, DMSO-d$_6$) δ = 145.7, 131.1, 129.0, 127.4, 116.3, 106.8, 29.1.

HRMS (ESI): calc. for $C_{14}H_{15}Br_2N_2^+$ $(M+H)^+$: 368.9597, found: 368.9598.

t$_R$ (LCMS, MeCN/H_2O/formic acid = 10/90/0.1 → 100/0/0.1 over 10 min) = 5.55 min.

UV/Vis (LCMS): λ_{max1} = 205 nm, λ_{max2} = 245 nm, λ_{max3} = 300 nm.

5.4.1.22 (*Z*)-2,9-Dibromo-11,12-dihydrodibenzo[*c,g*][1,2]diazocine (**5.22**)

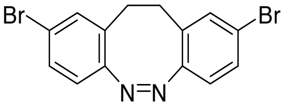

5.21 (371 mg, 1.0 mmol, 1.0 equiv.) was dissolved in 15 mL DCM. *m*CPBA (77%, 449 mg, 2.0 mmol, 2.00 equiv.) was added in portions over a time of 1 h under continuous stirring. The flask was capped and wrapped in aluminum foil to keep the reaction in the dark and the mixture was stirred at r.t. over the weekend. 10 mL of an aq. $Na_2S_2O_3$ solution (10%) were added, followed by extraction with 10 mL DCM and washing with 10 mL of 1 M aq. NaOH (4x). The aq. layers were back extracted with additional 5 x 10 mL DCM and the combined organic layers were washed against 40 mL water (2x) and 40 mL brine (2x). After drying over $MgSO_4$, all volatiles were removed *in vacuo*. The crude product was adsorbed on silica and loaded on a 4 x 15 cm column of silica, followed by elution with DCM/hexanes (1/5). The product containing impure fractions were combined, concentrated to dryness and purified by flash column chromatography another two times under the same conditions but on longer and wider 2 x 20 cm columns of silica. **5.22** was obtained as a yellow, slightly reddish-orange solid (110 mg, 0.30 mmol, 30%).

^{1}H NMR (400 MHz, $CDCl_3$) δ = 7.28 (dd, *J* = 8.4, 2.0 Hz, 2H), 7.16 (d, *J* = 2.0 Hz, 2H), 6.72 (d, *J* = 8.3 Hz, 2H), 2.99 – 2.88 (m, 2H), 2.79 – 2.65 (m, 2H).

^{13}C NMR (101 MHz, $CDCl_3$) δ = 154.1, 132.6, 130.2, 130.0, 120.8, 120.7, 31.4.

HRMS (EI): calc. for $C_{14}H_{10}Br_2N_2$ ($M^{+\square}$): 363.9211, found: 363.9202.

t$_R$ (LCMS, MeCN/H_2O/formic acid = 10/90/0.1 → 100/0/0.1 over 10 min) = 6.40 min.

UV/Vis (LCMS): λ_{max1} = 202 nm, λ_{max2} = 240 nm, λ_{max3} = 299 nm, λ_{max4} = 328 nm.

5.4.1.23 (*Z*)-di-*tert*-Butyl-(11,12-dihydrodibenzo[*c*,*g*][1,2]diazocine-2,9-diyl)-dicarbamate (**5.23**)

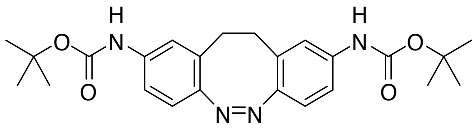

Pd_2dba_3 (8.1 mg, 8.8 μmol, 0.05 equiv.) and XantPhos (98%, 10.0 mg, 17 μmol, 0.10 equiv.) were transferred into a Schlenk tube. The flask was evacuated and backfilled with argon for three times, before 2.0 mL anhydrous 1,4-dioxane were added. The reaction mixture was stirred for 30 min. *tert*-Butyl-carbamate (104 mg, 0.89 mmol, 5.1 equiv.), **5.22** (64.4 mg, 0.176 mmol, 1.0 equiv.) and Cs_2CO_3 (347.0 mg, 1.07 mmol, 6.0 equiv.) were added sequentially together with an additional 2.0 mL of anhydrous 1,4-dioxane. The reaction was capped and stirred overnight at 100 °C. After the reaction mixture was allowed to cool to r.t., it was extracted with 20 mL EtOAc against 25 mL water (3x). The aq. layers were back extracted with additional 3 x 20 mL EtOAc and the combined organic layers were washed with 30 mL aq. sat $NaHCO_3$ (2x), 20 mL brine (3x), dried over $MgSO_4$ and concentrated to dryness. The resulting crude material was absorbed on silica and loaded on a 2.5 x 25 cm column of silica, followed by elution with DCM/hexanes (2 / 1 → 1 / 0). TLC (ninhydrin staining) showed that the product containing fractions also contained residuals of *tert*-butyl-carbamate. Therefore, product containing fractions were combined, concentrated *in vacuo* and repurified by flash column chromatography (5 / 1 = DCM/EtOAc) on a 2.5 x 20 cm column of silica, whereby the sample was loaded adsorbed on silica. **5.23** was obtained as a lemon-yellow solid (45.0 mg, 103 μmol, 59%).

^{1}H NMR (400 MHz, $CDCl_3$) δ = 7.14 (s, 2H), 7.03 (dd, *J* = 8.5, 2.2 Hz, 2H), 6.79 (d, *J* = 8.4 Hz, 2H), 6.40 (s, 2H), 2.82 (s, 4H), 1.48 (s, 18H).

^{13}C NMR (101 MHz, $CDCl_3$) δ = 152.6, 150.8, 137.3, 129.3, 120.4, 118.9, 116.6, 80.9, 32.0, 28.4.

HRMS (ESI): calc. for $C_{24}H_{31}N_4O_4^+$ $(M+H)^+$: 439.2340, found: 439.2345.

t$_R$ (LCMS, MeCN/H_2O/formic acid = 10/90/0.1 → 100/0/0.1 over 10 min) = 5.90 min.

UV/Vis (LCMS): λ_{max1} = 204 nm, λ_{max2} = 238 nm, λ_{max3} = 259 nm, λ_{max4} = 302 nm, λ_{max5} = 333 nm, λ_{max6} = 408 nm.

5.4.1.24 (*Z*)-11,12-Dihydrodibenzo[*c,g*][1,2]diazocine-2,9-diamine (**5.24**)

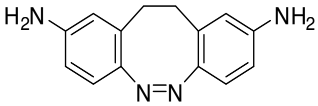

5.23 (44.8 mg, 0.102 mmol) was transferred into a 4 mL dram vial with EtOAc, the solvent was removed *in vacuo* and the sample was dried under HV. 0.75 mL neat TFA were added slowly accompanied by red discoloration. The vial was capped and the reaction was monitored by LCMS. After 35 min of stirring, the reaction was judged to be complete, and the TFA was removed by a stream of nitrogen. The residue was extracted with EtOAc (approx. 1 L) against 0.2 M aq. NaOH and the aq. layers were back extracted with additional EtOAc. The combined organic layers were washed against aq. sat $NaHCO_3$ (2x) and brine, dried over $MgSO_4$ and concentrated to dryness. Purification of the crude, red solid by flash column chromatography (5% MeOH/DCM) on a 2 x 7 cm column of silica yielded **5.24** as a yellow-brownish solid (19.8 mg, 0.0831 mmol, 81%).

^{1}H NMR (400 MHz, $CDCl_3$) δ = 6.71 (d, *J* = 8.3 Hz, 2H), 6.45 (dd, *J* = 8.4, 2.4 Hz, 2H), 6.30 (d, *J* = 2.4 Hz, 2H), 3.59 (s, 4H), 2.72 (s, 4H).

^{13}C NMR (101 MHz, $CDCl_3$) δ = 147.8, 145.2, 129.8, 121.6, 115.3, 113.3, 32.1.

HRMS (ESI): calc. for $C_{14}H_{15}N_4^+$ $(M+H)^+$: 239.1291, found: 239.1292.

t_R (LCMS, MeCN/H_2O/formic acid = 10/90/0.1 → 100/0/0.1 over 7 min) = 1.51 min.

UV/Vis (LCMS): λ_{max1} = 245 nm, λ_{max2} = 338 nm, λ_{max3} = 415 nm.

5.4.1.25 *tert*-Butyl (*Z*)-(2-((9-amino-11,12-dihydrodibenzo[*c,g*][1,2]diazocin-2-yl)amino)-2-oxoethyl)carbamate (**5.25**)

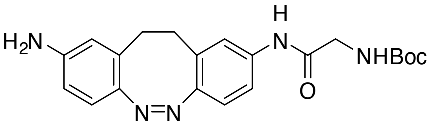

5.24 (19.8 mg, 0.0831 mmol, 1.00 eq.), *N*-Boc-Gly-OH (7.6 mg, 0.043 mmol, 0.52 eq.) and HBTU (31.7 mg, 0.0836 mmol, 1.01 eq.) were transferred into a 4 mL dram vial. The vial was capped, evacuated and backfilled with nitrogen for three times, before 1.0 mL dry THF were added. After DIPEA (29.0 µL, 0.166 mmol, 2.00 eq.) was added dropwise, the reaction mixture was stirred for 1 h at 0 °C overnight at room temperature. All volatiles were removed *in vacuo* and the residue was extracted with EtOAc against 1 mM aq. HCl, additional brine was added for breaking the emulsion. The collected aq. layers were back extracted with EtOAc and the combined organic layers were washed with water and brine. After drying over $MgSO_4$ and concentration *in vacuo*, the crude material was adsorbed on silica and loaded on a 2 x 14 cm column of silica. Elution with EtOAc/DCM (1 / 1) yielded the desired product as a yellow, slightly brown-greenish solid (14.9 mg, 0.0377 mmol, 45%).

^{1}H-NMR (400 MHz, $CDCl_3$) δ = 8.14 (bs, 1H), 7.33 (s, 1H), 7.18 (d, *J* = 8.5 Hz, 1H), 6.79 (d, *J* = 8.5 Hz, 1H), 6.71 (d, *J* = 8.3 Hz, 1H), 6.44 (dd, *J* = 8.3, 2.4 Hz, 1H), 6.26 (d, *J* = 2.3 Hz, 1H), 5.22 (bs, 1H), 3.86 (d, *J* = 6.0 Hz, 2H), 3.60 (bs, 2H), 2.80 – 2.65 (m, 4H), 1.46 (s, 10H).

^{13}C-NMR (101 MHz, $CDCl_3$) δ = 167.9, 152.1, 147.7, 145.6, 136.2, 129.8, 129.3, 121.5, 120.4, 120.2, 118.0, 115.5, 115.3, 113.4, 81.0, 38.8, 32.2, 31.8, 28.4.

HRMS (ESI): calc. for $C_{21}H_{26}N_5O_3^+$ $(M+H)^+$: 396.2030, found: 396.2034.

t_R (LCMS, MeCN/H_2O/formic acid = 10/90/0.1 → 100/0/0.1 over 7 min) = 3.44 min.

UV/Vis (LCMS): λ_{max1} = 243 nm, λ_{max2} = 308 nm, λ_{max3} = 341 nm, λ_{max4} = 414 nm.

5.4.1.26 *tert*-Butyl (*Z*)-(2-oxo-2-((9-((1-phenethylpiperidin-4-yl)amino)-11,12-dihydrodibenzo[*c*,*g*][1,2]diazocin-2-yl)amino)ethyl)carbamate (**5.26**)

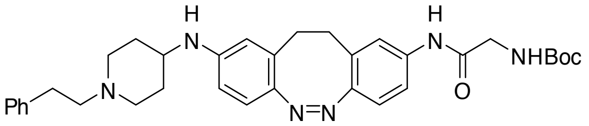

N-Phenethylpiperidin-4-one (98%, 39.4 mg, 0.190 mmol, 0.99 eq.), $NaBH(OAc)_3$ (97%, 58.7 mg, 0.269 mmol, 1.41 eq.) and AcOH (10.8 µL, 0.189 mmol, 0.99 eq.) were added to **5.25** (75.4 mg, 0.191 mmol, 1.00 eq.) in a 4 mL dram vial. The vial was capped, the mixture was put under a nitrogen atmosphere and 1.8 mL of anhydrous DCE was added. After the dark solution was stirred overnight at r.t., the sample was transferred into a 100 mL round-bottom flask with DCM and the grass-green solution was adsorbed on celite, loaded on a 3.5 x 14 cm column of silica and eluted with 2-8% MeOH/DCM. The desired product was obtained as a yellow, slightly greenish solid (64.7 mg, 0.111 mmol, 58%).

^{1}H NMR (400 MHz, MeOD-d_4) δ = 7.37 (s, 1H), 7.33 – 7.27 (m, 3H), 7.27 – 7.19 (m, 4H), 6.75 (d, *J* = 8.5 Hz, 1H), 6.70 (d, *J* = 8.5 Hz, 1H), 6.47 (dd, *J* = 8.6, 1.8 Hz, 1H), 6.31 (d, *J* = 2.3 Hz, 1H), 3.80 (s, 2H), 3.40 (tt, *J* = 9.7, 3.9 Hz, 1H), 3.27 (d, *J* = 12.7 Hz, 2H), 2.97 – 2.90 (m, 4H), 2.83 – 2.64 (m, 6H), 2.07 (dd, *J* = 11.5, 2.7 Hz, 2H), 1.58 (q, *J* = 10.2 Hz, 2H), 1.45 (s, 9H).

Note: The signals of two N_{sek}-H are not observed due solvent proton exchange.

^{13}C NMR (101 MHz, MeOD-d$_4$) δ = 170.5, 158.6, 152.7, 148.4, 147.2, 139.4, 138.4, 131.3, 130.8, 129.8, 129.7, 127.7, 122.7, 121.7, 120.9, 119.3, 114.1, 112.2, 80.7, 60.2, 52.9, 45.0, 33.2, 32.8, 32.7, 31.4, 28.7.

Note: One signal is covered by the MeOD-d$_4$ solvent peaks (see HSQC spectrum).

HRMS (ESI): calc. for $C_{34}H_{43}N_6O_3^+$ (M+H)$^+$: 583.3391, found: 583.3378.

t_R (LCMS, MeCN/H$_2$O/formic acid = 10/90/0.1 → 100/0/0.1 over 10 min) = 3.48 min.

UV/Vis (LCMS): λ_{max1} = 205 nm, λ_{max2} = 246 nm, λ_{max3} = 309 nm, λ_{max4} = 357 nm, λ_{max5} = 431 nm.

5.4.1.27 *tert*-Butyl (*Z*)-(2-oxo-2-((9-(*N*-(1-phenethylpiperidin-4-yl)propion-amido)-11,12-dihydrodibenzo[*c*,*g*][1,2]diazocin-2-yl)amino)ethyl)carbamate (**5.31**)

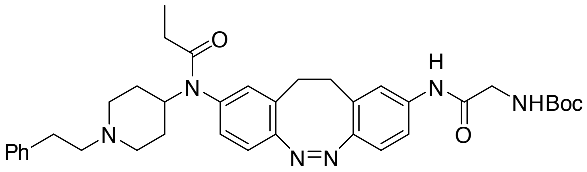

5.26 (44.6 mg, 0.0765 mmol, 1.00 eq.) was dissolved in 3.8 mL anhydrous DCM in a 4 mL dram vial under a nitrogen atmosphere. DIPEA (22.8 µL, 0.131 mmol, 1.71 eq.) and a 1.144 M solution of propionylchloride in DCM (73.6 µL, 0.0842 mmol, 1.10 eq.) were added accompanied by a color change of the solution from green to red. The vial was capped, flushed with nitrogen and wrapped in aluminum foil to keep the reaction mixture in the dark. After stirring at r.t. for 1.5 h, reaction progress was checked by LCMS, judged to be incomplete and more of the propionylchloride solution was added (20.1 *µ*L, 0.0230 mmol, 0.30 eq.). After another 2 h of stirring, the reaction was checked again by LCMS, judged to be incomplete and more of the propionylchloride solution (10.0 µL, 0.0114 mmol, 0.15 eq.) was added. The reaction mixture was stirred at r.t. overnight, followed by loading the sample directly on a 2.5 x 22 cm column of silica for purification (DCM/MeOH/AcOH/H$_2$O = 90 / 10 / 0.6 / 0.6). The desired product was obtained as a yellowish solid (22.4 mg, 0.0351 mmol, 46%).

Note: Complex ^{1}H NMR and ^{13}C NMR spectra, possibly because of multiple configurations with high energy barriers. The product was clean according to LCMS.

HRMS (ESI): calc. for $C_{37}H_{47}N_6O_4^+$ (M+H)$^+$: 639.3653, found: 639.3662.

t_R (LC-MS, MeCN/H$_2$O/formic acid = 10/90/0.1 → 100/0/0.1 over 10 min) = 3.40 min.

UV/Vis (LC-MS): λ_{max1} = 236 nm, λ_{max2} = 258 nm, λ_{max3} = 318 nm, λ_{max4} = 404 nm.

5.4.1.28 (*Z*)-*N*-(9-(2-Aminoacetamido)-11,12-dihydrodibenzo[*c*,*g*][1,2]diazocin-2-yl)-*N*-(1-phenethylpiperidin-4-yl)propionamide (**5.27**)

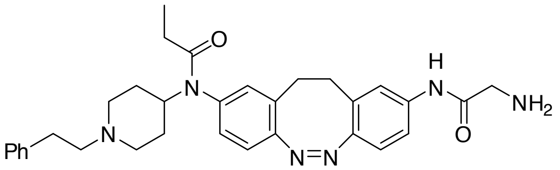

5.31 (21.7 mg, 0.0340 mmol) was loaded into a scintillation vial and dissolved in 3 mL anhydrous EtOAc under an argon atmosphere. 3 mL of EtOAc saturated with HCl gas were added slowly. The reaction mixture was stirred for 1.5 h at r.t. accompanied by a discoloration from green to red and by formation of a red precipitate. The reaction progress was checked by LCMS, judged to be incomplete and 0.5 mL HCl saturated EtOAc were added. After another 45 min of stirring, LCMS was measured again and 0.5 mL HCl saturated EtOAc were added once again. The reaction mixture was stirred for a further 1 h, followed by filtration through a cotton wool filled pipette and washing of the remaining red precipitate with anhydrous EtOAc. The precipitate was eluted with anhydrous MeOH and concentrated to dryness, yielding a brown-yellow solid. The solid was resolved in 0.5 mL of DMSO and filtered through a syringe filter (PTFE 0.4) which was rinsed with additional 0.5 mL DMSO. Purification by HPLC yielded the desired product as a pale yellow solid (9.9 mg, 0.018 mmol, 53%).

^{1}H NMR (400 MHz, DMSO-*d*$_6$) δ 10.45 (s, 1H), 9.25 (s, 1H), 8.11 (s, 3H), 7.45 – 7.19 (m, 7H), 7.10 – 6.81 (m, 4H), 4.65 (s, 1H), 3.72 (d, *J* = 5.8 Hz, 2H), 3.56 (s, 2H), 3.27 – 3.06 (m, 4H), 2.99 – 2.70 (m, 6H), 1.94 (d, *J* = 13.5 Hz, 2H), 1.71 – 1.47 (m, 2H), 1.28 (d, *J* = 30.9 Hz, 2H), 0.67 (s, 3H).

Note: Doubly charged FA salt.

HRMS (ESI): calc. for $C_{32}H_{39}N_6O_2^+$ [M+H]$^+$: 539.3129, found: 539.3136.

t_R (LCMS, MeCN/H$_2$O/formic acid = 10/90/0.1 → 100/0/0.1 over 10 min) = 2.20 min.

UV/Vis (LCMS): λ_{max1} = 236 nm, λ_{max2} = 257 nm, λ_{max3} = 317 nm, λ_{max4} = 404 nm.

5.4.2 Crystallographic Data

Crystallographic data of 2,2'-(ethane-1,2-diyl)bis(4-bromoaniline).

net formula	$C_{14}H_{14}Br_2N_2$
M_r/g mol^{-1}	370.09
crystal size/mm	0.040 × 0.030 × 0.020
T/K	100.(2)
radiation	MoKα
diffractometer	'Bruker D8 Venture TXS'
crystal system	monoclinic
space group	'P 1 21/c 1'
a/Å	7.2468(2)
b/Å	13.6374(5)
c/Å	6.8983(3)
α/°	90
β/°	100.3960(10)
γ/°	90
V/Å^3	670.55(4)
Z	2
calc. density/g cm^{-3}	1.833
μ/mm^{-1}	6.028
absorption correction	Multi-Scan
transmission factor range	0.6749–0.7457
refls. measured	6842
R_{int}	0.0392
mean σ(I)/I	0.0358
θ range	3.354–27.482
observed refls.	1323
x, y (weighting scheme)	0.0071, 0.5928
hydrogen refinement	H(C) constr, H(N) refall
refls in refinement	1533
parameters	90
restraints	0
$R(F_{\text{obs}})$	0.0232
$R_w(F^2)$	0.0532
S	1.098
shift/error$_{\text{max}}$	0.001
max electron density/e Å^{-3}	0.461
min electron density/e Å^{-3}	–0.331

Crystallographic data of (*Z*)-2,9-dibromo-11,12-dihydrodibenzo[*c*,*g*][1,2]diazocine.

net formula	$C_{14}H_{10}Br_2N_2$
M_r/g mol^{-1}	366.06
crystal size/mm	0.030 × 0.030 × 0.010
T/K	100.(2)
radiation	MoKα
diffractometer	'Bruker D8 Venture TXS'
crystal system	monoclinic
space group	'P 1 21/c 1'
a/Å	9.0147(3)
b/Å	17.1183(5)
c/Å	8.4172(3)
α/°	90
β/°	99.8120(10)
γ/°	90
V/Å^3	1279.91(7)
Z	4
calc. density/g cm^{-3}	1.900
μ/mm^{-1}	6.315
absorption correction	Multi-Scan
transmission factor range	0.6740–0.7457
refls. measured	14150
R_{int}	0.0356
mean σ(I)/I	0.0318
θ range	3.285–28.280
observed refls.	2700
x, y (weighting scheme)	0.0145, 0.9564
hydrogen refinement	constr
refls in refinement	3161
parameters	163
restraints	0
$R(F_{\text{obs}})$	0.0235
$R_w(F^2)$	0.0488
S	1.034
shift/error$_{\text{max}}$	0.003
max electron density/e Å^{-3}	0.483
min electron density/e Å^{-3}	−0.430

5.4.3 Plasmids, Cell Culture and Electrophysiology

HEK-GIRK cells were a kind gift of Sonja Kleinlogel.[110] They were maintained in standard growth medium DMEM/10% FCS with 400 ug/mL G418. Transfections were performed as described previously.[115]

The SNAP-MOR plasmids featured:

SNAP_MOR (from Helen Farrants): mGluR5 non-cleavable signal peptide, HA-epitope, SNAP-tag, PGLG linker, MOR (rat)

SNAP_(MOR) (J.T. Williams): HA cleavable signal peptide, FLAG-tag without enterokinase cleavage site, SNAP-tag 8x GS linker, MOR (mouse)

Patch solutions contained the following:

F4', internal Kgluconate, dilute 80:10:10 for end conc							
substrate	c (mM)	M (g/mol)	V (L)	n (mmol)	m (mg)		final conc
KCl	15	74.55	0.05	0.75	55.9125		12
Kgluconat	175	234.25	0.05	8.75	2049.688		140
HEPES	12.5	238.31	0.05	0.625	148.9438		10
NaCl	5	58.44	0.05	0.25	14.61		4
MgATP	40	507.18	0.01	0.4	202.872		4
Na2GTP	4	567.14	0.01	0.04	22.6856		0.4
						osmo	330.8

HEK_GIRK external solution, high K+, pH 7.4 with KOH, updated Josh recipe						
						10x
substrate	c (mM)	M (g/mol)	V (L)	n (mmol)	m (mg)	(m in g)
NaCl	25	58.44	0.5	12.5	730.5	7.305
KCl	120	74.55	0.5	60	4473	44.73
MgCl2	1	203.3	0.5	0.5	101.65	1.0165
CaCl2	2	147.02	0.5	1	147.02	1.4702
HEPES	10	238.31	0.5	5	1191.55	11.9155

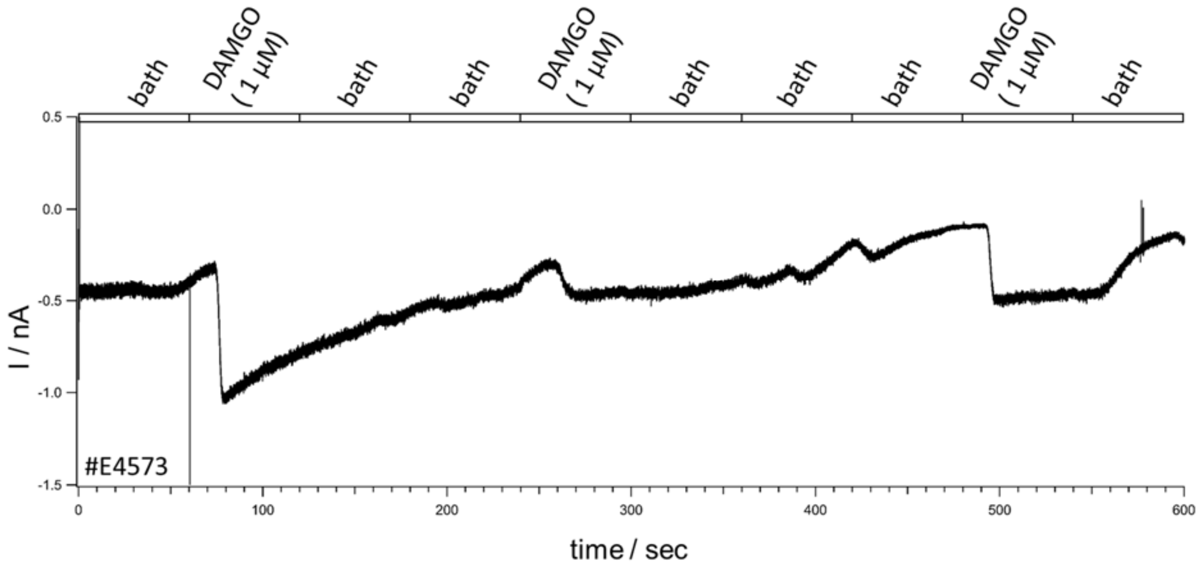

Supporting Figure 6. HEK-GIRK transfected with SNAP_MOR (from JT Williams). DAMGO was washed in as positive control to confirm functional expression of SNAP_MOR.

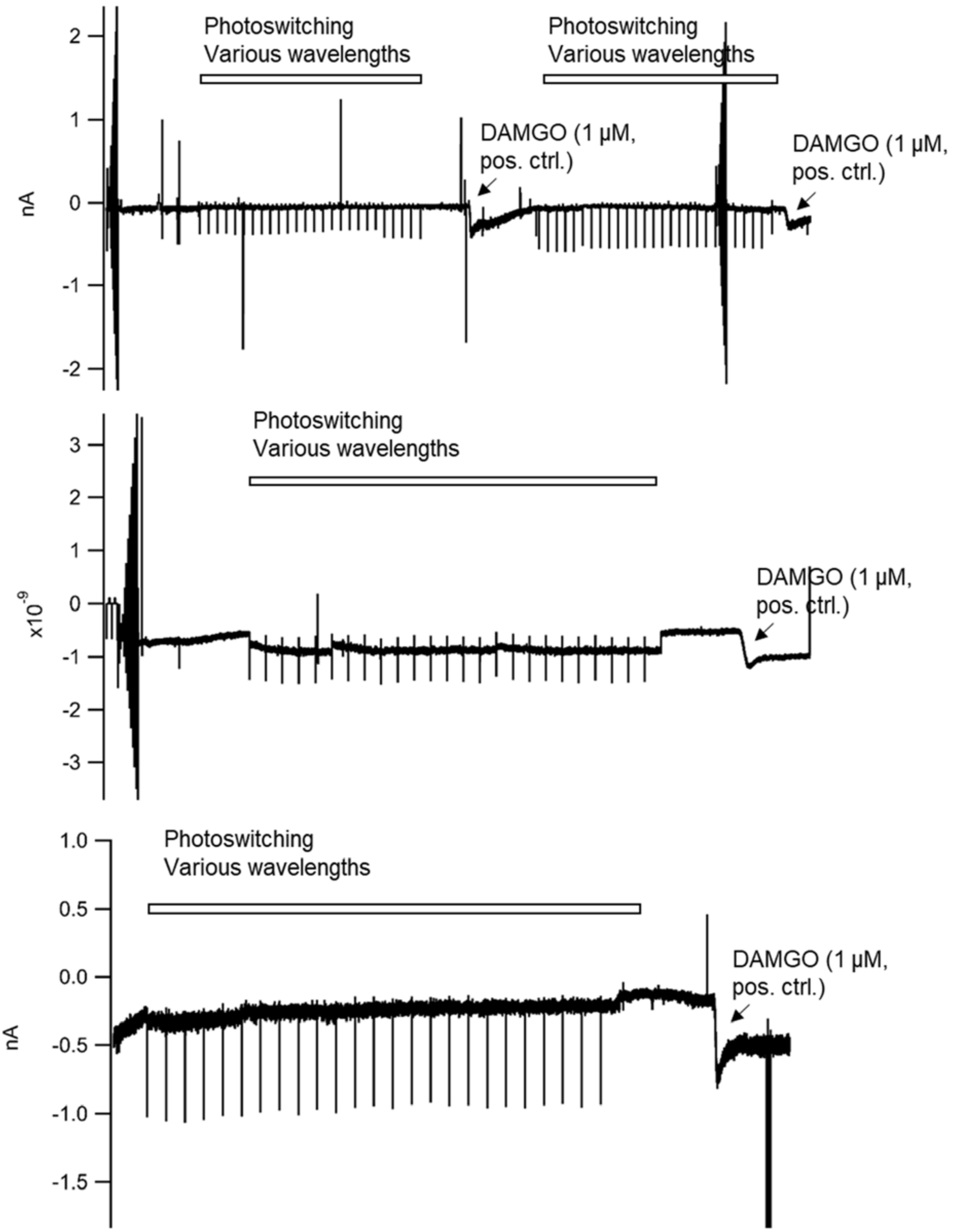

Supporting Figure 7. HEK-GIRK transfected with SNAP_MOR (from JT Williams). **5.27** (50 *μ*M) was washed in. Then, photoswitching was attempted using various wavelengths. The switching was performed at a holding potential of -80 mV to maximize GIRK currents. No light-dependent current was observed. DAMGO was washed in at the end of the experiment as a positive control to confirm expression of SNAP_MOR and GIRK. The spikes are capacitive currents from changing the membrane potential, or from interference from the perfusion system and are not edited out.

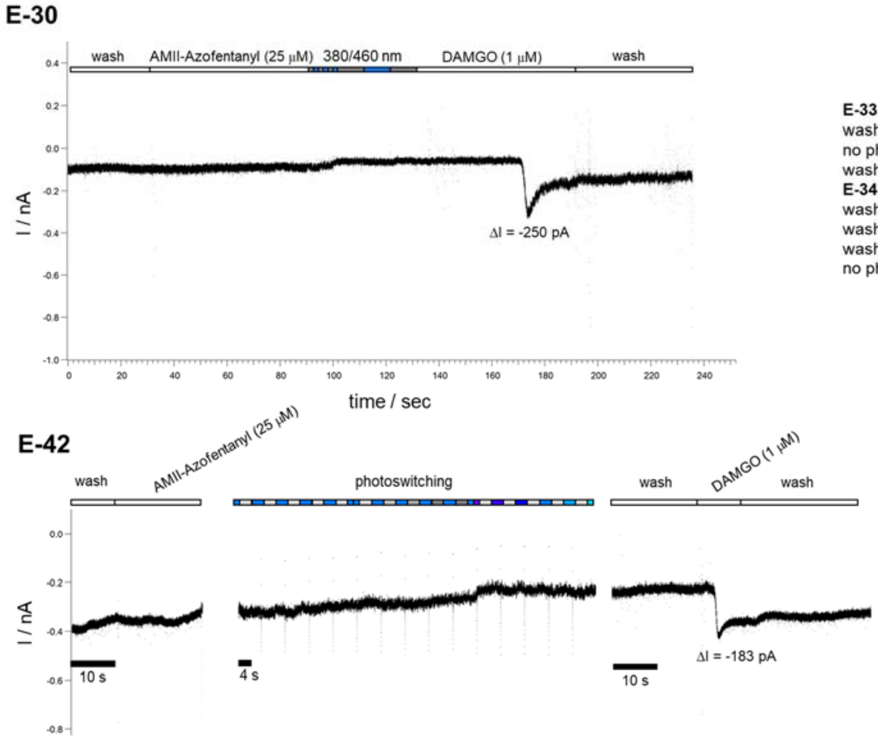

E-33:
wash-in AM-II (25 µM)
no photoswitching
wash-in DAMGO (1 µM) ΔI = -65 pA
E-34:
wash-in DAMGO (1 µM) ΔI= = -345 pA
washout
wash-in of AM-II (25 µM)
no photoswitching

E-44:
wash-in AM-II (25 µM)
no photoswitching
wash-in DAMGO (1 µM) ΔI = -138 pA

Supporting Figure 8. Electrophysiological characterization of AM-II.

AzoDAMGO patching
HEK-GIRK (100 ng mOR, 50 ng YFP)
60 mM K+ extracellular, F4 intracellular
#E3826

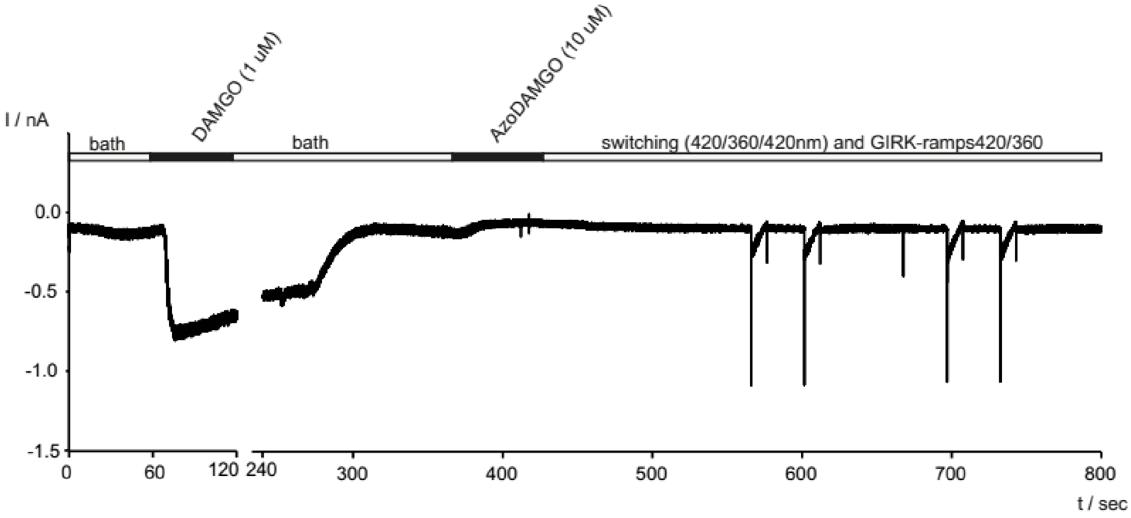

Summary:
10 uM AzoDAMGO: #E4826,#E4827, #E4828 (n=3)
50 uM AzoDAMGO : #E4829, #E4830, #E4833, E3835, E4836 (n=4)

At 10 uM no effect was observed (no washin current, no switching)
At 50 uM there might be an antagonistic effect (?), but no switching

Supporting Figure 9. Electrophysiological characterization of AzoDAMGO.

5.4.4 Spectral Data

5.4.4.1 *tert*-Butyl (*E*)-(2-((4-((4-aminophenyl)diazenyl)phenyl)amino)-2-oxoethyl)carbamate (**3.6**)

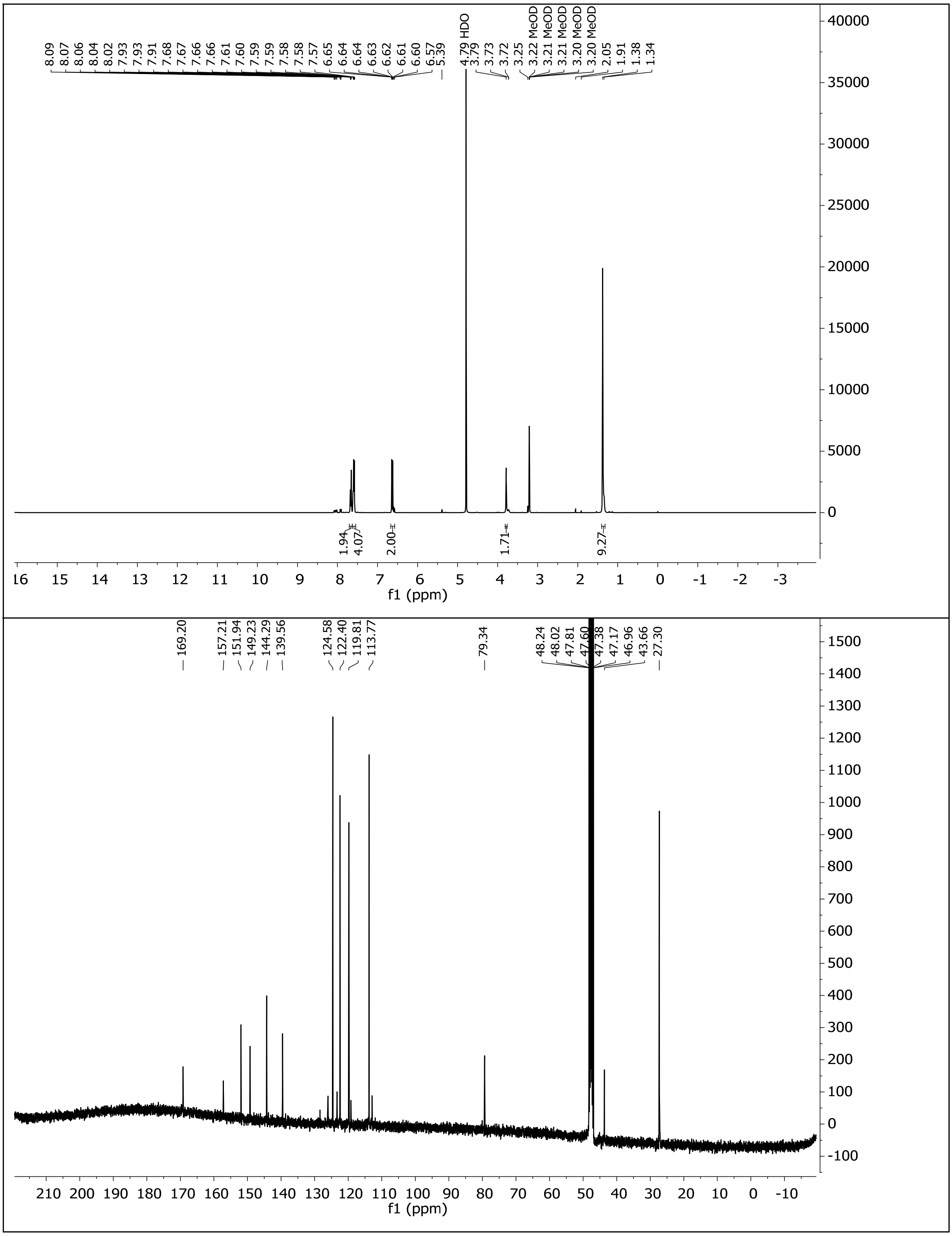

5.4.4.2 *tert*-Butyl (*E*)-(2-oxo-2-((4-((4-((1-phenethylpiperidin-4-yl)amino)phenyl)diazenyl)phenyl)amino)ethyl)carbamate (**5.11**)

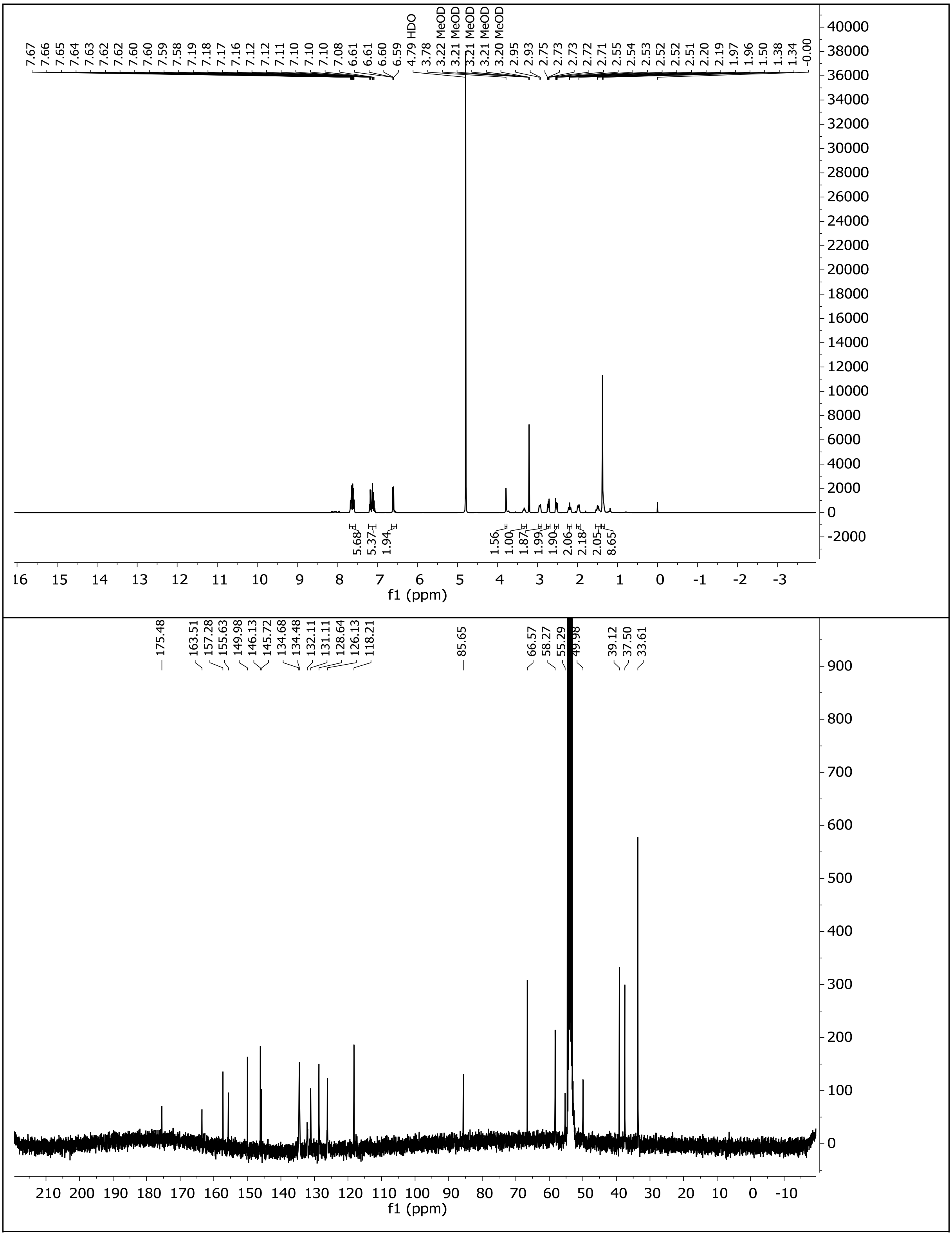

5.4.4.3 *tert*-Butyl (*E*)-(2-oxo-2-((4-((4-(*N*-(1-phenethylpiperidin-4-yl)propionamido)phenyl)diazenyl)phenyl)amino)ethyl)carbamate (**5.12**)

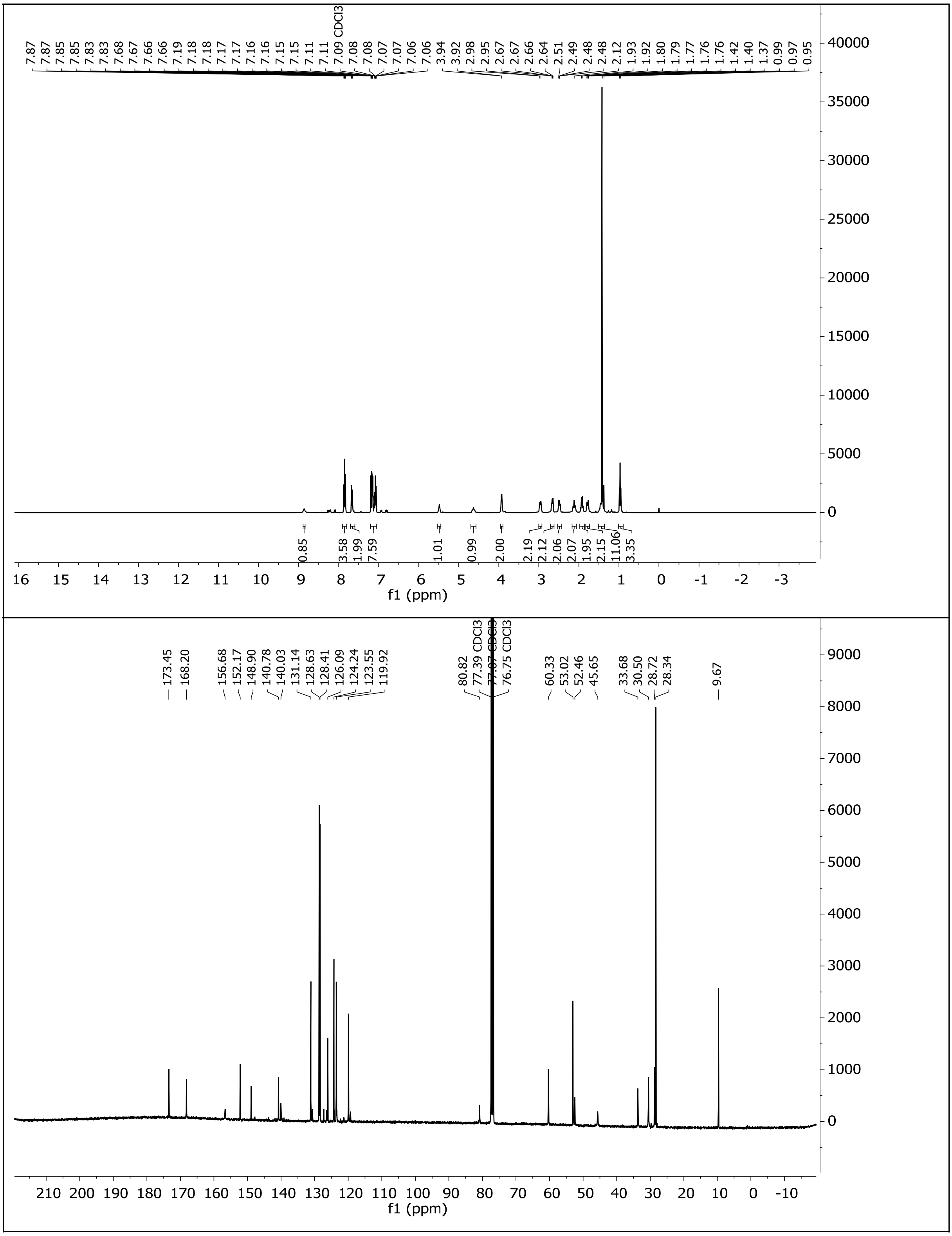

5.4.4.4 (*E*)-*N*-(4-((4-(2-Aminoacetamido)phenyl)diazenyl)phenyl)-*N*-(1-phenethylpiperidin-4-yl)propionamide (**5.13**)

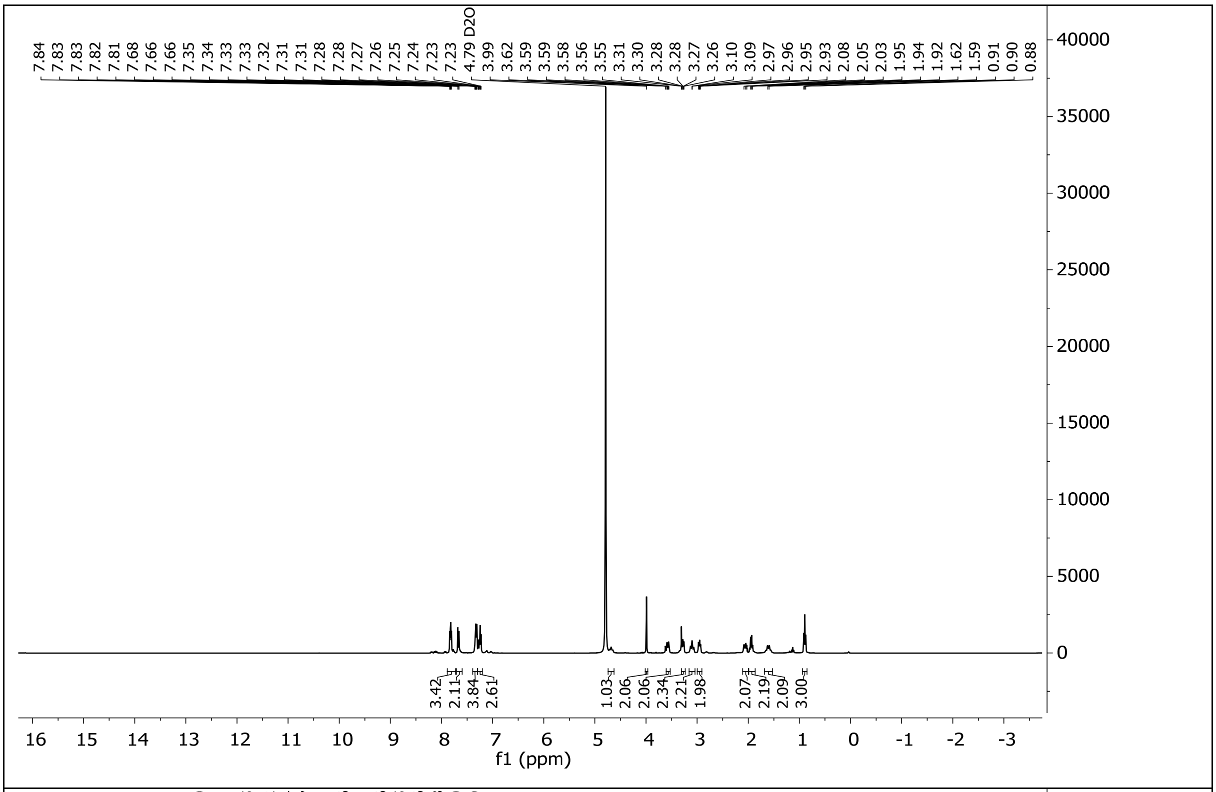

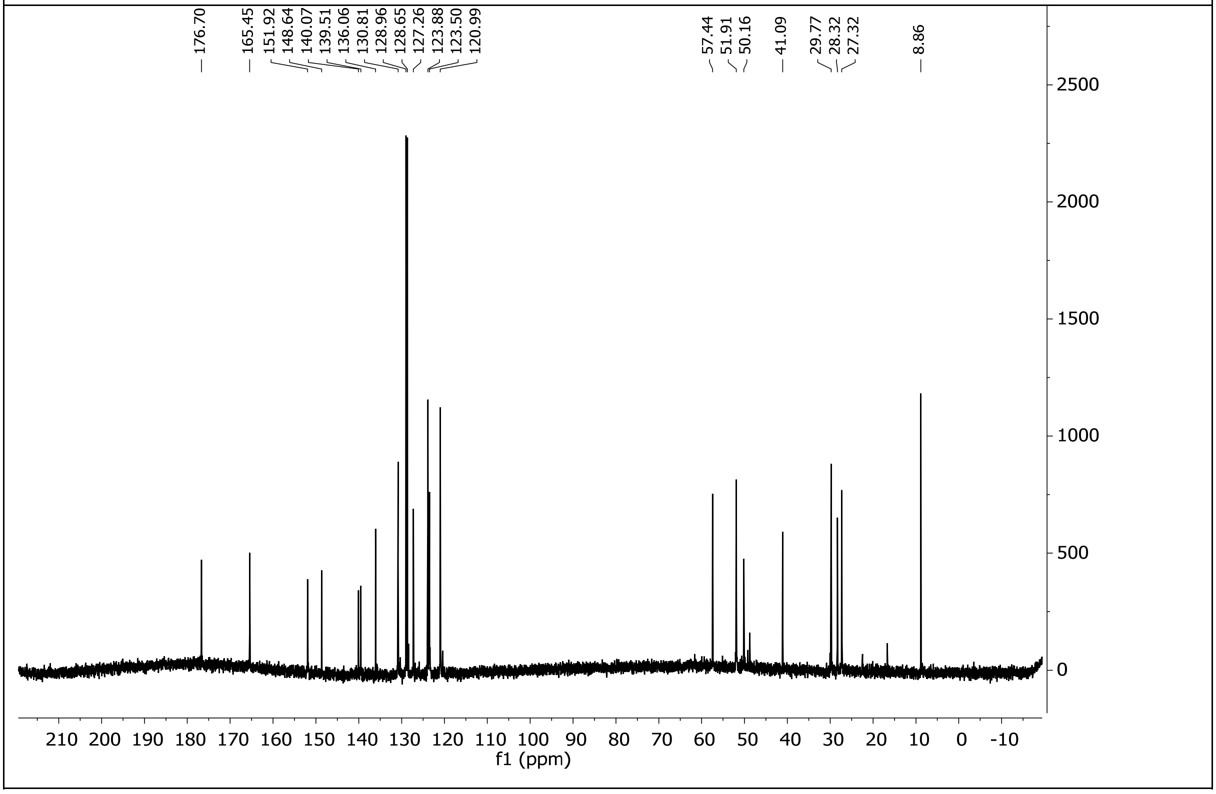

5.4.4.5 BG-DBCO

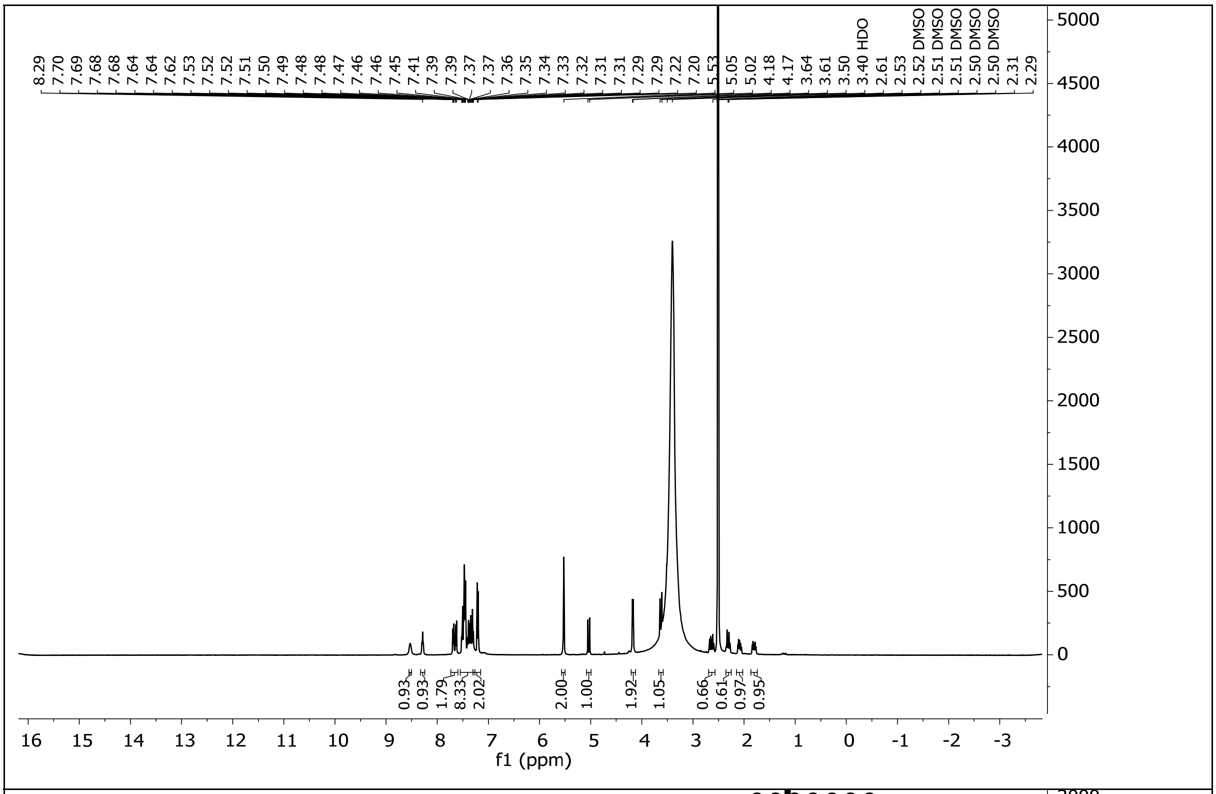
8.29
7.70
7.69
7.68
7.68
7.64
7.64
7.62
7.53
7.52
7.52
7.51
7.50
7.49
7.48
7.48
7.47
7.46
7.46
7.45
7.41
7.39
7.39
7.37
7.37
7.36
7.35
7.34
7.33
7.32
7.31
7.31
7.29
7.29
7.22
7.20
5.53
5.05
5.02
4.18
4.17
3.64
3.61
3.50
3.40 HDO
2.61
2.53
2.52 DMSO
2.51 DMSO
2.51 DMSO
2.50 DMSO
2.50 DMSO
2.31
2.29
0.93
0.93
1.79
8.33
2.02
2.00
1.00
1.92
1.05
0.66
0.61
0.97
0.95
5000
4500
4000
3500
3000
2500
2000
1500
1000
500
0
16 15 14 13 12 11 10 9 8 7 6 5 4 3 2 1 0 -1 -2 -3
f1 (ppm)

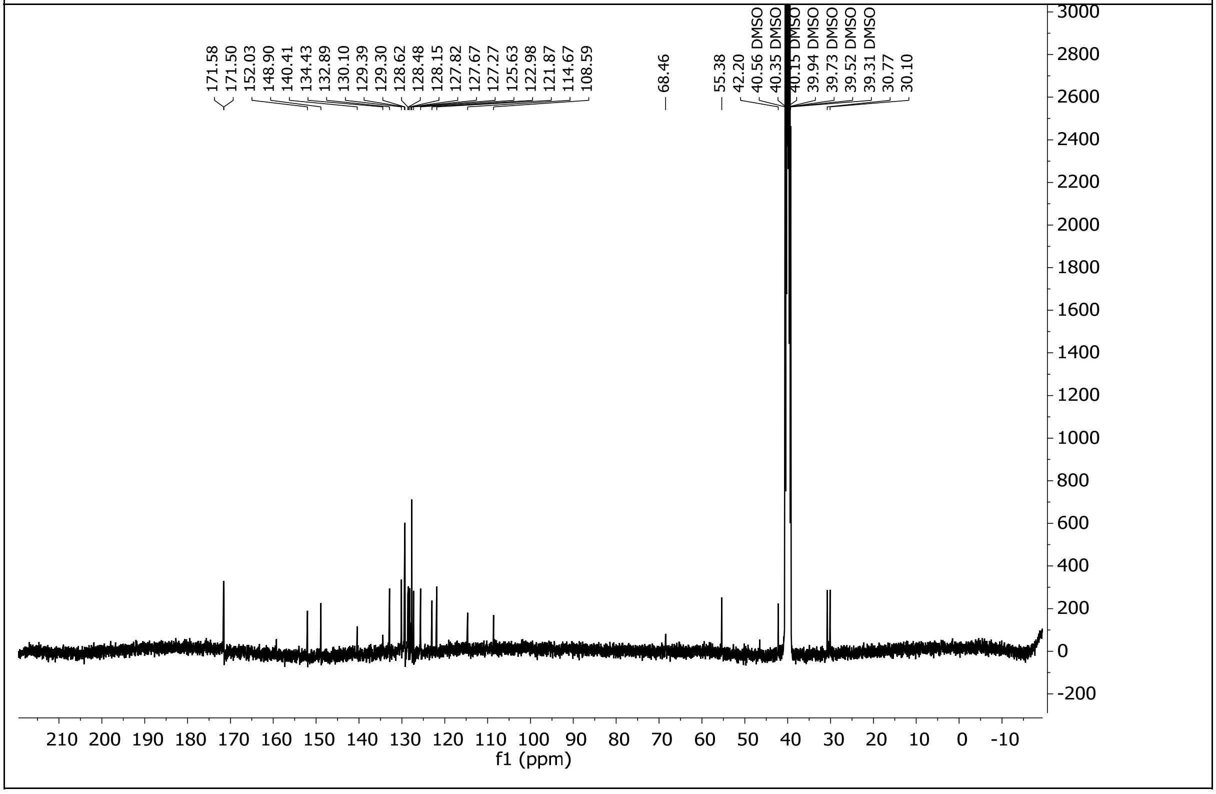
171.58
171.50
152.03
148.90
140.41
134.43
132.89
130.10
129.39
129.30
128.62
128.48
128.15
127.82
127.67
127.27
125.63
122.98
121.87
114.67
108.59
68.46
55.38
42.20
40.56 DMSO
40.35 DMSO
40.15 DMSO
39.94 DMSO
39.73 DMSO
39.52 DMSO
39.31 DMSO
30.77
30.10
3000
2800
2600
2400
2200
2000
1800
1600
1400
1200
1000
800
600
400
200
0
-200
210 200 190 180 170 160 150 140 130 120 110 100 90 80 70 60 50 40 30 20 10 0 -10
f1 (ppm)

5.4.4.6 *tert*-Butyl (3-(methyl(phenyl)amino)propyl)carbamate (**5.3**)

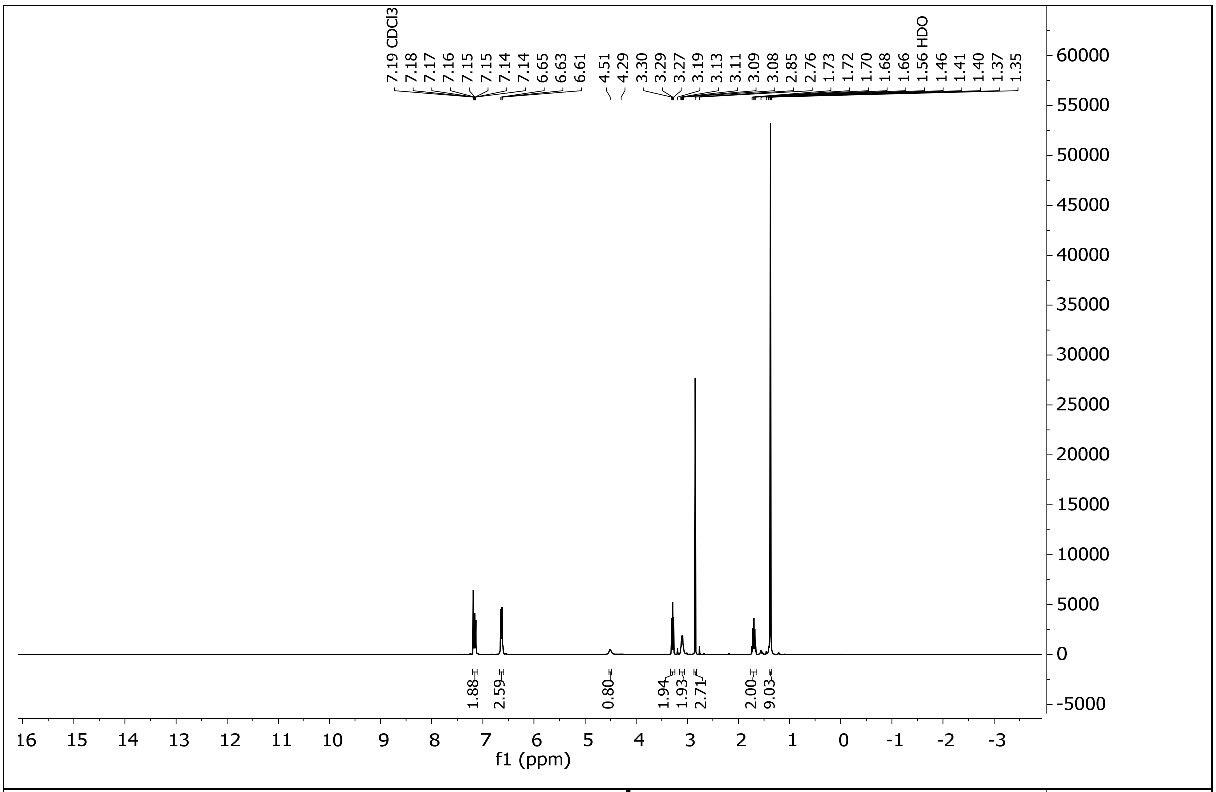

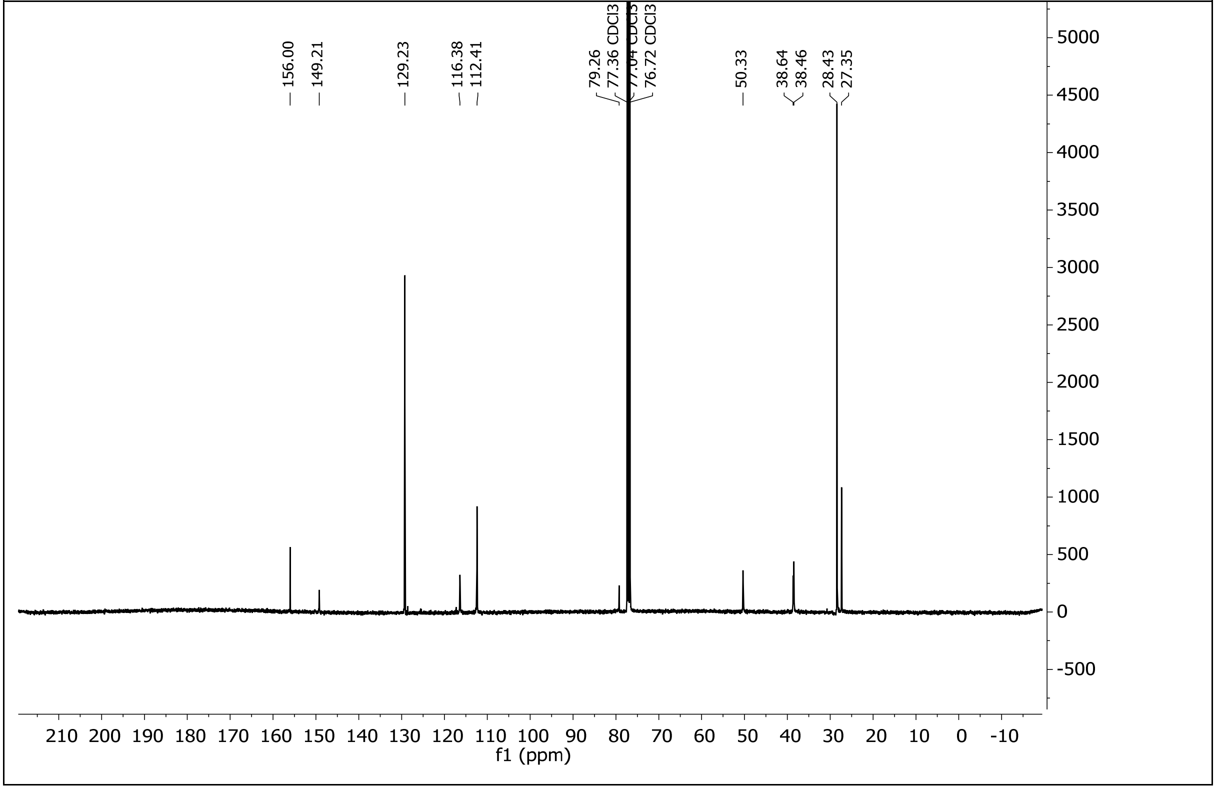

5.4.4.7 *tert*-Butyl (*E*)-(3-(methyl(4-((4-nitrophenyl)diazenyl)phenyl)amino)propyl)carbamate (**5.4**)

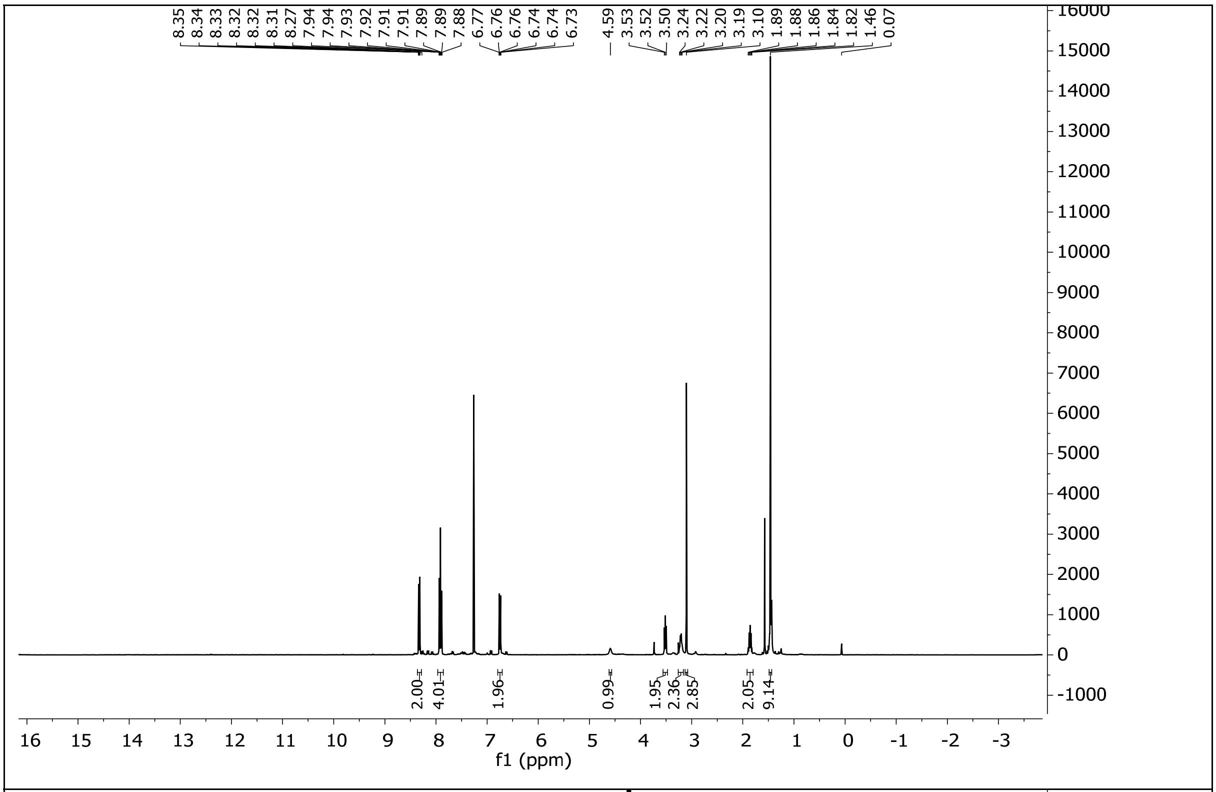

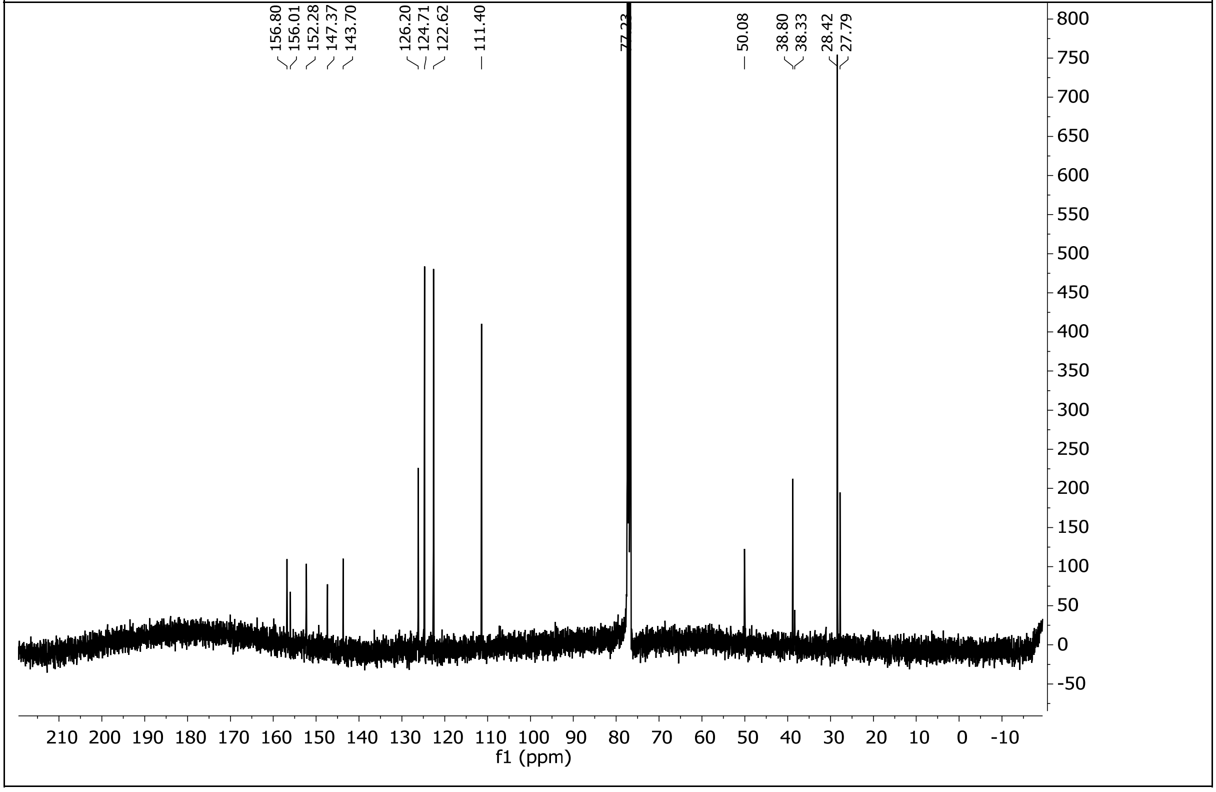

5.4.4.8 *tert*-Butyl (*E*)-(3-((4-((4-aminophenyl)diazenyl)phenyl)(methyl)amino)propyl)carbamate (**5.5**)

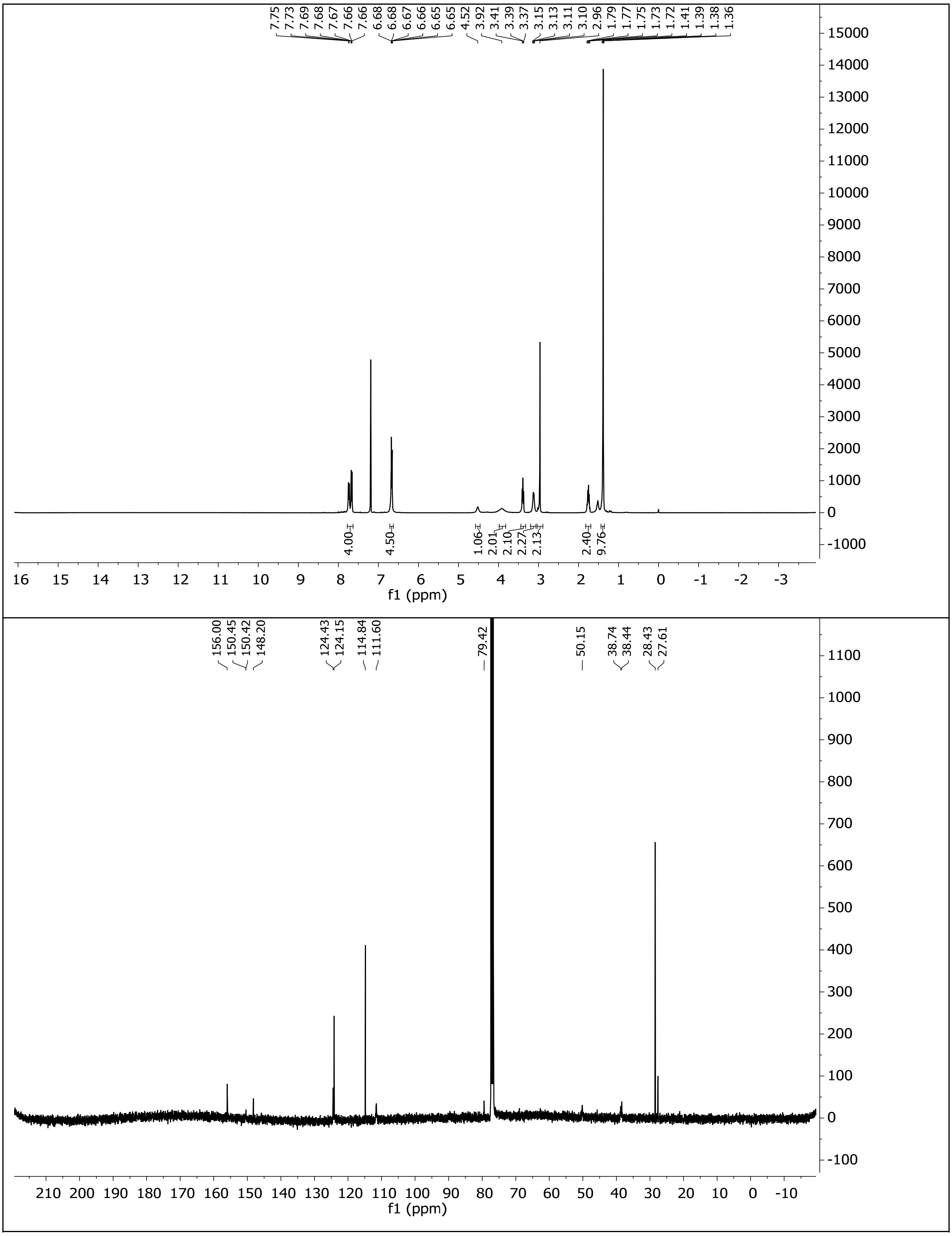

5.4.4.9 *tert*-butyl (*E*)-(3-(methyl(4-((4-((1-phenethylpiperidin-4-yl)amino)phenyl)diazenyl)phenyl)amino)propyl)carbamate (**5.6**)

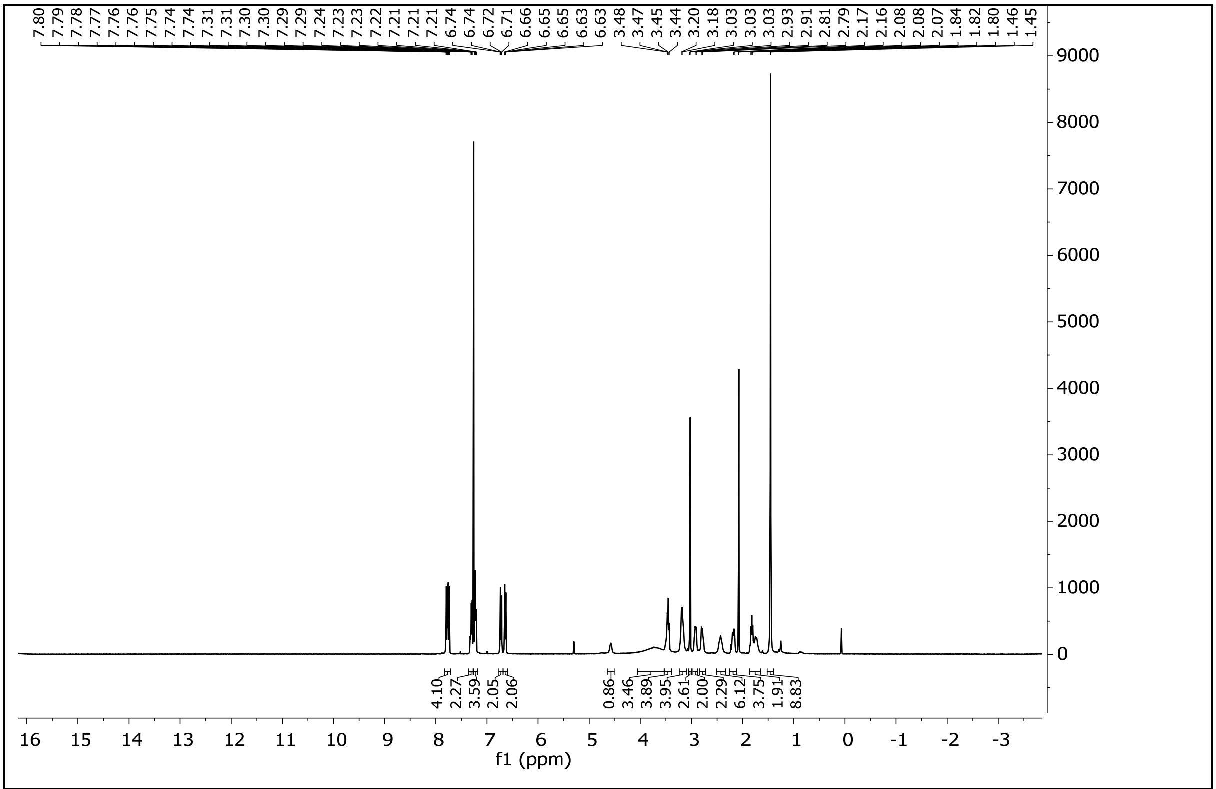

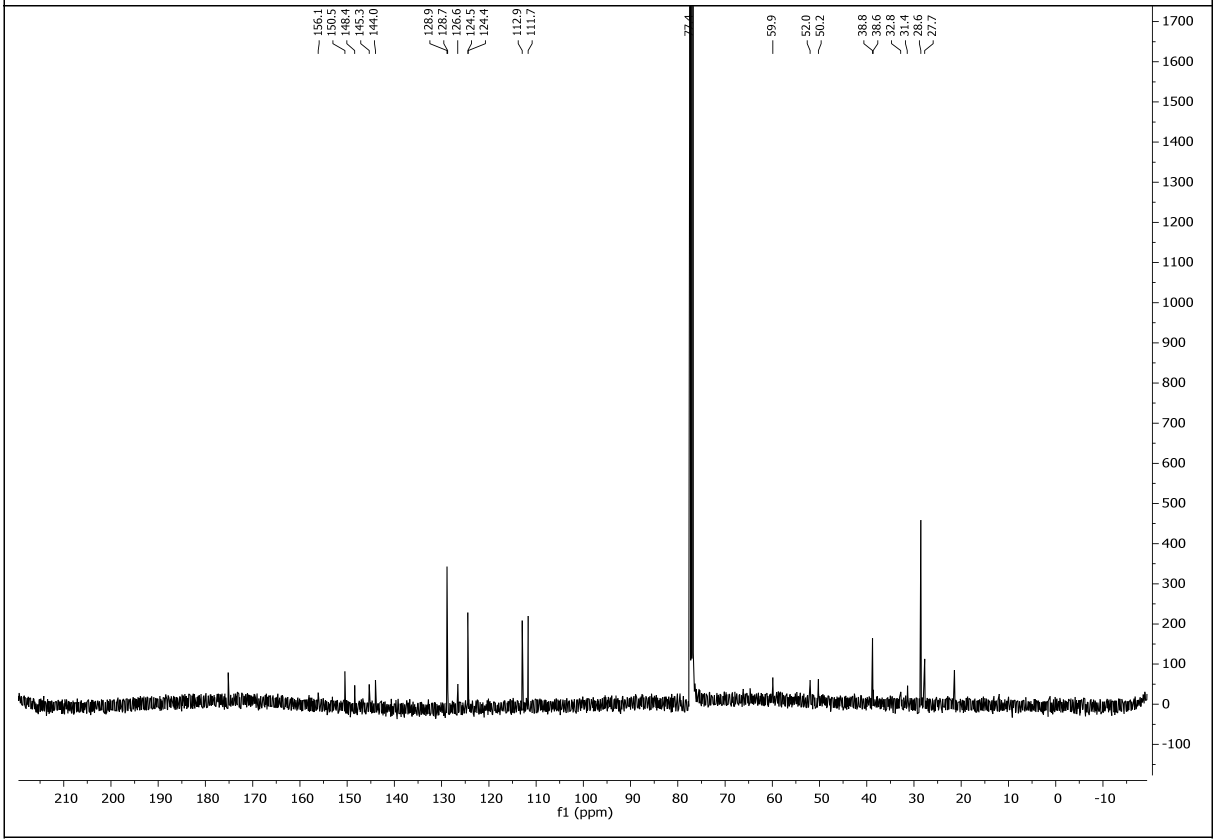

5.4.4.10 *tert*-butyl (*E*)-(3-(methyl(4-((4-(*N*-(1-phenethylpiperidin-4-yl)propionamido)phenyl)diazenyl)phenyl)amino)propyl)carbamate (**5.7**)

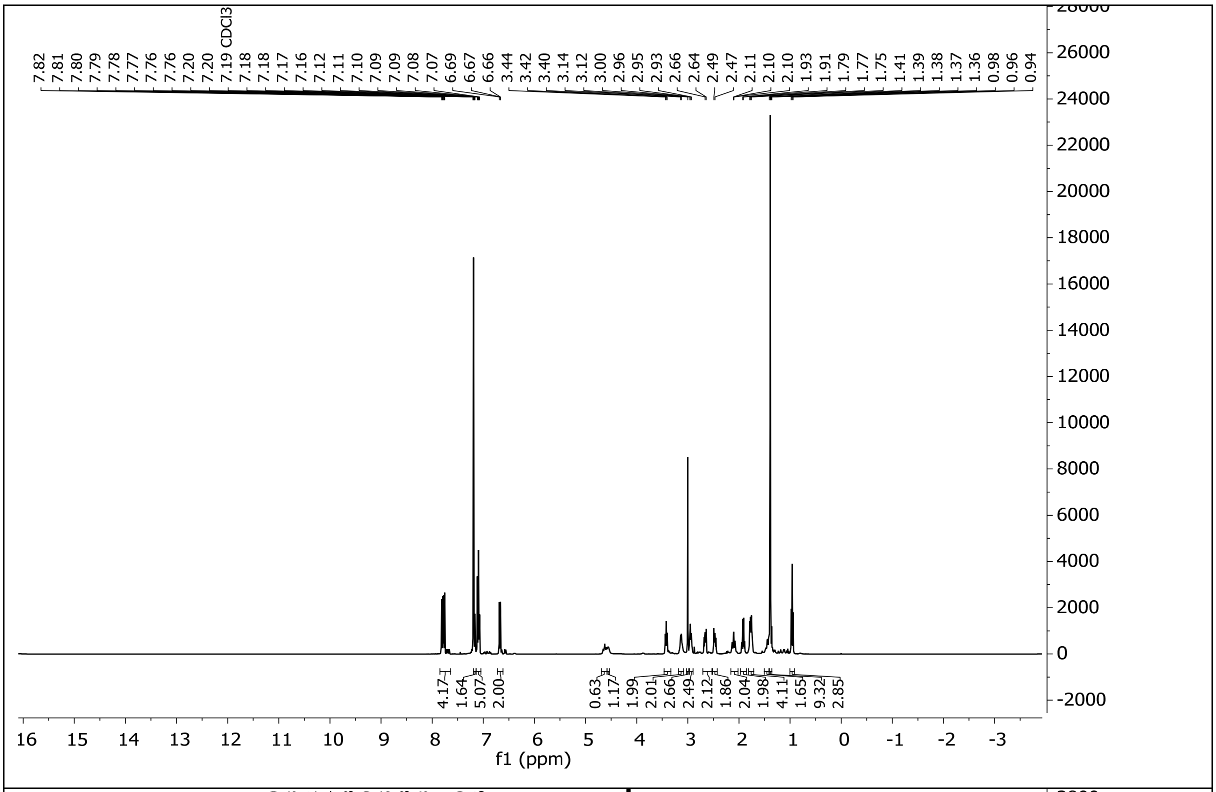

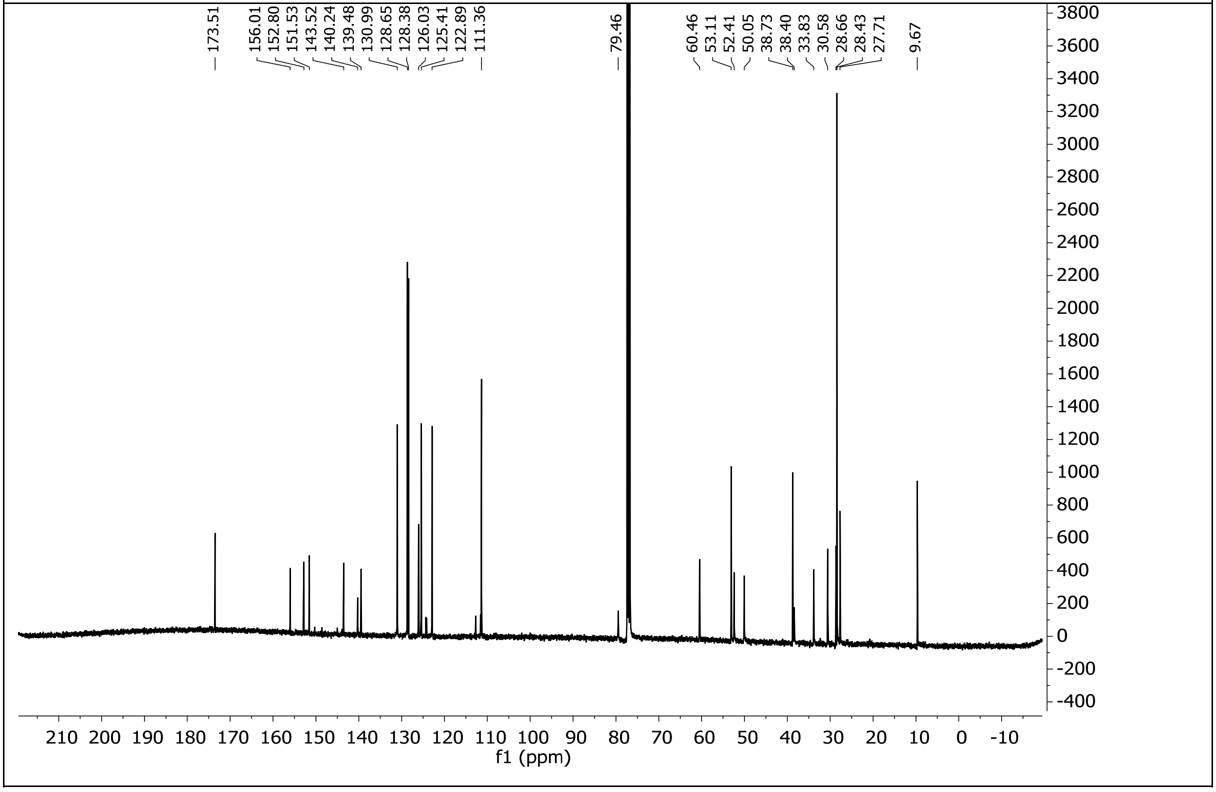

5.4.4.11 (*E*)-*N*-(4-((4-((3-aminopropyl)(methyl)amino)phenyl)diazenyl)phenyl)-*N*-(1-phenethylpiperidin-4-yl)propionamide dihydrochloride (**5.8**)

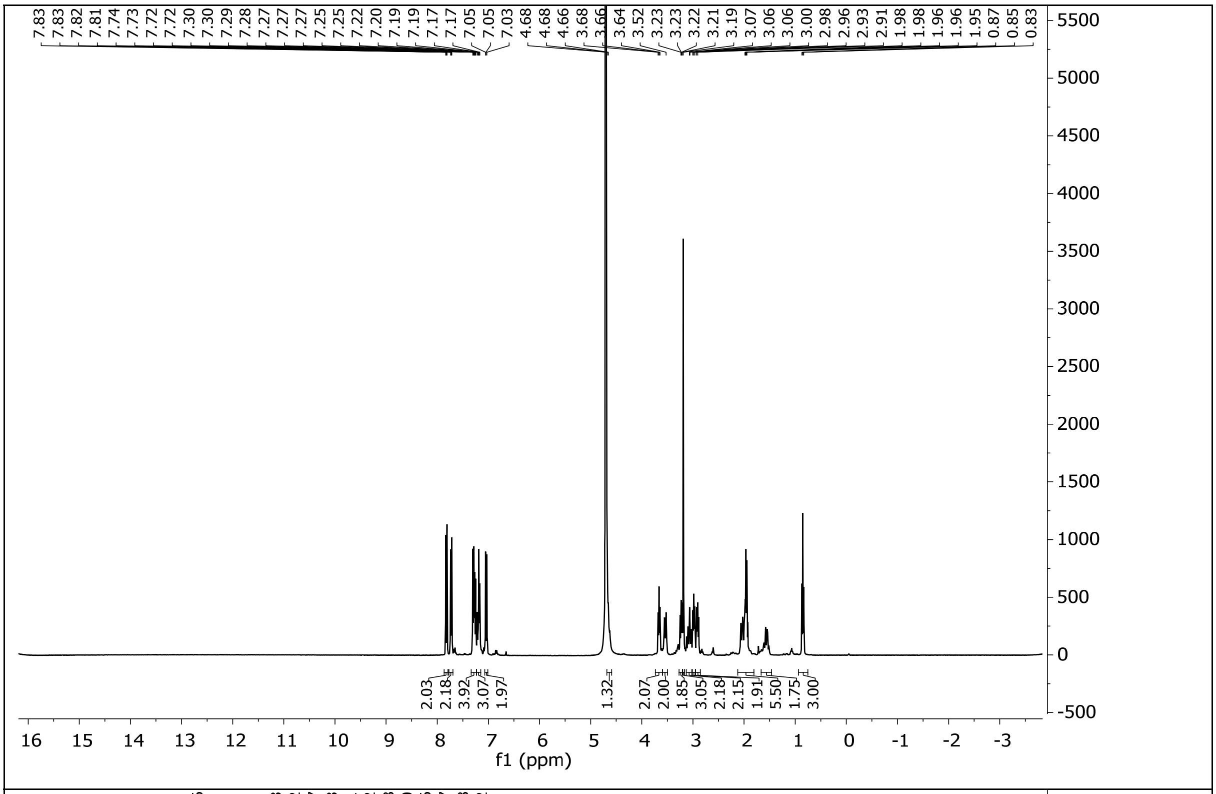

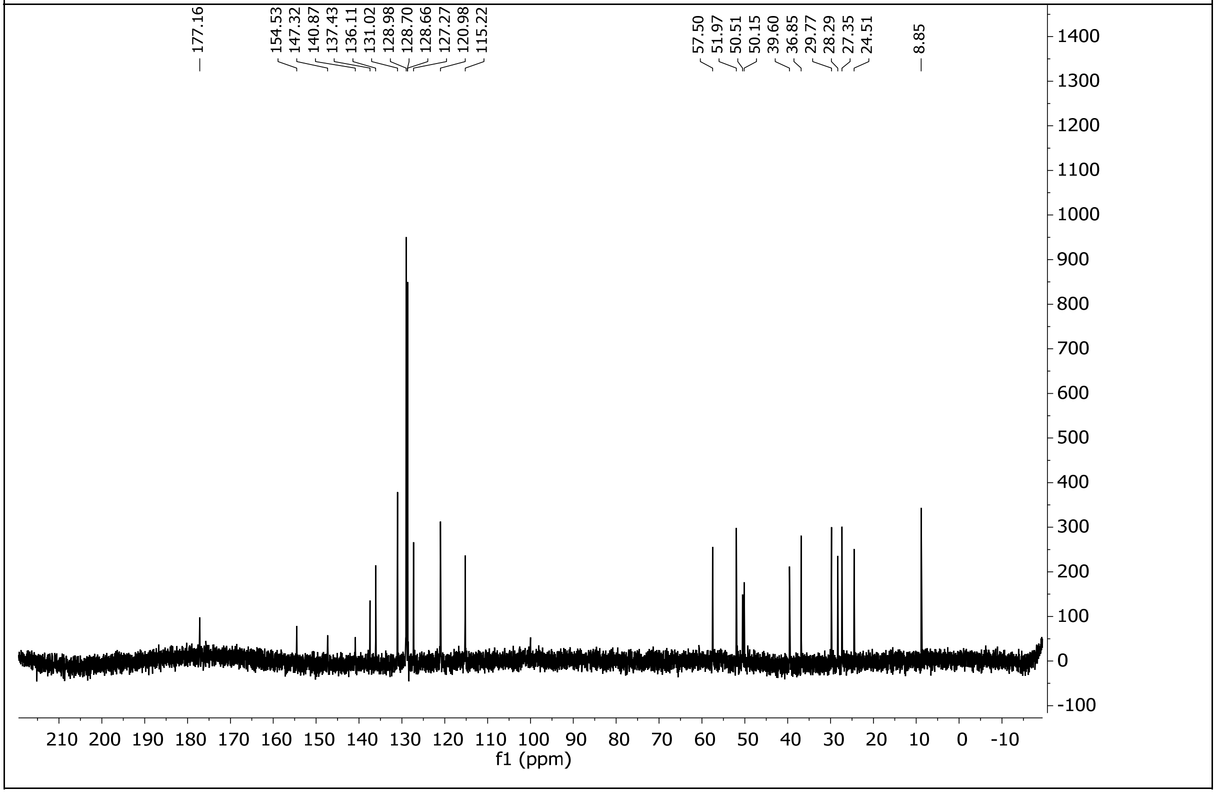

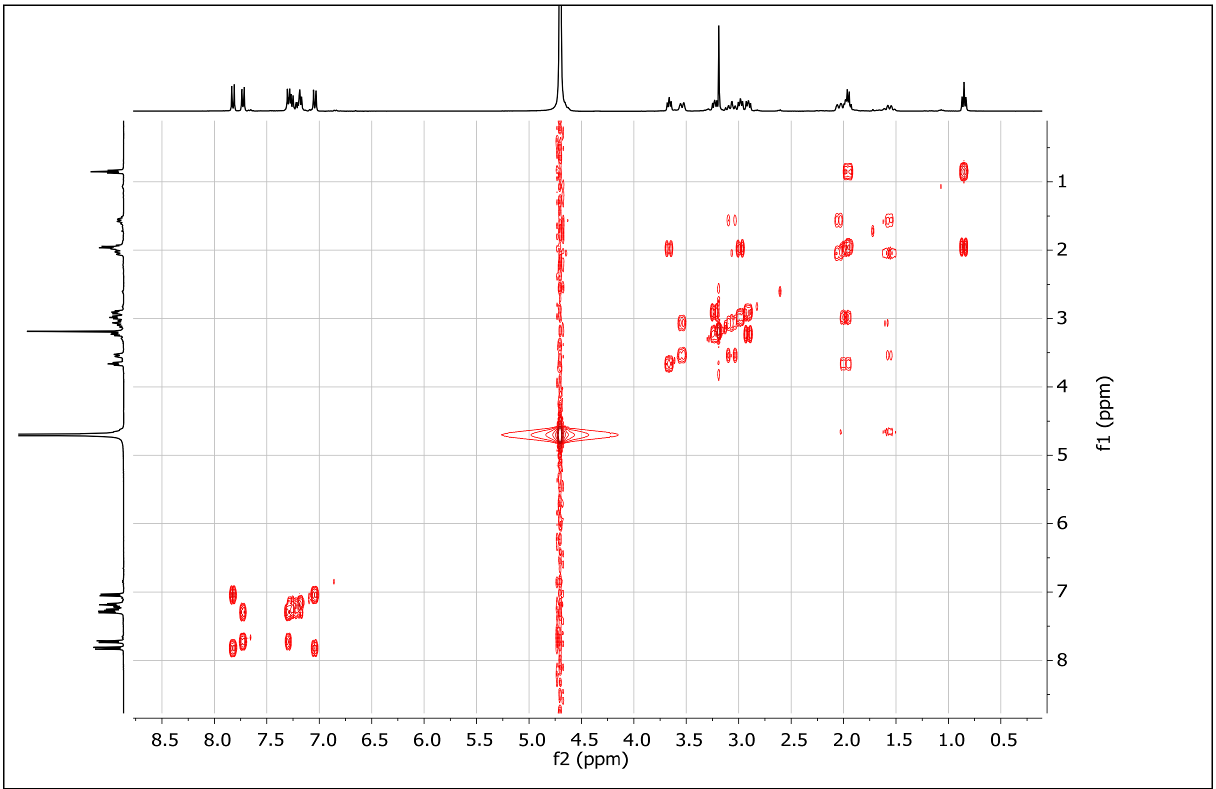
8.5
8.0
7.5
7.0
6.5
6.0
5.5
5.0
4.5
4.0
3.5
3.0
2.5
2.0
1.5
1.0
0.5
f2 (ppm)
1
2
3
4
5
6
7
8
f1 (ppm)

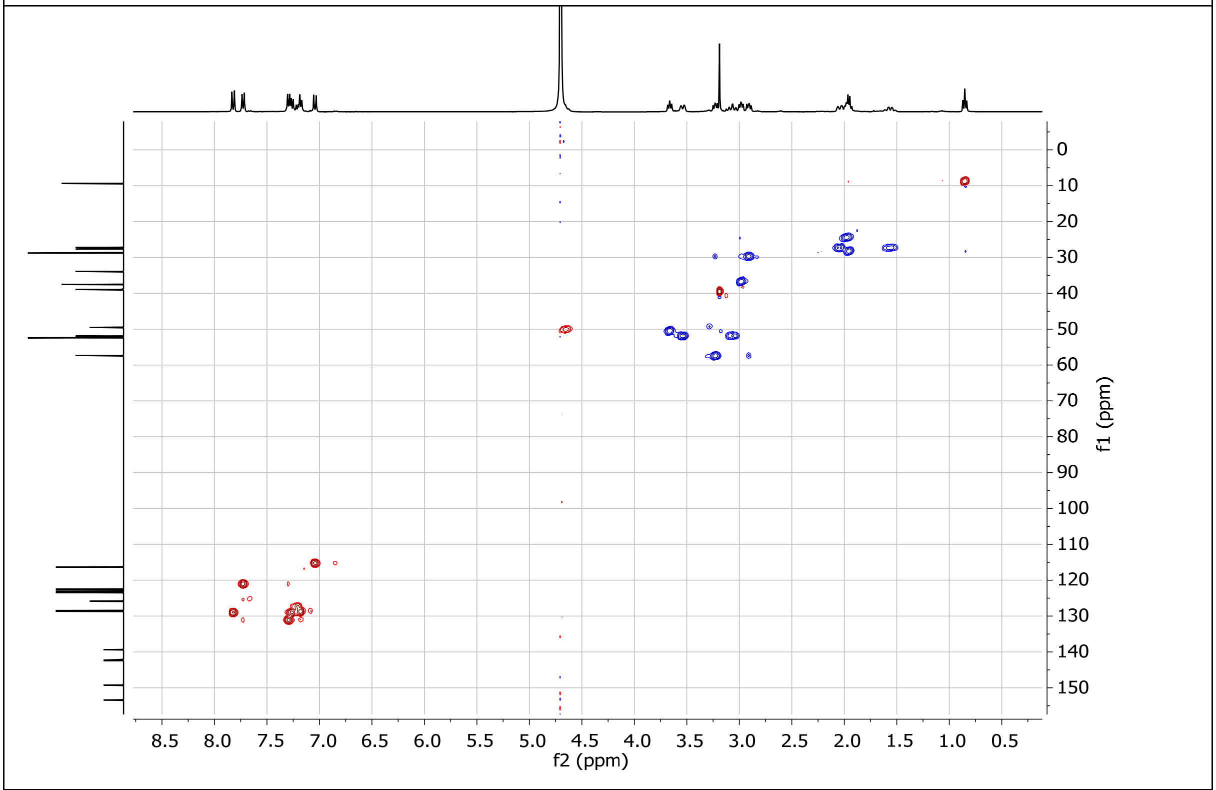
8.5
8.0
7.5
7.0
6.5
6.0
5.5
5.0
4.5
4.0
3.5
3.0
2.5
2.0
1.5
1.0
0.5
f2 (ppm)
0
10
20
30
40
50
60
70
80
90
100
110
120
130
140
150
f1 (ppm)

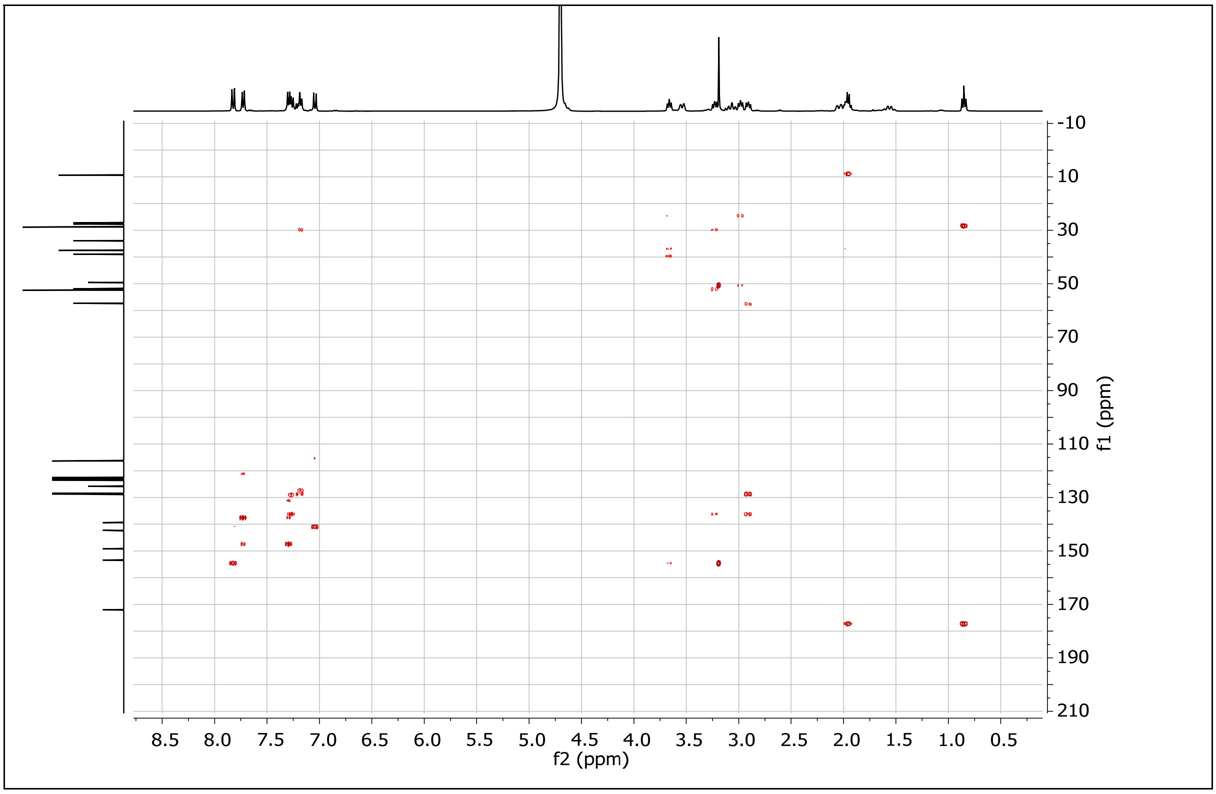
-10
10
30
50
70
90
110
130
150
170
190
210
f1 (ppm)
8.5
8.0
7.5
7.0
6.5
6.0
5.5
5.0
4.5
4.0
3.5
3.0
2.5
2.0
1.5
1.0
0.5
f2 (ppm)

5.4.4.12 (*E*)-1-(8-(4-((4-(((2-amino-9*H*-purin-6-yl)oxy)methyl)benzyl)amino)-4-oxobutanoyl)-8,9-dihydro-1*H*-dibenzo[b,f][1,2,3]triazolo[4,5-d]azocin-1-yl)-*N*-(3-((4-((4-(*N*-(1-phenethylpiperidin-4-yl)propionamido)phenyl)diazenyl)phenyl)-λ^2-azaneyl)propyl)-3,6,9,12,15,18,21,24,27,30,33,36-dodecaoxanonatriacontan-39-amide (**5.15**)

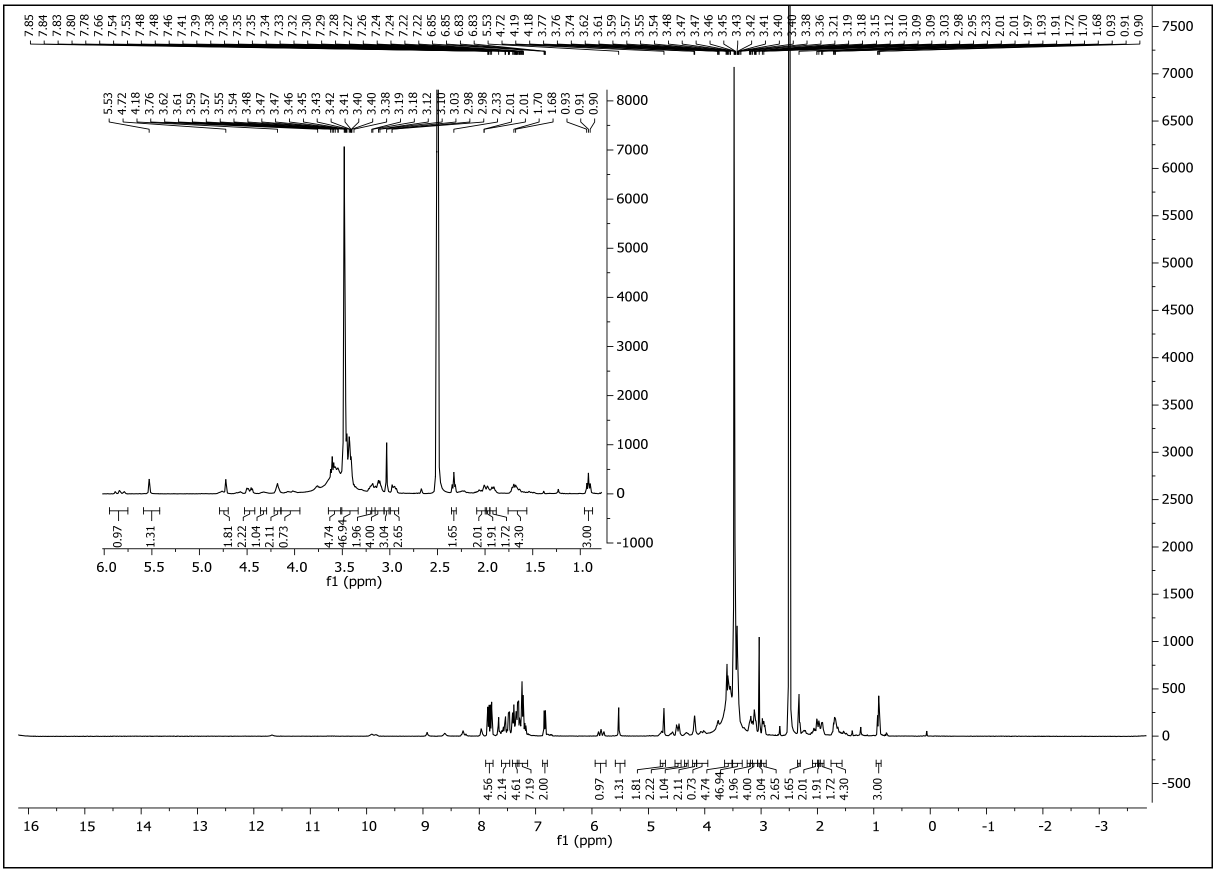

5.4.4.13 2,2'-(Ethane-1,2-diyl)bis(4-bromoaniline) (**5.21**)

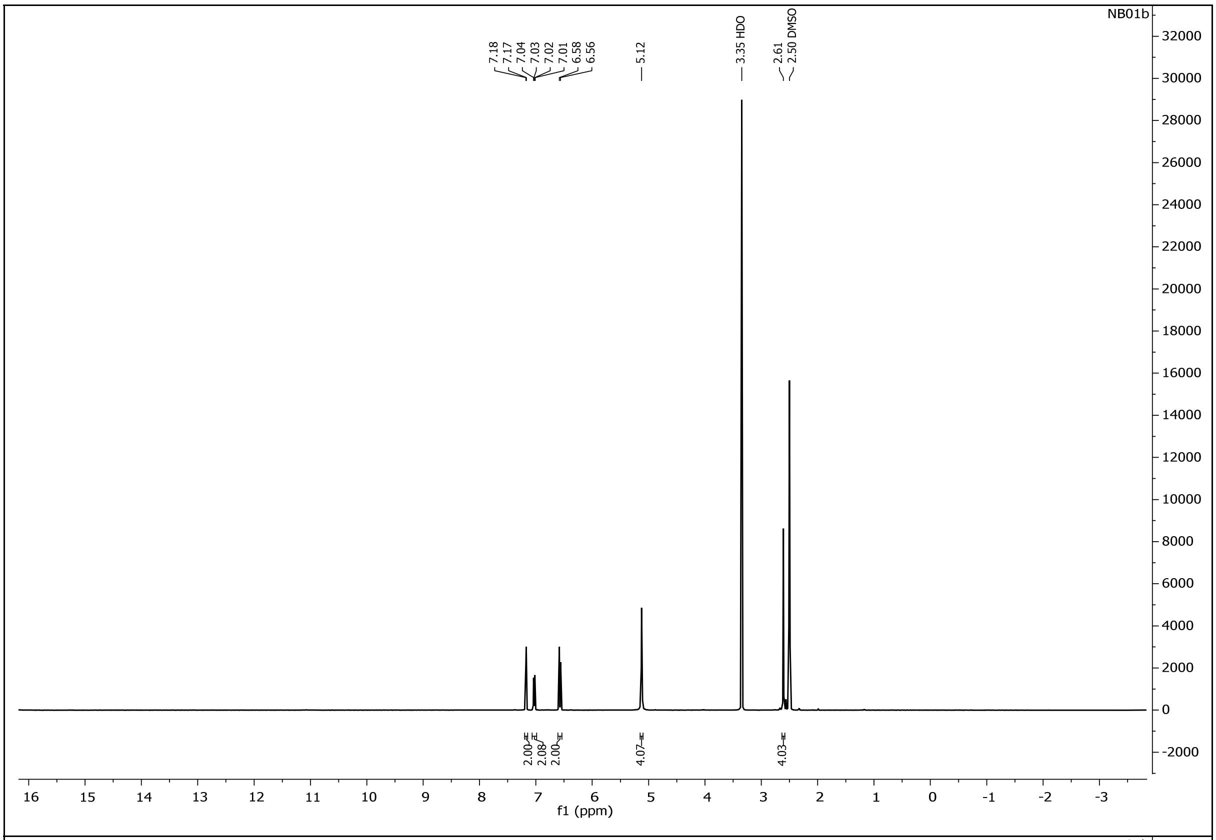

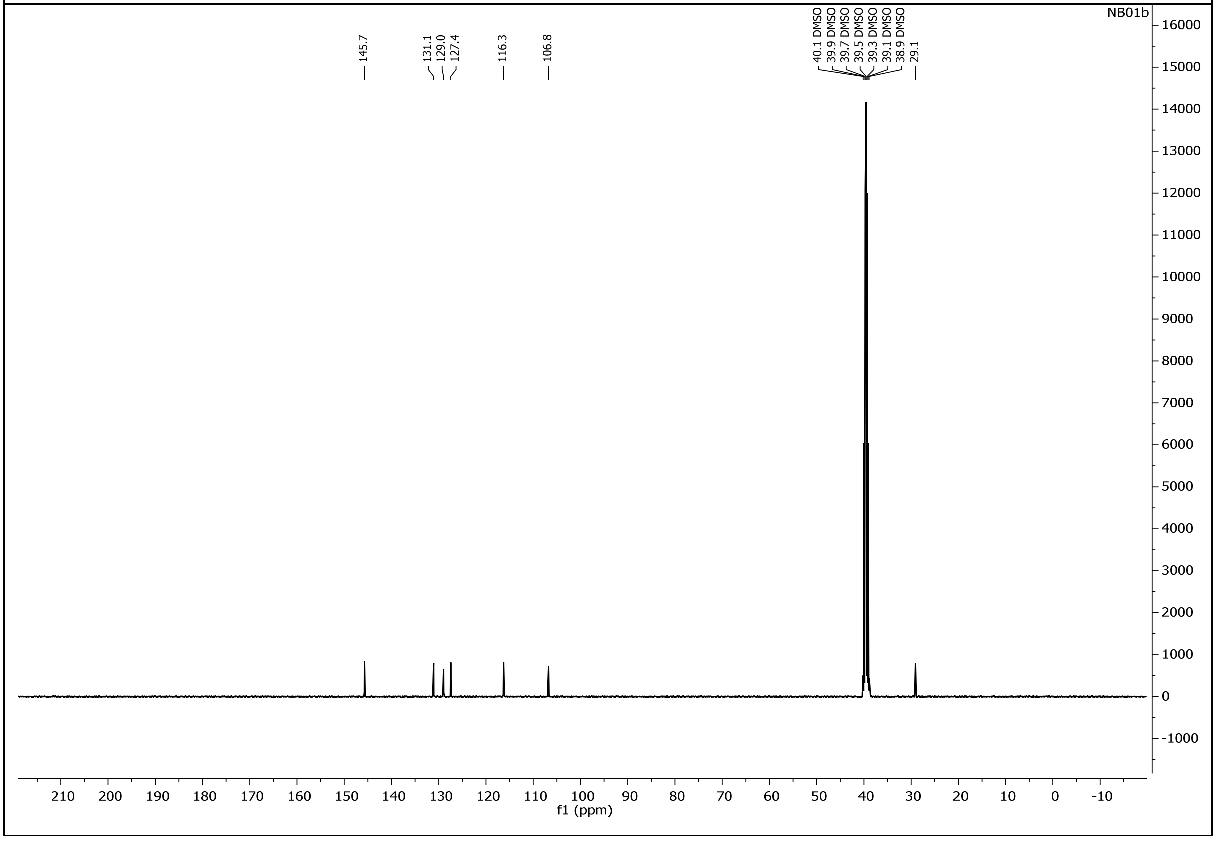

5.4.4.14 (*Z*)-2,9-dibromo-11,12-dihydrodibenzo[*c*,*g*][1,2]diazocine (**5.22**)

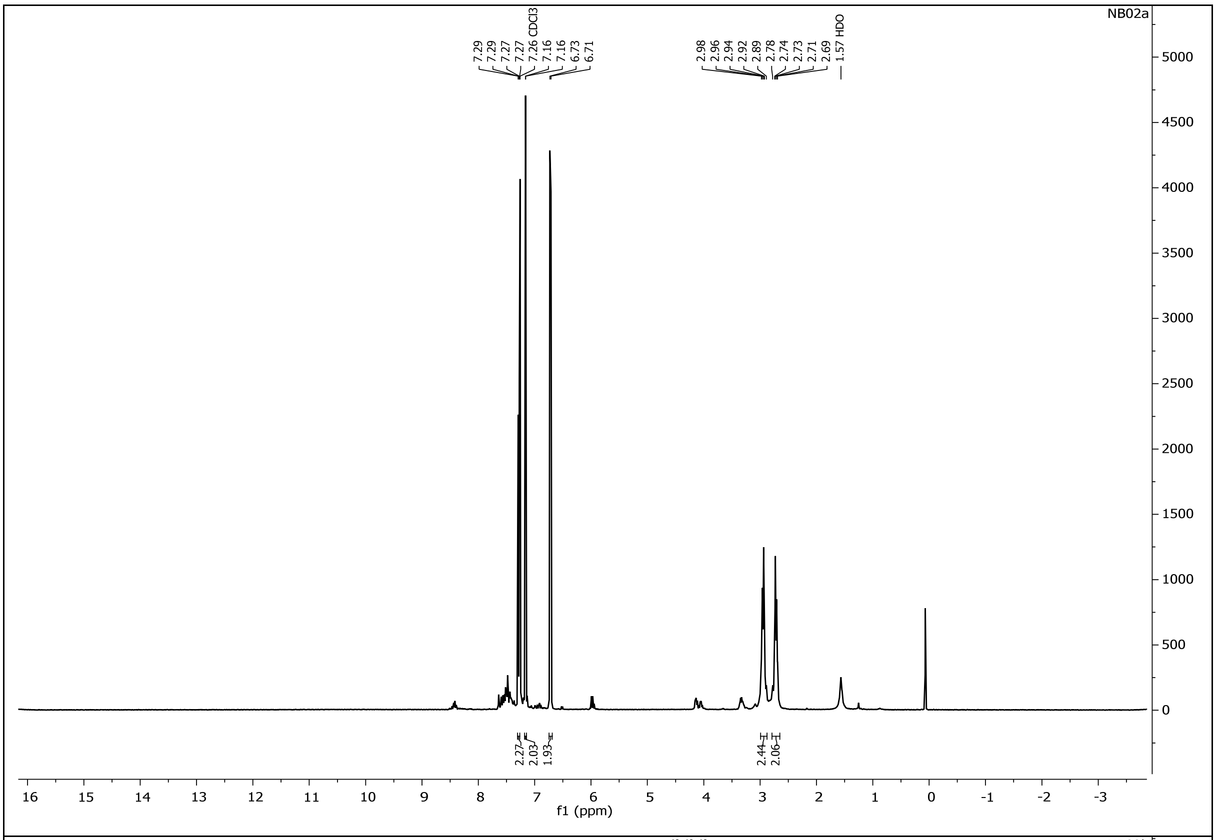

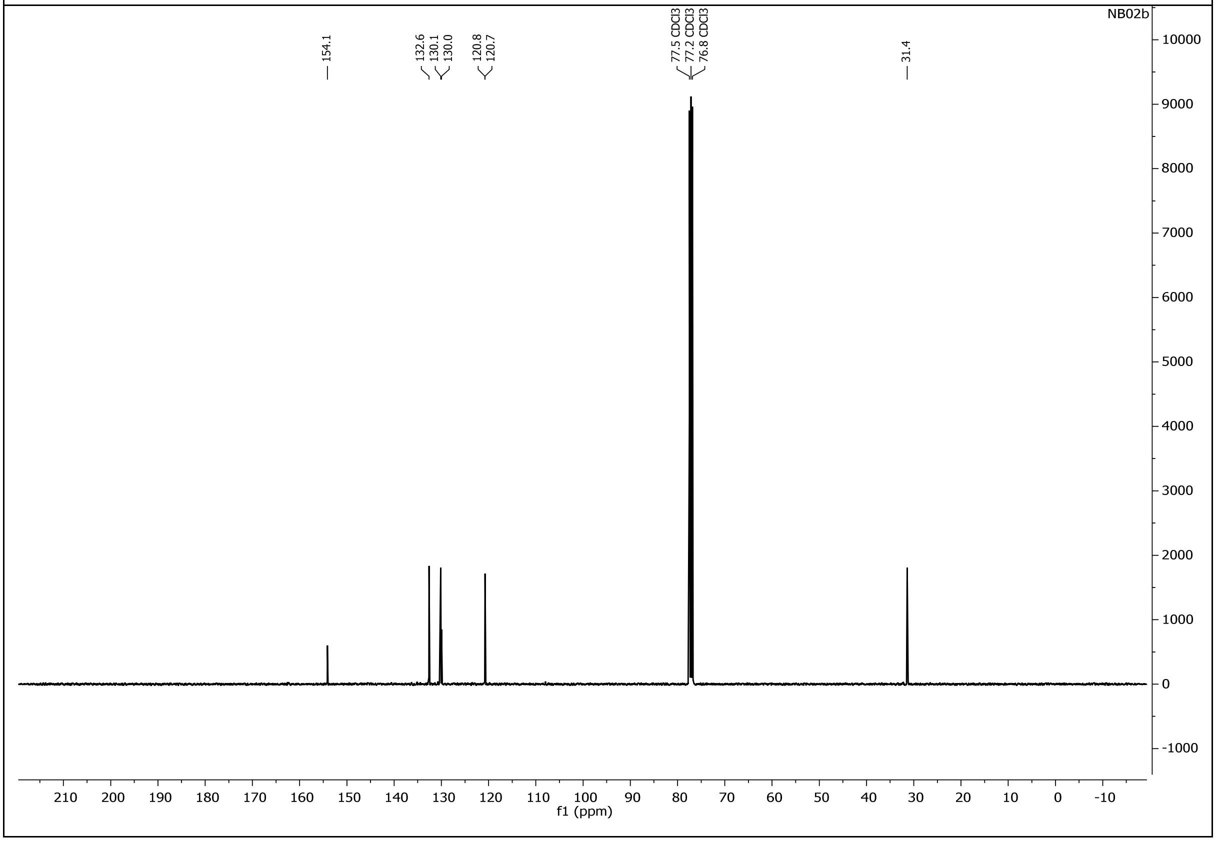

5.4.4.15 (*Z*)-di-tert-butyl-(11,12-dihydrodibenzo[*c*,*g*][1,2]diazocine-2,9-diyl)-dicarbamate (**5.23**)

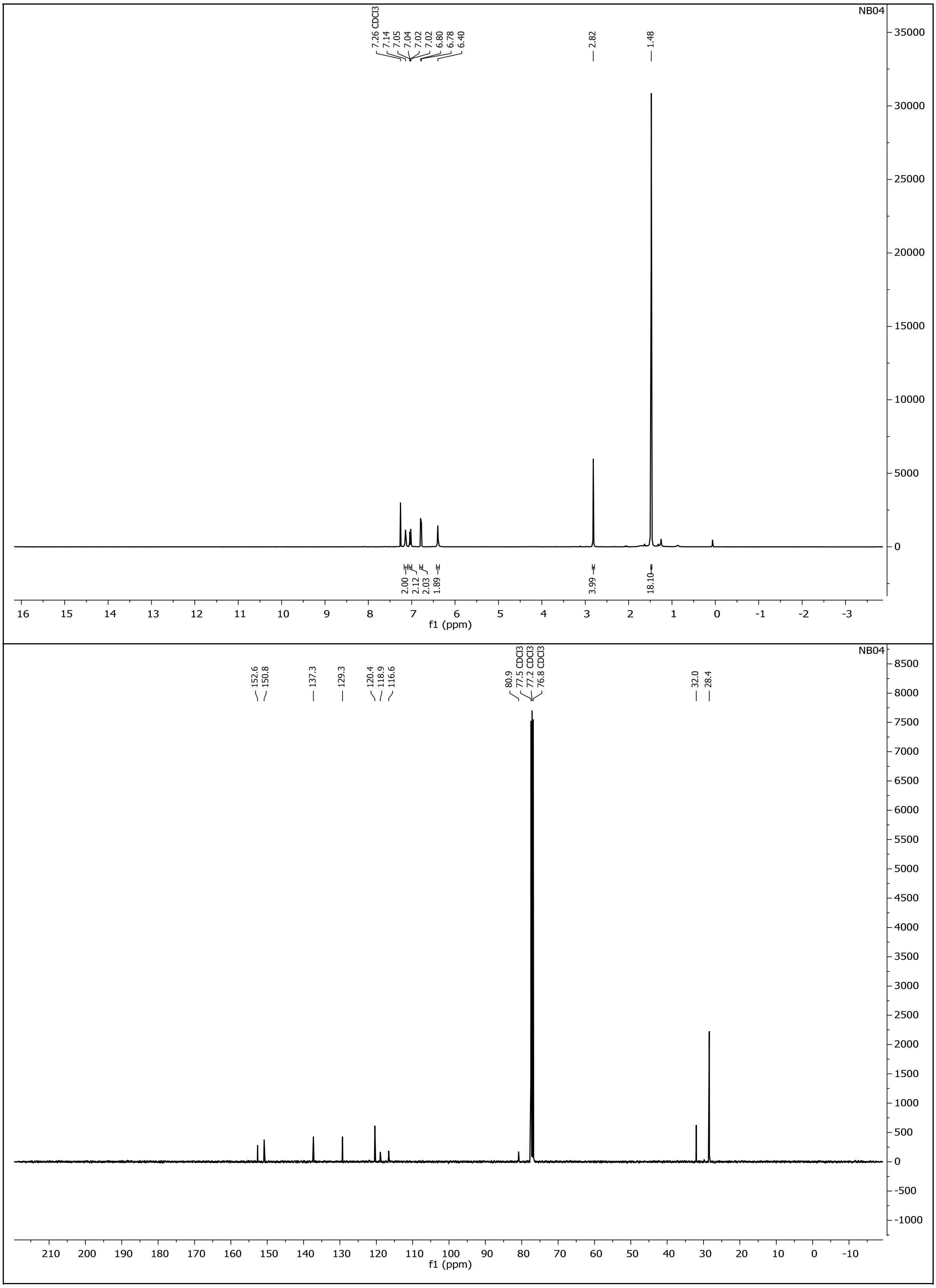

5.4.4.16 (*Z*)-11,12-dihydrodibenzo[*c*,*g*][1,2]diazocine-2,9-diamine (**5.24**)

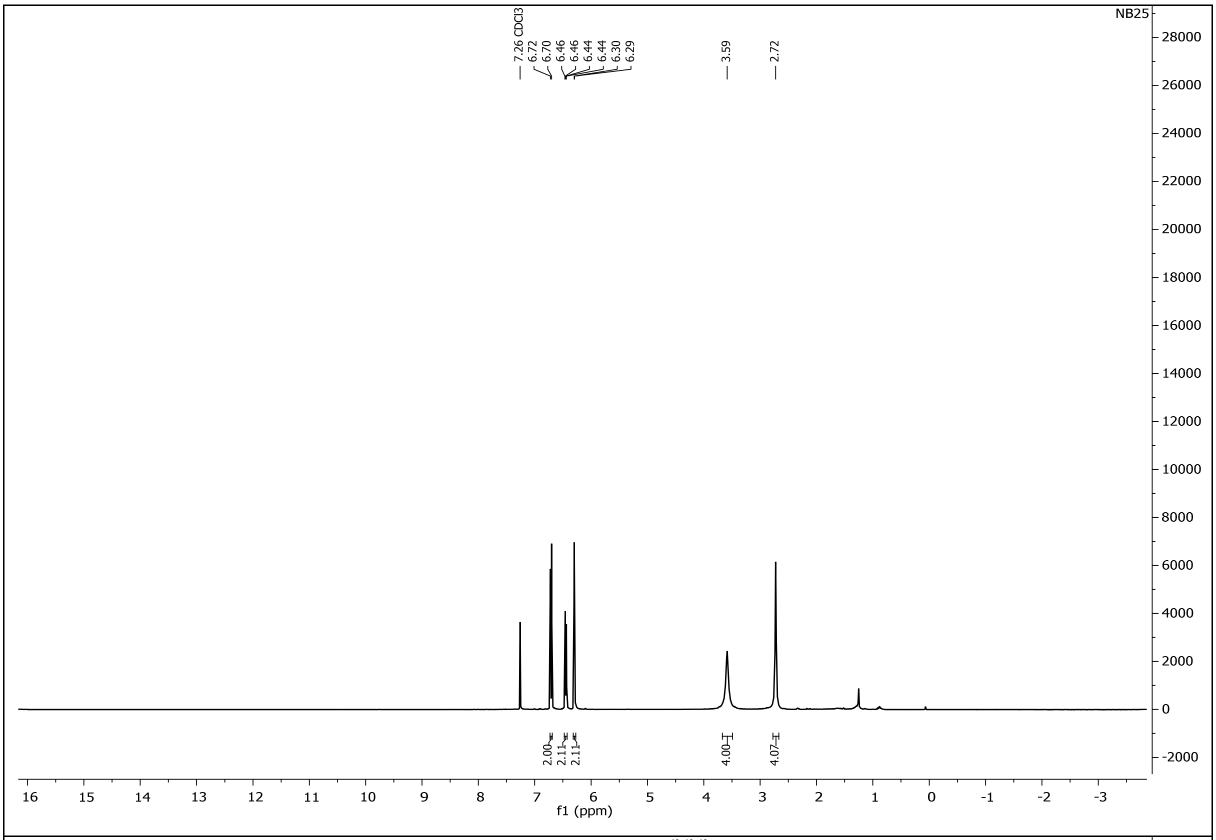

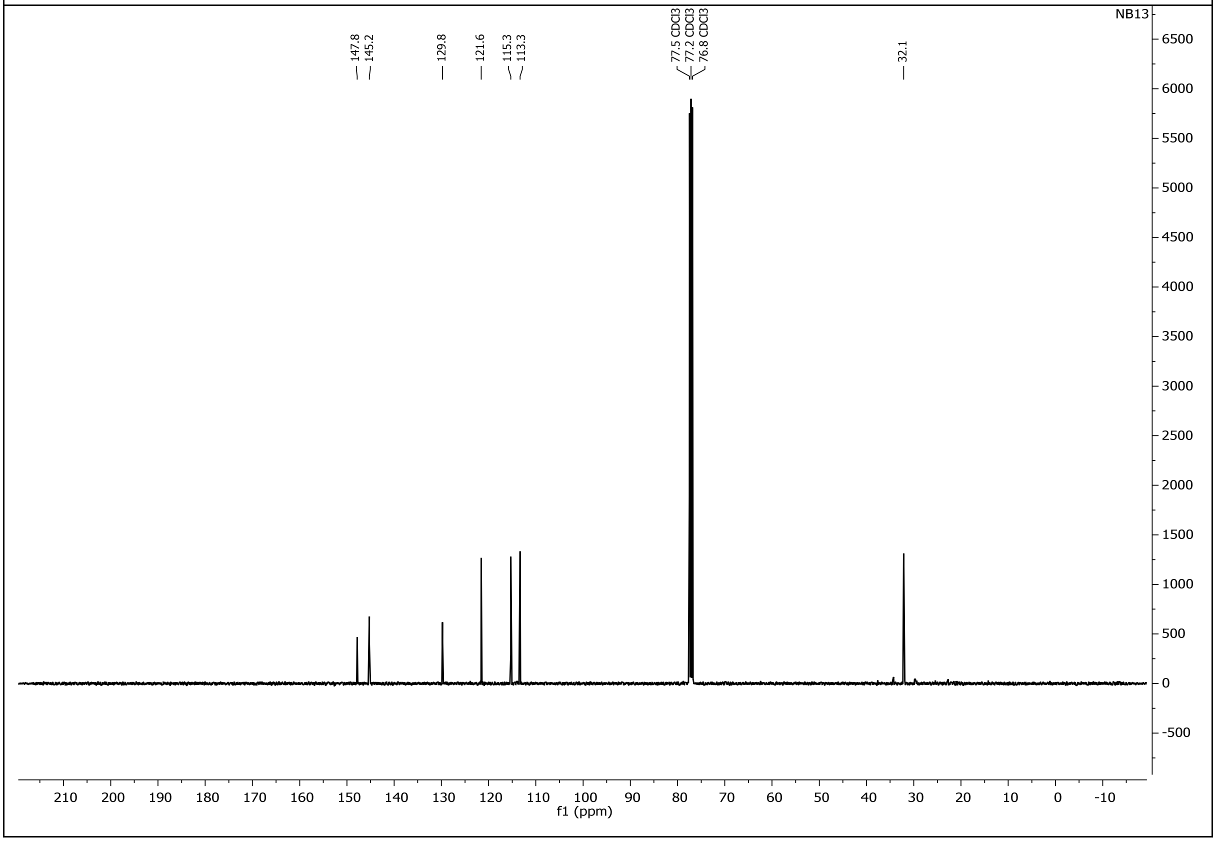

5.4.4.17 *tert*-butyl (*Z*)-(2-((9-amino-11,12-dihydrodibenzo[*c,g*][1,2]diazocin-2-yl)amino)-2-oxoethyl)carbamate (**5.25**)

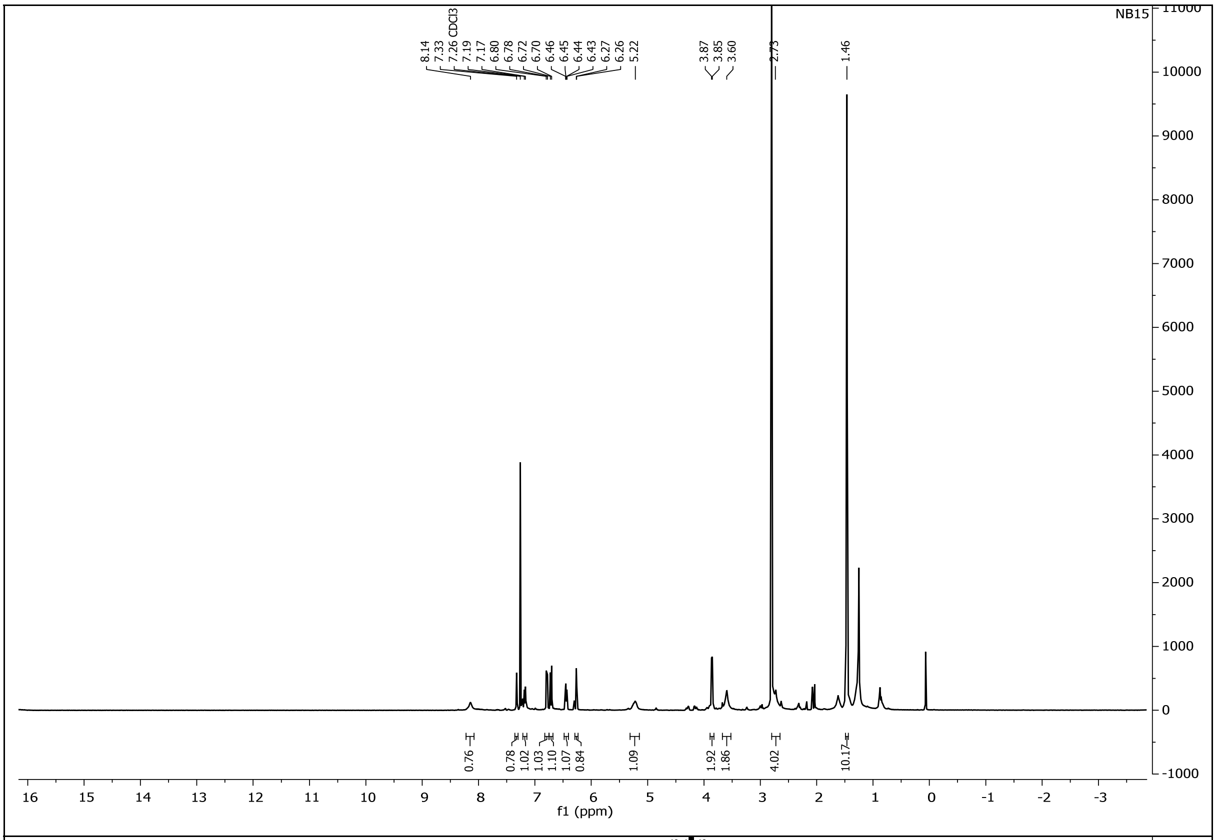

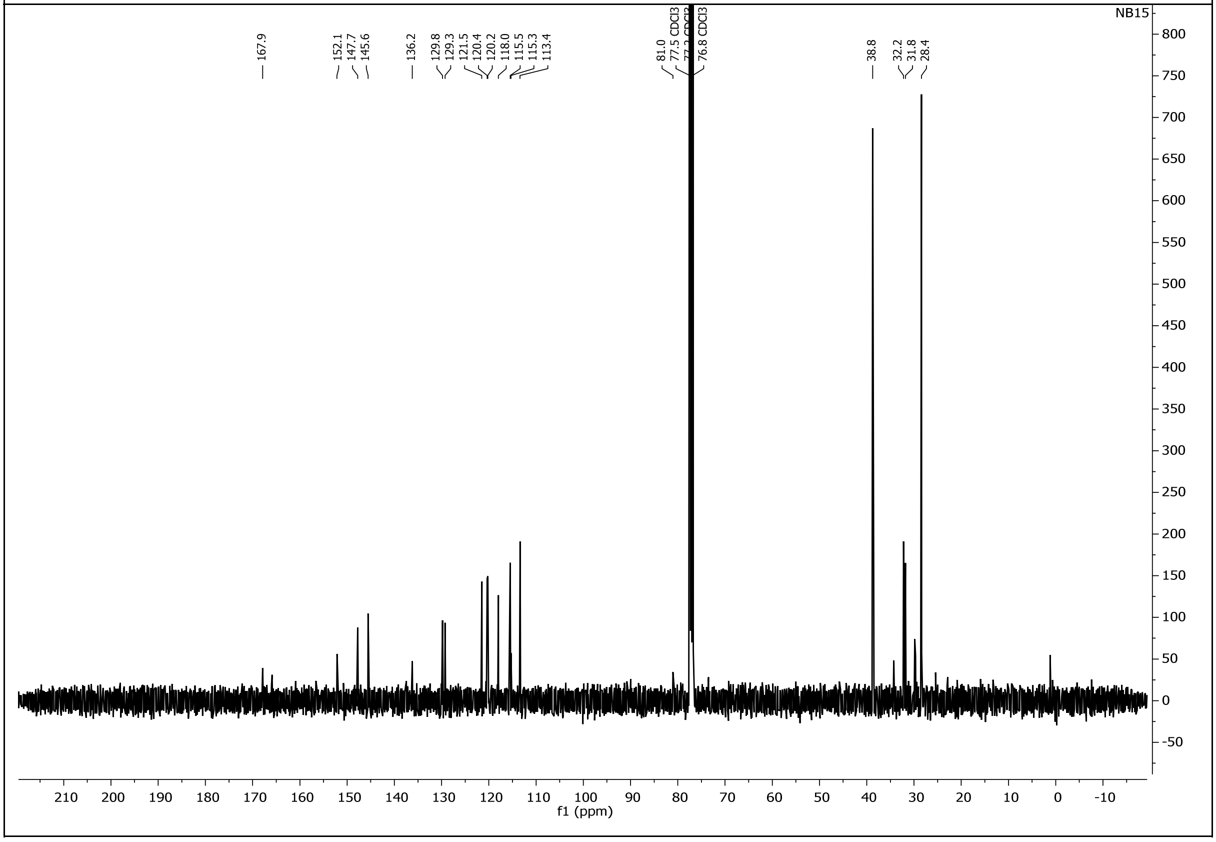

5.4.4.18 *tert*-Butyl (*Z*)-(2-oxo-2-((9-((1-phenethylpiperidin-4-yl)amino)-11,12-dihydrodibenzo[*c*,*g*][1,2]diazocin-2-yl)amino)ethyl)carbamate (**5.26**)

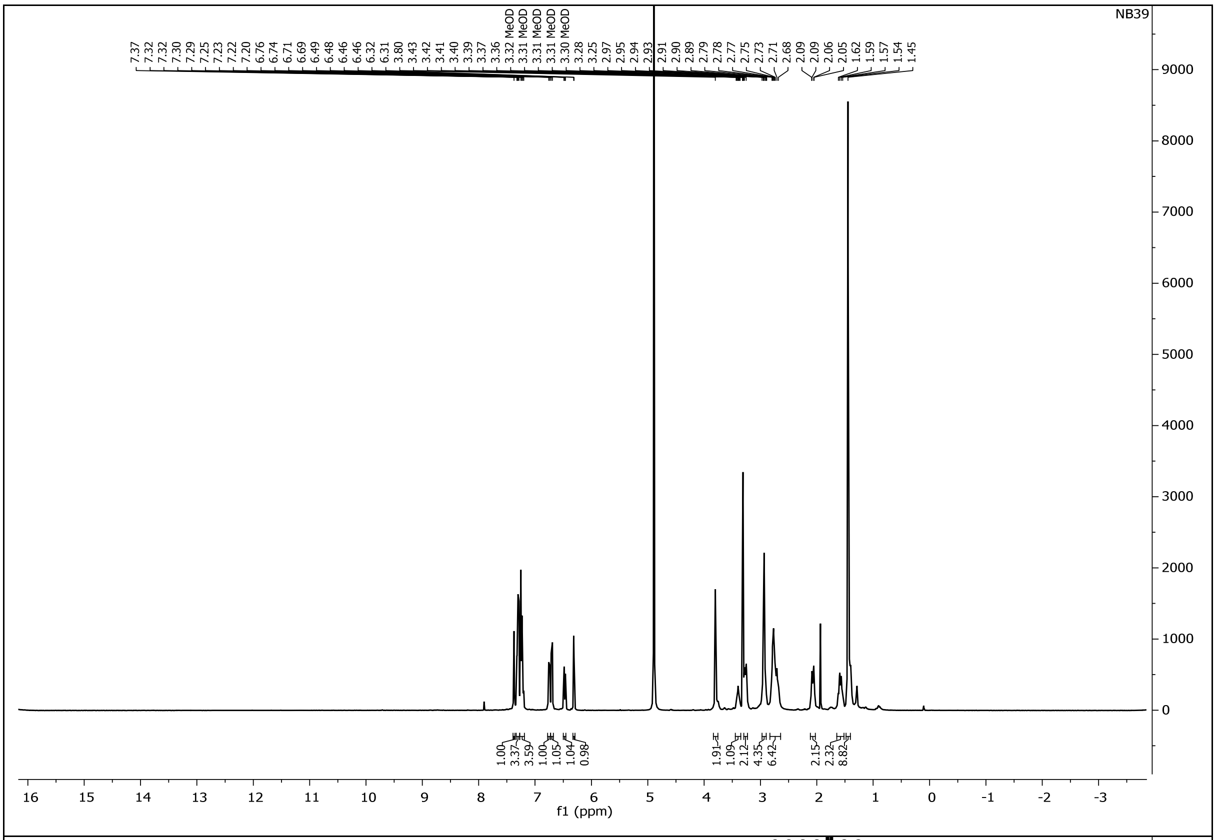

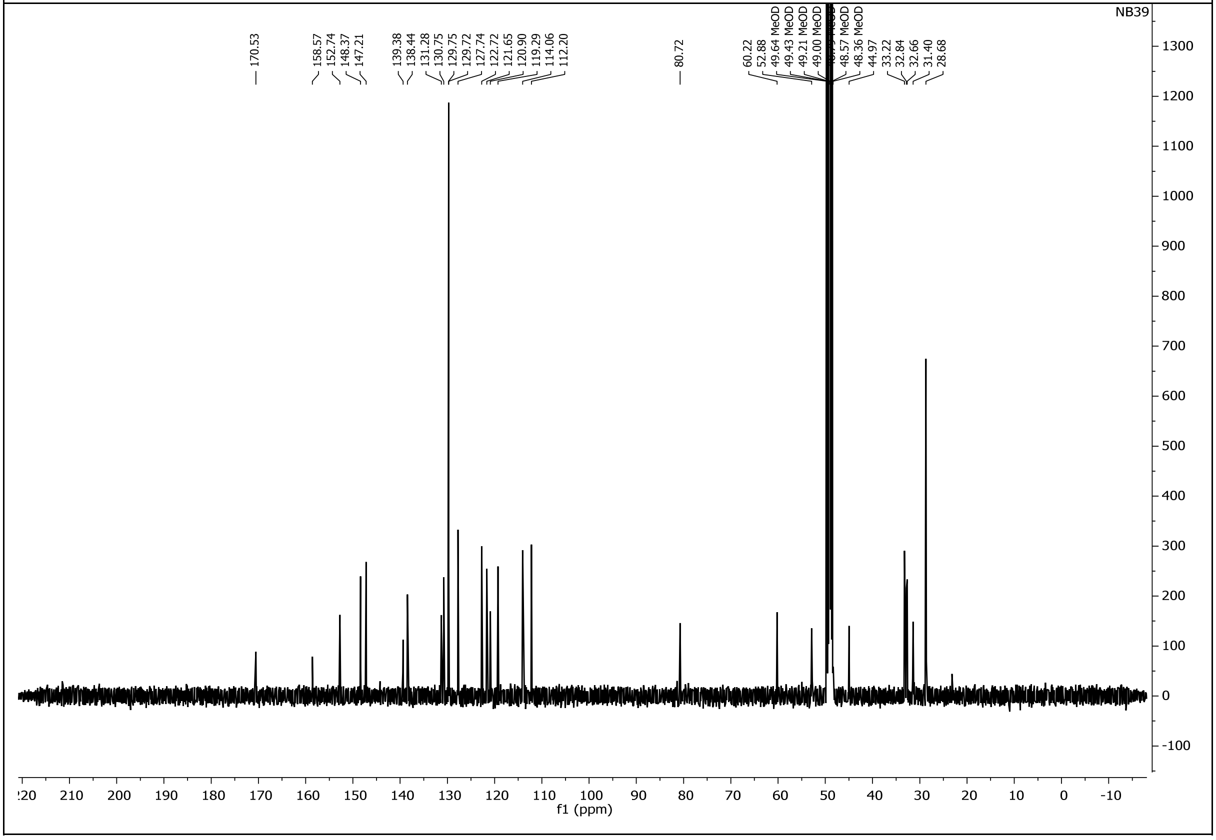

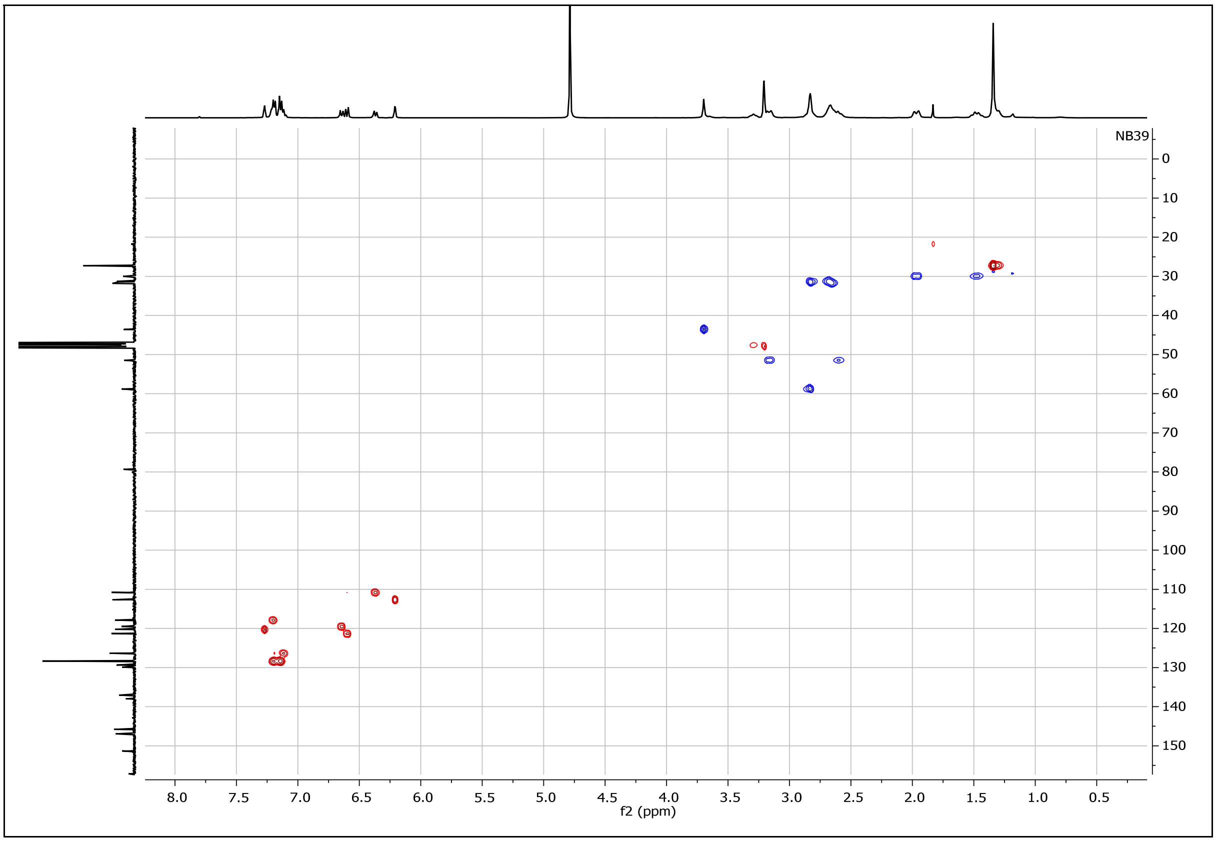
NB39
0
10
20
30
40
50
60
70
80
90
100
110
120
130
140
150
8.0
7.5
7.0
6.5
6.0
5.5
5.0
4.5
4.0
3.5
3.0
2.5
2.0
1.5
1.0
0.5
f2 (ppm)

5.4.4.19 (*Z*)-*N*-(9-(2-aminoacetamido)-11,12-dihydrodibenzo[*c*,*g*][1,2]diazocin-2-yl)-*N*-(1-phenethylpiperidin-4-yl)propionamide (**5.27**)

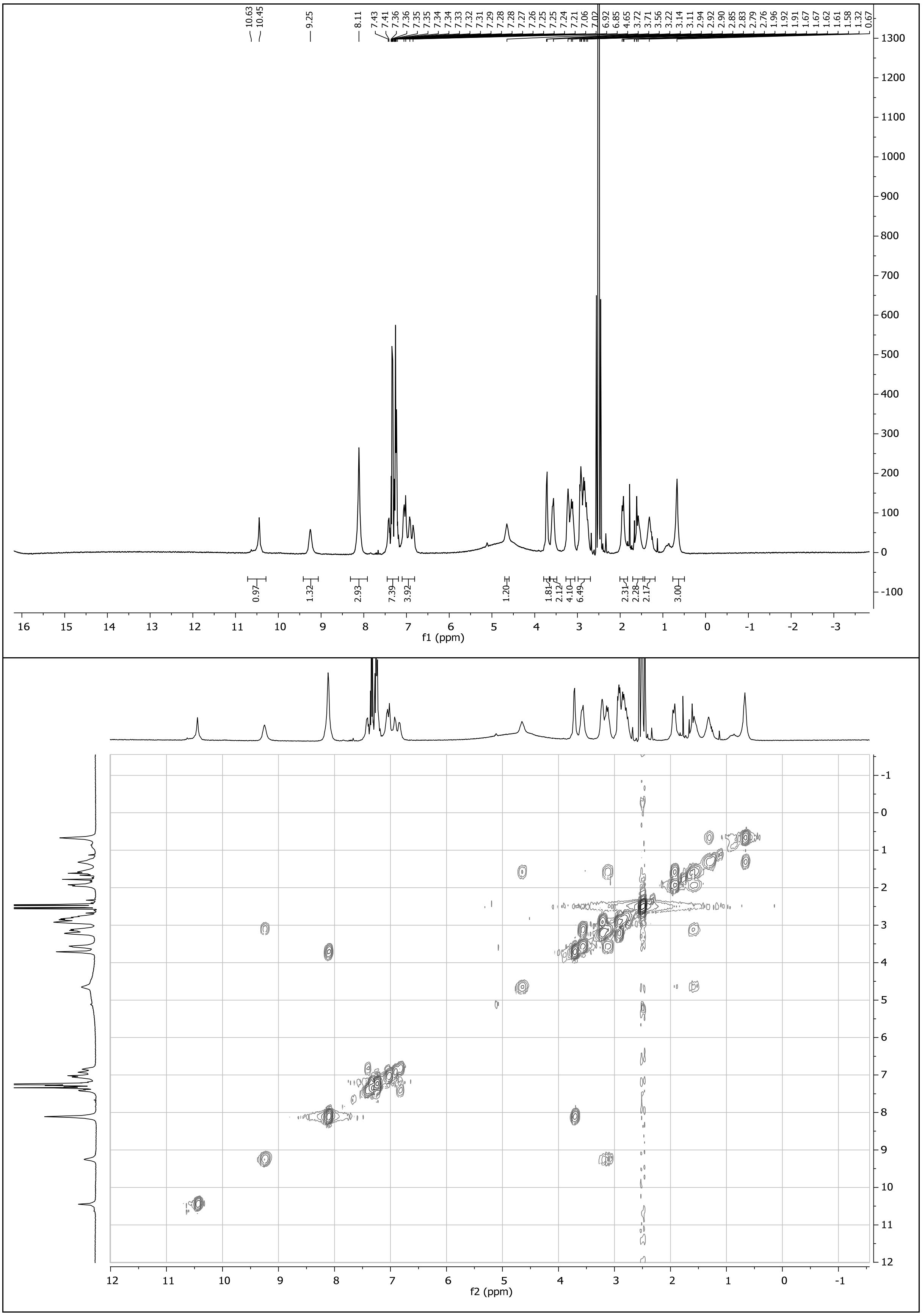

6 Optical Control of the Smoothened Receptor

6.1 Introduction

Most of our understanding of how genes drive development of animals stems from pioneering work on embryogenesis of the fruit fly *Drosophila melanogaster*,[116] which was awarded with the 1995 Nobel prize in physiology or medicine to Lewis, Nüsslein-Volhard and Wieschaus. Multiple genes were isolated that are vital for *Drosophila* embryogenesis by mutational studies and were named after the according mutants phenotype. Mutants with impaired genes involved in the Hedgehog (Hh) signaling pathway loose polarity of the evolving body segments, leading to flies with pronounced 'spikes' sticking out of their unusually short body. Today, the molecular components of the Hh signaling axis are identified: in absence of ligand, the Patched receptor is inhibiting Smoothened, keeping it sequestered in vesicles. After activation of Patched by the ligand Hh and the cell-surface co-receptor iHog, Smoothened is recruited to the plasma membrane where it activates Gli transcription regulator proteins, which in turn trigger transcription of target genes (Figure 35b).[63]

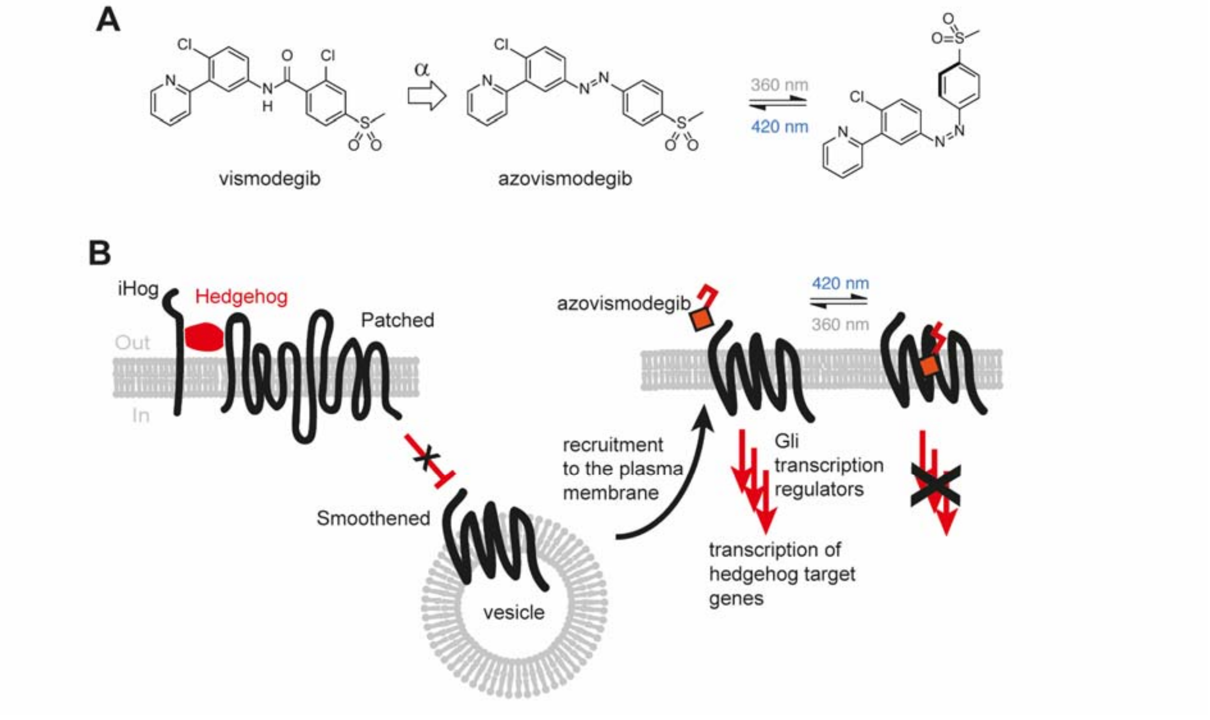

Figure 35. **Design of azovismodegib and the Hedgehog signaling pathway**. **a)** Azologization strategy for azovismodegib. **b)** In its inactive state, smoothened remains sequestered in vesicles by inhibition through patched. Upon stimulation of Patched by iHog and Hedgehog, the inhibition of Smoothened is relieved. Smoothened is then recruited to the plasma membrane where it recruits a protein complex and activates Gli transcription regulator proteins, ultimately leading to transcription of hedgehog target genes.

In humans, mutations of Smoothened are involved in basal cell carcinomas (BCC), which is the most prevalent form of cancer in Caucasians.[117] Vismodegib (Erivedge®) is a small-molecule antagonist which was approved for treatment of BCC in 2012, representing the first therapeutic targeting the Hh signaling pathway.[118] Vismodegib contains a *N*-aryl benzamide, which is a structural motif suitable for replacement by a diazene according to Trauner's azologization strategy (Figure 35a).[78] Furthermore, the conformation adopted by Vismodegib in the crystal structure with Smoothened suggest that azovismodegib should be accommodated in the proteins binding pocket in its *trans*- but not in its *cis*-configuration.[119]

6.2 Results and Discussion

Commencing with a Sandmeyer reaction of aniline **6.1** with potassium iodide afforded the iodoarene **6.2** in 44% yield. The 2-pyridyl ring was attached by Negishi-coupling with 2-bromopyridine yielded the biaryl **6.3** in 27%; this reaction proved to be a bottleneck due to the complex and tedious preparation of the reactive zinc species and unreliable yields. Attempts to improve the synthesis by using 2-pyridyl boronic acids or boronic esters to access the desired product *via* Suzuki coupling were tried and proved unsuccessful. **6.3** was reduced to aniline **6.4** in 90% yield by a suspension of powdered iron in a mixture of ethanol and acetic acid. Finally, azovismodegib **(6.6)** was obtained after Baeyer-Mills reaction of **6.4** with 1-(methylsulfonyl)-4-nitrosobenzene in 76% yield.

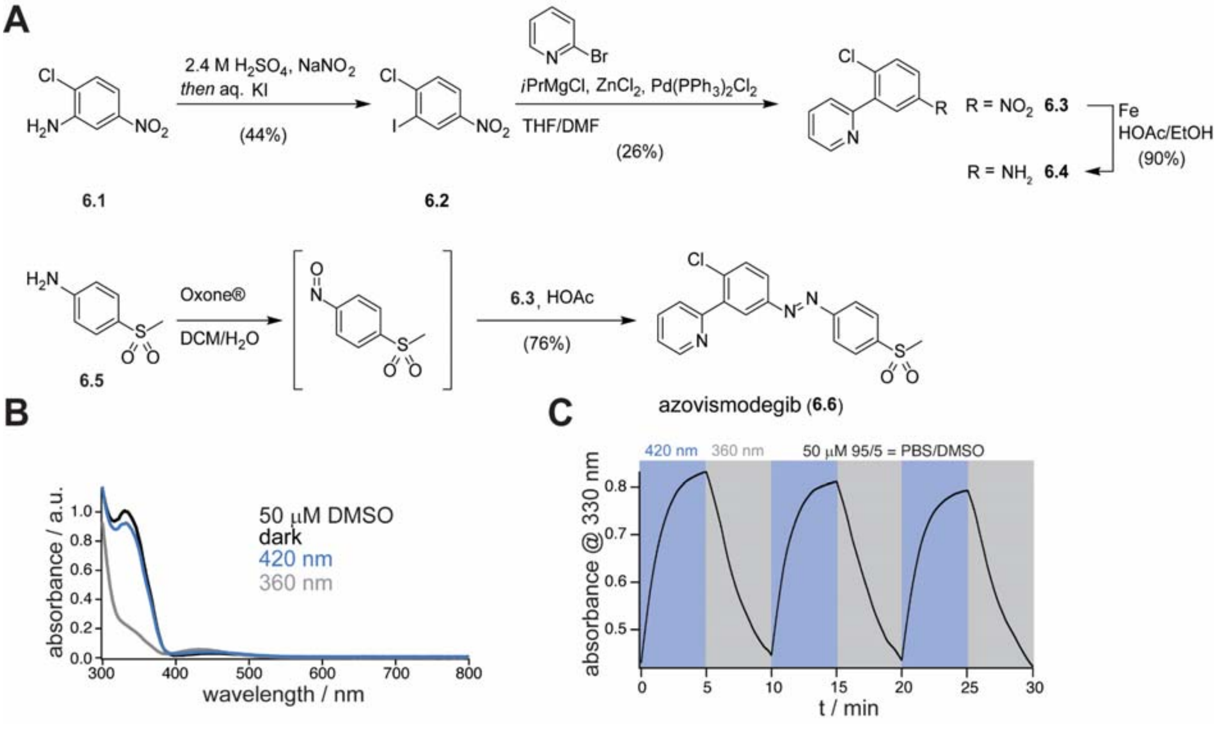

Figure 36. **Synthesis and UV/Vis-spectroscopy of azovismodegib. a)** Synthesis of azovismodegib in a four-step reaction sequence. **b)** UV/Vis spectra of azovismodegib (50 *μ*M in DMSO) were recorded in the dark and under illumination with the optimal wavelength for

switching to the *cis*-isomer (360 nm) or to the *trans*-isomer (420 nm). **c)** Switching was performed in aqueous buffer (50 μM in 95/5 = PBS/DMSO) while recording the absorbance at the absorbance maximum (330 nm) over time (τ(360 nm) = 3.73 ± 0.04 min, τ(420 nm) = 1.33 ± 0.002 min).

Azovismodegib was then tested for photoswitching. After performing a wavelength screen, optimal wavelengths for *cis*/*trans*-photoswitching were determined to be 360 nm and 420 nm. UV/Vis Spectra of azovismodegib were then recorded in the dark and under illumination with UV (360 nm) or blue light (420 nm). In addition, the kinetics of photoswitching were measured by recording the extinction at the absorbance maximum while switching UV/blue light (Figure 36c).

6.3 Summary and Outlook

Azovismodegib was accessed through a brief synthesis in four steps from commercially available starting materials. Azovismodegib behaves like a 'normal' photoswitch with bistable photostationary states and photoswitching kinetics as expected for azobenzenes with this electronic substitution pattern. At this stage, azovismodegib is being investigated for biological activity by collaborators (Ben Myers, University of Utah). To this end, NIH/3t3 cells stably expressing a Gli-responsive Firefly luciferase reporter (Shh LIGHT2 cells)[120] will be stimulated by the smoothened agonist SAG in presence of azovismodegib and under illumination with light of the appropriate wavelengths.

If azovismodegib exhibits light-dependent antagonism on Smoothened, it will be employed in more complex settings. The Hedgehog signaling axis gives the developing animal polarity, *e.g.* determines where the anterior (head) or posterior (tail) ends are. There are still many gaps in our knowledge of how this polarity arises.[121,122] With azovismodegib, we want to provide a tool which allows for a spatially defined inhibition of Smoothened. This could break down details of Hedgehog signaling in dependence of location in the developing animal, *e.g.* in *Drosophila*.

6.4 Supporting Information

6.4.1 Synthesis

6.4.1.1 1-Chloro-2-iodo-4-nitrobenzene (**6.2**)

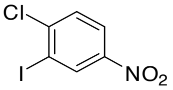

2-Chloro-5-nitroaniline (2.00 g, 11.6 mmol, 1.0 equiv.) was dissolved in 2.4 M H_2SO_4 (32 mL) and a $NaNO_2$ (0.91 g, 13.2 mmol, 1.1 equiv.) solution in water (130 mL) was added dropwise over 10 min at 0 °C. The resulting mixture was stirred for 1h at 0 °C. Then a KI (3.47 g, 13.2 mmol, 1.8 equiv.) solution in water (14 mL) was added dropwise over 15 min *via* dropping funnel at 0 °C. After addition of KI was completed, the mixture was stirred for another 2 h at room temperature. The reaction mixture was extracted with EtOAc against sodium thiosulfat solution three times. The combined organic layers were washed against brine, dried over $MgSO_4$ and concentrated in vacuo. The crude product was recrystallized from a mixture of hot *i*PrOH (13.6 mL) and hexane (5.40 mL). **6.2** was obtained as a tan powder in a yield of 44% (1.44 g, 5.10 mmol).

^{1}H-NMR (400 MHz, $CDCl_3$) δ = 8.71 (d, *J* = 2.5 Hz, 1H), 8.17 (dd, *J* = 8.8, 2.6 Hz, 1H), 7.61 (d, *J* = 8.8 Hz, 1H).

^{13}C-NMR (101 MHz, $CDCl_3$) δ = 145.9, 135.1, 129.6, 124.2, 100.0, 98.0.

HRMS (EI): *m/z* calc. for $C_6H_3ClINO_2$ $(M^+)^+$: 282.8897, found: 282.8892.

Note: Too unpolar for LCMS, no elution.

6.4.1.2 (2-Chloro-5-nitrophenyl)pyridine (**6.3**)

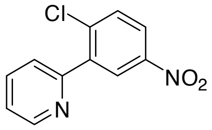

2-Bromopyridine (0.43 mL, 4.52 mmol, 1.6 equiv.) was added to dry THF (5 mL) under argon and *i*PrMgCl (3.47 mL, 4.52 mmol, 1.6 equiv.) was added dropwise at 0 °C. The mixture was stirred for 1 h at room temperature. $ZnCl_2$ (717 mg, 4.52 mmol, 1.6 equiv.) was sublimated under argon, and dissolved in dry THF (5 mL). The pyridine-2-ylmagnesium bromide solution was added to the $ZnCl_2$ solution and heated to 50 °C for 1h (solution 1). 1-Chloro-2-iodo-4-nitrobenzene (800 mg, 2.82 mmol, 1 equiv., **6.2**), bis(triphenylphosphine)palladium-(II)-chloride (60 mg, 0.09 mmol, 0.03 equiv.) and triphenylphosphine (89 mg, 0.34 mmol, 0.12 equiv.) were dissolved in dry DMF (5 mL) under argon (Solution 2). Solution 1 was added to solution 2 and heated to 60 °C overnight. The reaction mixture was cooled to room temperature, ethyl acetate (100 mL) and 2 M NaOH (100 mL) were added and stirred for 10 min. The solution was filtered over celite and washed with ethyl acetate (50 mL). The organic layer was separated and the aq. layer was extracted with ethyl acetate (3 x 100 mL). The combined organic layers were washed with brine and dried over $MgSO_4$. The product was purified by flash column chromatography (EtOAc/hexanes = 1/9). 2-(2-chloro-5-nitrophenyl)pyridine (**6.3**) was obtained as brown crystals in a yield of 26% (173 mg, 0.73 mmol).

TLC (EtOAc/hexanes = 1/9) = 0.35.

^{1}H-NMR (400 MHz, $CDCl_3$) δ (d, *J* = 4.9 Hz, 1H), 8.45 (d, *J* = 2.8 Hz, 1H), 8.14 (dd, *J* = 8.8, 2.8 Hz, 1H), 7.78 (td, *J* = 7.7, 1.7 Hz, 1H), 7.67 – 7.57 (m, 2H), 7.33 (dd, *J* = 7.6, 4.9 Hz, 1H).

HRMS (ESI): *m/z* calc. for $C_{11}H_8ClN_2O_2^+$ $(M+H)^+$: 235.0269, found: 235.0269.

***t*$_R$** (LCMS; MeCN/H_2O/formic acid = 10/90/0.1 → 100/0/0.1 over 10 min) = 7.53 min.

UV/Vis (LCMS): λ_{max1} = 194 nm, λ_{max2} = 226 nm, λ_{max3} = 270 nm.

6.4.1.3 4-Chloro-3-(pyridine-2-yl)aniline (**6.4**)

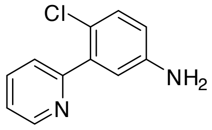

2-(2-Chloro-5-nitrophenyl)pyridine (20 mg, 0.09 mmol, 1.0 equiv., **6.3**) was dissolved in a mixture of acetic acid/ethanol (1:1, 2 ml) and added to a suspension of Fe (29mg, 0.51 mmol, 6.0 equiv.) in acetic acid/ethanol (1:2; 5 ml). The reaction mixture was heated to 60 °C for 4 h. The reaction mixture was allowed to cool to room temperature, filtered over celite, washed with EtOAc (30 mL) and concentrated *in vacuo*. The oily residue was diluted in EtOAc (30 mL), washed with aq. sat. $NaHCO_3$ (2 x 25 mL), water (2 x 10 mL), brine (30 mL) and dried over $MgSO_4$. The crude material was purified by flash column chromatography (EtOAc/ hexanes = 4:1). The desired product was obtained in a yield of 90%.

TLC (EtOAc/hexanes = 4/1) = 0.30.

^{1}H-NMR (400 MHz, $CDCl_3$) δ = 8.69 (d, *J* = 4.5 Hz, 1H), 7.82 – 7.70 (m, 1H), 7.66 (d, *J* = 7.9 Hz, 1H), 7.29 – 7.26 (m, 1H), 7.22 (d, *J* = 8.5 Hz, 1H), 6.92 (d, *J* = 2.8 Hz, 1H), 6.65 (dd, *J* = 8.5, 2.8 Hz, 1H), 3.74 (s, 2H).

^{13}C-NMR (101 MHz, $CDCl_3$) δ = 155.9, 148.4, 144.4, 138.5, 134.8, 129.7, 123.9, 121.3, 120.0, 116.7, 115.4.

HRMS (ESI): *m/z* calc. for $C_{11}H_{10}ClN_2^+$ $(M+H)^+$: 205.0527, found: 205.0527.

t_R (LCMS; MeCN/H_2O/formic acid = 10/90/0.1 → 100/0/0.1 over 10 min) = 3.20 min.

UV/Vis (LCMS): λ_{max1} = 193 nm, λ_{max2} = 231 nm, λ_{max3} = 270 nm.

Notes: Impurities (silicon grease).

6.4.1.4 (*E*)-2-(2-Chloro-5-((4-(methylsulfonyl)phenyl)diazenyl)phenyl)pyridine (**6.6**)

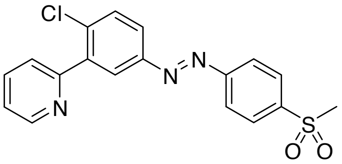

4-(Methylsulfonyl)aniline (1.71 g, 10 mmol, 1.0 equiv.) was dissolved in a biphasic mixture of DCM/water (40 mL / 40 mL) and Oxone® (6.18 g, 10 mmol) was added in one portion. The reaction mixture was stirred vigorously at r.t. for 2h while it changed color to a bright green. The reaction mixture was diluted with water (100 mL) and DCM (100 mL). The organic layer was separated and dried over $MgSO_4$ and concentrated *in vacuo*. A part of the solid residue (48 mg, 0.26 mmol, 1.5 equiv.) was used without further purification for the next step. It was added to **6.4** (56 mg, 0.17 mmol, 1.0 equiv.) dissolved in AcOH (5 mL). The reaction mixture was stirred at r.t. for 2 days before it was neutralized with aq. sat. $NaHCO_3$ and extracted with DCM. The organic layer was washed with aq. sat. $NaHCO_3$, water and brine for it was dried over $MgSO_4$ and concentrated *in vacuo*. The crude material was purified by flash column chromatography (DCM / EtOAc = 9 / 1). The desired product was obtained as an orange solid in 76% yield (47 mg, 0.13 mmol).

TLC (DCM/EtOAc = 1/9) = 0.52.

^{1}H NMR (400 MHz, $CDCl_3$) δ 8.77 (d, *J* = 4.8 Hz, 1H), 8.23 (d, *J* = 2.4 Hz, 1H), 8.07 (q, *J* = 8.5 Hz, 4H), 7.95 (dd, *J* = 8.6, 2.4 Hz, 1H), 7.82 (td, *J* = 7.7, 1.7 Hz, 1H), 7.72 (d, *J* = 7.9 Hz, 1H), 7.66 (d, *J* = 8.5 Hz, 1H), 7.35 (dd, *J* = 7.5, 4.9 Hz, 1H), 3.11 (s, 3H).

^{13}C NMR (101 MHz, $CDCl_3$) δ 155.9, 155.1, 150.8, 149.8, 142.0, 140.2, 136.1, 136.0, 131.2, 128.6, 126.4, 124.8, 124.1, 123.6, 122.9, 44.6.

HRMS (ESI): *m/z* calc. $C_{18}H_{15}ClN_3O_2S^+$ $(M+H)^+$: 372.0568, found: 372.0564.

t_R (LCMS; MeCN/H_2O/formic acid = 10/90/0.1 → 100/0/0.1 over 10 min) = 5.20.

UV/Vis (LCMS): λ_{max1} = 235nm, λ_{max2} = 226 nm, λ_{max3} = 273 nm, λ_{max4} = 327 nm.

6.4.2 Spectral Data

6.4.2.1 1-Chloro-2-iodo-4-nitrobenzene (**6.2)**

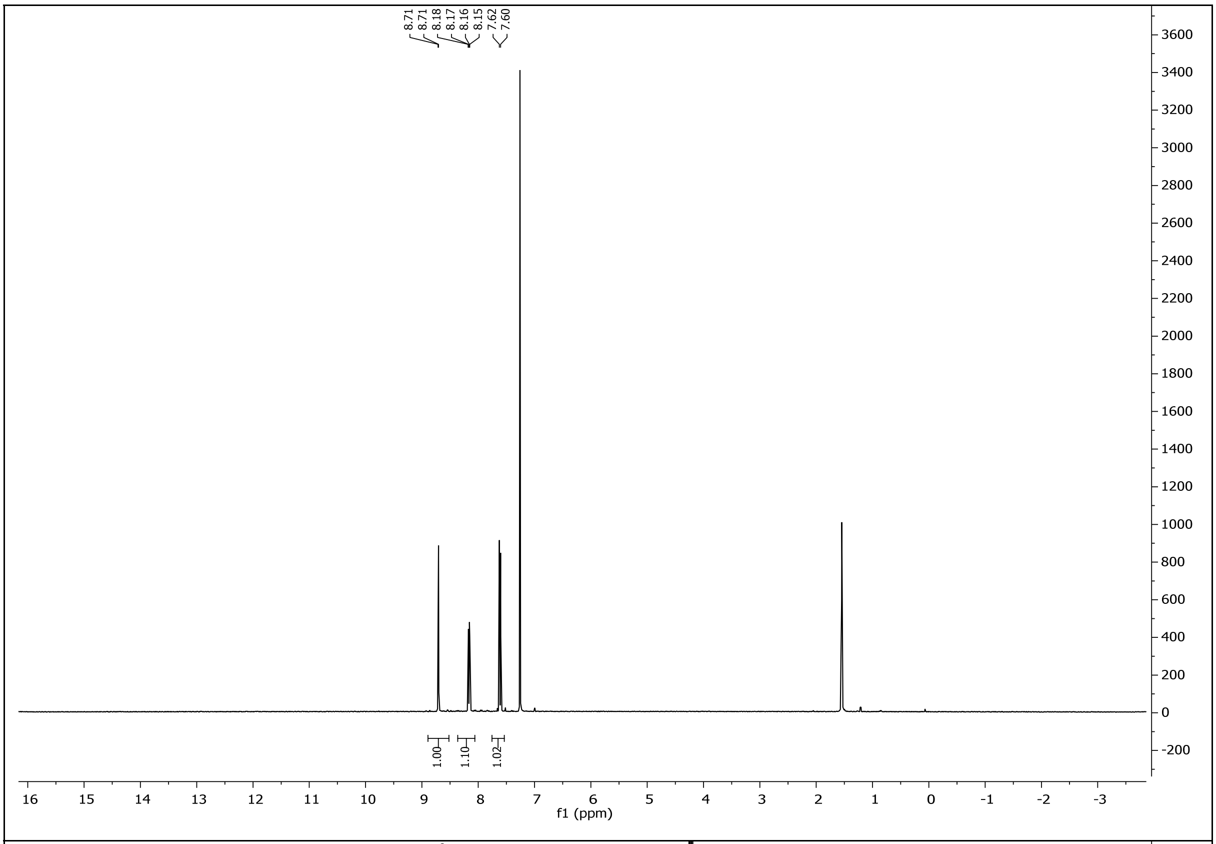

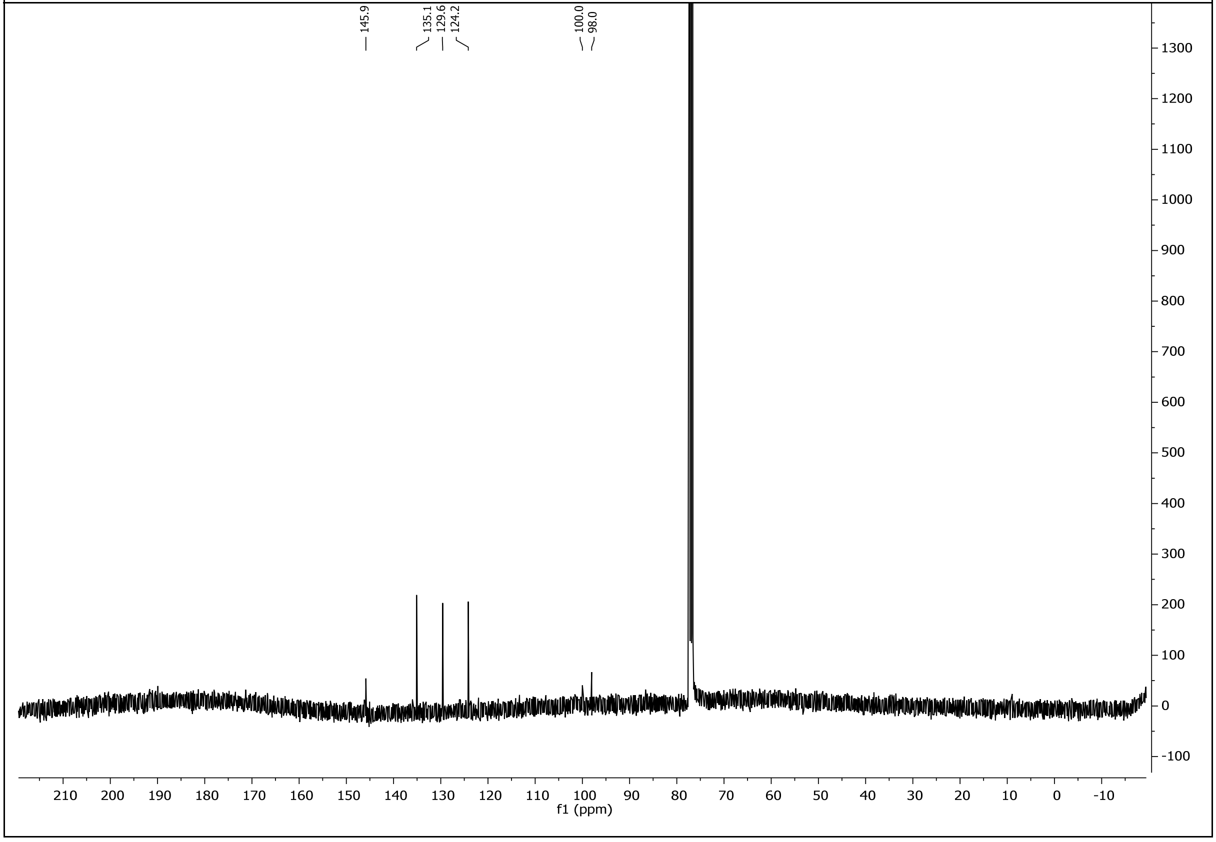

6.4.2.2 2-(2-Chloro-5-nitrophenyl)pyridine **(6.3)**

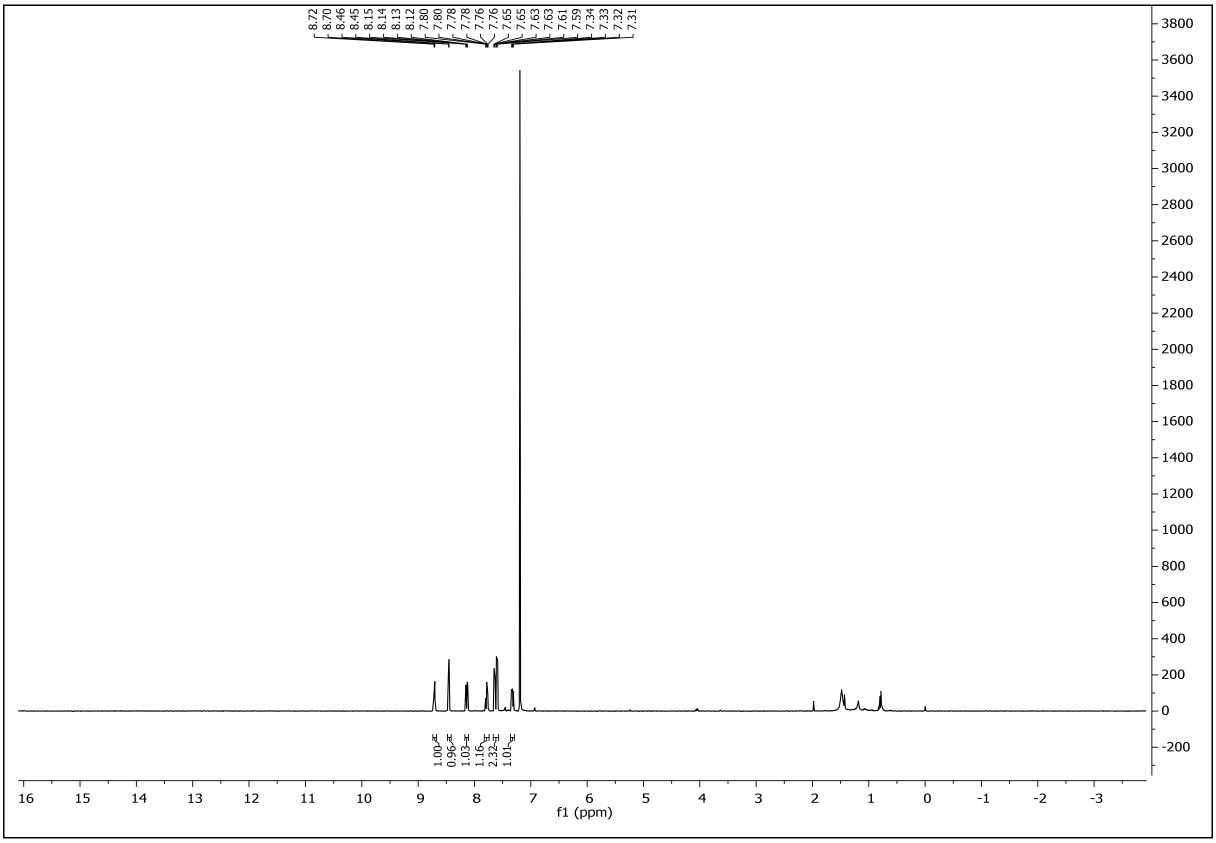

6.4.2.3 4-Chloro-3-(pyridine-2-yl)aniline **(6.4)**

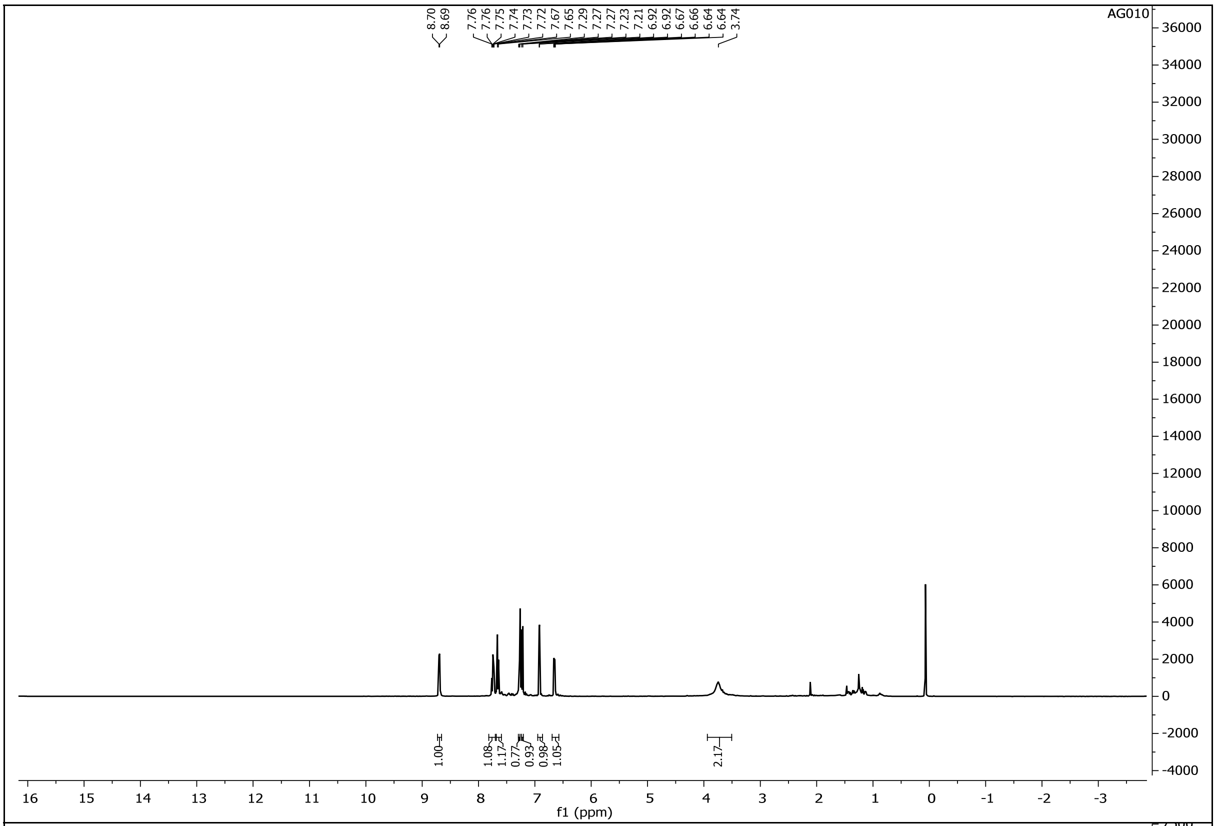

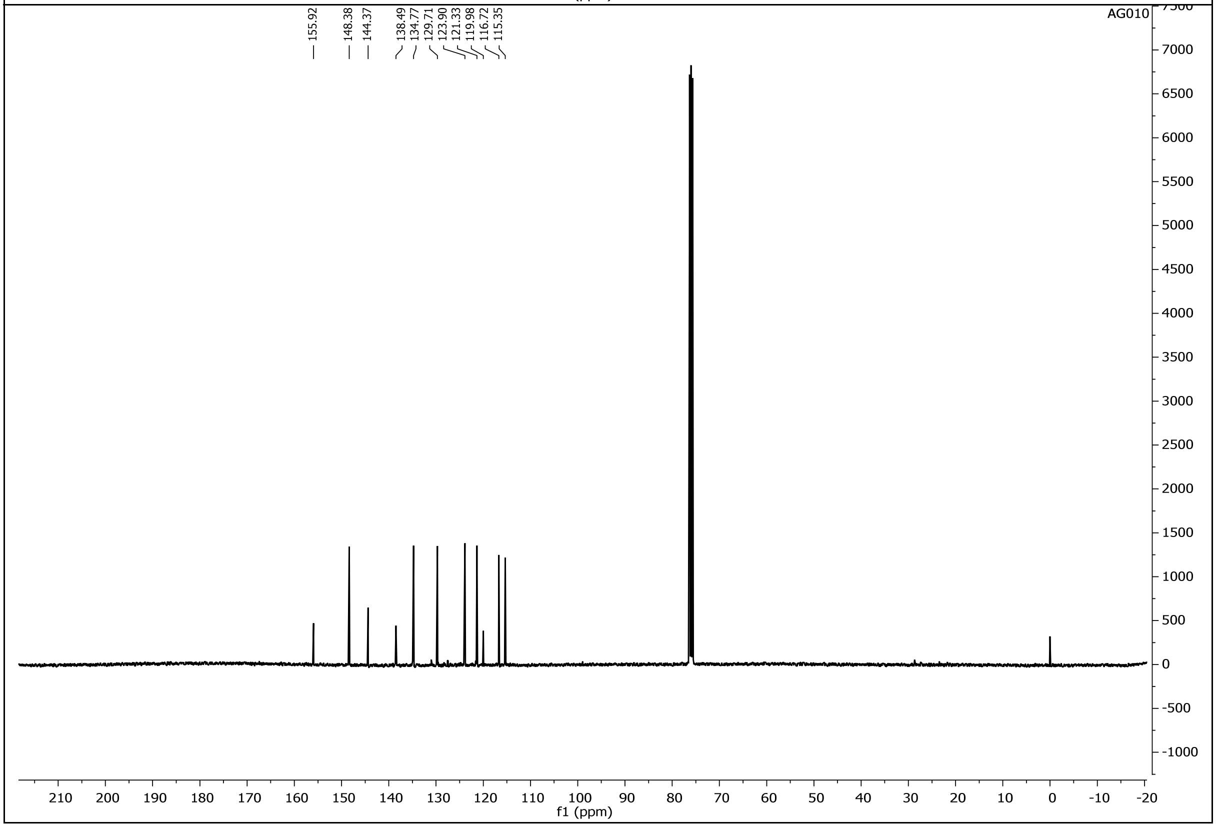

6.4.2.4 (*E*)-2-(2-Chloro-5-((4-(methylsulfonyl)phenyl)diazenyl)phenyl)pyridine **(6.6)**

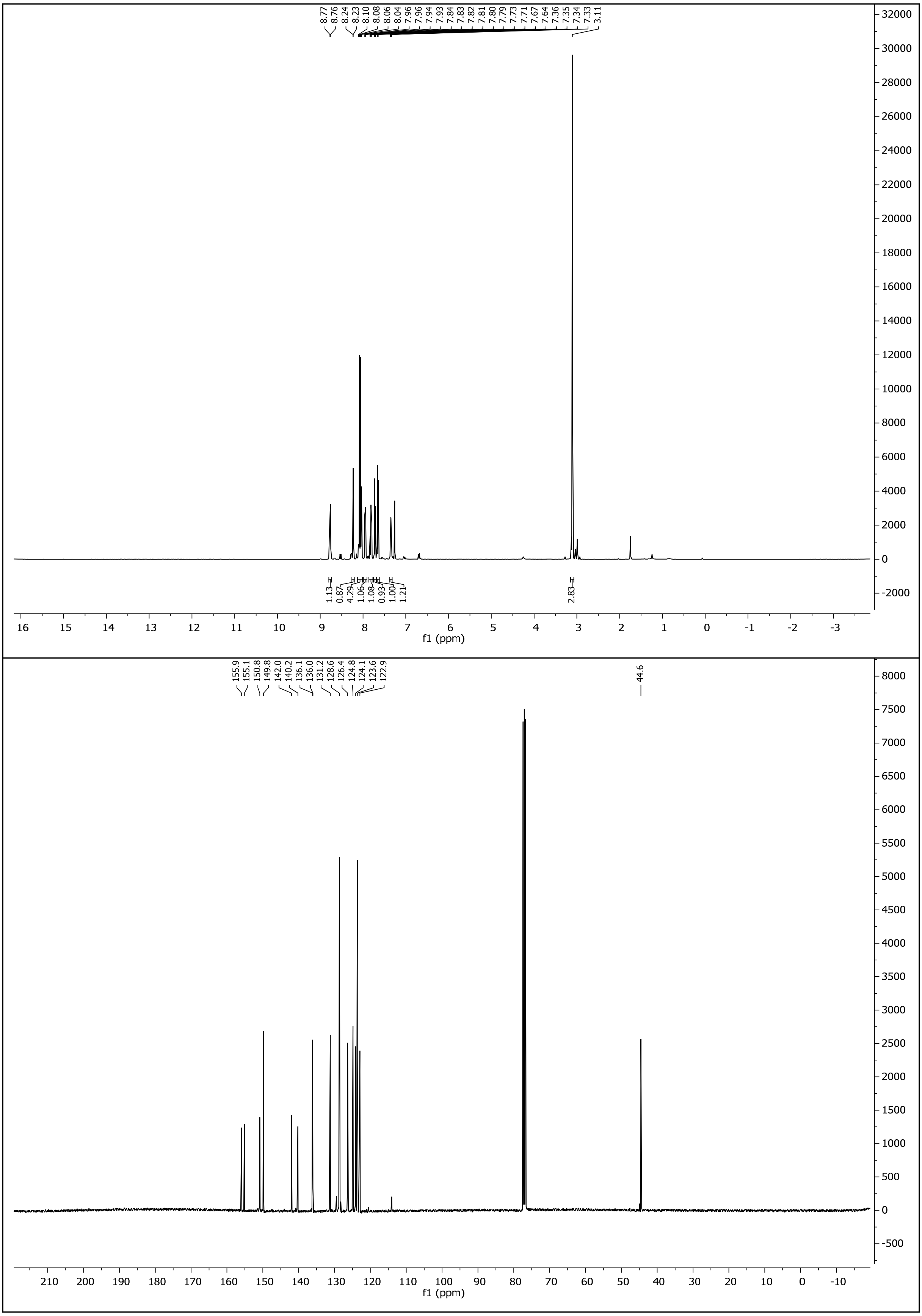

7 Photoswitchable Receptor Tyrosine Kinase Inhibitors

7.1 Introduction

Cancer is one of the biggest challenges of modern societies. According to Siegel *et al.*, more than one out of three individuals in the US are likely to suffer from some kind of invasive cancer in their lifetime, and one out of four deaths in the US is caused by cancer.[123] Cancer is a disease characterized by uncontrolled cell growth and the spread of its cells from the site of origin to other sites in the body.[124] The development of human cancer is multistep process during which several distinct biological capabilities are acquired: the so-called hallmarks of cancer. Defined by Hanahan and Weinberg in 2000, these hallmarks are characteristics shared by most types of cancer, namely the capability for autonomous growth signaling, evasion of growth inhibitory signals, evasion of apoptotic cell death, unlimited replicative potential, angiogenesis (the formation of new blood vessels), and invasion and metastasis.[125] Since RTKs are key regulators of cell growth and cell cycle growth, mutation or overexpression of RTKs is often closely linked to mutagenesis. As such, they constitute an important drug target for cancer therapy.[126] Tyrosine-kinase-inhibitors (TKIs) can be ATP-mimetics, which block the ATP binding pocket of the tyrosine kinase (TK) domain, therefore blocking auto-phosphorylation and locking the RTK in its auto-inhibited state.

A major drawback of TKIs is the lack of selectivity against tumor cells versus normal cells. As a result, chemotherapy with TKIs is often accompanied by harsh side-effects.[127] Indeed, photoswitchable drugs could offer a solution to this issue. After systemic application of a photoswitchable drug by oral uptake, it is distributed in the body in its dark adapted, inactive form. Tumor cells would then be locally exposed to light, and the photoswitchable drug is turned ON, resulting in RTK inhibition. Only the illuminated area, *i.e.* the tumor, is exposed to the active drug, limiting off-target effects in healthy, surrounding tissue. This approach combines the precision of radiotherapy with the efficacy of chemotherapy and represents another leap that photopharmacology could take.

Axitinib is a small molecule TKI which showed promising results in the treatment of various cancer types. For instance, it reduced growth of breast cancer in xenograft tumor mouse models and is now approved by the FDA for treatment of metastatic renal cell carcinoma (mRCC). It is acting through inhibition of the vascular endothelial growth factor receptors (VEGFR) 1-3, mast/stem cell growth factor receptor (c-KIT) and the platelet-derived growth factor receptor (PDGFR).[128,129] Axitinib is a TKI that blocks the ATP-binding site. For productive binding of ATP, the juxtamembrane domain (JM) has to switch from JM_{in} to JM_{out}, which allows the DFG motif to switch from its inactive ‘out’ to its active ‘in’ position. Crystal structures of

Axitinib in complex with non-phosporylated VEGFR2 revealed that it acts by blocking the JM_{in} to JM_{out} transition, thereby locking the RTK in its auto-inhibited state.[130] Key interactions of Axitinib with the protein are two hydrogen bonds and one hydrophobic stabilization between the amide head group with D146, E885 and I804 of VEGFR2. The pyrazol nitrogen atoms are acting as hydrogen bond donor or acceptor to the protein backbone.[130] The vinylpyridine moiety is mostly responsible for solubility an the metabolic and pharmacokinetic properties of the drug.

We envisioned that Axintinib could be turned into a photoswitchable drug by replacing the diarylethene moiety by a diazene.

7.2 Results and Discussion

First, unsuccessful syntheses were aimed at installing phenylhydrazine *via* cross-coupling with the 3-halogenated benzopyrazol. Subsequent oxidation of the resulting diarylhydrazine would then give the diazene. Therefore, the synthetic route was changed (Scheme 13). **7.1** was condensed with hydrazine to yield the aminoindazole **7.2**. **7.2** was reacted with 2-nitrosopyridine[131] in a Baeyer-Mills reaction to give access to the heterocyclic azobenzene **7.3**. The final AzoAxitinib **7.5** was then obtained by Pd-catalyzed cross-coupling with aryl thiol **7.4**. To fine tune photophysical properties, one diazene with a benzene instead of the pyridine and one red-shifted variant were synthesized. Since cross couplings with **7.10**, the benzene-analogue of **7.3** were unsuccessful. Therefore, the reaction sequence was reversed. To this end, **7.1** was cross-coupled to aryl thiol **7.4** to yield diaryl sulfide **7.6.** Subsequent condensation with hydrazine gave access to **7.7.** Sandmeyer reaction with potassium iodide yielded the 3-iodo derivative that was used for X-ray crystallography after recrystallization from ethanol. **7.7** was then reacted in a Baeyer-Mills reaction with nitrosobenzene to yield **7.8**: The red-shifted variant **7.9** was obtained by diazotation of **7.7** and subsequent capture with *N,N*-diethylaniline.

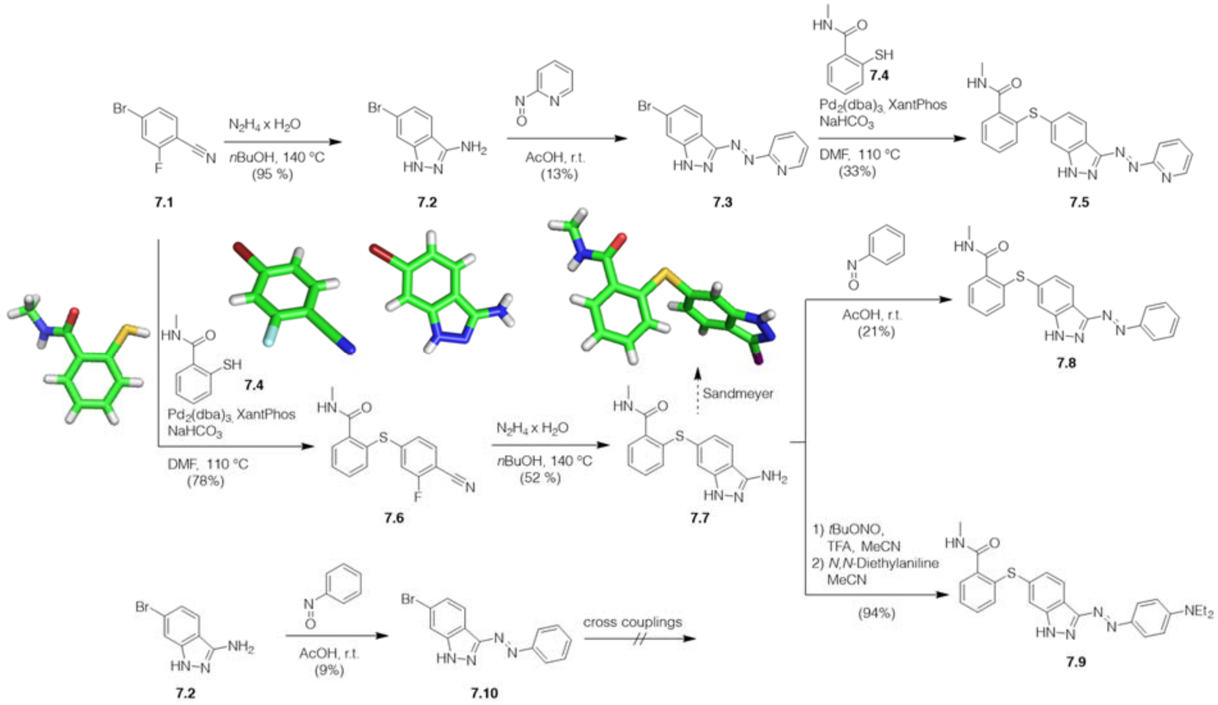

Scheme 13. **Synthesis of AzoAxitinibs 7.5, 7.8 and 7.9.**

The three photoswitches were then evaluated for their photophysical properties by UV/Vis spectroscopy (Figure 36). The photoswitches behave very similar, they all relax back to the *trans*-isomer in the dark. The optimal wavelengths for the *cis*-isomerization of pyridine-diazene **7.5** is 380 nm, which is the same wavelength for the phenyl-diazene **7.8**. Both absorption spectra are very similar, but the kinetics of photoisomerization are different. **7.5** *cis*-isomerizes significantly slower with $\tau = 0.22$ min compared to $\tau = 0.14$ min for **7.8**. Both **7.5** and **7.8** isomerize back to the trans under thermal conditions in the dark. The *trans*-isomerization of **7.5** is slower with $\tau = 0.17$ min compared to $\tau = 0.10$ min for **7.8**. For azobenzenes, substitution in *para*-position of the diazene bond with an electron-donating substituent leads to red-shifting of the cis-isomerization while the thermal backrelaxation to *trans* is proceeding faster. This is not the0 case for the heterocyclic azobenzenes shown here, when an electron-donating diethylamine is installed on **7.8**, the rate of back-relaxation is slowed. The red-shifted **7.9** is isomerized to *cis* with blue light (460 nm), with $\tau = 0.13$ min. The backrelaxation to trans in the dark is significantly slower with $\tau = 0.42$ min.

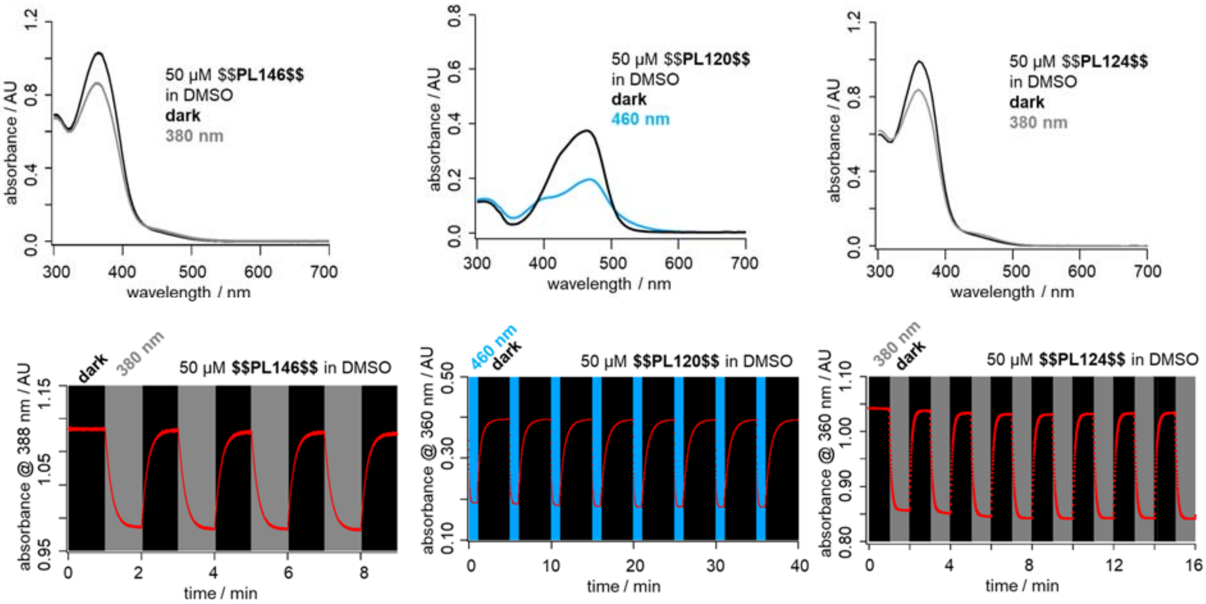

Figure 37. **UV/Vis spectroscopy of AzoAxitinibs 7.5, 7.9 and 7.8. 7.5** τ(cis) = 0.22 ± 0.001 min, τ(trans) = 0.17 ± 0.0002 min; **7.9** τ(cis) = 0.13 ± 0.007 min, τ(trans) = 0.42 ± 0.001 min; **7.8** τ(cis) = 0.14 ± 0.003 min, τ(trans) = 0.10 ± 0.0001 min;

7.5 was evaluated for light-dependent bioactivity by a proliferation (MTT) assay of HUVEC cells (human umbilical vein endothelial cells, kind gift from Carlo Mümmler, CPC Munich). In the dark, **7.5** inhibited cell proliferation with IC50 = 67 nM (Figure 38). Under illumination with violet light (390 nm), the IC50 decreased to 183 nM.

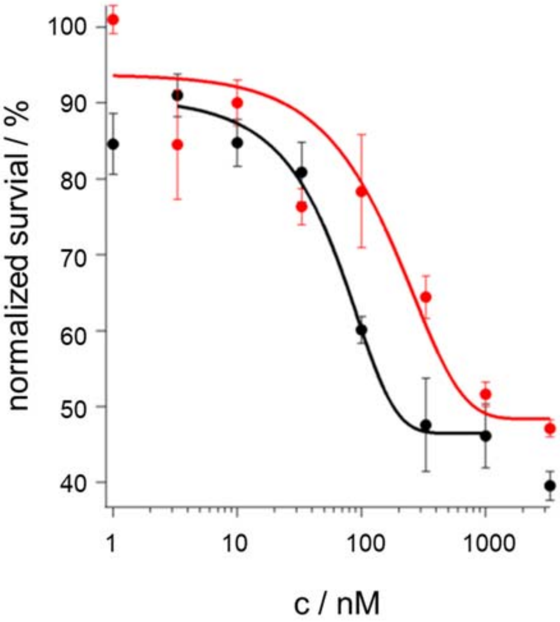

Figure 38. **MTT assay with HUVEC cells and 7.5.** Red: 390 nm, black: dark; error bars represent standard deviation. Survival was normalized to vehicle control (0.2% DMSO). IC_{50} (dark) = 67 nM; IC_{50} (390 m) = 183 nM.

7.3 Summary and Outlook

Here, photoswitchable variants of the cancer drug Axitinib were described. Proliferation assays indicated that the installation of the photoswitch was not deleterious to the inhibitory effects of Axitinib. Nevertheless, the difference in IC_{50} between *trans*- and *cis*- isomers of AzoAxitinib **7.5** is only ~3-fold. As an assay method, proliferation is a downstream phenotypic effect, is dependent on many effects, and can lead to misleading conclusions. To better understand the structure-activity relationship (SAR) of *cis*- and *trans*-AzoAxitinib, more simple assays, such as phosphorylation assays should be employed. This could help with the design of improved photoswitches with higher differences in affinity upon photoisomerization.

AzoAxitinib **7.5** represents a new type of photoswitch that features an indazole and a pyridine. Indeed, the photophysical properties of AzoAxitinib **7.5** are very similar to common azobenzene derivatives. This class of indazole-containing diazene was only recently described by Travieso-Puente *et al.*[132] Their synthesis featured a nucleophilic aromatic substitution to form the 5-membered indazole-ring and is limited to strongly electron-deficient aromatics. On the other hand, the azo-bonds of AzoAxitinibs **7.5**, **7.8** and **7.9** were installed *via* well-known Baeyer-Mills reactions or diazotation from the 3-amino indazole derivative. As such, these syntheses represent a facile method of constructing this type of photoswitch and expands the ‘azologable’ space even further.

7.4 Supporting Information

HUVEC cells were grown in EGM2 medium (Lonza), supplemented with 10% FCS. Cells were seeded on two 96w plates (5000 cells/well). After 1d, cells were starved in 1%FCS/EBM2 (Lonza). Compound was applied, one plate was kept in the dark and one was illuminated by an LED array at 390 nm (72 LEDs) from above, 50 ms light pulses every 3 seconds. 1-2h after compound application, 2 μL/well VEGF (human, 1 ng/μL) was added. The next day, 10 μL MTT/PBS was added, and the MTT assay was performed as previously described.[62]

7.4.1 Synthesis

7.4.1.1 2-Mercapto-*N*-methylbenzamide (**7.4**)

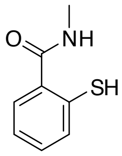

Synthesis of **7.4** was carried out according to a literature procedure.[133] Briefly, methylamine-hydrochloride (2.00 g, 29.6 mmol, 2.0 equiv.) was suspended in dry DCM (20 mL) and cooled to 0°C. $AlMe_3$ (2 M in toluene, 14.9 mL, 29.8 mmol, 2.0 equiv.) was added dropwise. The mixture was stirred at 0 °C for 15 min and allowed to warm to r.t. After the gas evolution ceased, *N*-methyl thiosalicylate (2.50 g, 14.86 mmol, 1.0 equiv.) was added dropwise. The yellow reaction mixture was heated to reflux for 6 h. Then, the reaction mixture was cooled to r.t. and carefully quenched with 1 M aq. HCl. The organic layer was separated and the aqueous layer was extracted with DCM (3 x 30 mL). The combined organic layers were dried over $MgSO_4$ and evaporated. Recrystallization from diethyl ether yielded **7.4** as colorless crystals (1.33 g, 7.92 mmol, 53%) suitable for single-crystal X-ray diffraction.

^{1}H NMR (400 MHz, $CDCl_3$) δ = 7.39 (dd, *J* = 7.7, 1.4 Hz, 1H), 7.28 (dd, *J* = 7.9, 1.3 Hz, 1H), 7.21 (td, *J* = 7.6, 1.5 Hz, 1H), 7.08 (td, *J* = 7.5, 1.3 Hz, 1H), 6.33 (s, 1H), 4.73 (s, 1H), 2.94 (d, *J* = 4.9 Hz, 3H).

^{13}C NMR (101 MHz, $CDCl_3$) δ = 169.5, 132.9, 132.9, 130.8, 130.5, 128.0, 125.0, 26.7.

HRMS (ESI): *m/z* calc. for $C_8H_8NOS^-$ [M-H]**-**: 166.0332, found: 166.0321.

t$_R$ (LCMS, MeCN/H_2O/formic acid = 90/10/0.1 → 10/90/0.1 over 7 min) = 2.57 min.

UV/Vis (LCMS): λ_{max} = 297 nm.

7.4.1.2 6-Bromo-1*H*-indazol-3-amine (**7.2**)

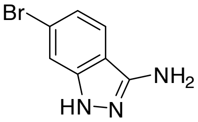

7.2 was synthesized according to a patent procedure.[134] Briefly, 4-bromo-2-fluoro-benzonitrile (1.00 g, 5.00 mmol, 1.0 equiv.) and hydrazine hydrate (785 µL, 25.0 mmol, 5 equiv.) were dissolved in *n*-butanol (6 mL) and refluxed for 2 h. The reaction mixture was allowed to cool to r.t., before filtering over a glass frit. The colorless crystals were washed with EtOAc and dried in vacuo to yield the desired product (1.01 g, 4.76 mmol, 95%).

^{1}H NMR (400 MHz, DMSO-*d*$_6$) d = 7.64 (d, *J* = 8.5 Hz, 1H), 7.47–7.38 (m, 1H), 7.02 (d, *J* = 8.7 Hz, 1H), 5.48 (s, 2H).

^{13}C NMR (101 MHz, DMSO-*d*$_6$) d = 149.8, 142.5, 122.6, 120.8, 120.3, 113.5, 112.3.

HRMS (ESI): *m/z* calc. for $C_7H_7BrN_3^+$ [M+H]$^+$: 211.9818, found: 211.9817.

7.4.1.3 (*E*)-6-Bromo-3-(pyridin-2-yldiazenyl)-1*H*-indazole (**7.3**)

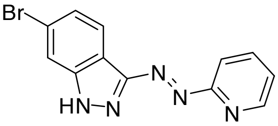

The 2-nitrosopyridine was prepared according to a published procedure.[131] The crude nitroso compound was extracted and washed according to the original procedure. The product containing DCM layers were then carefully concentrated to dryness with the rotary evaporator at ~25 °C and the crude tan material was stored at -20°C until further use.

7.2 (500 mg, 2.4 mmol, 1.0 equiv.) was suspended in AcOH (15 mL) and crude 2-nitrosopyridine (384 mg, th. 3.6 mmol, th. 1.5 equiv.) was added in one portion. The reaction mixture immediately turned green. The reaction mixture was allowed to stir for a few hours before it was extracted with DCM against sat. aq. $NaHCO_3$ (3x). The combined organic layers were concentrated *in vacuo* before purification by flash column chromatography (dry load on silica) to yield the product as a yellow solid (98 mg, 0.32 mmol, 13%).

^{1}H NMR (400 MHz, DMSO-*d*$_6$) δ 14.27 (s, 1H), 8.80 – 8.72 (m, 1H), 8.25 (d, *J* = 8.6 Hz, 1H), 8.08 (td, *J* = 7.7, 1.7 Hz, 1H), 7.94 (s, 1H), 7.84 (d, *J* = 8.0 Hz, 1H), 7.60 (dd, *J* = 7.3, 4.8 Hz, 1H), 7.56 (dd, *J* = 8.6, 1.5 Hz, 1H).

^{13}C NMR (101 MHz, DMSO) δ 163.7, 155.6, 150.0, 142.7, 139.4, 128.2, 126.3, 124.7, 121.4, 114.1, 113.4, 112.3.

HRMS (ESI): *m/z* calc. for $C_{12}H_9BrN_5^+$ $[M+H]^+$: 302.0036, found: 302.0037.

***t*$_R$** (LCMS, MeCN/H_2O/formic acid = 90/10/0.1 → 10/90/0.1 over 7 min) = 4.16 min.

UV/Vis (LCMS): λ_{max} = 361 nm.

7.4.1.4 (*E*)-*N*-Methyl-2-((3-(pyridin-2-yldiazenyl)-1*H*-indazol-6-yl)thio)benzamide (**7.5**)

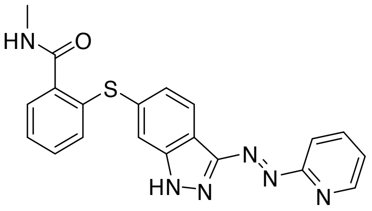

7.3 (90 mg, 0.30 mmol, 1.0 equiv.), **7.4** (50 mg, 0.30 mmol, 1.0 equiv.), $Pd_2(dba)_3$ (5.5 mg, 6 μmol, 0.02 equiv.), XantPhos (7.0 mg, 12 μmol, 0.04 equiv.) and $NaHCO_3$ (28 mg, 0.33 mmol, 1.1 equiv.) were combined in a Schlenk flask. The flask was evacuated and backfilled with nitrogen for three times, before dry DMF (1 mL) was added. The reaction mixture was heated to 120 °C for 24 h before it was allowed to cool to r.t. The reaction mixture was extracted with EtOAc against sat. aq. $NaHCO_3$ (3x). The combined organic layers were washed with water and brine, dried over $MgSO_4$ and concentrated *in vacuo*. The desired product was obtained after flash column chromatography (dry load, 5% MeOH/DCM) as an orange solid (38 mg, 98 μmol, 33%).

^{1}H NMR (400 MHz, DMSO-*d*$_6$) δ 14.19 (s, 1H), 8.75 (dd, *J* = 4.9, 1.6 Hz, 1H), 8.42 (q, *J* = 4.6 Hz, 1H), 8.30 (d, *J* = 8.4 Hz, 1H), 8.08 (td, *J* = 7.8, 1.8 Hz, 1H), 7.84 (d, *J* = 8.1 Hz, 1H), 7.65 (s, 1H), 7.59 (dd, *J* = 7.4, 4.8 Hz, 1H), 7.51 (dd, *J* = 7.0, 2.1 Hz, 1H), 7.39 – 7.28 (m, 3H), 7.11 (dd, *J* = 7.3, 1.7 Hz, 1H), 2.76 (d, *J* = 4.5 Hz, 3H).

^{13}C NMR (101 MHz, DMSO) δ 168.3, 163.7, 155.7, 149.9, 142.5, 139.4, 138.0, 135.2, 135.1, 131.1, 130.9, 128.9, 128.3, 127.1, 126.2, 123.9, 114.7, 113.4, 112.5, 40.6, 40.6, 40.4, 40.4, 40.2, 40.2, 39.9, 39.7, 39.5, 39.3, 26.6.

HRMS (ESI): *m/z* calc. for $C_{20}H_{17}N_6OS^+$ $[M+H]^+$: 389:1179, found: 389.1178.

***t*$_R$** (LCMS, MeCN/H_2O/formic acid = 90/10/0.1 → 10/90/0.1 over 7 min) = 3.53 min.

UV/Vis (LCMS): λ_{max} = 380 nm.

7.4.1.5 2-((4-Cyano-3-fluorophenyl)thio)-*N*-methylbenzamide (**7.6**)

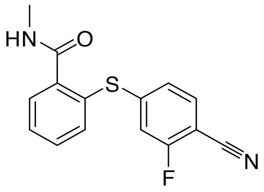

7.4 (600 mg, 3.00 mmol, 1.0 equiv.), $Pd_2(dba)_3$ (28 mg, 30 *µ*mol, 0.01 equiv.), XantPhos (35 mg, 60 *µ*mol, 0.02 equiv.) and $NaHCO_3$ (277 mg, 3.30 mmol, 1.1 equiv.) were combined in a Schlenk flask. The flask was evacuated and backfilled with nitrogen for three times, before dry *N*-methylpyrrolidinone (3 mL) was added. The reaction mixture was stirred at r.t. for 30 min before 4-bomo-2-fluorobenzonitrile **7.1** (506 mg, 3.00 mmol, 1.0 equiv.; dissolved in 3 mL N-methylpyrrolidinone) was added dropwise. The reaction mixture was heated to 50 °C for 5 h before it was allowed to cool to r.t. The reaction mixture was extracted with DCM against water (3x). The combined organic layers were washed with water, sat aq. LiCl, brine, dried over $MgSO_4$ and concentrated *in vacuo*. The desired product was obtained after flash column chromatography (2% MeOH/DCM) as a white solid (670 mg, 2.34 mmol, 78%).

^{1}H NMR (400 MHz, $CDCl_3$) δ 7.59 (dd, *J* = 5.6, 2.6 Hz, 1H), 7.44 (dt, *J* = 16.4, 5.9 Hz, 4H), 6.99 (d, *J* = 8.3 Hz, 1H), 6.90 (d, *J* = 9.5 Hz, 1H), 6.29 (s, 1H), 3.04 – 2.70 (m, 3H).

^{13}C NMR (101 MHz, $CDCl_3$) δ 168.2, 164.4, 161.8, 147.9, 147.8, 140.6, 135.8, 133.3, 131.3, 129.9, 128.9, 128.4, 123.8, 123.8, 115.3, 115.1, 113.9, 98.3, 98.1, 77.4, 77.1, 76.8, 26.8.

HRMS (ESI): *m/z* calc. for $C_{15}H_{12}FN_2OS^+$ $[M+H]^+$: 287.0649, found: 287.0650.

7.4.1.6 2-((3-Amino-1*H*-indazol-6-yl)thio)-*N*-methylbenzamide (**7.7**)

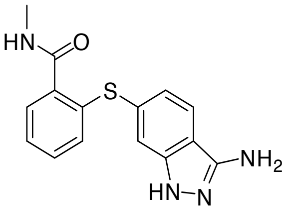

7.6 (573 mg, 2.00 mmol, 1.0 equiv.) and hydrazine hydrate (0.5 mL; 10.0 mmol, 5 equiv.) were combined in *n*BuOH (~7 mL). The reaction mixture was refluxed overnight before it was allowed to cool to r.t. The reaction mixture was extracted with EtOAc against sat. aq. $NaHCO_3$ (3x). The combined organic layers were washed with brine, dried over $MgSO_4$ and concentrated to dryness. The crude material was purified by C18 reverse-phase column chromatography (100/0 → 60/40 = 1 mM aq. HCl/MeCN) to yield the product as colorless crystals (311 mg, 1.04 mmol, 52%).

For X-Ray crystallography, the product was dissolved in MeCN and *t*BuONO was added. After 30 min, aq. KI solution was added. Single crystals suitable for X-Ray crystallography were obtained by crystallization from hot EtOH.

^{1}H NMR (400 MHz, Methanol-*d*$_4$) δ 7.52 (d, *J* = 8.3 Hz, 1H), 7.33 – 7.26 (m, 1H), 7.24 (s, 1H), 7.18 – 7.08 (m, 2H), 7.04 – 6.97 (m, 1H), 6.83 (dd, *J* = 8.4, 1.6 Hz, 1H), 3.97 (q, *J* = 7.1 Hz, 1H), 2.74 (s, 3H), 1.89 (s, 1H), 1.18 – 1.06 (m, 1H).

^{13}C NMR (101 MHz, Methanol-*d*$_4$) δ 170.4, 149.2, 142.3, 137.0, 135.7, 133.8, 130.8, 130.2, 127.5, 126.2, 122.6, 120.6, 113.6, 113.2, 48.3, 48.1, 47.9, 47.8, 47.6, 47.4, 47.2, 47.0, 25.4.

HRMS (ESI): *m/z* calc. for $C_{15}H_{15}N_4OS^+$ [M+H]$^+$: 299.0961, found: 299.0962.

7.4.1.7 (*E*)-*N*-Methyl-2-((3-(phenyldiazenyl)-1*H*-indazol-6-yl)thio)benzamide (**7.8**)

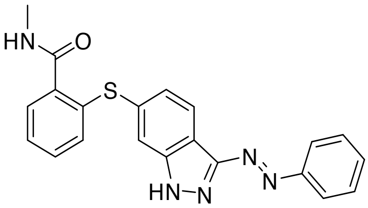

7.7 (52 mg, 0.17 mmol, 1.0 equiv.) was dissolved in 2 mL AcOH and nitrosobenzene (21 mg, 0.20 mmol, 1.2 equiv.) was added in one portion. The reaction mixture was heated overnight at 60 °C before it was allowed to cool to r.t. and extracted with DCM against aq. sat. $NaHCO_3$ (3x). The combined organic layers were washed with brine, dried over $MgSO_4$ and concentrated *in vacuo*. Purification by flash column chromatography (5% MeOH/DCM) yielded the product as an orange solid (14 mg, 37 *μ*mol, 21%).

^{1}H NMR (400 MHz, DMSO-*d*$_6$) δ 13.97 (s, 1H), 8.42 (q, *J* = 4.6 Hz, 1H), 8.34 (d, *J* = 8.4 Hz, 1H), 7.98 (d, *J* = 7.5 Hz, 2H), 7.67 – 7.55 (m, 4H), 7.54 – 7.48 (m, 1H), 7.37 – 7.26 (m, 3H), 7.08 (d, *J* = 7.4 Hz, 1H), 2.77 (d, *J* = 4.3 Hz, 3H).

HRMS (ESI): *m/z* calc. for $C_{21}H_{18}N_5OS^+$ [M+H]$^+$: 388.1223, found: 388.1226.

7.4.1.8 (*E*)-2-((3-((4-(Diethylamino)phenyl)diazenyl)-1*H*-indazol-6-yl)thio)-*N*-methylbenzamide (**7.9**)

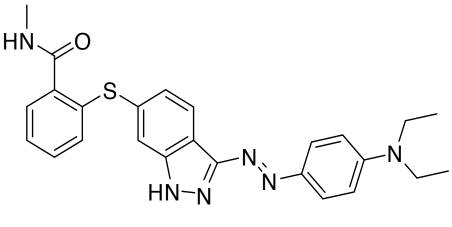

7.7 (30 mg, 0.10 mmol, 1.0 equiv.) and TFA (23 µL, 0.30 mmol, 3.0 equiv.) were combined in MeCN (15 mL). The reaction mixture was cooled to 0 °C before *t*BuONO (16 µL, 0.12 mmol, 1.2 equiv.) was added. After 45 min, *N,N*-diethylaniline (0.16 mL, 1.00 mmol, 10.0 equiv.) was added dropwise. Stirring was continued at 0 °C for 45 min, before the reaction mixture was allowed to warm to r.t. and all volatiles were removed *in vacuo*. The residue was purified by flash column chromatography (DCM → 5%MeOH/DCM) to yield the product as an orange-red solid (43 mg, 94 µmol, 94%).

^{1}H NMR (400 MHz, $CDCl_3$) δ 12.37 (s, 0H), 8.31 (d, *J* = 8.4 Hz, 1H), 7.91 – 7.83 (m, 2H), 7.72 (s, 1H), 7.49 – 7.41 (m, 1H), 7.19 (s, 1H), 7.12 (d, *J* = 8.4 Hz, 1H), 7.13 – 6.97 (m, 4H), 6.63 (d, *J* = 8.8 Hz, 2H), 6.51 (q, *J* = 4.9 Hz, 1H), 3.35 (q, *J* = 7.1 Hz, 4H), 2.88 (d, *J* = 4.7 Hz, 3H), 1.13 (t, *J* = 7.0 Hz, 7H).

^{13}C NMR (101 MHz, $CDCl_3$) δ 169.2, 156.3, 150.3, 143.5, 142.5, 135.6, 135.5, 133.0, 131.0, 130.9, 128.4, 126.8, 126.6, 125.4, 124.6, 114.8, 113.8, 111.0, 44.7, 27.0, 12.7.

HRMS (ESI): *m/z* calc. for $C_{25}H_{27}N_6OS^+$ $[M+H]^+$: 459.1962, found: 459.1967.

t_R (LCMS, MeCN/H_2O/formic acid = 90/10/0.1 → 10/90/0.1 over 7 min) = 5.33 min.

UV/Vis (LCMS): λ_{max} = 482 nm.

7.4.2 Spectral Data

7.4.2.1 2-Mercapto-*N*-methylbenzamide (**7.4**)

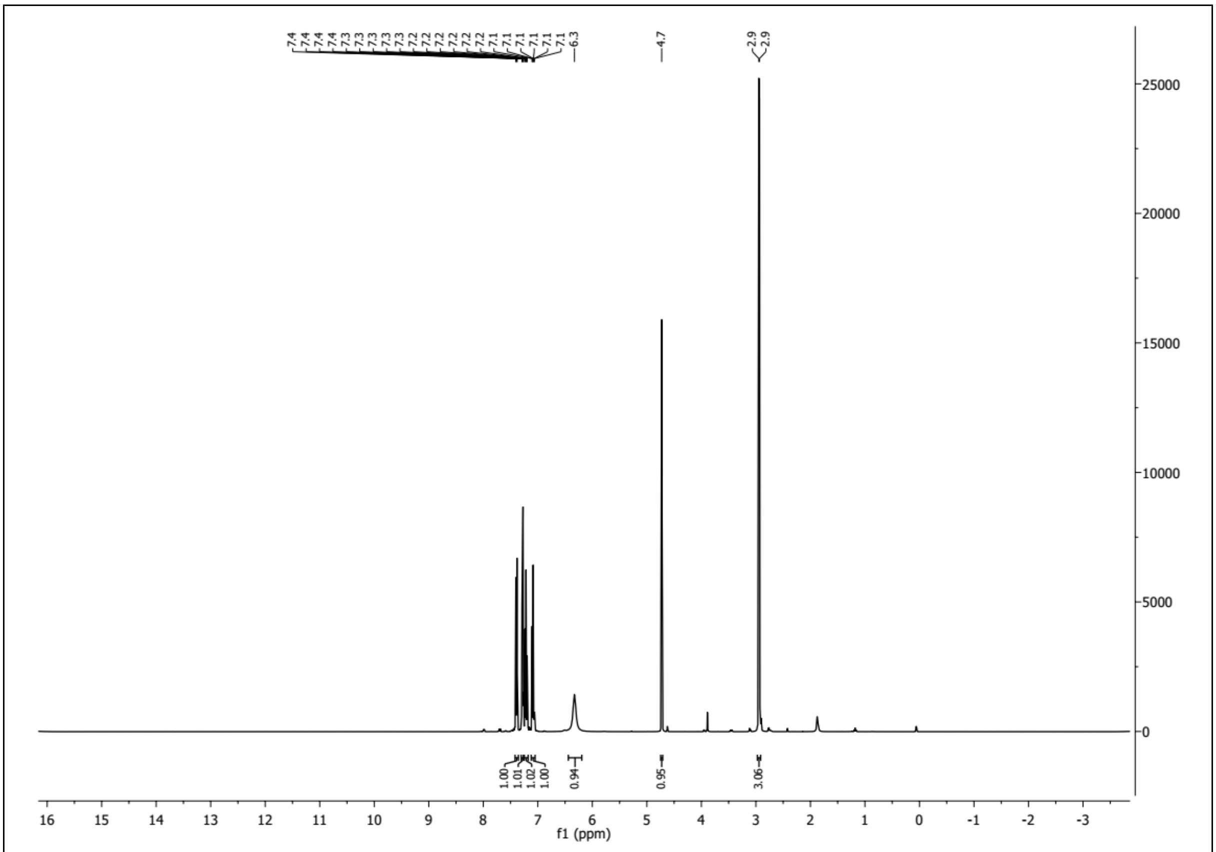

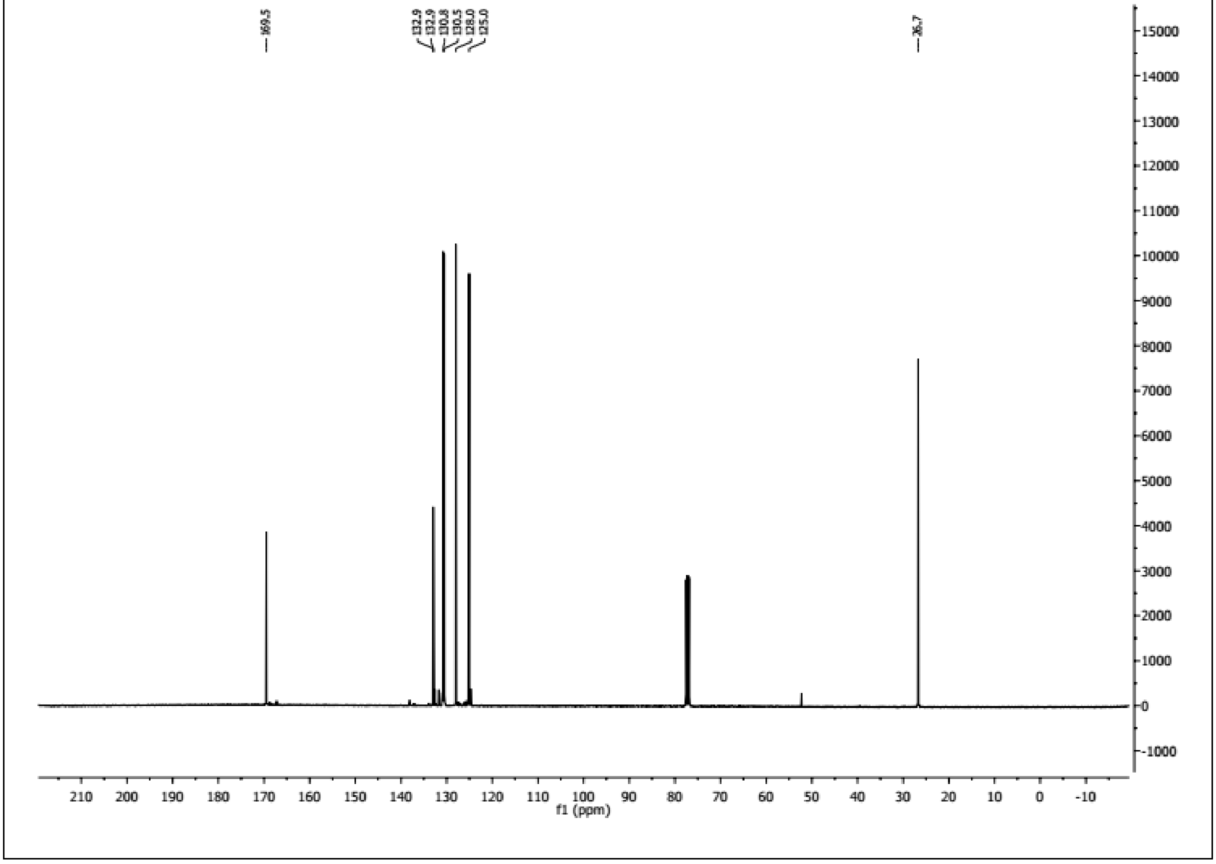

7.4.2.2 6-Bromo-1*H*-indazol-3-amine (**7.2**)

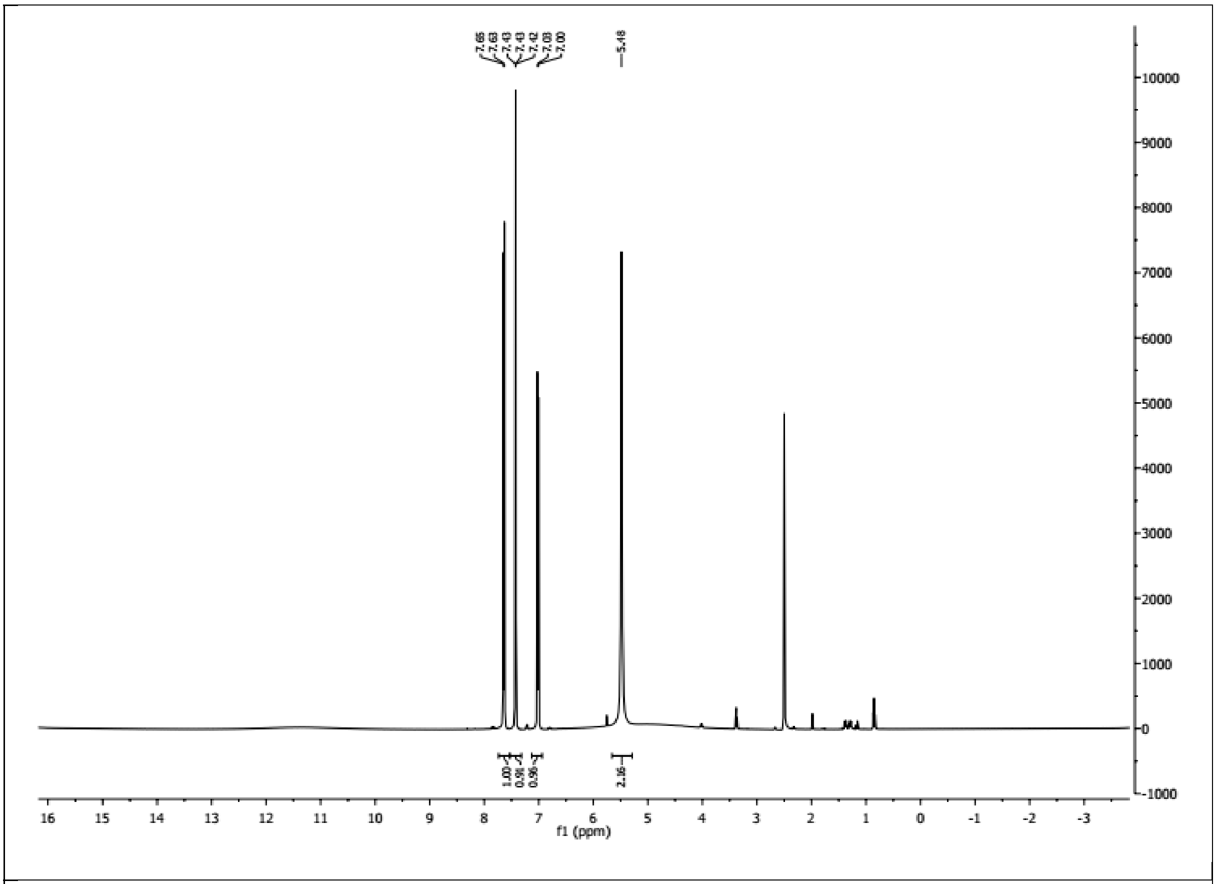

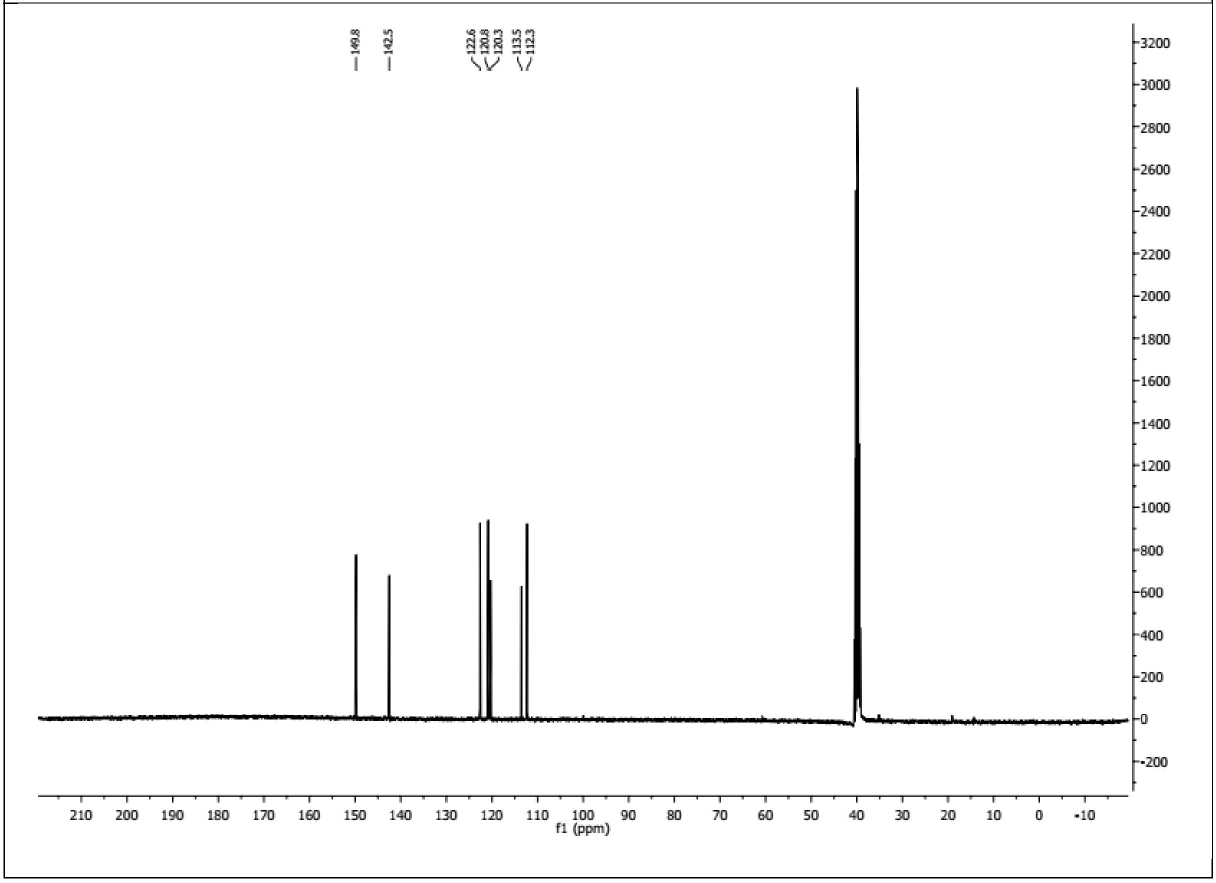

7.4.2.3 (*E*)-6-Bromo-3-(pyridin-2-yldiazenyl)-1*H*-indazole (**7.3**)

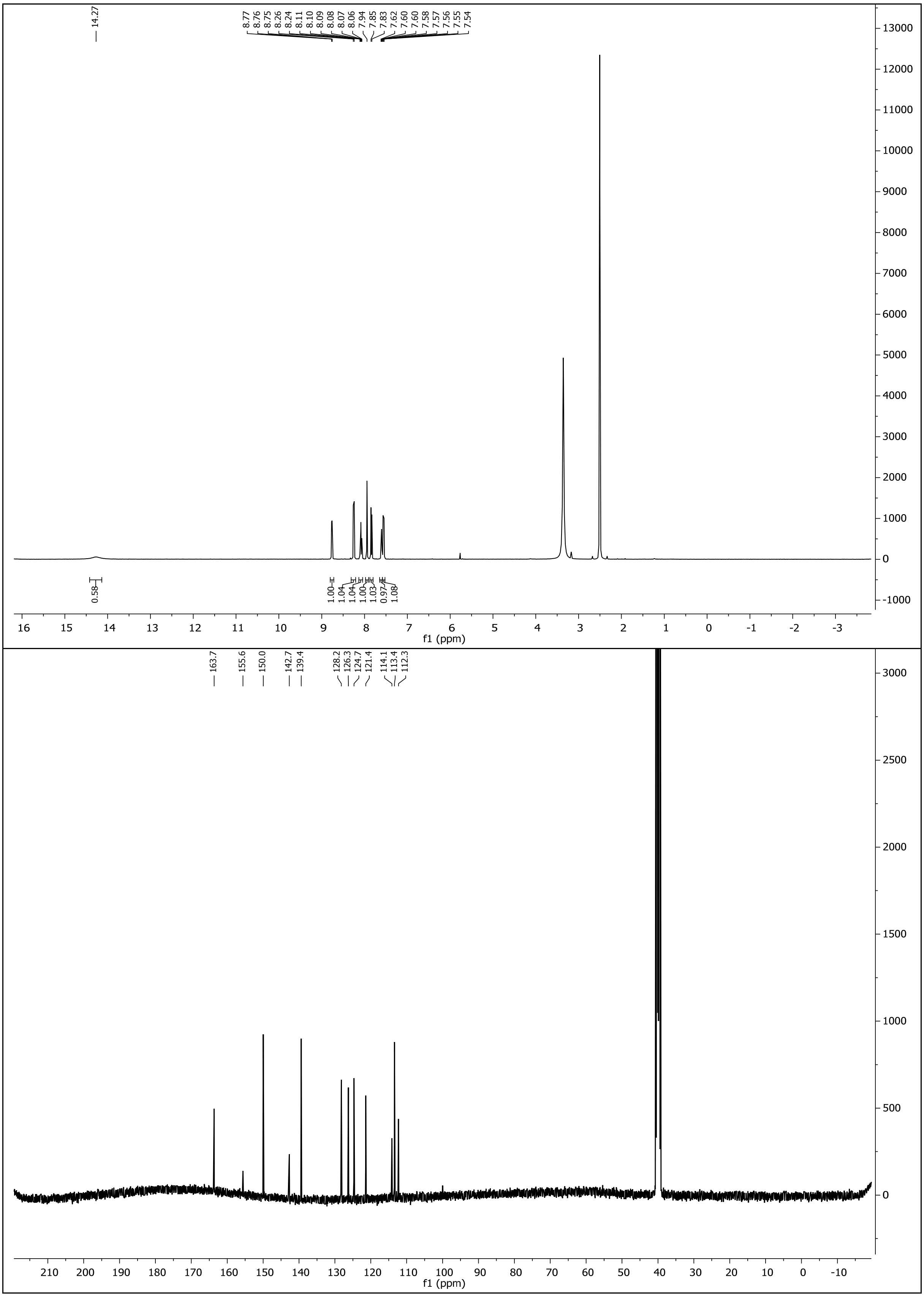

7.4.2.4 (*E*)-*N*-Methyl-2-((3-(pyridin-2-yldiazenyl)-1*H*-indazol-6-yl)thio)benzamide (**7.5**)

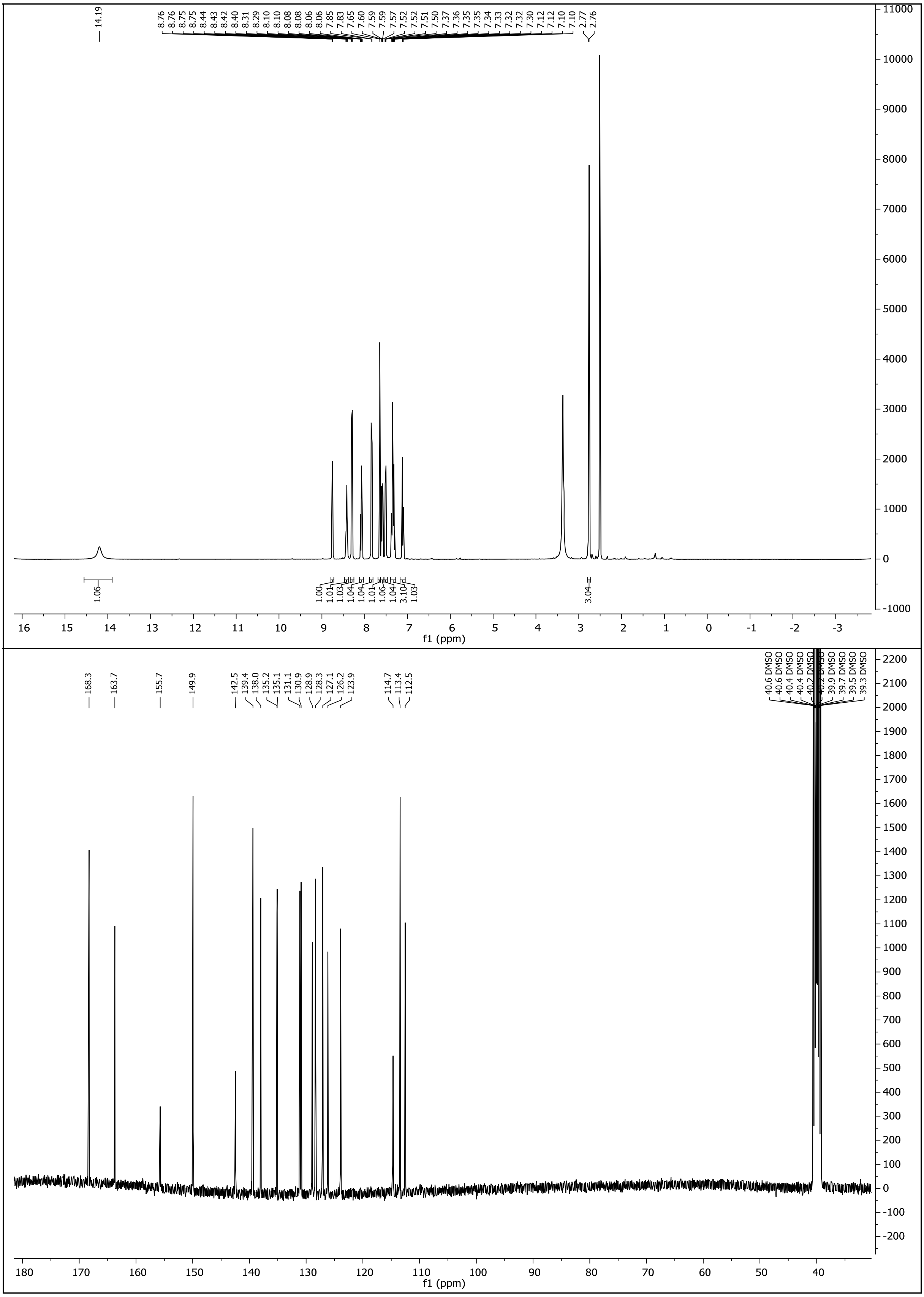

7.4.2.5 2-((4-Cyano-3-fluorophenyl)thio)-*N*-methylbenzamide (**7.6**)

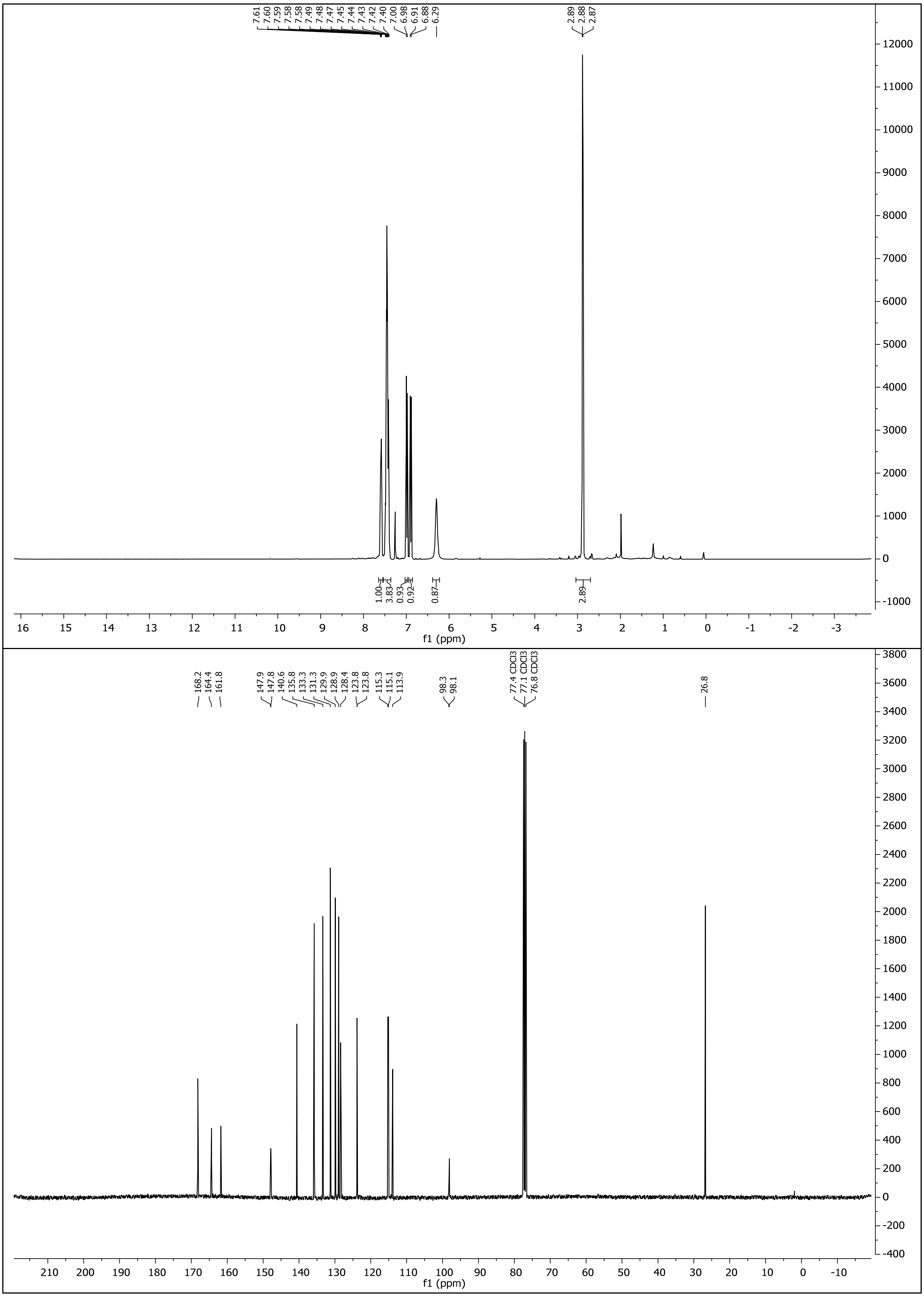

7.4.2.6 2-((3-Amino-1*H*-indazol-6-yl)thio)-*N*-methylbenzamide (**7.7**)

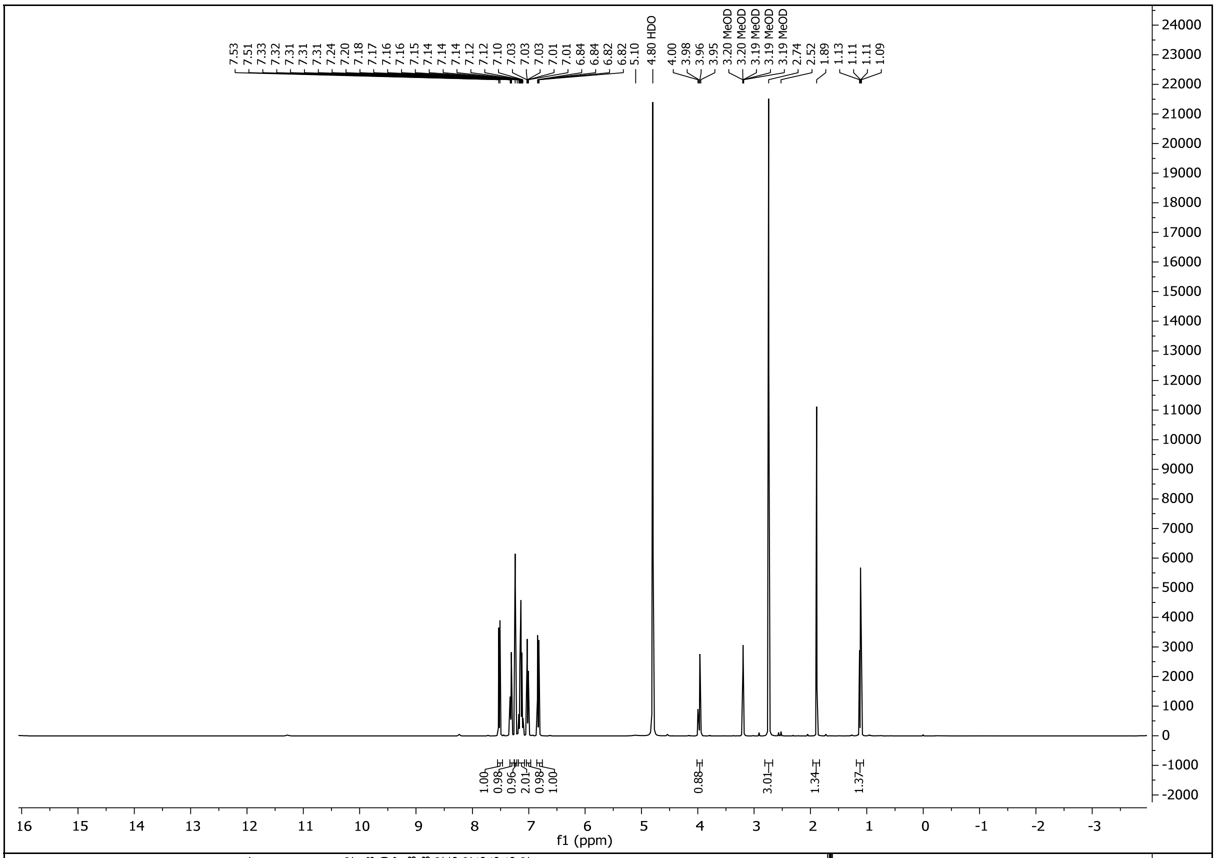

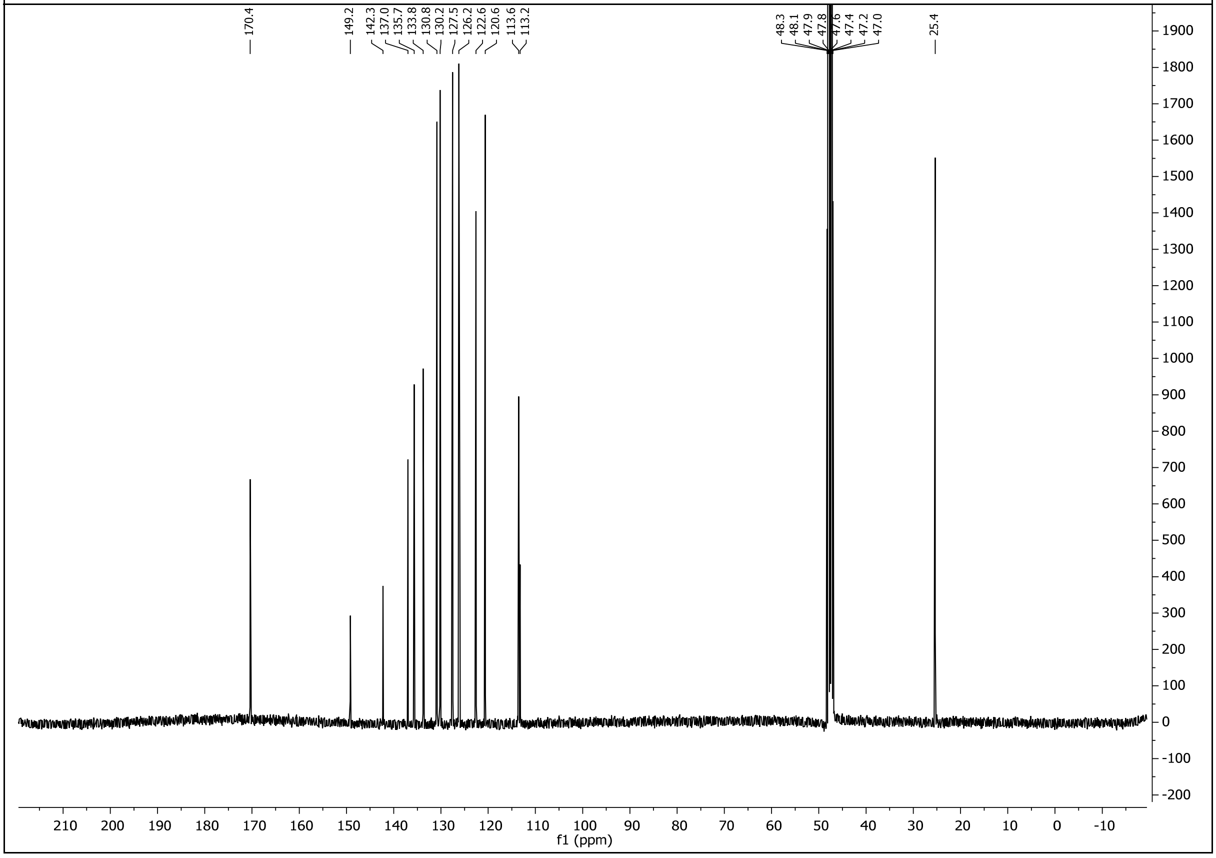

7.4.2.7 (*E*)-*N*-Methyl-2-((3-(phenyldiazenyl)-1*H*-indazol-6-yl)thio)benzamide (**7.8**)

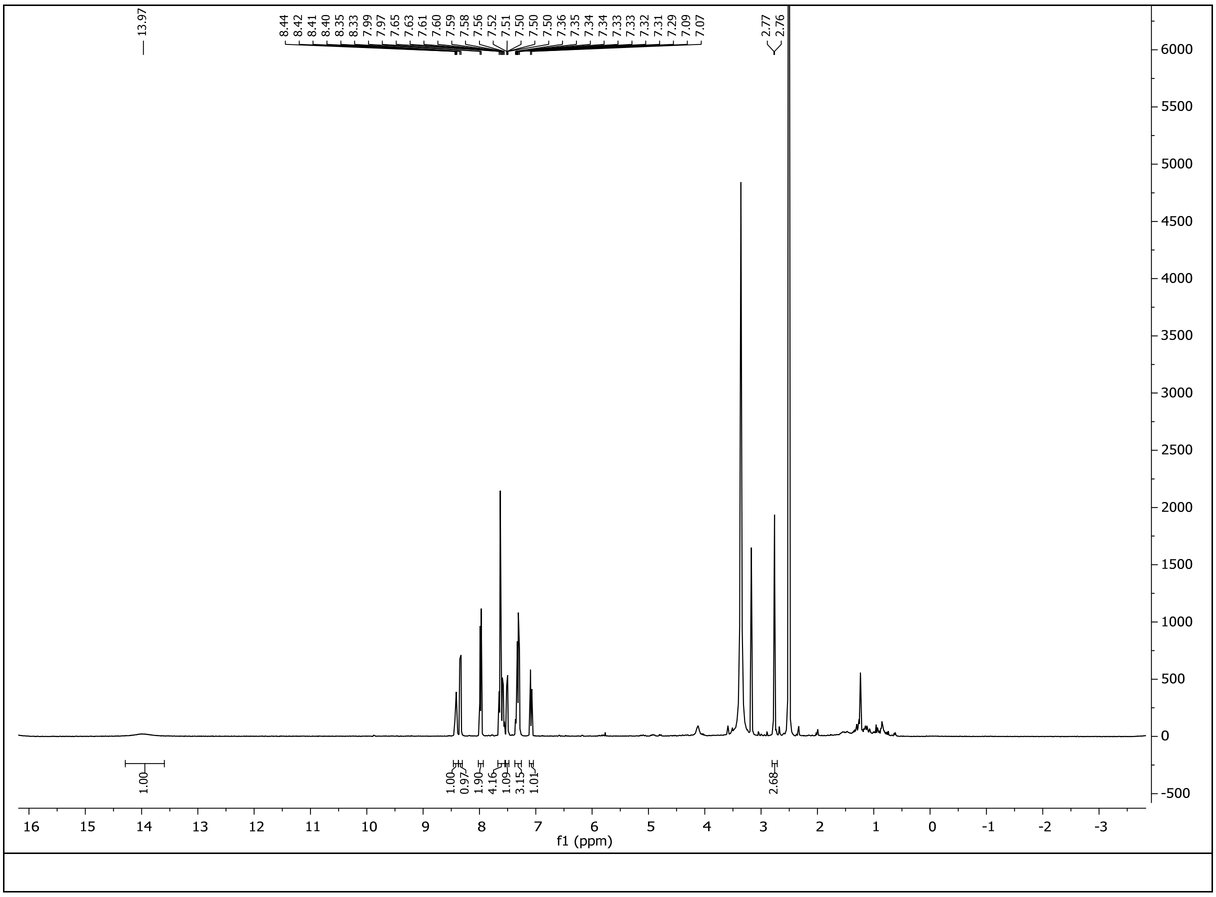

7.4.2.8 (*E*)-2-((3-((4-(Diethylamino)phenyl)diazenyl)-1*H*-indazol-6-yl)thio)-*N*-methylbenzamide (**7.9**)

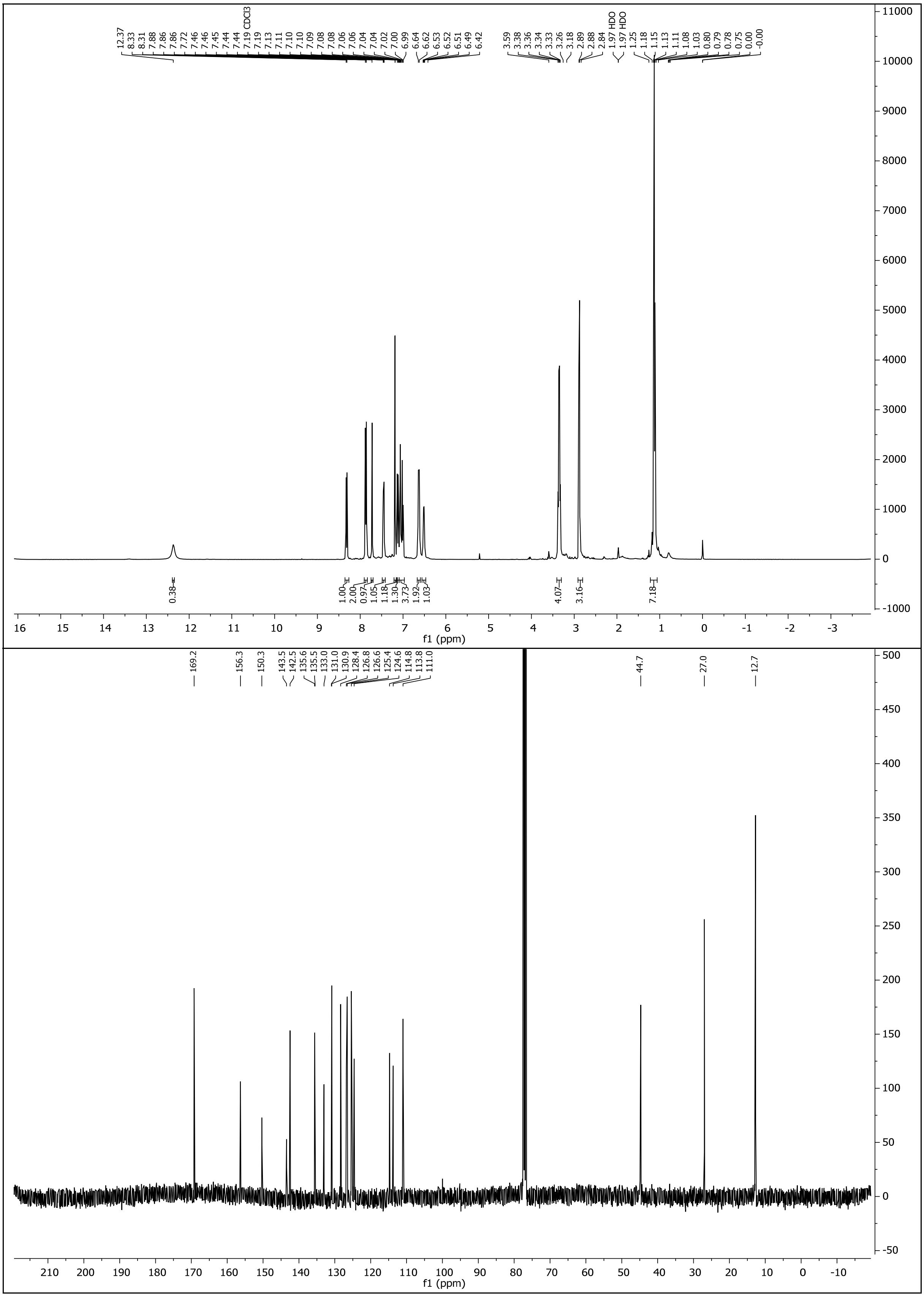

7.4.3 Crystallographic Data

7.4.3.1 2-Mercapto-*N*-methylbenzamide (**7.4**)

net formula	C_8H_9NOS
M_r/g mol^{-1}	167.229
crystal size/mm	0.3977 x 0.1142 x 0.0658
T/K	120(2)
radiation	Mo$K\alpha$
diffractometer	'Oxford XCalibur'
crystal system	triclinic
space group	'P 1'
a/Å	9.7638(9)
b/Å	9.7897(12)
c/Å	9.8755(5)
α/°	89.387(7)
β/°	71.641(7)
γ/°	66.939(10)
V/Å^3	817.42(15)
Z	4
calc. density/g cm^{-3}	1.3589(2)
μ/mm^{-1}	0.334
absorption correction	'multi-scan'
transmission factor range	0.92723–1.00000
refls. measured	11668
R_{int}	?
mean σ(I)/I	0.0837
θ range	4.199–28.742
observed refls.	8114
x, y (weighting scheme)	0.1041,
hydrogen refinement	mixed
Flack parameter	0.66(6)
refls in refinement	11668
parameters	410
restraints	3
R(F_{obs})	0.0610
R_w(F_2)	0.1654
S	0.955
shift/error$_{max}$	0.001
max electron density/e Å^{-3}	0.617
min electron density/e Å^{-3}	-0.502
BASF 0.32, HKLF 5 data.	

7.4.3.2 4-Bromo-2-fluoro-benzonitrile (**7.1**)

net formula	C_7H_3BrFN
M_r/g mol^{-1}	200.01
crystal size/mm	0.110 x 0.090 x 0.050
T/K	100(2)
radiation	MoKα
diffractometer	'Bruker D8Venture'
crystal system	triclinic
space group	'P -1'
a/Å	3.9527(4)
b/Å	8.8216(8)
c/Å	9.7528(9)
α/°	80.482(3)
β/°	86.764(3)
γ/°	81.885(3)
V/Å^3	331.84(5)
Z	2
calc. density/g cm^{-3}	2.002
µ/mm^{-1}	6.119
absorption correction	'multi-scan'
transmission factor range	0.6099-0.7454
refls. measured	5776
R_{int}	0.0322
mean σ(I)/I	0.0290
θ range	3.416-26.37
observed refls.	1245
x, y (weighting scheme)	0.0487, 0.2691
hydrogen refinement	constr.
refls in refinement	1354
parameters	91
restraints	0
R(F_{obs})	0.0292
R_w(F_2)	0.0809
S	1.143
shift/error$_{max}$	0.001
max electron density/e Å^{-3}	0.981
min electron density/e Å^{-3}	-0.448

7.4.3.3 6-Bromo-1*H*-indazol-3-amine (**7.2**)

net formula	C_7H_3BrFN
M_r/g mol^{-1}	212.06
crystal size/mm	0.070 x 0.050 x 0.040
T/K	100(2)
radiation	Mo$K\alpha$
diffractometer	'Bruker D8Venture'
crystal system	monoclinic
space group	'P 21'
a/Å	9.4410(4)
b/Å	3.9016(2)
c/Å	9.5096(5)
α/°	90
β/°	92.4411(15)
γ/°	90
V/Å^3	349.97(3)
Z	2
calc. density/g cm^{-3}	2.012
μ/mm^{-1}	5.797
absorption correction	'multi-scan'
transmission factor range	0.6641-0.7456
refls. measured	8262
R_{int}	0.0286
mean σ(I)/I	0.0321
θ range	3.107-27.49
observed refls.	1505
x, y (weighting scheme)	0.0083, 0.0066
hydrogen refinement	mixed
Flack parameter	0.008(6)
refls in refinement	1589
parameters	109
restraints	1
R(F_{obs})	0.0170
R_w(F_2)	0.0335
S	1.076
shift/error$_{max}$	0.001
max electron density/e Å^{-3}	0.316
min electron density/e Å^{-3}	-0.234

7.4.3.4 2-((3-Iodo-1*H*-indazol-6-yl)thio)-*N*-methylbenzamide

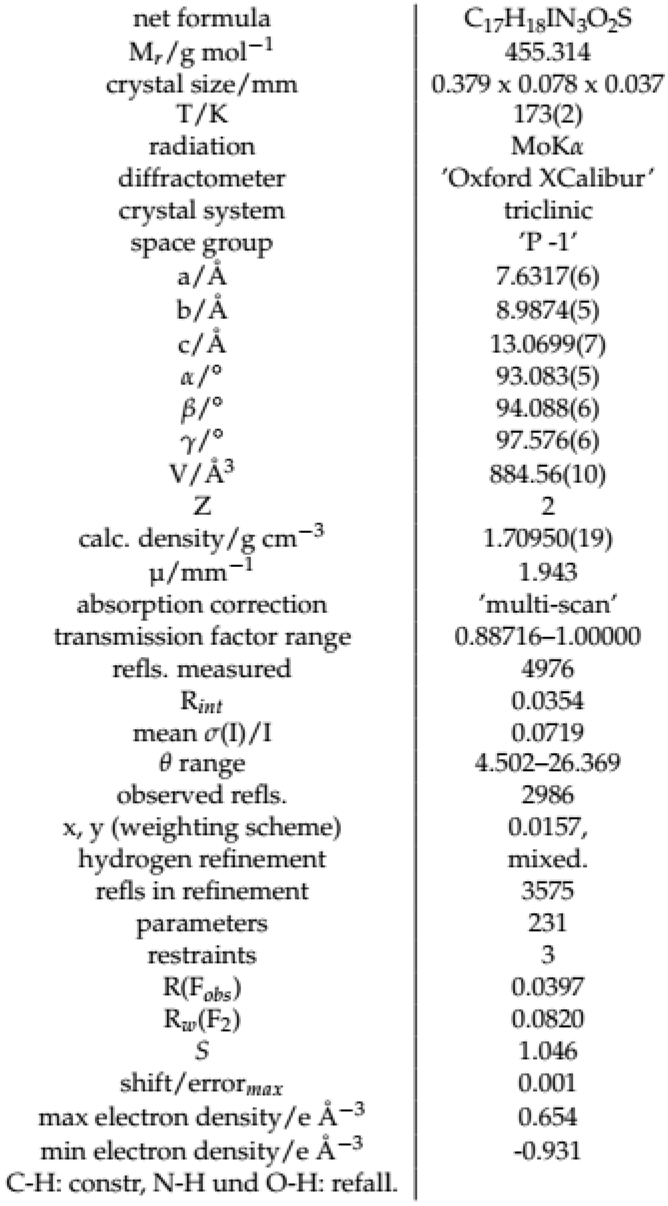

net formula	$C_{17}H_{18}IN_3O_2S$
M_r/g mol^{-1}	455.314
crystal size/mm	0.379 x 0.078 x 0.037
T/K	173(2)
radiation	MoKα
diffractometer	'Oxford XCalibur'
crystal system	triclinic
space group	'P -1'
a/Å	7.6317(6)
b/Å	8.9874(5)
c/Å	13.0699(7)
α/°	93.083(5)
β/°	94.088(6)
γ/°	97.576(6)
V/Å^3	884.56(10)
Z	2
calc. density/g cm^{-3}	1.70950(19)
μ/mm^{-1}	1.943
absorption correction	'multi-scan'
transmission factor range	0.88716–1.00000
refls. measured	4976
R_{int}	0.0354
mean σ(I)/I	0.0719
θ range	4.502–26.369
observed refls.	2986
x, y (weighting scheme)	0.0157,
hydrogen refinement	mixed.
refls in refinement	3575
parameters	231
restraints	3
R(F_{obs})	0.0397
R_w(F_2)	0.0820
S	1.046
shift/error$_{max}$	0.001
max electron density/e Å^{-3}	0.654
min electron density/e Å^{-3}	-0.931
C-H: constr, N-H und O-H: refall.	

8 Further Synthesis and Biology

8.1 ExONatide

This work was published as:

Podewin, T.; Ast, J.; Broichhagen, J.; Fine, N.H.F., Nasteska, D.; **Leippe, P.;** Gailer, M., Buenaventura, T.; Kanda, N.; Jones, B.J., M'Kadmi, C.; Baneres, J.-L.; Marie, J.; Tomas, A., Trauner, D.; Hoffmann-Röder, A.; Hodson, D.J. Conditional and Reversible Activation of Class A and B G Protein-Coupled Receptors Using Tethered Pharmacology. *ACS Cent. Sci.* **2018**, *4* (2), 166–179.

8.1.1 Supporting Information

N-(4-(((2-Amino-9*H*-purin-6-yl)oxy)methyl)benzyl)-1-(3-(pyridin-2-yldisulfanyl)propanamido)-3,6,9,12-tetraoxapentadecan-15-amide (BG-PEG$_4$-SSpy)

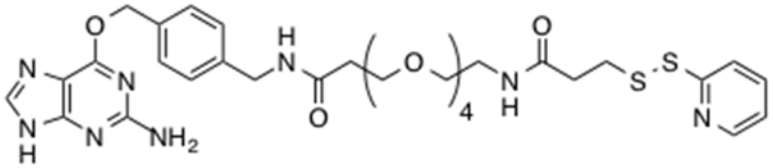

6-((4-(Aminomethyl)benzyl)oxy)-9*H*-purin-2-amine (12.0 mg, 44 µmol, 1.1 equiv.), PEG$_4$-SDPD (ThermoScientific #26128, 22.0 mg, 44.0 µmol, 1.0 equiv.) and DIPEA (10.5 µL, 60 µmol, 1.5 equiv.) were combined in anhydrous DMF (1.0 mL) under a nitrogen atmosphere. After stirring for 1 h at r.t., the crude reaction mixture was syringe filtered and subjected to RP-HPLC. The product containing fractions were combined, concentrated *in vacuo* and freeze-dried to obtain 17.0 mg (24.0 µmol) of the desired product as a white solid in 60% yield.

Note: The multiplet at 2.52 – 2.45 ppm was obscured by the solvent signal and was assigned by 2D-COSY analysis.

^{1}H NMR (800 MHz, DMSO-d$_6$) δ [ppm] 12.44 (s, 1H), 8.45 (ddd, J = 4.8, 1.9, 0.9 Hz, 1H), 8.35 (t, J = 6.0 Hz, 1H), 8.04 (t, J = 5.7 Hz, 1H), 7.82 (ddd, J = 8.0, 7.5, 1.9 Hz, 1H), 7.80 (d, J = 4.3 Hz, 1H), 7.76 (dt, J = 8.1, 1.1 Hz, 1H), 7.44 (d, J = 7.7 Hz, 2H), 7.26 (d, J = 7.9 Hz, 2H), 7.24 (ddd, J = 7.4, 4.8, 1.1 Hz, 1H), 6.28 (s, 2H), 5.45 (s, 2H), 4.27 (d, J = 5.9 Hz, 2H), 3.62 (t, J = 6.4 Hz, 2H), 3.48 (d, J = 4.6 Hz, 12H), 3.39 (t, J = 5.9 Hz, 2H), 3.19 (q, J = 5.8 Hz, 2H), 3.00 (t, J = 7.1 Hz, 2H), 2.53 – 2.52 (m, 2H), 2.37 (t, J = 6.4 Hz, 2H).

^{13}C NMR (201 MHz, DMSO-d$_6$) δ [ppm] 170.1, 169.8, 159.8, 159.6, 159.2, 155.2, 149.6, 139.3, 137.8, 135.2, 128.5, 127.2, 121.1, 119.1, 113.5, 109.5, 69.8, 69.7, 69.5, 69.5, 69.0, 66.9, 66.5, 41.8, 39.9, 38.6, 36.1, 34.5, 34.1.

HRMS (ESI): m/z calc. for $C_{32}H_{41}N_8O_7S_2^-$ [M-H]$^-$: 713.2545, found: 713.2545.

UV/VIS (LCMS): λ_{max1} = 197 nm; λ_{max2} = 214 nm; λ_{max3} = 286 nm.

t_R (LCMS, MeCN/H$_2$O/formic acid = 10/90/0.1 → 100/0/0.1 over 10 min) = 4.479 min.

t_R (RP-HPLC, MeCN/H$_2$O/TFA = 5/95/0.1 → 80/20/0.1 over 60 min) = 21.1 min.

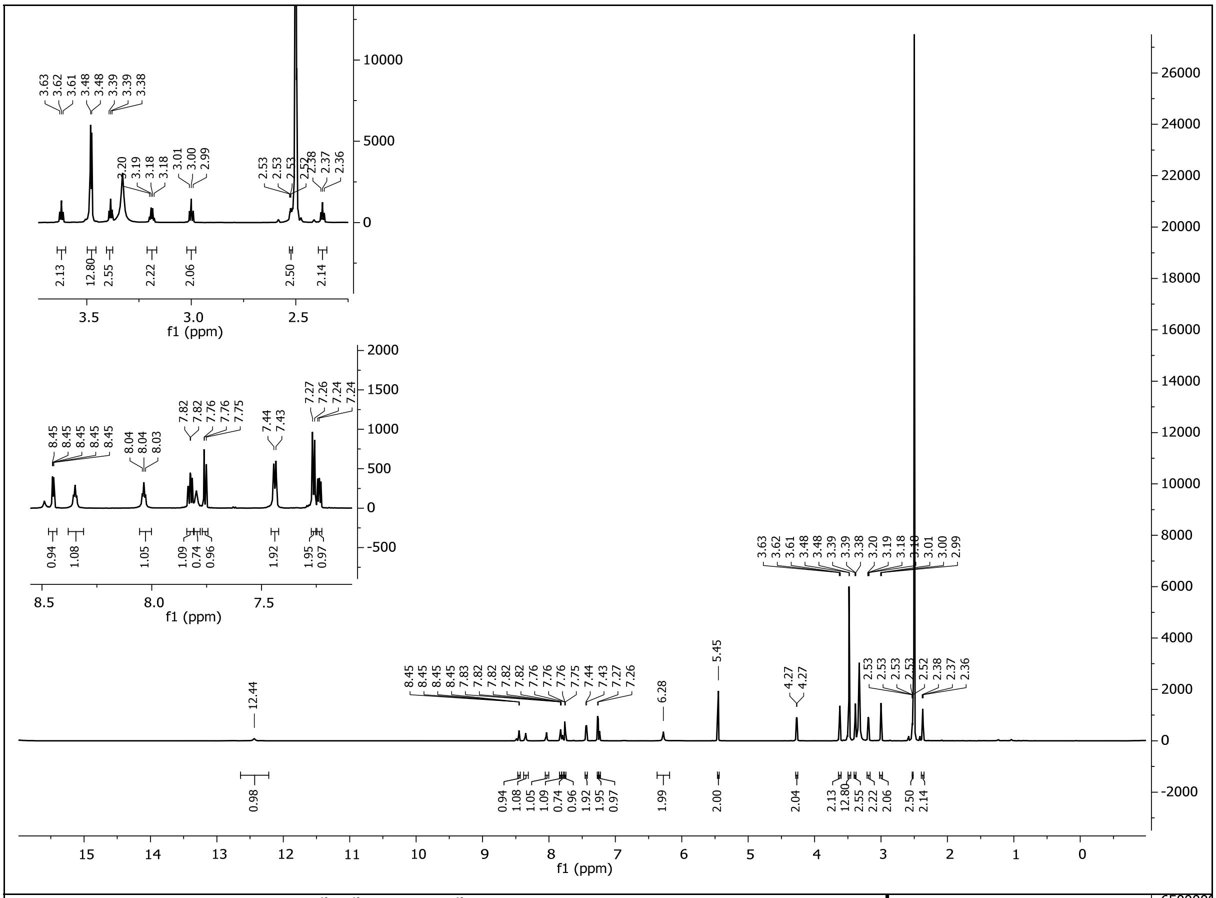
3.63 3.62 3.61 3.48 3.48 3.39 3.39 3.38
3.20 3.19 3.18 3.18 3.01 3.00 2.99
2.53 2.53 2.53 2.52 2.38 2.37 2.36
2.13 12.80 2.55 2.22 2.06 2.50 2.14
10000
5000
0
3.5
3.0
2.5
f1 (ppm)
8.45 8.45 8.45 8.45 8.45 8.04 8.04 8.03 7.82 7.82 7.76 7.76 7.75 7.44 7.43 7.27 7.26 7.24 7.24
0.94 1.08 1.05 1.09 0.74 0.96 1.92 1.95 0.97
2000
1500
1000
500
0
-500
8.5
8.0
7.5
f1 (ppm)
12.44
8.45 8.45 8.45 8.45 7.83 7.82 7.82 7.82 7.82 7.76 7.76 7.76 7.75 7.44 7.43 7.27 7.26
6.28
5.45
4.27 4.27
3.63 3.62 3.61 3.48 3.48 3.39 3.39 3.38 3.20 3.19 3.18 3.18 3.01 3.00 2.99
2.53 2.53 2.53 2.53 2.52 2.38 2.37 2.36
0.98
0.94 1.08 1.05 1.09 0.74 0.96 1.92 1.95 0.97
1.99
2.00
2.04
2.13 12.80 2.55 2.22 2.06
2.50 2.14
26000
24000
22000
20000
18000
16000
14000
12000
10000
8000
6000
4000
2000
0
-2000
15
14
13
12
11
10
9
8
7
6
5
4
3
2
1
0
f1 (ppm)

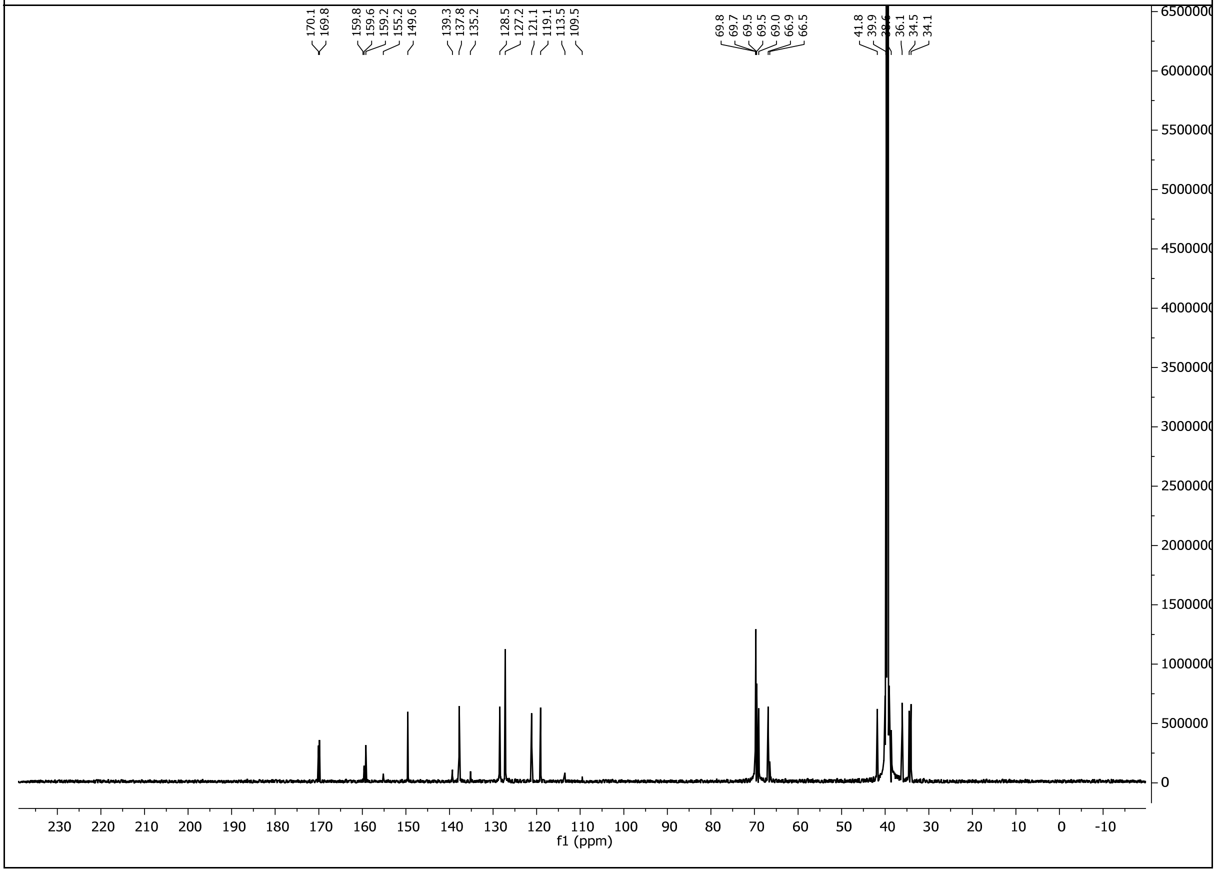
170.1 169.8
159.8 159.6 159.2 155.2 149.6
139.3 137.8 135.2
128.5 127.2 121.1 119.1 113.5 109.5
69.8 69.7 69.5 69.5 69.0 66.9 66.5
41.8 39.9 36.1 34.5 34.1
6500000
6000000
5500000
5000000
4500000
4000000
3500000
3000000
2500000
2000000
1500000
1000000
500000
0
230
220
210
200
190
180
170
160
150
140
130
120
110
100
90
80
70
60
50
40
30
20
10
0
-10
f1 (ppm)

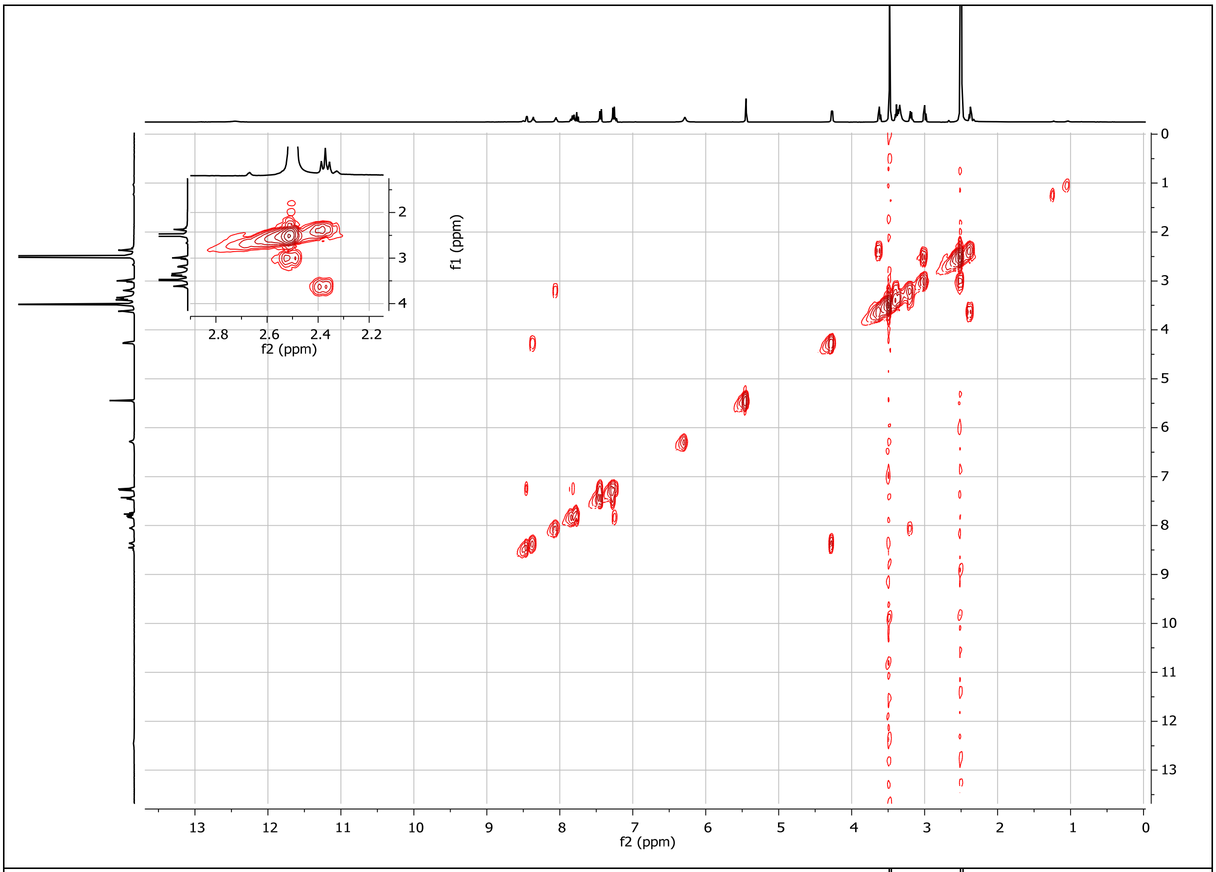
f2 (ppm)
f1 (ppm)
13
12
11
10
9
8
7
6
5
4
3
2
1
0
2.8
2.6
2.4
2.2

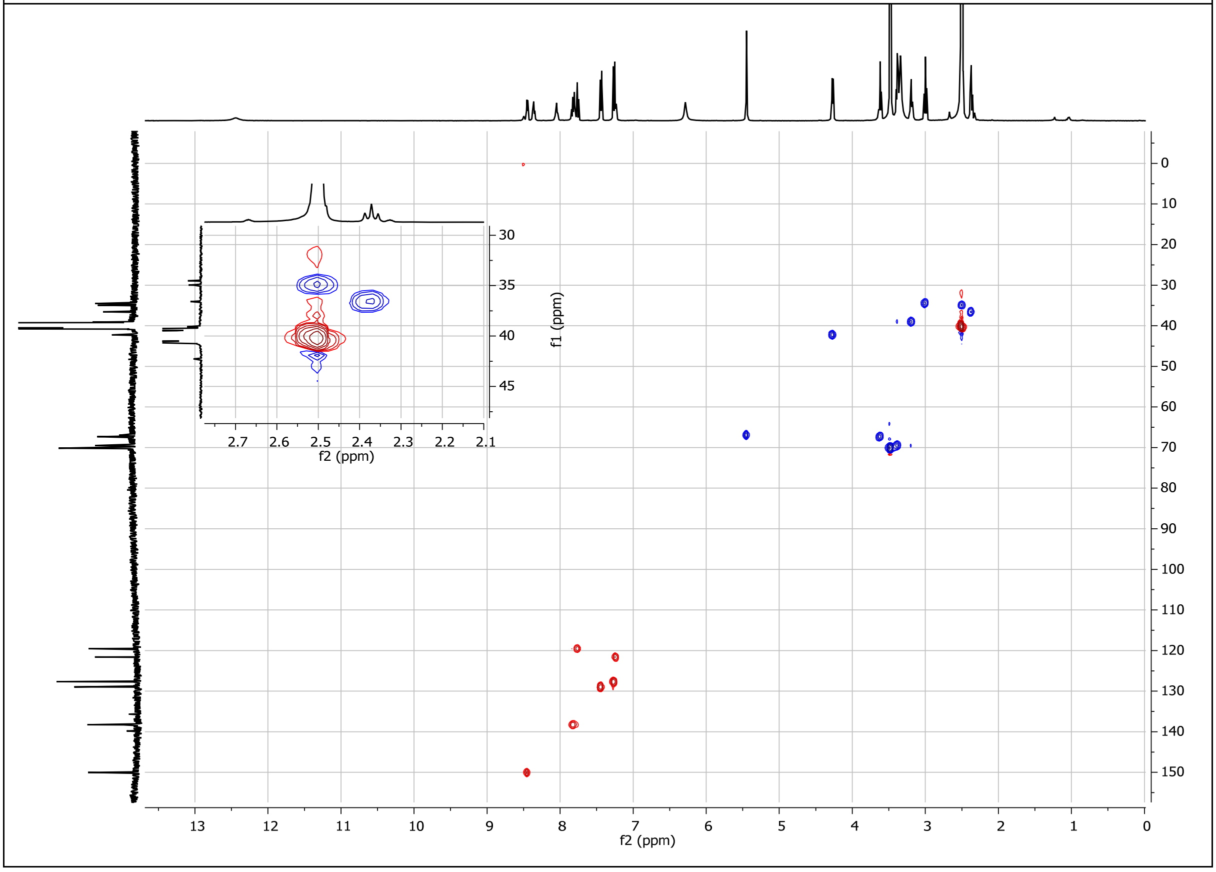
f2 (ppm)
f1 (ppm)
0
10
20
30
40
50
60
70
80
90
100
110
120
130
140
150
2.7
2.6
2.5
2.4
2.3
2.2
2.1
35
45

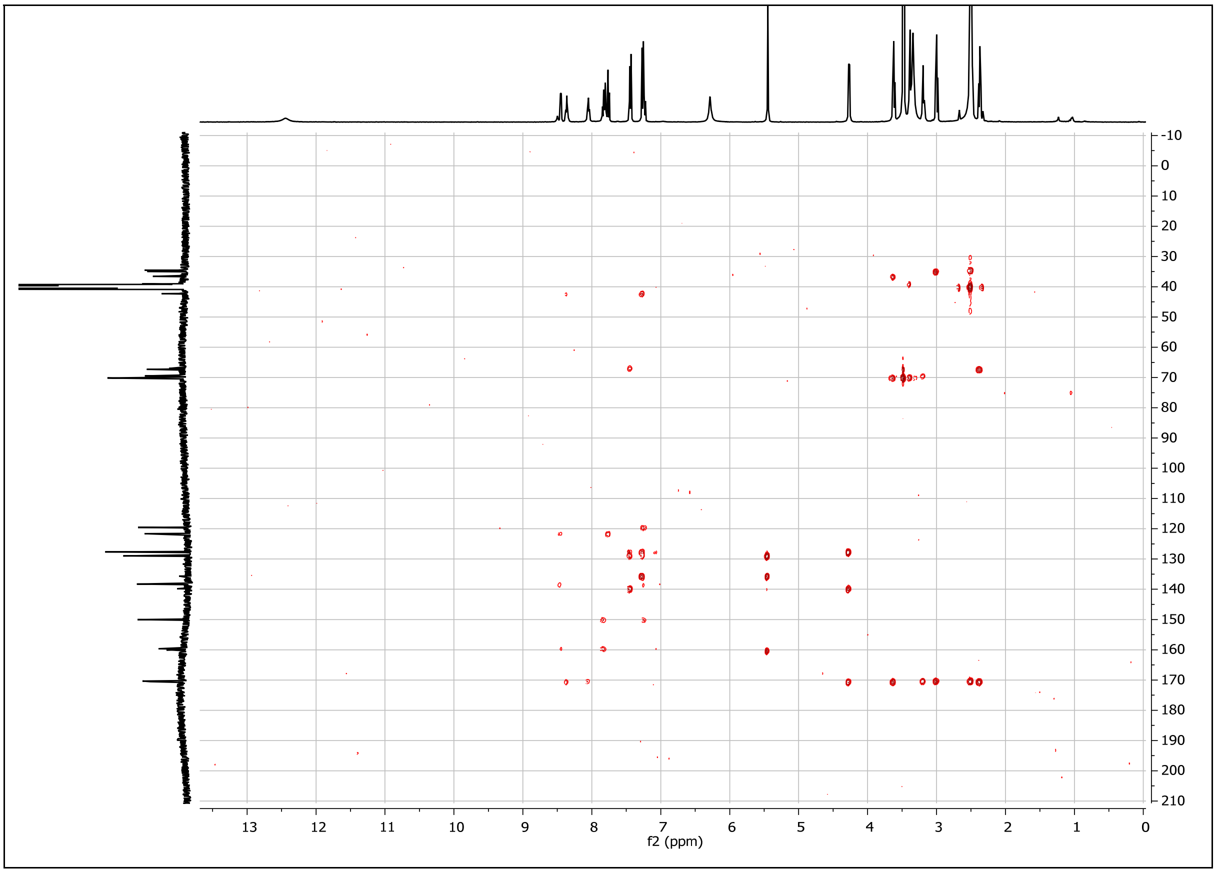
f2 (ppm)
13
12
11
10
9
8
7
6
5
4
3
2
1
0
-10
0
10
20
30
40
50
60
70
80
90
100
110
120
130
140
150
160
170
180
190
200
210

8.2 APCs for mGluR2

Similar to the ideas outlined in chapter 3.2.2, an APC for the mGluR2 was synthesized. Synthesis and characterization is summarized in Figure 39.

Electrophysiological characterization was carried out in HEK293T cells transfected with GIRK1/2 and mGlur2 (rat). No photoswitchable effects of the APC were observed, the data is not shown here. One reason for these negative experiments might be bad quality of the anti-mGluR2 antibody, multiple unspecific bands were detected by immunoblotting of HEK293T cells transfected with mGluR2 (see Figure 39e).

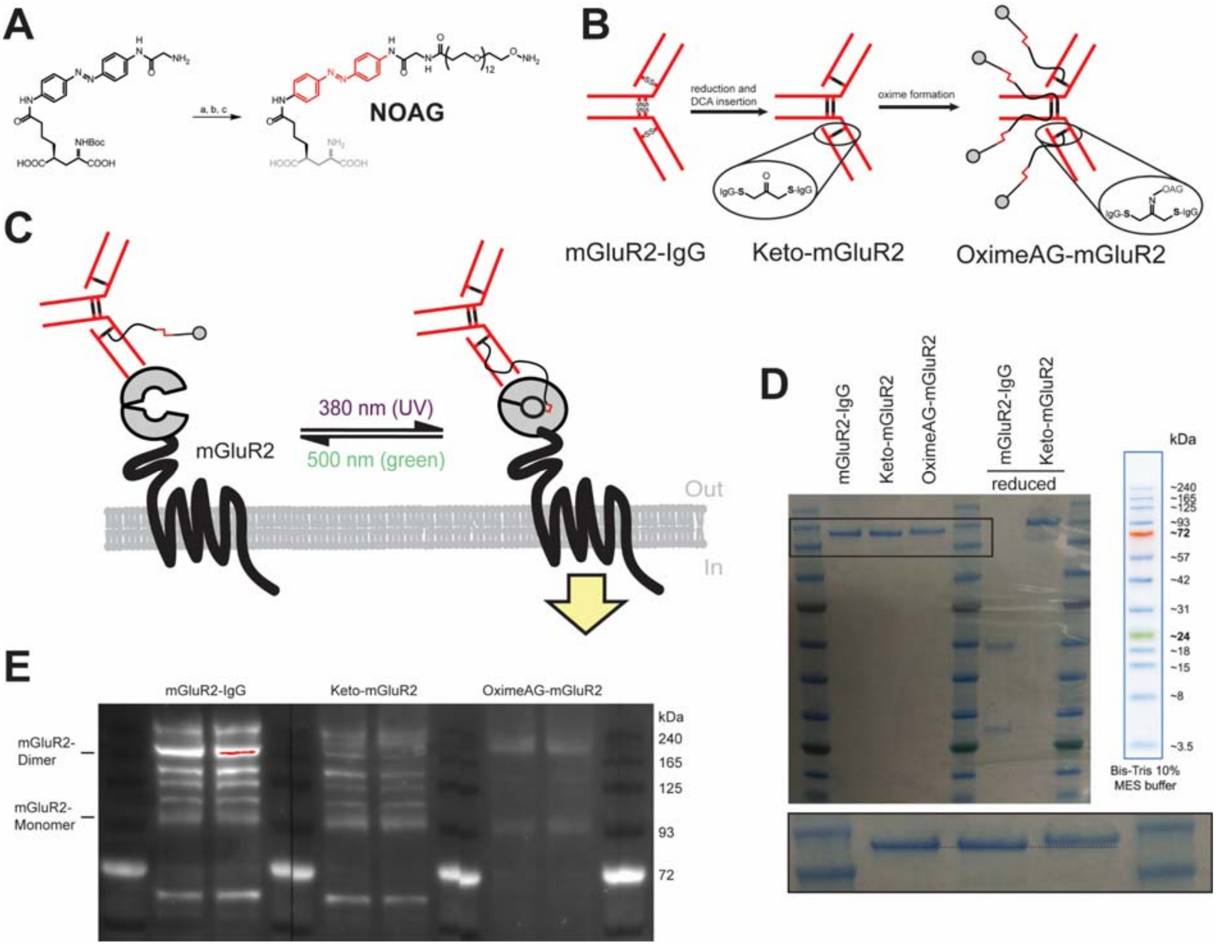

Figure 39. **APCs for mGluR2. a)** Synthesis of the photoswitchable NOAG molecule **b)** APC conjugation reactions. **c)** The APC binds to the native mGluR2 and illumination with light of different wavelengths enables optical control. **d)** Coomassie stained SDS-PAGE gel verifies successful synthesis of APC (OximeAG-mGluR2). **e)** Lysate of HEK293T cells transfected with mGluR2 was subjected to immunoblotting.

8.2.1 Supporting Information

Synthesis of NOAG

Azoglutamate[28] (4.0 mg, 6.1 μmol, 1.0 equiv.) was combined with Phth-NO-PEG$_{12}$-(CH$_2$)$_2$-C(O)NHS (Iris Biotech #PEG4630, 6.3 mg, 7.3 μmol, 1.2 equiv.) and DIPEA (4.2 μL, 24 μL, 4.0 equiv.) in dry DMF (0.5 mL). The reaction mixture was stirred at r.t. for 3h. The reaction mixture was acidified by addition of a few drops of FA and charged on a Waters Sep-Pack 2g C18 column. Elution with a gradient of H_2O/MeCN +0.1% FA yielded the product as an orange glaze (1.1 mg).

TFA (200 μL) was then added and allowed to stand for 15 min before the TFA was removed in a gentle stream of nitrogen. For deprotection of the phthalimide, 2M $MeNH_2$ in THF (500 μL) was added and sonicated for 30 min. The residue was acidified by addition of FA and charged on a Waters Sep-Pack 2g C18 column. Elution with a gradient of H_2O/MeCN +0.1% FA yielded the product as an orange glaze (1.2 mg, 1.09 μmol, 18% over 3 steps).

For HRMS analysis, the product was reacted with a drop of acetone to form the oxime.

HRMS (ESI): calc. for $C_{53}H_{86}N_7O_{20}^+$ (M+acetone+H)$^+$: 1140.5922, found: 1140.5960; calc. for $C_{53}H_{84}N_7O_{20}^-$ (M+acetone-H)$^+$: 1138.5777, found: 1138.5773.

Synthesis of Keto-mGluR2

Stock solutions:

- A 0.1 mg/mL stock solution of anti-mGluR2 (ATSBio #AB-N32) was prepared by diluting 77 μL of 1.3 mg/mL stock (100 μg, $6.41 * 10^{-10}$ mol) with 923 μL of 0.25M pH 7.3 TRIS buffer.
- A 20 mg/mL stock solution of dichloroacetone (DCA, Sigma-Aldrich #168548) was prepared by dissolving 39.2 mg of DCA in 1.96 mL DMSO.
- A 4 mM stock solution of TCEP.HCl was prepared by diluting 10 μL of 0.5M TCEP.HCl with 1.25 mL milliQ water. The 0.5M stock solution of TCEP.HCl was prepared by dissolving 37.4 mg of TCEP.HCl in 0.260 mL milliQ water.

In a 1.5 mL Eppendorf tube at room temperature, 17 μL of 20 mg/mL DCA was combined with 1000 μL of 0.1 mg/mL mGluR2-IgG 4000:1 DCA:IgG). The tube was vortexed, spun down and cooled to 4°C. In a separate microcentrifuge tube, 50 μL of 4mM TCEP.HCl was added and cooled to 4°C. Using a pipette, the entire volume of the mGluR2-IgG/DCA solution was added to the TCEP.HCl solution and the resulting solution was mixed thoroughly by repeated pipetting (300:1 TCEP:IgG). The reaction mixture was stored at 4°C overnight. The antibody was purified the next morning by membrane filtration using an Amicon centrifugal filter with 10kDa MWCO (10min, 14000rcf). After concentration, the retentate was diluted to ~500uL with PBS pH 7.4

and concentration was repeated. In total, seven concentration steps were performed, using PBS pH 7.4 as diluent each time. The final retentate was collected via centrifugation according to the manufacturer's instructions into a tared tube and then weighed to determine the retentate volume (47.9 mg = 47.9 μL, assuming d = 1 mg/uL). The concentration of Keto-mGluR2 was determined by absorbance spectroscopy: A_{280} = 0.882, corresponding to 0.65 mg/mL using ε_{280} of 1.36 mL mg^{-1} cm^{-1}. Recovery of Keto-mGluR2 was 31% (31.1 μg).

Synthesis of Azo-mGluR2

Stock solutions:

- A 1M stock solution of 3,5-diaminobenzoic acid (DABA, Sigma-Aldrich #D12805) was freshly prepared by dissolving 49.6 mg DABA in 326uL DMSO.

A 1.5 mL Eppendorf tube was charged sequentially with PBS (18.9 μL), DMSO (7.5 μL, final conc.: 30vol/vol%), DABA (6 μL, final conc.: 0.1 M), AoAG (AminooxyAzoGlutamate, PL421C, 4.5 μL of 6.5 mM DMSO stock, 29 nmol, 300 equiv.) and Keto-mGluR2 (23 μL, 15 μg, 96 pmol, 1 equiv.). The resulting solution was mixed thoroughly by repeated pipetting and stored at room temperature overnight. The reaction mixture was stored at room temperature, protected from light, overnight. The next morning, the reaction was diluted to ~500 μL by addition of PBS pH 7.4 and the antibody was purified by membrane filtration using an Amicon centrifugal filter with 10kDa MWCO (10min, 14000rcf) using the same procedure as described for Keto-mGluR2 purification. The final retentate was collected via centrifugation according to the manufacturer's instructions into a tared tube and then weighed to determine the retentate volume (43.0 mg = 43.0 μL, assuming d = 1 mg/μL). The concentration of OximeAG-mGluR2 was determined by absorbance spectroscopy: A_{280} = 0.245, corresponding to 180 μg/mL using ε_{280} of 1.36 $mL \cdot mg^{-1} \cdot cm^{-1}$. A second absorbance peak at 380 nm was observed, indicative of successful conjugation: A_{378} = 0.090 corresponding to 4.59 μM using ε_{378} of 19611 $L \cdot mg^{-1} \cdot cm^{-1}$. The calculated conjugation ratio of photoswitch is OximeAG/IgG = (4.59 μM * 43.0 μL) / (180 μg * 43.0 μL/156 kDa) = 3.97. Recovery of OximeAG-mGluR2 was 16% (7.74ug) over two steps (ketone insertion and oxime condensation).

Absorptionspectra

Keto-mGluR2

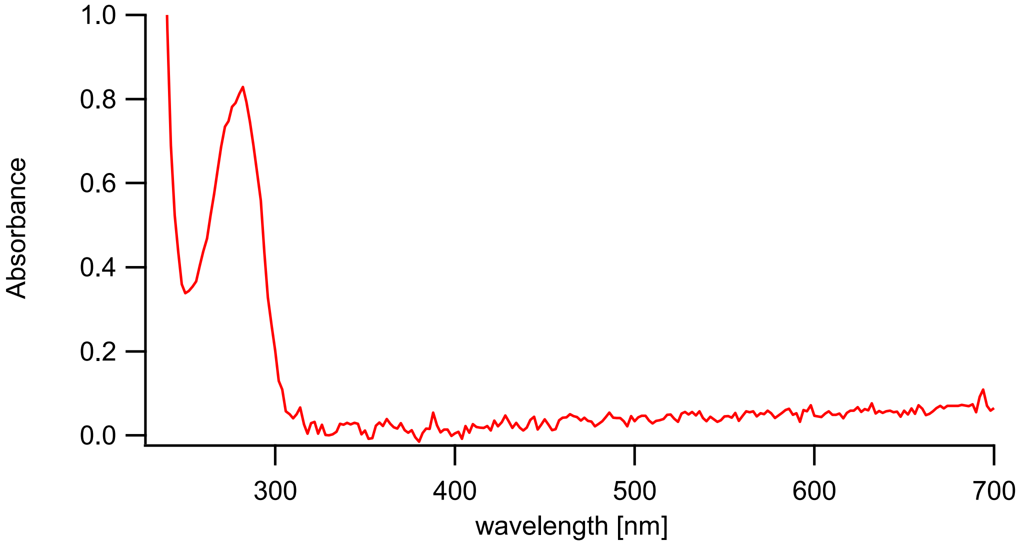

OximeAG-mGluR2

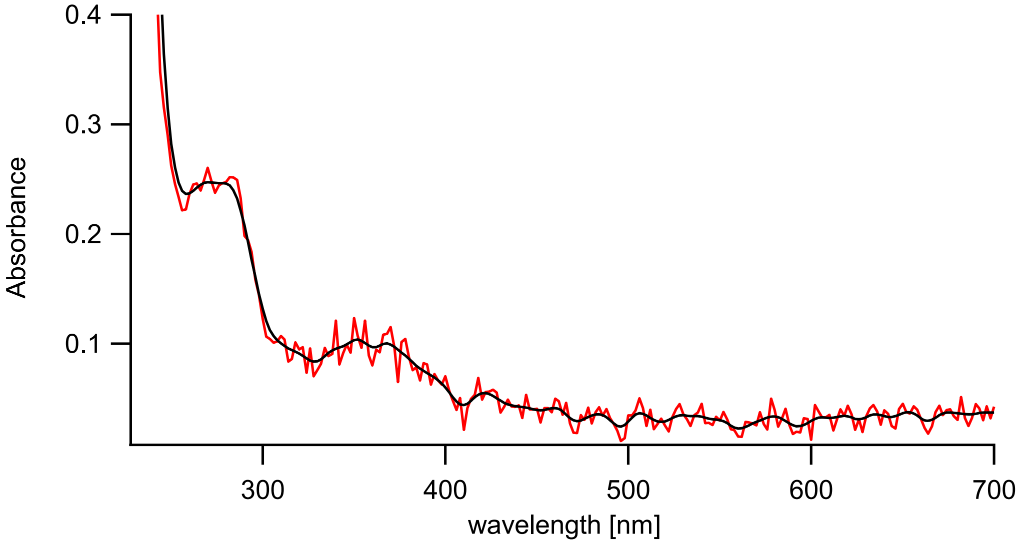

SDS-PAGE of Keto-mGluR2 and OximeAG-mGluR2

Samples (1 µg/lane) were analyzed by SDS-PAGE on a NuPage 4-12% Bis-Tris gel with MES running buffer at 180V for ca. 45min:

The gel was removed from its plastic casing and stained using InstantBlue Coomassie (Expedeon). Both unmodified and modified antibodies were observed to migrate near the 165kDa MW marker, consistent with an intact IgG (~156 kDa). The reduced mGluR2-IgG migrated as two bands near the 24kDa and 57kDa MW markers, consistent with complete reduction of the interchain disulfide bonds yielding separate HC (~50kDa) and LC (~25kDa). The reduced Keto-mGluR2 migrated near the 165kDa MW marker, consistent with successful crosslinking with DCA, where reduction-insensitive thioether bonds have replaced disulfides.

The band for the OximeAG-mGluR2 conjugate migrates slightly slower than the starting IgG, indicative of an increase in molecular weight after conjugation (see zoom-in).

8.3 Photocleavable dimerizers and oligomerizers

Coumarins are widely used as photoremovable ‘photocaging’ groups. Usually, payloads are attached in 4-position and released upon irradiation with UV-light (Figure 40a). In comparison with other photoremovable groups, *e.g.* *o*-nitrobenzyl, coumarin cages exhibit high absorbance coefficients at reasonably long wavelengths, together with fast release-rates.[135]

Other uses can be envisioned. Often, biological processes are driven by proximity alone, which can be taken advantage of by chemical tools, *i.e.* rapamycin induced dimerization.[136] However, most chemical tools are irreversible. Recently, we reversibly enabled conditional control over SNAP-tagged GLP1-R and GHS-R1a by inclusion of a reductively-cleavable disulfide bridge into the designs of benzylguanine-linked peptide agonists, termed ExONatide and GhrelON.[137] An improvement over this method could involve the use of photolabile groups, to allow the cleavage to proceed by illumination (Figure 40b). To this end, a few building blocks were synthesized to allow for further modification.

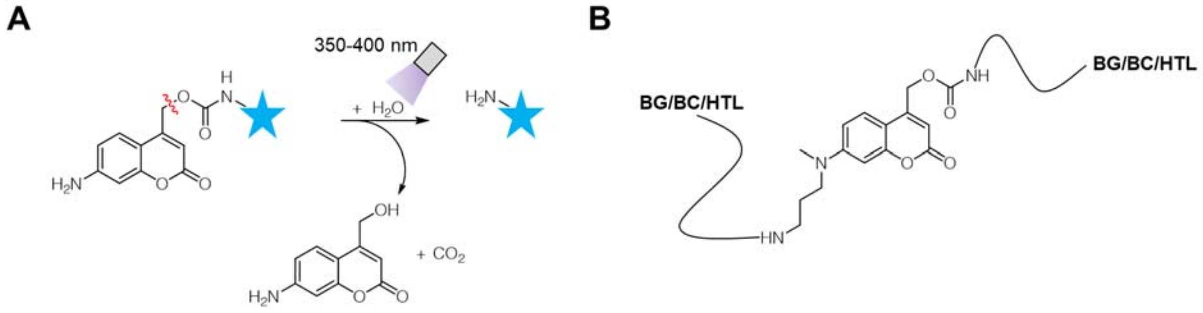

Figure 40. **Design of photocleavable dimerizers or oligomerizers.** BG = benzyl guanine, BC = benzyl cytosine, HTL = Halo-tag ligand.

8.3.1 Synthesis

8.3.1.1 *tert*-Butyl (3-((4-(Chloromethyl)-2-oxo-2*H*-chromen-7-yl)(methyl)amino)propyl) carbamate (**8.1**)

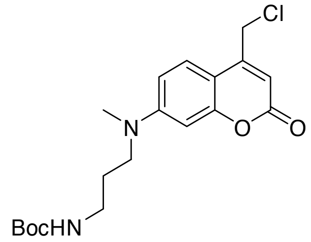

7-amino-4-(chloromethyl)-2H-chromen-2-one was prepared according to a published synthesis route.[138] *N*-(*tert*-Butoxycarbonyl)-3-aminopropionaldehyde was prepared by standard Boc-protection of 3-aminopropanol and subsequent DMP oxidation.

7-Amino-4-(chloromethyl)-2H-chromen-2-one (245 mg, 1.2 mmol, 1.0 equiv.), triacetoxyborohydride (447 mg, 2.8 mmol, 2.3 equiv.), glacial acetic acid (127 *μ*L, 2.2 mmol, 1.8 equiv.) and *N*-(*tert*-Butoxycarbonyl)-3-aminopropionaldehyde were mixed in DCE (10 mL). The reaction mixture was stirred at r.t. for 3 h before addition of aq. formaldehyde (37%, 95 *μ*L, 1.3 mmol, 1.1 equiv.), glacial acetic acid (57 *μ*L, 1.0 mmol, 0.8 eq) and triacetoxyborohydride (160 mg, 1.2 mmol, 1.0 eq.). The reaction mixture was stirred at r.t. for a further 4.5 h before it was extracted with DCM against sat. $NaHCO_3$ (2x), water (1x) and brine (1x). The organic layer was dried over $MgSO_4$, concentrated *in vacuo* and purified by flash column chromatography (2/98 = MeOH/DCM) to obtain 160 mg (0.42 mmol) of a light yellow solid in 35% yield.

^{1}H NMR (400 MHz, $CDCl_3$): δ 7.45 (d, J = 9.0 Hz, 1H), 6.64 (dd, J = 9.0, 2.6 Hz, 1H), 6.52 (d, J = 2.6 Hz, 1H), 6.21 (t, J = 0.9 Hz, 1H), 4.57 (d, J = 0.8 Hz, 2H), 3.46 (dd, J = 14.7, 7.3 Hz, 2H), 3.19 (q, J = 6.6 Hz, 2H), 3.03 (s, 3H), 1.81 (p, J = 7.0 Hz, 2H), 1.45 (s, 9H).

^{13}C NMR (101 MHz, $CDCl_3$): δ 161.6, 156.3, 156.0, 151.8, 149.8, 125.1, 109.7, 109.0, 106.8, 98.4, 79.6, 50.0, 41.5, 38.7, 31.0, 28.4, 27.5.

HRMS (ESI): calc. for $C_{19}H_{26}ClN_2O_4^+$ $(M+H)^+$: 381.1576, found: 381.1578.

8.3.1.2 *tert*-Butyl (2-(methyl(4-methyl-2-oxo-2*H*-chromen-7-yl)amino)ethyl)carbamate (**8.2**)

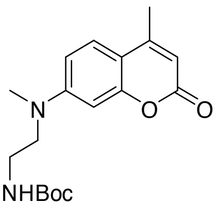

7-Bromo-4-methylcoumarin was prepared according to a published procedure.[139] *tert*-Butyl (2-(methylamino)ethyl)carbamate was prepared according to a published procedure.[140]

7-Bromo-4-methylcoumarin (46.6 mg, 195 µmol, 1.0 equiv.), *tert*-butyl (2-(methylamino)ethyl)carbamate (40.8 mg, 234 µmol, 1.2 equiv.), cesium carbonate (190.6 mg585 µmol, 3.0 equiv.), RuPhos (9.1 mg, 19.5 µmol, 0.1 equiv.) and RuPhos Pd G3 (16.3 mg, 19.5 µmol, 0.1 equiv.) were combined in a schlenk tube. The schlenk tube was evacuated and backfilled three times with argon before addition of dry 1,4-dioxane (1 mL). The reaction mixture was heated to 100°C and stirred for 3.5 h before LCMS analysis indicated consumption of all starting material. The reaction mixture was filtered over celite, the filter cake was washed with EtOAc. The solvent was removed *in vacuo* and the crude residue was purified by flash column chromatography (EtOAc/hexanes = 1/3 -> 1/2 -> 1/1) to yield the product as a white solid (31.5 mg, 94.8 µmol) in 49% yield.

^{1}H NMR (599 MHz, $CDCl_3$): δ 7.37 (d, J = 9.0 Hz, 1H), 6.69 – 6.64 (m, 1H), 6.50 (d, J = 2.6 Hz, 1H), 5.95 (d, J = 1.2 Hz, 1H), 4.78 (s, 1H), 3.53 (t, J = 6.7 Hz, 2H), 3.31 (q, J = 6.5 Hz, 2H), 3.03 (s, 3H), 2.32 (d, J = 1.2 Hz, 3H), 1.42 (s, 9H).

^{13}C NMR (151 MHz, $CDCl_3$): δ [ppm] = 162.1, 156.1, 155.9, 152.9, 152.0, 125.6, 109.9, 109.5, 108.8, 98.2, 79.7, 51.8, 38.8, 38.2, 28.5, 18.6.

HRMS (ESI): calc. for $C_{18}H_{25}N_2O_4^+$ $(M+H)^+$: 333.1809, found: 333.1808.

t

t_R (LCMS; MeCN/H_2O/formic acid = 10/90/0.1 → 100/0/0.1 over 10 min) = 7.723 min.

UV/Vis (LCMS): $\lambda_{max1,2,3}$ = 278, 314, 369 nm.

8.3.1.3 *tert*-Butyl (2-((4-(hydroxymethyl)-2-oxo-2H-chromen-7-yl)(methyl)amino)ethyl) carbamate (**8.3**)

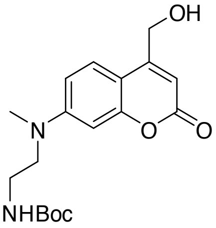

8.2 (276 mg, 0.830 mmol, 1.0 equiv.) and SeO_2 (184 mg, 1.66 mmol, 2.0 equiv.) were combined in dry *meta*-xylene. The reaction mixture was heated to reflux for 7 h before the reaction was judged to be incomplete by LCMS. More SeO_2 (55.0 mg, 0.495 mmol, 0.6 equiv.) was added and the reaction mixture heated to reflux 16 h. The reaction mixture was allowed to cool to r.t. and filtered over celite. The celite was washed with a copious amount of EtOAc before the organic layer was concentrated *in vacuo*. The blackish residue was redissolved in MeOH (10 mL), cooled to 0 °C and $NaBH_4$ (53.0 mg, 1.40 mmol, 1.6 equiv.) was added in portions. After stirring for 1 h, the reaction was quenched by addition of a few drops of water. The reaction mixture was extracted with EtOAc (3x) and DCM (3x) against water. The combined organic layers were dried over $MgSO_4$ and concentrated *in vacuo*. The residue was purified on a Waters Sep-Pak© 5g C18 column (water/MeCN + 0.1% FA, 100/0 -> 80/20, 5% increments). Product containing fractions were identified by LCMS, combined and freeze-dried. The tan product was obtained in 10% yield over 2 steps (30 mg, 0.086 mmol).

^{1}H NMR (400 MHz, $CDCl_3$): δ 7.33 (d, J = 9.0 Hz, 1H), 6.68 (d, J = 10.0 Hz, 1H), 6.55 (d, J = 2.4 Hz, 1H), 6.30 (s, 1H), 4.83 (s, 2H), 4.72 (s, 1H), 3.54 (t, J = 6.8 Hz, 2H), 3.32 (q, J = 6.5 Hz, 2H), 3.05 (s, 3H), 1.43 (s, 9H).

^{13}C NMR (101 MHz, $CDCl_3$): δ 162.2, 156.1, 155.9, 154.3, 151.7, 124.4, 109.0, 107.2, 106.3, 98.5, 79.7, 61.0, 51.8, 38.8, 38.0, 28.4.

t_R (LCMS; $MeCN/H_2O$/formic acid = 10/90/0.1 → 100/0/0.1 over 10 min) = 6.23 min.

UV/Vis (LCMS): $\lambda_{max1,2,3}$ = 209, 246, 374 nm.

HRMS (ESI): calc. for $C_{18}H_{25}N_2O_5^+$ $(M+H)^+$: 349.1758, found: 349.1764.

8.3.1.4 (9*H*-Fluoren-9-yl)methyl (2-((4-(hydroxymethyl)-2-oxo-2H-chromen-7-yl)(methyl)amino)ethyl)carbamate (**8.4**)

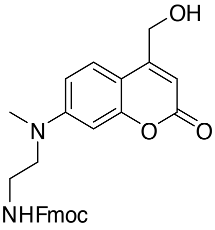

To **8.3** (30.0 mg, 0.086 mmol, 1.0 equiv.) was added neat TFA (1 mL). After 10 min at r.t., volatiles were removed by a gentle stream of nitrogen. The residue was redissolved in DMF (0.5 mL), DIPEA (0.060 mL, 0.344 mmol, 4.0 equiv.) and Fmoc-OSu (35.0 mg, 0.103 mmol, 1.2 equiv.)O were added. The reaction was stirred for 30 min before the crude mixture was loaded on a Waters Sep-Pak© 2g C18 column and eluted with a gradient of water and MeCN (water/MeCN + 0.1% FA, 100/0 -> 80/40, 5% increments). Product containing fractions were identified by LCMS, combined and freeze-dried. The product was obtained as a tan solid in 46% yield over 2 steps (19.0 mg, 0.040 mmol).

^{1}H NMR (400 MHz, $CDCl_3$): *δ* 7.67 (d, J = 7.6 Hz, 2H), 7.44 (d, J = 7.5 Hz, 2H), 7.31 (t, J = 7.4 Hz, 2H), 7.20 (d, J = 9.2 Hz, 2H), 6.62 – 6.54 (m, 1H), 6.47 (s, 1H), 6.17 (s, 1H), 4.90 (d, J = 7.6 Hz, 1H), 4.62 (s, 2H), 4.33 (d, J = 6.8 Hz, 2H), 4.02 (t, J = 6.8 Hz, 1H), 3.49 (t, J = 6.5 Hz, 2H), 3.32 (q, J = 6.4 Hz, 2H), 2.93 (s, 3H).

^{13}C NMR (101 MHz, $CDCl_3$): *δ* 156.5, 155.9, 154.3, 151.8, 143.8, 141.3, 127.7, 127.1, 125.0, 124.4, 120.0, 108.8, 107.1, 106.3, 98.4, 66.7, 60.9, 51.5, 47.3, 38.6, 38.4.

HRMS (ESI): calc. for $C_{28}H_{27}N_2O_5^+$ $(M+H)^+$: 471.1915, found: 471.1917.

***t*$_R$** (LCMS; MeCN/H_2O/formic acid = 10/90/0.1 → 100/0/0.1 over 10 min) =7.76 min.

UV/Vis (LCMS): $\lambda_{max1,2,3}$ = 207, 256, 301, 372 nm.

8.3.2 Spectral Data

8.3.2.1 *tert*-Butyl (3-((4-(Chloromethyl)-2-oxo-2*H*-chromen-7-yl)(methyl)amino)propyl) carbamate (**8.1**)

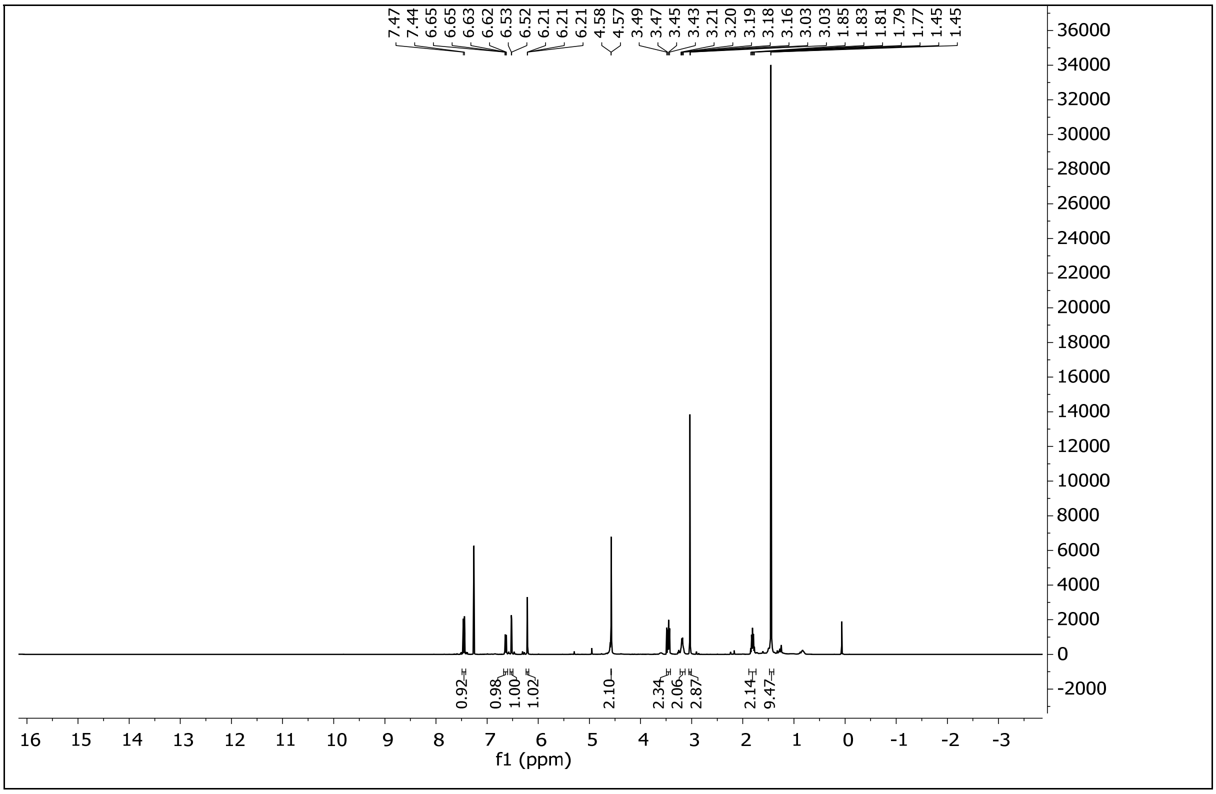

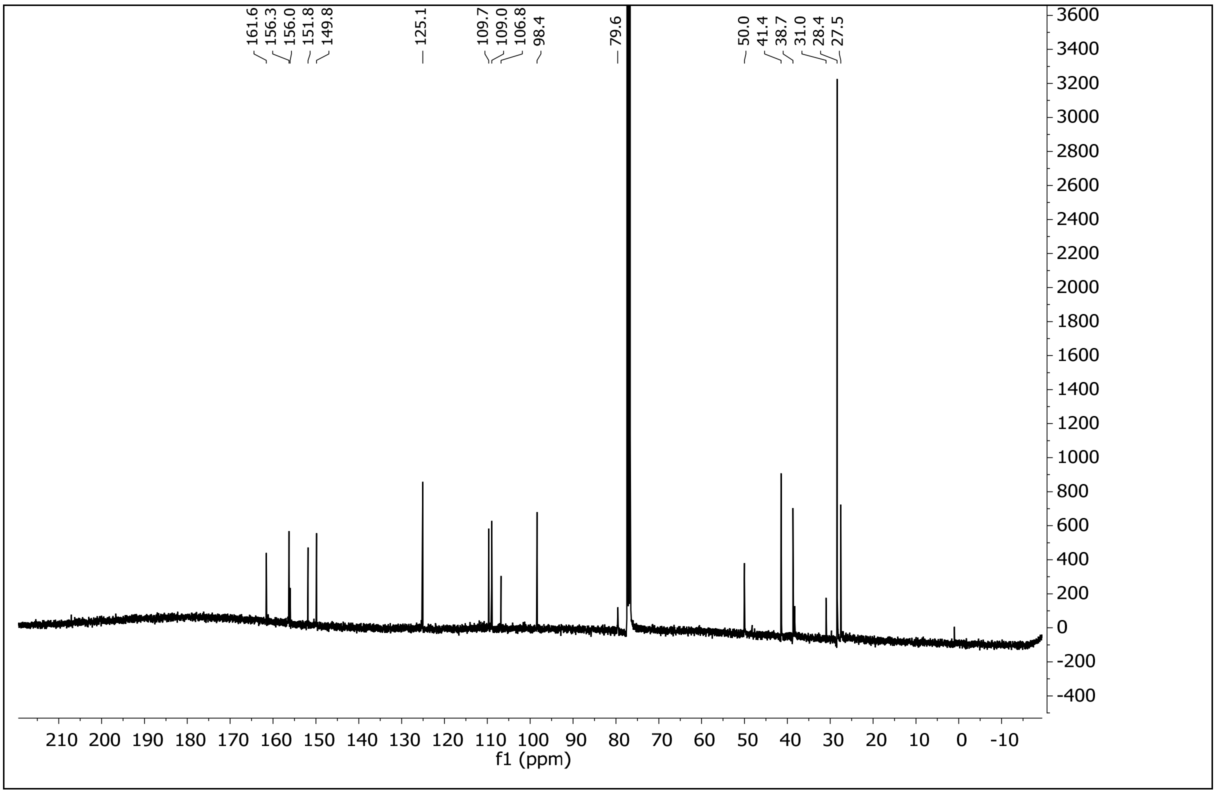

8.3.2.2 *tert*-Butyl (2-(methyl(4-methyl-2-oxo-2*H*-chromen-7-yl)amino)ethyl)carbamate (**8.2**)

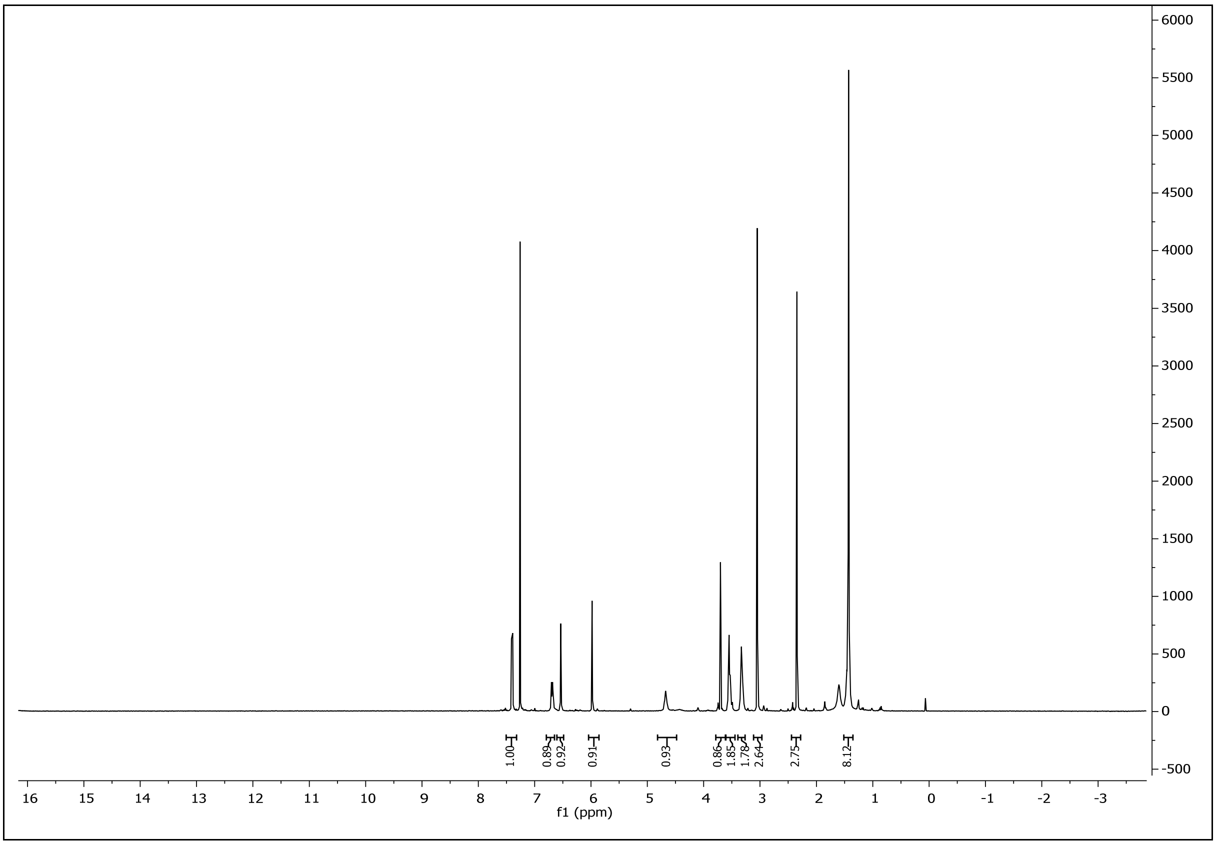

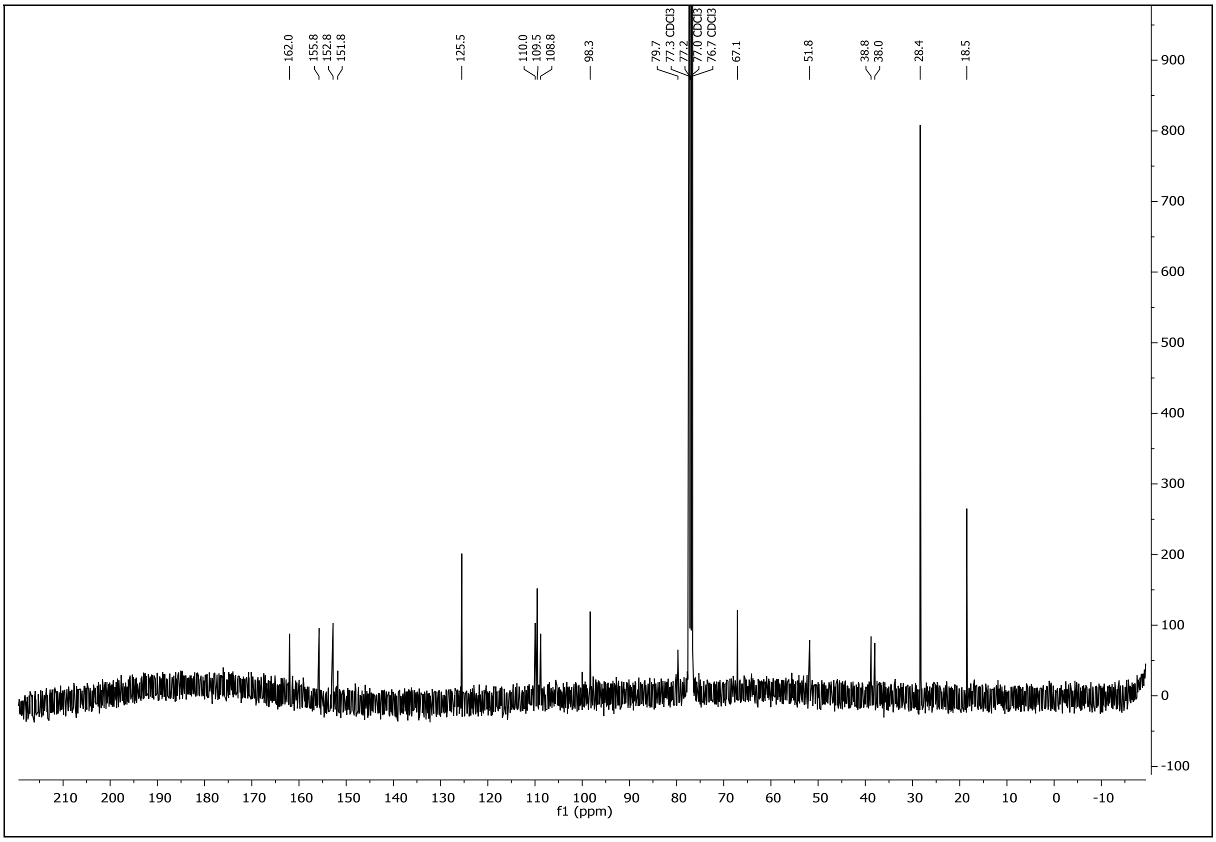

8.3.2.3 *tert*-Butyl (2-((4-(hydroxymethyl)-2-oxo-2H-chromen-7-yl)(methyl)amino)ethyl) carbamate (**8.3**)

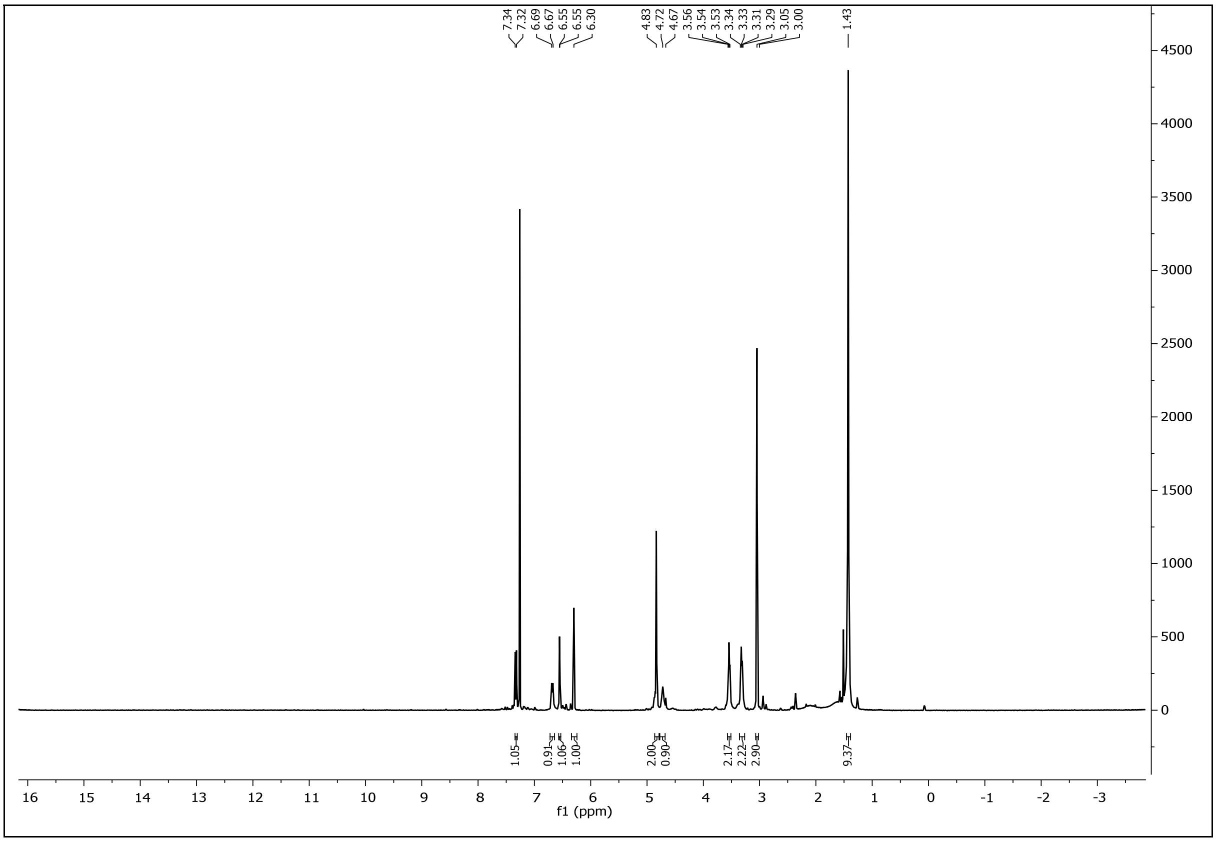

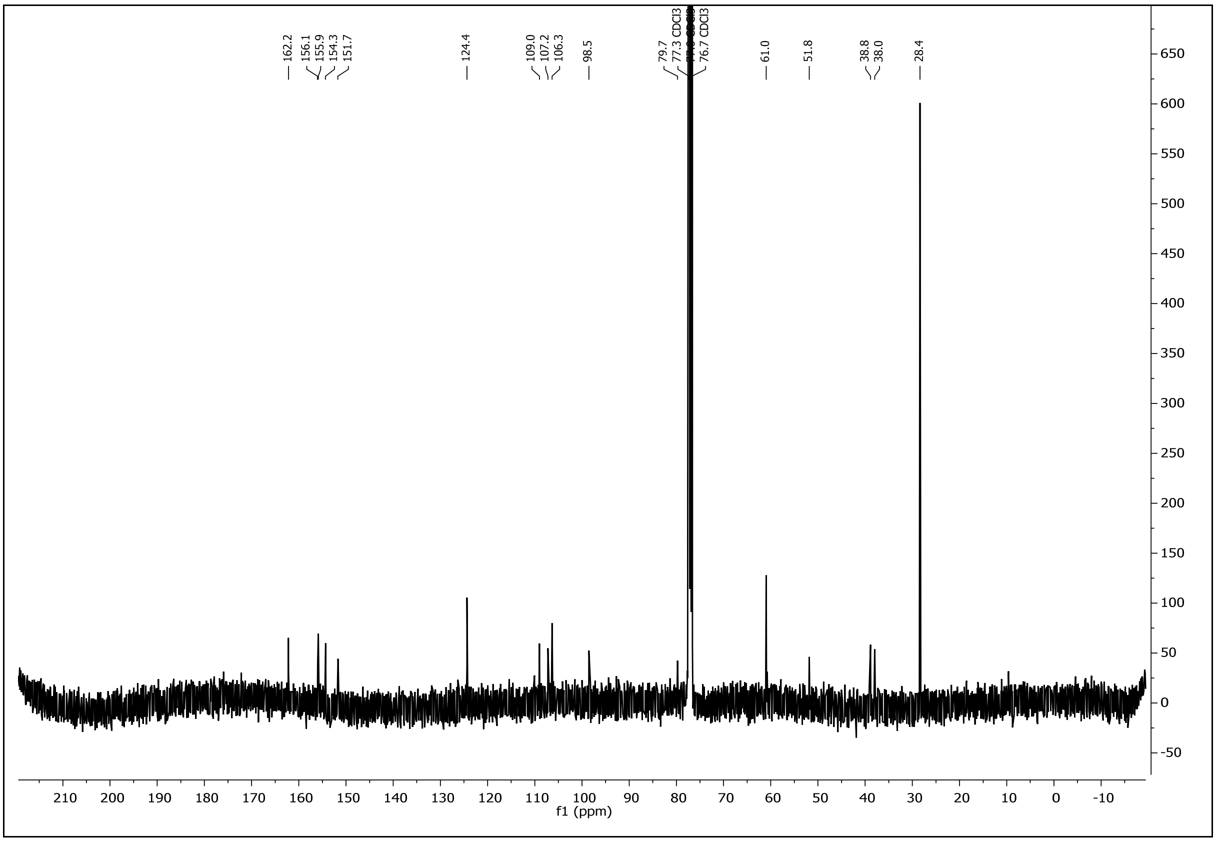

8.3.2.4 (9*H*-Fluoren-9-yl)methyl (2-((4-(hydroxymethyl)-2-oxo-2H-chromen-7-yl)(methyl)amino)ethyl)carbamate (**8.4**)

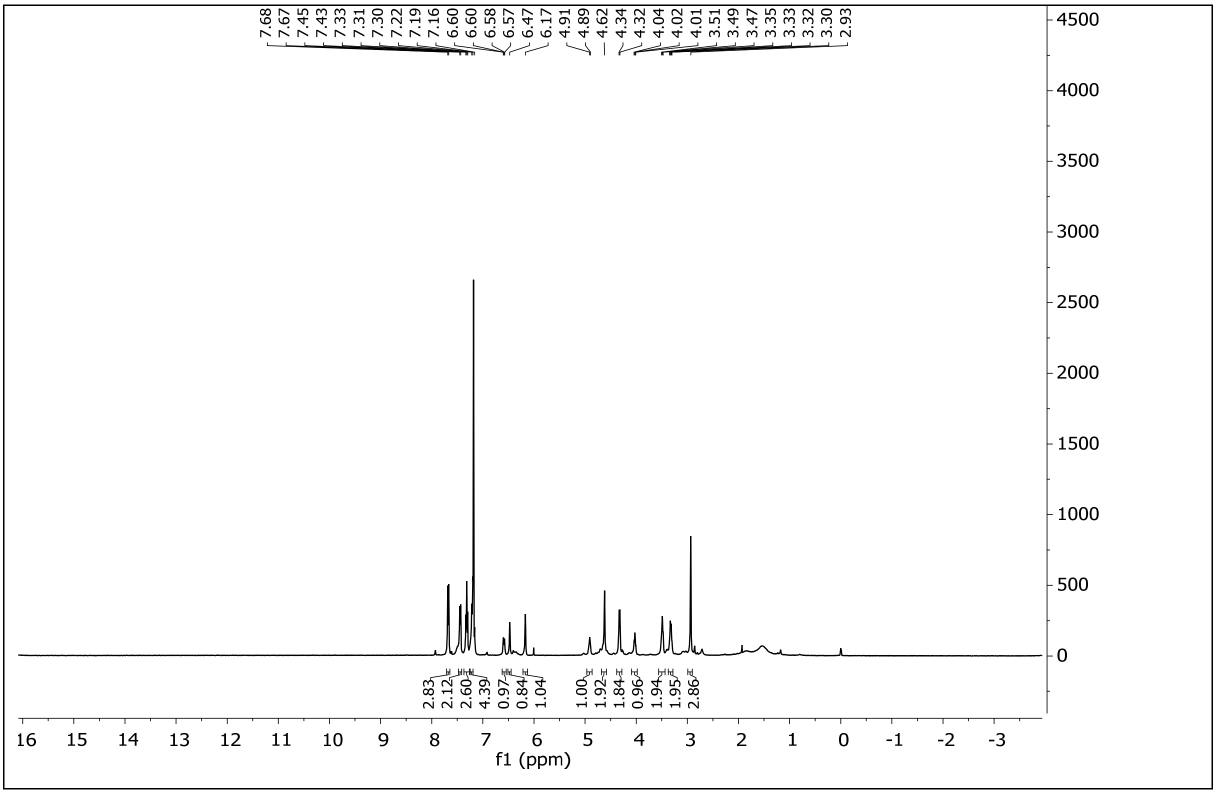

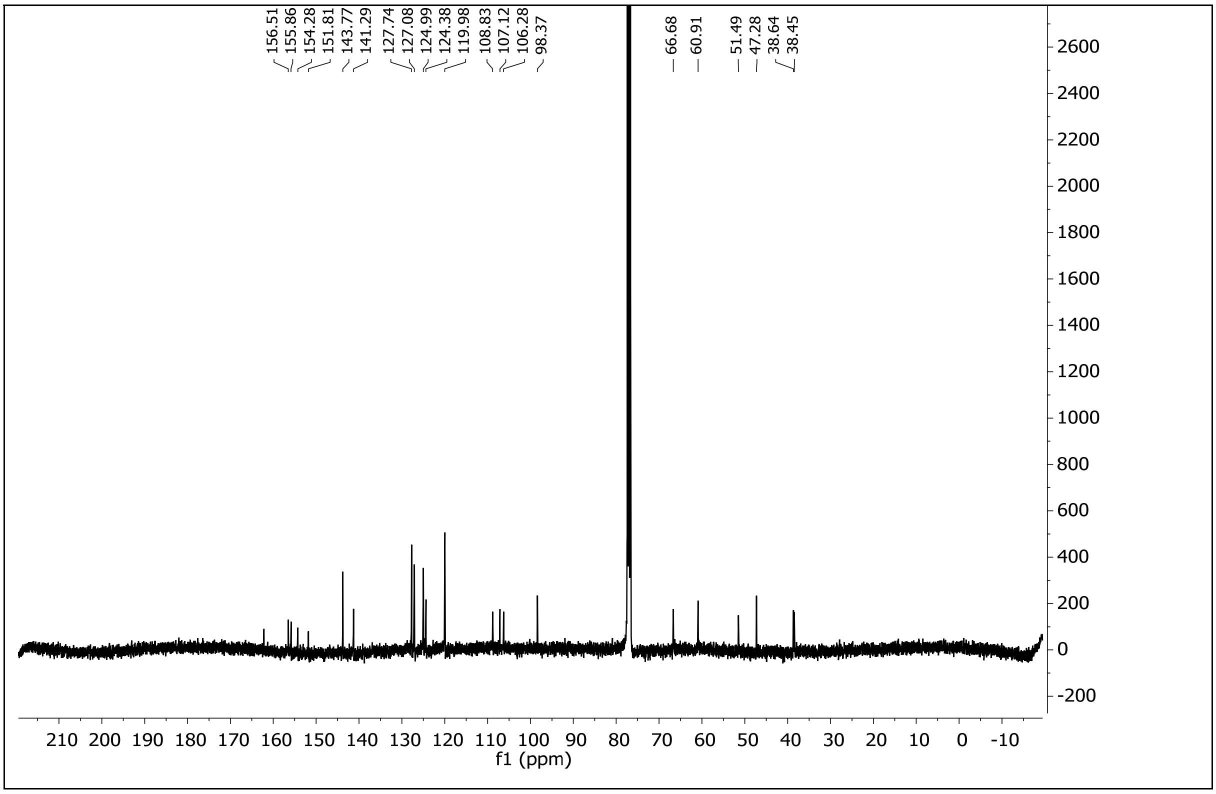

9 Appendix

9.1 General Remarks Regarding Synthetic Procedures Including Spectroscopy and Spectrometry

All reactions were carried out with magnetic stirring and, if moisture- or air- sensitive, under nitrogen or argon atmosphere using standard Schlenk techniques in oven-dried glassware (140 °C oven temperature). External bath temperatures were used to record all reaction temperatures. Low temperature reactions were carried out in a Dewar vessel filled with distilled water/ice (0 °C). High temperature reactions were conducted using a heated silicon oil bath in reaction vessels equipped with a reflux condenser or in a sealed flask. Tetrahydrofuran (THF) was distilled over sodium and benzophenone prior to use. Dichloromethane (CH_2Cl_2), triethylamine (Et_3N), diisopropylethylamine (DIPEA) and diisopropylamine (DIPA) were distilled over calcium hydride under a nitrogen atmosphere. All other solvents were purchased from Acros Organics as ‘extra dry’ reagents. All other reagents with a purity > 95% were obtained from commercial sources (Sigma Aldrich, Acros, Alfa Aesar and others) and used without further purification.

Normal phase flash column chromatography was carried out with Merck silica gel 60 (0.040-0.063 mm). **Reverse phase flash column chromatography** was carried out with

Macherey-Nagel POLYGOPREP® 100-50 C_{18} silica gel or on Waters Sep-Pak® C8 or C18 columns. **Analytical thin layer chromatography** (TLC) was carried out using Merck silica gel 60 F254 glass-backed plates and visualized under UV light at 254 nm.

NMR spectra (^{1}H NMR and ^{13}C NMR) were recorded in deuterated chloroform ($CDCl_3$) on a Bruker Avance III HD 400 MHz spectrometer equipped with a CryoProbe™, a Varian VXR400 S spectrometer, a Bruker AMX600 spectrometer or a Bruker Avance III HD 800 MHz spectrometer equipped with a CryoProbe™ and are reported as follows: chemical shift δ in ppm (multiplicity, coupling constant J in Hz, number of protons) for ^{1}H NMR spectra and chemical shift δ in ppm for ^{13}C NMR spectra. Multiplicities are abbreviated as follows: s = singlet, d = doublet, t = triplet, q = quartet, quint = quintet, br = broad, m = multiplet, or combinations thereof. Residual solvent peaks of $CDCl_3$ (δH = 7.26 ppm, δC = 77.16 ppm), d_4-MeOH (δH = 3.31 ppm δC = 49.00 ppm) were used as an internal reference. NMR spectra were assigned using information ascertained from COSY, HMBC, HSQC and NOESY experiments.

High resolution mass spectra (HRMS) were recorded on a Varian MAT CH7A or a Varian MAT 711 MS instrument by electron impact (EI) or electrospray ionization (ESI) techniques at the Department of Chemistry, Ludwig-Maximilians-University Munich.

LCMS was performed on an Agilent 1260 Infinity HPLC System, MS-Agilent 1100 Series, Type: 1946D, Model: SL, equipped with an Agilent Zorbax Eclipse Plus C18 (100 x 4.6 mm, particle size 3.5 micron) RP column with a constant flow-rate of 1 or 2 mL/min.

X-ray data collections were performed either on an Oxford Diffraction Xcalibur diffractometer, on a Bruker D8Quest diffractometer or on a Bruker D8Venture at 100 K or at 173 K using MoKα-radiation (λ = 0.71073 Å, graphite monochromator). The CrysAlisPro software (version 1.171.33.41) [CrysAlisPro, Oxford Diffraction Ltd., Version 1.171.33.41 (release 06-05-2009 CrysAlis171.NET)] was applied for the integration, scaling and multi-scan absorption correction of the data. The structures were solved by direct methods with SIR97218 and refined by least-squares methods against F2 with SHELXL-97. All non-hydrogen atoms were refined anisotropically. The hydrogen atoms were placed in ideal geometry riding on their parent atoms

UV/Vis spectroscopy was performed using a VARIAN Cary 50 Scan UV/Vis spectrometer. Compound solution was placed in a standard quartz cuvette (d = 1 cm) illuminated by a light fiber cable from above.

All yields are isolated, unless otherwise specified.

9.2 Abbreviations

A	Ampere
Å	Angstrom
a.u.	Arbitrary units
Ac	Acetyl
ADC	antibody-drug conjugate
AMPA	α-amino-3-hydroxy-5-methyl-4-isoxazolepropionic acid receptor, GluA
ANP	atrial natriuretic peptide
APC	antibody-photoswitch conjugate
Asc	Ascorbate
BC	2-((4-(aminomethyl)benzyl)oxy)pyrimidin-4-amine, benzyl cytosine
BG	6-((4-(aminomethyl)benzyl)oxy)-7*H*-purin-2-amine, benzyl guanine
BGAG	Benzyl guanine azobenzene glutamate
BINA	Biphenyl-indanone A
BME	β-mercaptoethanol
Boc	*tert*-butoxycarbonyl
br	broad
brsm	based on recovered starting material
BSA	bovine serum albumin
Bu	butyl
C	Celsius
COSY	correlation spectroscopy
CRD	cysteine-rich domain
CuAAC	Copper-catalyzed azide-alkyne-cylcoaddition
DABA	3,5-diaminobenzoic acid
DBCO	dibenzocyclooctyne
DCA	1,3-dichloroacetone
DCE	1,2-dichloroethane
DCM	dichloromethane
DIPEA	ethyldiisopropylamine
DMEM	Dulbecco’s modified eagle medium
DMF	*N,N*-dimethylformamide

DMSO	Dimethylsulfoxide
DNA	desoxyribonculeic acid
EC50	half-maximal effective concentration
EGFR	epidermal growth factor receptor
EI	electron impact
equiv.	equivalents
ESI	electrospray ionization
Et	ethyl
FA	formic acid
FBS	ftal bovine serum
FCS	Fetal calf serum
Fmoc	fluorenylmethoxycarbonyl
FP	Fluorescent proteinj
g	gram
GFP	green fluorescent protein
GHS-R1a	growth hormone secretagogue receptor 1a
GIRK	G protein-coupled inward rectifying receptor
GLP1-R	glucagon-like peptide 1 receptor
GLP-1R	glucagon-like peptide-1 receptor
GPCR	G protein-coupled receptor
GVBD	germinal vesicle breakdown
HEPES	4-(2-hydroxyethyl)-1-piperazineethanesulfonic acid
HRMS	high-resolution mass spectrometry
HRP	Horseradish peroxidase
HV	High vacuum
Hz	Hertz
IC50	half-maximal inhibitory concentration
IR	Insulin Receptor
LB	luria broth
LBD	ligand binding domain
LCMS	liquid chromatography–mass spectrometry
LF	lipofectaime
MAG	maleimide azobenzene glutamate
MAP	mitogen-activated protein

M_{eff}	effective molarity
Met	hepatocyte growth factor receptor
mGluR	metabotropic glutamate receptor
NMDA	*N*-methyl-D-aspartate receptor
NMR	nuclear magnetic resonance
PAGE	polyacrylamide gel electrophoresis
PBS	phosphate buffered saline
PCL	Photochromic ligand
PEG	polyethylene glycol
Ph	phenyl
PORTL	Photoswitchable orthogonal remotely-tethered ligand
ppm	parts per million
PTL	Photoswitchable tethered ligand
RGCs	retinal ganglion cells
s	seconds
SAR	structure-activity relationship
SM	small molecule
SpAAC	Strain-promoted azide-alkyne-cycloaddition
TEA	Triethylamine
TFA	trifluoroacetic acid
TK	tyrosine kinase
TLC	thin layer chromatography
TM	transmembrane
VFT	Venus flytrap
VKR	venus kinase receptor
WB	western blot

9.3 References

1. Lerch, M. M., Hansen, M. J., van Dam, G. M., Szymanski, W. & Feringa, B. L. Emerging Targets in Photopharmacology. *Angew. Chem. Int. Ed.* **55,** 10978–10999 (2016).
2. Laprell, L. *et al.* Restoring Light Sensitivity in Blind Retinae Using a Photochromic AMPA Receptor Agonist. *ACS Chem. Neurosci.* **7,** 15–20 (2016).
3. Barber, D. M. *et al.* Optical control of AMPA receptors using a photoswitchable quinoxaline-2,3-dione antagonist. *Chem. Sci.* **8,** 611–615 (2016).
4. Laprell, L. *et al.* Optical control of NMDA receptors with a diffusible photoswitch. *Nat. Commun.* **6,** 8076 (2015).
5. Schönberger, M. & Trauner, D. A Photochromic Agonist for μ-Opioid Receptors. *Angew. Chem. Int. Ed.* **53,** 3264–3267 (2014).
6. Banghart, M. R. *et al.* Photochromic Blockers of Voltage-Gated Potassium Channels. *Angew. Chem. Int. Ed.* **48,** 9097–9101 (2009).
7. Mourot, A. *et al.* Rapid optical control of nociception with an ion-channel photoswitch. *Nat. Methods* **9,** 396–402 (2012).
8. Podewin, T. *et al.* Optical control of a receptor-linked guanylyl cyclase using a photoswitchable peptidic hormone. *Chem. Sci.* **8,** 4644–4653 (2017).
9. Fehrentz, T., Schönberger, M. & Trauner, D. Optochemical Genetics. *Angew. Chem. Int. Ed.* **50,** 12156–12182 (2011).
10. Merino, E. & Ribagorda, M. Control over molecular motion using the cis–trans photoisomerization of the azo group. *Beilstein J. Org. Chem.* **8,** 1071–1090 (2012).
11. Levitz, J. *et al.* Optical control of metabotropic glutamate receptors. *Nat. Neurosci.* **16,** 507–516 (2013).
12. Berlin, S. *et al.* A family of photoswitchable NMDA receptors. *Elife* **5,** e12040 (2016).
13. Donthamsetti, P. *et al.* Optical Control of Dopamine Receptors Using a Photoswitchable Tethered Inverse Agonist. *J. Am. Chem. Soc.* (2017). doi:10.1021/jacs.7b07659

14. Banghart, M., Borges, K., Isacoff, E., Trauner, D. & Kramer, R. H. Light-activated ion channels for remote control of neuronal firing. *Nat. Neurosci.* **7,** 1381–1386 (2004).

15. Sandoz, G., Levitz, J., Kramer, R. H. & Isacoff, E. Y. Optical Control of Endogenous Proteins with a Photoswitchable Conditional Subunit Reveals a Role for TREK1 in GABAB Signaling. *Neuron* **74,** 1005–1014 (2012).

16. Janovjak, H., Szobota, S., Wyart, C., Trauner, D. & Isacoff, E. Y. A light-gated, potassium-selective glutamate receptor for the optical inhibition of neuronal firing. *Nat. Neurosci.* **13,** 1027–1032 (2010).

17. Volgraf, M. *et al.* Allosteric control of an ionotropic glutamate receptor with an optical switch. *Nat. Chem. Biol.* **2,** 47–52 (2006).

18. Tochitsky, I. *et al.* Optochemical control of genetically engineered neuronal nicotinic acetylcholine receptors. *Nat. Chem.* **4,** 105–111 (2012).

19. Lemoine, D. *et al.* Optical control of an ion channel gate. *Proc. Natl. Acad. Sci.* **110,** 20813–20818 (2013).

20. Szobota, S. *et al.* Remote Control of Neuronal Activity with a Light-Gated Glutamate Receptor. *Neuron* **54,** 535–545 (2007).

21. Caporale, N. *et al.* LiGluR Restores Visual Responses in Rodent Models of Inherited Blindness. *Mol. Ther.* **19,** 1212–1219 (2011).

22. Wyart, C. *et al.* Optogenetic dissection of a behavioural module in the vertebrate spinal cord. *Nature* **461,** 407–410 (2009).

23. Stephanopoulos, N. & Francis, M. B. Choosing an effective protein bioconjugation strategy. *Nat. Chem. Biol.* **7,** 876–884 (2011).

24. Hermanson, G. T. *Bioconjugate techniques*. (Elsevier/AP, 2013).

25. DuBay, K. H. *et al.* A Predictive Approach for the Optical Control of Carbonic Anhydrase II Activity. *ACS Chem. Biol.* **13,** 793–800 (2018).

26. Tsai, Y.-H., Essig, S., James, J. R., Lang, K. & Chin, J. W. Selective, rapid and optically switchable regulation of protein function in live mammalian cells. *Nat. Chem.* **7,** 554–561 (2015).

27. Blackman, M. L., Royzen, M. & Fox, J. M. Tetrazine Ligation: Fast Bioconjugation Based on Inverse-Electron-Demand Diels–Alder Reactivity. *J. Am. Chem. Soc.* **130,** 13518–13519 (2008).

28. Broichhagen, J. *et al.* Orthogonal Optical Control of a G Protein-Coupled Receptor with a SNAP-Tethered Photochromic Ligand. *ACS Cent. Sci.* **1,** 383–393 (2015).

29. Lang, K. & Chin, J. W. Bioorthogonal Reactions for Labeling Proteins. *ACS Chem. Biol.* **9,** 16–20 (2014).

30. Keppler, A. *et al.* A general method for the covalent labeling of fusion proteins with small molecules in vivo. *Nat. Biotechnol.* **21,** 86–89 (2003).

31. Cisbio. *http://www.cisbio.com/usa/drug-discovery/start-pre-clonedplasmids (accessed July 12, 2017).*

32. Shields, B. C. *et al.* Deconstructing behavioral neuropharmacology with cellular specificity. *Science* **356,** eaaj2161 (2017).

33. Niswender, C. M. & Conn, P. J. Metabotropic Glutamate Receptors: Physiology, Pharmacology, and Disease. *Annu. Rev. Pharmacol. Toxicol.* **50,** 295–322 (2010).

34. Krishnamurthy, V. M., Semetey, V., Bracher, P. J., Shen, N. & Whitesides, G. M. Dependence of Effective Molarity on Linker Length for an Intramolecular Protein–Ligand System. *J. Am. Chem. Soc.* **129,** 1312–1320 (2007).

35. Levitz, J. *et al.* Dual optical control and mechanistic insights into photoswitchable group II and III metabotropic glutamate receptors. *Proc. Natl. Acad. Sci.* 201619652 (2017). doi:10.1073/pnas.1619652114

36. Courtesy of and adapted from Dr. Johannes Broichhagen.

37. Berry, M. H. *et al.* Restoration of patterned vision with an engineered photoactivatable G protein-coupled receptor. *Nat. Commun.* **8,** 1862 (2017).

38. Gaub, B. M. *et al.* Restoration of visual function by expression of a light-gated mammalian ion channel in retinal ganglion cells or ON-bipolar cells. *Proc. Natl. Acad. Sci.* **111,** E5574–E5583 (2014).

39. Spark grabs FDA nod for Luxturna, a breakthrough gene therapy likely bearing a pioneering price | FiercePharma. Available at: https://www.npr.org/sections/health-shots/2017/12/19/571962226/first-gene-therapy-for-inherited-disease-gets-fda-approval. (Accessed: 12th April 2018)

40. Chudasama, V., Maruani, A. & Caddick, S. Recent advances in the construction of antibody–drug conjugates. *Nat. Chem.* (2016). doi:10.1038/nchem.2415

41. Helma, J., Cardoso, M. C., Muyldermans, S. & Leonhardt, H. Nanobodies and recombinant binders in cell biology. *J. Cell Biol.* **209,** 633–644 (2015).

42. Schumacher, D., Helma, J., Schneider, A. F. L., Leonhardt, H. & Hackenberger, C. P. R. Nanobodies: Chemical Functionalization Strategies and Intracellular Applications. *Angew. Chem. Int. Ed.* **57,** 2314–2333 (2018).

43. Farrants, H. *et al.* SNAP-tagged nanobodies enable reversible optical control of a G protein-coupled receptor via a remotely tethered photoswitchable ligand. (2018). doi:10.1101/266247

44. Kirchhofer, A. *et al.* Modulation of protein properties in living cells using nanobodies. *Nat. Struct. Mol. Biol.* **17,** 133–138 (2010).

45. Scholler, P. *et al.* Allosteric nanobodies uncover a role of hippocampal mGlu2 receptor homodimers in contextual fear consolidation. *Nat. Commun.* **8,** 1967 (2017).

46. Group II mGlu Receptors | mGlu2 | mGlu3. *Tocris Bioscience* Available at: https://www.tocris.com/pharmacology/glutamate-metabotropic-group-ii-receptors. (Accessed: 12th April 2018)

47. Lemmon, M. A. & Schlessinger, J. Cell Signaling by Receptor Tyrosine Kinases. *Cell* **141,** 1117–1134 (2010).

48. Vicogne, J. *et al.* An unusual receptor tyrosine kinase of Schistosoma mansoni contains a Venus Flytrap module. *Mol. Biochem. Parasitol.* **126,** 51–62 (2003).

49. Vanderstraete, M. *et al.* Venus Kinase Receptors Control Reproduction in the Platyhelminth Parasite Schistosoma mansoni. *PLOS Pathog.* **10,** e1004138 (2014).

50. Vogel, K. J., Brown, M. R. & Strand, M. R. Ovary ecdysteroidogenic hormone requires a receptor tyrosine kinase to activate egg formation in the mosquito *Aedes aegypti*. *Proc. Natl. Acad. Sci.* **112,** 5057–5062 (2015).

51. Vanderstraete, M. *et al.* The venus kinase receptor (VKR) family: structure and evolution. *BMC Genomics* **14,** 1 (2013).

52. Goodsell, D. S. Insulin Receptor. *RCSB Protein Data Bank* (2015). doi:10.2210/rcsb_pdb/mom_2015_2

53. Ferrell, J. E. Building a cellular switch: more lessons from a good egg. *BioEssays* **21,** 866–870 (1999).

54. El-Etr, M., Schorderet-Slatkine, S. & Baulieu, E. E. Meiotic maturation in Xenopus laevis oocytes initiated by insulin. *Science* **205,** 1397–1399 (1979).

55. Felder, C. B., Graul, R. C., Lee, A. Y., Merkle, H.-P. & Sadee, W. The Venus flytrap of periplasmic binding proteins: an ancient protein module present in multiple drug receptors. *AAps Pharmsci* **1,** 7–26 (1999).

56. Ahier, A. *et al.* A New Family of Receptor Tyrosine Kinases with a Venus Flytrap Binding Domain in Insects and Other Invertebrates Activated by Aminoacids. *PLoS ONE* **4,** e5651 (2009).

57. Li, E. & Hristova, K. Receptor tyrosine kinase transmembrane domains. *Cell Adhes. Migr.* **4,** 249–254 (2010).

58. Ward, C. W., Menting, J. G. & Lawrence, M. C. The insulin receptor changes conformation in unforeseen ways on ligand binding: Sharpening the picture of insulin receptor activation. *BioEssays* **35,** 945–954 (2013).

59. Ye, Z. C. & Sontheimer, H. Astrocytes protect neurons from neurotoxic injury by serum glutamate. *Glia* **22,** 237–248 (1998).

60. mGlu2 receptor | Metabotropic glutamate receptors | IUPHAR/BPS Guide to PHARMACOLOGY. Available at: http://www.guidetopharmacology.org/GRAC/ObjectDisplayForward?objectId=290. (Accessed: 20th April 2018)

61. Libermann, T. A. *et al.* Amplification, enhanced expression and possible rearrangement of EGF receptor gene in primary human brain tumours of glial origin. *Nature* **313,** 144–147 (1985).

62. Borowiak, M. *et al.* Photoswitchable Inhibitors of Microtubule Dynamics Optically Control Mitosis and Cell Death. *Cell* **162,** 403–411 (2015).

63. Alberts, B. *et al. Molecular Biology of the Cell.* (Garland Science, 2002).

64. Carpi, N., Carpi, N., Piel, M., Azioune, A. & Fink, J. Micropatterning on glass with deep UV. *Protoc. Exch.* (2011). doi:10.1038/protex.2011.238

65. Pitaval, A., Christ, A., Curtet, A., Tseng, Q. & Théry, M. Probing Ciliogenesis Using Micropatterned Substrates. in *Methods in Enzymology* **525,** 109–130 (Elsevier, 2013).

66. Malherbe, P. *et al.* Identification of Essential Residues Involved in the Glutamate Binding Pocket of the Group II Metabotropic Glutamate Receptor. *Mol. Pharmacol.* **60,** 944–954 (2001).

67. Mahen, R. *et al.* Comparative assessment of fluorescent transgene methods for quantitative imaging in human cells. *Mol. Biol. Cell* **25,** 3610–3618 (2014).

68. Regot, S., Hughey, J. J., Bajar, B. T., Carrasco, S. & Covert, M. W. High-Sensitivity Measurements of Multiple Kinase Activities in Live Single Cells. *Cell* **157,** 1724–1734 (2014).

69. Kudo, T. *et al.* Live-cell measurements of kinase activity in single cells using translocation reporters. *Nat. Protoc.* **13,** 155–169 (2017).

70. Bindels, D. S. *et al.* mScarlet: a bright monomeric red fluorescent protein for cellular imaging. *Nat. Methods* **14,** 53–56 (2016).

71. Hodgkin, A. L. & Huxley, A. F. Action Potentials Recorded from Inside a Nerve Fibre. *Nature* **144,** 710–711 (1939).

72. Wulff, H., Castle, N. A. & Pardo, L. A. Voltage-gated potassium channels as therapeutic targets. *Nat. Rev. Drug Discov.* **8,** 982–1001 (2009).

73. Garcia, M. L. & Kaczorowski, G. J. Potassium Channels as Targets for Therapeutic Intervention. *Sci. Signal.* **2005,** pe46–pe46 (2005).

74. Fortin, D. L. *et al.* Photochemical control of endogenous ion channels and cellular excitability. *Nat. Methods* (2008). doi:10.1038/nmeth.1187

75. Tochitsky, I. *et al.* Restoring Visual Function to Blind Mice with a Photoswitch that Exploits Electrophysiological Remodeling of Retinal Ganglion Cells. *Neuron* **81,** 800–813 (2014).

76. Tochitsky, I. *et al.* How Azobenzene Photoswitches Restore Visual Responses to the Blind Retina. *Neuron* **92,** 100–113 (2016).

77. Goodsell, D. https://pdb101.rcsb.org/motm/38, accessed on 20180322.

78. Broichhagen, J., Frank, J. A. & Trauner, D. A Roadmap to Success in Photopharmacology. *Acc. Chem. Res.* **48,** 1947–1960 (2015).

79. Barber, D. M. *et al.* Optical control of neuronal activity using a light-operated GIRK channel opener (LOGO). *Chem. Sci.* **7,** 2347–2352 (2016).

80. French, R. J. & Shoukimas, J. J. Blockage of squid axon potassium conductance by internal tetra-N-alkylammonium ions of various sizes. *Biophys. J.* **34,** 271–291 (1981).

81. Honoré, E. The neuronal background K2P channels: focus on TREK1. *Nat. Rev. Neurosci.* **8,** 251–261 (2007).

82. Fink, M. *et al.* Cloning, functional expression and brain localization of a novel unconventional outward rectifier K+ channel. *EMBO J.* **15,** 6854–6862 (1996).

83. Vivier, D., Bennis, K., Lesage, F. & Ducki, S. Perspectives on the Two-Pore Domain Potassium Channel TREK-1 (TWIK-Related K $^+$ Channel 1). A Novel Therapeutic Target?: Miniperspective. *J. Med. Chem.* **59,** 5149–5157 (2016).

84. Göb, E. *et al.* The two-pore domain potassium channel KCNK5 deteriorates outcome in ischemic neurodegeneration. *Pflüg. Arch. - Eur. J. Physiol.* **467,** 973–987 (2015).

85. Steinberg, E. A., Wafford, K. A., Brickley, S. G., Franks, N. P. & Wisden, W. The role of K2P channels in anaesthesia and sleep. *Pflüg. Arch. - Eur. J. Physiol.* **467,** 907–916 (2015).

86. Piechotta, P. L. *et al.* The pore structure and gating mechanism of K2P channels: K2P channel gating. *EMBO J.* **30,** 3607–3619 (2011).

87. Koh, D.-S., Jonas, P., Bräu, M. E. & Vogel, W. A TEA-insensitive flickering potassium channel active around the resting potential in myelinated nerve. *J. Membr. Biol.* **130,** 149–162 (1992).

88. Lein, E. S. *et al.* Genome-wide atlas of gene expression in the adult mouse brain. *Nature* **445,** 168–176 (2007).

89. Sack, J. T., Stephanopoulos, N., Austin, D. C., Francis, M. B. & Trimmer, J. S. Antibody-guided photoablation of voltage-gated potassium currents. *J. Gen. Physiol.* **142,** 315–324 (2013).

90. Beck, S. *et al.* Fluorophore-assisted light inactivation: A high-throughput tool for direct target validation of proteins. *PROTEOMICS* **2,** 247–255 (2002).

91. Hu, Q. Y. & Allan, M. *Methods for making conjugates from disulfide-containing proteins*. (Google Patents, 2017).

92. Hu, Q. Y. & Imase, H. *Methods for oxime conjugation to ketone-modified polypeptides*. (Google Patents, 2016).

93. Kienzler, M. A. *et al.* A Red-Shifted, Fast-Relaxing Azobenzene Photoswitch for Visible Light Control of an Ionotropic Glutamate Receptor. *J. Am. Chem. Soc.* **135,** 17683–17686 (2013).

94. Hammond, C. *Cellular and molecular neurophysiology*. (Elsevier/AP, Academic Press is an imprint of Elsevier, 2015).

95. Traynelis, S. F. *et al.* Glutamate Receptor Ion Channels: Structure, Regulation, and Function. *Pharmacol. Rev.* **62,** 405–496 (2010).

96. Schmitz, L. J. M. *et al.* The AMPA receptor-associated protein Shisa7 regulates hippocampal synaptic function and contextual memory. *eLife* **6,** (2017).

97. Tomita, S. *et al.* Stargazin modulates AMPA receptor gating and trafficking by distinct domains. *Nature* **435,** 1052–1058 (2005).

98. Choi, C. & Nitabach, M. N. Membrane-Tethered Ligands: Tools for Cell-Autonomous Pharmacological Manipulation of Biological Circuits. *Physiology* **28,** 164–171 (2013).

99. Los, G. V. *et al.* HaloTag: A Novel Protein Labeling Technology for Cell Imaging and Protein Analysis. *ACS Chem. Biol.* **3,** 373–382 (2008).

100. Sobolevsky, A. I., Rosconi, M. P. & Gouaux, E. X-ray structure, symmetry and mechanism of an AMPA-subtype glutamate receptor. *Nature* **462,** 745–756 (2009).

101. Chang, P. K.-Y., Verbich, D. & McKinney, R. A. AMPA receptors as drug targets in neurological disease – advantages, caveats, and future outlook. *Eur. J. Neurosci.* **35,** 1908–1916 (2012).

102. Henley, J. M. & Wilkinson, K. A. Synaptic AMPA receptor composition in development, plasticity and disease. *Nat. Rev. Neurosci.* **17,** 337–350 (2016).

103. Yamashita, T. & Kwak, S. The molecular link between inefficient GluA2 Q/R site-RNA editing and TDP-43 pathology in motor neurons of sporadic amyotrophic lateral sclerosis patients. *Brain Res.* **1584,** 28–38 (2014).

104. Greger, I. H., Watson, J. F. & Cull-Candy, S. G. Structural and Functional Architecture of AMPA-Type Glutamate Receptors and Their Auxiliary Proteins. *Neuron* **94,** 713–730 (2017).

105. Wolter, M., Klapars, A. & Buchwald, S. L. Synthesis of N-Aryl Hydrazides by Copper-Catalyzed Coupling of Hydrazides with Aryl Iodides. *Org. Lett.* **3,** 3803–3805 (2001).

106. Li, S. *et al.* Synthesis and biological evaluation of fentanyl acrylic derivatives. *RSC Adv.* **7,** 20015–20019 (2017).

107. Salam, M. The Opioid Epidemic: A Crisis Years in the Making. *The New York Times* (2018).

108. Smydo, J. Delayed respiratory depression with fentanyl. *Anesth. Prog.* **26,** 47–48 (1979).

109. Williams, J. T. *et al.* Regulation of -Opioid Receptors: Desensitization, Phosphorylation, Internalization, and Tolerance. *Pharmacol. Rev.* **65,** 223–254 (2013).

110. Wyk, M. van, Pielecka-Fortuna, J., Löwel, S. & Kleinlogel, S. Restoring the ON Switch in Blind Retinas: Opto-mGluR6, a Next-Generation, Cell-Tailored Optogenetic Tool. *PLOS Biol.* **13,** e1002143 (2015).

111. Siewertsen, R. *et al.* Highly Efficient Reversible *Z–E* Photoisomerization of a Bridged Azobenzene with Visible Light through Resolved S $_1$ (nπ*) Absorption Bands. *J. Am. Chem. Soc.* **131,** 15594–15595 (2009).

112. Sell, H., Näther, C. & Herges, R. Amino-substituted diazocines as pincer-type photochromic switches. *Beilstein J. Org. Chem.* **9,** 1–7 (2013).

113. Samanta, S., Qin, C., Lough, A. J. & Woolley, G. A. Bidirectional Photocontrol of Peptide Conformation with a Bridged Azobenzene Derivative. *Angew. Chem. Int. Ed.* **51,** 6452–6455 (2012).

114. Mostad, A. *et al.* A Refinement of the Crystal Structure of cis-Azobenzene. *Acta Chem. Scand.* **25,** 3561–3568 (1971).

115. Frank, J. A. *et al.* Photoswitchable fatty acids enable optical control of TRPV1. *Nat. Commun.* **6,** 7118 (2015).

116. Nüsslein-Volhard, C. & Wieschaus, E. Mutations affecting segment number and polarity in Drosophila. *Nature* **287,** 795–801 (1980).

117. Ruat, M., Hoch, L., Faure, H. & Rognan, D. Targeting of Smoothened for therapeutic gain. *Trends Pharmacol. Sci.* **35,** 237–246 (2014).

118. Gunzner, J. L. *et al.* Pyridyl inhibitors of hedgehog signalling. (2011).

119. Byrne, E. F. X. *et al.* Structural basis of Smoothened regulation by its extracellular domains. *Nature* **535,** 517 (2016).

120. Taipale, J. *et al.* Effects of oncogenic mutations in Smoothened and Patched can be reversed by cyclopamine. *Nature* **406,** 1005–1009 (2000).

121. Ingham, P. W., Nakano, Y. & Seger, C. Mechanisms and functions of Hedgehog signalling across the metazoa. *Nat. Rev. Genet.* **12,** 393–406 (2011).

122. Briscoe, J. & Thérond, P. P. The mechanisms of Hedgehog signalling and its roles in development and disease. *Nat. Rev. Mol. Cell Biol.* **14,** 416–429 (2013).

123. Siegel, R., Naishadham, D. & Jemal, A. Cancer statistics, 2013. *CA. Cancer J. Clin.* **63,** 11–30 (2013).

124. Pecorino, L. *Molecular biology of cancer: mechanisms, targets, and therapeutics*. (Oxford University Press, 2016).

125. Hanahan, D. & Weinberg, R. A. Hallmarks of Cancer: The Next Generation. *Cell* **144,** 646–674 (2011).

126. Luo, J., Solimini, N. L. & Elledge, S. J. Principles of Cancer Therapy: Oncogene and Non-oncogene Addiction. *Cell* **136,** 823–837 (2009).

127. Schmidinger, M. & Bellmunt, J. Plethora of agents, plethora of targets, plethora of side effects in metastatic renal cell carcinoma. *Cancer Treat. Rev.* **36,** 416–424 (2010).

128. Wilmes, L. J. *et al.* AG-013736, a novel inhibitor of VEGF receptor tyrosine kinases, inhibits breast cancer growth and decreases vascular permeability as detected by dynamic contrast-enhanced magnetic resonance imaging. *Magn. Reson. Imaging* **25,** 319–327 (2007).

129. Escudier, B. & Gore, M. Axitinib for the Management of Metastatic Renal Cell Carcinoma. *Drugs R. D.* **11,** 113–126 (2011).

130. McTigue, M. *et al.* Molecular conformations, interactions, and properties associated with drug efficiency and clinical performance among VEGFR TK inhibitors. *Proc. Natl. Acad. Sci.* **109,** 18281–18289 (2012).

131. Taylor, E. C., Tseng, C. P. & Rampal, J. B. Conversion of a primary amino group into a nitroso group. Synthesis of nitroso-substituted heterocycles. *J. Org. Chem.* **47,** 552–555 (1982).

132. Travieso-Puente, R. *et al.* Arylazoindazole Photoswitches: Facile Synthesis and Functionalization via S $_N$ Ar Substitution. *J. Am. Chem. Soc.* **139,** 3328–3331 (2017).

133. Correa, A., Tellitu, I., Domínguez, E. & SanMartin, R. Novel Alternative for the N–S Bond Formation and Its Application to the Synthesis of Benzisothiazol-3-ones. *Org. Lett.* **8,** 4811–4813 (2006).

134. Gray, N., Zhou, W. & Deng, X. *Indazole compounds and their uses*. (Google Patents, 2013).

135. Klán, P. *et al.* Photoremovable Protecting Groups in Chemistry and Biology: Reaction Mechanisms and Efficacy. *Chem. Rev.* **113,** 119–191 (2013).

136. Stanton, B. Z., Chory, E. J. & Crabtree, G. R. Chemically induced proximity in biology and medicine. *Science* **359,** eaao5902 (2018).

137. Podewin, T. *et al.* Conditional and Reversible Activation of Class A and B G Protein-Coupled Receptors Using Tethered Pharmacology. *ACS Cent. Sci.* **4,** 166–179 (2018).

138. Cürten, B., Kullmann, P. H. M., Bier, M. E., Kandler, K. & Schmidt, B. F. Synthesis, Photophysical, Photochemical and Biological Properties of Caged GABA, 4-[[(2H-1-Benzopyran-2-one-7-amino-4-methoxy) carbonyl] amino] Butanoic Acid¶. *Photochem. Photobiol.* **81,** 641 (2005).

139. Liu, X. *et al.* Aziridinyl Fluorophores Demonstrate Bright Fluorescence and Superior Photostability by Effectively Inhibiting Twisted Intramolecular Charge Transfer. *J. Am. Chem. Soc.* **138,** 6960–6963 (2016).

140. Li, H., Hao, M., Wang, L., Liang, W. & Chen, K. Preparation of Mono Boc-Protected Unsymmetrical Diamines. *Org. Prep. Proced. Int.* **41,** 301–307 (2009).